STATE OF CALIFORNIA DEPARTMENT OF TRANSPORTATION

TECHNICAL REPORT DOCUMENTATION PAGE

TR0003 (REV. 10/98)

1. REPORT NUMBER	2. GOVERNMENT ASSOCIATION NUMBER	3. RECIPIENT'S CATALOG NUMBER
CA98-0005		

4. TITLE AND SUBTITLE	5. REPORT DATE
Evaluation and Implementation of an Improved Methodology for Earthquake Ground Response Analysis: Uniform Treatment of Uncertainties in Source, Path, and Site Effects.	December, 2008
	6. PERFORMING ORGANIZATION CODE

7. AUTHOR(S)	8. PERFORMING ORGANIZATION REPORT NO.
Walter Silva[1], Clifford Roblee[2]	

9. PERFORMING ORGANIZATION NAME AND ADDRESS	10. WORK UNIT NUMBER
[1]Pacific Engineering and Analysis 311 Pomona Avenue El Cerrito, CA 94530 [2]California Department of Transportation Division of Research and Innovation, MS-5 5900 Folsom Blvd. Sacramento, CA 95819	11. CONTRACT OR GRANT NUMBER DRI Research Task No. 0005 Contract No. 65V395

12. SPONSORING AGENCY AND ADDRESS	13. TYPE OF REPORT AND PERIOD COVERED
California Department of Transportation Division of Research and Innovation, MS-83 1227 O Street Sacramento, CA 95814	Final Report
	14. SPONSORING AGENCY CODE 913

15. SUPPLEMENTAL NOTES

.

16. ABSTRACT

Shortly after the 1994 Northridge Earthquake, Caltrans geotechnical engineers charged with developing site-specific response spectra for high priority California bridges initiated a research project aimed at broadening their perspective from simple geotechnical site response analyses to a more comprehensive seismological approach. The project was centered on a series of seminars on seismological theory and analyses using a pair of stochastic numerical ground motion models that allowed uniform treatment of uncertainties in recognized earthquake source, path, and site effects. The project was not intended to produce a "report" per se, but rather, was meant to strengthen the knowledge and perspective of practicing engineers. Nevertheless, hard copy of seminar notes and a portion of the analyses have now been recovered, scanned and compiled into this volume for their archival and educational value.

Seven sets of seminar notes and two application examples are presented. Two seminars provide an overview of site-specific specification of ground motion from a seismological perspective. Another seminar provides background on seismological instrumentation and processing of strong-motion recordings. A pair of seminars addresses empirical attenuation models and outlines the variety of numerical ground motion modeling approaches. The final pair of seminars systematically explore source, path and site effects on ground motion and various strategies employed to capture these effects for purposes of prediction. The two application examples use the stochastic model to explore the impacts and uncertainties of geotechnical site effects within the context of the broader seismological problem.

17. KEY WORDS	18. DISTRIBUTION STATEMENT
Earthquake; Engineering Seismology; Ground Motion Analysis; Stochastic Modeling; Source, Path, Site Effects; Uncertainty and Variability	No restrictions. This document is available to the public through the National Technical Information Service, Springfield, VA 22161

19. SECURITY CLASSIFICATION (of this report)	20. NUMBER OF PAGES	21. PRICE
Unclassified	530 Pages	

Division of Research & Innovation

Evaluation and Implementation of an Improved Methodology for Earthquake Ground Response Analysis

Uniform Treatment of Uncertainties in Source, Path, and Site Effects

Final Report

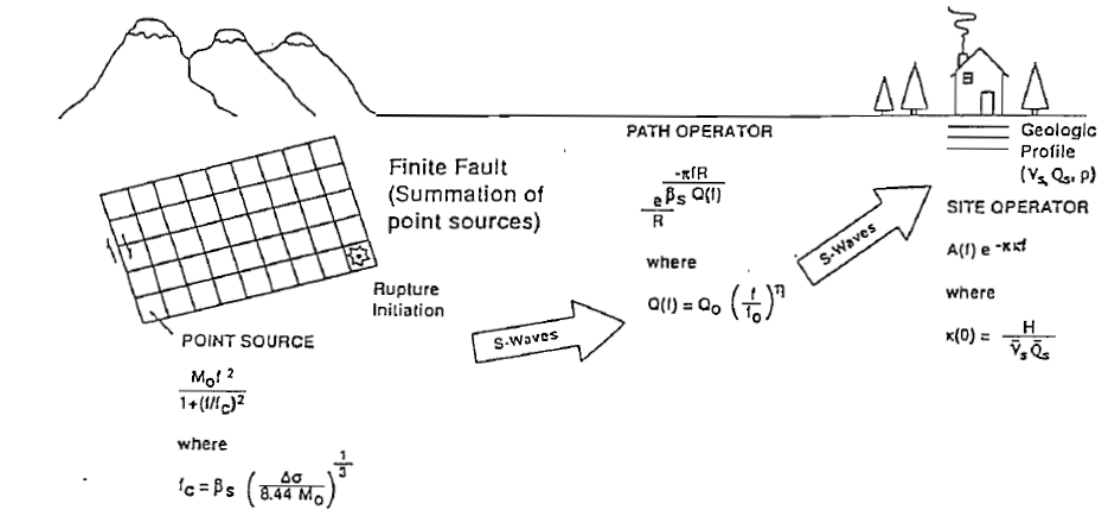

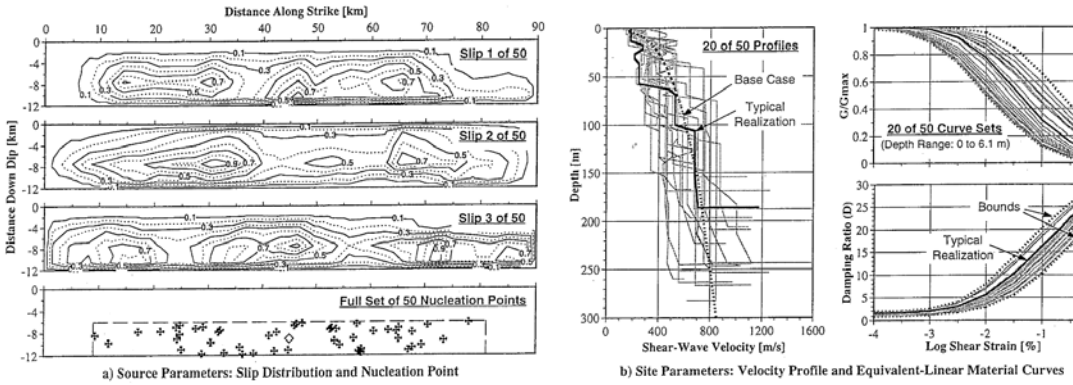

a) Source Parameters: Slip Distribution and Nucleation Point

b) Site Parameters: Velocity Profile and Equivalent-Linear Material Curves

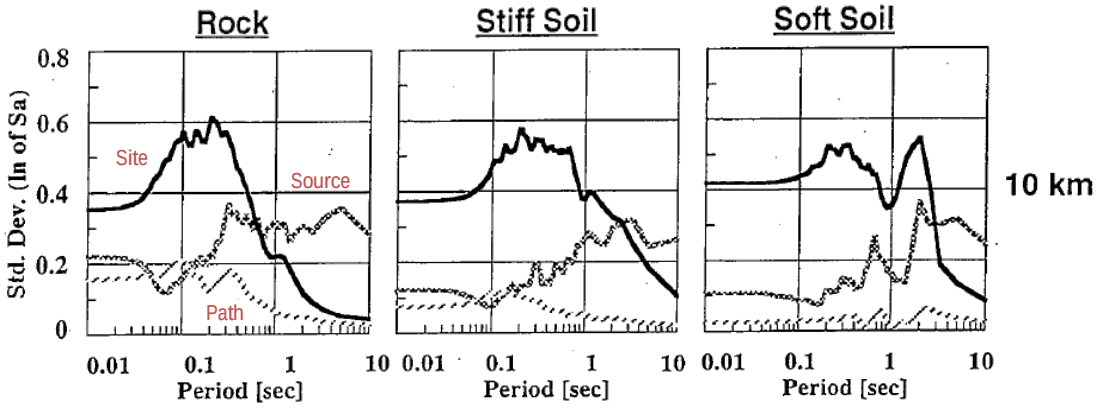

Report CA98-0005
December 2008

Evaluation and Implementation of an Improved Methodology for Earthquake Ground Response Analysis

Uniform Treatment of Source, Path and Site Effects

Final Report

Report No. CA98-0005

December 2008

Prepared By:

Pacific Engineering and Analysis
311 Pomona Avenue.
El Cerrito, CA 94530

California Department of Transportation
Division of Research and Innovation, MS-5
5900 Folsom Blvd.
Sacramento, CA 95816

Prepared For:

California Department of Transportation
Division of Research and Innovation, MS-83
1227 O Street
Sacramento, CA 95814

DISCLAIMER STATEMENT

This document is disseminated in the interest of information exchange. The contents of this report reflect the views of the authors who are responsible for the facts and accuracy of the data presented herein. The contents do not necessarily reflect the official views or policies of the State of California or the Federal Highway Administration. This publication does not constitute a standard, specification or regulation. This report does not constitute an endorsement by the Department of any product described herein.

For individuals with sensory disabilities, this document is available in Braille, large print, audiocassette, or compact disk. To obtain a copy of this document in one of these alternate formats, please contact: the Division of Research and Innovation, MS-83, California Department of Transportation, P.O. Box 942873, Sacramento, CA 94273-0001.

Evaluation and Implementation of an Improved Methodology for Earthquake Ground Response Analysis

Uniform Treatment of Source, Path and Site Effects

Final Report

Abstract:

Shortly after the 1994 Northridge Earthquake, Caltrans geotechnical engineers charged with developing site-specific response spectra for high priority California bridges initiated a research project aimed at broadening their perspective from simple geotechnical site response analyses to a more comprehensive seismological approach. The project was centered on a series of seminars on seismological theory and analyses using a pair of stochastic numerical ground motion models that allowed uniform treatment of uncertainties in recognized earthquake source, path, and site effects. The project was not intended to produce a "report" per se, but rather, was meant to strengthen the knowledge and perspective of practicing engineers. Nevertheless, hard copy of seminar notes and a portion of the analyses have now been recovered, scanned and compiled into this volume for their archival and educational value.

Seven sets of seminar notes and two application examples are presented. Two seminars provide an overview of site-specific specification of ground motion from a seismological perspective. Another seminar provides background on seismological instrumentation and processing of strong-motion recordings. A pair of seminars addresses empirical attenuation models and outlines the variety of numerical ground motion modeling approaches. The final pair of seminars systematically explore source, path and site effects on ground motion and various strategies employed to capture these effects for purposes of prediction. The two application examples use the stochastic model to explore the impacts and uncertainties of geotechnical site effects within the context of the broader seismological problem.

Evaluation and Implementation of an Improved Methodology for Earthquake Ground Response Analysis

Uniform Treatment of Source, Path and Site Effects

Contents

Seminar 4 – Empirical Attenuation Models (9/29/94, 49 p.)

a) General References
b) Review: Instrumentation and Data Processing
c) Introductory Comments
d) Development of Predictive Equations
e) Summary of Predictive Relations
f) Comparisons of Predictive Relations
g) Future Trends

Seminar 5 – Numerical Ground Motion Models (10/27/94, 37 p.)

a) General References
b) Review: Empirical Attenuation Models
c) Introductory Comments
d) Background
    1) Purely Theoretical Method
    2) Empirical Green Function Method
    3) Empirical Source Function Method
    4) Stochastic Finite Fault Method
e) Empirical Green/Source Function Method
f) Stochastic Finite Fault Model
    1) Point Source Model
    2) Finite Fault Model
    3) Uncertainty in Model Parameters

Seminar 6 – Source, Path, and Site Effects in Strong Ground Motion (12/1/94, 49 p.)

a) General References
b) Introductory Comments
c) Source Effects
    1) Directivity
    2) Site Location
    3) Slip Distribution
    4) Fault Dip
    5) Stress Drop
d) Propagation Path Effects
    1) Crustal Damping
    2) Geometric Attenuation
e) Site Effects
    1) Rock Sites
    2) Soil Sites

Seminar 7 – Global Site Effects (1/26/95, 59 p.)

a) General References
b) Introduction
c) Global or Non 1-D Site Effects
    1) Topographic Effects
    2) Alluvial Valley Effects
    3) Variability of Observed 2-Dimensional Site Effects

d) 1-D Site Effects
    1) Site Classification
    2) Soil Versus Rock
    3) Mechanism of 1-D Site Effects
    4) Approaches to Modeling Nonlinear 1-D Site Effects

Application Example A – Variability in Site-Specific Seismic Ground Motion Design Predictions

Application Example B – Case Study: Site-Specific Motions at I-10 La Cienega Bridge in LA

Evaluation and Implementation of an Improved Methodology for Earthquake Ground Response Analysis

Uniform Treatment of Source, Path and Site Effects

Seminar 1

(6/30/94, 127 p.)

Site Specific Specification of Ground Motion: An Overview, Part 1

a) Introductory Comments
b) Seismological Background
    1) Seismic Source Theory
    2) Point Source Ground Motion Model
        a) Source Effects
        b) Path Effects
        c) Site Effects
    3) Magnitude Scales
c) Measures of Strong Ground Motion
    1) A, V, D, Response Spectra, Fourier Spectra
d) Features of Strong Ground Motion: Illustrations from Recordings
    1) Rock vs. Soil
    2) Magnitude Effects
    3) Effects of Damping at Rock Sites
    4) Nonlinear Soil Response
    5) Directivity, Near-Source Effects

CALTRANS

SEMINAR ON STRONG GROUND MOTION

Seminar 1; June 30, 1994

Site Specific Specifications of Strong Ground Motions: An Overview

a) Introductory Comments

1) Purpose of seminar series: provide technology transfer to enhance in-house capability in characterizing strong ground motion for engineering design.

2) Planned ten 3 hour seminars approximately bi-weekly: $\approx$ 2½ hr presentation, ½-1 hr discussion sessions (question/answer?).

3) Seminar to concentrate on fundamental aspects of strong ground motion as well as recent developments (stable, state-of-practice). Cover everything from definition of an earthquake (dislocation in a homogenous elastic solid) to numerical modeling of complex sources with an emphasis on factors which control strong ground motions. Concentrate on stable features of strong ground motions, how predictable they are (empirically or through modeling), and which aspects or parameters of the source, path, or site exert controlling influences. Additionally, we'll relate these source, path, and site parameters to physical concepts and investigate how best to determine their median values and uncertainties.

4) Last seminar will concentrate on a case study: implement our approach in characterizing strong ground motions as well as uncertainty for an actual project.

5) Appendix 1 shows the tentative seminar outline and schedule.

6) General References:

1990 Reiter: Earthquake Hazard Analysis, Issues and Insights. Columbia

University Press.

1981 Kasahara: Earthquake Mechanics. Cambridge University Press.

1958 Richter: Elementary Seismology. W.H. Freeman and Co.

1985 Bullen and Bolt: An Introduction to the Theory of Seismology

1980 Aki and Richards: Quantative Seismology. W.H. Freeman and Co.

EERI Monograph Series. Seed and Idriss, Hudson, Newmark and Hall.

b) Seismological Background

1) Seismic Source Theory

Earthquake Definition: Broad definition; process within the earth which generates elastic wave energy (large number of sources of elastic wave energy, Table 1). Restricted definition for us. Tectonic Earthquake: Seismicity associated with tectonic or other natural forces and whose rates are unaffected by human activity (induced seismicity: mining, reservoir, thermal load).

Earthquake Model: Dislocation (crack) in a homogenous elastic medium under uniform shear strain. Introduction of crack results in a reduction in strain Δe and

stress $\Delta\sigma$ (static stress drop) where $\Delta e = k\frac{D}{h}$, D is displacement and κ depends on crack geometry.

$$\Delta\sigma = 2\mu\ \Delta e = 2\mu\ k\frac{D}{h} \quad , \qquad \mu = \text{shear modulus}$$

$$\approx 3 \times 10^{11} \text{ dyne/cm}^2 \text{ for the crust}$$

A more general relation

$\Delta\sigma = k\mu \left(\frac{[D]}{l}\right)$ *where* l is a characteristic rupture or fault (crack) dimension. The term $\frac{[D]}{l}$ is a strain change averaged over a scale length. Static stress drop then depends on the shear strength, fault slip, and "size" of the fault as well as geometry through the constant κ.

For ∞ SS rectangular fault $\Delta\sigma = \frac{2}{\pi}\,\mu\,\frac{[D]}{w}$, w = *fault width* (1)

For circular fault $\Delta\sigma = \frac{7}{16}\,\pi\,\mu\,\frac{[D]}{a}$, a = *fault radius* (2)

Circular fault relation applied to finite rectangular faults: $L \cdot W = \pi a^2$

$$\Delta\sigma = \frac{7}{16}\,\pi\mu\,\frac{[D]}{\left(\frac{L\cdot w}{\pi}\right)^{1/2}} \qquad (3)$$

The circular fault equation (using L and W) is a common relation used to evaluate static stress drop. From observations, $\Delta\sigma$ appears to be independent of magnitude with a an average value of about 30 bars for California earthquakes (inter-plate). This value may be higher for intra-plate events.

Constant $\Delta\sigma$ implies that the term $\left(\frac{[D]}{l}\right)$ or strain drop is also constant. To see this, we introduce the seismic moment

$M_o = \mu\, A\, [D]$, A = fault area. (4)

This is a force (μ A) times a distance or length ([D]) and describes the strength of a

double couple (zero torque) shear dislocation force system. The seismic moment and stress drop are directly related to the energy released

$$w = \frac{\Delta\sigma}{2\mu} M_o \quad . \tag{5}$$

For circulate faults from (2)

$$\Delta\sigma = \frac{7}{16} \pi \mu \frac{[D]}{(\frac{A}{\pi})^{1/2}} \tag{6}$$

using $M_o = \mu A [D]$

giving $M_o = (\frac{16}{7\pi^{3/2}}) \Delta\sigma A^{3/2}$ (7)

or $\log M_o = \log (\frac{16}{7\pi^{3/2}}) + \log \Delta\sigma + 3/2 \log A$ (8)

Then $M_o \propto A^{3/2}$ for $\Delta\sigma \approx$ constant.

Figure 1 shows plot of log A verses log M_o for inter- and intra-plate earthquakes.

Inter-plate: Earthquakes which occur along or parallel to major plate boundaries: includes subduction and transform fault thrust earthquakes.

Intra-plate: Earthquakes which occur clearly within a plate boundary: fault planes not along

plate boundary (San Fernando, Kern County).

From Figure 1, the linearity of log S (area) verses log M_o with a ⅔ slope is clear. Most earthquakes have stress drops between 10-100 bars. The average stress drop is about 60 bars.

Inter-plate ≈ 30 bars

Intra-plate ≈ 100 bars

This result is one of the most fundamental observations in seismology.

Radiation Pattern, Near And Far Field Terms

For a slip D ($\bar{x}$, t) distributed on a surface Σ, the displacement $\bar{u}$ in spherical co-ordinates can be written as:

$$\begin{bmatrix} u_r \\ u_\theta \\ u_\phi \end{bmatrix} : \begin{matrix} \text{P - wave} \\ \text{SV - wave} \\ \text{SH - wave} \end{matrix}$$

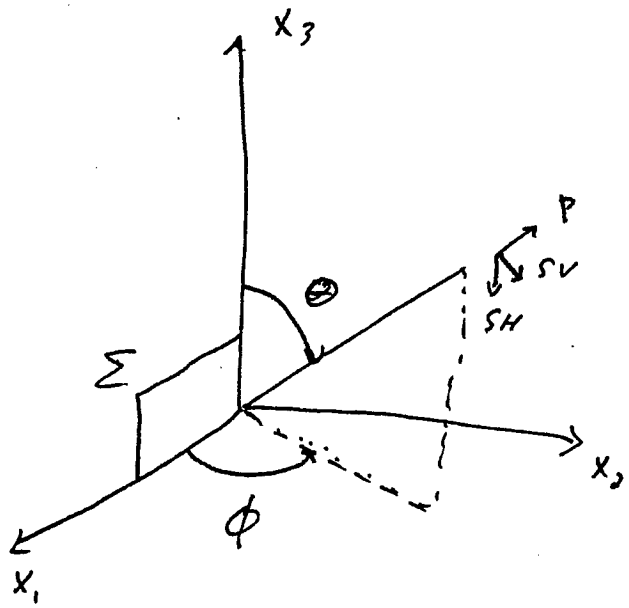

$$\begin{bmatrix} u_r(r,\theta,\phi,t') \\ u_\theta(\quad) \\ u_\phi(\quad) \end{bmatrix} = \frac{1}{4\pi\mu r^4} \begin{bmatrix} 9\sin^2\theta\sin 2\phi \\ -3\sin 2\theta\sin 2\phi \\ -6\sin\theta\cos 2\phi \end{bmatrix} \mu \int_{\frac{\Sigma}{2}}^{+} \int_{\frac{r}{\alpha}}^{r/\beta} \tau\, D(\vec{x}, t'-\tau)\, d\tau\, ds$$

$$+ \frac{1}{4\pi\alpha^2 r^2} \begin{bmatrix} 4\sin^2\theta\sin 2\phi \\ -\sin 2\theta\sin 2\phi \\ -2\sin\theta\cos 2\phi \end{bmatrix} \mu \int_{\frac{\Sigma}{2}}^{+} D(\vec{x}, t'-\tfrac{r}{2})\, ds$$

$$+ \frac{1}{4\pi\beta^2 r^2} \begin{bmatrix} -3\sin^2\theta\sin 2\phi \\ \frac{3}{2}\sin 2\theta\sin 2\phi \\ 3\sin\theta\cos 2\phi \end{bmatrix} \mu \int_{\frac{\Sigma}{2}}^{+} D(\vec{x}, t'-\tfrac{r}{\beta})\, ds$$

$$+ \frac{1}{4\pi\alpha^2 r} \begin{bmatrix} \sin^2\theta\sin 2\theta \\ 0 \\ 0 \end{bmatrix} \mu \int_{\frac{\Sigma}{2}}^{+} \dot{D}(\vec{x}, t'-\tfrac{r}{2})\, ds$$

$$+ \frac{1}{4\pi\beta^2 r} \begin{bmatrix} 0 \\ \frac{1}{2}\sin 2\theta\sin 2\phi \\ \sin\theta\cos 2\phi \end{bmatrix} \mu \int_{\frac{\Sigma}{2}}^{+} \dot{D}(\vec{x}, t'-\tfrac{r}{\beta})\, ds \qquad (9)$$

The 5 terms behave roughly as

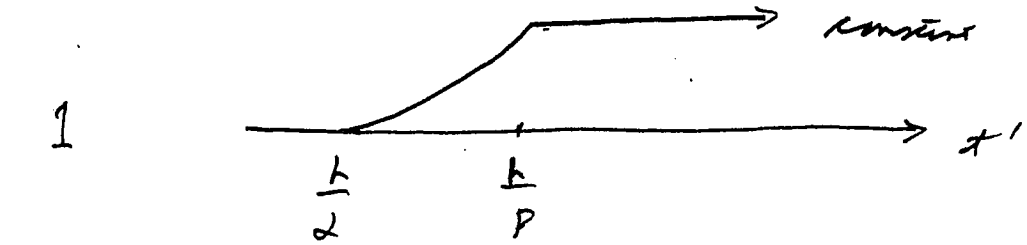

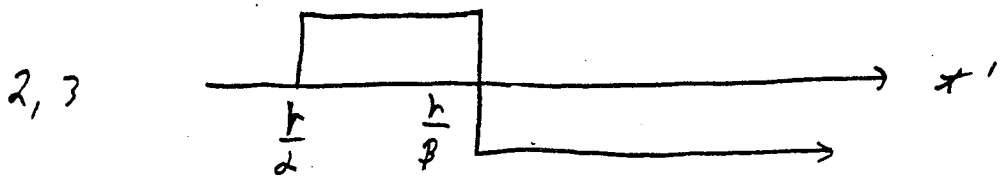

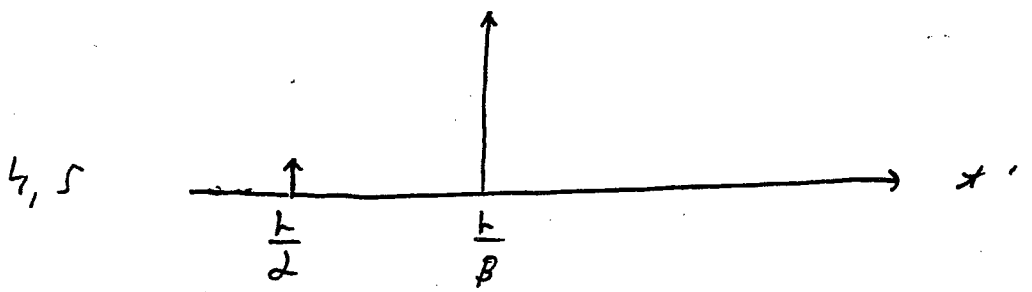

Features of interest:

1) 1st 3 terms are "near-field" and attenuate as r^{-2}

2) Near-field terms mix P- and S-waves

3) Near-field terms are proportional to slip D

4) Last 2 terms are "far-field" and attenuate as r^{-1}

5) Far-field terms separate P- and S-waves (some of us would have chosen another field if this were not the case!)

6) Far-field terms are proportional to slip velocity $\dot{D}$

7) Amplitude of S-waves > P-waves by $\frac{\beta^3}{\alpha^3} \approx 5$, *for Poisson solid* $\sigma = (0.25)$

8) Radiation pattern in θ, $\emptyset$ for far field terms: Figure 2

9) M_o contained in far-field $\mu \int_\Sigma \dot{D}\, ds$ term. Ignoring coefficients

$u = \mu \int \dot{D}\, ds$ and consider

$\int_{-\infty}^{\infty} u(t')\, dt'$ or average value of

displacement: same as f=o or zero frequency part of Fourier amplitude spectrum.

$$\int_{-\infty}^{\infty} u\, dt' = \mu \int_{\frac{\Sigma^+}{2}} \int_{-\infty}^{\infty} \dot{D}\left(\vec{\xi}, \tau - \frac{h}{c}\right) dt'\, ds \qquad c = \alpha, \beta$$

$$= \mu \int_{\Sigma^+_J} [D(\vec{x}, \infty) - D(\vec{x}, -\infty)] \, dS$$

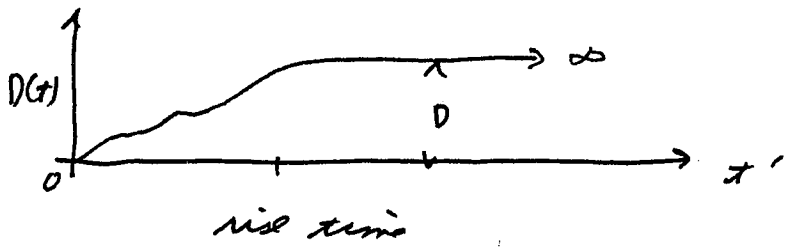

$$= \mu D \int_{\Sigma^+_J} dS$$

$$= \mu D A = M_0 \qquad (10)$$

Important results: seismic moment M_o is the average surface displacement or, equivalently, the D.C. term in the Fourier amplitude spectrum computed from earthquake recordings (corrected for radiation pattern and damping (material and radiation). It is therefor a true measure of the gross size only and the measurement is done at very low frequencies where material damping and wave scattering are minimal.

To look at how ground motion should behave at frequencies other than DC, we need a source model: a function (time or frequency) showing the characteristics of $D(\bar{x}, t)$ in the far field.

2) Point-Source Ground Motion Model

a) Source Effects

Character of dislocation time history

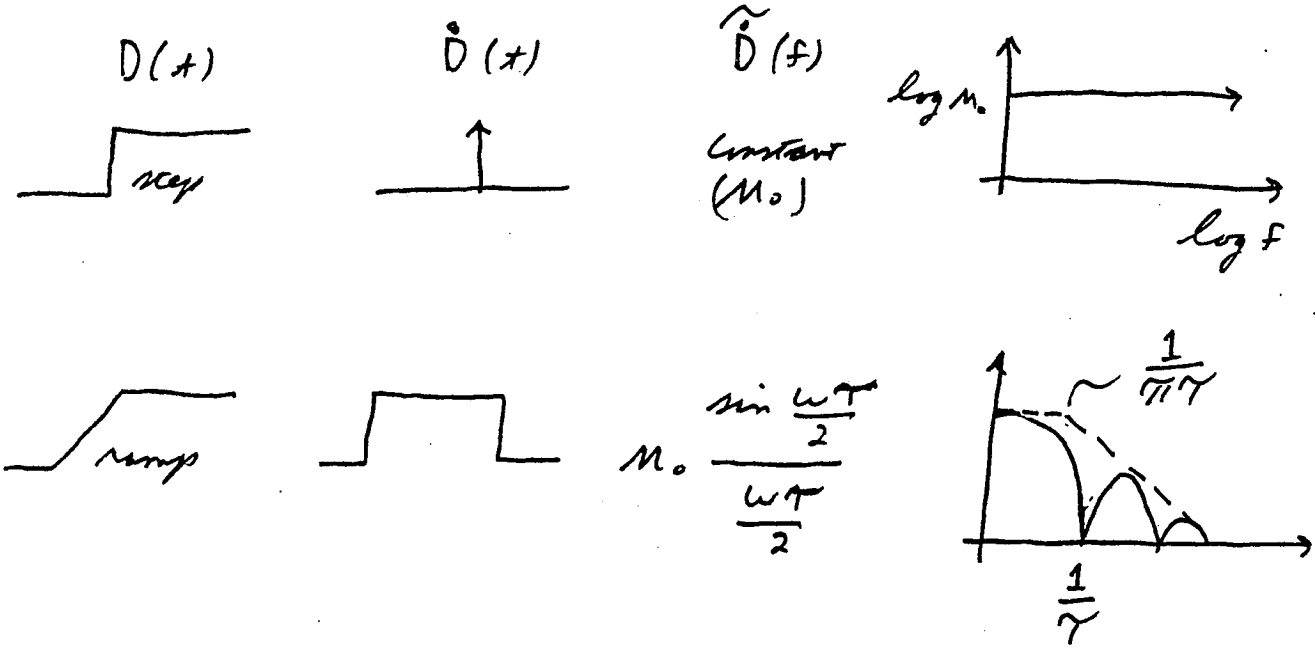

Effects of source finiteness

another sinc function

multiplies spectrum

$$\frac{\sin \frac{\omega \tau_c}{2}}{\frac{\omega \tau_c}{2}}$$

due to diffraction effects

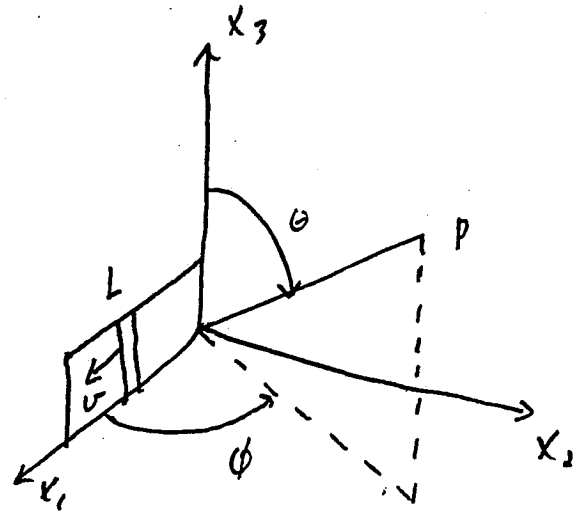

V = rupture velocity

results in another corner: $\tau_c = L \left(\frac{1}{V} - \frac{\sin\theta \cos\phi}{c} \right)$ $c = \alpha, \beta$ (11)

ramp + finiteness

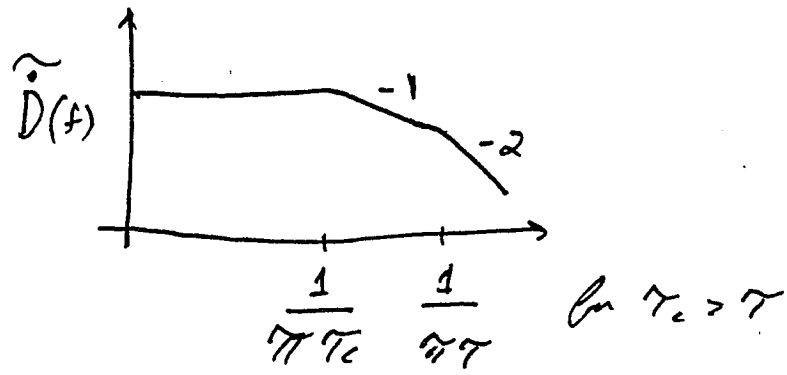

look at τc term : $\theta = \frac{\pi}{2}$, $\tau_c = (\tau_R - \frac{L}{c}\cos\phi)$ $\tau_R = \frac{L}{v}$ rupture time

$\tau_c < \tau_R$ propagation toward site

$> \tau_R$ " away from "

Effects on spectrum : neglect rise time

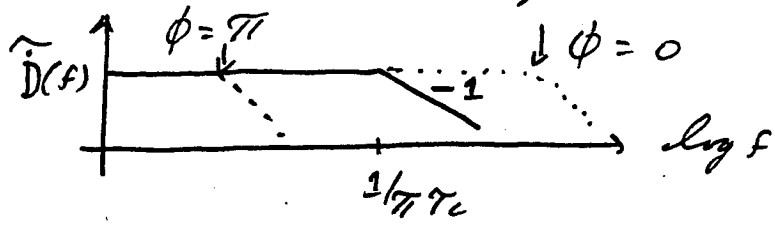

$\emptyset = 0$ directivity toward site, increase in spectral content

$\emptyset = \pi$ directivity array from site, decrease in spectral content

Effects of directivity for <u>simple</u> model: shift in corner frequency due to diffraction of a finite source.

For real earthquake at strong motion frequencies 0.1 - 50 Hz, effects of finiteness are much more complicated due to

1) presence of asperities (non uniform slip)

2) nonuniform rupture velocity

3) variable rise time

4) path and site effects (difficult to compare recordings at two different sites to isolate

source effects).

For strong motions, directivity effects appear to be most significant at low frequencies: < 1 Hz.

Brune Source: circular fault, effects of rise time and finiteness combined

$$\tilde{\dot{D}}(f) = \frac{M_o}{1 + \left(\frac{f}{f_c}\right)^2} \quad (12)$$

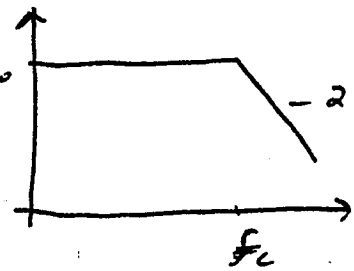

$$f_c^3 = \frac{\beta^3}{8.44} \frac{\Delta\sigma}{M_o} \quad (13)$$

scaling relation: specifies how source spectrum changes shape with earthquake size

2 parameter source model: M_o, $\Delta\sigma$ completely and uniquely describe source spectrum.

M_o related to magnitude

$\Delta\sigma \approx$ constant, Brune stress drop related to effective stress: Difference between dynamic fractional stress and stress just prior to an earthquake. Sometimes referred to as dynamic stress drop. Unfortunately static (computed from area) $\Delta\sigma$ and Brune stress drops are not the same in concept or value.

$\Delta\sigma$ static $\approx$ 30 bars California

$\Delta\sigma$ Brune (Dynamic, RMS) $\approx$ 100 bars California (Table 2)

From the equation for fc and the spectral shape, the high frequency source strength is very sensitive to $\Delta\sigma$ as fc $\sim$ $(\Delta\sigma)$ ⅓. For California earthquakes, assuming $\Delta\sigma \approx$ 100 bars

fc $\approx$ 300 $e^{-1.15M}$, **M** = moment magnitude

M	fc (Hz)
0	300
3	9
5	1
6	0.3
7	0.1
8	0.03

For the Brune source, the Fourier amplitude spectrum of acceleration looks like

$$\frac{f^2 M_0}{1 + \left(\frac{f}{f_c}\right)^2}$$

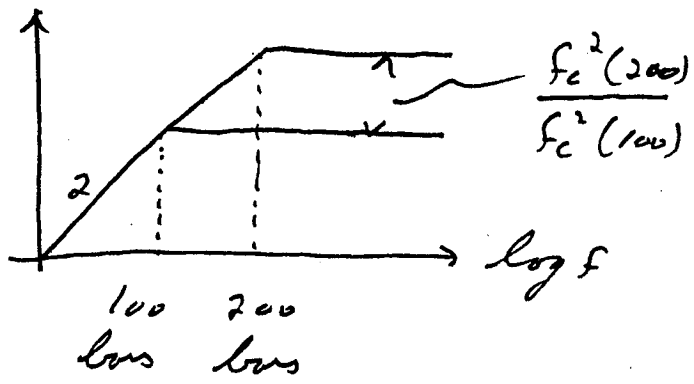

so high frequencies depend strongly on $\Delta\sigma$. For the Brune source, the fault radius, a, is given by

$$a = 0.37\,\beta/fc$$

From the scaling relation fc ($\Delta\sigma$, M_o) we can see how the source spectrum changes with earthquake size (M_o).

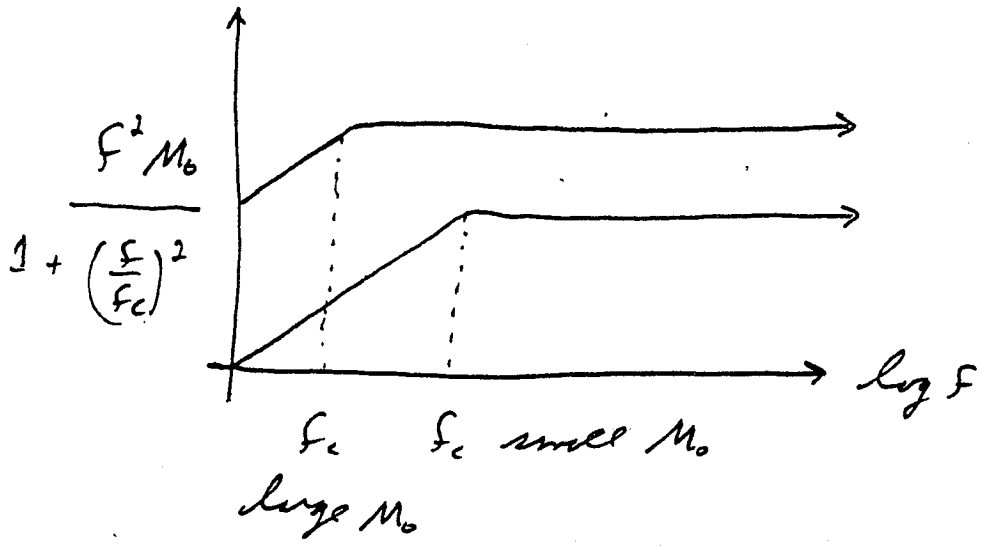

N.b.: change in f_c with M_o from Equation (13) $f_c \sim M_o^{-\frac{1}{3}}$ results in magnitude dependent response spectral shape

b) Path Effects

1) Damping

The Brune source acceleration spectrum is flat in acceleration at high frequencies. As the seismic radiation propagates, material damping through scattering and intrinsic absorption roll off the source spectrum

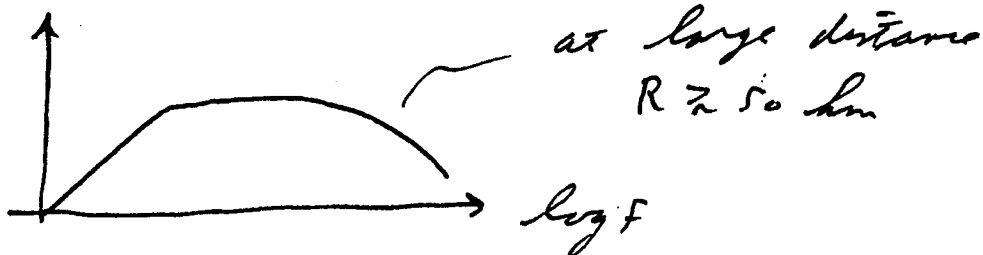

term to represent material damping

$e^{-\frac{\pi f R}{\beta Q(f)}}$, R = hypocentral distance

Q(f): frequency dependent deep crustal damping $Q \approx \frac{1}{2\eta}$

$\approx 150\ f^{0.6}$ WNA

$500\ f^{0.65}$ ENA

2) Geometric attenuation (radiation damping)

$\frac{1}{R}$, $\frac{1}{\sqrt{R}}$ $(R \gtrsim 100\ km)$

can also accommodate post-critical reflections through a generalized G(R) term.

c) Site Effects

a) Rock sites: the site term (for rock sites) generally has the forms

$A(f)\ e^{-\pi\kappa f}$ where

A(f) is amplification due to the velocity gradient from source depth to the site.

High frequency asymptote is

$\sim \sqrt{\frac{\beta_0}{\beta_1}} \sim \sqrt{\frac{3.2}{0.6}} \approx 2.3$

β_0, shear wave velocity at source

β_1, shear wave velocity at site (surface)

for soft rock (WNA) and

~ 1

for hard rock (ENA).

κ: kappa, frequency independent shallow crustal damping 1-2 km

$\approx$ 0.04 sec WNA

Table 3

$\approx$ 0.008 sec ENA

and is strongly correlated to rock strength.

Figure 3 shows kappa values plotted verses average shear-wave velocity over about 100 ft at rock sites which recorded the 1989 Loma Prieta earthquake. The average values is about 0.04 sec.

Figure 4 shows soft and hard rock velocity gradients.

Figure 5 shows soft and hard rock site terms.

For rock sites, the point source model takes the form

$$\hat{a}(f) = C \frac{M_o f^2}{1 + \left(\frac{f}{f_c}\right)^2} \cdot \frac{e^{-\frac{\pi f R}{Q(f)\beta}}}{R} \cdot A(f)\, e^{-\pi \kappa f} \qquad (14)$$

source · path · site

$$C = \frac{1}{\rho \beta^3} \cdot 2 \cdot 0.63 \cdot \frac{1}{\sqrt{2}}$$

where: 2 = free surface effect

0.63 = average radiation pattern

$1/\sqrt{2}$ = partition of energy onto one component

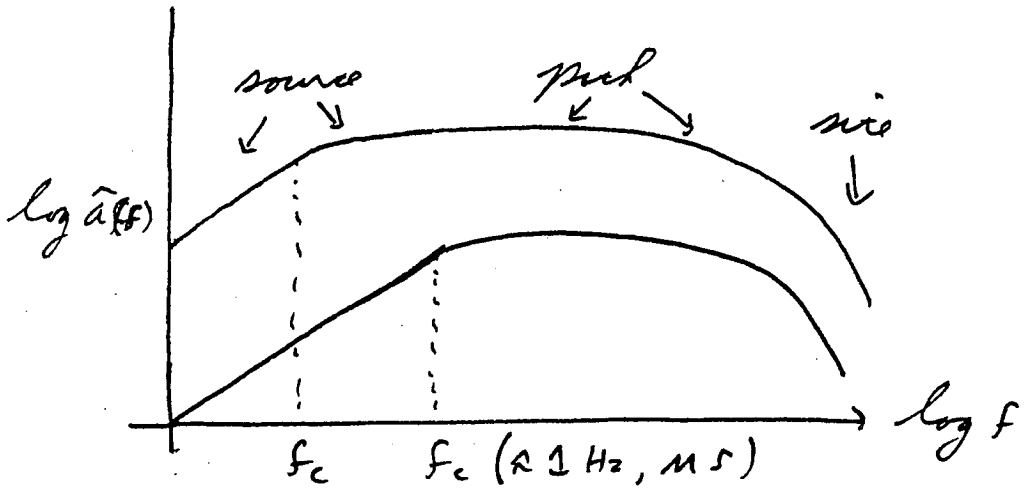

Figures 6,7 shows Fourier amplitude spectrum computed from recordings compared to model

Table 4 shows model predictions at R = 10 km for WNA and ENA parameters.

b) Soil Sites:

The effect of a soil column on strong ground motion is identical to that for rock sites: amplification through a velocity gradient competing with deamplification through damping (material and scattering). Because soils are generally softer than rock, liklehood is greater for nonlinear response.

Currently the distinction between rock and soil sites is becoming less clear. Figures 8 and 9 show shear-wave velocity profiles for "rock" and "soil" sites. Interestingly, over shallow portions of the profiles, rock and soil sites have similar velocities. Also of note: the variability of rock velocities appears to be greater than for soil. This suggests that

variability of ground motions should be higher at rock sites at high frequencies. If the increased variability exists to greater depths, this inference extends to lower frequencies as well.

The general effect of a soil column ($>$ 20 ft) on strong ground motions is to amplify at low frequencies by about 2-3 (5% damped response spectra) and to deamplify at high frequencies ($\approx$ 0.6) relative to rock. The spectral shape (response spectra) must then be different for rock and for soil. Additionally, nonlinear material response will cause changes in the frequency range of the amplification to deamplification crossover.

Figure 10 shows deep soil-to-rock 5% damped response spectral ratios from regression analyses on the empirical strong motion data base. The Figure shows excellent evidence of nonlinear material response as the amplification decreases as rock motion increases.

The classical approach to specifying site effects is the vertically propagating shear-wave model using the rock outcrop motion as control or input motion.

Examples of computed site effects for a generic soil profile (Figure 11) are shown in Figures 12 and 13 for 5% damped response spectra as functions of profile thickness. Figure 12 demonstrates nonlinearity at an oscillator frequency of 2.5 Hz and Figure 13 shows amplifications for various frequencies for a control motion level of 0.5g.

In general, site effects, apart from earthquake size, represent the greatest source of

variability in strong ground motions.

3) Magnitude Scales

Magnitude scales have the general formula

$$M = \log A + f(d, h) + C_S + C_R$$

where A = amplitude measured on some instrument (corrected for instrument response)

f = correction function of distance and depth

C_S = station correction

C_R = regional correction.

Magnitude scales such as these are measures of the source spectrum over a narrow frequency band roughly corresponding to the maximum magnification of the particular recording system. Because the shape of the source, spectrum changes with earthquake size, magnitude scales defined in this way do not give the same number for the same size earthquake. There at least 18 different magnitude scales of this type plaguing the seismological community and all of them, being based on narrow-band measures of amplitude, will saturate; under-estimate earthquake size.

To show this, Figure 14 shows a sketch of the Brune source spectra ($\Delta\sigma$ = 100 bars) along with bandwidth of the M_L and M_S scales. M_L begins to saturate around 6.5 and M_S around 7.5. Figure 15 shows relationships between several scales and Appendix 3 gives definitions of several common scales. Table 5 lists period ranges for various scales.

From Figure 14, it is apparent that only seismic moment, M_o, scales properly with size because it is at zero or very low frequency, away from any corners. As a result moment magnitude was introduced and defined as

$$\mathbf{M} = (\log M_o - 16.05)/1.5$$

or

$$\log M_o = 1.5\,\mathbf{M} + 16.1\ .$$

The seismic moment is generally measured at periods exceeding 10 sec for large earthquakes ($> \mathbf{M}\,5$) from the low frequency portion of the displacement spectra computed from recordings by inverting Equation 14.

EXAMPLE OF SATURATION		
	M_S	M
1906 SF	8.3	7.8
1960 Chile	8.3	9.5

d) Measures of Strong Ground Motion

1) Time Domain: Ground motions due to earthquakes recorded on seismographs which are sensitive to ground acceleration over a wide bandwidth (accelerographs) are referred to as strong ground motions. In general, the gains are low factor of 10-100 compared to sensitive seismographs ($\approx 10^6$). Typical instrument acceleration sensitivity:

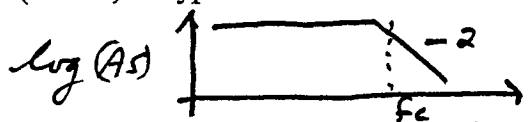

The accelerograph passes ground acceleration without distortion up to its corner frequency. Beyond that it acts like a low-pass filter.

Figures 16 and 17 show 3 component acceleration time histories recorded at deep soil sites located at about the same rupture distances ($\approx$ 25 km) from the M 7.4 Landers earthquake. These records are uncorrected for instrument response (removal of the acceleration sensitivity).

Of interest, the vertical motions show higher frequencies than the horizontal with larger motions earlier in the records. These observations suggest that these verticals are dominated by P-waves ($\alpha > \beta$) and that P-waves have significantly less soil damping than S-waves.

Additionally, the Yermo site (Figure 16) has a shorter duration of strong motion than Desert Hot Springs (Figure 17). This is a result of directivity and our τ_c from Equation 11.

For velocity and displacement, the acceleration time histories are integrated either in the time or frequency domains (Appendix 2). Figures 18 and 19 show A, V, and D time histories for the Yermo and Desert Hot Springs sites. Note for Yermo, the effects of rupture directivity (toward Yermo) not only shortens the duration but results in much larger velocity and displacement time histories. Interestingly, directivity has less of an effect on the acceleration amplitude, suggesting a predominately low frequency phenomena.

2) Frequency Domain:

a) Fourier spectra

Complex representation of a real time history a(t):

$$a(t) = \int_{-\infty}^{\infty} \tilde{a}(f)\, e^{i2\pi f}\, df$$

This equation assumes that any time history can be decomposed into harmonics of frequency f of near zero spacing df. The weighting function for continuous f (frequencies) is the complex function ã(f).

$$\tilde{a}(f) = \int_{-\infty}^{\infty} a\ (t)\ e^{-i2\pi ft}\ dt \quad .$$

The modulus of ã(f) is the Fourier amplitude spectrum and describes how the energy contained in a(t) is distributed with <u>frequency.</u>

The phase of ã(f) is the Fourier phase spectrum and describes how the energy contained in a(t) is distributed in <u>time.</u>

$$\tilde{a}(f) = \tilde{a}_R(f) + i\ \tilde{a}_I(f)$$

$$= \sqrt{\tilde{a}_R^2\ (f) + \tilde{a}_I^2\ (f)}\ e^{i\phi(f)}$$

$|\tilde{a}(f)|$ = Fourier amplitude spectrum

energy $\propto |\tilde{a}(f)|^2$

$$\Phi(f) = \tan^{-1}\left(\frac{\tilde{a}_I(f)}{\tilde{a}_R(f)}\right)$$

$\Phi(f)$ = Fourier phase spectrum

= specifies relative delay between spectral components $|\tilde{a}(f)|$. (Appendix 2).

Figures 20-24 illustrate some interesting features of Fourier spectra for the Landers (M 7.4) earthquake at the site Lucern (D $\approx$ 2 km). Figure 20 shows Fourier amplitude spectra computed 1) from recorded motions and 2) point source model including a 20 ft thick stiff generic soil profile. Both data and model have filters (HP 2 pole at 0.1 Hz, Lp 4 pole at 30 Hz).

1) spectra looks like our sketches

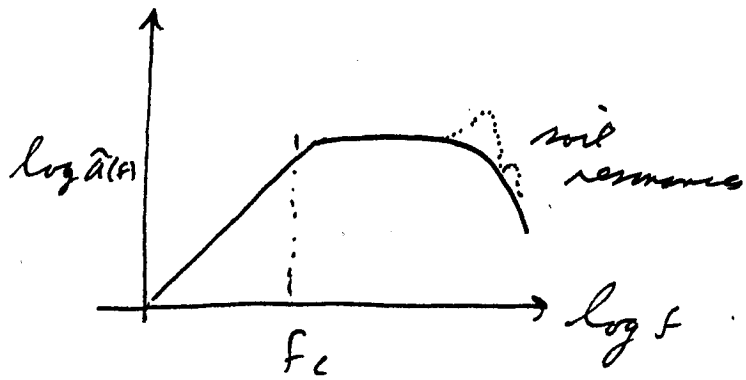

2) point source does very well for M 7.5, D $\approx$ 2 km.

Figure 21 shows corresponding response spectra.

Figures 22-24 show recorded A, V, D and computed A, V, D by adding phase spectrum from recording to model ã(f).

1) recorded and computed motions appear very similar,

2) Φ(f): phase spectrum describes how energy distributed in time,

3) easy way to generate synthetic time histories if Φ(f) is available from recordings or a suitable model.

b) Response Spectra: Simple harmonic oscillator subjected to a force (ground acceleration).

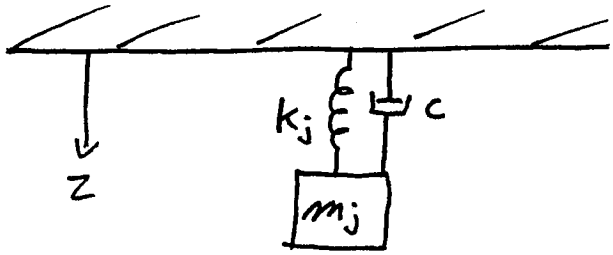

z : absolute motion of ground

x : absolute motion of mass

y = x-z, relative mass motion (positive for spring extension)

For dynamic equilibrium $\Sigma f = 0$

$$m_j \ddot{x} + c \dot{y} + \kappa_j y = 0$$

$$\ddot{x} = \ddot{y} + \ddot{z}$$

$$m_j (\ddot{y} + \ddot{z}) + c \dot{y} + \kappa_j y = 0$$

$$\ddot{y} + 2\eta\omega_j \dot{y} + \omega_j^2 y = -\ddot{z}$$

η = fraction of critical damping

Taking Fourier transforms or assuming $y \sim \sin \omega_e t$, $z \sim \sin \omega_e t$, where ω_e is the earth or ground radial frequency we have

$$-\omega_e^2 \tilde{y}(f_e) + i2\eta\omega_j\omega_e \tilde{y}(f_e) + \omega_j^2 \tilde{y}(f_e) = \omega_e^2 \tilde{z}(f_e)$$

rearranging and looking at modulus (and neglecting 2 π terms)

$$\hat{y}(f_e) = \frac{f_e^2}{\left[\left(f_j^2 - f_e^2\right)^2 + \left(2\zeta f_j f_e\right)^2\right]^{\frac{1}{2}}} \cdot \left(-\hat{z}(f_e)\right) + \text{phase}$$

$$= H(f_j, f_e, \zeta) \cdot \left(-z(f_e)\right), \text{ neglecting phase}$$

↑ relative displacement F.S.

↑ oscillator Transfer function

↑ absolute ground displacement F.S.

$-f_e^2(-z(f_e))$: absolute ground acceleration F.S.

Look at transfer function and F.S. of absolute ground displacement

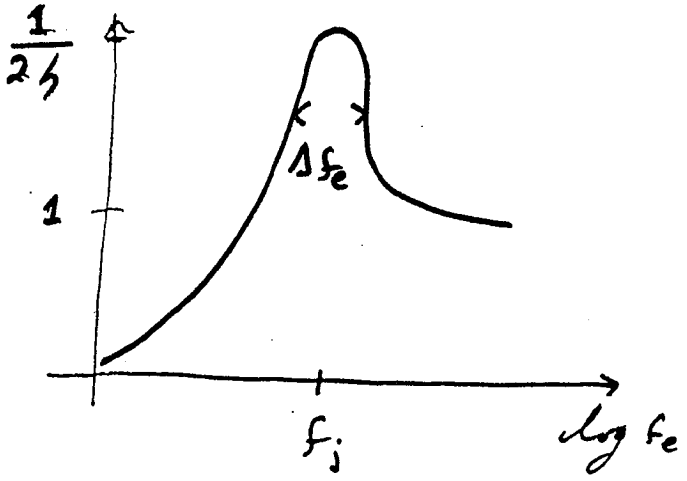

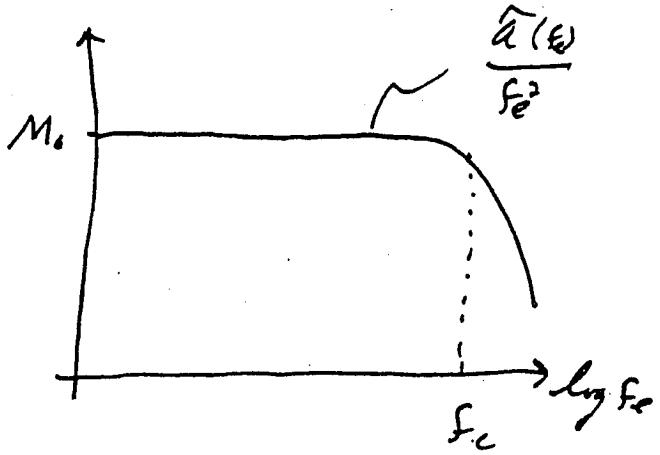

Δf_e = width of resonance peat at ½ amplitude

$$\frac{\Delta f_e}{f_j} = \frac{\sqrt{3}\,\Delta}{\pi} = \sqrt{3}\,\frac{2\zeta}{\sqrt{1-\zeta^2}} \quad \zeta \ll 1 \quad \simeq \sqrt{3}\,2\zeta \approx \frac{\sqrt{3}}{Q}$$

where Δ = logrithimic decrement

Important points:

1) For fixed frequency, f_j, as damping η increases Δf_e increases

2) For fixed damping, η, as frequency f_j increases Δf_e increases

Figure 25 shows $H(f_j, f_e, h)$ for f_j = 1, 10, 30 Hz

Relative displacement F.S. is a product of the absolute ground displacement F.S. and oscillator transfer function whose window Δf_e increases in width with increasing f_j (oscillator frequency).

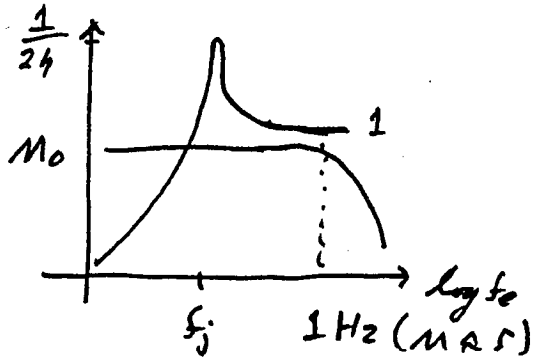

$f_j << 1$ Hz

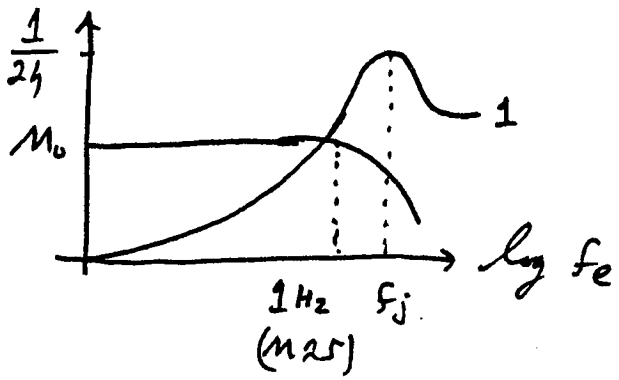

$f_j >> 1$ Hz

At low f_j, because Δf_e is very narrow $\tilde{y}(f_e)$ windows $\tilde{z}(f_e)$ near f_j

At high f_j, because Δf_e is very wide $\tilde{y}(f_e)$ windows $\tilde{z}(f_e)$ over a wide range of f_e.

Definitions of Response Spectrum

$$SD = \left| Y(t) \right|_{max} = \left| \int_{-\infty}^{\infty} \tilde{y}(f_e)\, e^{2\pi i f_e t}\, df_e \right|_{max} \quad \text{relative displacement}$$

$$SV = \left| \dot{y}(t) \right|_{max} = \left| 2\pi i \int_{-\infty}^{\infty} f_e\, \tilde{y}(f_e)\, e^{2\pi i f_e t}\, df_e \right|_{max} \quad \text{relative velocity}$$

$$SA = \left| \ddot{x}(t) \right|_{max} \quad \left| (2\pi)^2 \int_{-\infty}^{\infty} f_e^2 \left(\tilde{y}(f_e) + \tilde{z}(f_e) \right) e^{2\pi i f_e t}\, df_e \right|_{max} \quad \text{absolute acceleration}$$

↑ not $\ddot{y}$

Why not relative acceleration $|\ddot{y}(t)|_{max}$?

Actually of no use: interested in inertial force on structure $m_j \ddot{x}$. Mass times absolute

acceleration.

$c\dot{y}$, viscous force

κy , spring force

SV not of much interest either. Real interest is in SD because of spring force: strain energy in structure $\propto y^2$. Also SD provides an additional and convenient way of evaluating SA.

To see this the "pseudo" spectra are introduced

$PSV = 2\pi f_j \ SD$ pseudo relative velocity

$PSA = (2\pi)^2 f_j^2 \ SD$ pseudo absolute acceleration

SD: relative displacement is $\propto$ to maximum strain energy in the structure (spring)

$$E(t) = \frac{1}{2} \kappa_j \, y^2(t)$$

$$E_{max} = \frac{1}{2} \kappa_j \, y(t)^2 \, |_{max} = \frac{1}{2} \kappa_j \, (SD)^2$$

$$\frac{E_{max}}{m} = \frac{1}{2} \frac{\kappa_j}{m_j} (SD)^2 = \frac{1}{2} (2\pi f_j)^2 \, (SD)^2 = \frac{1}{2} \, (PSV)^2$$

SA: absolute acceleration $\propto$ maximum inertial forces on structure $m_j\ddot{x}$. Convenient to have a relationships between SA and PSA.

Recall the oscillator equation

$$\ddot{y} + 2\eta\omega_j \dot{y} + \omega_j^2 y = -\ddot{z}$$

for a small $\dot{y}$ term

$$\ddot{y} + \ddot{z} \approx -\omega_j^2 y$$

$$\ddot{y} + \ddot{z}\Big|_{max} = SA \quad , \quad y\Big|_{max} = SD,$$

$$PSA = -(2\pi)^2 \ f_j^2 \ y\Big|_{max}$$

$\therefore$ SA $\approx$ PSA , for small $\dot{y}$ term

Recap:

y : relative displacement between mass and ground with the governing equation

$$\ddot{y} + 2\eta w_j \dot{y} + w_j^2 y = -\ddot{z}$$

$SD = y(t)\Big|_{max}$ relative displacement

$SV = \dot{y}(t)\Big|_{max}$ relative velocity

$SA = \ddot{y}(t) + \ddot{z}(t)\Big|_{max}$ absolute acceleration

$PSV = \omega_j SD$ pseudo relative velocity

$PSA = \omega_j^2 SD \approx SA$ pseudo absolute acceleration $\approx$ absolute acceleration

Asymptotic values for response spectra; look at the transfer function representation

$$\hat{Y}(f_e) = -\frac{f_e^2}{\left[\left(f_j^2 - f_e^2\right)^2 + \left(2\zeta f_e f_j\right)^2\right]^{\frac{1}{2}}} \cdot \hat{Z}(f_e)$$

$f_j \Rightarrow 0 \qquad T \Rightarrow \infty$

Consider SD

$$\hat{Y}(f_e) = -\frac{1}{} \cdot \hat{Z}(f_e)$$

= F.S. of ground displacement

$SD(f_j \Rightarrow 0) = Z(t)\Big|_{max}$ maximum ground displacement

Consider SV and PSV

$$2\pi f_e \hat{Y}(f_e) = -2\pi f_e \cdot \hat{Z}(f_e)$$

= F.S. of ground velocity

$SV(f_j \Rightarrow 0) = V(t)\Big|_{max}$ maximum ground velocity

$PSV(f_j \Rightarrow 0) = 2\pi f_j SD = 0$

Consider SA and PSA

$$(2\pi)^2 f_e^2 \tilde{y}(f_e) = -(2\pi)^2 f_e^2 \tilde{z}(f_e)$$

$$(2\pi)^2 f_e^2 \left(\tilde{y}(f_e) + \tilde{z}(f_e)\right) = 0$$

F.S. of absolute acceleration $\ddot{y}$

$$SA(f_j \Rightarrow 0) = \ddot{y} + \ddot{z} \Big| = 0$$

max

$$PSA(f_j \Rightarrow 0) = (2\pi)^2 f_j^2 SD = 0$$

Figure 26 shows an example of SD (a), SV and PSV (b), and PSA (c) on log-log axes. Note SD $\Rightarrow z_{max}$ at $f_j \Rightarrow 0$ and the general shape of the spectrum looks like $\tilde{a}(f_e)/f_e^2$, Fourier amplitude spectrum of our ω^2 model. For spectral velocity SV $\Rightarrow \dot{z}_{max}$ at $f_j \Rightarrow 0$ and PSV $\Rightarrow 0$. The PSA plot (c) looks like our $\tilde{a}(f_e)$ and saturates to $\ddot{z}_{max}$ at high frequency.

The variability of the spectral ordinates appears to decrease with increasing f_j due to the accompanying increase in Δf_e: the wider window in the transfer function has a smoothing effect.

PSA saturates to PGA at high f_j, i.e. when f_j exceeds the dominant energy in $\tilde{a}(f)$.

Figure 27 shows a conventional "tripartite" plot of PSV along with peak values of $\ddot{z}$, $\dot{z}$, and z. The PSV increases with a 1 slope in the low frequency range, has a mid frequency range flat in velocity, and then decreases with $\approx$ 1 + slope at high frequencies. The PSV spectrum is anchored at low frequency to z_{max} and at high frequency to max $\ddot{z}_{max}$.

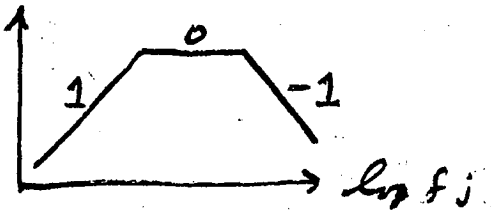

d) Features of Strong Ground Motion

The following figure sets illustrate:

1) Motions on rock sites compared to motions on soil sites,

2) Effects of magnitude on Fourier amplitude spectra and on 5% damped response spectra,

3) Effects of damping (kappa) at rock sites,

4) Nonlinear soil response,

5) Rupture directivity and near-source effects.

Table 1 Earth Disturbances Recorded by Seismographs*

A. Continuous disturbances
   1. Artificial
      Traffic
      Machinery
   2. Natural (microseisms)
      Meteorological: storms, wind, frost
      Water in motion: surf, streams, waterfalls
      Volcanic tremor

B. Single disturbances
   1. Artificial (chiefly explosions)
      Blasting: quarry or road work, geophysical exploration
      Explosives tests
      Demolitions
      Bombing and bomb tests
      Gunfire
      Accidental large detonations
   2. Natural (including earthquakes)
      I. Minor causes
         Collapse of caves
         Large slides and slumps
         Rockbursts in mines
         Meteorites
      II. Volcanic shocks
         Superficial, explosive
         Magmatic or eruptive
      III. Tectonic shocks
         Shallow or normal (depths not over 60 kilometers)
         Intermediate (depths 70 to 300 kilometers)
         Deep (depths 300 to 720 kilometers)

* This table, and the following discussion, show the problems involved in defining the term "earthquake." Authors have differed extremely. Some have practically restricted the meaning to tectonic shocks, others accept only volcanic shocks in addition; some include artificial shocks, and a few have framed definitions so broad as to include microseisms.

Table 2

STRESS DROP SUMMARY

ACTIVE REGIONS

M	M Range	$\Delta\sigma$ (Bars) Inversion	$\Delta\sigma$ (Bars) RMS2	σ_{ln} Inversion	σ_{ln} RMS2	N
3.0	2.8 - 3.2	13.0	3.2	0.35	0.42	4 (3)*
3.5	3.3 - 3.7	52.0	18.1	0.42	0.64	14 (11)*
4.0	3.8 - 4.2	66.1	48.9	0.84	0.85	19 (17)*
4.5	4.3 - 4.7	71.2	58.4	0.65	0.84	11
5.0	4.8 - 5.2	121.3	109.4	0.84	0.79	12
5.5	5.3 - 5.7	104.9	118.4	0.58	0.55	8
6.0	5.8 - 6.2	77.6	92.3	0.74	0.57	9
6.5	6.3 - 6.7	88.4	100.6	0.37	0.30	7
7.0	6.8 - 7.2	107.0	112.5	0.33	0.21	3
7.5	7.3 - 7.7	143.7	176.3	0.26	0.41	2
3.0-7.5	2.8 - 7.7	71.4	58.9	0.82	1.08	90
All 5.0-7.5	4.8 - 7.7	101.2	108.2	0.68	0.60	41
Main 5.0-7.5	4.8 - 7.7	108.2	118.0	0.50	0.44	23
After 5.0-7.5	4.8 - 7.7	92.9	96.8	0.85	0.74	18

STABLE CONTINENTAL INTERIORS

All	2.1 - 7.2	88.8	0.99	36
Main	3.0 - 7.2	89.3	1.00	20
After	2.1 - 5.4	88.1	0.97	16

*Number of earthquakes available for RMS stress drops.

TABLE 3

KAPPA VALUES FOR "AVERAGE" SITE CONDITIONS IN WNA AND ENA

Tectonic Regime	"Average" Site Condition	N	Median Kappa (sec)	σ_{ln}	Range Of Kappa For This Site Condition (sec)
WNA	Hard rock	11	0.026	0.58	0.010-0.060
	Weathered hard rock	9	0.035	0.52	0.015-0.100
	Soft rock	15	0.045	0.51	0.015-0.080
	Sheared rock	4	0.062	0.41	0.040-0.120
	Combined	39	0.037	0.59	0.010-0.120
ENA	Hard rock	16	0.007	0.42	0.004-0.016
	Soft rock	3	0.017	0.09	0.015-0.018
	Sheared rock	1	0.025		0.025
	Combined	20	0.008	0.55	0.004-0.025

Note: In WNA, The Parkfield, EPRI soil sites are excluded from this table. In ENA, the Painesville, Ohio soil sites are excluded from this table.

*"Average" Site Condition is defined as;

Hard Rock: WNA as granite, schist, carbonate, slate
ENA as granitic pluton, carbonate, sites in Canadian Shield region (Saguenay, New Hampshire).

Weathered Hard Rock: WNA as weathered granitic rock and tonalite

Soft Rock: WNA as sandstone and breccias
ENA as sandstone and claystone

Sheared Rock: WNA as site near fault zone (Gilroy #6) or greenstone site in Franciscan (Redwood City, Hayward).
ENA as site near fault zone (Nahanni River Site #1)

TABLE 4

MOMENT MAGNITUDE, CORNER FREQUENCY, PEAK ACCELERATION, AND PEAK PARTICLE VELOCITY AT R = 10 KM FOR STANDARD WNA AND ENA PARAMETERS

WNA

M	f_C (Hz)	A_P (g)	f_P^{**} (Hz)	V_P (cm/s)	f_P (Hz)	V_P/A_P (cm/s/g)
2.5	17.594	0.003	15.03	0.05	9.93	15.73
3.5	5.563	0.020	10.47	0.43	6.37	21.46
4.5	1.759	0.072	7.84	2.50	3.91	34.80
5.5	0.556	0.178	6.86	9.73	2.45	54.52
6.5	0.176	0.378	6.56	32.17	1.55	85.00
7.5	0.056	0.756	6.48	87.95	1.13	116.40

ENA

M	f_C (Hz)	A_P (g)	f_P (Hz)	V_P (cm/s)	f_P^{**} (Hz)	V_P/A_P (cm/s/g)
2.5	19.244	0.017	38.70	0.09	25.54	5.49
3.5	6.084	0.055	31.15	0.51	14.55	9.28
4.5	1.924	0.133	27.43	2.17	7.92	16.37
5.5	0.608	0.283	25.98	8.22	4.32	29.07
6.5	0.192	0.567	25.47	28.63	2.44	50.46
7.5	0.061	1.104	25.32	81.76	1.67	74.03

**Predominant frequencies estimated from random process theory

TABLE 5

MAGNITUDE SCALES

Scale	T (sec)	λ_{max} (km)	Related scales
M_L	0.1 ~ 3	10	m_{bLg}
M_s	~ 20	70	M_{GR}, M_R, M_D, M_Z, M_V, M_{JMA}
m_B	0.5 ~ 12	70	
m_b	~ 1	10	m_{bLg}
Moment magnitude	10 ~ ∞	∞	M_M, M_w, M_E, M_t
M_C	-	-	
M_I	-	-	M_K

Notation

T Period

λ_{max} Maximum wave length

M_L Local magnitude, Richter (1935)

M_s Surface-wave magnitude, Gutenberg (1945a)

m_B Body-wave magnitude, Gutenberg (1945b), Gutenberg and Richter (1956)

m_b Short-period body-wave magnitude reported in "Earthquake Data Reports" and "Bulletin of International Seismological Center"

m_{bLg} Lg-wave magnitude, e.g., Nuttli (1973)

M_{GR} Magnitude used in Gutenberg and Richter (1954)

M_R Magnitude used in Richter (1958)

M_D Magnitude used in Duda (1965)

M_Z Surface-wave magnitude determined from the vertical-component seismograms (e.g., Earthquake Data Reports)

M_V Surface-wave magnitude defined by Vaněk et al. (1962)

M_{JMA} Magnitude scale used by the Japan Meteorological Agency

M_M Moment magnitude by Brune and Engen (1969)

M_w Kanamori (1977)

M_E Purcaru and Berckhemer (1978)

M_t Tsunami magnitude regressed against M_w, Abe (1979)

M_C Coda (or duration magnitude), e.g., Bisztricsány (1959), Tsumura (1967), Real and Teng (1973)

M_I Magnitude determined from intensity data and macro-seismic data, e.g., Nuttli and Zollweg (1974). Nuttli et al., (1979), Utsu (1979).

M_K Kawasumi (1951)

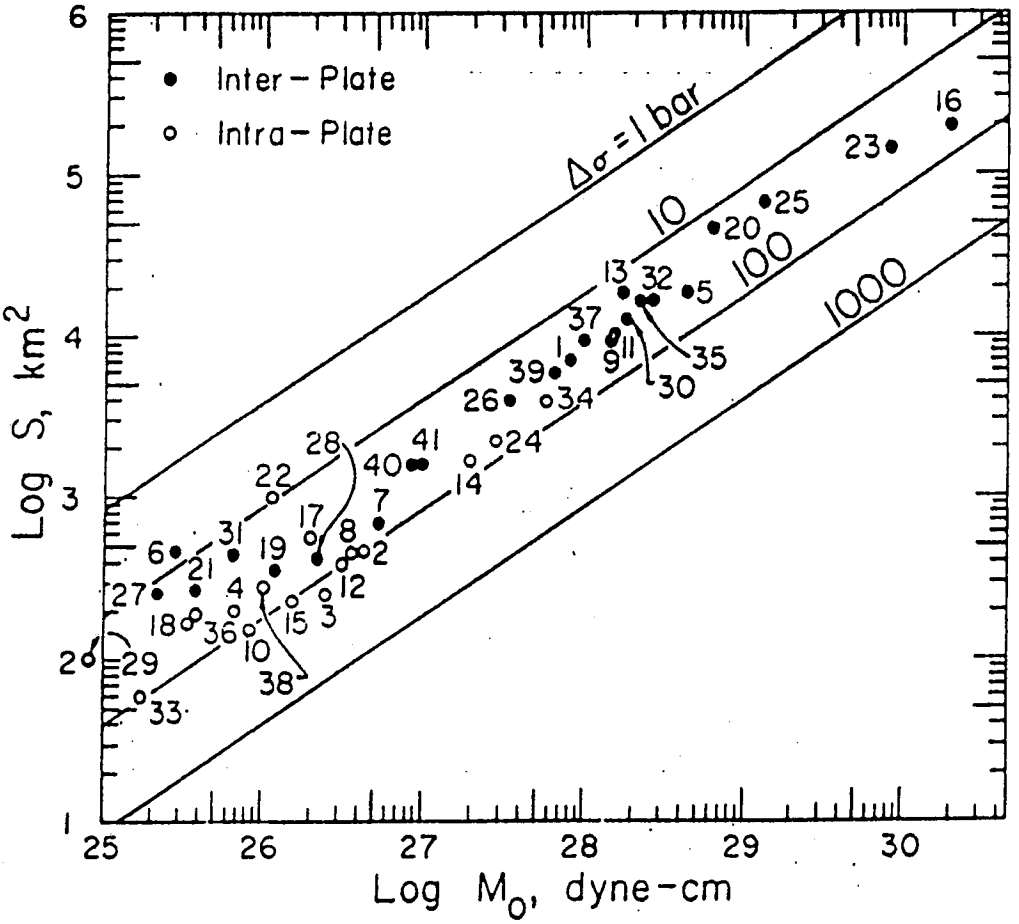

Figure 1. Relation between S (fault surface area) and M_o (seismic moment). The straight lines give the relations for circular cracks with constant $\Delta\sigma$ (stress drop).

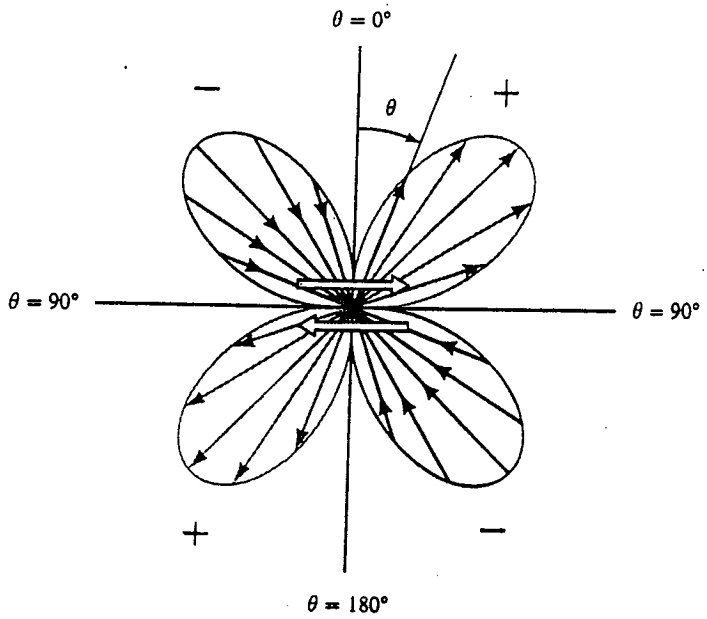

(a)

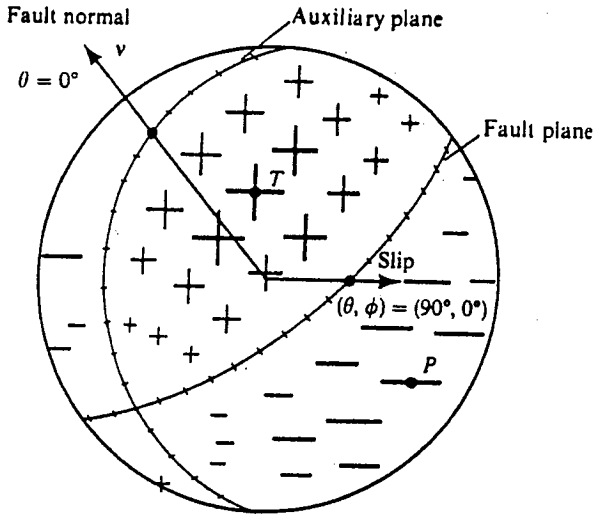

(b)

Figure 2.

Diagrams for the radiation pattern of the radial component of displacement due to a double couple, i.e., sin 2θ cos ϕf. (a) The lobes are a locus of points having a distance from the origin that is proportional to sin 2θ. The diagram is for a plane of constant azimuth, and the pair of arrows at the center denotes the shear dislocation. Note the alternating quadrants of inward and outward directions. In terms of far-field P-wave displacement, plus signs denote outward displacement (if $M_0(t - r/\alpha)$ is positive), and minus signs denote inward displacement. (b) View of the radiation pattern over a sphere centered on the origin. Plus and minus signs of various sizes denote variation (with θ, ϕ) of outward and inward motions. The fault plane and the auxiliary plane are nodal lines (on which sin 2θ cos $\phi = 0$).

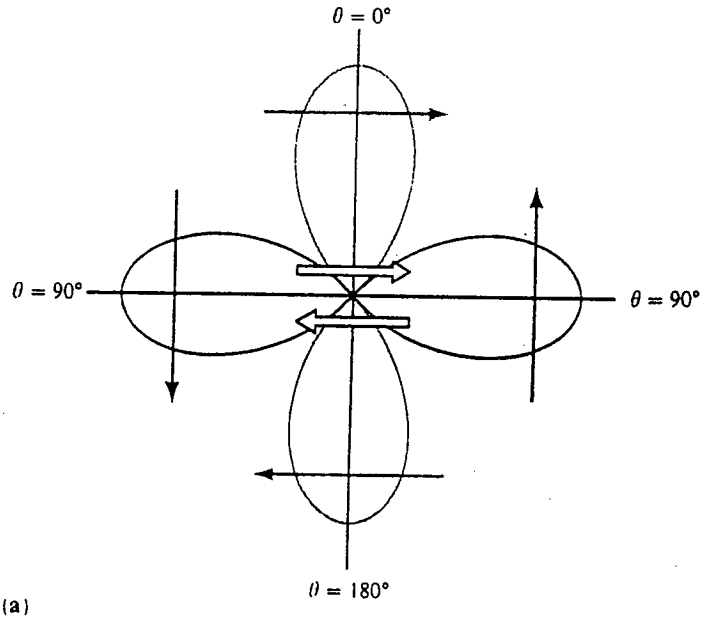

(a)

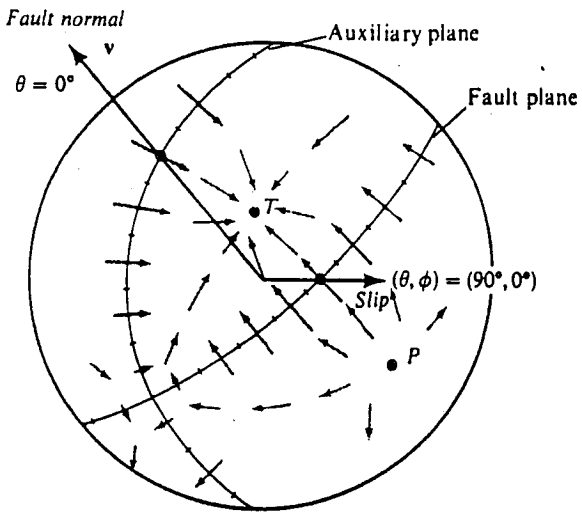

(b)

Figure 2. (cont.)

Diagrams for the radiation pattern of the transverse component of displacement due to a double couple, i.e., $\cos 2\theta \cos \phi\hat{\theta} - \cos \theta \sin \phi\hat{\phi}$. (**a**) The four-lobed pattern in plane $\{\phi = 0, \phi = \pi\}$. The central pair of arrows shows the sense of shear dislocation, and arrows imposed on each lobe show the direction of particle displacement associated with the lobe. If applied to the far-field S-wave displacement, it is assumed that $M_0(t - r/\beta)$ is positive. (**b**) Off the two planes $\theta = \pi/2$ and $\{\phi = 0, \phi = \pi\}$, the $\hat{\phi}$ component is nonzero, hence (a) is of limited use. This diagram is a view of the radiation pattern over a whole sphere centered on the origin, and arrows (with varying size and direction) in the spherical surface denote the variation (with θ, ϕ) of the transverse motions.

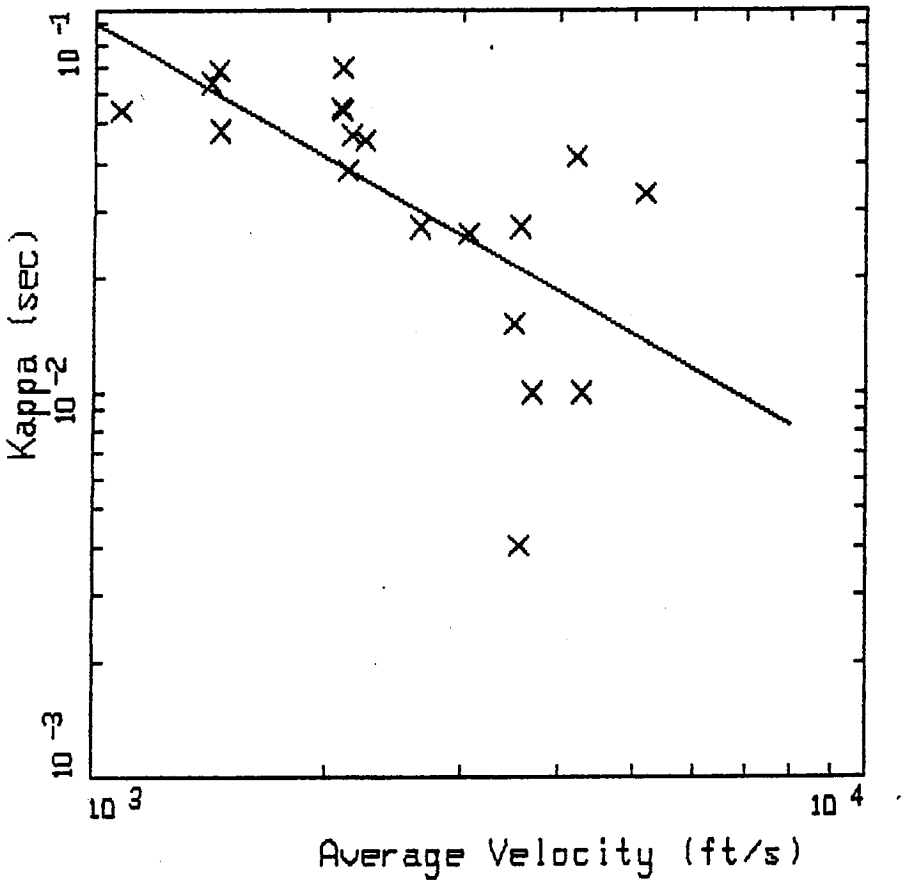

ROCK SITES (WNA)

KAPPA VS AVERAGE (OVER 100 FT) VELOCITY

LEGEND

× DATA

——— LOG(KAPPA) = 2.40939 - 1.15099 * LOG(VELOCITY IN FT/S)

Figure 3.

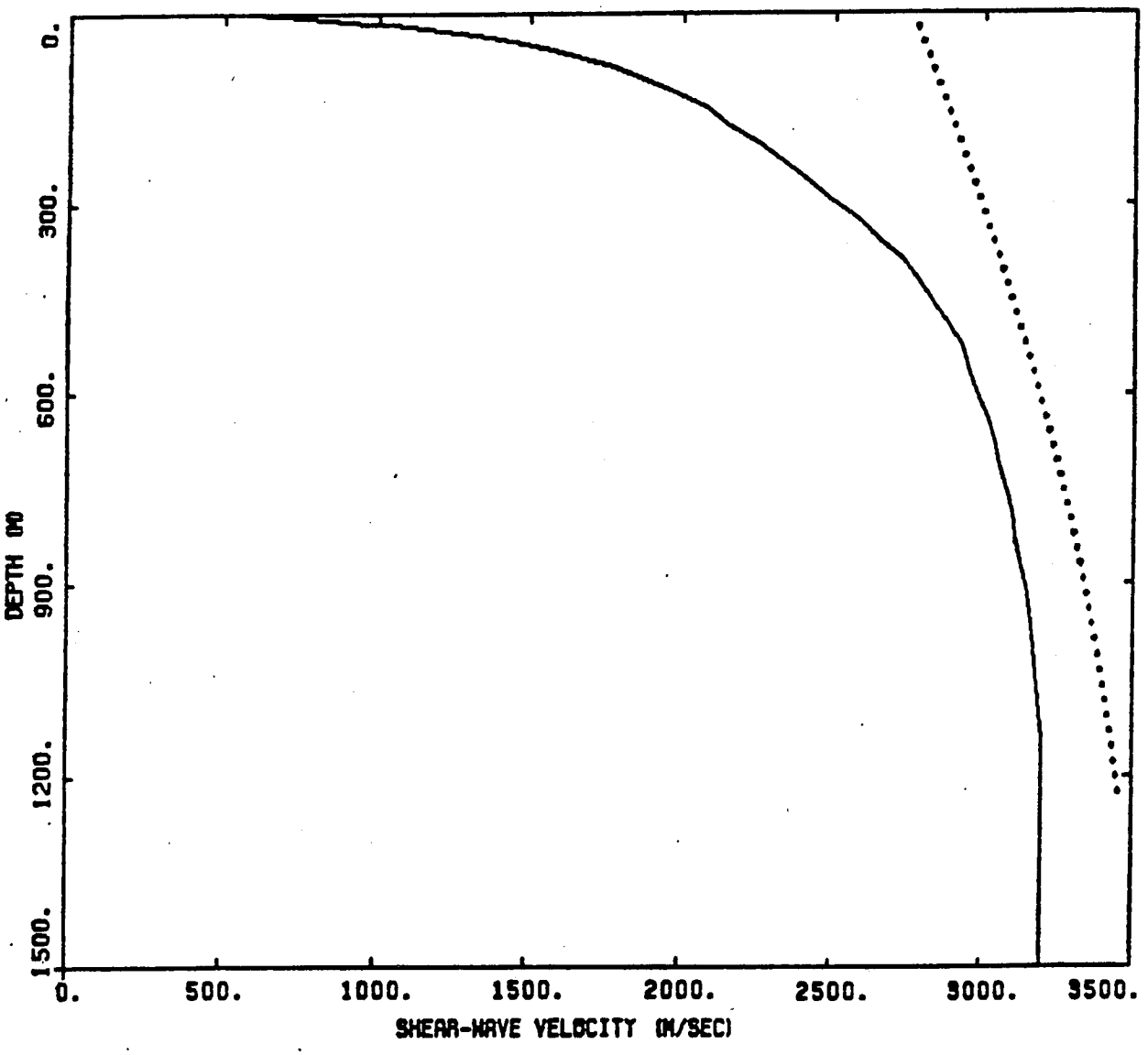

Figure 4. Comparison of average shear-wave velocity profile for WNA (Boore; personal communication, 1988) (solid line) with quadratic fit to ENA well log profile (Moodus) (dotted line).

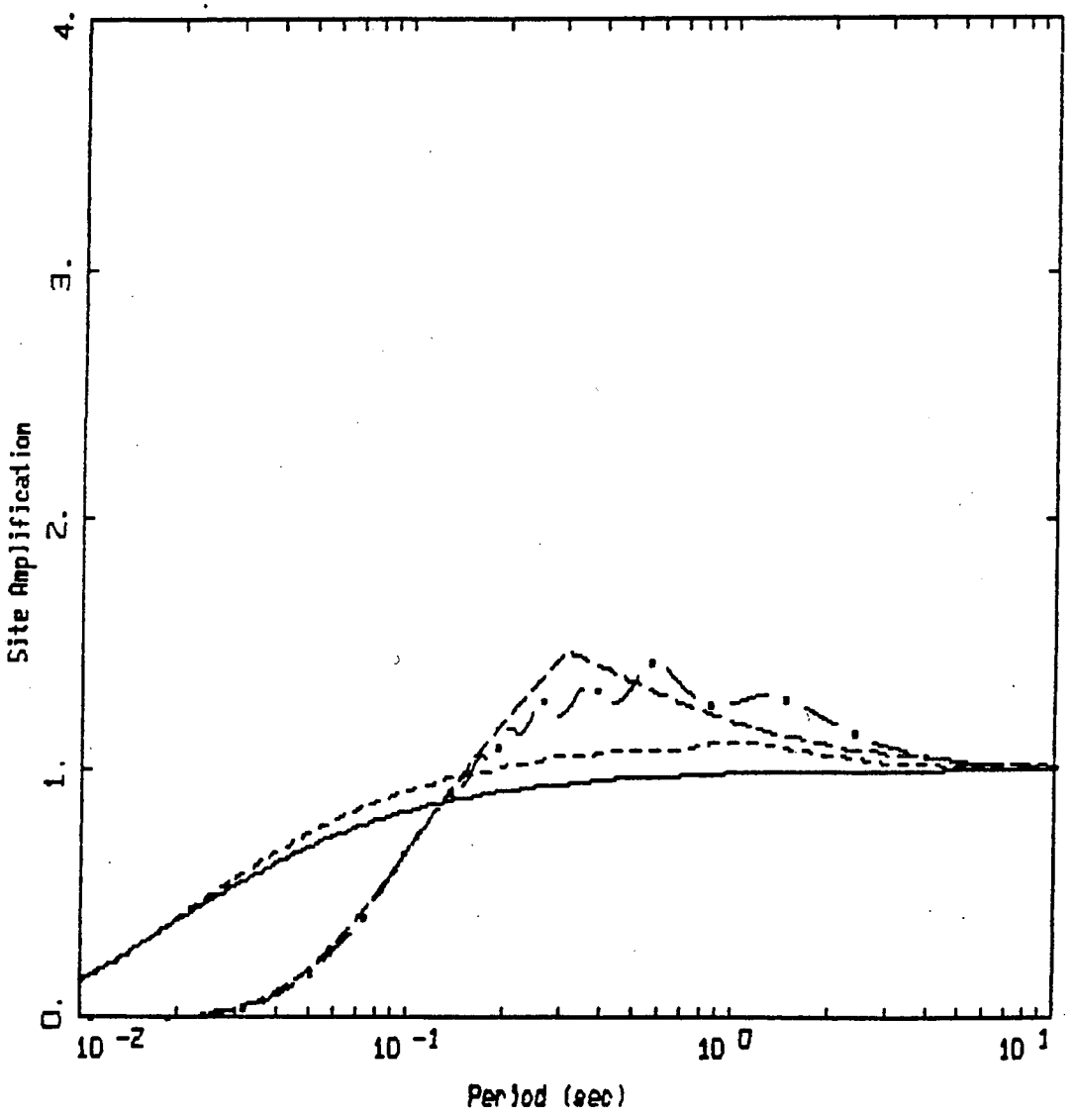

Figure 5. Upper set of curves: comparison of amplification factors computed by response analysis using WNA shear-wave velocity profile (Table 2-5) and $Q_s = 0.007 * \beta_R$ ($Q_S \geq 6$) (dash-dotted) with Boore's (1986) amplification factors combined with a kappa operator (κ = 0.04 sec) (long-dashed). Lower set of curves: amplification factors computed by response analysis using ENA shear-wave velocity profile (Table 2-6) and $Q_S = 0.029 * \beta_R$ compared to unity with a kappa operator (κ = 0.006 sec).

MODEL DEVELOPMENT

SIGNIFICANT OBSERVATIONS

1a) FOURIER ACCELERATION SPECTRAL DENSITY APPROXIMATELY CONSTANT BETWEEN LOW-AND HIGH- FREQUENCY CUT OFFS (HANKS, 1982)

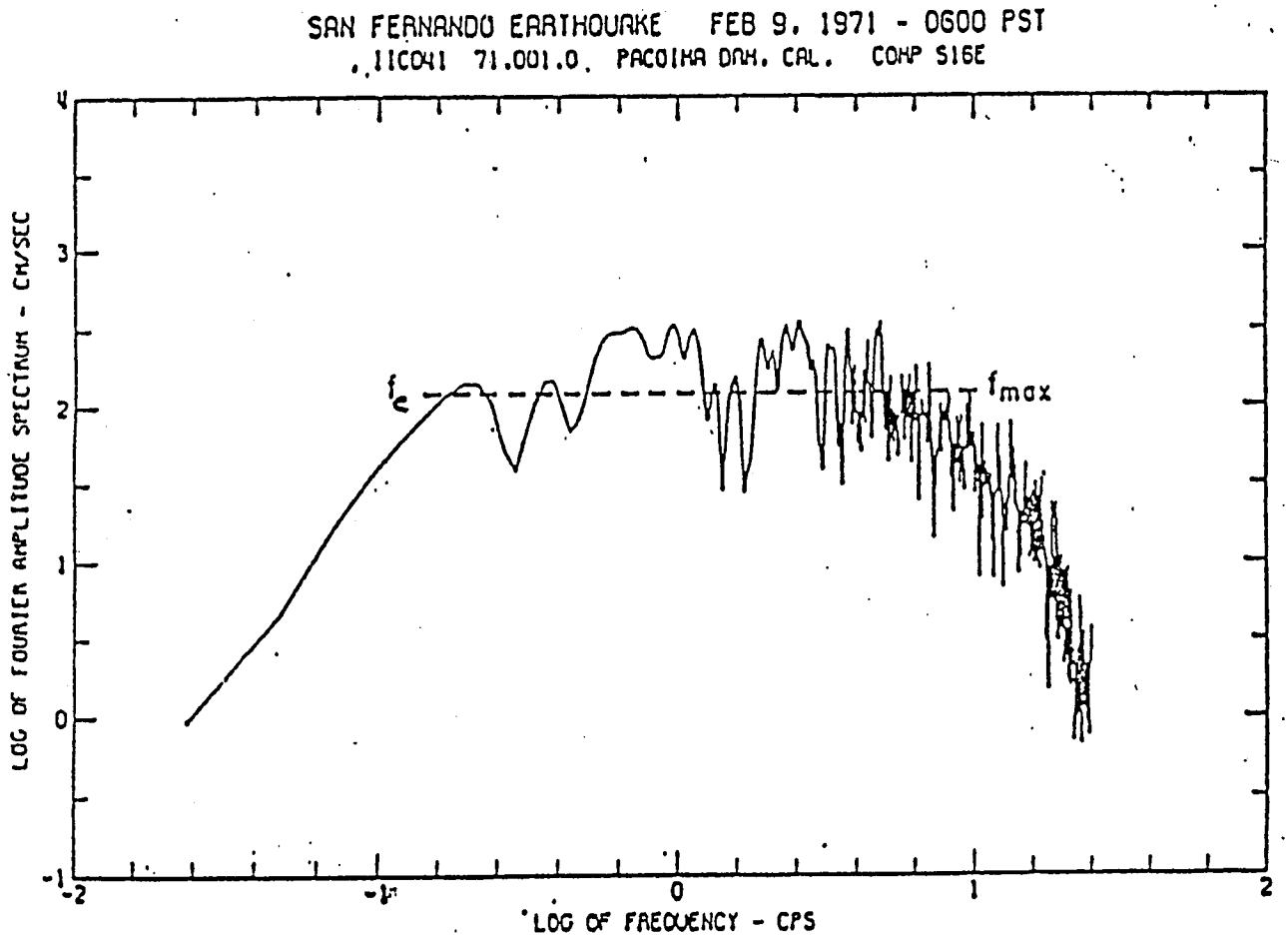

Figure 6. Whole-record spectrum of the San Fernando earthquake (9 February 1971; M_L = 6.4) at Pacoima Dam (S16E component). f_0 and f_{max} are estimated as indicated. Modified from Trifunac *et al.* (1973).

2) HIGH-FREQUENCY CUTOFF DUE TO NEAR SURFACE (1-2 km) DAMPING IN CRUSTAL ROCKS (ANDERSON AND HOUGH, 1984).

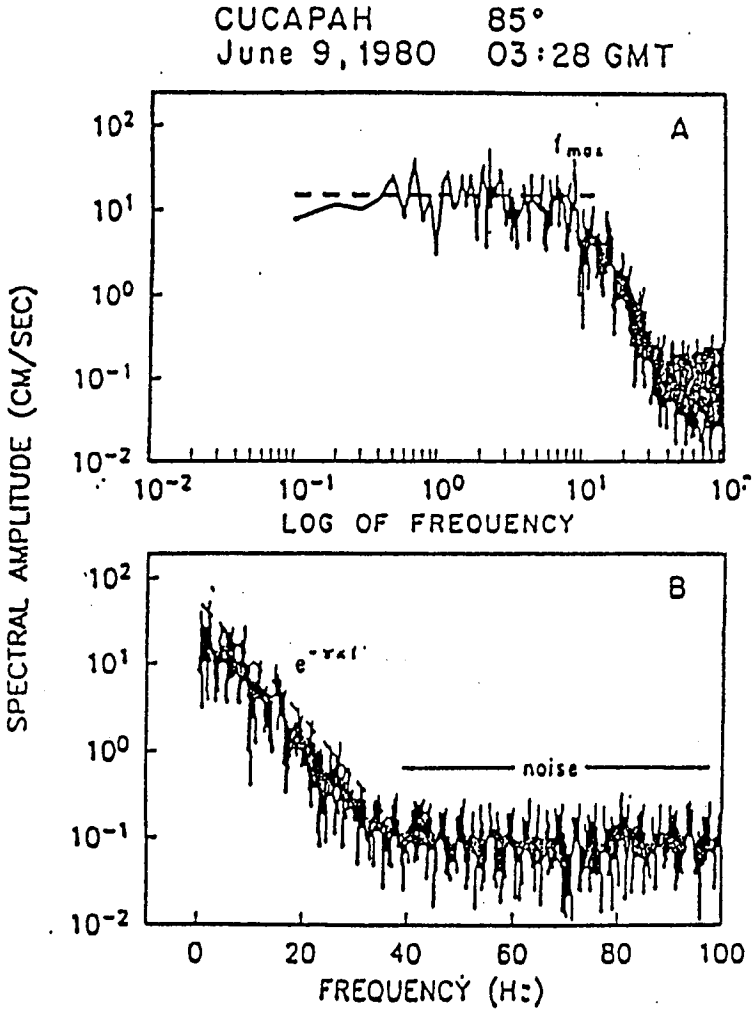

Figure 7. Fourier amplitude spectrum of the N85°E component of strong ground acceleration recorded at Cucapah during the Mexicali Valley earthquake of 9 June 1980 (M_L 6.2). Accelerograph was a digital recorder which samples at a rate of 200/sec. (A) Log-log axies. (B) Linear-log axes.

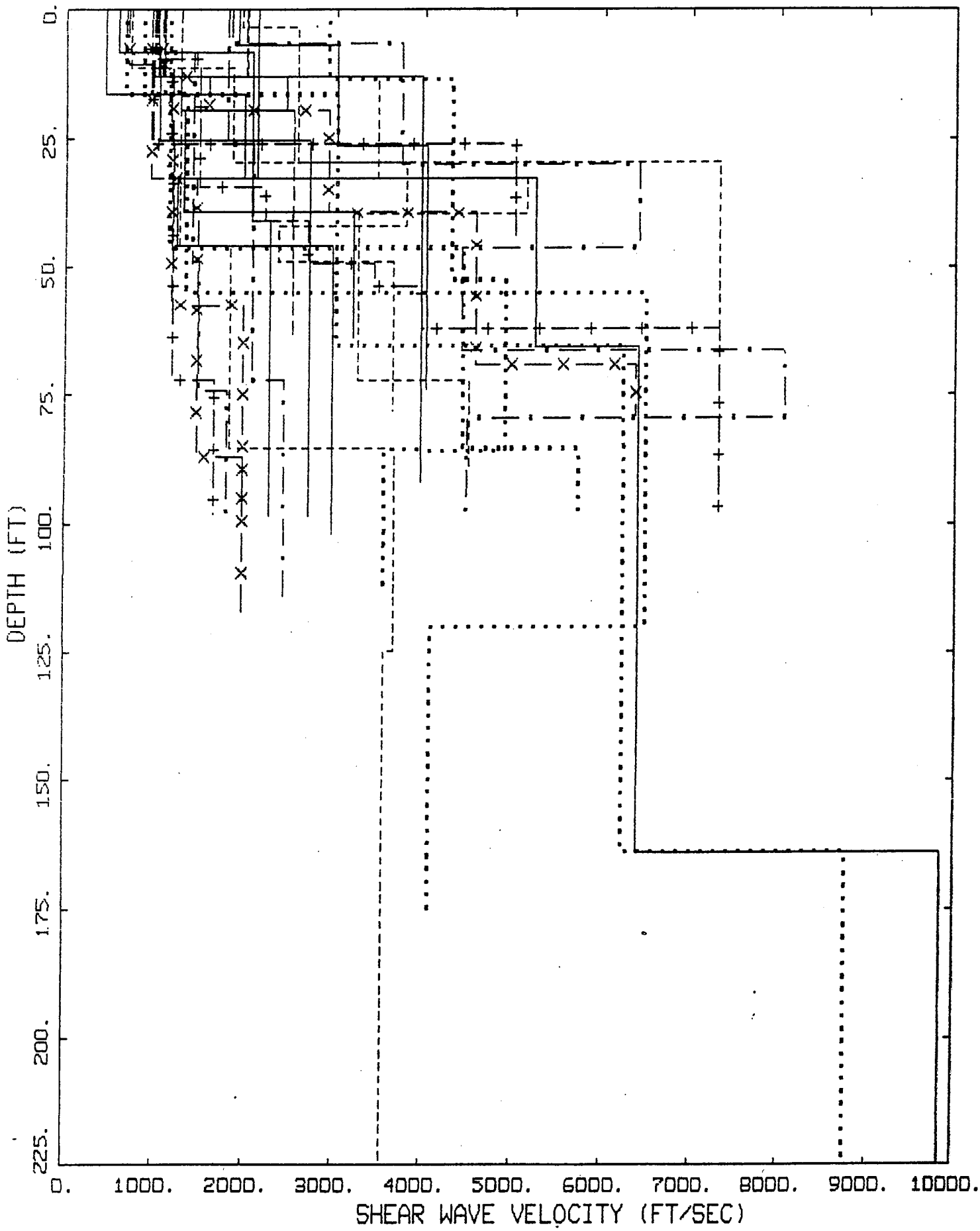

Figure 8. ROCK PROFILES

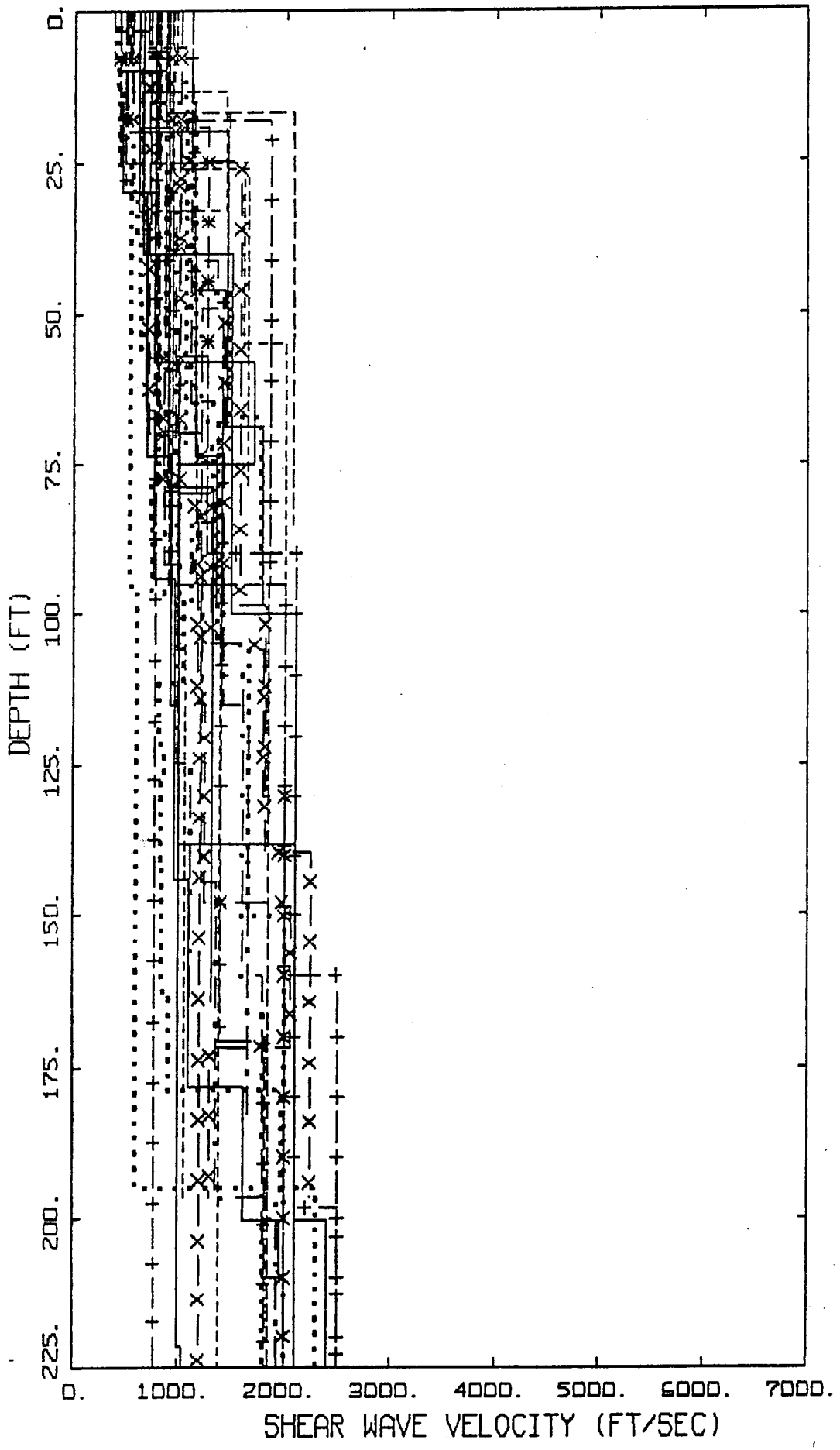

Figure 9. SOIL PROFILES

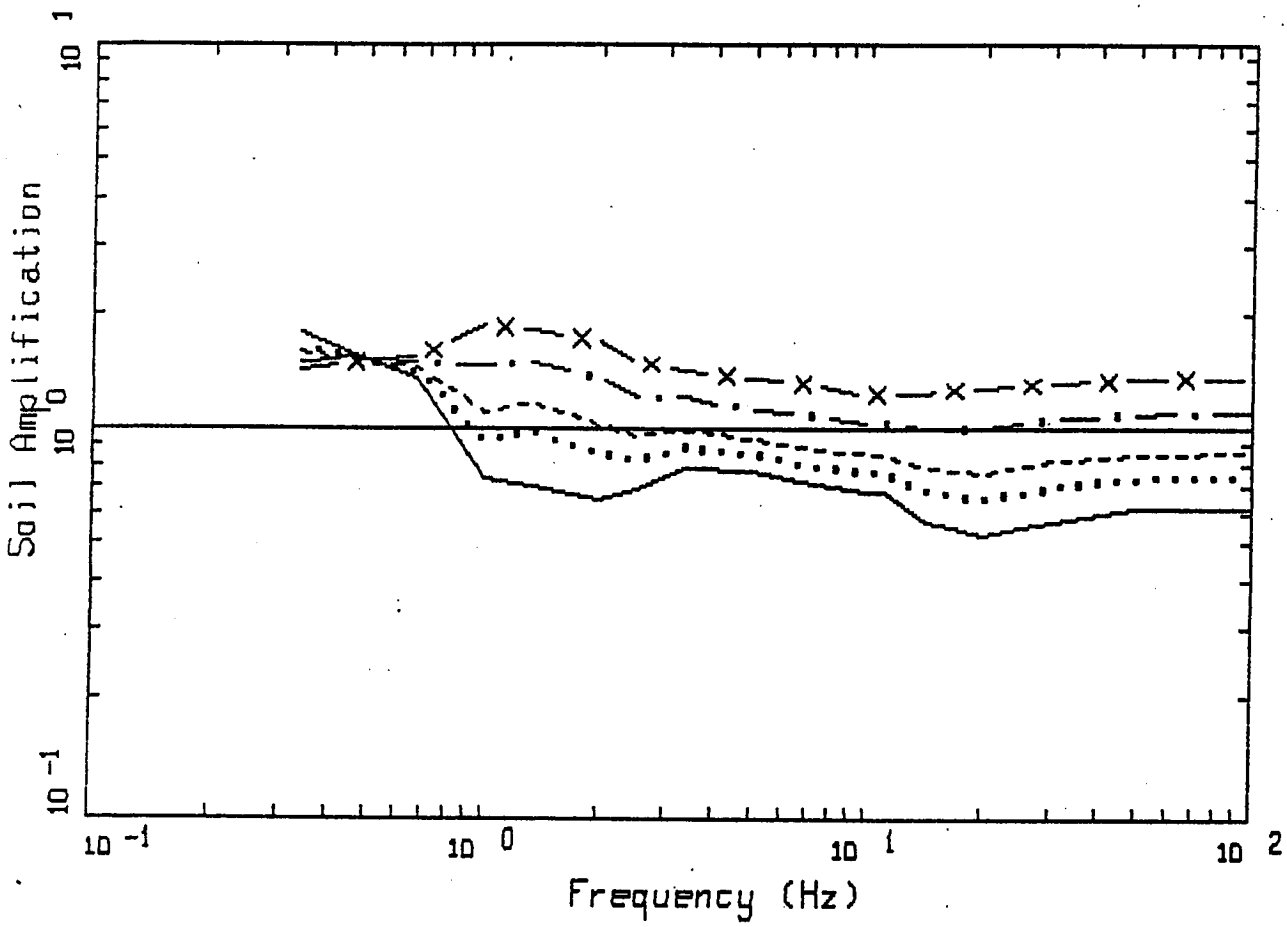

WNA EMPIRICAL M 6.5
DEEP, FIRM

LEGEND

R = 1.0 KM, ROCK PGA = 0.73 g
R = 5.0 KM, ROCK PGA = 0.40 g
R = 10.0 KM, ROCK PGA = 0.25 g
R = 25.0 KM, ROCK PGA = 0.11 g
R = 50.0 KM, ROCK PGA = 0.06 g

Figure 10.

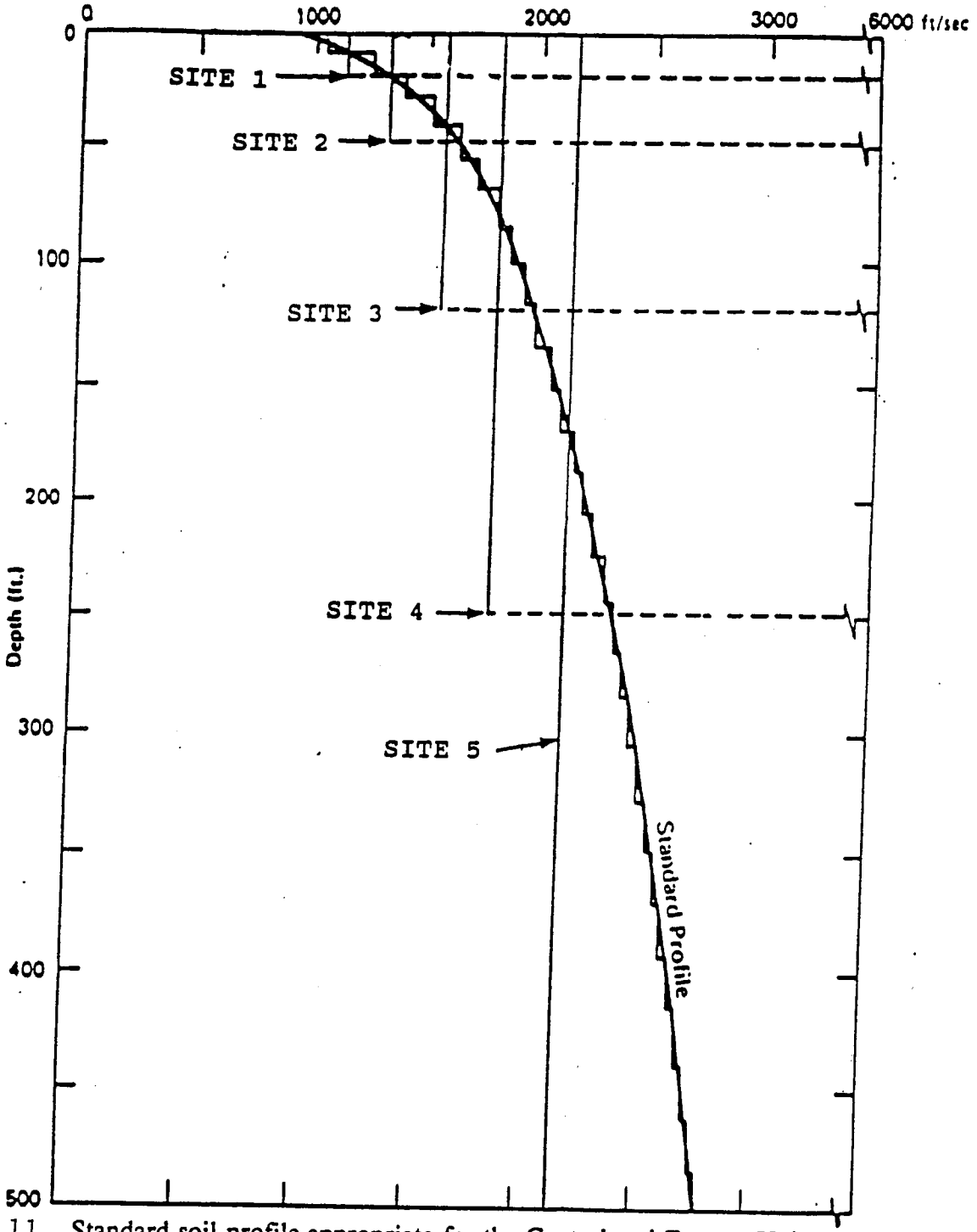

Figure 11. Standard soil profile appropriate for the Central and Eastern United States sites (gradient). Site categories 1-5 are indicated by their respective soil column depths. Constant shear-wave velocity profiles represent averages (over travel time) of the gradient profiles for each site category.

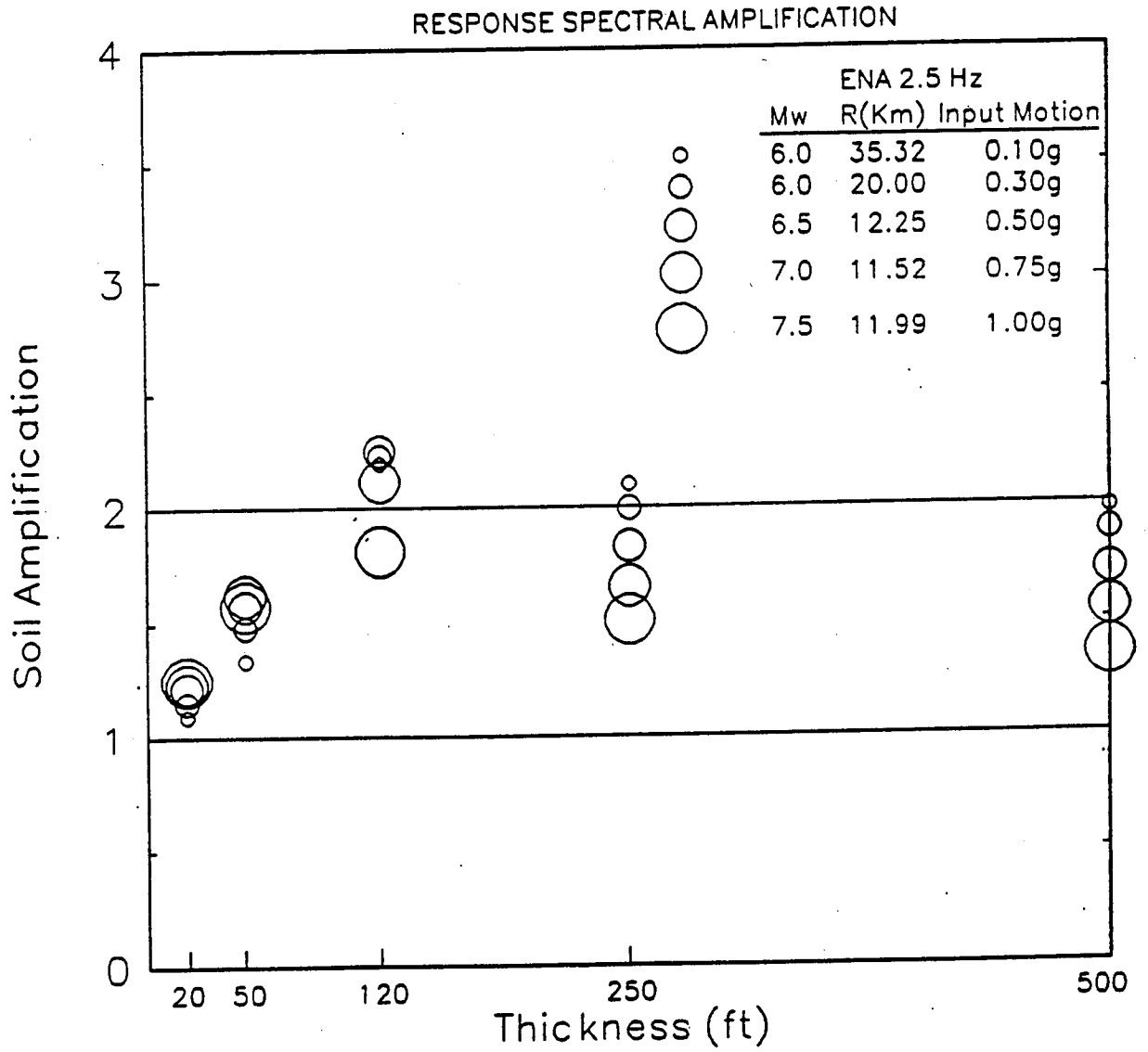

Figure 12. Plot of median 5% damped response spectral amplification factors computed for the five site categories (Table 6-2) at a frequency of 2.5 Hz. Size of symbol indicates level of input (rock outcrop) acceleration (0.1, 0.3, 0.5, 0.75, 1 g).

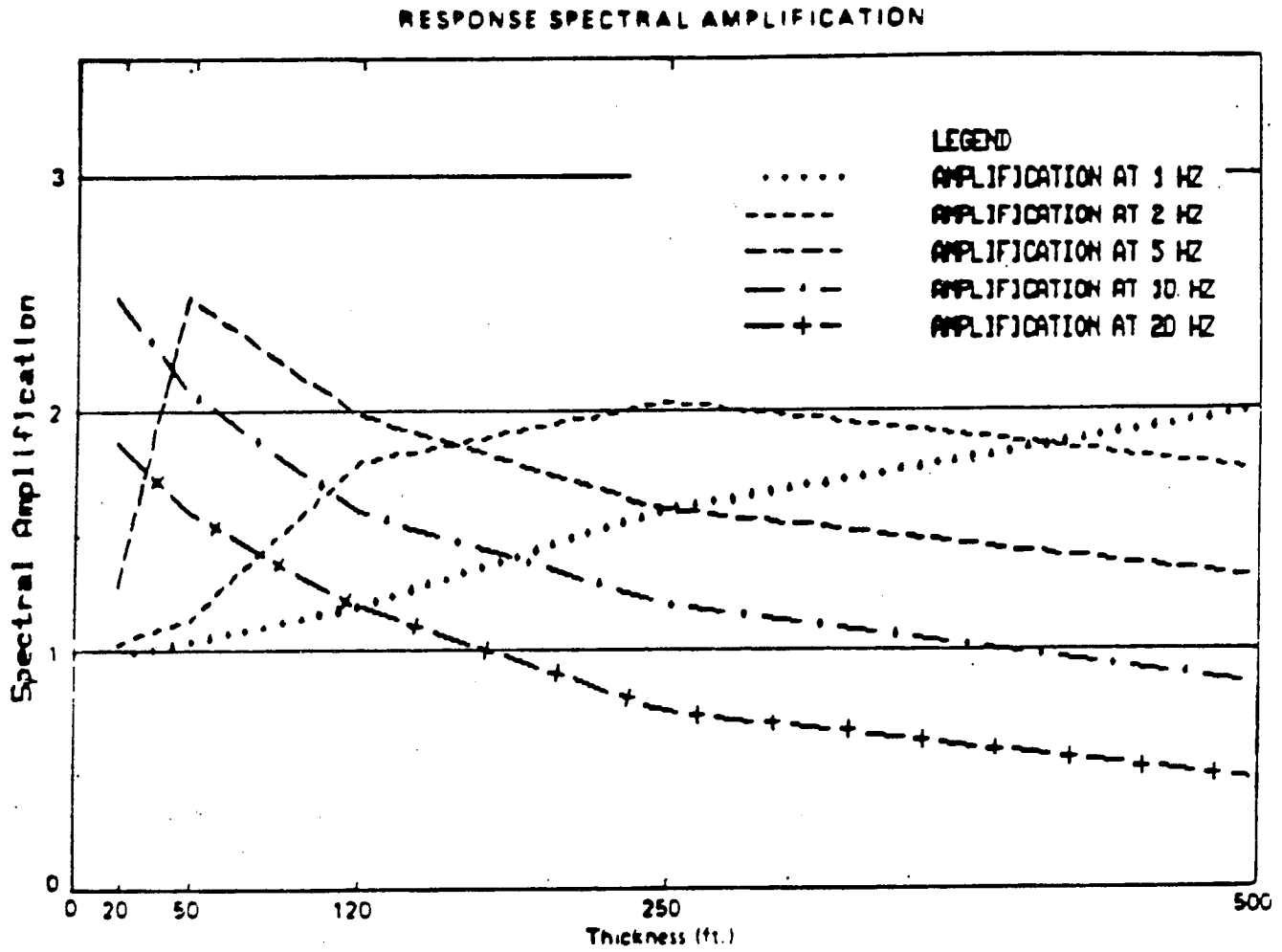

Figure 13. Plot of computed 5% response spectral amplification factors for five site categories (Figure 22) for a 0.5 g level of input (rock outcrop) motion. Curves represent frequencies of 1, 2, 5, 10 and 20 Hz.

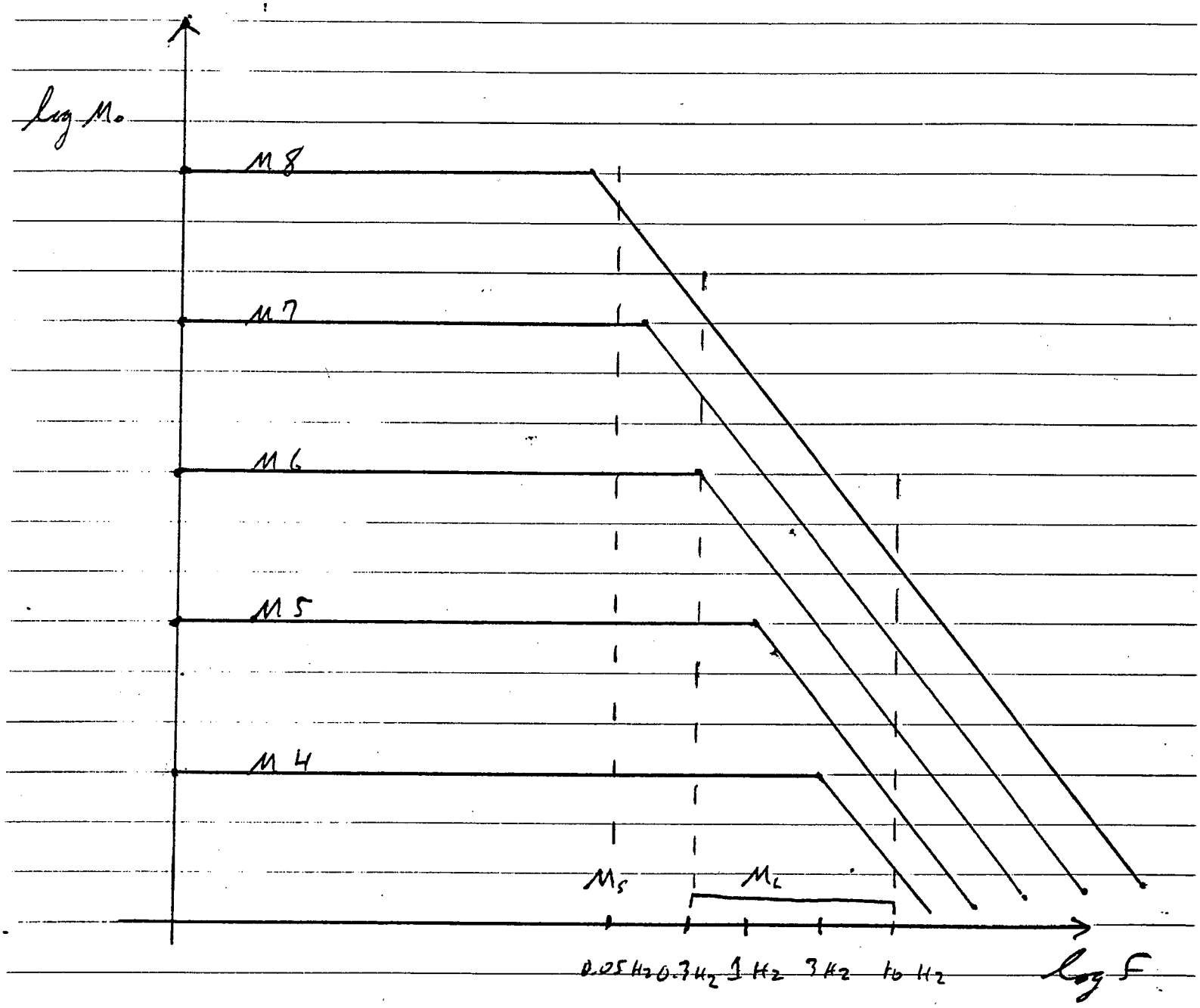

Figure 14.

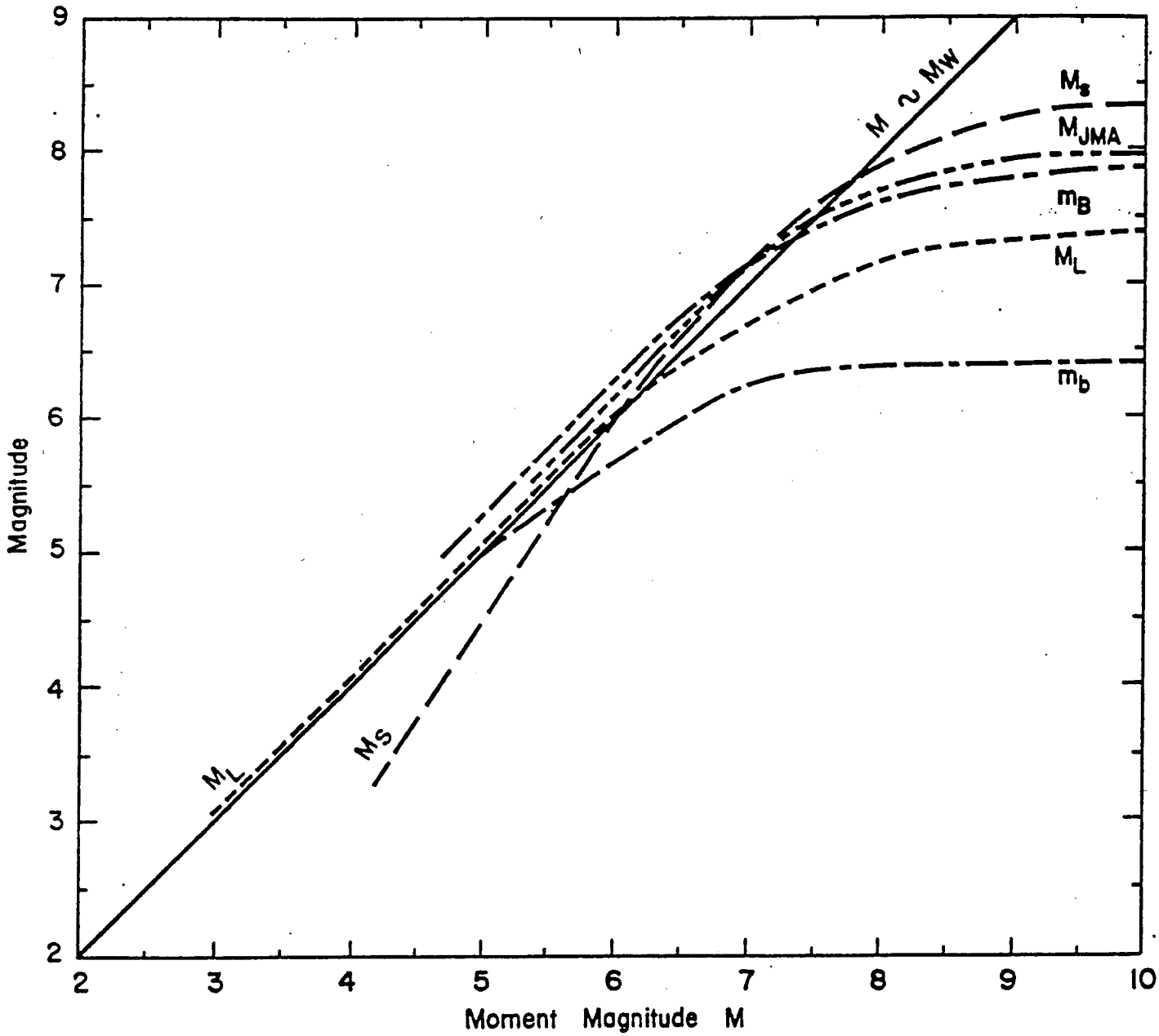
9
8
7
6
5
4
3
2
Magnitude
2
3
4
5
6
7
8
9
10
Moment Magnitude M
M ≃ Mw
Ms
MJMA
mB
ML
mb
ML
Ms

Figure 15.

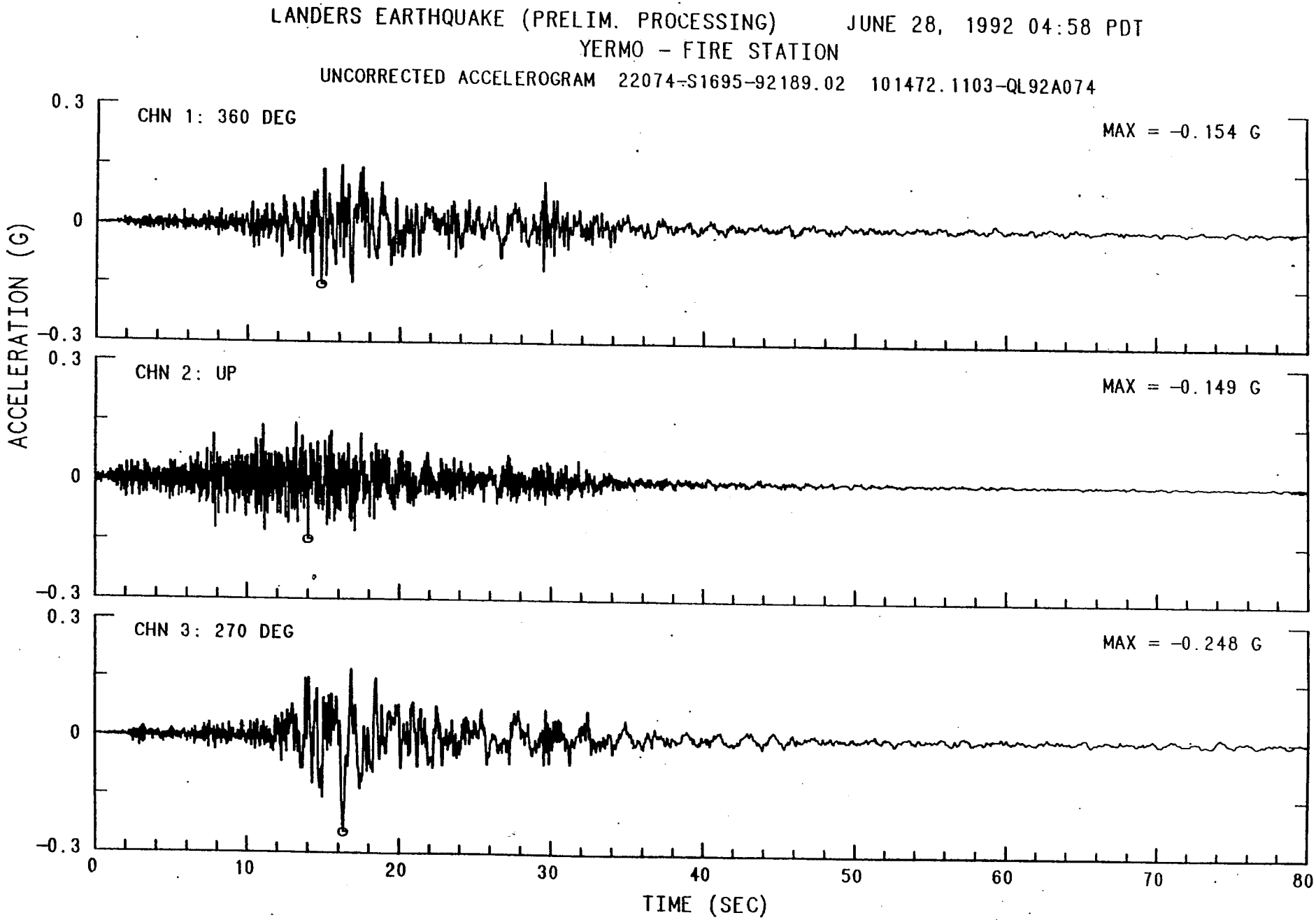
LANDERS EARTHQUAKE (PRELIM. PROCESSING) JUNE 28, 1992 04:58 PDT
YERMO - FIRE STATION
UNCORRECTED ACCELEROGRAM 22074-S1695-92189.02 101472.1103-QL92A074
CHN 1: 360 DEG
MAX = -0.154 G
CHN 2: UP
MAX = -0.149 G
CHN 3: 270 DEG
MAX = -0.248 G
ACCELERATION (G)
0.3
0
-0.3
0
10
20
30
40
50
60
70
80
TIME (SEC)

Figure 16.

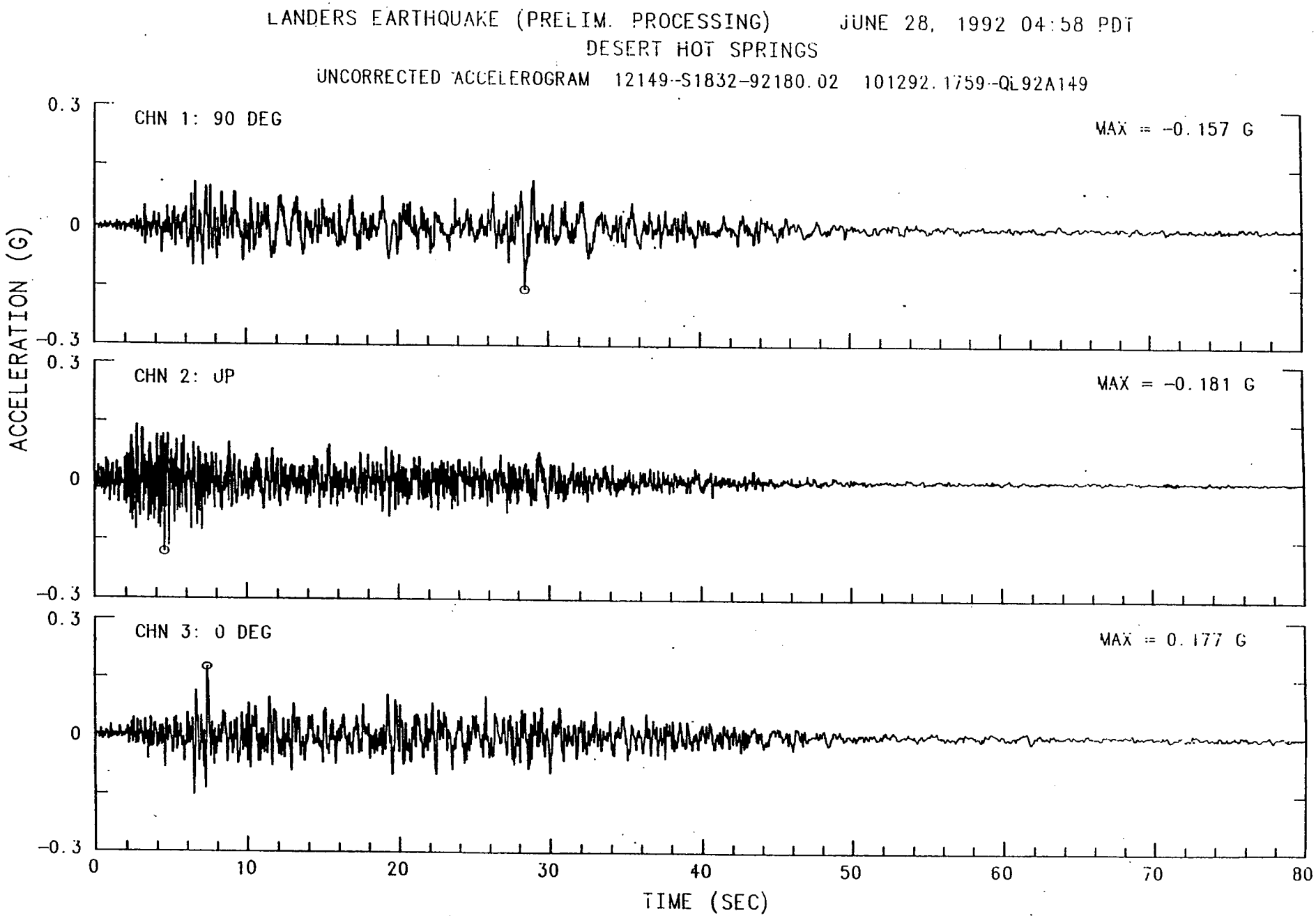
LANDERS EARTHQUAKE (PRELIM. PROCESSING) JUNE 28, 1992 04:58 PDT
DESERT HOT SPRINGS
UNCORRECTED ACCELEROGRAM 12149-S1832-92180.02 101292.1759-QL92A149
CHN 1: 90 DEG
MAX = -0.157 G
CHN 2: UP
MAX = -0.181 G
CHN 3: 0 DEG
MAX = 0.177 G
ACCELERATION (G)
0.3
0
-0.3
0
10
20
30
40
50
60
70
80
TIME (SEC)

Figure 17.

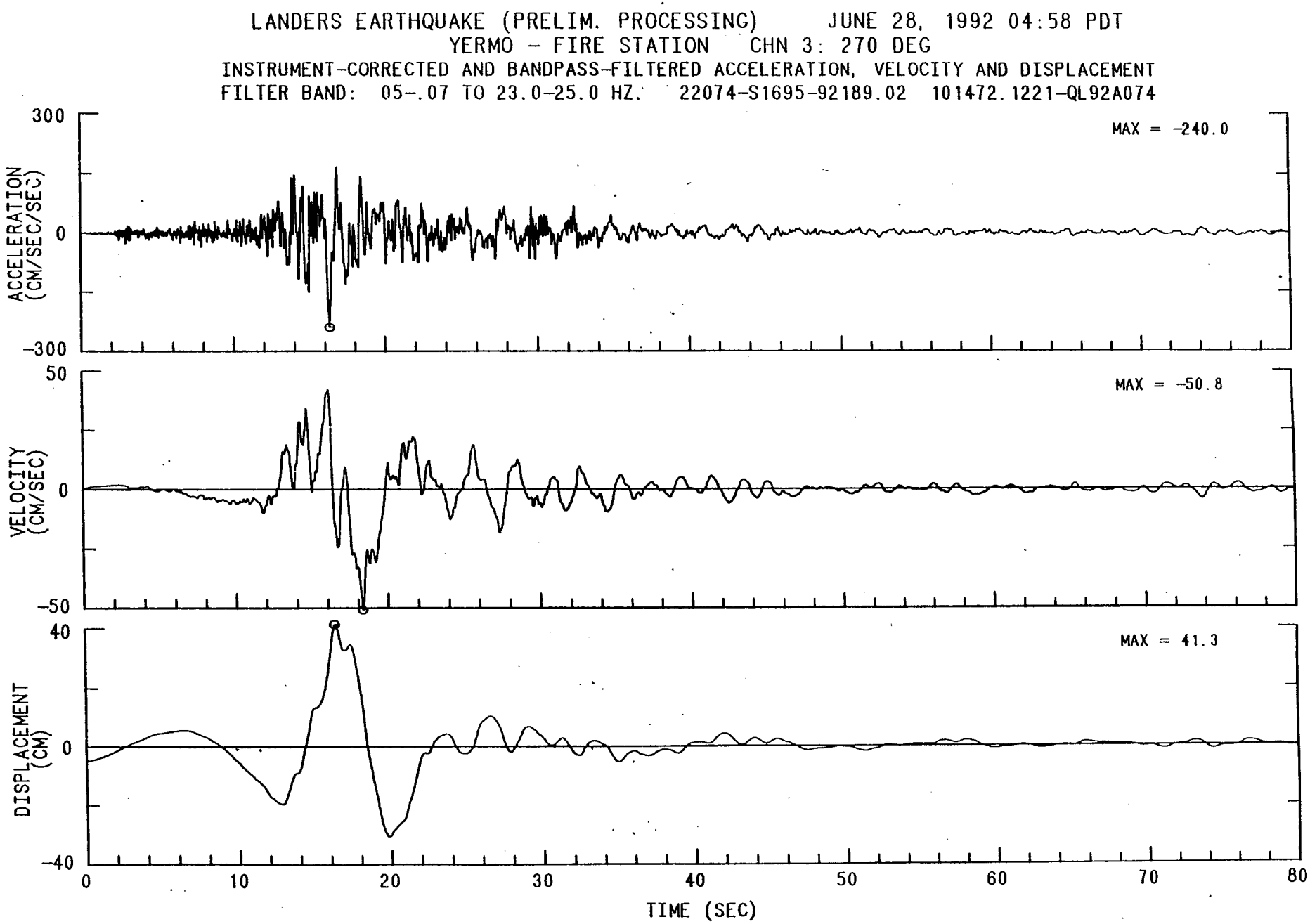
LANDERS EARTHQUAKE (PRELIM. PROCESSING) JUNE 28, 1992 04:58 PDT
YERMO - FIRE STATION CHN 3: 270 DEG
INSTRUMENT-CORRECTED AND BANDPASS-FILTERED ACCELERATION, VELOCITY AND DISPLACEMENT
FILTER BAND: 05-.07 TO 23.0-25.0 HZ. 22074-S1695-92189.02 101472.1221-QL92A074
ACCELERATION (CM/SEC/SEC)
MAX = -240.0
VELOCITY (CM/SEC)
MAX = -50.8
DISPLACEMENT (CM)
MAX = 41.3
TIME (SEC)

Figure 18.

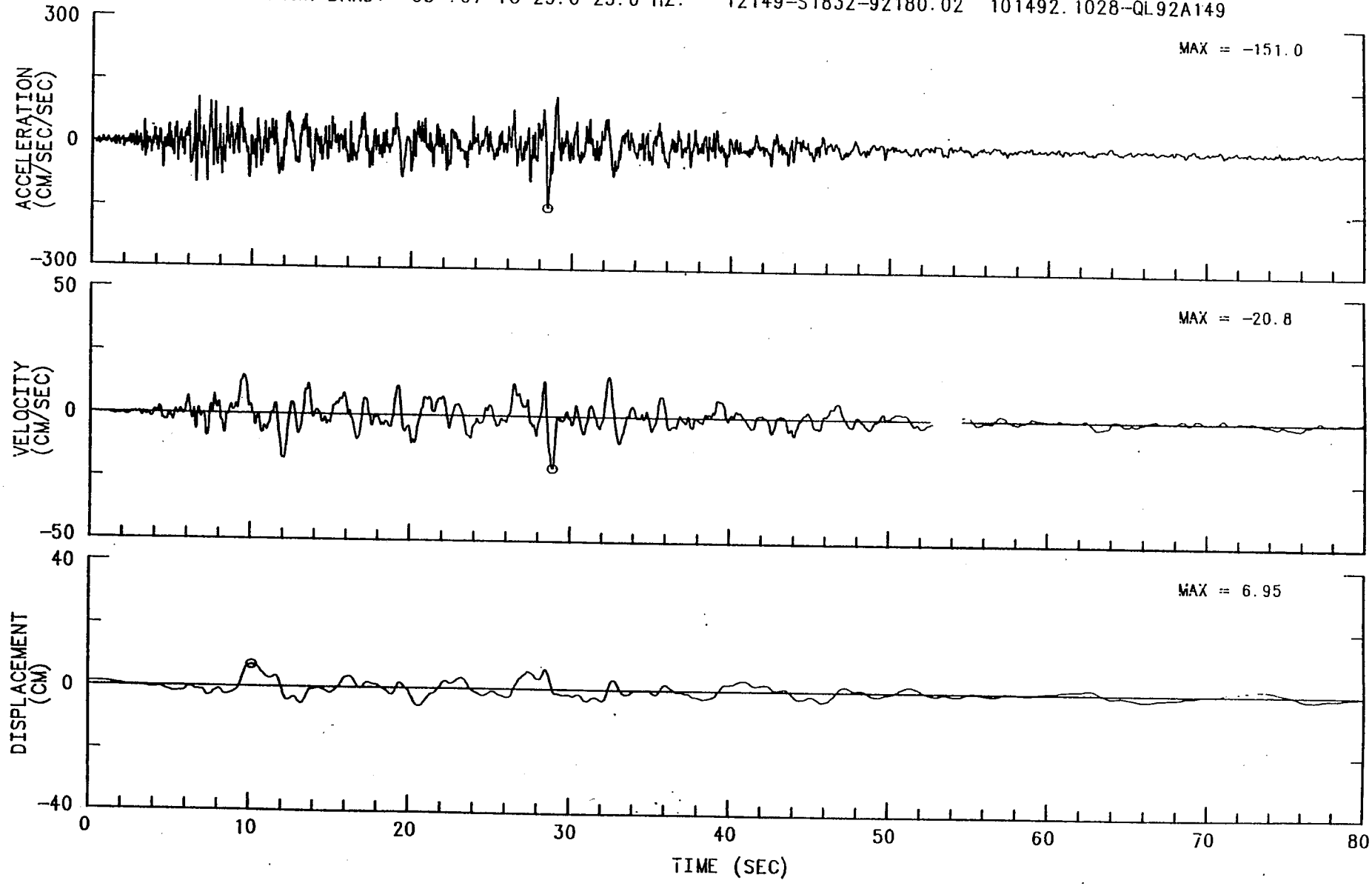
LANDERS EARTHQUAKE (PRELIM. PROCESSING) JUNE 28, 1992 04:58 PDT
DESERT HOT SPRINGS CHN 1: 90 DEG
INSTRUMENT-CORRECTED AND BANDPASS-FILTERED ACCELERATION, VELOCITY AND DISPLACEMENT
FILTER BAND: 05-.07 TO 23.0-25.0 HZ. 12149-S1832-92180.02 101492.1028-QL92A149
ACCELERATION (CM/SEC/SEC)
MAX = -151.0
VELOCITY (CM/SEC)
MAX = -20.8
DISPLACEMENT (CM)
MAX = 6.95
TIME (SEC)

Figure 19.

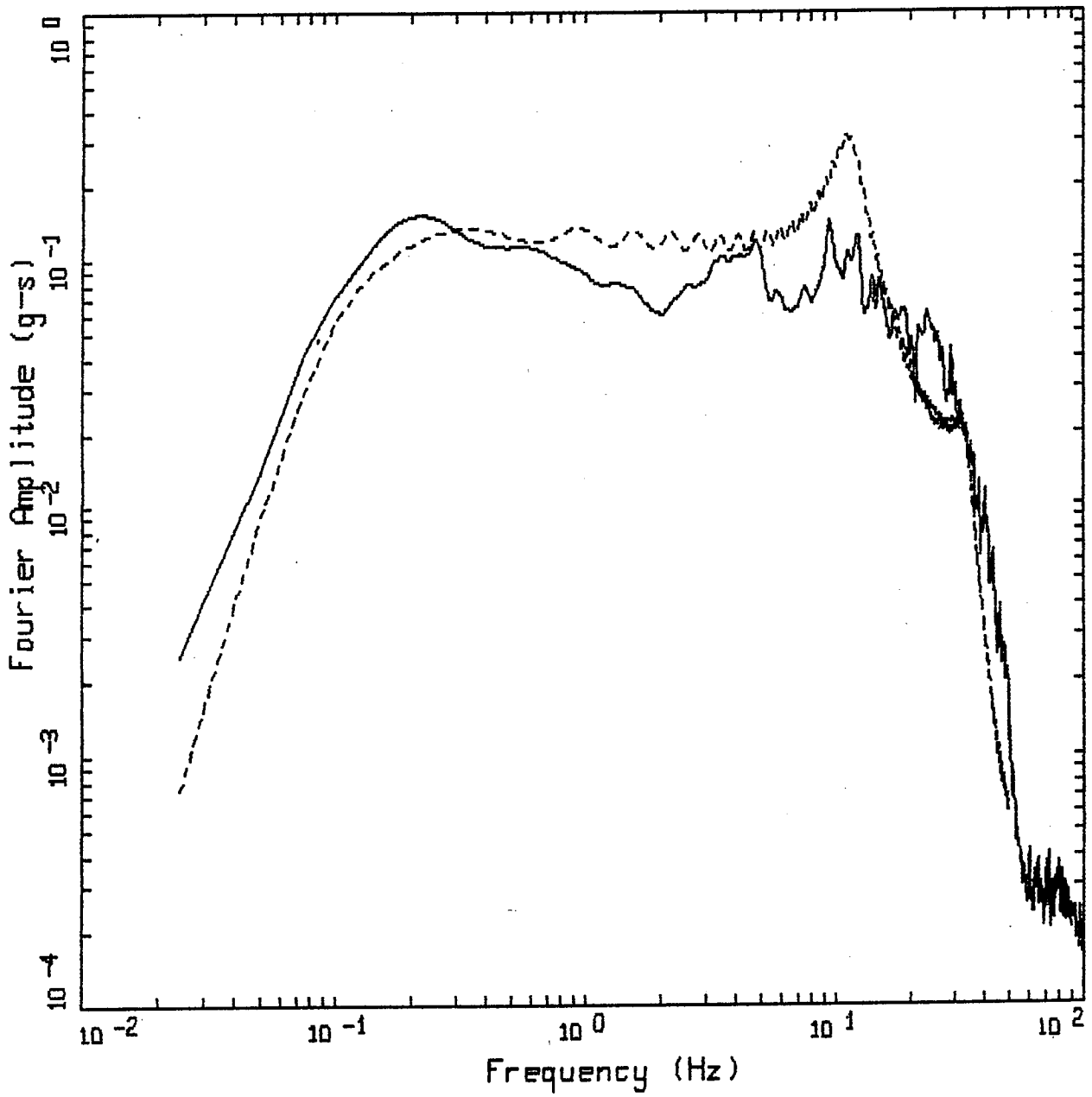

LANDERS EARTHQUAKE 06/28/92
LUCERNE TRANSVERSE COMPONENT

LEGEND

——— FROM RECORDINGS (1-HZ SMOOTHING)

----- RVT: 20FT ENA PROFILE

Figure 20.

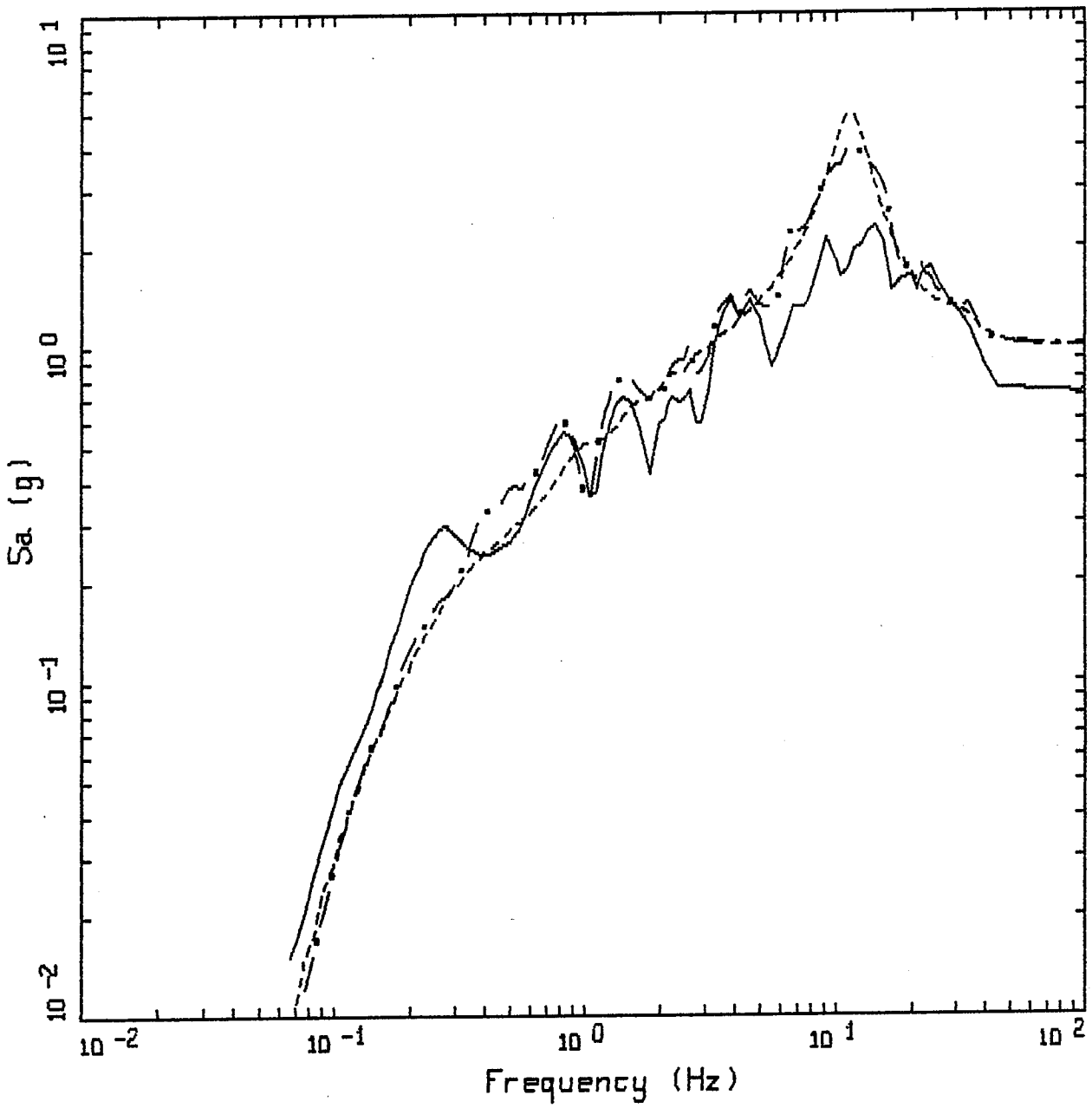

LANDERS EARTHQUAKE 06/28/92
TRANSVERSE COMPONENT

LEGEND

——— 5 %, FROM RECORDINGS, PGA = 0.72 g

- - - - - 5 %, RVT: 20FT ENA PROFILE, PGA = 0.97 G

—·— 5 %, SDF: 20FT ENA PROFILE, PGA = 0.97 G

Figure 21.

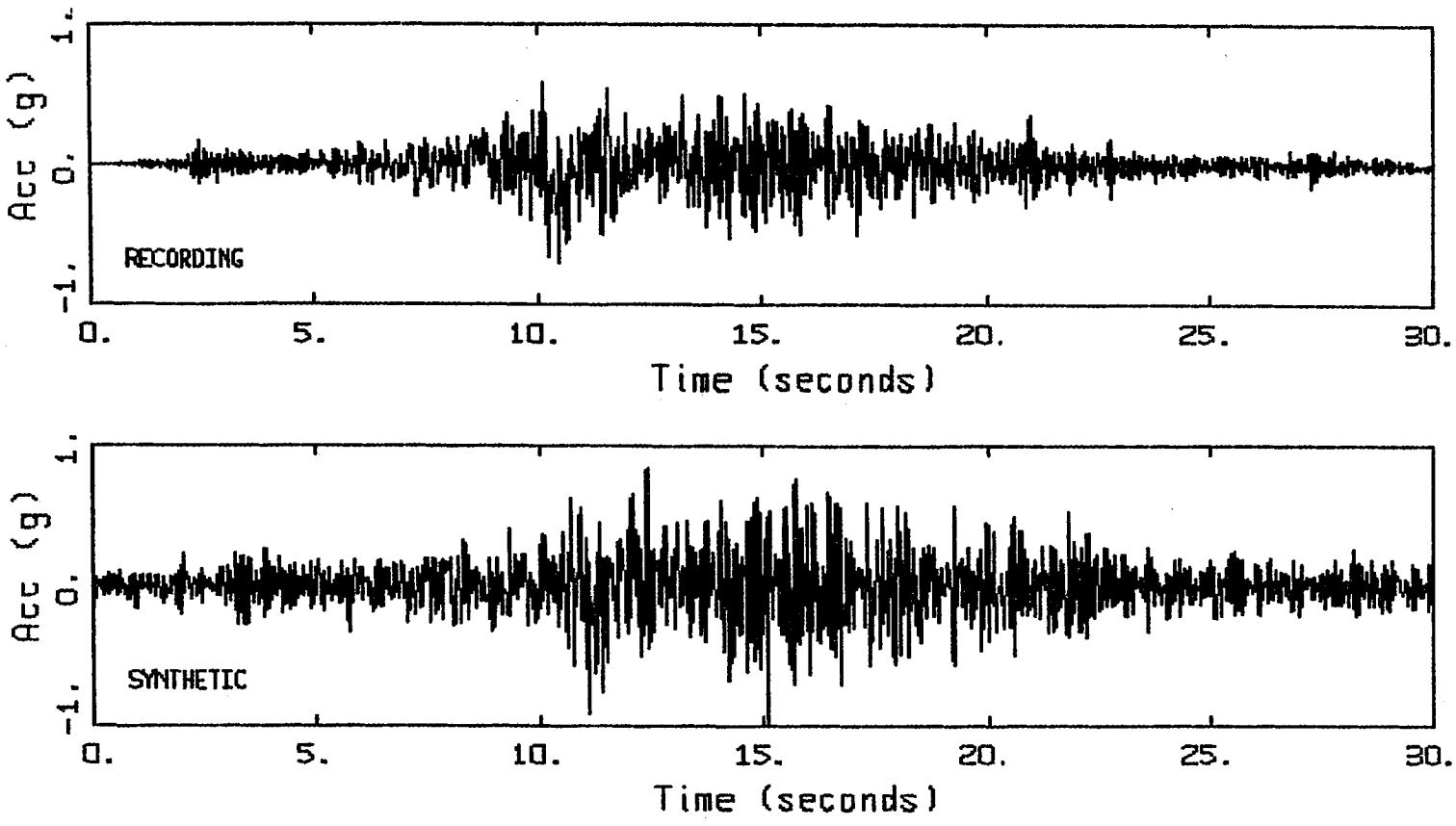

LANDERS EARTHQUAKE 06/28/92, TRANSVERSE COMPONENT

Figure 22.

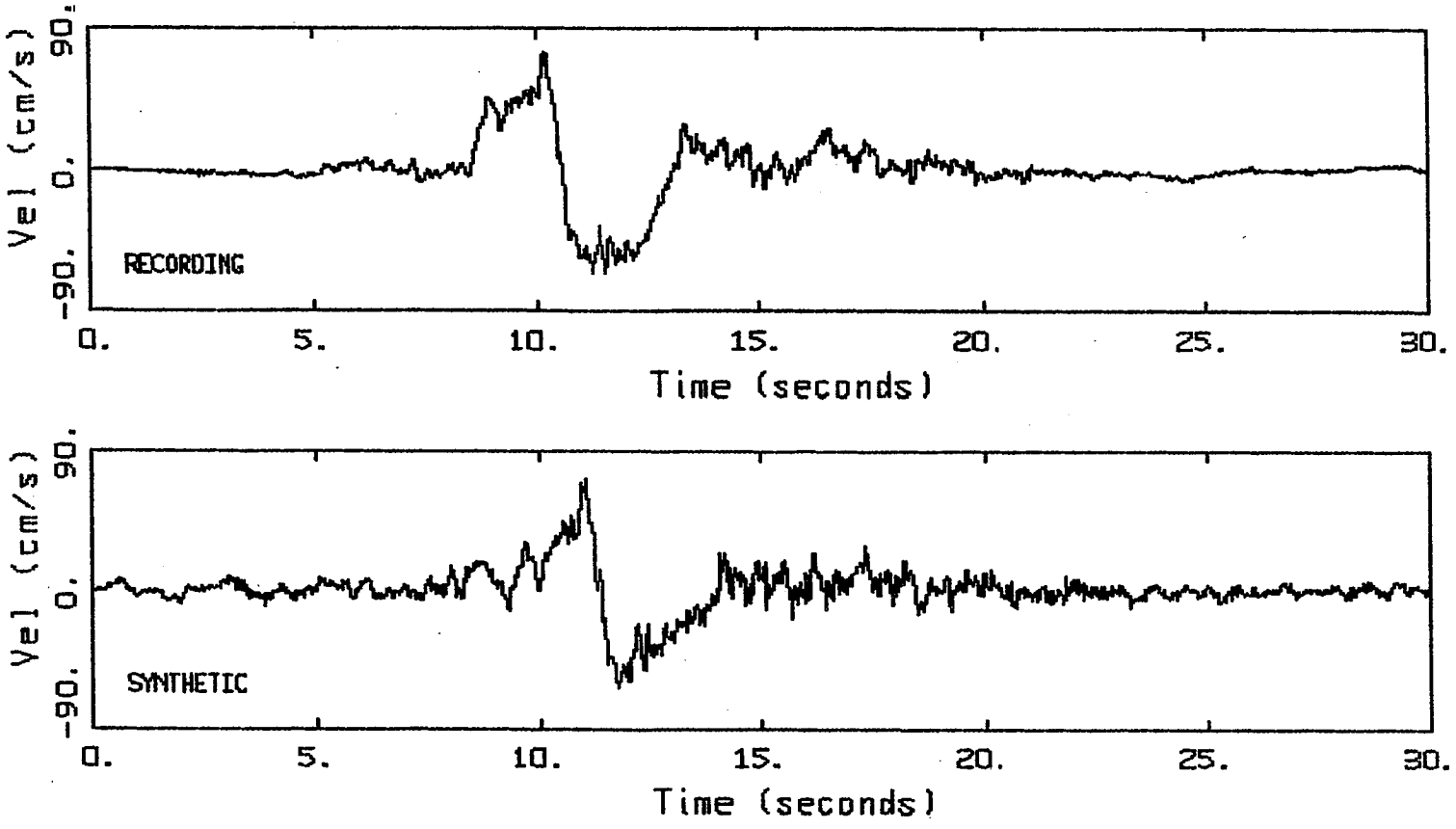

LANDERS EARTHQUAKE 06/28/92, TRANSVERSE COMPONENT

Figure 23.

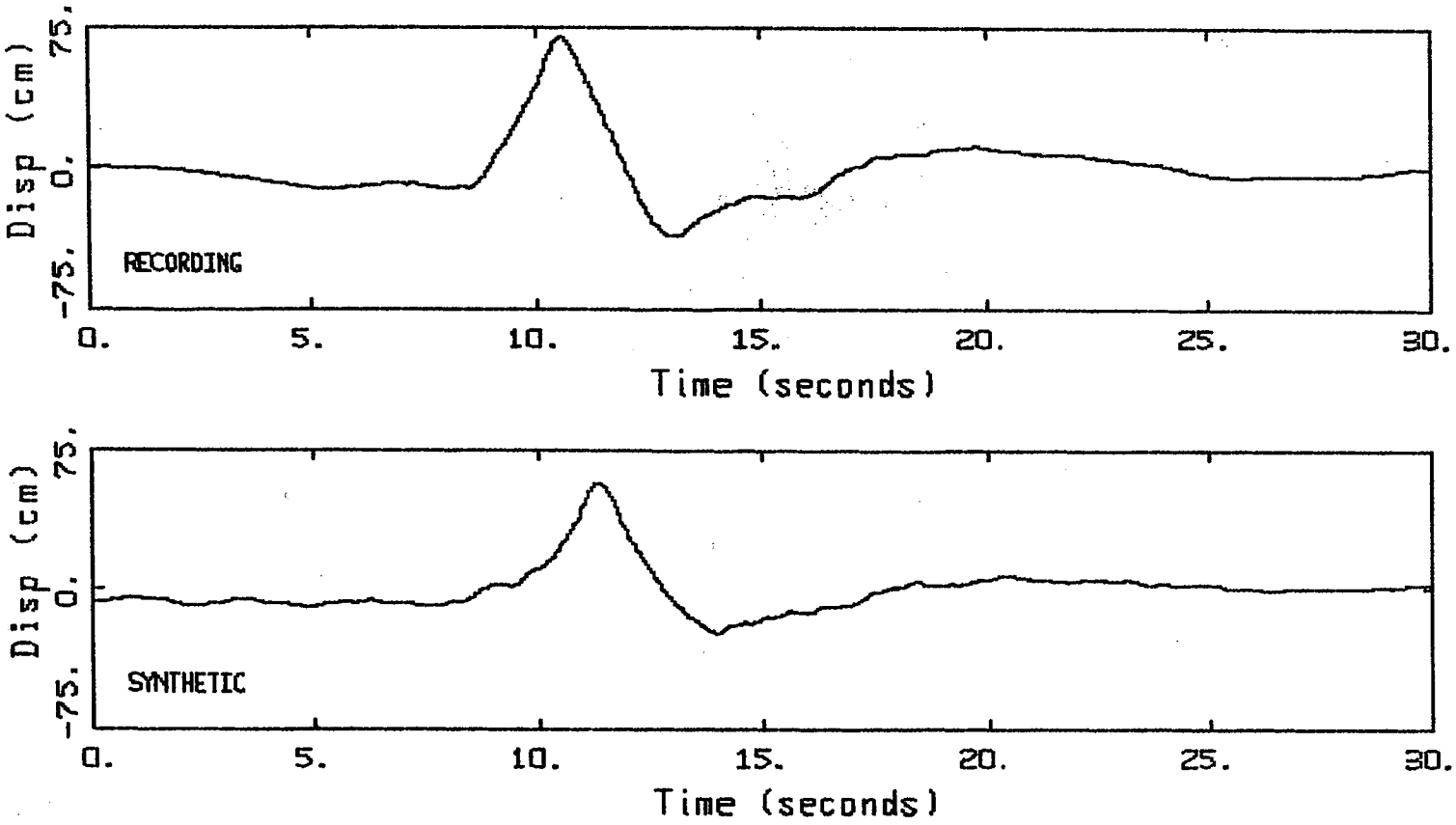

LANDERS EARTHQUAKE 06/28/92, TRANSVERSE COMPONENT

Figure 24.

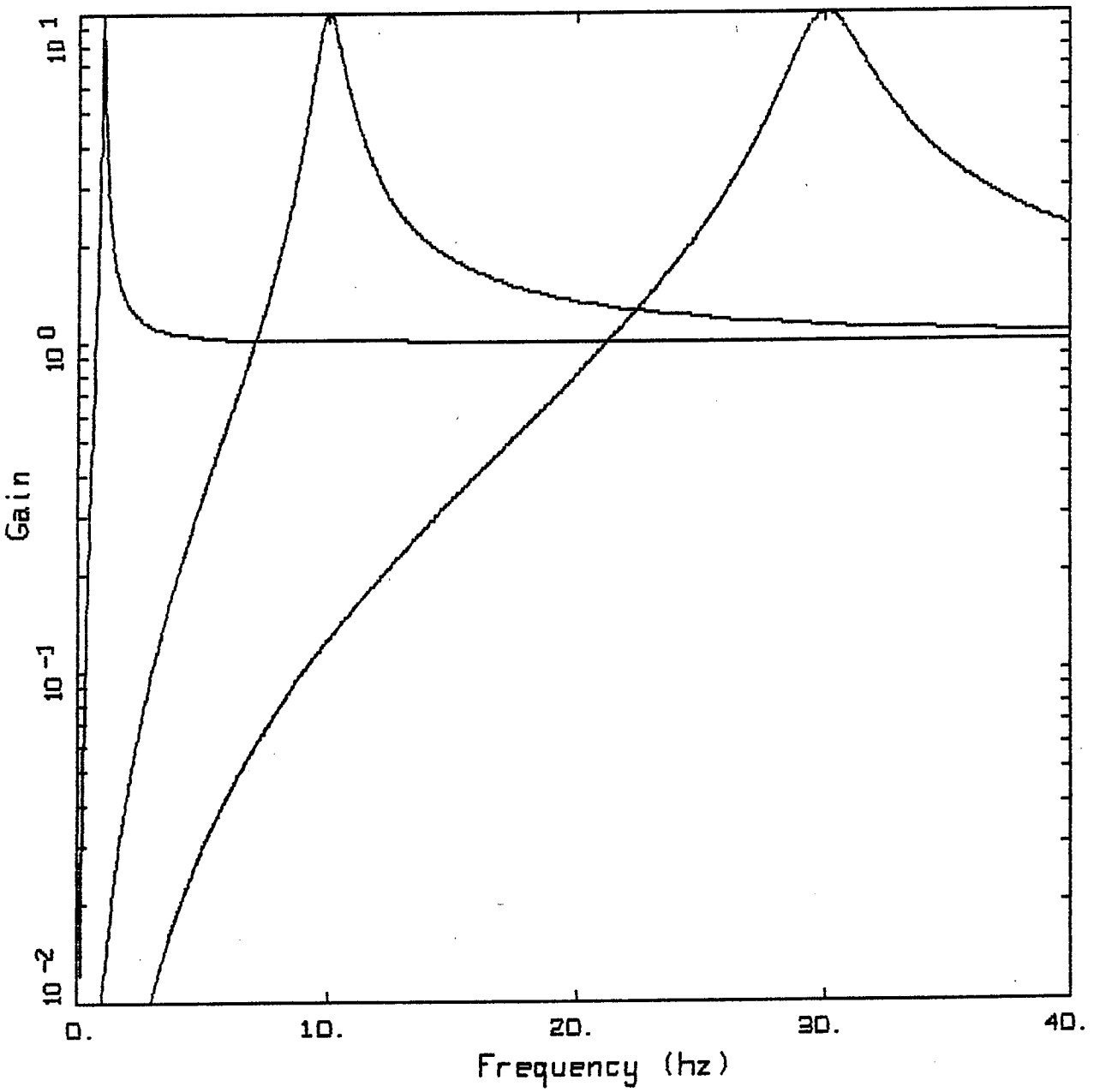

OSCILLATOR TRANSFER FUNCTION, DAMPING = 5%

LEGEND

NATURAL FREQUENCY = 1.0 HZ

NATURAL FREQUENCY = 10.0 HZ

NATURAL FREQUENCY = 30.0 HZ

Figure 25.

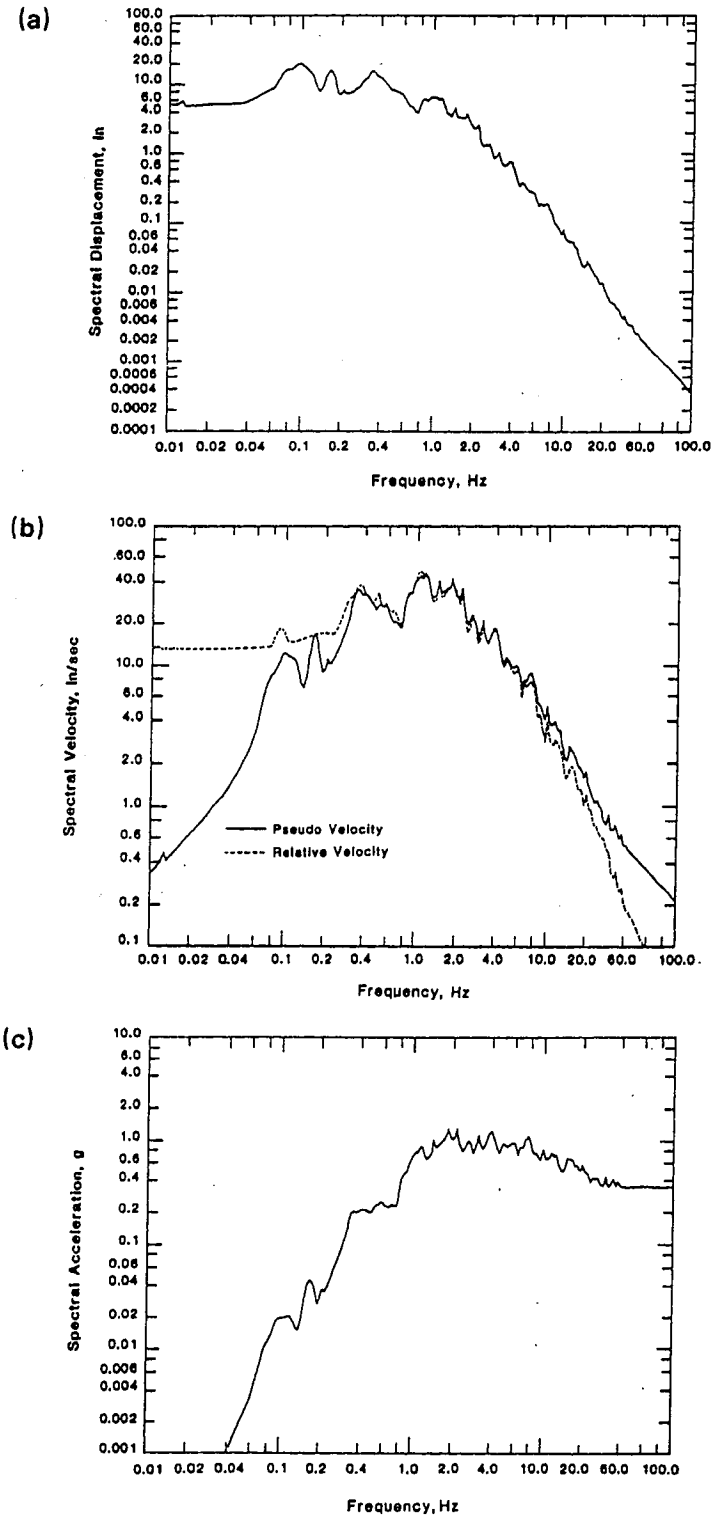

Figure 26. (a) Displacement response spectrum, (b) Velocity response spectra, (c) Acceleration response spectrum for El Centro earthquake (SOOE, 1940); damping ratio, ζ = 0.02.

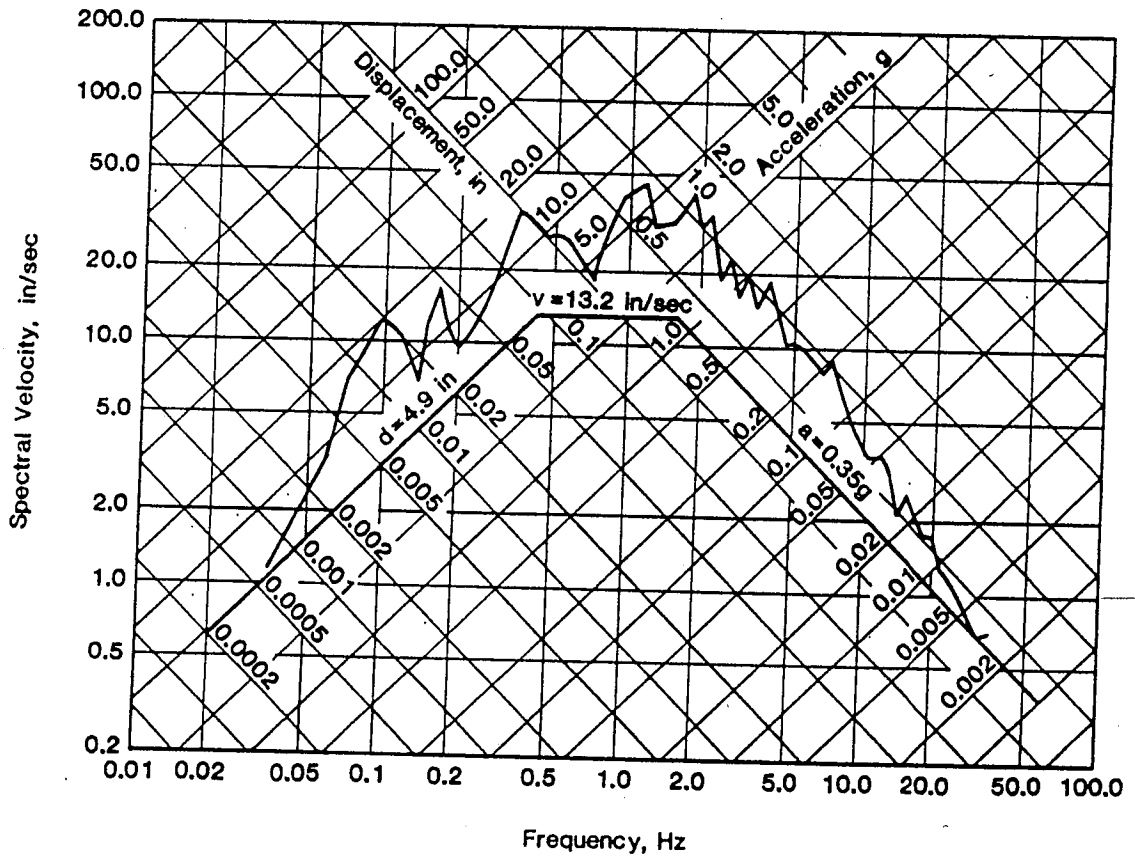

Figure 27. Tripartite response spectrum for El Centro earthquake (SOOE, 1940); damping ration, $\zeta = 0.02$.

1) Figures 28 - 36 illustrating general differences in strong ground motions at typical rock and deep stiff soil sites.

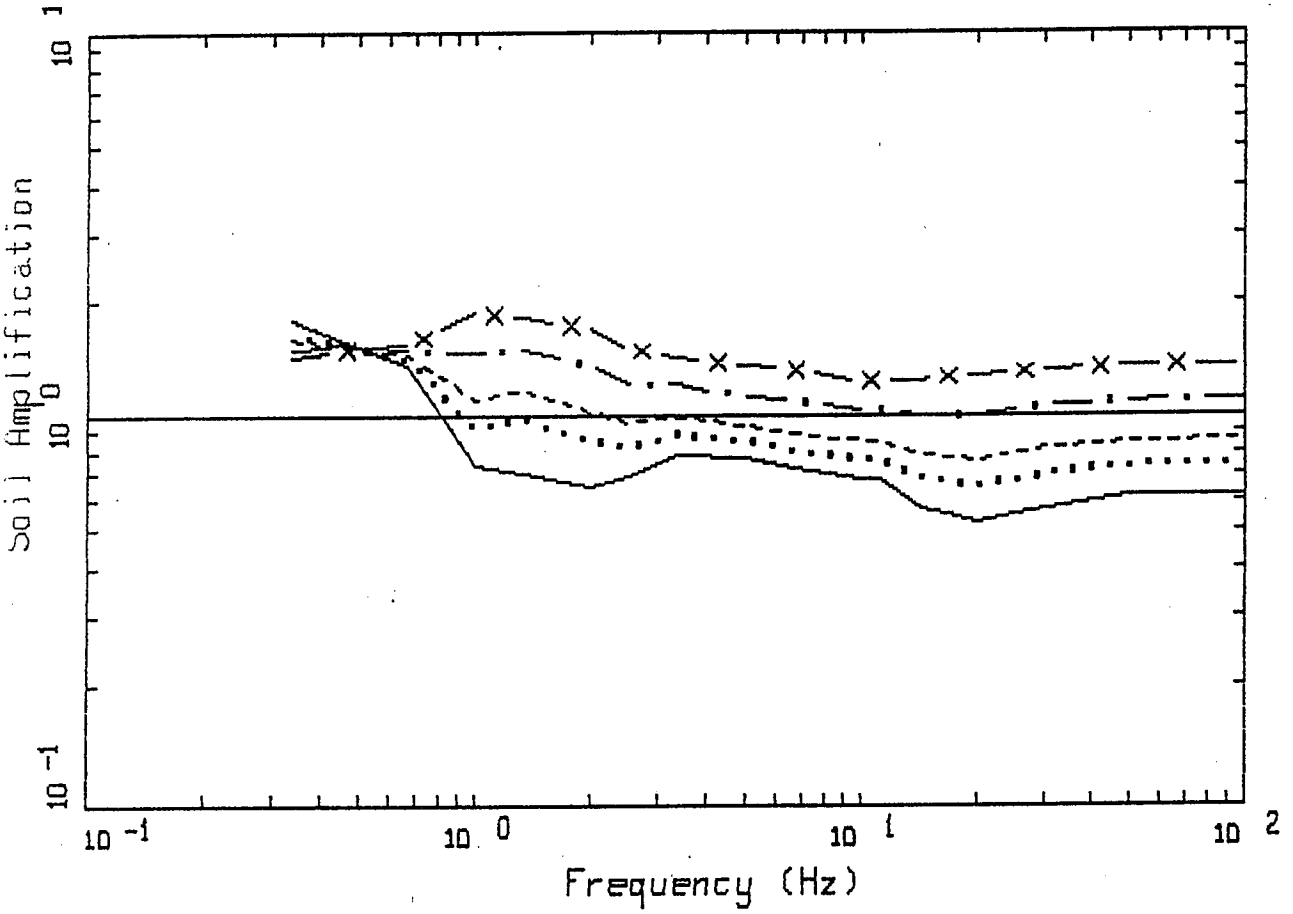

WNA EMPIRICAL M 6.5
DEEP, FIRM

LEGEND

———	R = 1.0 KM, ROCK PGA = 0.73 g
. . . .	R = 5.0 KM, ROCK PGA = 0.40 g
- - - - -	R = 10.0 KM, ROCK PGA = 0.25 g
— . —	R = 25.0 KM, ROCK PGA = 0.11 g
—×—	R = 50.0 KM, ROCK PGA = 0.06 g

Figure 28.

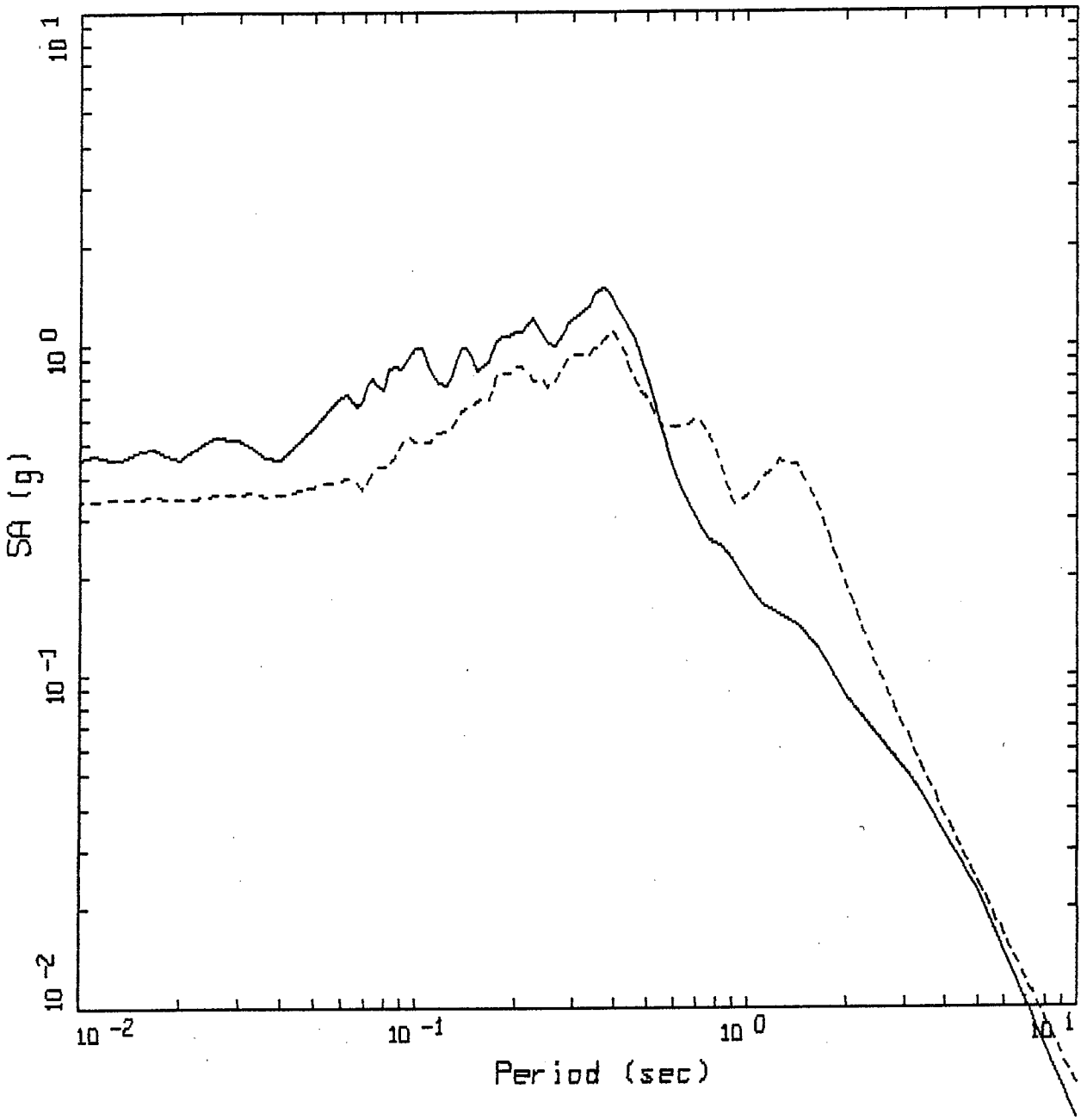

LOMA PRIETA, M = 6.9

LEGEND

GILROY 1, rock

GILROY 2, deep stiff soil (650 ft)

Figure 29.

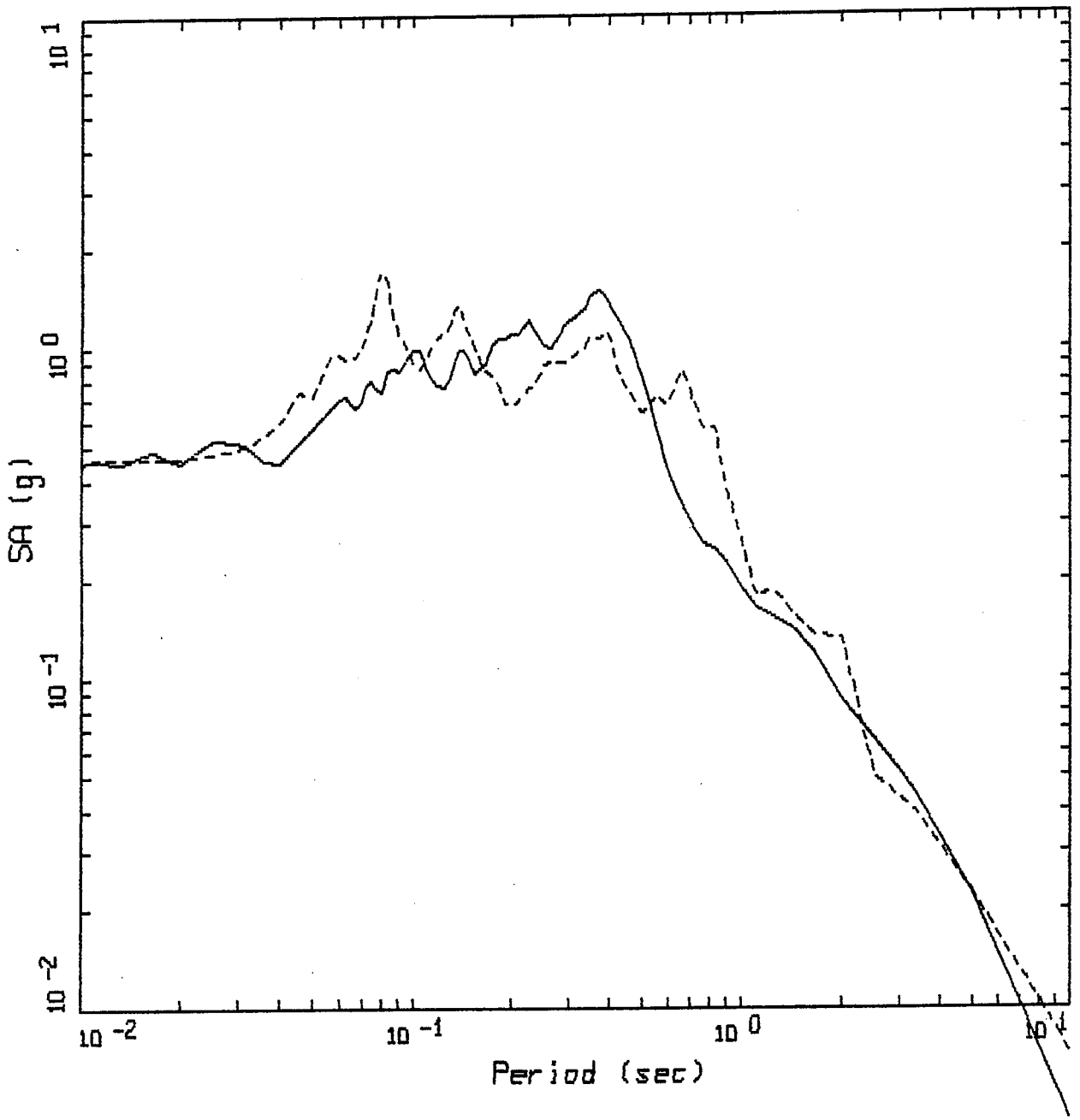
SA (g)
10 1
10 0
10 -1
10 -2
10 -2
10 -1
10 0
Period (sec)
LOMA PRIETA, M = 6.9
LEGEND
GILROY 1, rock, recorded motions
GILROY 1, rock, computed motions

Figure 30.

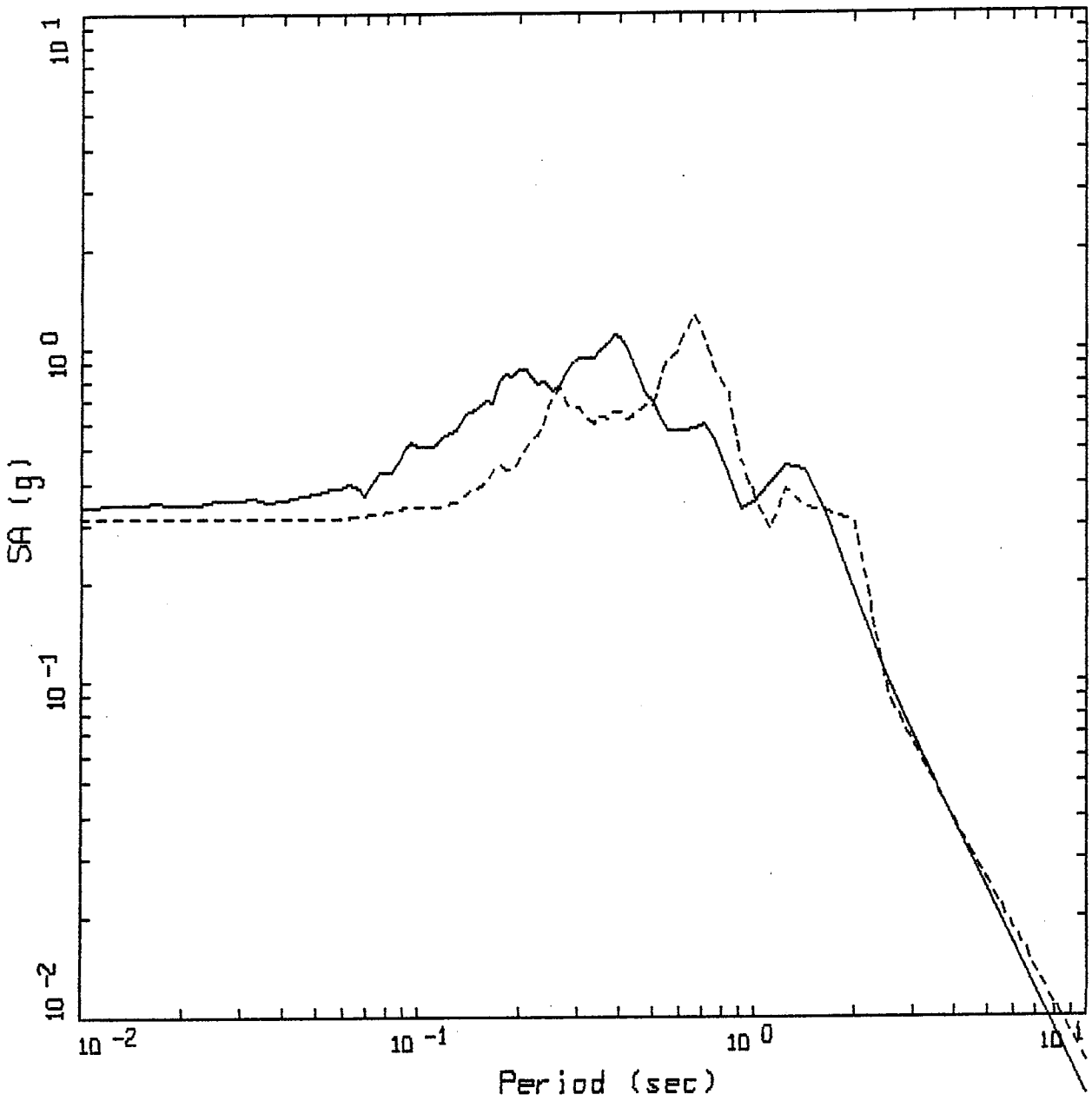

LOMA PRIETA, M = 6.9

LEGEND

——— GILROY 2, deep stiff soil (650 ft), recorded motions

----- GILROY 2, deep stiff soil (650 ft), computed motions

Figure 31.

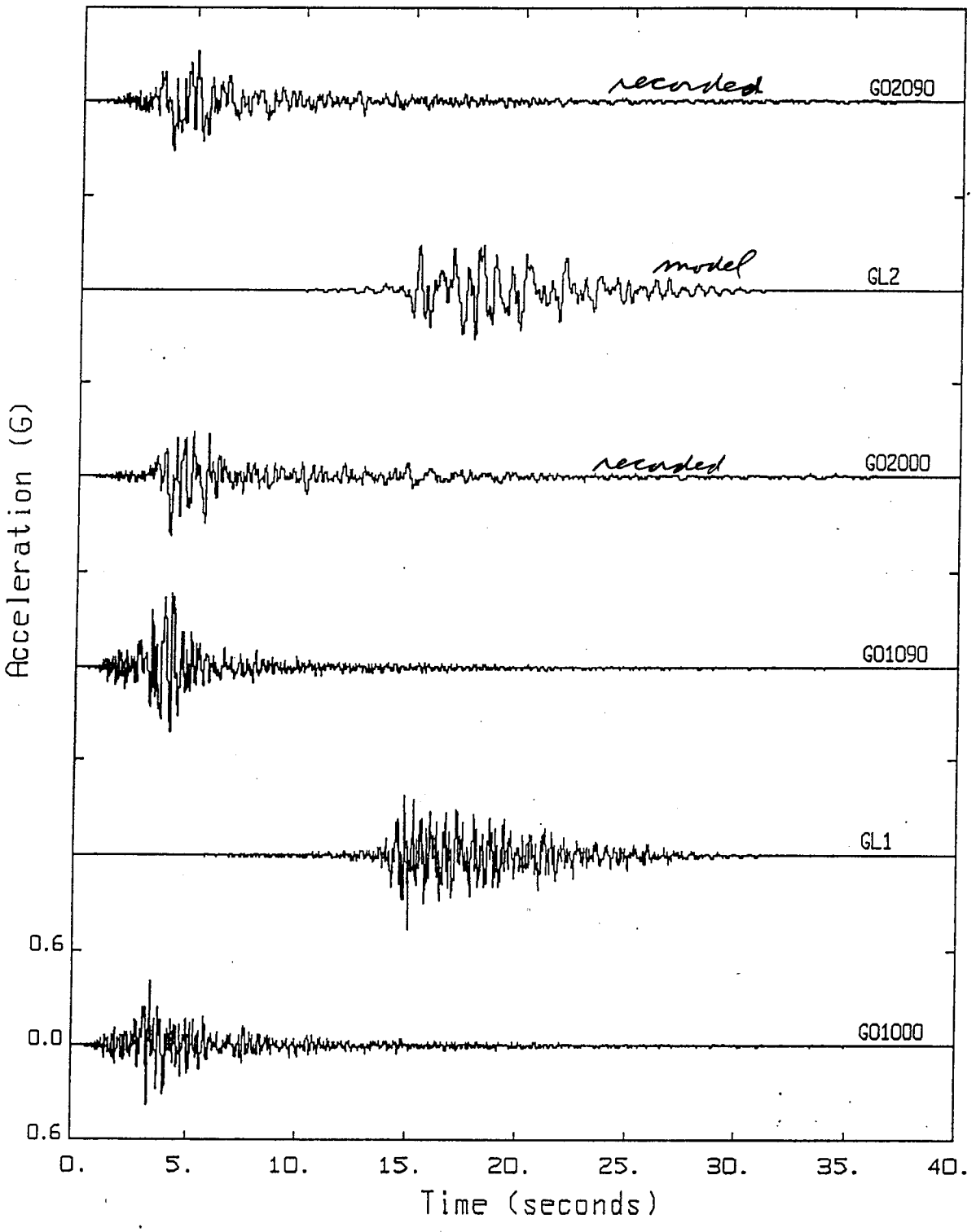

Figure 32. LOMA PRIETA

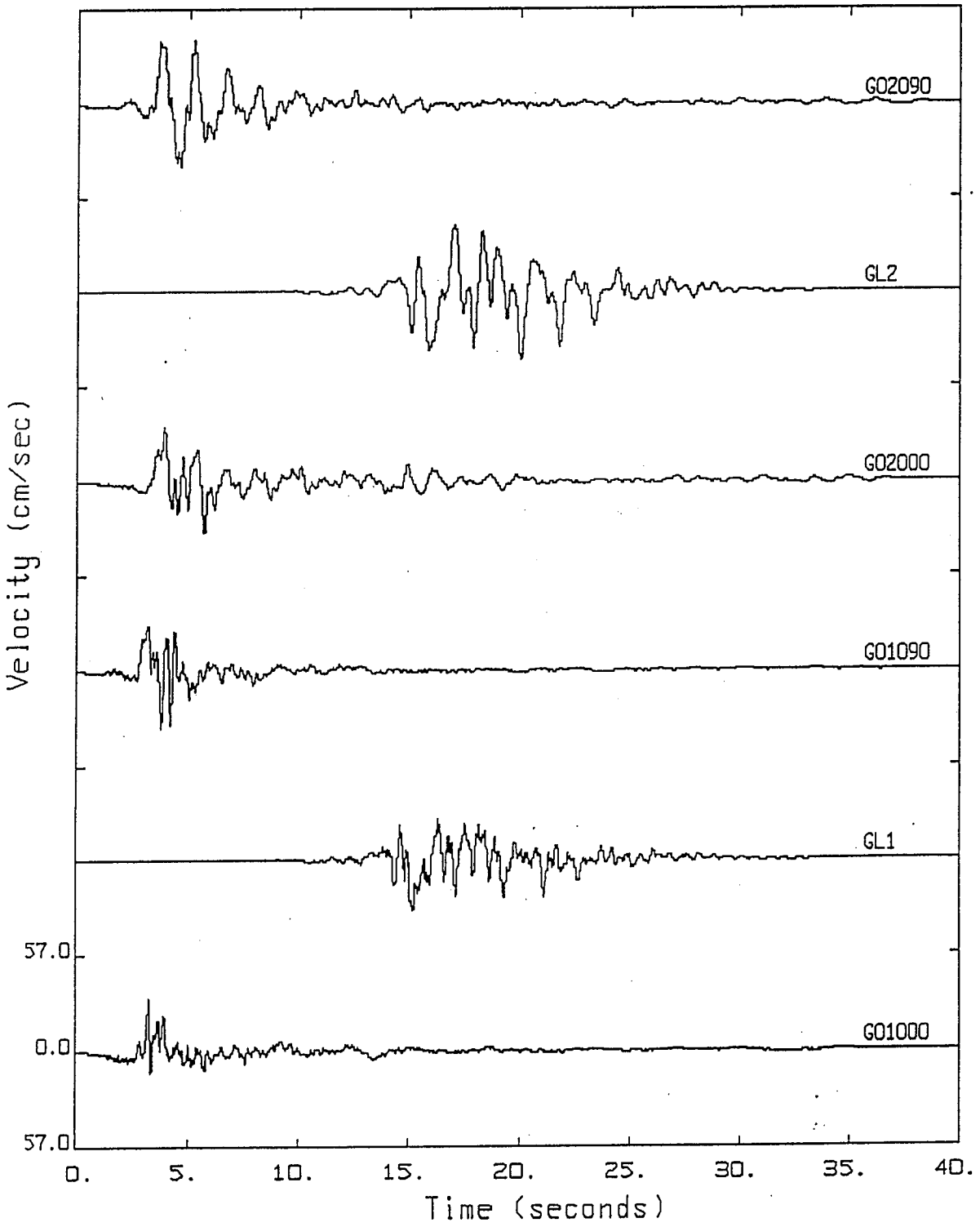

Figure 33. LOMA PRIETA

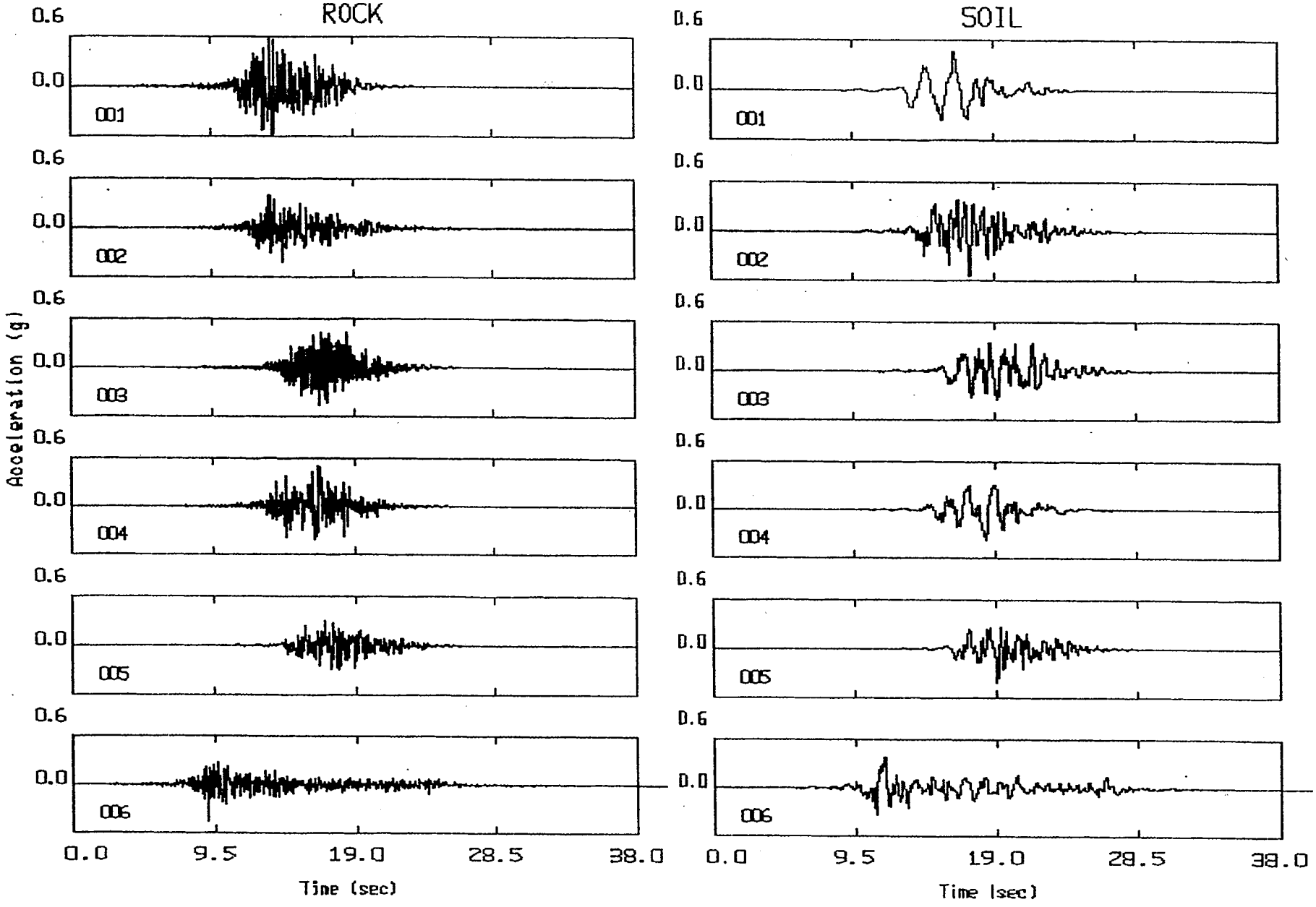

Figure 35.

M 7, Parametric Variations

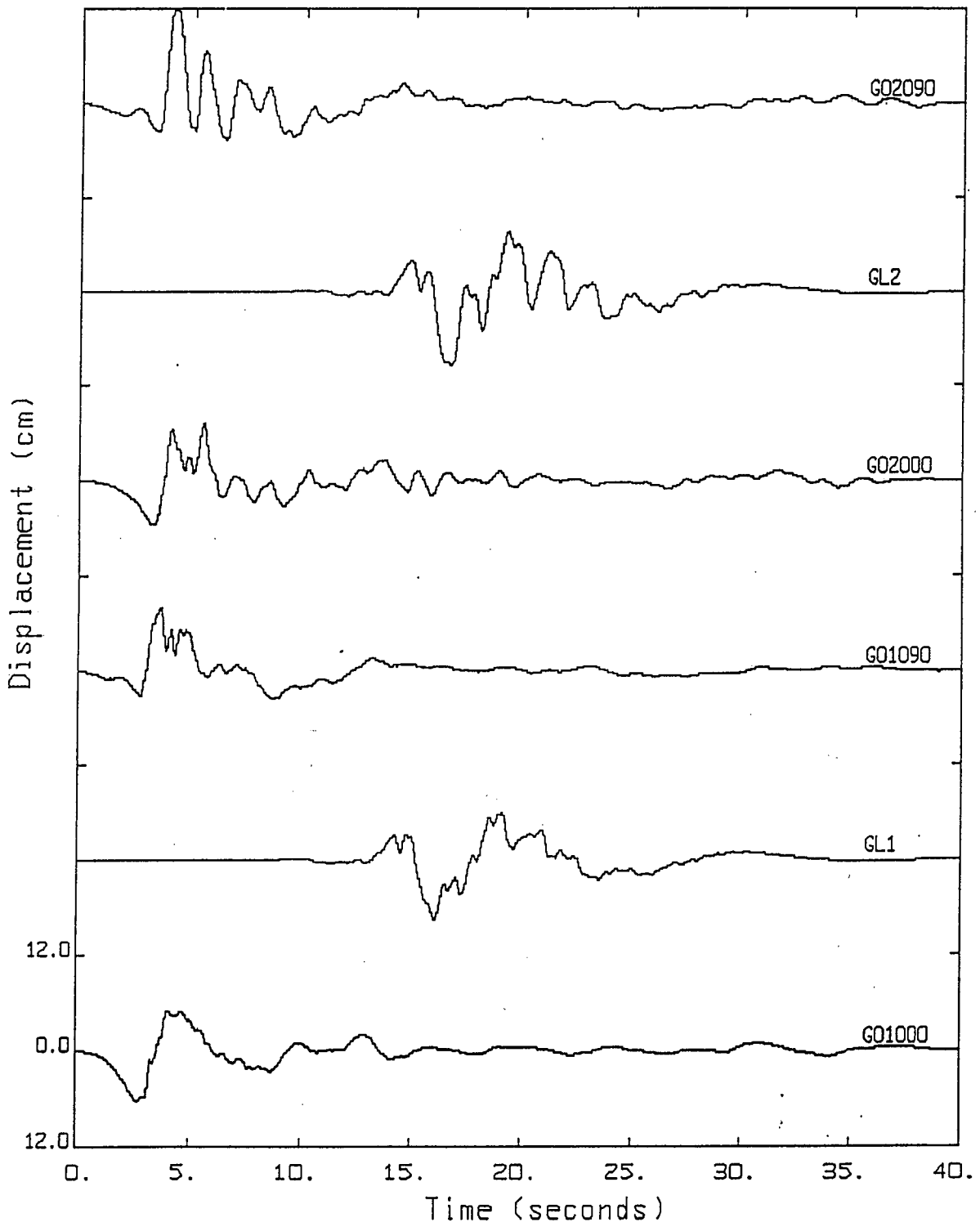

Figure 34. LOMA PRIETA

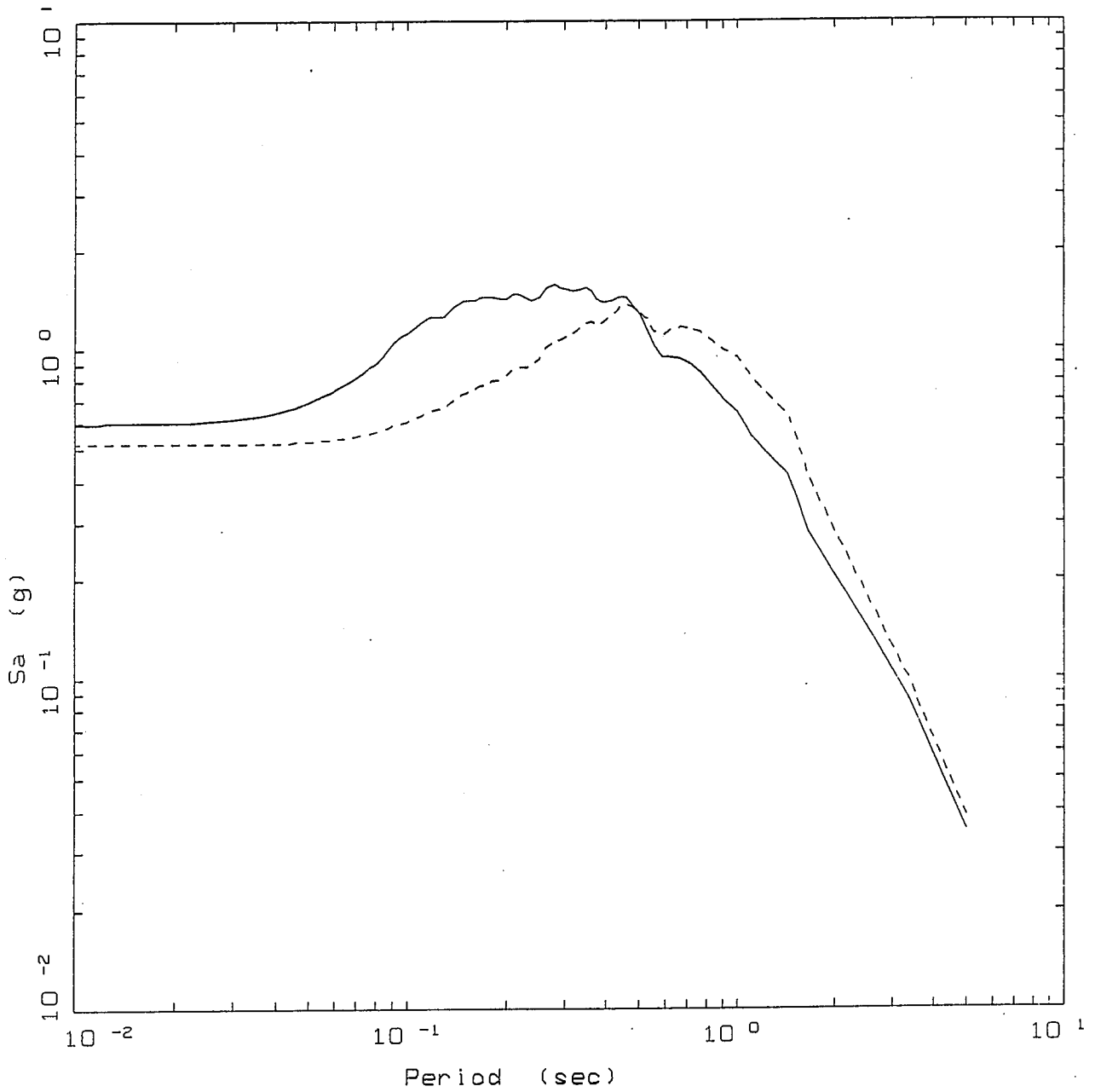

HAYWARD, M 6.8
SITES 6, 7, & 8, D = 0.2 KM

LEGEND

——— 5 %, ALL FOCI, ROCK SITE, PGA = 0.599 G

- - - - - 5 %, ALL FOCI, SOIL SITE, PGA = 0.519 G

Figure 36.

2) Figures 37 - 43 illustrating the effects of earthquake magnitude on strong ground motions at rock sites.

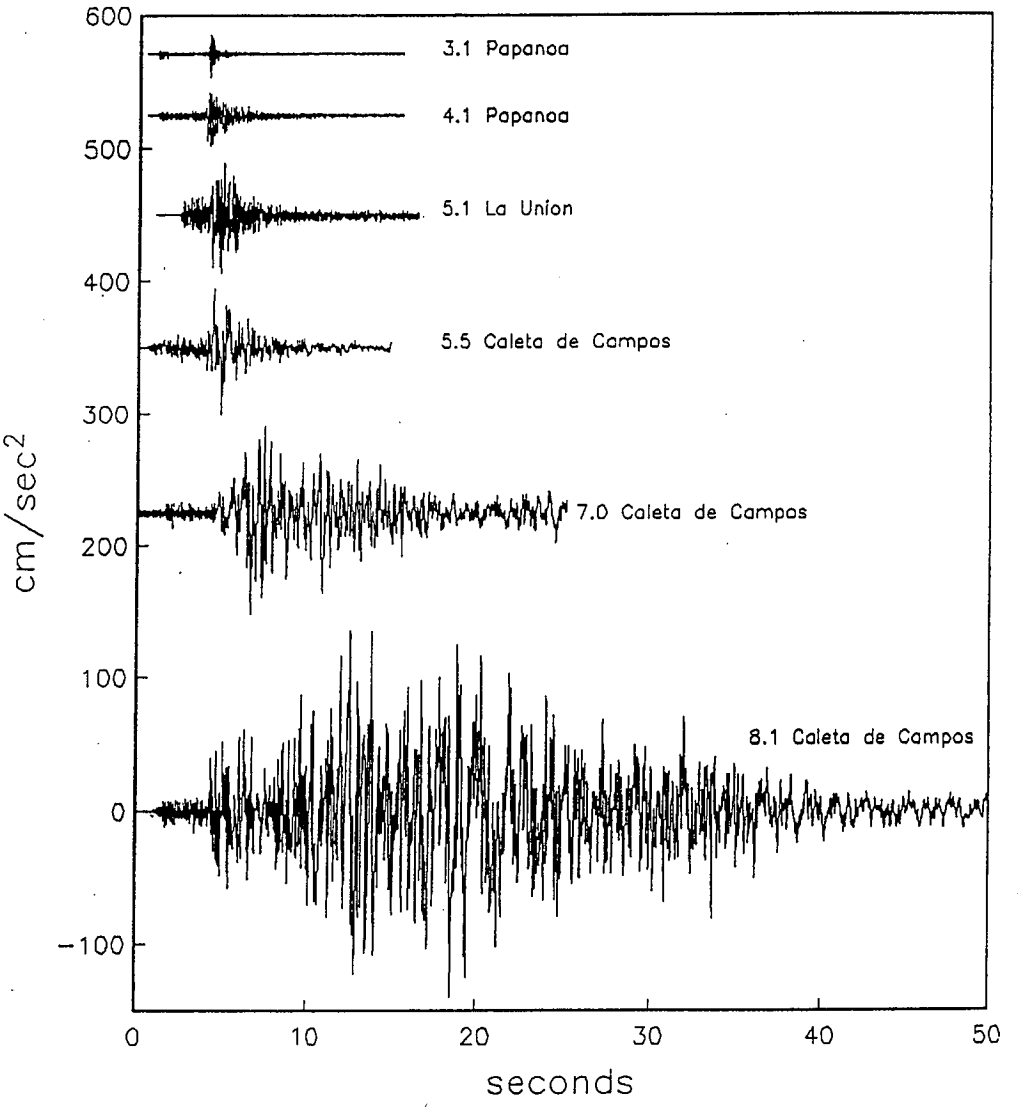

Figure 37. - An example of accelerograms recorded in 1985 and 1986 on the Guerrero accelerograph array. All events have epicenters about 25 km from the station, and all stations are on hard rock.

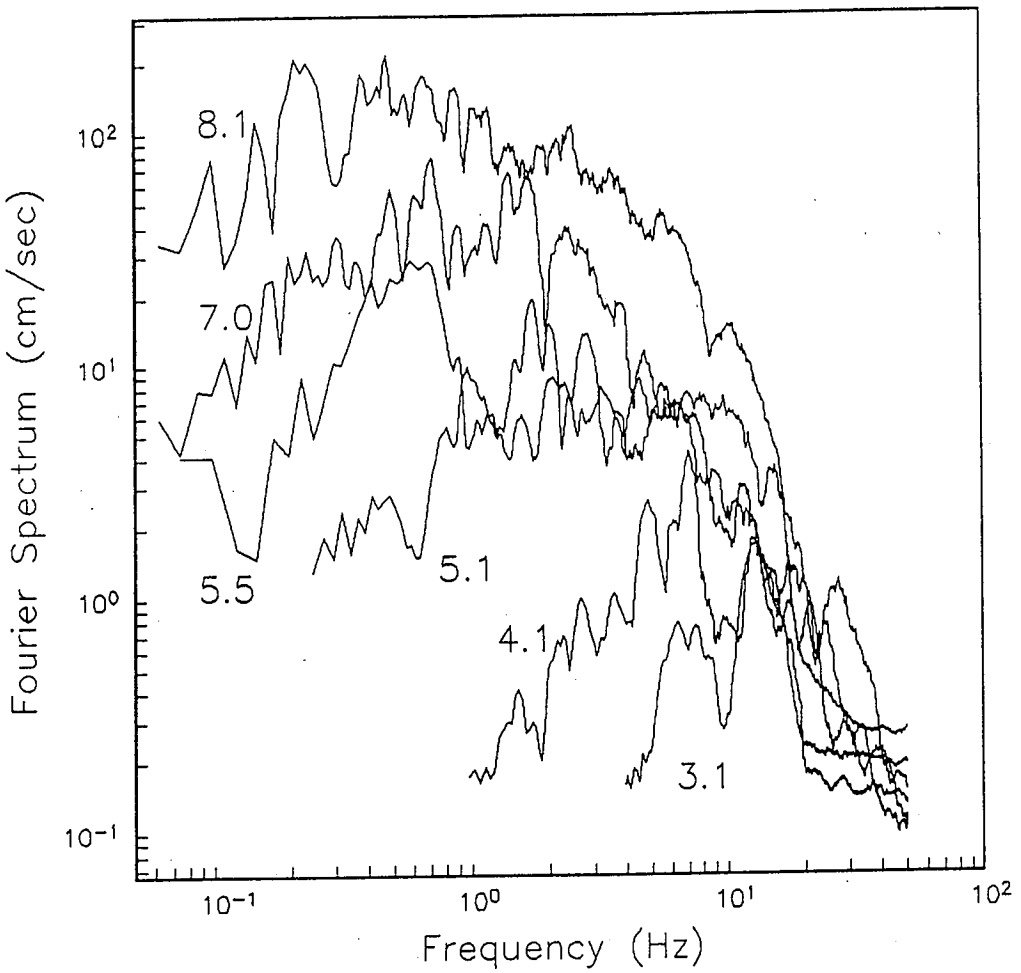

Figure 38. - Fourier amplitude spectra (whole record).

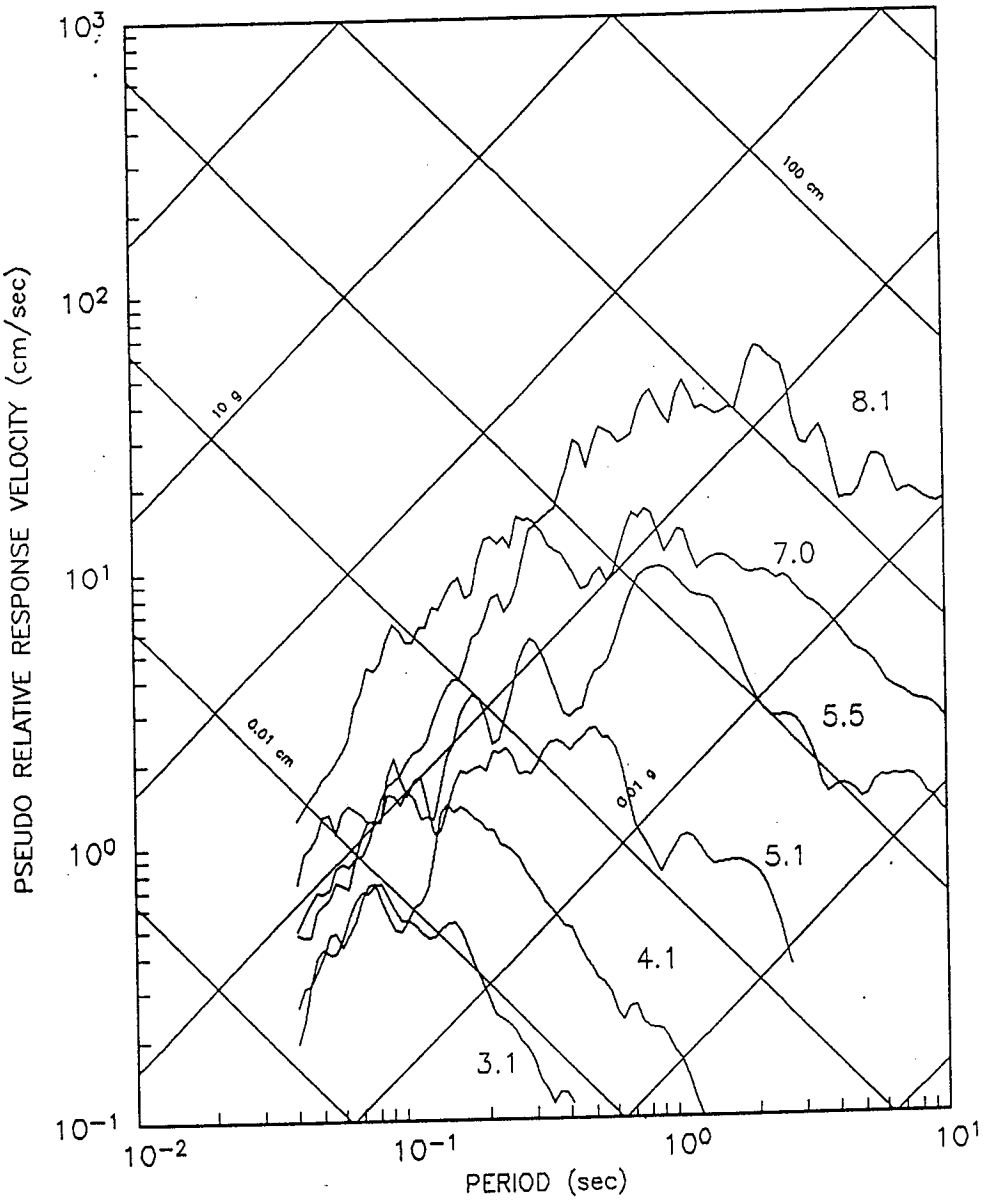

Figure 39. - Response spectra (5% damped, Pseudorelative velocity) corresponding to the acceleration traces.

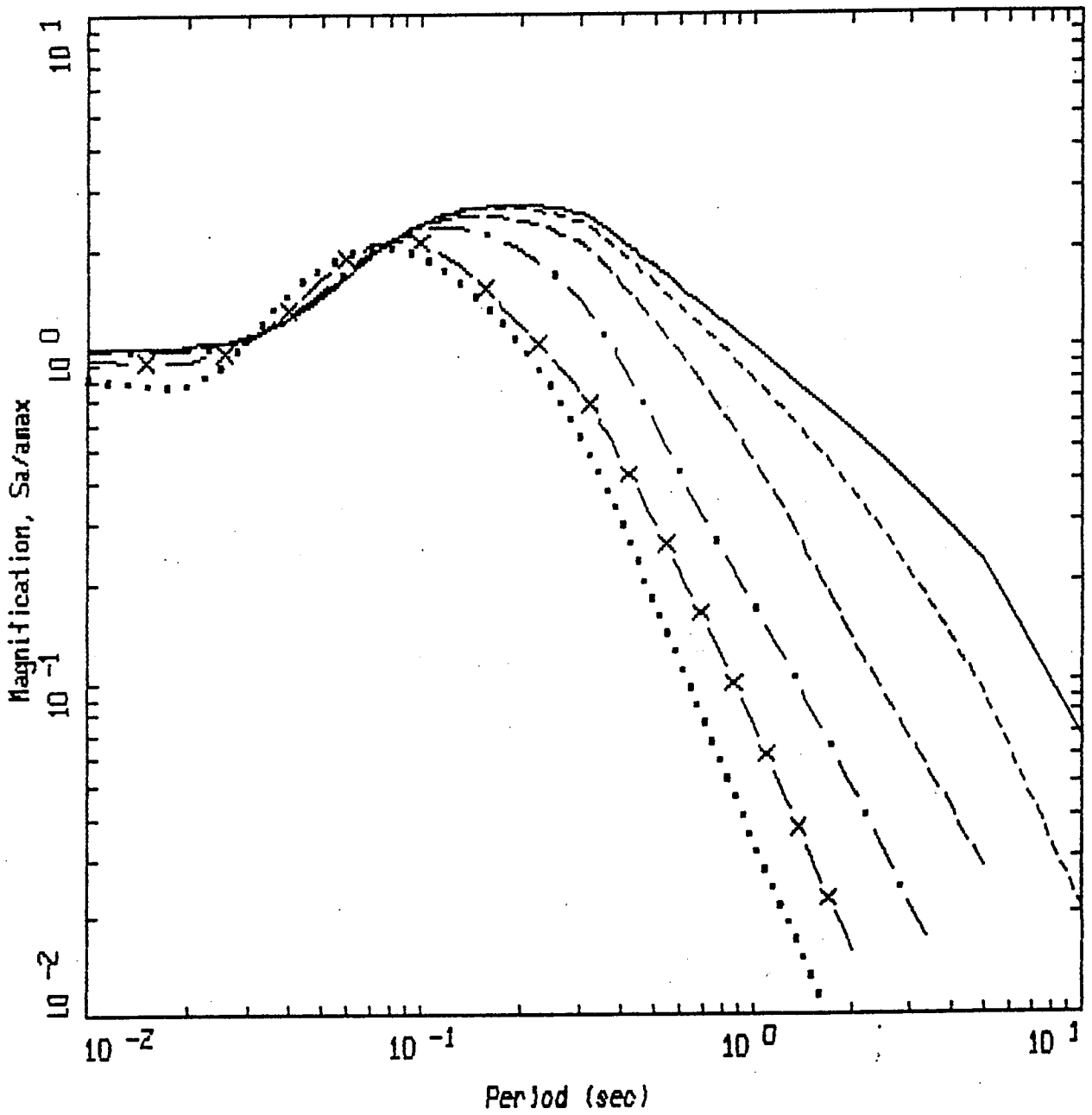

Figure 40. Comparison of 5%-damped response spectral shapes (Sa/a) computed for WNA parameters (Table 2-3). Note the shift in peak response to longer period with increasing moment magnitude. Starting with the lowest curve, M = 2.5, 3.5, 4.5, 5.5, 6.5 and 7.5.

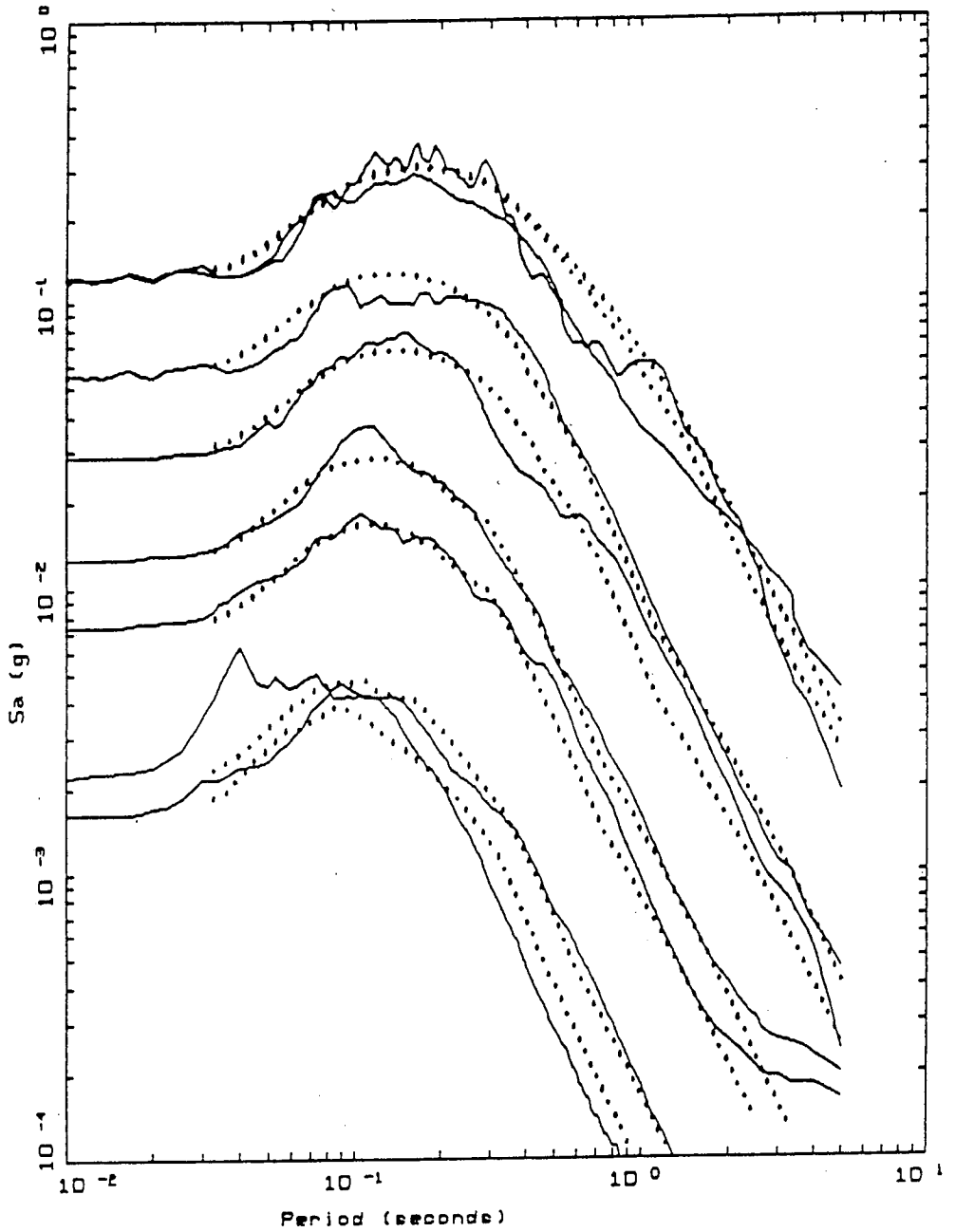

Figure 41. Average 5% absolute acceleration response spectra computed from recordings of the Coalinga aftershocks recorded at rock sites Magnitude (M_L) categories are 2.5, 3.0, 3.5, 3.9, 4.2, 4.6, 5.2 and 5.9 (solid line). Dotted line shows WNA model calculations suing a kappa of 0.045 sec for the magnitude (M) categories (3.0, 3.5, 4.0, 4.25, 4.5, 4.6, 5.3, and 5.5) and scaled to the average peak accelerations of the recorded motions.

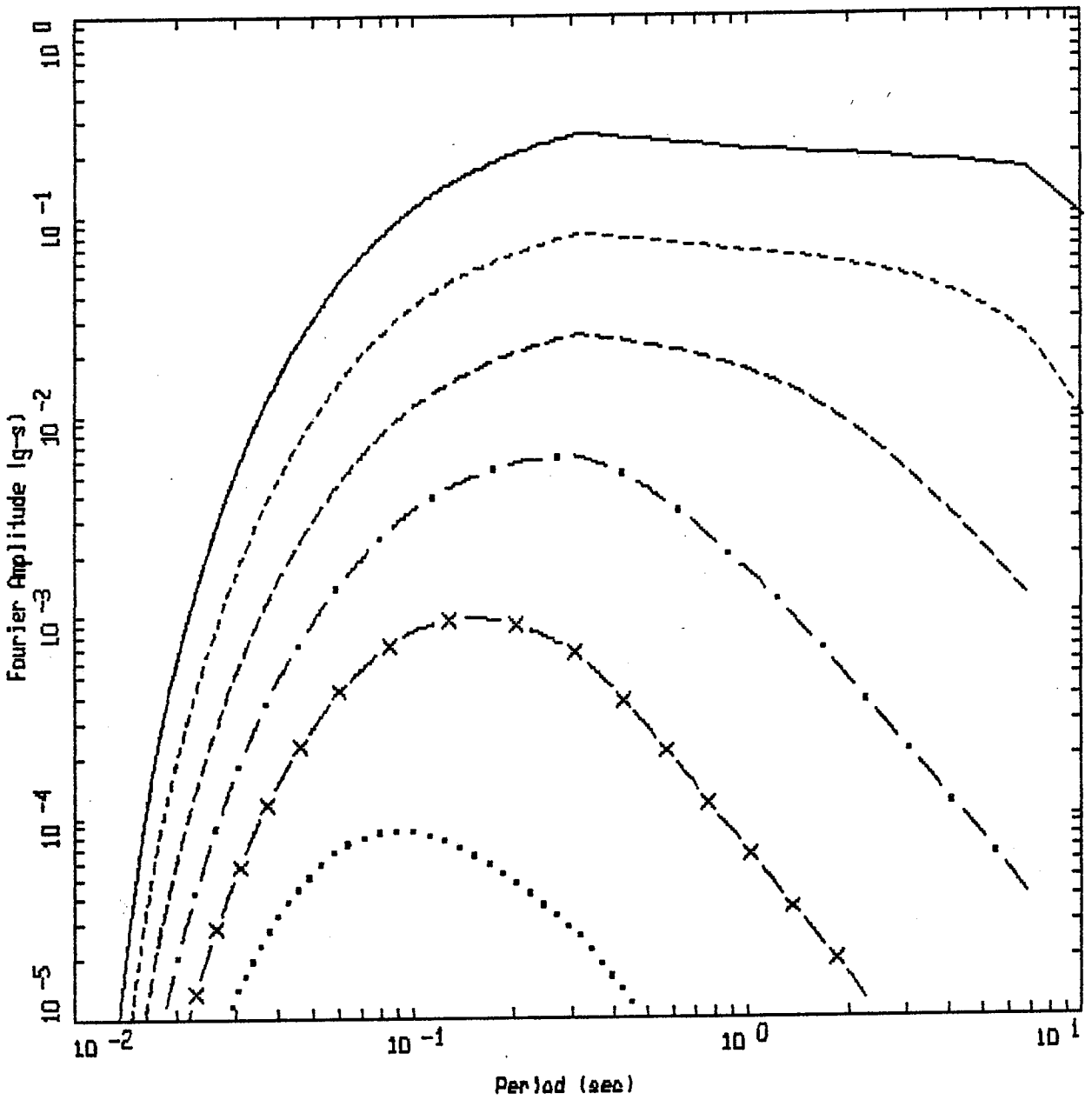

WNA SPECTRA
ROCK, R= 10 KM

LEGEND

WNA M=7.5
WNA M=6.5
WNA M=5.5
WNA M=4.5
WNA M=3.5
WNA M=2.5

Figure 42.

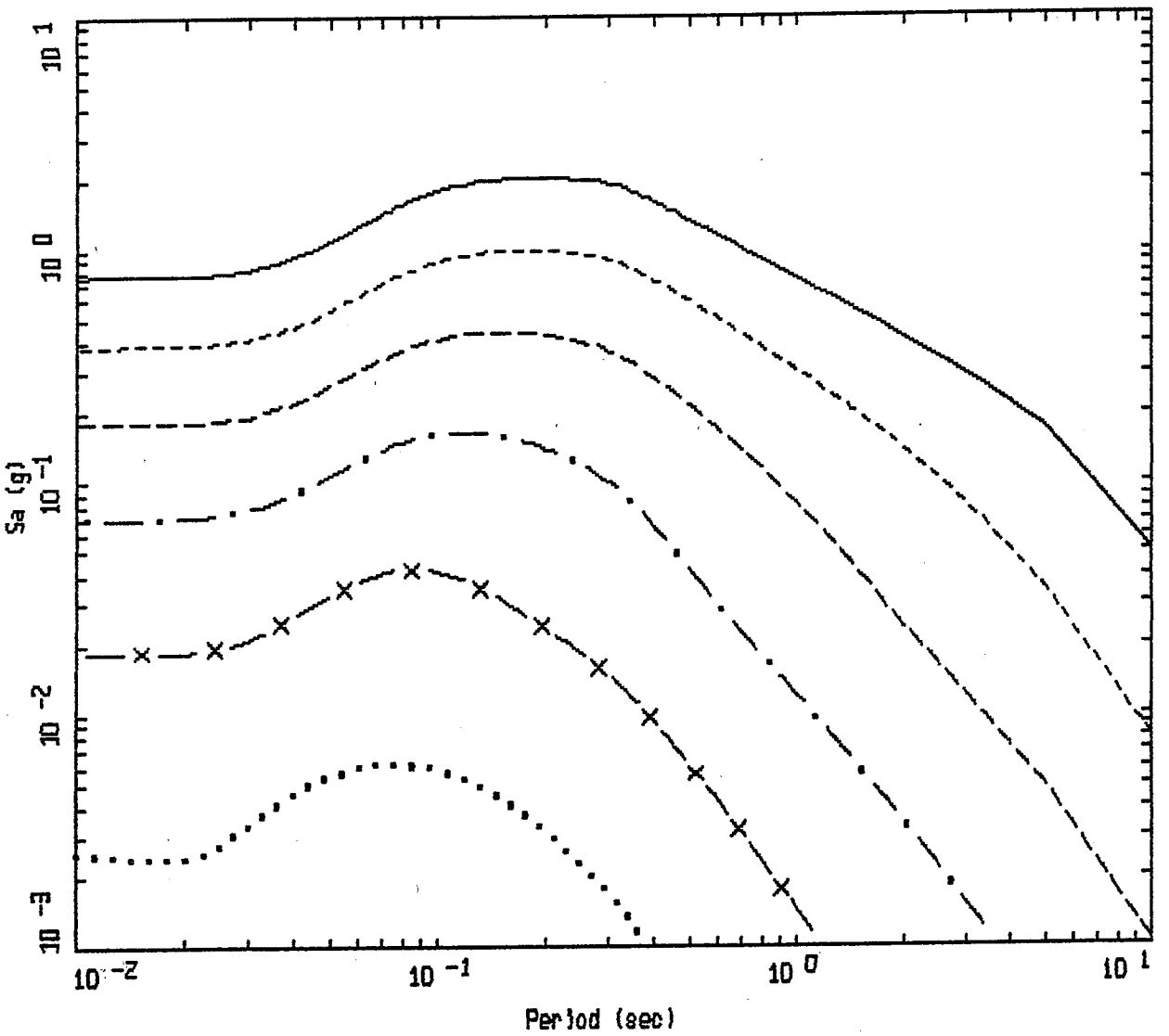

WNA SPECTRA
ROCK, R= 10 KM

LEGEND
WNA M=7.5
WNA M=6.5
WNA M=5.5
WNA M=4.5
WNA M=3.5
WNA M=2.5

Figure 43.

3) Figures 44 - 56 illustrating the effects of damping (kappa) at rock sites.

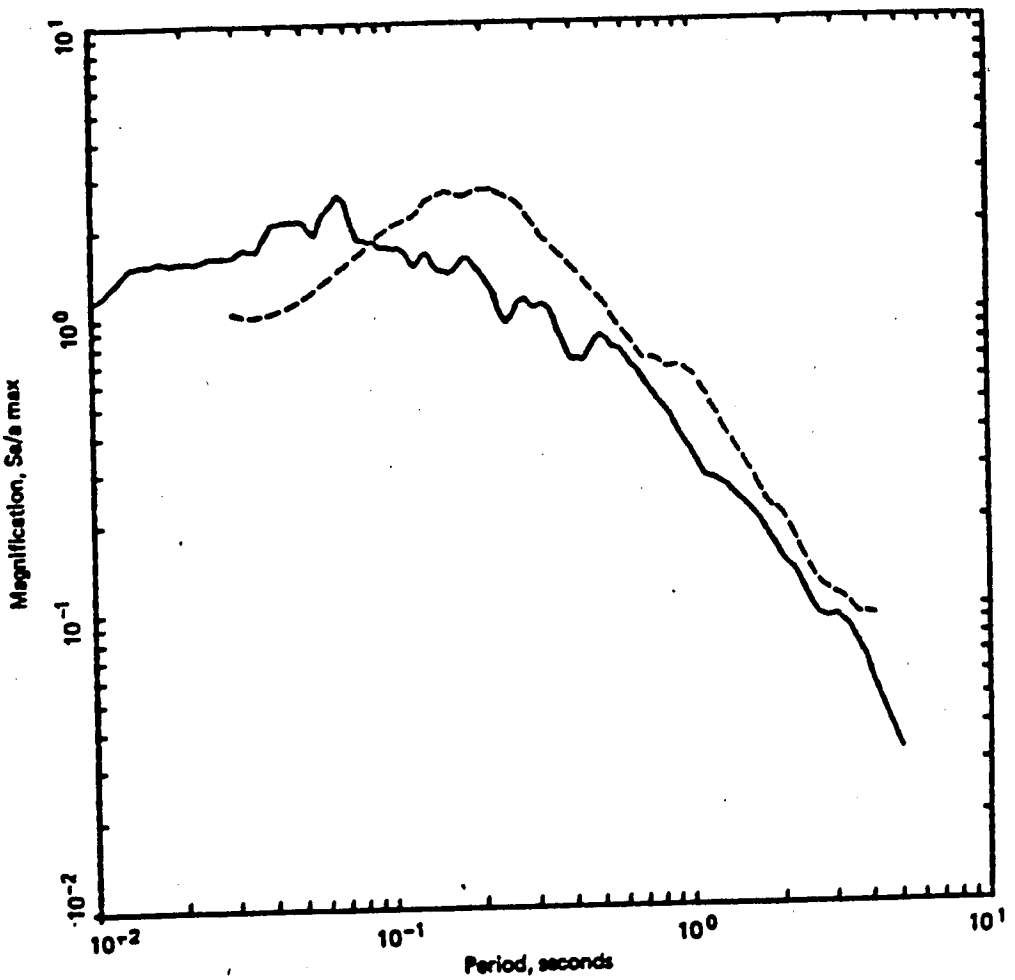

Figure 44. Comparison of average 5% damped response spectral shapes (Sa/a_{max}) computed from strong motion data recorded at rock sites in ENA (solid line) and WNA (dashed line). ENA average shape is from recordings of the m_b = 6.4 Nahanni aftershock. The WNA average shape is from recordings of the San Fernando M_L = 6.4 and Imperial Valley M_L = 6.6 events.

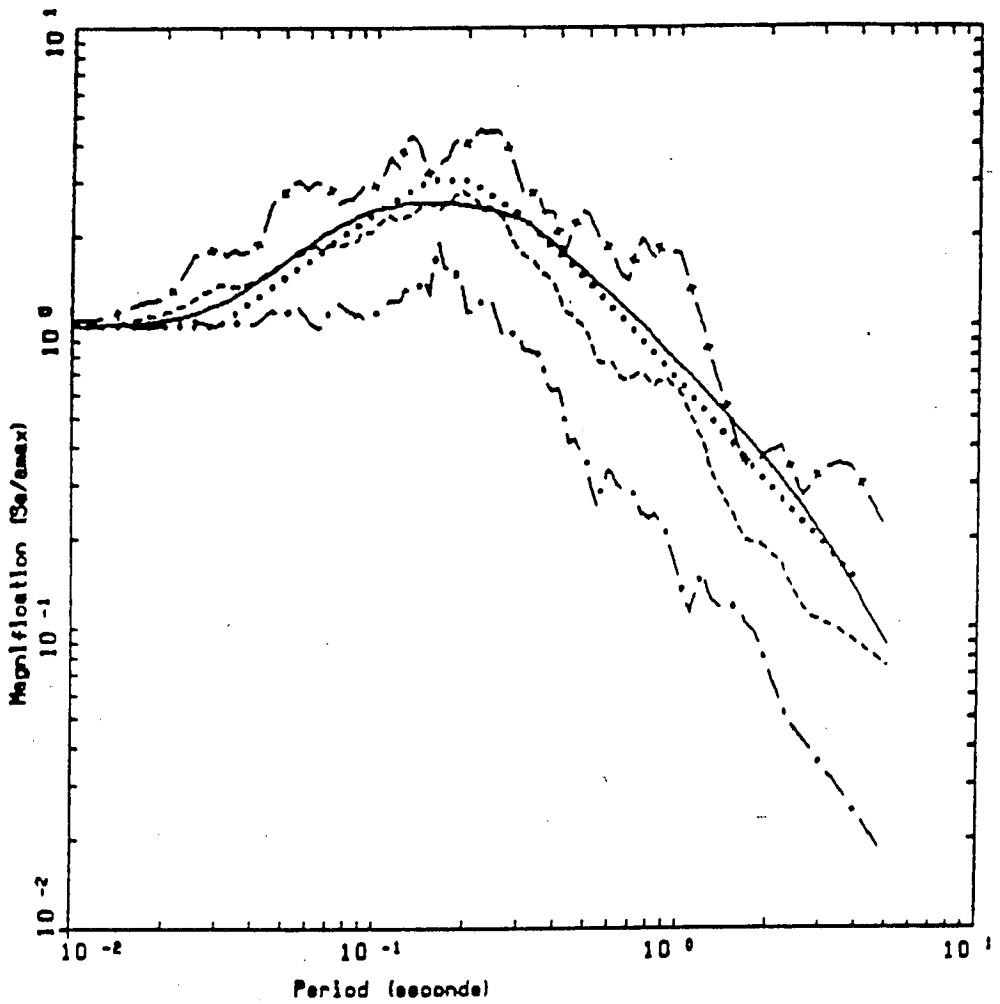

Figure 45. Plot of average 5% spectral shape for all stations for the magnitude 6.4 San Fernando earthquake. Solid line is the BLWN model shape computed with WNA parameters at 25 km for a moment magnitude 6.4 using a kappa of 0.030 sec. Dotted lines is the Joyner-Boore (1985) shape for R = 25 km and M = 6.4.

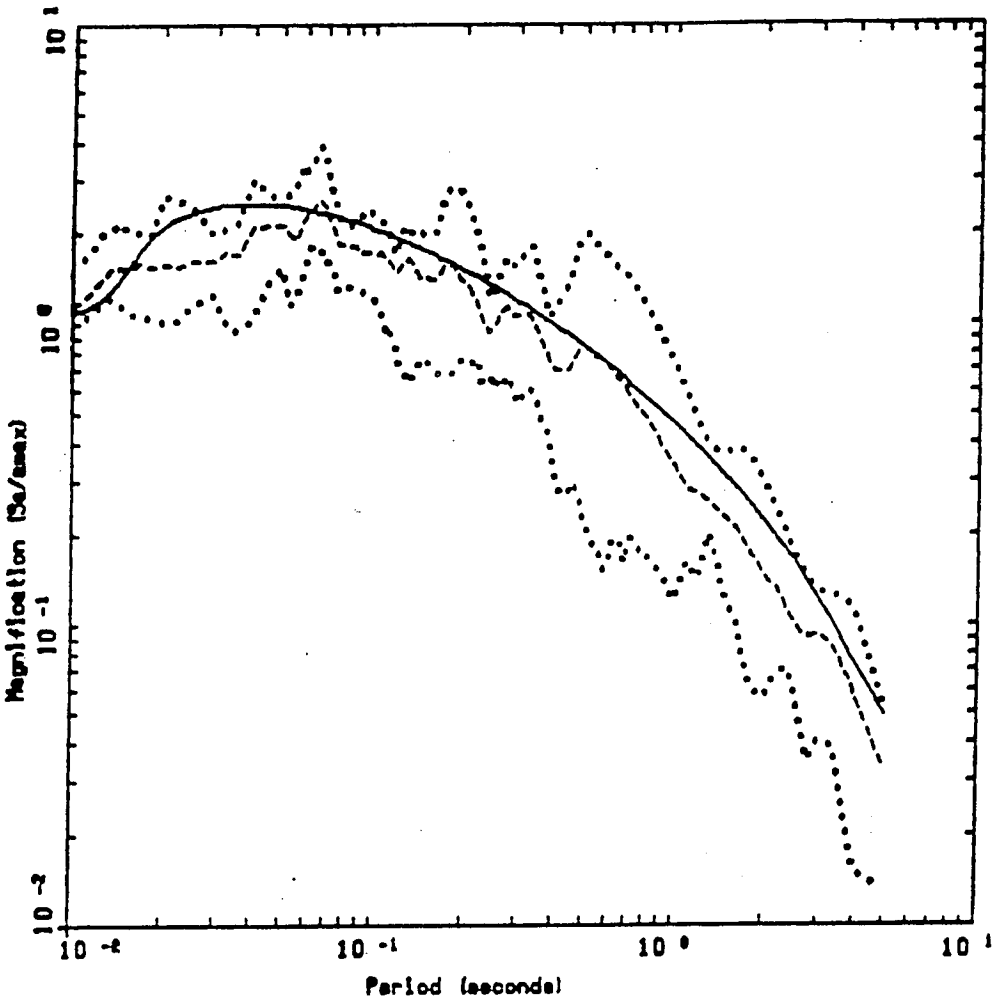

Figure 46. Plot of average 5% spectral shape for all stations for the magnitude 6.4 Nahanni earthquake. Solid line is the BLWN model shape computed with ENA parameters at 10 km for a moment magnitude 6.5 using a kappa of 0.008 sec.

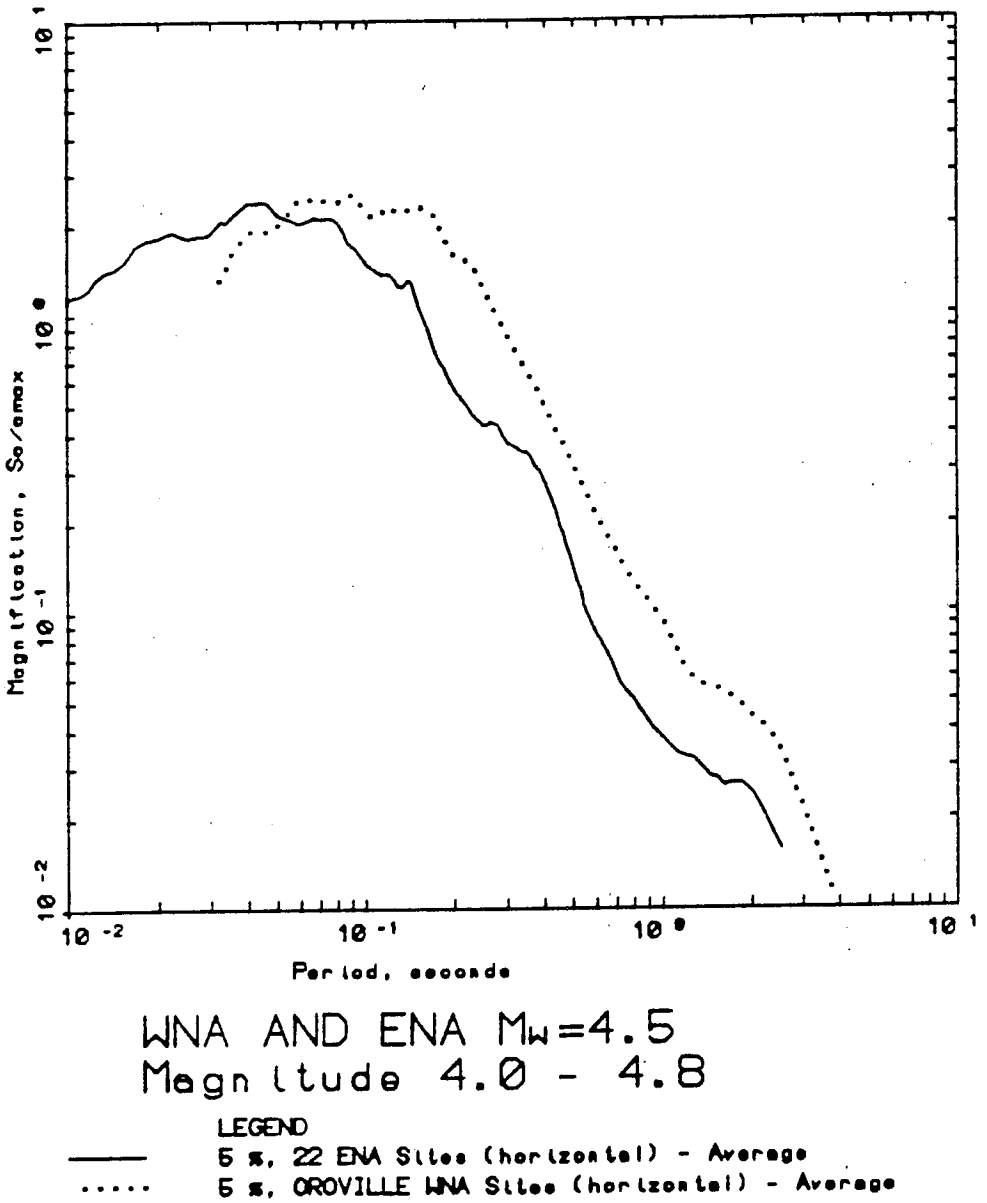

Figure 47. Comparison of average 5% damped response spectral shapes (Sa/a_{max}) computed from strong motion data recorded at rock sites in ENA (solid line) and WNA (dotted line). The WNA average shape is from aftershocks of the Oroville earthquake listed in Table 5. The ENA average shape is from recordings listed in Table 6.

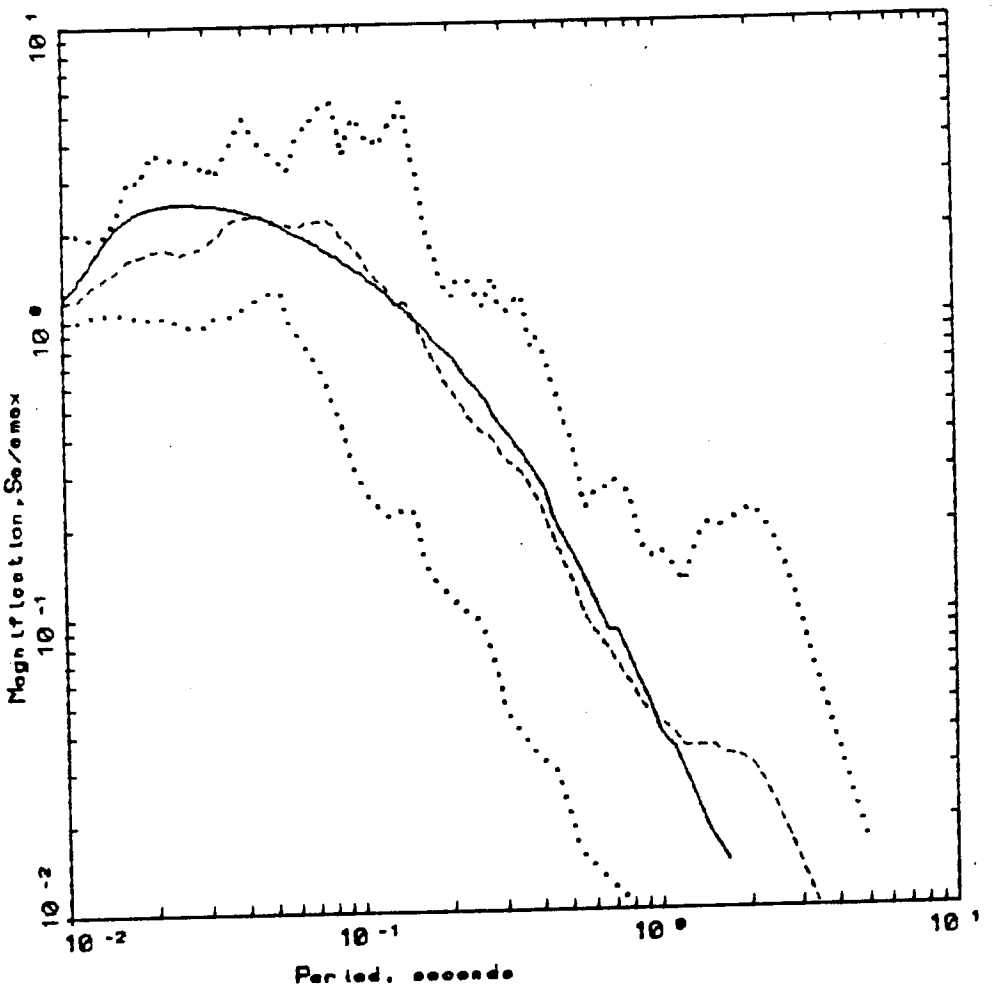

Figure 48. Comparison of predicted response spectral shape (solid line) for a moment magnitude (M_W) 4.5 earthquake at a distance of 8 km using ENA parameters (Table 1) with average shape computed from recorded data (Table 6, dashed line). The dotted lines represent the extremes of the shapes computed from the recorded data.

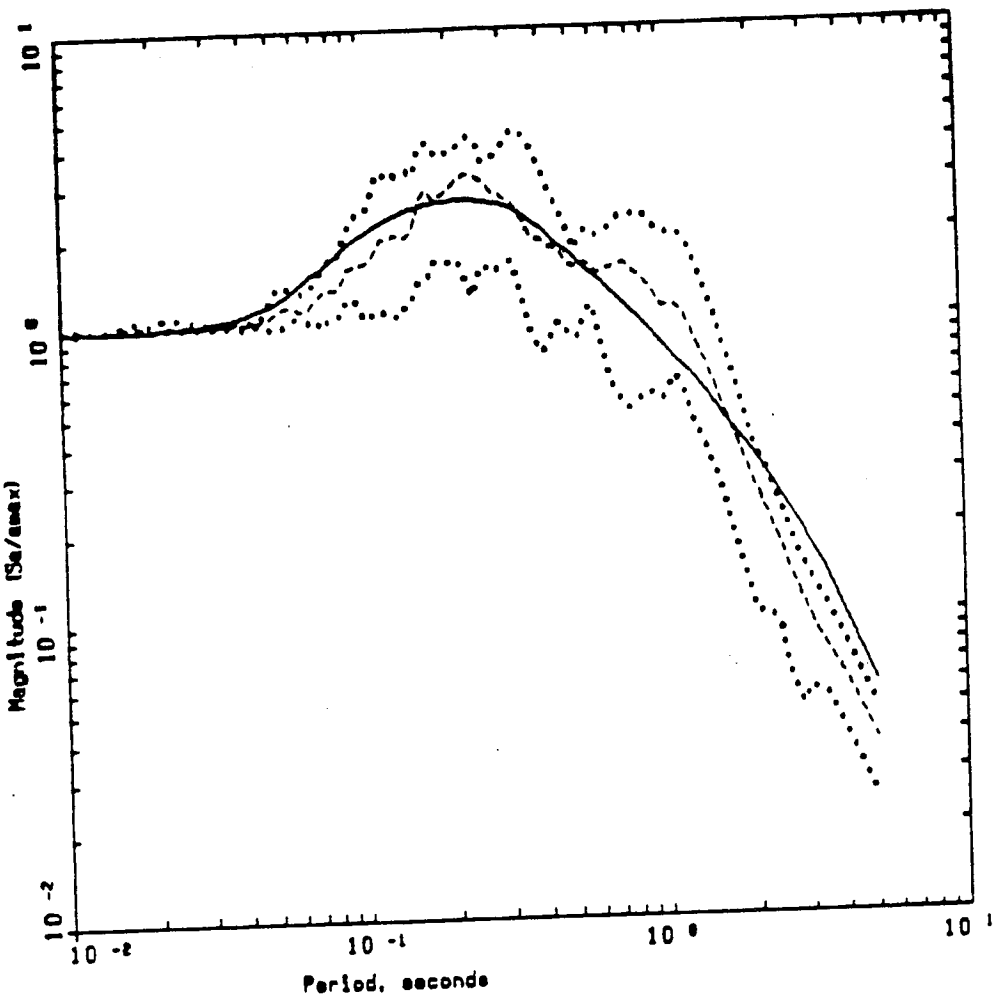

Figure 50. Plot of average 5% spectral shape for station GA-6 over the magnitude range of 5.9 - 6.1 for the Gilroy Array. Solid line is the BLWN model shape computed with WNA parameters at 10 km for a moment magnitude 6.0 using a kappa of 0.055 sec.

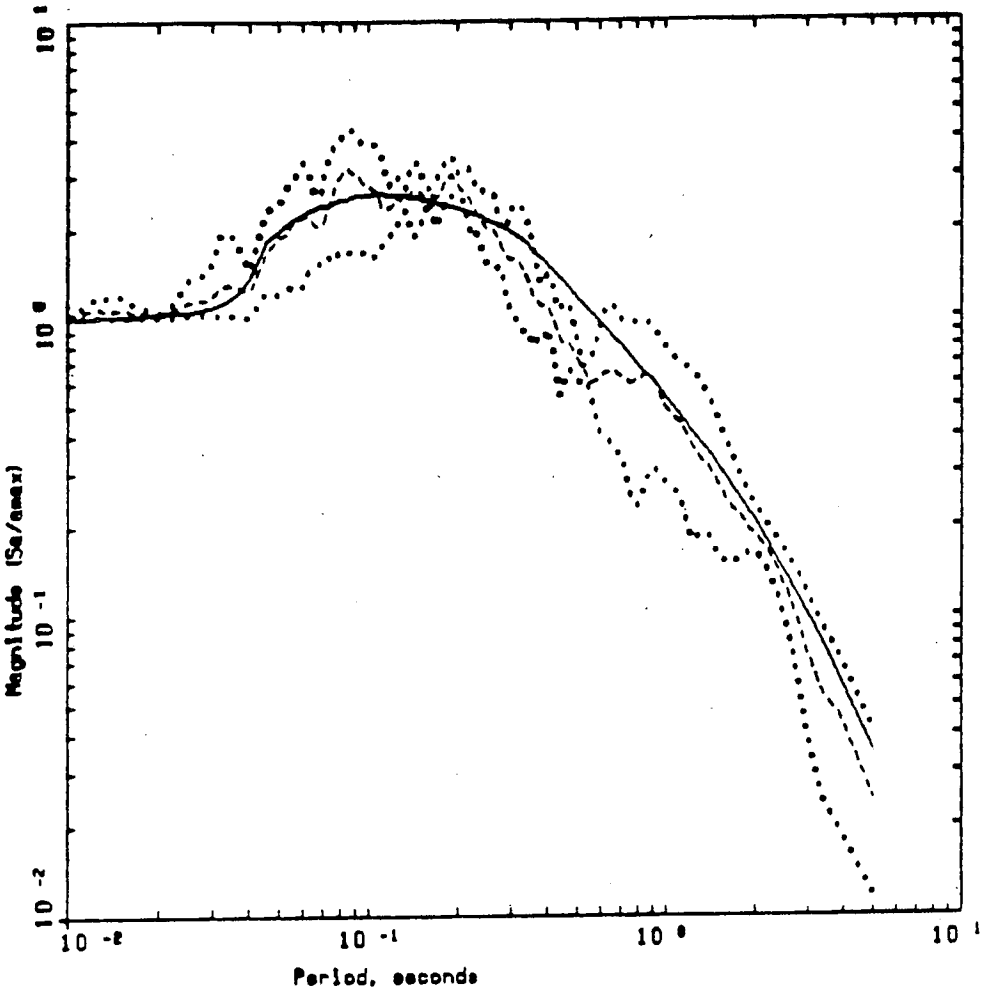

Figure 51. Plot of average 5% spectral shape for station GA-1 over the magnitude range of 5.9 - 6.1 for the Gilroy Array. Solid line is the BLWN model shape computed with WNA parameters at 10 km for a moment magnitude 6.0 using a kappa of 0.025 sec.

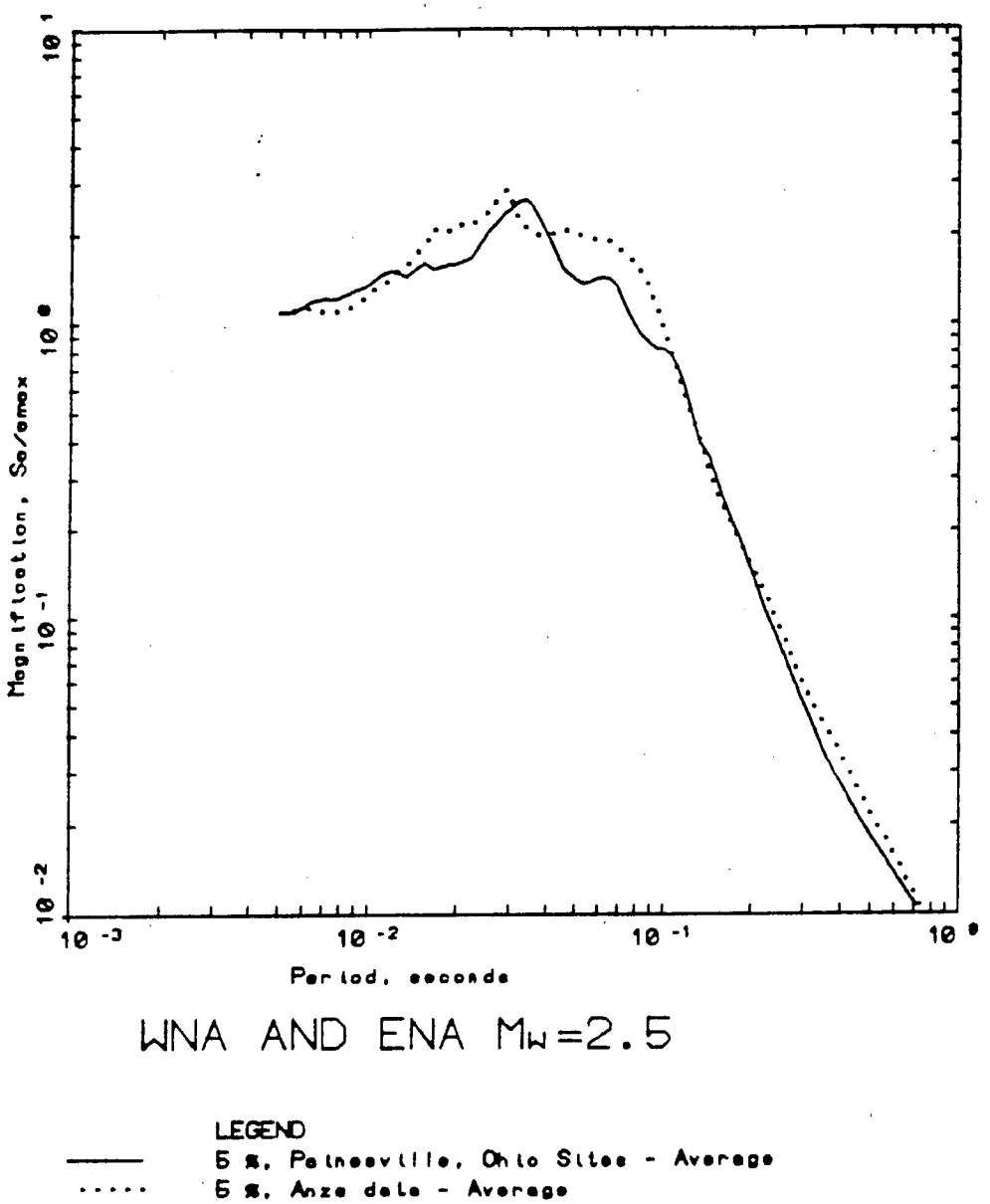

Figure 52. Comparison of average 5% response spectral shapes (Sa/a_{max}) computed from strong motion data recorded at rock sites in ENA (solid line) and WNA (dotted line).

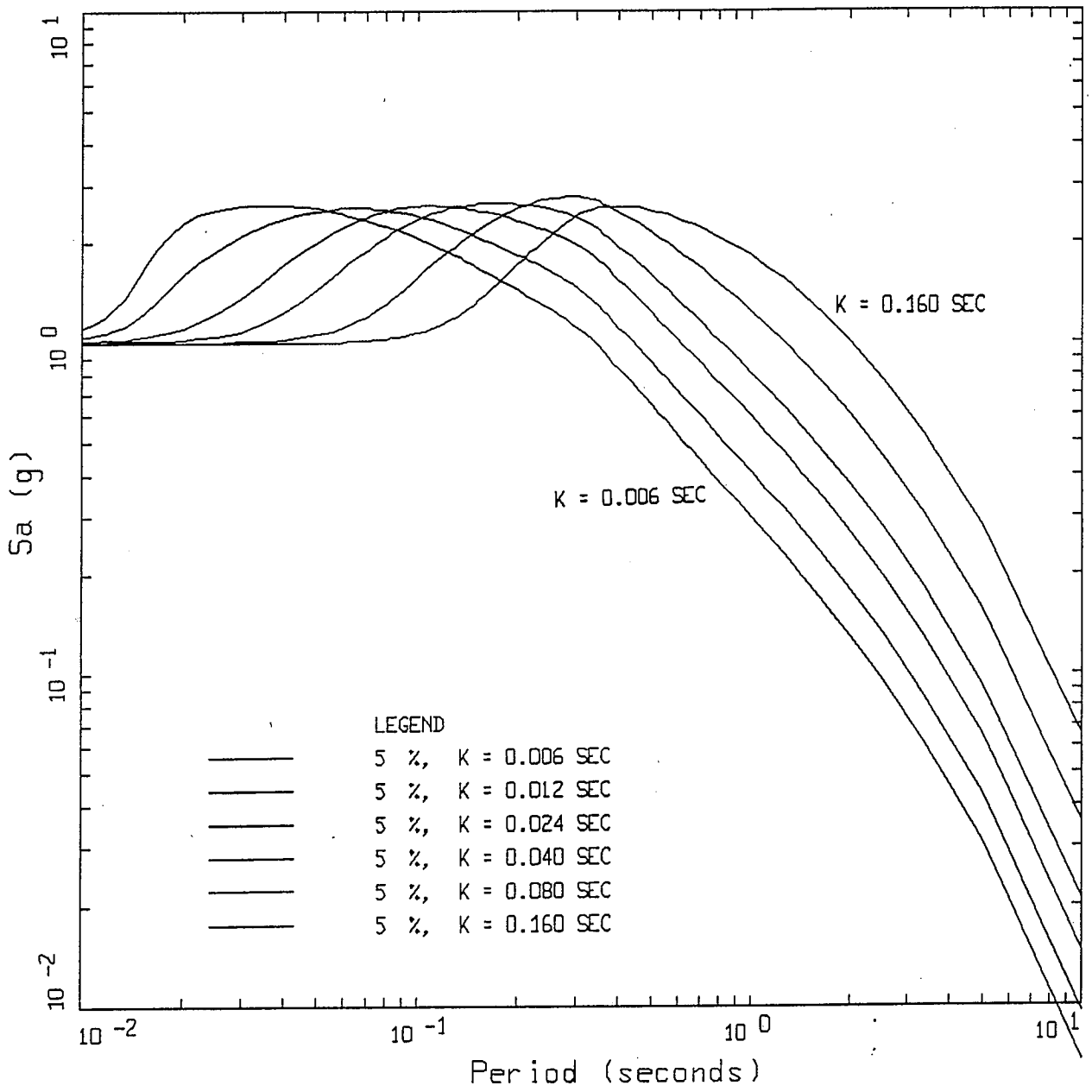

Figure 53. The effects of kappa on 5% damped response spectral shapes computed for a M 6.5 earthquake at 10 km using WNA parameters. As kappa increases, the peak shifts to longer periods and remains essentially constant in amplitude.

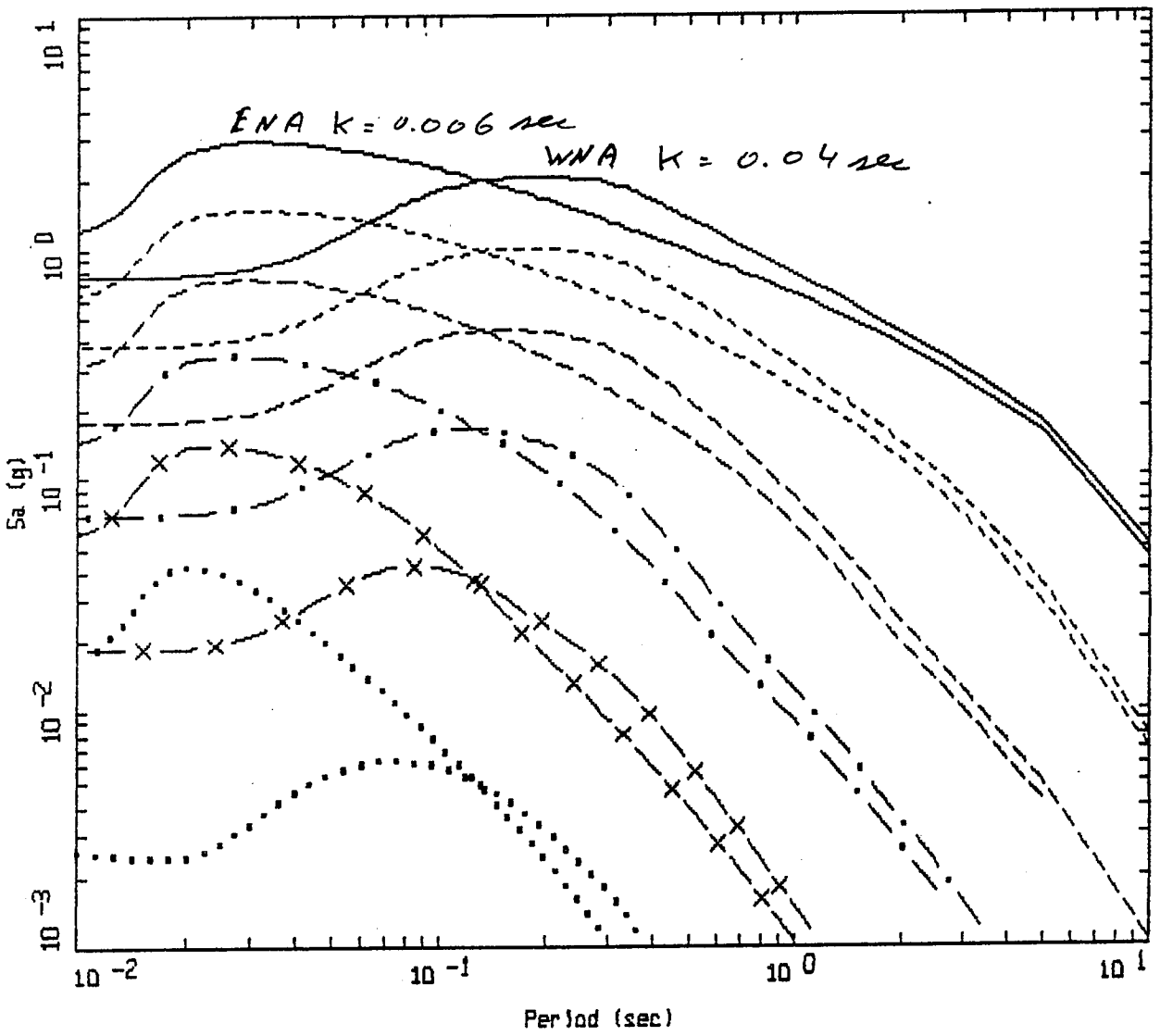

WNA AND ENA SPECTRA
ROCK, R= 10 KM

LEGEND

ENA M=7.5
ENA M=6.5
ENA M=5.5
ENA M=4.5
ENA M=3.5
ENA M=2.5
WNA M=7.5
WNA M=6.5
WNA M=5.5
WNA M=4.5
WNA M=3.5
WNA M=2.5

Figure 54.

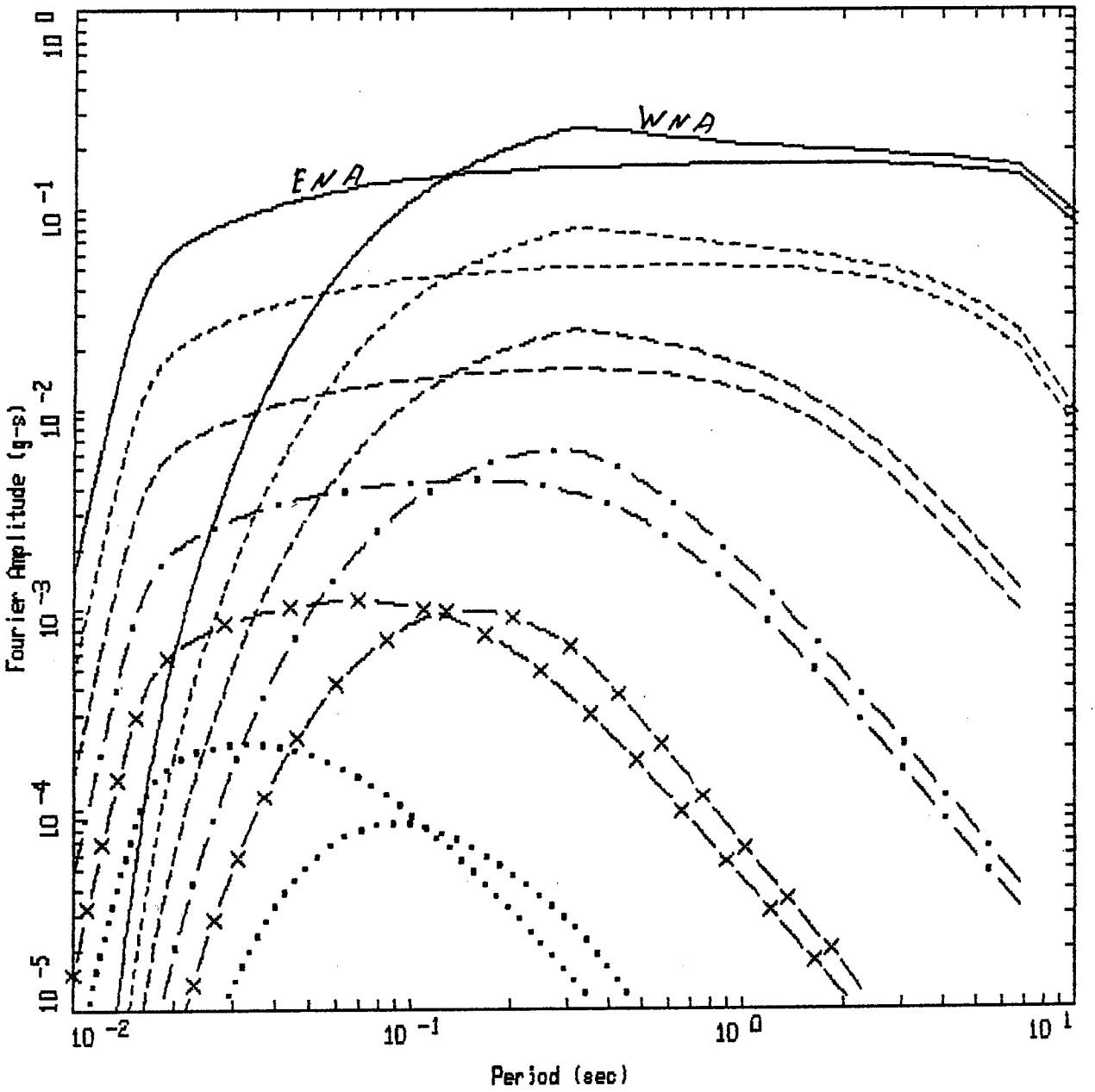

WNA AND ENA SPECTRA
ROCK, R= 10 KM

LEGEND

ENA M=7.5
ENA M=6.5
ENA M=5.5
ENA M=4.5
ENA M=3.5
ENA M=2.5
WNA M=7.5
WNA M=6.5
WNA M=5.5
WNA M=4.5
WNA M=3.5
WNA M=2.5

Figure 55.

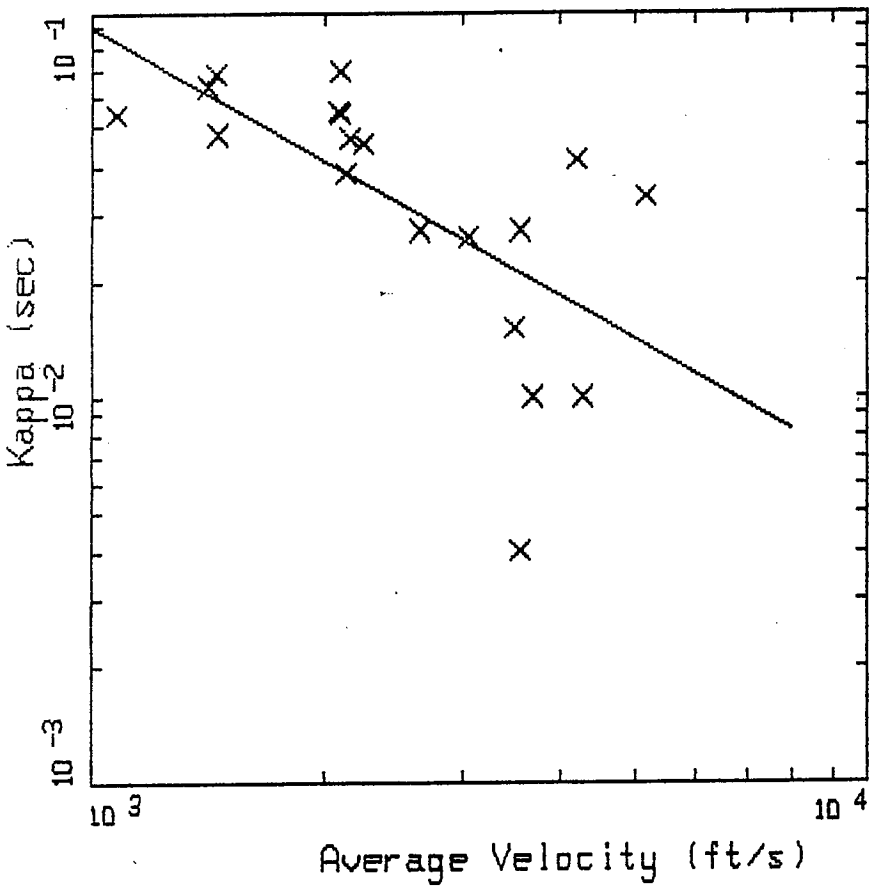

ROCK SITES (WNA)

KAPPA VS AVERAGE (OVER 100 FT) VELOCITY

LEGEND

× DATA

——— LOG(KAPPA) = 2.40939 - 1.15099 * LOG(VELOCITY IN FT/S)

Figure 56.

4) Figures 57 - 60 illustrating nonlinear soil response (includes 1 table).

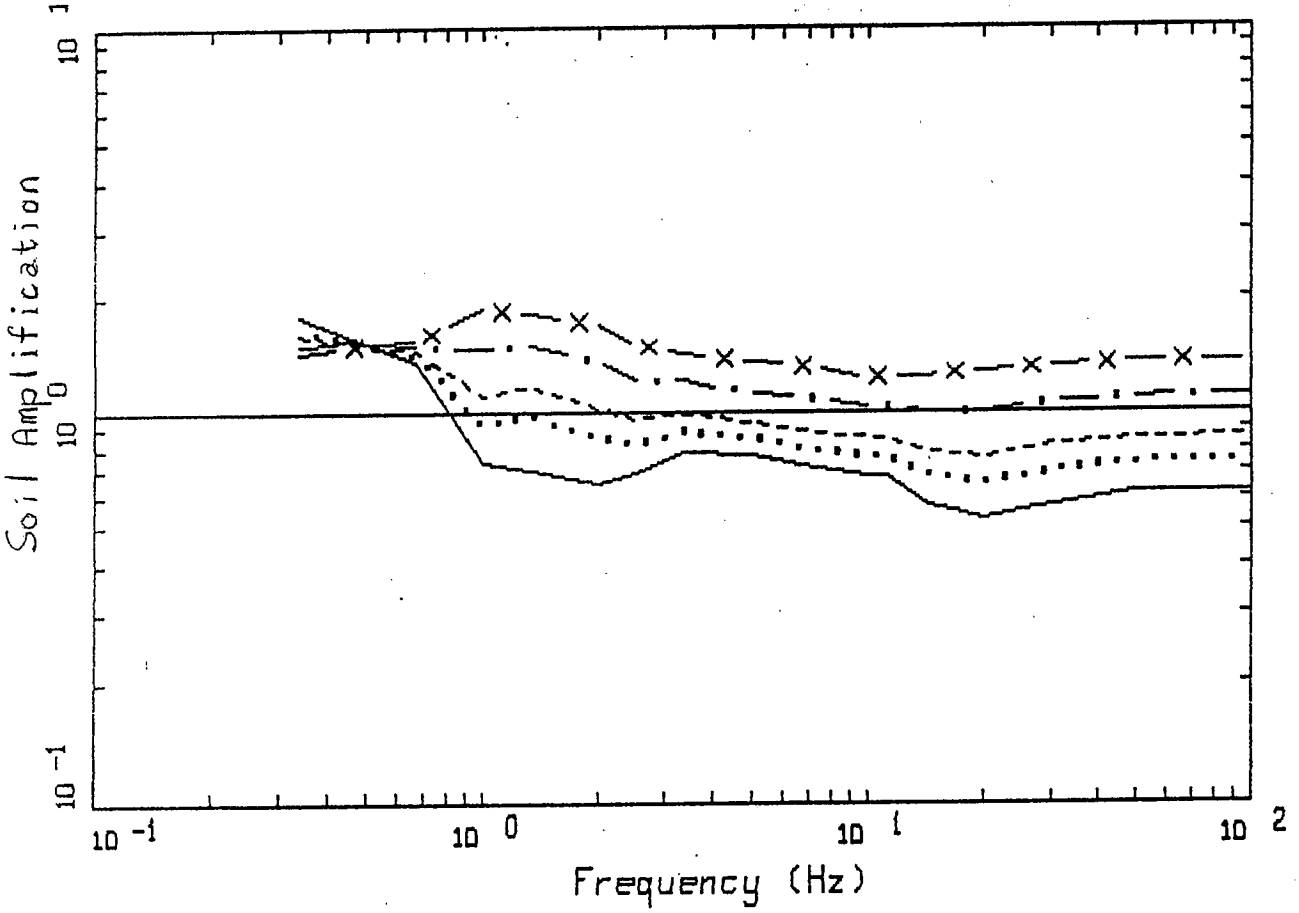

WNA EMPIRICAL M 6.5
DEEP, FIRM

LEGEND

R = 1.0 KM, ROCK PGA = 0.73 g
R = 5.0 KM, ROCK PGA = 0.40 g
R = 10.0 KM, ROCK PGA = 0.25 g
R = 25.0 KM, ROCK PGA = 0.11 g
R = 50.0 KM, ROCK PGA = 0.06 g

Figure 57.

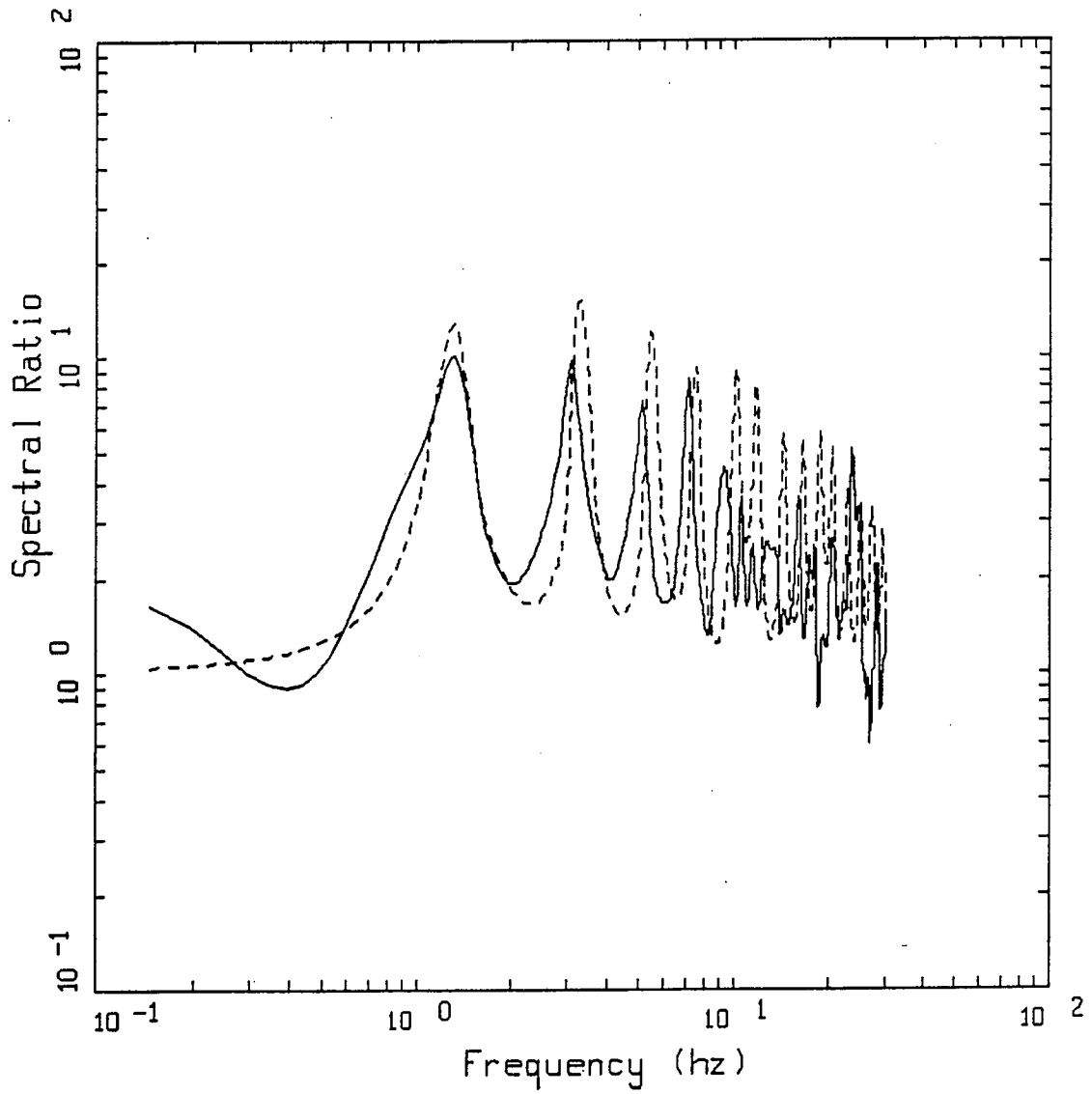

Figure 58. **Fourier amplitude spectral ratios, surface-to-154 ft, at reference site Lotung from LSST event 10 (solid) and computed using base-case shear-wave velocity profile: linear analysis. Numerator and denominator are smoothed with a 1/2 Hz wide triangular operator prior to taking ratios.**

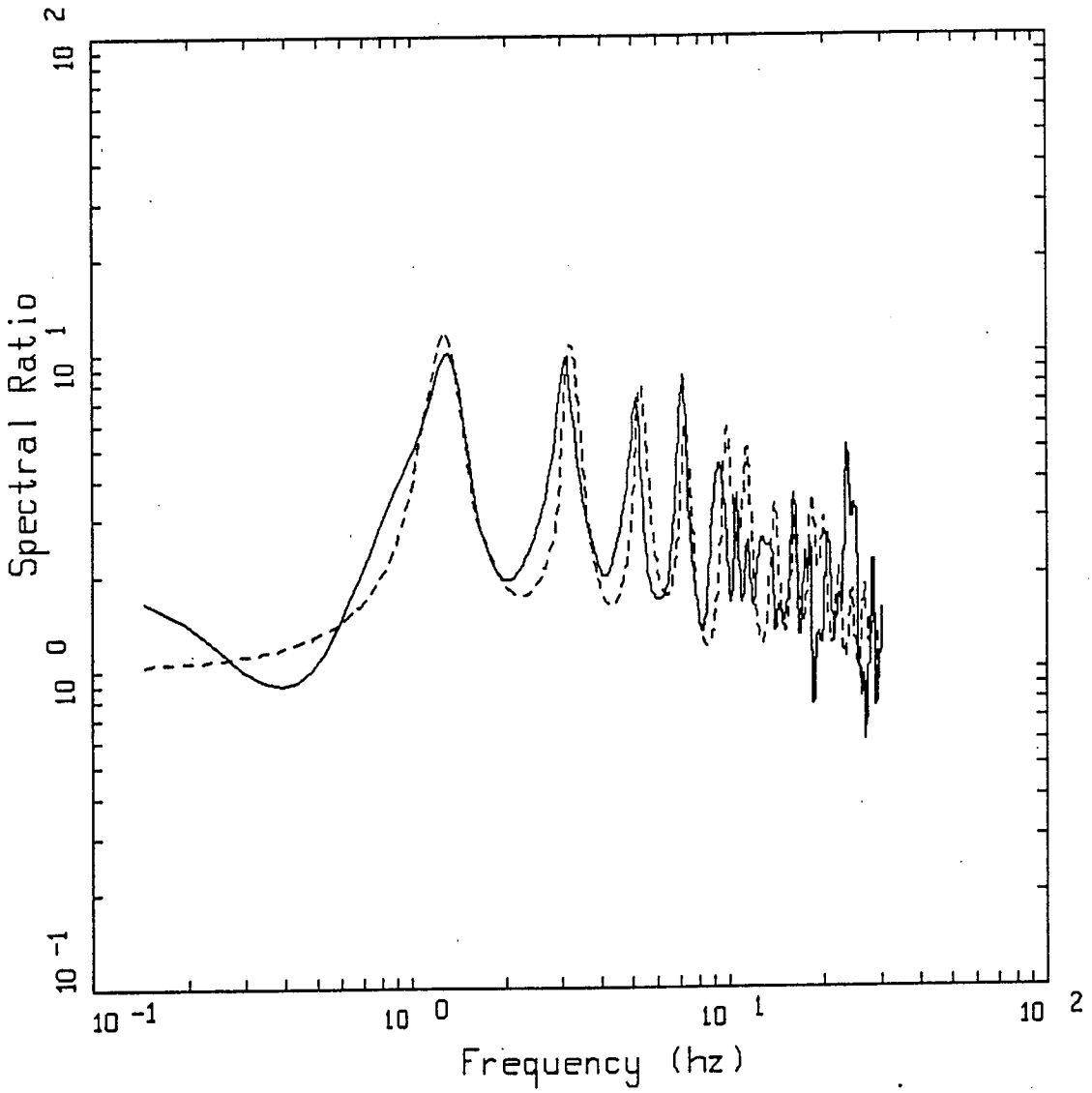

Figure 59. Fourier amplitude spectral ratios, surface-to-154 ft, at reference site Lotung from LSST event 10 (solid) and computed using base-case shear-wave velocity profile: equivalent-linear analysis. Numerator and denominator are smoothed with a 1/2 Hz wide triangular operator prior to taking ratios.

FREQUENCY AND AMPLITUDE OF FUNDAMENTAL RESONANCES

LSST Event	Surface AVG PGA (g)	F (Hz)	Amplitude
Surface/20 ft			
10	0.035	4.83	10.84
16	0.080	3.37	3.78
7	0.090	2.98	2.65
Surface/36 ft			
10	0.035	3.37	7.16
16	0.080	2.44	3.38
7	0.090	1.71	2.01
Surface/56 ft			
10	0.035	2.44	8.15
16	0.080	1.66	3.68
7	0.090	1.32	2.52
Surface/154 ft			
10	0.035	1.22	6.57
16	0.080	-----*	-----*
7	0.090	0.78	3.58

*Recording not available

Figure 60.

5) Figures 61 - 76 illustrating directivity and near-source effects.

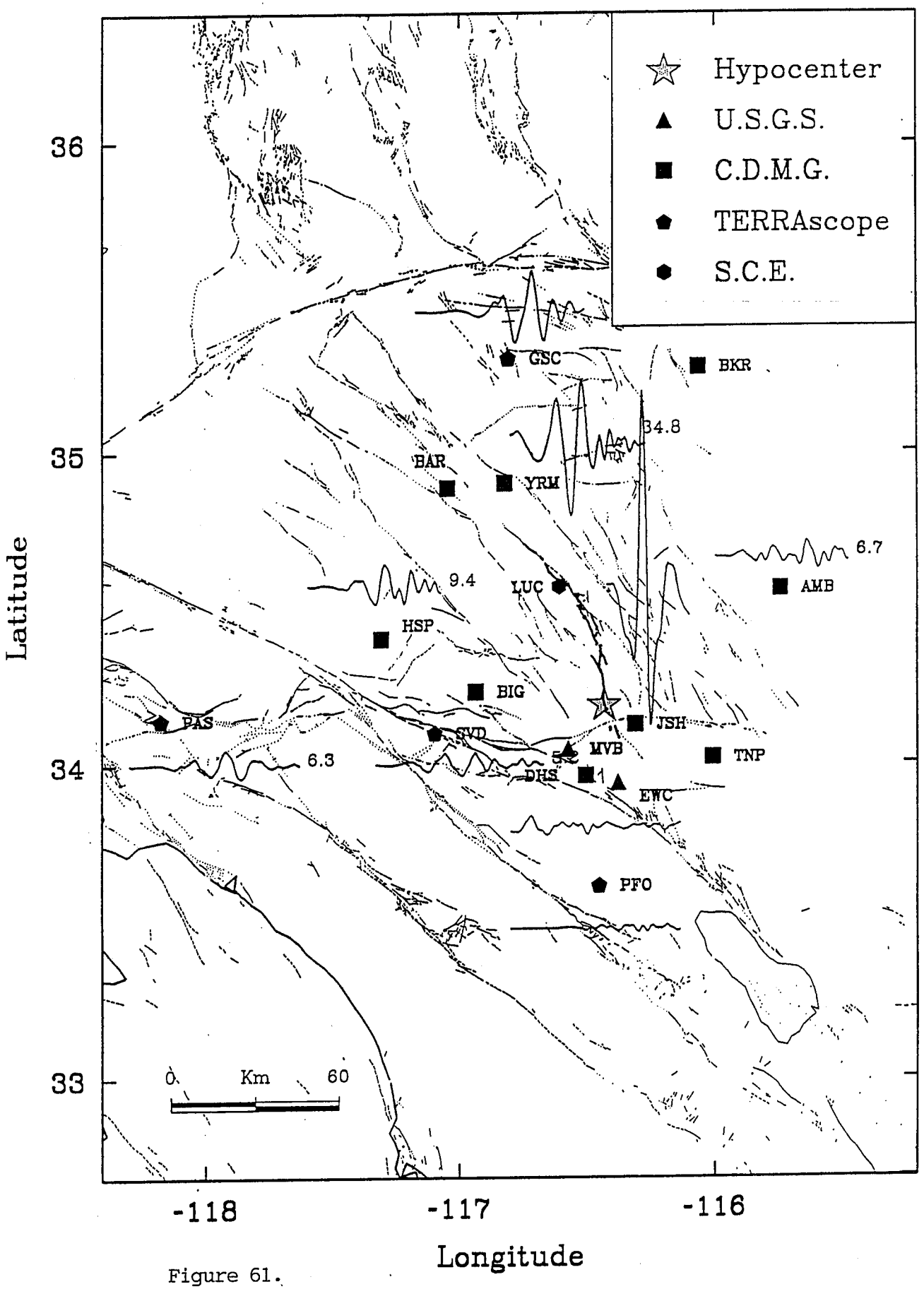
Hypocenter
U.S.G.S.
C.D.M.G.
TERRAscope
S.C.E.
GSC
BKR
34.8
BAR
YRM
6.7
AMB
9.4
LUC
HSP
BIG
JSH
PAS
SVD
MVB
TNP
6.3
DHS
EWC
PFO
0
Km
60
36
35
34
33
-118
-117
-116
Latitude
Longitude

Figure 61.

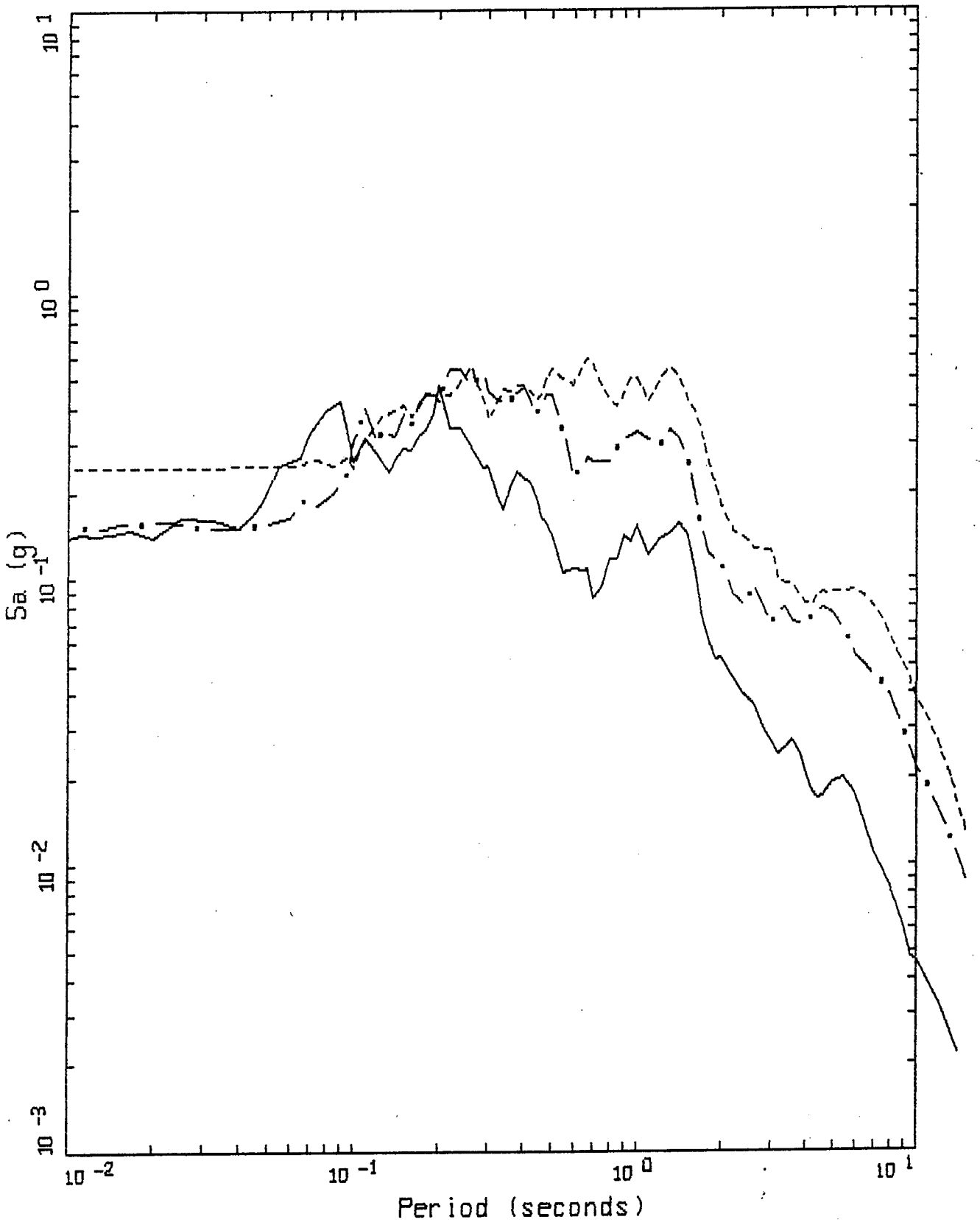
Sa (g)
Period (seconds)
LANDERS 06/28/92 1158
YERMO FIRE STATION
LEGEND
5 %, PE&A-CORRECTED DATA, COMP UP
5 %, PE&A-CORRECTED DATA, COMP 270
5 %, PE&A-CORRECTED DATA, COMP 360

Figure 62.

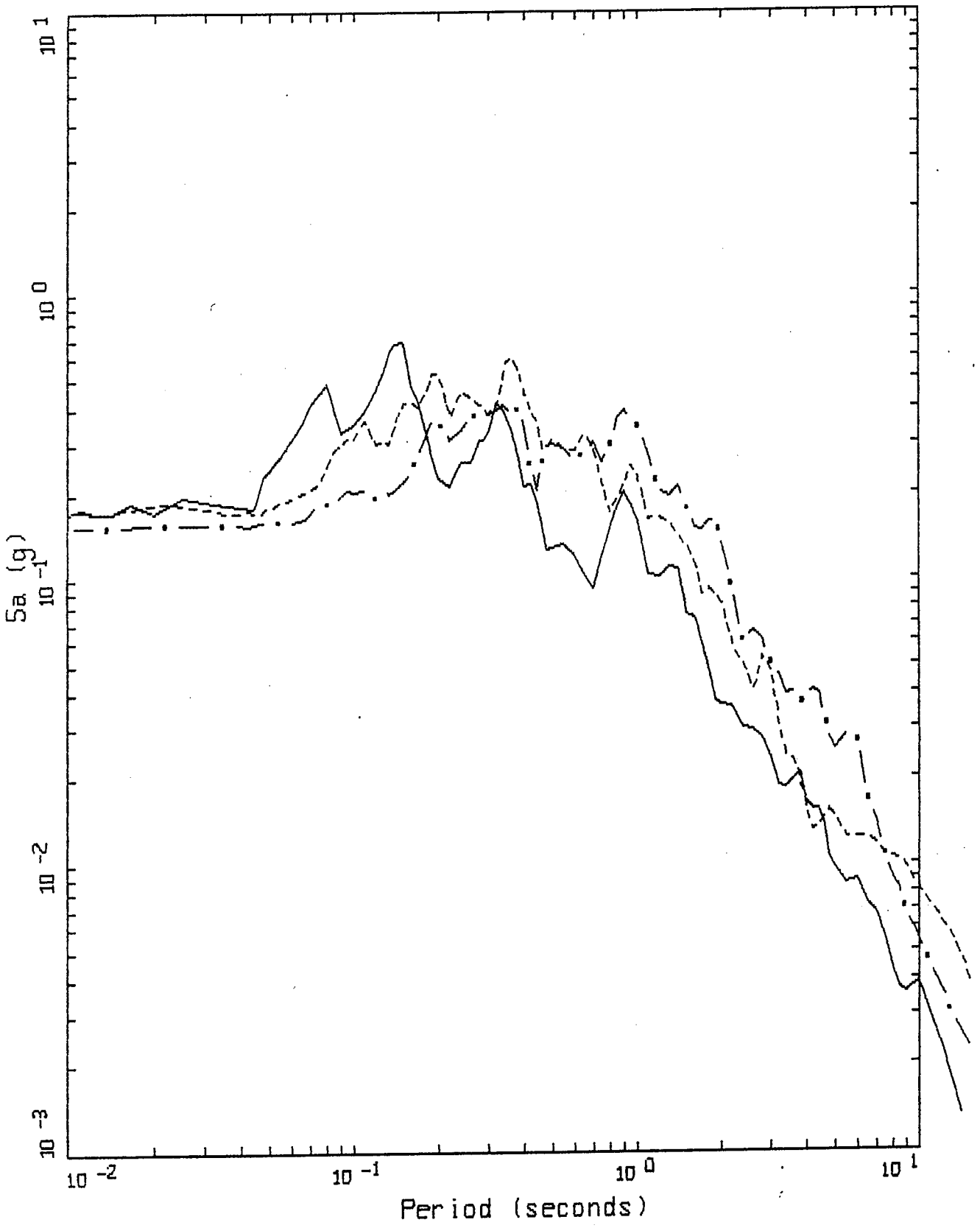

LANDERS 06/28/92 1158
DESERT HOT SPRINGS

LEGEND

——— 5 %, PE&A-CORRECTED DATA, COMP UP

----- 5 %, PE&A-CORRECTED DATA, COMP 000

—·— 5 %, PE&A-CORRECTED DATA, COMP 090

Figure 63.

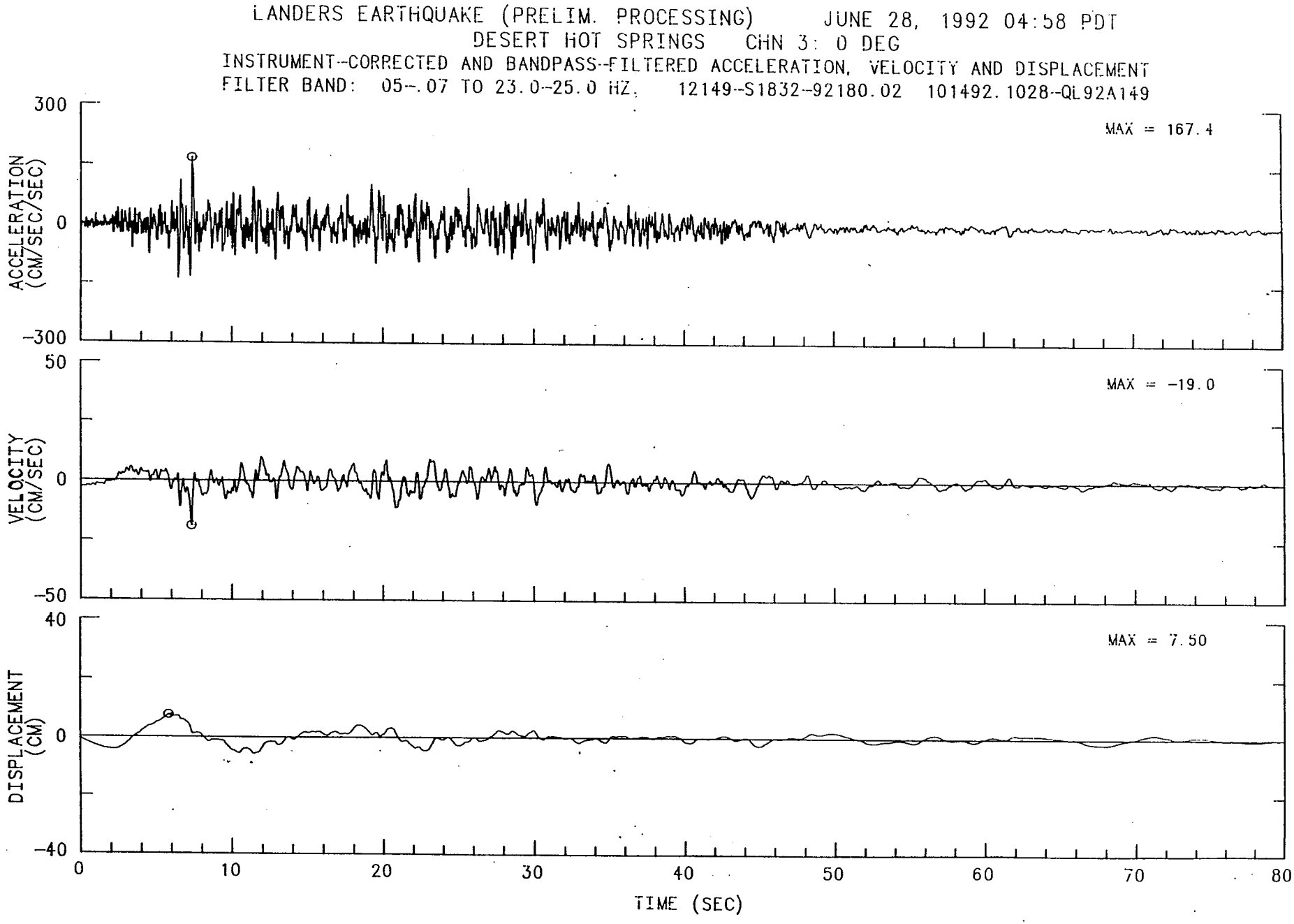
LANDERS EARTHQUAKE (PRELIM. PROCESSING) JUNE 28, 1992 04:58 PDT
DESERT HOT SPRINGS CHN 3: 0 DEG
INSTRUMENT-CORRECTED AND BANDPASS-FILTERED ACCELERATION, VELOCITY AND DISPLACEMENT
FILTER BAND: 05-.07 TO 23.0-25.0 HZ. 12149-S1832-92180.02 101492.1028-QL92A149
ACCELERATION (CM/SEC/SEC)
300
0
-300
MAX = 167.4
VELOCITY (CM/SEC)
50
0
-50
MAX = -19.0
DISPLACEMENT (CM)
40
0
-40
MAX = 7.50
0
10
20
30
40
50
60
70
80
TIME (SEC)

Figure 65.

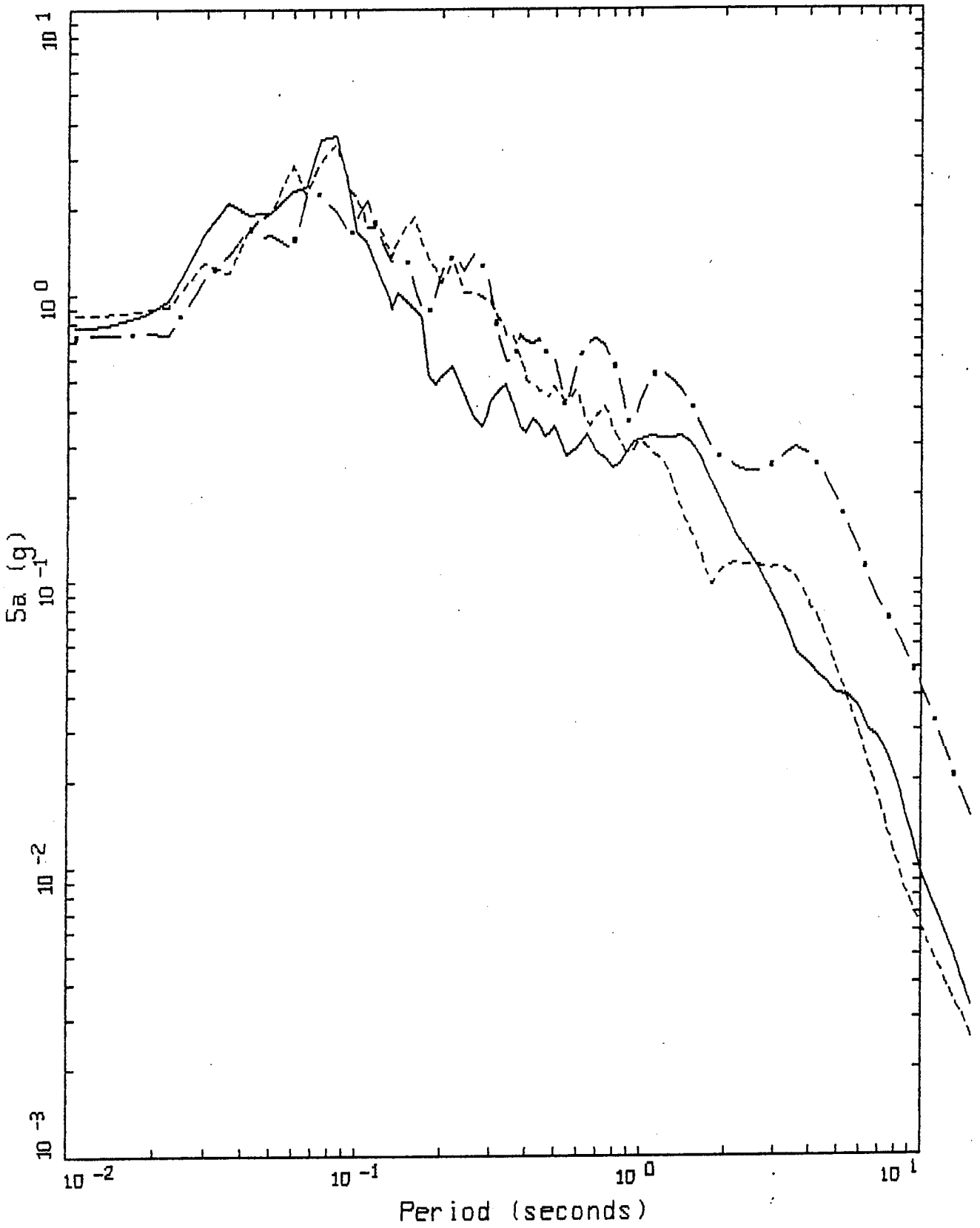

Figure 66. LANDERS 06/28/92 1158
LUCERNE

LEGEND

——— 5 %, PE&A-CORRECTED DATA, COMP VRT

- - - - - 5 %, PE&A-CORRECTED DATA, COMP LONGITUDINAL

— · — 5 %, PE&A-CORRECTED DATA, COMP TRANSVERSE

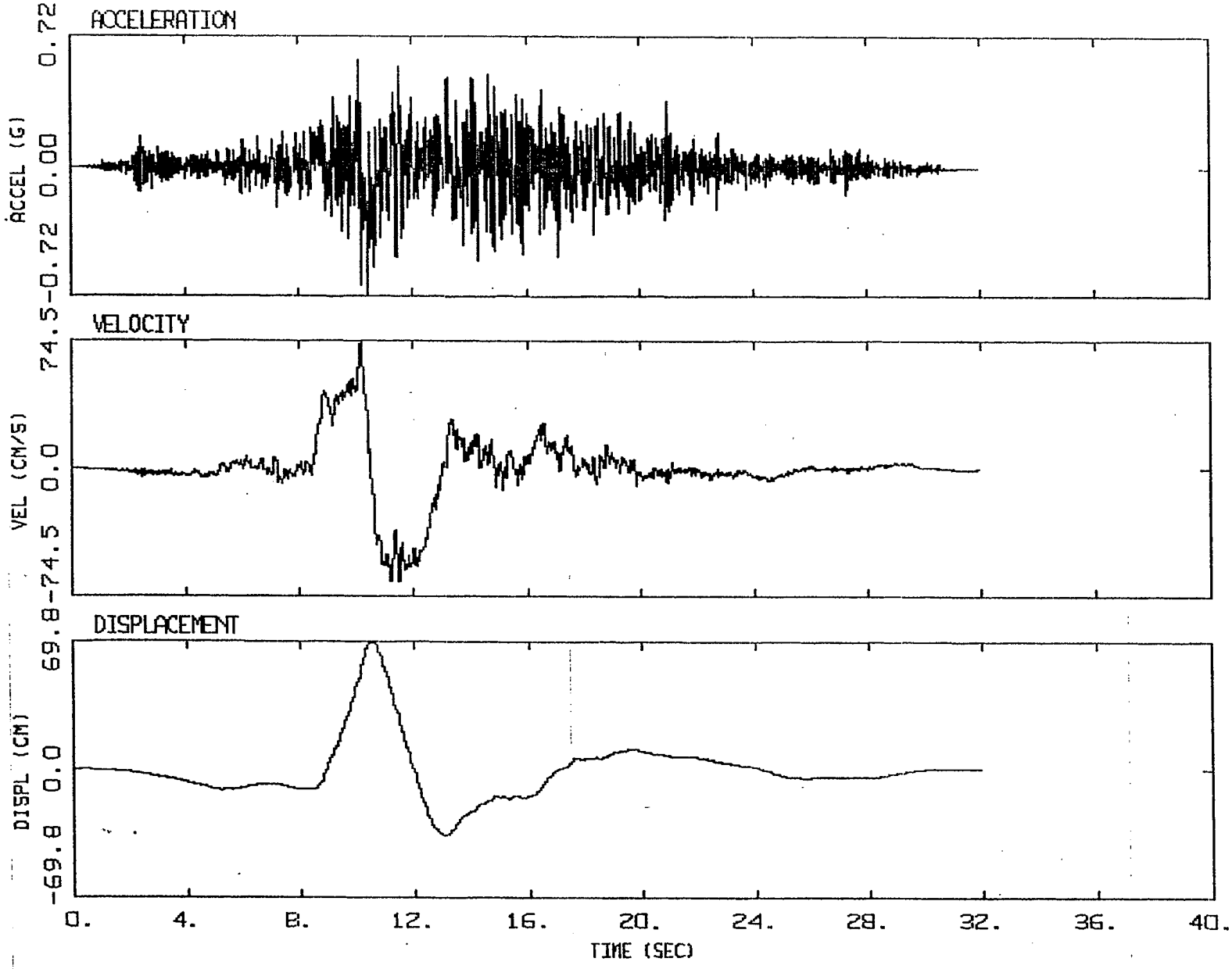

LANDERS 07/23/92 1849, SCE LUCERN, TR, D=??.? KM, SITE=???
INTEGRATED FROM CORRECTED AND BASE-CORRECTED ACCELERATIONS

Figure 67.

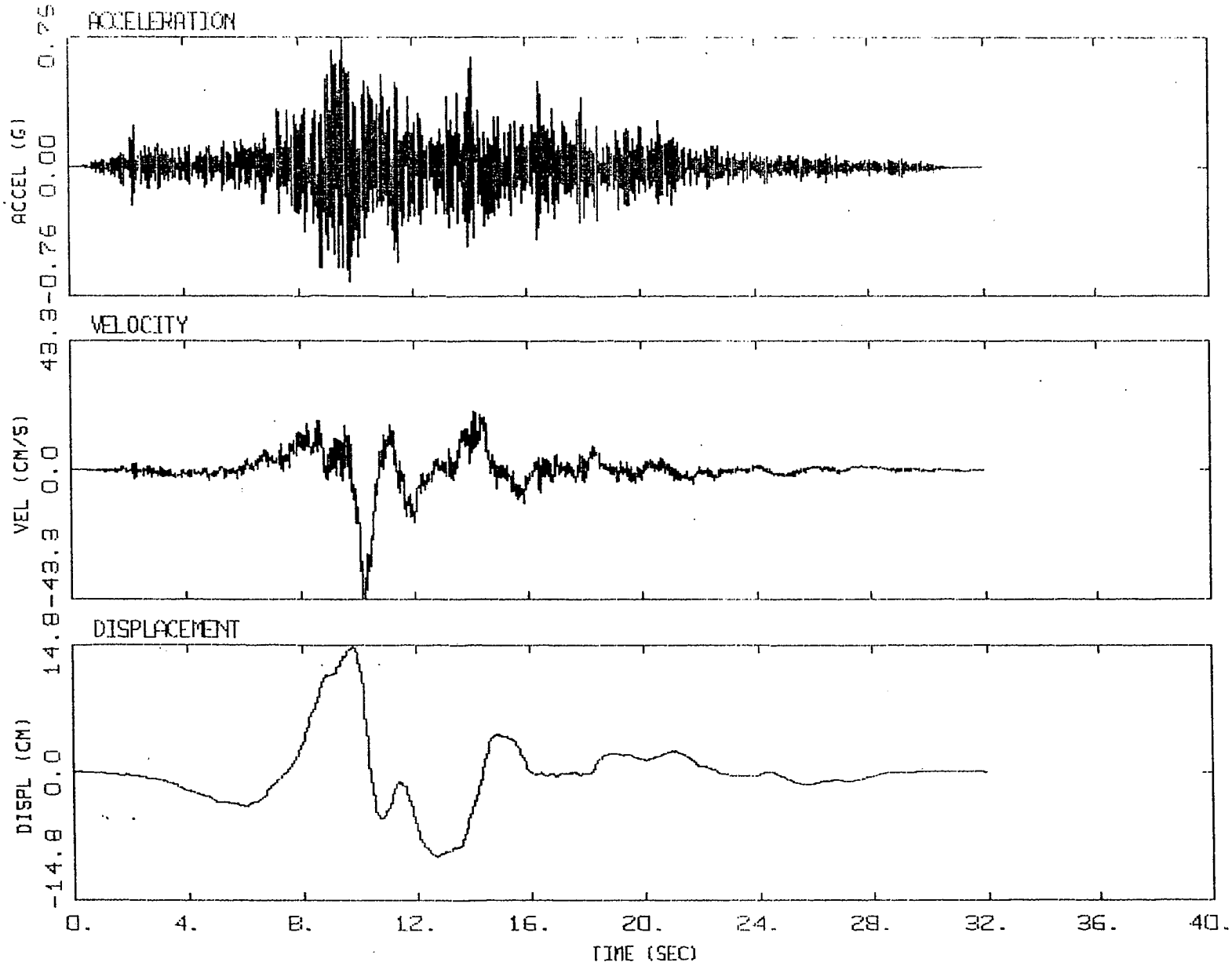

LANDERS 07/23/92 1849, SCE LUCERN, VRT, D=??.? KM, SITE=???
INTEGRATED FROM CORRECTED AND BASE-CORRECTED ACCELERATIONS

Figure 68.

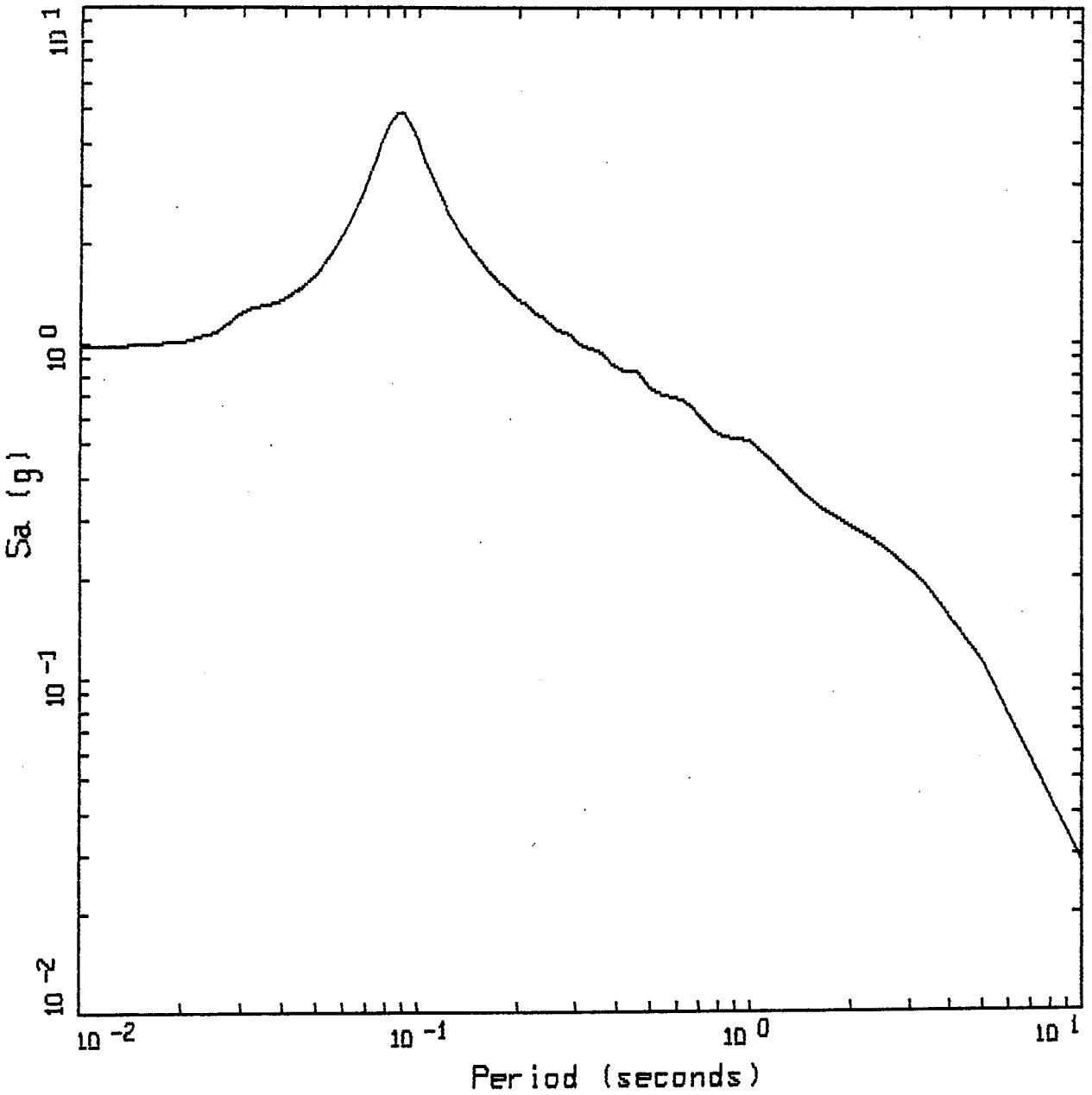

LANDERS EARTHQUAKE 06/28/92
MODELED AT LUCERNE

LEGEND

5 %, RVT: 20FT ENA PROFILE, PGA = 0.970 G

Figure 69.

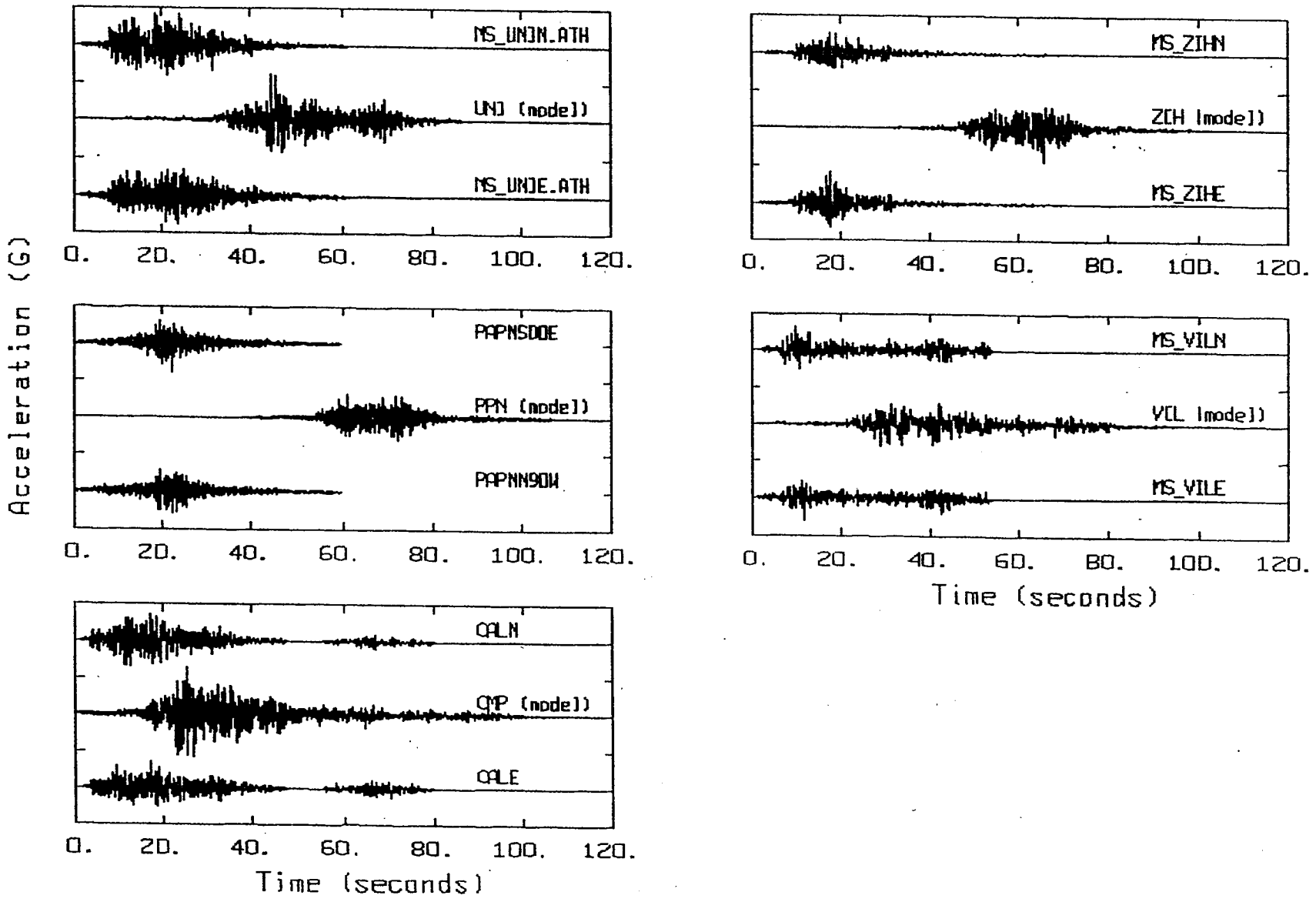
MS_UNIN.ATH
UNI (mode])
MS_UNIE.ATH
MS_ZIHN
ZIH (mode])
MS_ZIHE
PAPNSDOE
PPN (mode])
PAPNN90W
MS_VILN
VIL (mode])
MS_VILE
QALN
QMP (mode])
QALE
0. 20. 40. 60. 80. 100. 120.
Acceleration (G)
Time (seconds)
MICHOACAN EARTHQUAKE

Figure 70.

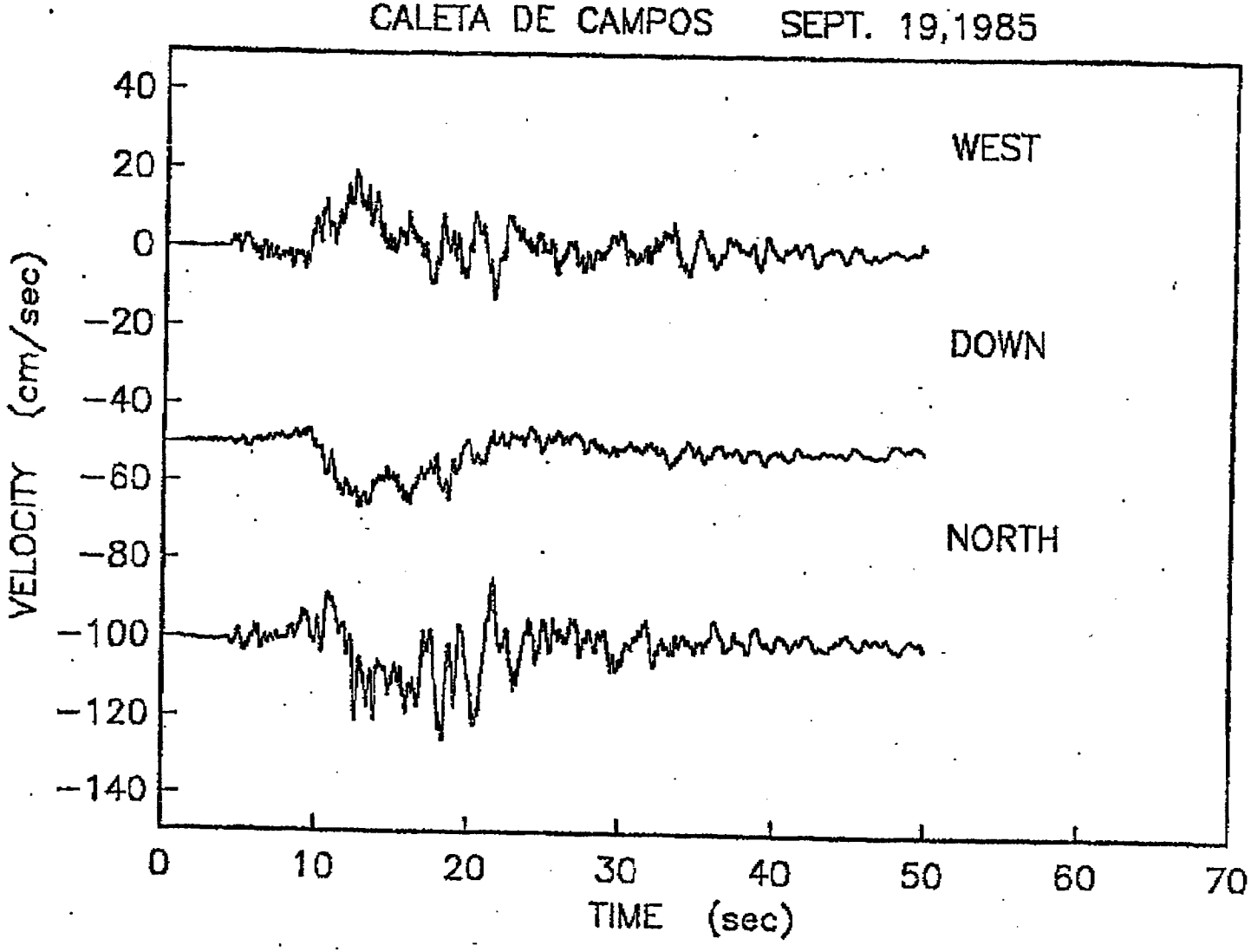
CALETA DE CAMPOS SEPT. 19,1985
WEST
DOWN
NORTH
VELOCITY (cm/sec)
40
20
0
-20
-40
-60
-80
-100
-120
-140
0
10
20
30
40
50
60
70
TIME (sec)

Figure 71.

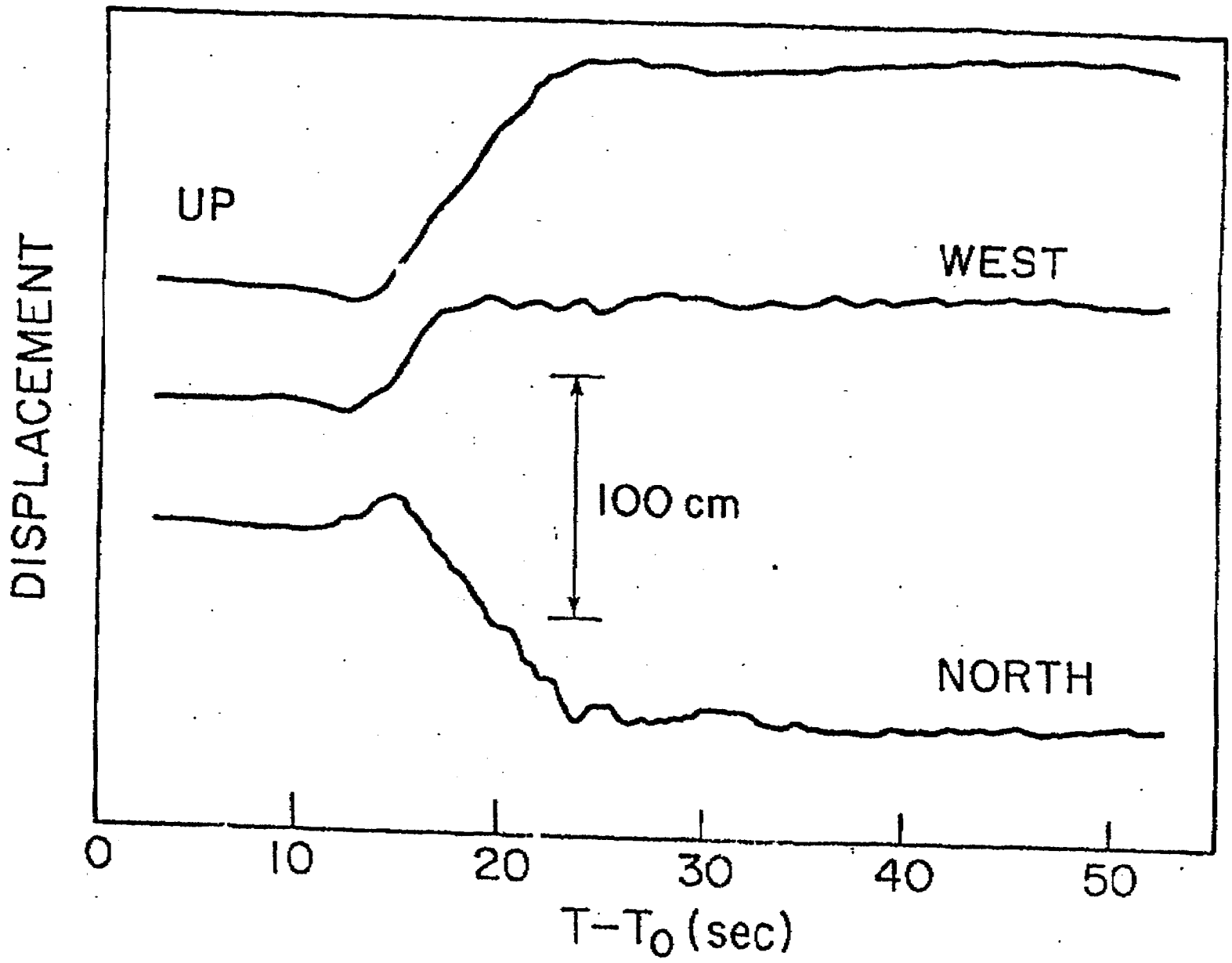

Figure 72.

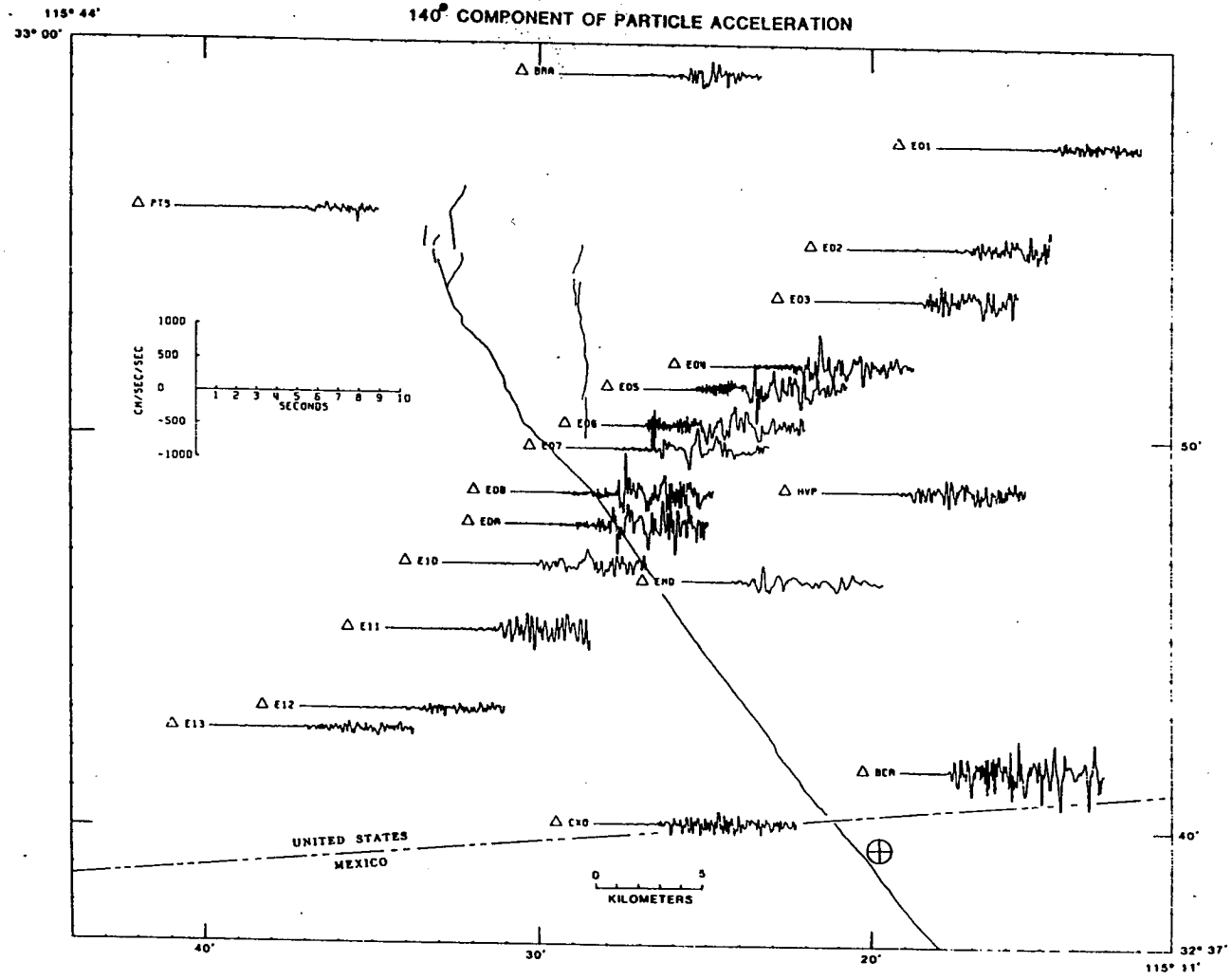

Figure 73. Main shock 140° component of particle acceleration.

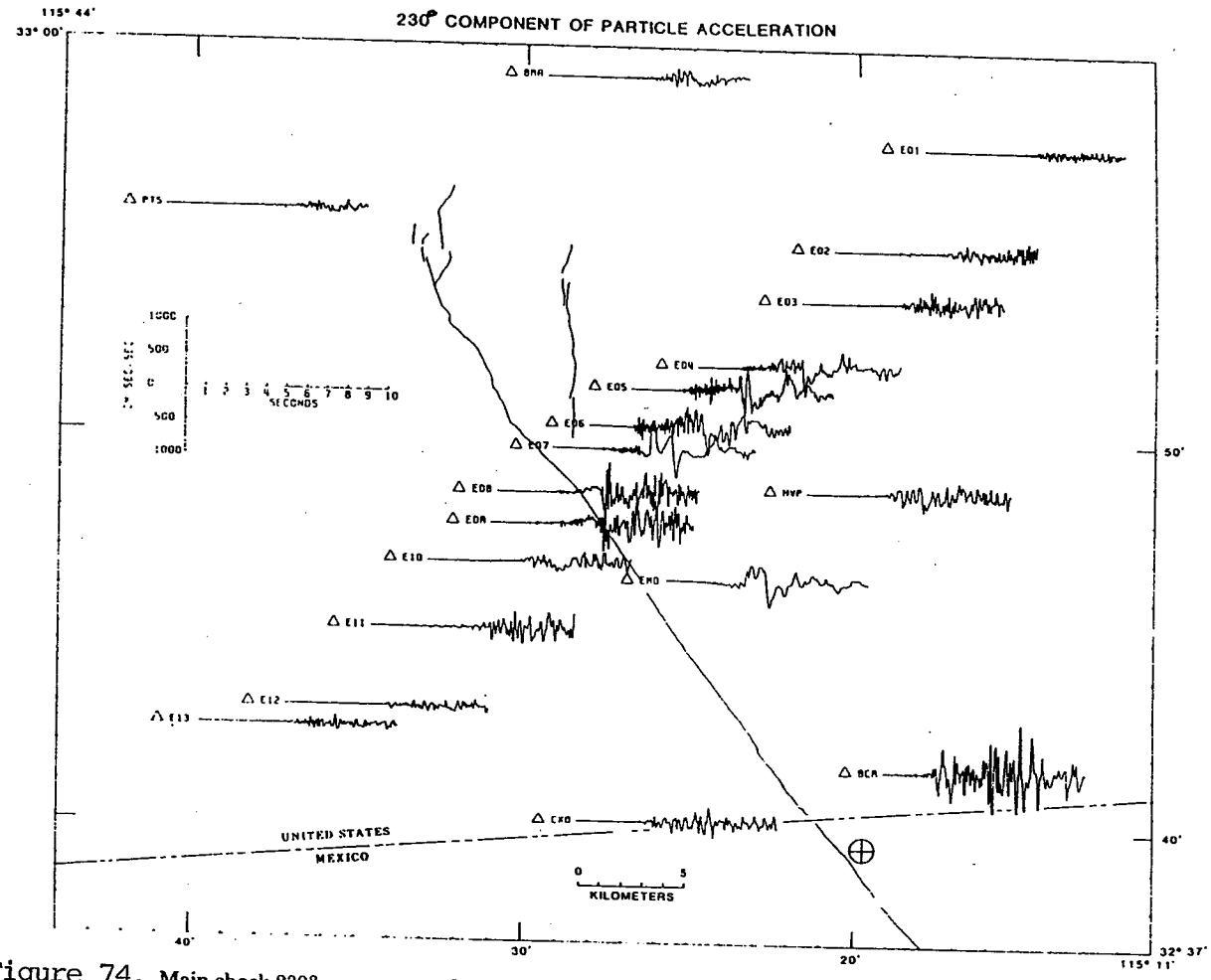

Figure 74. Main shock 230° component of particle acceleration.

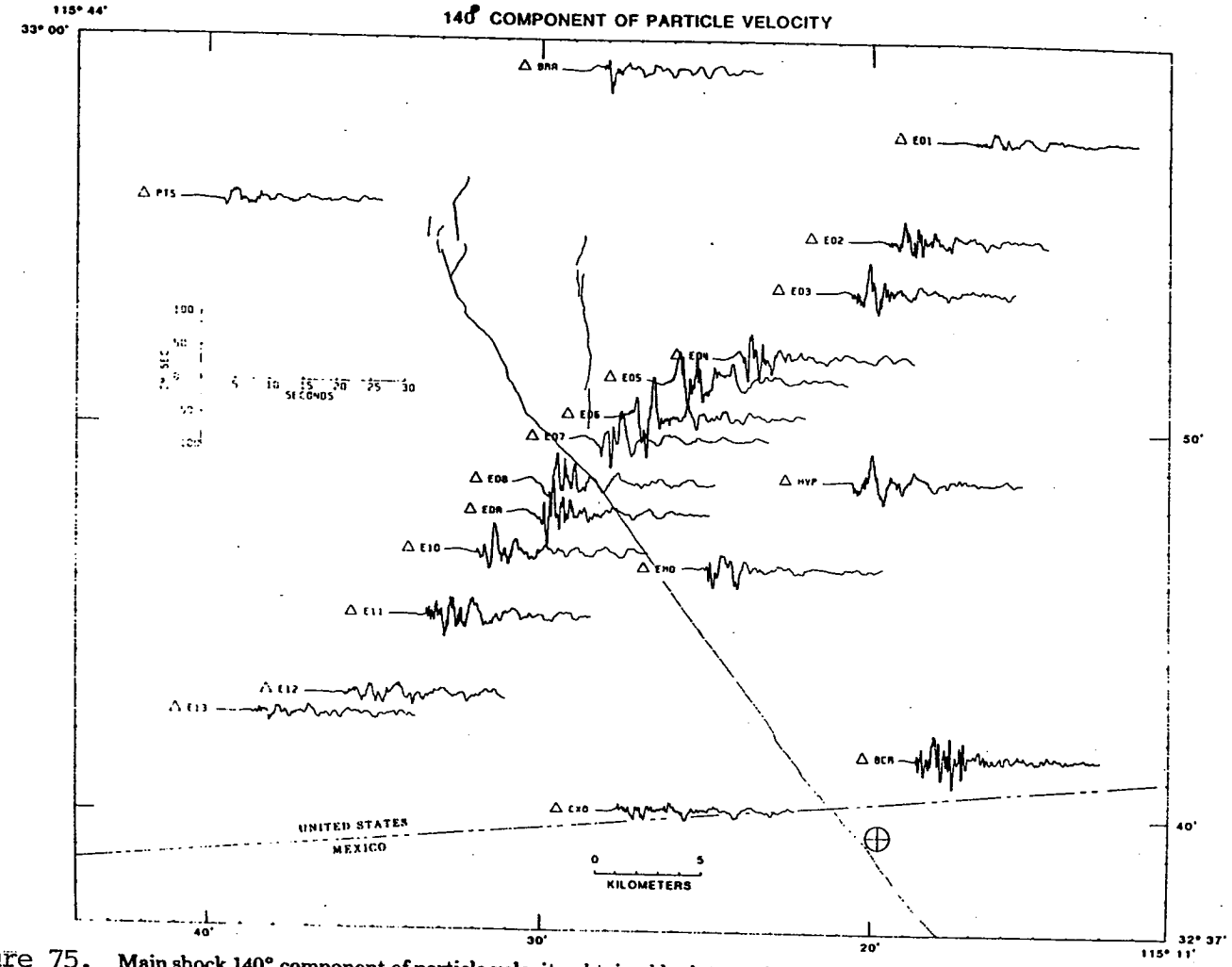

Figure 75. Main shock 140° component of particle velocity obtained by integrating the 140° component of particle acceleration. The first 30 sec after triggering is plotted.

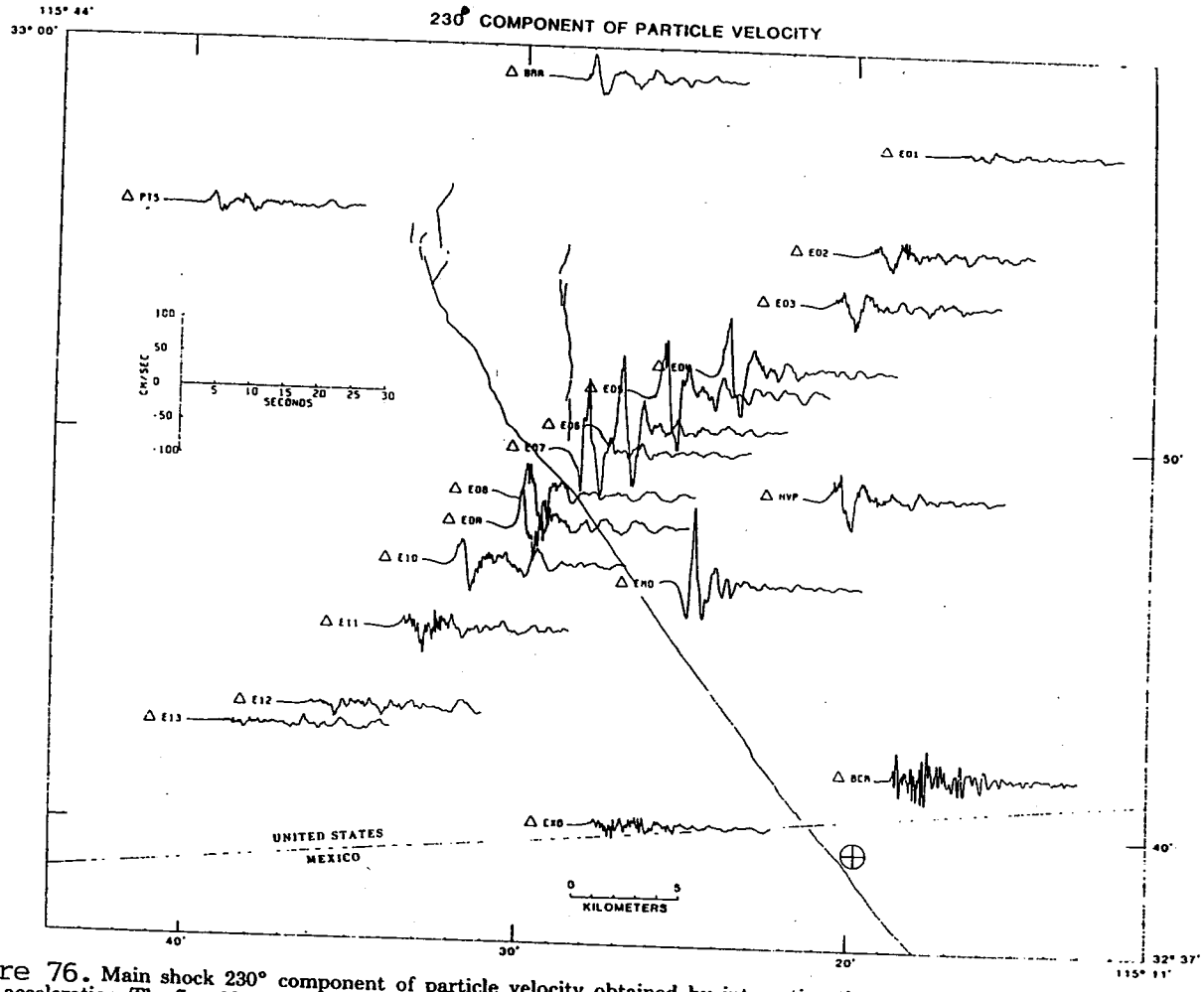

Figure 76. Main shock 230° component of particle velocity obtained by integrating the 230° component of the particle acceleration. The first 30 sec after triggering is plotted.

APPENDIX 2

NOTES ON FOURIER ANALYSIS

Any function which is periodic with period τ may be written as a Fourier series: expressed in terms of sines and cosines which are functions of frequency components ω_j. An acceleration time history can be written as

$$a(t) = A_o + \sum_{j=1}^{\infty} A_j \cos j\omega_o t + B_j \sin j\omega_o t$$

where A_j^2, B_j^2 represent the energy contained in a(t) for discrete frequency components

$$j\omega_o = \frac{j2\pi}{\tau}$$

where $A_j = \frac{4}{T}\int_o^{\frac{T}{2}} f(t) \cos j\omega_o t \, dt$

$$B_j = \frac{4}{T}\int_o^{\frac{T}{2}} f(t) \sin j\omega_o t \, dt$$

Complex Form

$$f(t) = \sum c_j e^{ij\omega_o t}$$

$$c_j = \frac{1}{T}\int_o^T f(t) \, e^{-ij\omega_o t} \, dt$$

For continuous spectra: $T \Rightarrow \infty$

$$j\,\omega_o = j\Delta\omega \Rightarrow \omega$$

$$f(t) = \frac{1}{2\pi} \int_{-\infty}^{\infty} F(\omega)\, e^{i\omega t}\, d\omega$$

$$F(\omega) = \int_{-\infty}^{\infty} f(t)\ e^{-i\omega t}\, dt$$

$F(\omega)$ = complex function

$= |F(\omega)|\ e^{i\phi(\omega)}$

Modulus · Phase

$$\Phi(\omega) = tan^{-1} \frac{Imag\ F(\omega)}{Real\ F(\omega)} \quad ,$$

modulus: Fourier amplitude spectrum; specifies how energy is distributed in frequency

example: Brune source spectrum

phase: Phase spectrum; specifies how energy is distributed in time (shape of time history).

example: $\Phi(\omega) = -\omega\tau$

phase spectrum $\Phi(\omega)$

To see the effect on f(t) of multiplying its complex spectrum $F(\omega)$ by $e^{i\omega\tau}$ start with

$$f(t) = \frac{1}{2\pi} \int_{-\infty}^{\infty} F(\omega)\ e^{i\omega t}\, dt$$

let $G(\omega) = F(\omega)\, e^{-i\omega\tau}$

$$g(t) = \frac{1}{2\pi}\int_{-\infty}^{\infty} G(\omega)\ e^{i\omega t}\, dt$$

$$= \frac{1}{2\pi}\int_{-\infty}^{\infty} F(\omega)\ e^{-i\omega(t-\tau)}\, dt$$

$$= f(t-\tau) \quad \textit{or delay by } \tau$$

f(t)

g(t)

Derivative property of Fourier transform

$$F(f(t)) = \int_{-\infty}^{\infty} f(t)\ e^{i\omega t}\, dt$$

$$F\left(\frac{df(t)}{dt}\right) = \int_{-\infty}^{\infty} \dot{f}(t)\ e^{-i\omega t}\, dt$$

integrate by parts

$$= f(t)\ e^{-i\omega t}\Big|_{-\infty}^{\infty} + i\omega \int_{-\infty}^{\infty} f(t)\ e^{-i\omega t}\, dt$$

$f(t) \Rightarrow 0 \quad t \Rightarrow \pm\infty$

$$= i\,\omega\, F\,(f(t))$$

The inverse operation applies to integration:

$$F\left(\int_{-\infty}^{t} f(x)\ dx\right) = \frac{1}{i\omega} F(f(t))$$

D.C. component of Fourier amplitude spectrum ($\omega = o$)

From

$$F(\omega) = \int_{-\infty}^{\infty} f(t)\ e^{-i\omega t}\ dt$$

$$\omega \Rightarrow 0$$

$$F(O) = \int_{-\infty}^{\infty} f(t)\ dt$$

then $\omega = 0$ component is the average of f(t).

APPENDIX 3

MEASURES OF EARTHQUAKE SIZE (MAGNITUDE)

The most common measure of the size of an earthquake is its magnitude. This important parameter is one of the most misunderstood concepts of strong motion seismology. The confusion arises because of the number of magnitude scales which the seismological community has evolved over the years. Kanamori (1983) lists 18 distinct magnitude scales each of which measures the source motion spectrum over a narrow frequency band that roughly corresponds to the maximum magnifation of a particular recording system (Nuttli and Herrmann, 1982). Because the shape of the source motion spectrum changes with earthquake size, the magnitude scales defined in this manner do not give the same number for the same size earthquakes. In addition, as the size of an earthquake increases, narrow bands of the source spectrum saturate and their amplitudes do not continue to increase. Magnitudes based upon these narrow-band measures must then saturate as well and, at some point, under-estimate earthquake size.

The magnitude scales that are important for strong ground motion assessment are the following:

(M_L) Local or Richter magnitude (Richter, 1935), which is, strictly speaking, appropriate to only southern California, measures displacement at frequencies between 0.3-10 Hz (Kanamori, 1983).

(M_s) Surface-wave magnitude was introduced by Gutenberg (1945a) and is a measure of

surface-wave energy at a period of approximately 20 sec.

(m_B) Body-wave magnitude was introduced by Gutenberg (1945b) to extend magnitudes to measure the size of deep earthquakes ($\geq$ 70 km) which, because of the depth of focus, do not excite 20 sec surface waves particularly well. The body wave phases used can be either P, PP, or S with periods ranging from approximately 0.5 to 12 sec (Kanamori, 1983). Maximum amplitudes are measured, which can be several seconds into the wavetrain.

(m_b) Body-wave magnitude. With the advent of the World-Wide Standardized Seismograph Network (WWSSN) around 1961-1963, the body-wave magnitude was computed from P-waves recorded by the short-period vertical component Benioff instrument. The seismographs have a natural frequency at about 1 Hz and the measurement is made during the first few cycles of the recorded P-wave. Because of this, the m_b measure does not represent the entire source (Kanamori, 1983) and underestimates the true size for m_b larger than about 5½ to 6 (Kanamori, 1983; Houston and Kanamori, 1986; Boore and Atkinson, 1987). The m_b measure was adopted as a standard by the U.S. Coast and Geodetic Survey in the 1960's.

(m_{Lg}) This scale was introduced by Nuttli (1973) and specifically designed for eastern North American earthquakes. The scale uses the amplitude of one-second period higher-mode Rayleigh waves recorded on vertical component short period WWSSN seismographs. This is the magnitude measure commonly used in performing seismic

hazard analyses in the central and eastern United States (Atkinson and Boore, 1987) and is also variously designated as M_N or m_n. The scale was originally established to be equivalent to m_b (Herrmann and Nuttli, 1981) and has been shown to be equivalent to M_L over the magnitude range M_L 3-5 (Herrmann and Nuttli, 1982; Kanamori, 1983). The m_{Lg} scale has been applied to records made by different instruments with predominant periods away from the nominal 1 sec period for which it was originally calibrated (Atkinson and Boore, 1987; Herrmann, 1987). As a result some caution is warranted in evaluating m_b - m_{Lg} and m_{Lg} - M_o (seismic moment) relationships (Atkinson and Boore, 1987, Boore and Atkinson, 1987; Herrmann, 1987; Toro and McGuire, 1987),

(M) Moment magnitude was first introduced by Brune and Engen (1969) and later developed into a generally applicable scale by Kanamori (1977) and Hanks and Kanamori (1979). It is the only scale fundamentally related to a physical parameter of the seismic source, the seismic moment.

The seismic moment (M_o) may be thought of as a measure of the zero-frequency amplitude of the earthquake source spectrum. It is related to static source parameters by

$$M_o = \mu A \bar{D} \qquad (1)$$

where μ is the rigidity of the source volume (usually taken as 3×10^{11} dyne/cm^2; Hanks and Kanamori, 1979), A is the fault area (length x width), and $\bar{D}$ is the average slip (Aki, 1967). Because seismic moment can be related directly to the energy radiated by a seismic source, a

magnitude scale based upon moment does not suffer the limitations imposed by narrow-band time domain measures (Hanks and Thatcher, 1972; Kanamori, 1977). In addition, the seismic moment can be accurately determined from seismograms directly or from spectral analyses. The seismic moment is related to moment magnitude **M** through

$$\log M_o = 1.5\,M + 16.1 \qquad \text{(Hanks and Kanamori, 1979)} \qquad (2).$$

Since its definition in 1979, moment magnitude has come into widespread use and, because of its unambiguous nature, is the preferred scale for characterizing the size of an earthquake. Because of the relationship involving fault area and slip, use of moment magnitude has the additional advantage of making it easier to relate earthquake occurrence rates to geologically determined slip rates.

REFERENCES

Aki, K. (1967). "Scaling law of seismic spectrum." *J. Geophys. Res.*, 73, 1217-1231.

Atkinson, G.M., and Boore, D.M. (1987). "On the m_N, M relation for eastern North America earthquakes." *Seism. Res. Letters,* 58(4).

Boore, D.M., and Atkinson, G.M. (1987). "Stochastic prediction of ground motion and spectral response parameters at hard-rock sites in eastern North America." *Bull. Seism. Soc. Am.*, 77(2), 440-467.

Brune and Engen (1969)

Gutenberg, B. (1945). "Amplitudes of surface waves and magnitudes of shallow earthquakes." *Bull. Seism. Soc. Am.*, 35, 3-12.

Gutenberg (1945a, B)

Hanks, T.C., and Kanamori, H. (1979). "A moment magnitude scale." *J. Geophys. Res.*, 84, 2348-2350.

Hanks, T.C., and Thatcher, W. (1972). "A graphical representation of seismic source parameters." *J. Geophys. Res.*, 77, 4393-4405.

Herrmann, R.B. (1987). "Broadband Lg magnitude." *Seis. Res. Letters,* 58(4).

Herrmann, R.B., Nuttli, O.W. (1982). "Magnitude: the relation of M_L to m_{bLg}." *Bull. Seism. Soc. Am.*, 72, 389-397.

Herrmann, R.B., and Nuttli, O.W. (1980). "Strong motion inves-tigations in the central United States." *Proc. Seventh World Conf. on Earthq. Engin.*, Istanbul., 2, 533-536.

Houston, H., and Kanamori H. (1986). "Source spectra of great earthquakes: teleseismic constraints on rupture processes and strong motion." *Bull. Seism. Soc. Am.*, 76, 19-42.

Kanamori, H. (1983). "Mechanism of the 1983 Coalinga earthquake determined from long-period surface waves." *The 1983 Coalinga, Calif. Earthquakes,* Calif. Dept. of Conser., Div. of Mines and Geology, Special Publ. 66, 233-240.

Kanamori, H. (1977). "The energy release in great earthquakes." *J. Geophys. Res.*, 82, 2981-2987.

Nuttli, O.W. (1973). "Seismic wave attenuation and magnitude relations for eastern North America." *J. Geophys. Res.*, 78, 876-885.

Nuttli, O.W., and Herrmann, R.B. (1981). "Consequences of earthquakes in the Mississippi Valley." *Am. Soc. Civil Engin.*, Meeting, St. Louis, MO. Preprint 81-519.

Nuttli, O.W., and Herrmann, R.B. (1984). "Ground motion of Mississippi Valley earthquakes." *J. Tech. Topics in Civil Engin.*, 110(1), 54-69.

Toro, G.R., and McGuire, R.K. (1987). "An investigation into earthquake ground motion characteristics in eastern North America." *Bull. Seism. Soc. Am.*, 77, 468-489.

Richter, C.F. (1935). "An instrumental earthquake magnitude scale." *Bull. Seism. Soc. Am.*, 25, 1-32.

Evaluation and Implementation of an Improved Methodology for Earthquake Ground Response Analysis

Uniform Treatment of Source, Path and Site Effects

Seminar 2

(7/6/94, 89 p.)

Site Specific Specification of Ground Motion: An Overview, Part 2

a) General References
b) Review Main Points from Seminar 1
c) Empirical Approach
d) Statistical Approach
e) Numerical Modeling Approach
f) Combined Approach
g) Spectral Matching
h) Case Studies

CALTRANS

SEMINAR ON STRONG GROUND MOTION

Seminar 2; July 6, 1994

Site Specific Specifications of Strong Ground Motions:An Overview(Continuation of Seminar 1)

a) General References:

1990 Reiter: Earthquake Hazard Analysis, Issues and Insights. Columbia University Press.

EERI Monograph Series. Seed and Idriss, Hudson, Newmark and Hall.

1993 I.M. Idriss: NIST GCR 93-625

1987 Silva and Lee: Waterways Experiment Station Report 24 (Paper S-73-1) (RASCAL code)

b) Review:

1) Model F.S. and PAA for a rock site

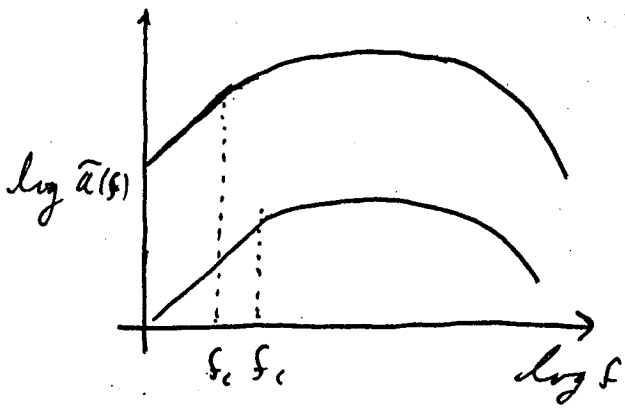

see Figure 1

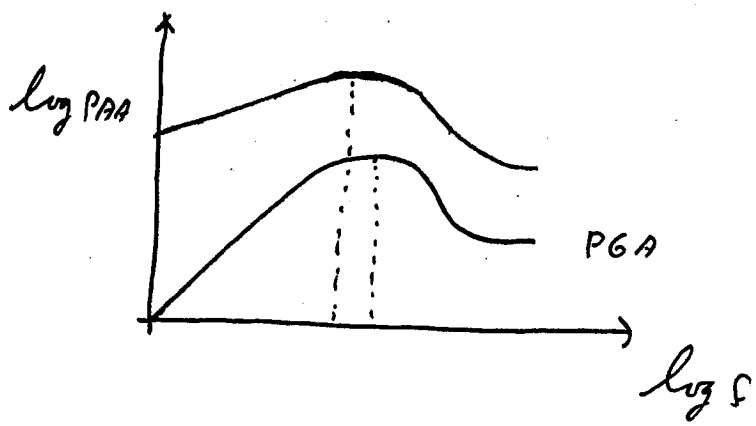

see Figure 2

based on point source, single corner frequency ω-square model (Brune)

$$\tilde{a}(f) = \frac{cM_o f^2}{1 + (\frac{f}{f_c})^2} \cdot \frac{e^{\frac{-\pi fR}{\beta Q(f)}}}{R} \cdot A(f) e^{-\pi \kappa f}$$

$$f_c^3 = \frac{\beta^3}{8 \cdot 44} \frac{\Delta\sigma}{M_o} \qquad \text{,source corner frequency}$$

2) Features of Strong Ground Motion

a) Rock verses soil

Figure 3 shows the empirical deep stiff soil amplification factors (5% damped response spectra) for varying levels of control (rock outcrop) motions. For control motions, exceeding ≈ 10%g, deep stiff soils amplify at low frequency (due to the velocity gradient) and deamplify at high frequency (due to damping). Figure 4 shows a "classical" example in the spectra computed from recordings at Gilroy 1 (rock) and Gilroy 2 (soil) from the 1989 M 6.9 Loma Prieta earthquake. The rupture distance is about 15 km (≈ 15 km GL1, ≈ 17 km GL2). The soil profile amplifies at periods from about 0.6 sec to 3 sec. Beyond about 3 sec, the wavelengths are greater than the profile depth (≈ 650 ft) and the control motions are largely unaffected by the soil column. At periods shorter than about 0.6 sec the soil column deamplifies. Figures 5, 6, and 7 show acceleration, velocity, and displacement time histories (recorded and computed) at the same two sites. The time histories reflect the features seen in the response spectra: accelerations show higher frequency content at the rock site and slightly higher motions, velocities show larger motions at the soil site, and displacements are about the same at both sites. The displacement time histories are associated with periods whose corresponding wavelengths are greater than the profile depth.

b) Magnitude Effects

The time domain effects of earthquake size amplitude and duration, are shown in Figure 8. Figure 9 illustrates the effects on 5% damped response spectral shapes.

c) Effects of Damping (kappa) at Rock Sites

The differences in 5% damped response spectral shapes for M $\approx$ 6.5 ENA (hard rock, κ = 0.008 sec) and WNA (soft rock, κ = 0.04 sec) recordings are shown in Figure 10. The difference in shapes is attributed to kappa or frequency independent damping in the top 1-2 km of the crust. Figure 11 shows computed effects of kappa in spectral shapes for WNA motions (includes A(f), amplification factors). Figure 12 shows pseudo absolute acceleration response spectra computed for WNA and ENA and Figure 13 shows measured kappa values plotted verses average shear-wave velocity over about 100 ft. These are rock sites which recorded the 1989 M 6.9 Loma Prieta earthquake.

d) Nonlinear Soil Response

Figure 14 shows change in empirical soil amplification with change in control motion (rock outcrop) level. Table 1 lists changes in predominate frequency and amplitude of the fundamental profile resonance peak for Lotung, Taiwan recordings of different size earthquakes. As the motions increase, the predominate frequency and amplitude decrease: shear modulus decreases and damping increases with increasing strain levels.

e) Directivity and Near-Source Effects

Figure 15 shows a plot of the fault trace, strong motion sites, and selected displacement time

histories for the 1992 M 7.2 Landers earthquake. Sites YRM (Yermo) and DHS (Desert Hot Springs) are at nearly the same fault distance ($\approx$ 25 km) from the ends of the fault. Rupture towards YRM (away from DHS) results in an increase in long period energy (relative to DHS) and is reflected in the larger displacements. Effects of rupture directivity also results in shorter durations at YRM relative to DHS (Figures 16 and 17). Site LUC (Figure 15) shows very large displacements (particularly on fault normal components), expected very close to large magnitude earthquakes. Figure 18 shows very long period (infinite) displacements recorded from a great earthquake (M 8.1 Michoachan, Mexico at a rupture distance of about 15 km). These represent the near-field terms in our model ($\sim \frac{1}{r^2 \alpha^2, \beta^2}$; *from Equation* (9), *Seminar* 1) .

Another important aspect of near-source motions is the high level of short period energy on the vertical component. Figure 19 shows response spectra computed from recordings at site Lucerne. At periods shorter than about 0.1 sec, the vertical component exceeds the horizontal and saturates to nearly the same PGA as the horizontal. The figure also illustrates the effects of a shallow soil (20 ft) and low kappa (κ = 0.02 sec). Figure 20 shows model prediction (point source) which match the recorded motions quite well.

c) Empirical Approach:

1) Distribution of Data

The empirical strong motion data base for crustal earthquakes occurring in tectonically active regions is comprised of about 100 earthquakes and about 1,500 components of recordings. Figures 21 and 22 show the distributions of sites and magnitudes for rock and soil sites respectively. The two figures reveal:

a) Very little data at close distances, particularly for **M** > 6.5,

b) Rock sites have significantly fewer recordings than soil sites.

The two figures clearly demonstrate the need for some kind of augmentation or guide in extrapolating the empirical data base. For **M** 5-6.5 at distances 10-70 km, soil site motions are well represented. For the same ranges, rock sites have significantly fewer recordings but are reasonably well represented. For **M** > 6.5 and at distances < 10 km, relations based on the empirical data are largely extrapolations relying almost totally on the selection of function forms and poorly determined coefficients (those coefficients which control near source motions).

2) Functional Forms

The empirical approach is the fitting of some function to the recorded motions (PGA, PGV, PGD, and response spectra).

$$y = f(M, D, S) \quad (1)$$

y, ground motion

M, magnitude

D, some measure of distance to source

S, site conditions

The fitting process generally involves minimizing the square error term

$$\sum (y_o - y_c)^2$$

$$\sum (y_o - f(M, D, S)^2 \quad (2).$$

The functional form is generally expressed as some variant on

$$\ln y = C_1 + C_2 M + C_3 \ln (D + C_4 e^{C_5 M}) + C_6 D + C_7 S \quad (3)$$

where C_j represent coefficients, S represents a site switch i.e. 0 rock site
1 soil site.

Seminar 4 will examine several functional forms in detail as well as the physical basis for Equation (3) in the context of our point-source model.

Figures 23-28 illustrate the effects of data distribution (M, D) on several empirical attenuation relations.

Figures 23 and 24 show PGA verses D for **M** 6.5 at soil and rock sites respectively. The soil site relations (Figure 23) show much closer agreement particularly at closer distances where there are significantly more soil data. Figures 25 and 26 are corresponding plots for **M** 7.5. The spread in the relations is larger than for **M** 6.5 at both rock and soil sites reflecting the effects of the lack of data to provide constraints. **M** 7.5 results are almost entirely extrapolations (Figures 21 and 22).

To examine the ranges in response spectra, Figures 27 and 28 show 5% damped spectral acceleration for a **M** 7.0 earthquake at a 1 km fault distance at soil and rock sites. The differences in the predicted motions are period dependent and similar to those reflected in the PGA relations with distance. This variability suggests that some additional guide in specification of ground motions for **M** > 6.5 and at distance < 10 km is desirable.

d) Statistical Approach

Sometimes referred to as the site dependent spectra or "method of representative data" approach. In this method, a suite of acceleragrams are selected that represent the magnitudes, paths, and site conditions of the design earthquake or earthquakes. Magnitudes are generally selected to be within 0.5 unit of the design magnitude and site conditions include attempting to have similar shear-wave velocity profiles.

Since the design earthquake is generally at close distances ($\leq$ 50 km) the effects of propagation path differences have usually been neglected. The resulting acceleragrams are then scaled, each by a constant factor to account for magnitude and distance differences, averaged, and fractiles computed. The approach is desirable in that site specific effects are accommodated and a statistically significant measure of dispersion is obtained. However, this naturally presupposes that "representative data" are available and also introduces a substantial element of subjectively in the selection of appropriate records. Questions also arise regarding appropriate scaling factors for distance and magnitude. As an illustrative example, Figure 29 shows a site shear-wave velocity profile and Figure 30 shows profiles at representative recording sites. Figure 31, shows 2% damped representative spectral velocities, scaled for M and D. Figure 32 shows computed fractiles based on the scaled data shown in Figure 31. In Figure 32, (a) and (b) represent the median and 1-sigma spectra respectively, (c) represents the largest component, and (d) represents a conservative design motion based on the method of representative data.

Another, perhaps slightly less site specific but similar approach is the use of site dependent shapes scaled to a design PGA value. Figure 33 shows an example of site dependent 5% damped response spectral shapes for rock, stiff, deep, and soft soil conditions. In this case, magnitude dependencies are not included nor is the effect of damping at rock sites. Curves such as these must only be implemented for the same magnitude, distance, and site conditions as the recordings used in producing the shapes.

e) **Numerical Modeling Approach**

1) Ground Motion Model:

Figure 34 depicts the point-source model as well as a general finite-source model. Seminar 5 on Numerical Ground Motion Models will discuss several finite-fault models in some detail with emphasis on the stochastic model. In the current application, only the stochastic point- and finite-source models are considered. As a result, since the point-source model has already been introduced, only a brief discussion of the stochastic finite source model will be presented.

Finite earthquake sources include the effects of rupture propagation and spatially variable moment release over a rupture surface. To model these effects, small stochastic point source models are simply distributed on a planar surface and progressively fired to simulate a propagating rupture. In general, a number of **M** 5 "subevents" are added to produce **M** 6-8 earthquakes. This process is depicted schematically in Figure 34. The point-source model in terms of path and site components is identical to the point-source model, an extremely convenient feature. For both ground motion models, the free parameters at fixed magnitude for rock sites are:

Point : source depth, $\Delta\sigma$, Q(f), A(f), κ(kappa)

Finite : slip model, hypocenter and mechanism, Q(f), A(f), κ(kappa).

For soil sites additional free parameters include soil profile (shear-wave velocity and unit weight) and, for equivalent-linear soil response, strain dependencies of shear modulus and damping.

Region specific components of the models include $\Delta\sigma$, source depth mechanism, Q(f), and generally A(f). Site specific parameters are kappa, the local soil profile, and material nonlinearisties. Table 2 lists the models parameters and typical methods to determine representative values. Seminar 5 will go into detail regarding determination of parameters and their uncertainties.

Two ways to implement the numerical modeling approach:

1) Generate "data" to produce a region- or site-specific attenuation relation,

2) Compute response spectra for the design earthquake.

The first approach is useful in applications to probabilistic analyses where a site specific attenuation relation is used along with several empirical relations. It can also be used to generate region specific attenuation relations for situations where few data exist: for example, Cascadia subduction zone earthquakes that may affect northern California.

An example of generating synthetic data and then developing a region/site specific attenuation relation is shown in Figure 35. In this application, the point-source model was used with suites of parameters shown in Table 3. Thirteen epicentral distances were used from 0 to 500 km (7,020 runs). A functional form (Equation 3) was chosen and a weighted regression performed (solid line in Figure 35).

The second approach will be illustrated in the case study (Section h).

f) Combined Approach

This approach generally involves combining the empirical with modeling to develop design ground motions. The usual procedure is to produce response spectra from several empirical relations and from numerical modeling. The suite of spectra are plotted together and a design spectrum judgementally drawn either to envelope the suite of predictions or to represent some average. This approach is illustrated in the case study as well.

g) Spectral Matching

This process refers to generating a synthetic time history whose response spectrum matches, in some sense, a target spectrum. Several techniques are available but most do not produce realistic

time histories (acceleration, velocity, and displacement). We'll concentrate on the method using the code RASCAL.

PROCEDURE

Uses an omega-square point source to compute initial fourier amplitude spectrum and RVT (Random Vibration Theory) to estimate an initial response spectrum,

SPECIFY

Target response spectrum (0.5-10% damping) and source parameters for stochastic point source: **M**, R, $\Delta\sigma$, β, ρ,

Form ratio of target to computed spectral velocity for correction factor to fourier amplitude spectrum,

Compute new response spectrum using RVT (RVT iterations, 2-4),

Extract phase spectrum from recorded motion with about same **M**, R, and site conditions as dominant earthquake target spectrum,

Combine with fourier amplitude spectrum to produce "realistic" time history,

Continue iterations using response spectrum computed from time history (SDF iterations, 4-6).

Results of the RASCAL spectral matching procedure are shown in Figures 36-38. Figure 36 shows the convergence properties of the RVT iterations. Figure 37 shows a design spectrum (target) and final spectral match and Figure 38 shows the resulting time histories.

h) Case Studies

Two Bureau of Reclamation Dams: Unity in northeastern Oregon and Spring Creek in northern California.

1) Unity Dam: M 6.25 at a distance (epicentral) of about 0.3 km. Figure 39 shows a schematic of the model. The site is a shallow 8m (26 ft) thick stiff soil site (Figure 40). Table 4 lists the model parameters and their uncertainties.

Figure 41 shows the randomized profiles. Figure 42 shows the modulus reduction and damping curves used along with upper- and lower- bounds for the randomization process. Figure 43 shows a suite of 20 of the 50 random degradation curves (Seminars 7, 8, and 9 will treat soil profile and degradation curve uncertainty and randomization).

The variation in 5% damped spectral accelerations for each parameter varied separately (50 realizations) based on Table 4 distributions are shown in Figure 44-51. The parameters uncertainty for variation of all parameters is shown in Figure 52.

To develop the design (SEE) response spectrum, the empirical spectra and model spectrum are compared in Figure 53. From the figure it is apparent the modeling has captured the site specific aspects of the seismic evaluation showing the effects of the shallow stiff soil column in the short period peak of the spectrum. The SEE was chosen to reflect the site specific results at short periods and to be more enveloping at longer periods where the dam response is most significant (about 0.8-2 sec).

Figure 54 shows the SEE design spectrum along with the spectral match and Figure 55 shows the resulting time histories. The phase spectrum for the RASCAL match was taken from a recording of a M 6.5 earthquake.

2) Spring Creek Dam: A rock site for a M 8.5 Cascadia subduction earthquake at a rupture distance of about 70 km. Figure 56 shows a plan view of the rupture surface and site location with

distances shown in Figure 57. In this case, the stochastic finite-fault was used and variation of slip model and nucleation point replace the point-source variation in stress drop. Table 5 lists the parameters and their uncertainties and Figure 58 shows three of the 50 random slip models. The nucleation zone is defined to be the lower half of the rupture surface and to 10% of the fault length at each end. Figure 59 shows an example (different project) of random nucleation points and the base case nucleation point at the center of the nucleation zone.

The variation of 5% damped spectral acceleration for each parameter varied are shown in Figures 60-64. The base case slip model used during parameter variations is simply taken as the first random slip model. (Seminar 9 will discuss the method of generating slip models in some detail). Figure 65 shows extreme cases for directivity at this site with spectra computed for north, middle, and southern foci (nucleation points). Interestingly, the middle focus results in the largest motions. This could be related to the base case slip model and the particular distribution of asperities.

The total parametric uncertainty (all parameters varied) is shown in Figure 66 and Figure 67, shows the median model spectrum compared to empirical spectra. The Crouse (1991) spectrum is for a soil site so the shape is quite different (Crouse (1991) only has soil spectra, it is shown since there are so few empirical relations for subduction zone earthquakes). The SSE spectrum is conservatively chosen to follow Youngs et al. (1988) at short periods and the modeling at long periods.

To perform the RASCAL spectral match a phase spectrum from a M 8.5 subduction earthquake recorded at a rock site at around 70 km distance is needed. To supply this, the stochastic finite fault was run to generate 50 time histories during the simulations which varied all the parameters. To calibrate the finite-fault code's ability to correctly model subduction earthquake time histories, the M 8.1 Michoacan earthquake was modeled at several sites. Figure 68 shows

the simulated average component compared to the two recorded motions at each site (all plotted to the same scale). Apparently the stochastic finite-fault simulates the amplitudes and durations quite well. A suite of time histories for a M 8.5 Cascadia earthquake representing variations of all parameters is shown in Figure 69. The actual selection of a time history could be based on a target duration, say 5-75% Arias Intensity but, in this case, a time history which was moderately long was selected. The spectral match is shown in Figure 70 and the resulting acceleration, velocity, and displacement time histories are shown in Figure 71.

TABLE 1

FREQUENCY AND AMPLITUDE OF FUNDAMENTAL RESONANCES

LSST Event	Surface AVG PGA (g)	F (Hz)	Amplitude
Surface/20 ft			
10	0.035	4.83	10.84
16	0.080	3.37	3.78
7	0.090	2.98	2.65
Surface/36 ft			
10	0.035	3.37	7.16
16	0.080	2.44	3.38
7	0.090	1.71	2.01
Surface/56 ft			
10	0.035	2.44	8.15
16	0.080	1.66	3.68
7	0.090	1.32	2.52
Surface/154 ft			
10	0.035	1.22	6.57
16	0.080	-----*	-----*
7	0.090	0.78	3.58

*Recording not available

TABLE 2

MODEL PARAMETERS

Parameter	How Determined
source depth	local seismicity or analogue
$\Delta\sigma$	small earthquakes, literature
slip model	randomly generated using a calibrated method
nucleation point	random within defined nucleation zone
mechanism	local/regional geology, local/regional seismicity
Q(f)	small earthquakes, literature
kappa	small earthquakes, relate to geology, literature
A(f)	local/regional crustal model
soil profile	downhole, crosshole, SASW, generic category
material nonlinearity	in-situ testing, laboratory testing, generic curves, literature

TABLE 3

INPUT PARAMETERS AND WEIGHTINGS FOR STOCHASTIC ATTENUATION RELATIONSHIPS

Parameter	Value	Weight
$\Delta\sigma$	25 bars 50 bars 75 bars 100 bars 150 bars	0.05 0.30 0.30 0.30 0.05
κ	0.02 sec 0.04 sec 0.08 sec	0.40 0.50 0.10
Q_o	150 370 600	0.20 0.60 0.20
M_w 5 and 6 Point Source Focal Depth	5 km 7 km 9 km 11 km	0.10 0.80 0.05 0.05
M_w 7 Point Source Focal Depth	8 km 10 km 12 km 14 km	0.8 0.1 0.05 0.05

TABLE 4

INPUT PARAMETERS AND UNCERTAINTIES FOR PARAMETRIC VARIATIONS FOR UNITY DAM

Parameter	Mean Value	Distribution	σ
Q_o	350	lognormal	0.18
η	0.30	normal	0.05
κ	0.04 sec	lognormal	0.30
$\Delta\sigma$	75 bars	lognormal	0.36
Source depth	10 km	uniform	$\pm$ 5 km
Soil v_S	-	lognormal	0.34
Modulus Reduction	-	normal	0.11
Modulus Damping	-	normal	4.0%
Half-Space v_S	1219 m/sec	lognormal	0.17

TABLE 5

INPUT PARAMETERS AND UNCERTAINTIES FOR PARAMETRIC VARIATIONS - SOUTHERN CASCADIA SUBDUCTION ZONE INTERFACE EARTHQUAKE

Parameter	Mean or Median Value	Distribution	σ*
Q_0	273	lognormal	0.18
η	0.66	normal	0.05
κ	0.02 sec	lognormal	0.30

* For lognormal distributions, σ is actually σ_{ln}

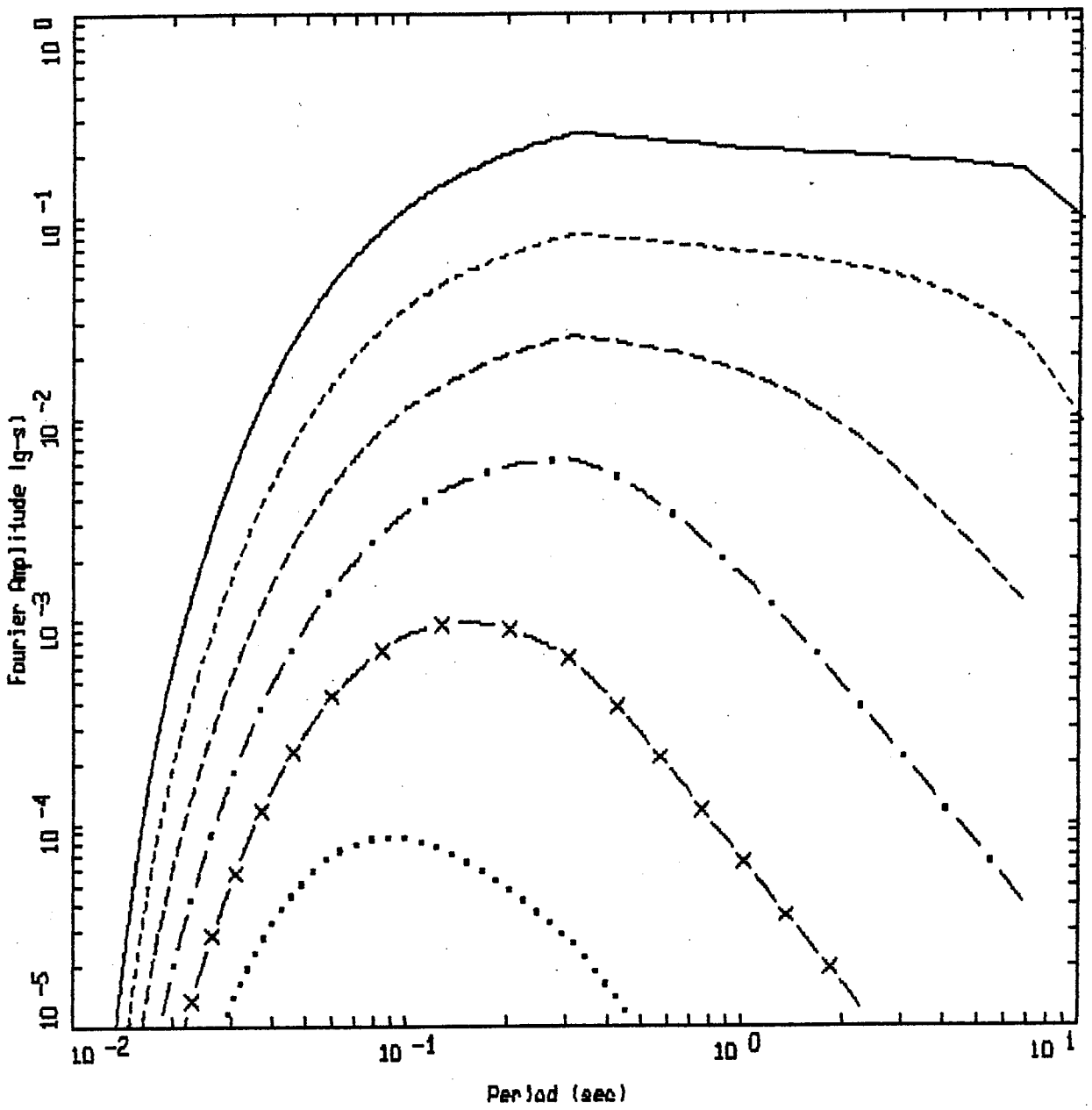

WNA SPECTRA
ROCK, R= 10 KM

LEGEND
WNA M=7.5
WNA M=6.5
WNA M=5.5
WNA M=4.5
WNA M=3.5
WNA M=2.5

Figure 1.

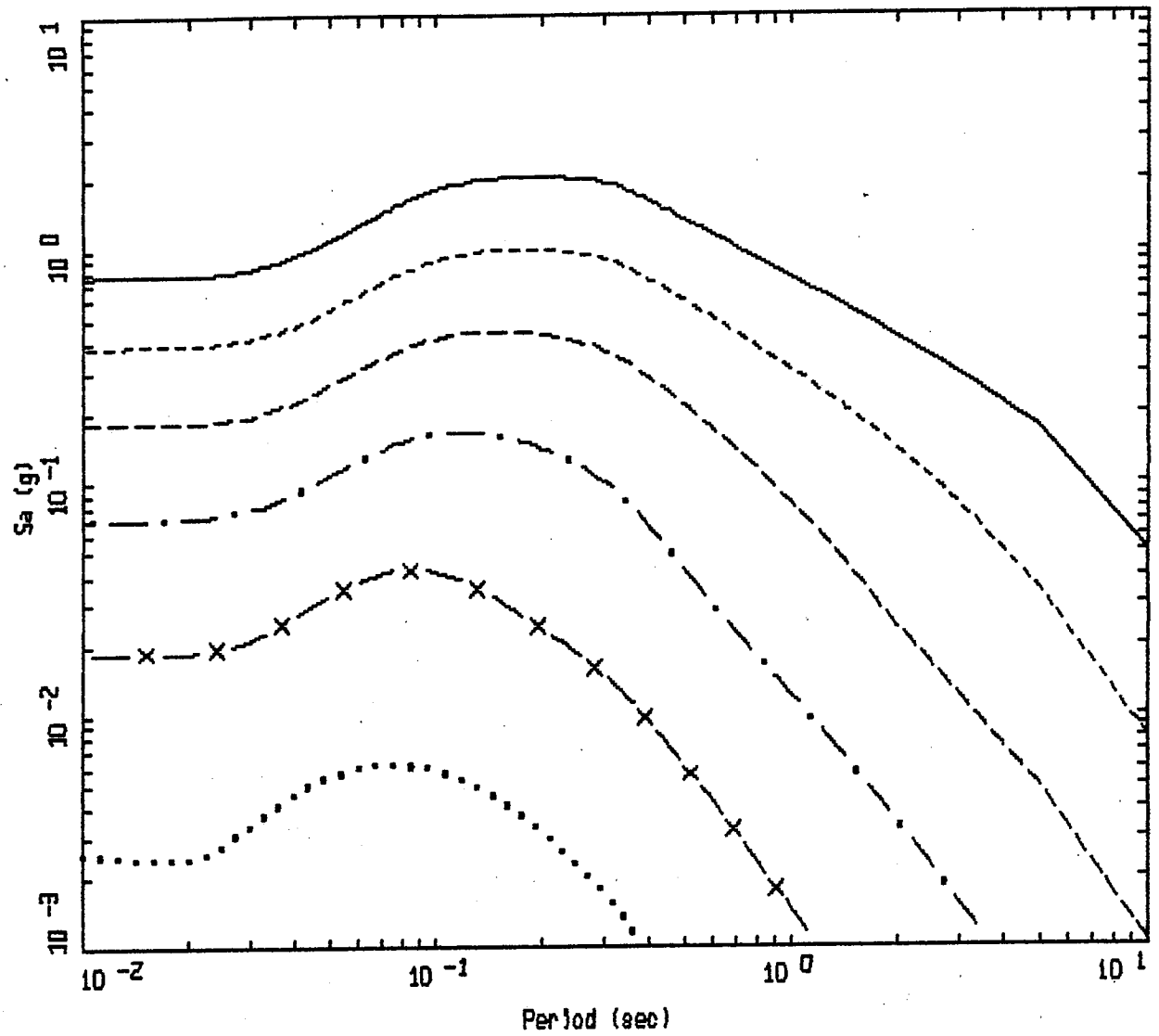

WNA SPECTRA
ROCK, R= 10 KM

LEGEND
WNA M=7.5
WNA M=6.5
WNA M=5.5
WNA M=4.5
WNA M=3.5
WNA M=2.5

Figure 2.

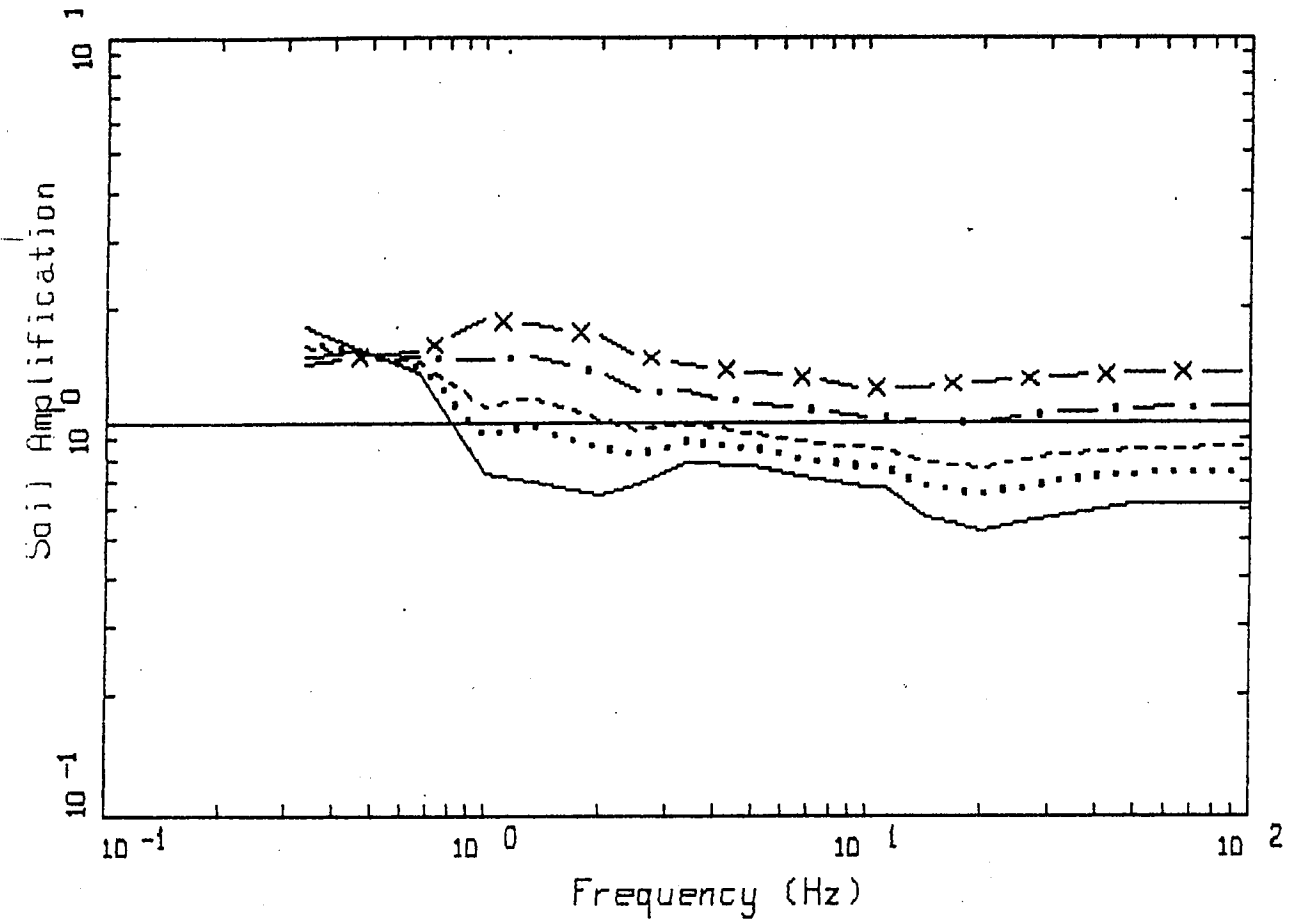

WNA EMPIRICAL M 6.5
DEEP, FIRM

LEGEND

R = 1.0 KM, ROCK PGA = 0.73 g
R = 5.0 KM, ROCK PGA = 0.40 g
R = 10.0 KM, ROCK PGA = 0.25 g
R = 25.0 KM, ROCK PGA = 0.11 g
R = 50.0 KM, ROCK PGA = 0.06 g

Figure 3.

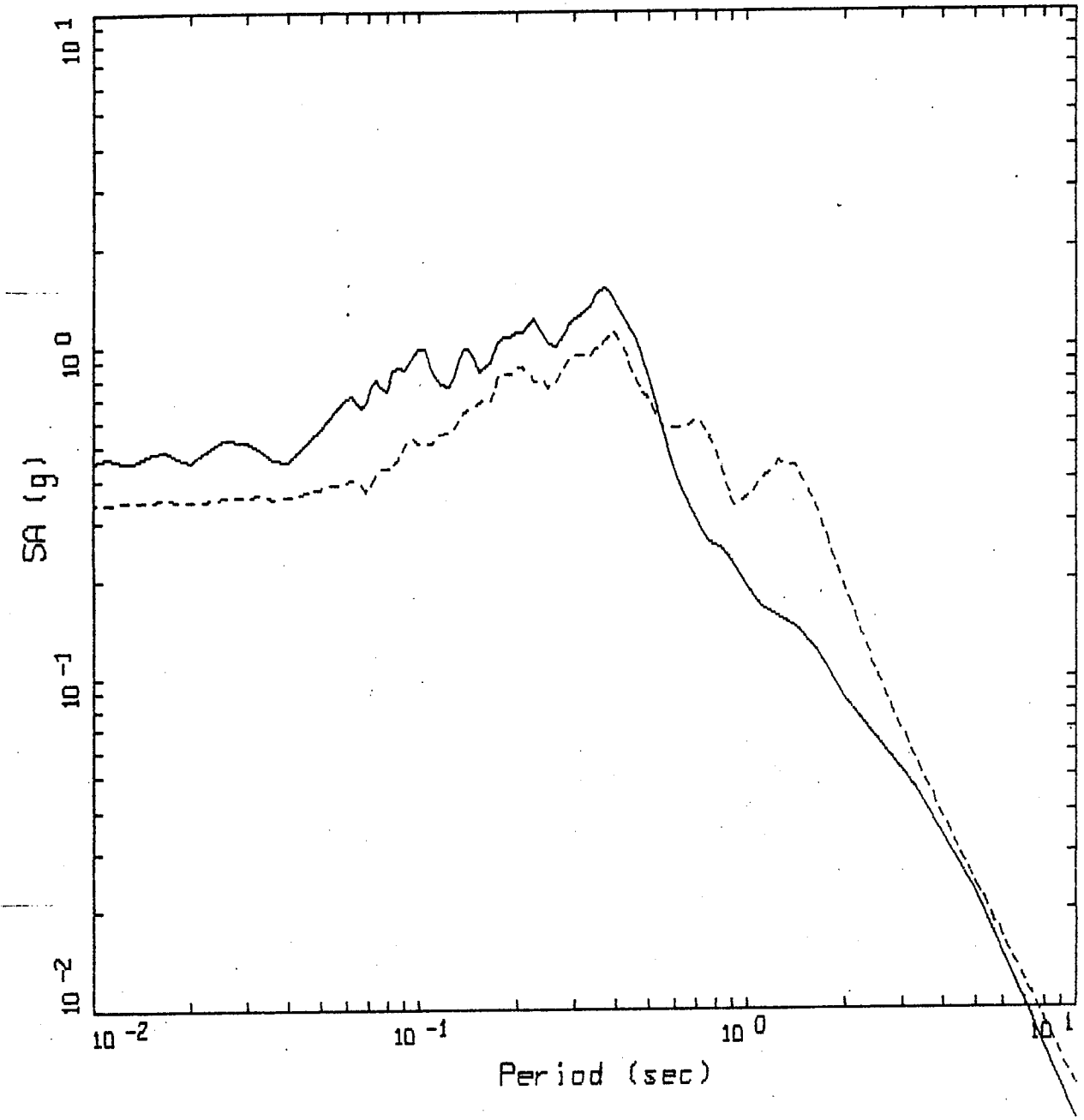

LOMA PRIETA, M = 6.9

LEGEND

——— GILROY 1, rock

----- GILROY 2, deep stiff soil (650 ft)

Figure 4.

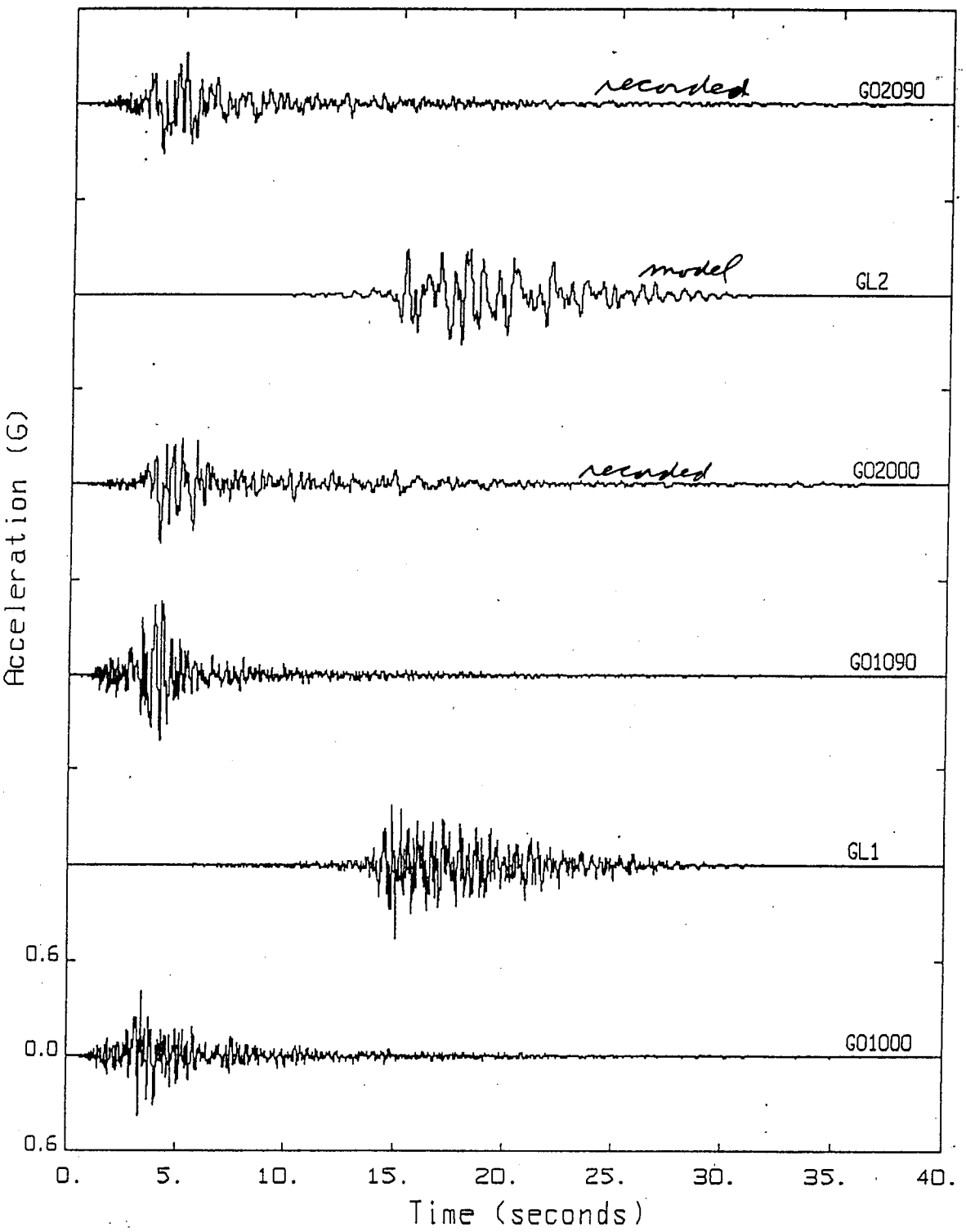

Figure 5. LOMA PRIETA

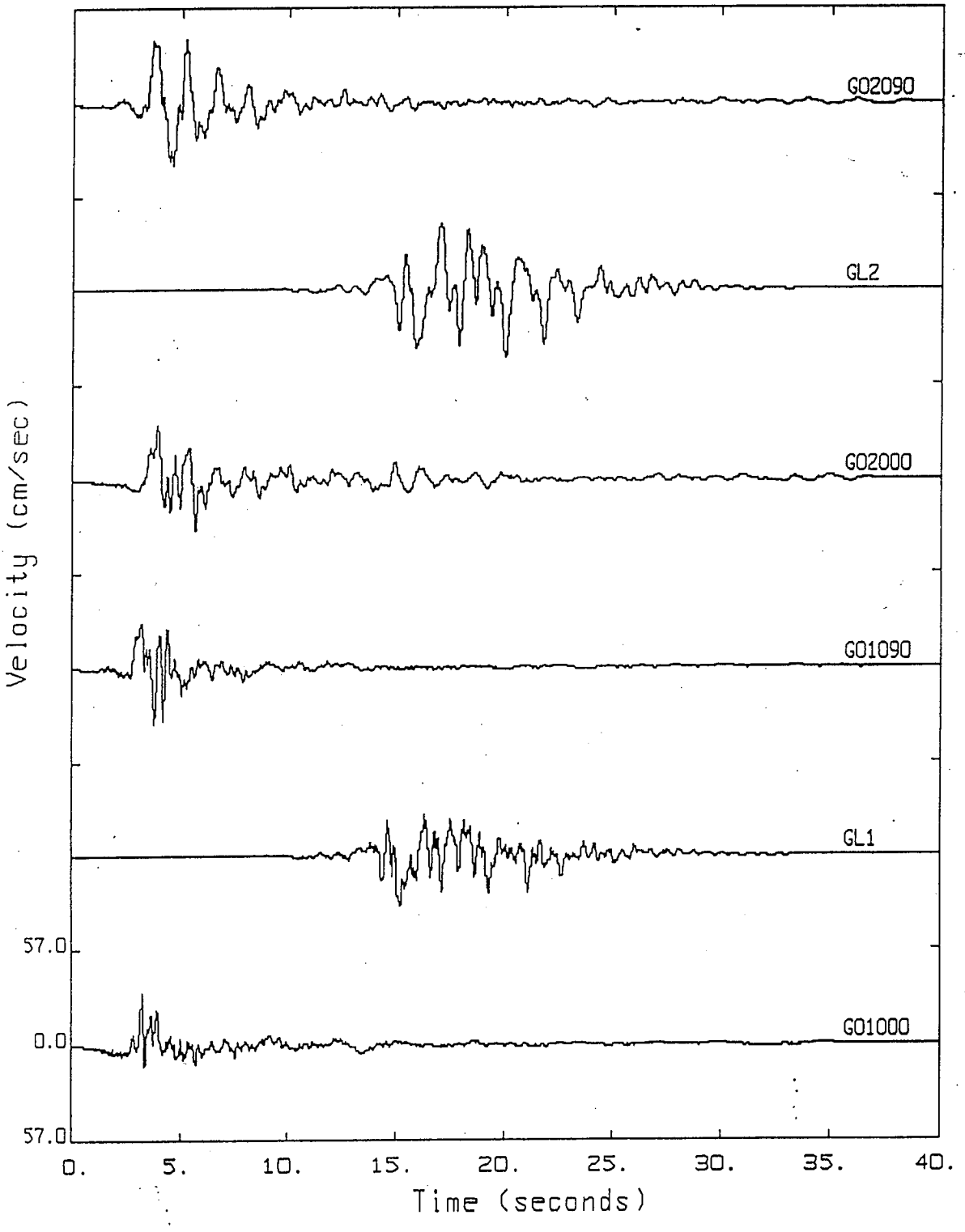

Figure 6. LOMA PRIETA

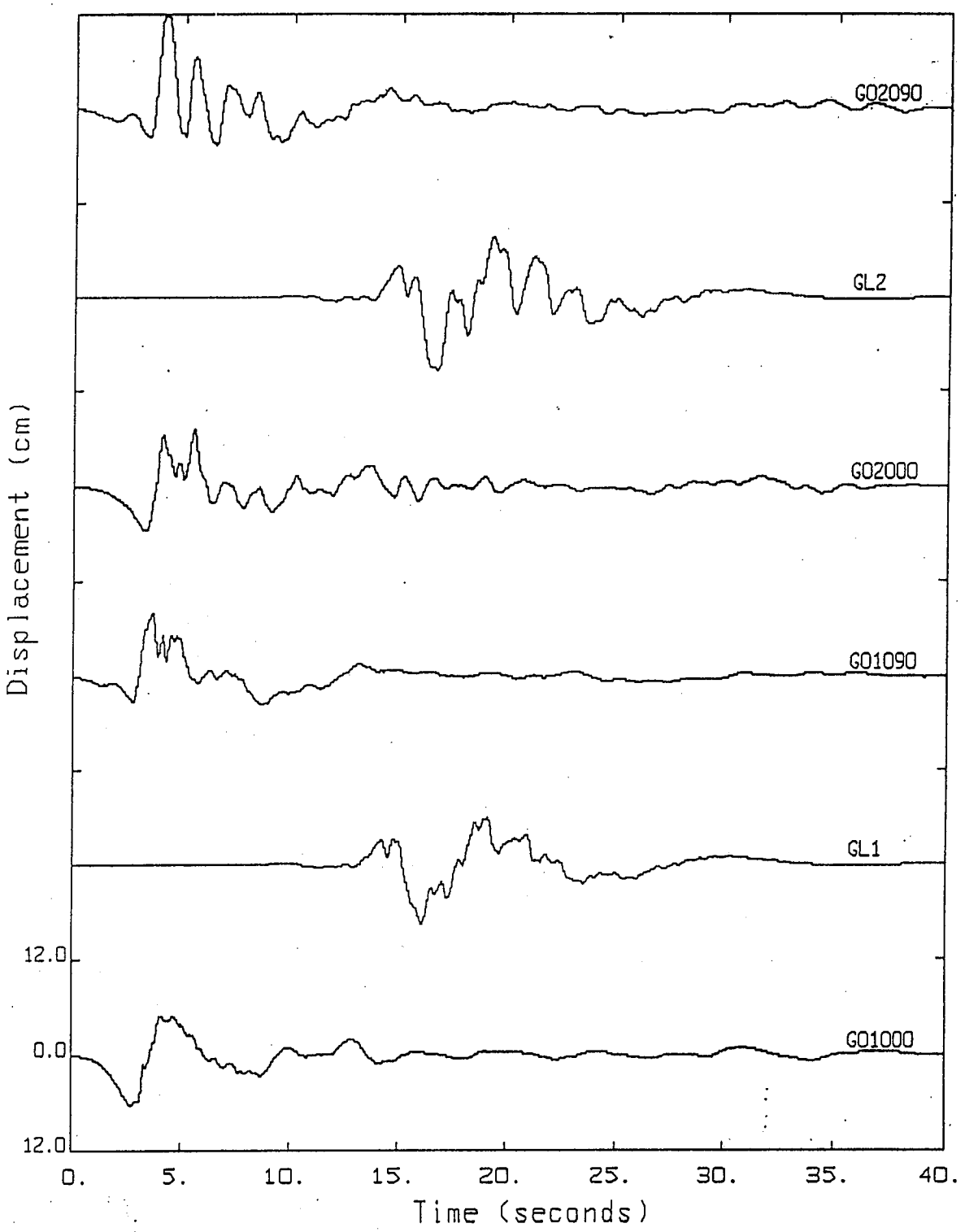

Figure 7. LOMA PRIETA

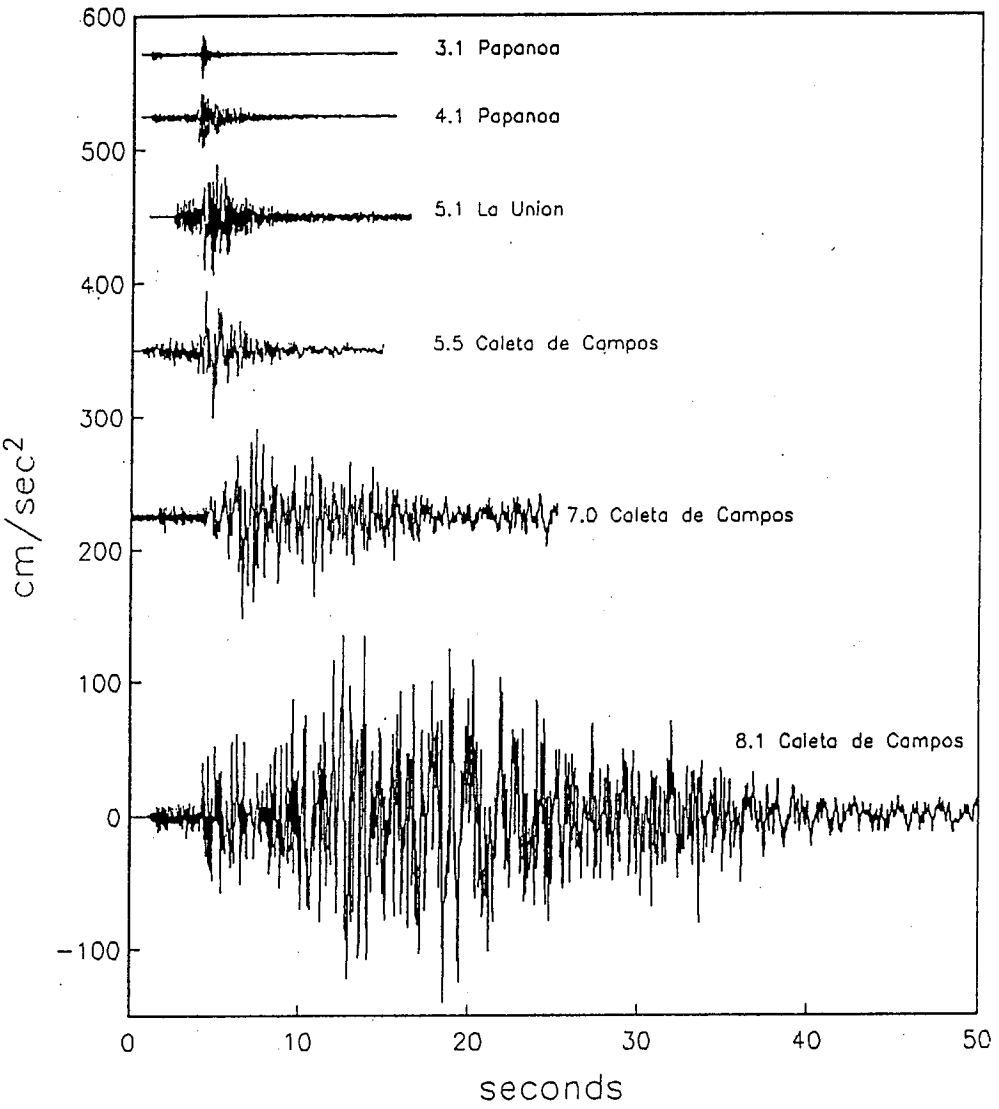

Figure 8. - An example of accelerograms recorded in 1985 and 1986 on the Guerrero accelerograph array. All events have epicenters about 25 km from the station, and all stations are on hard rock.

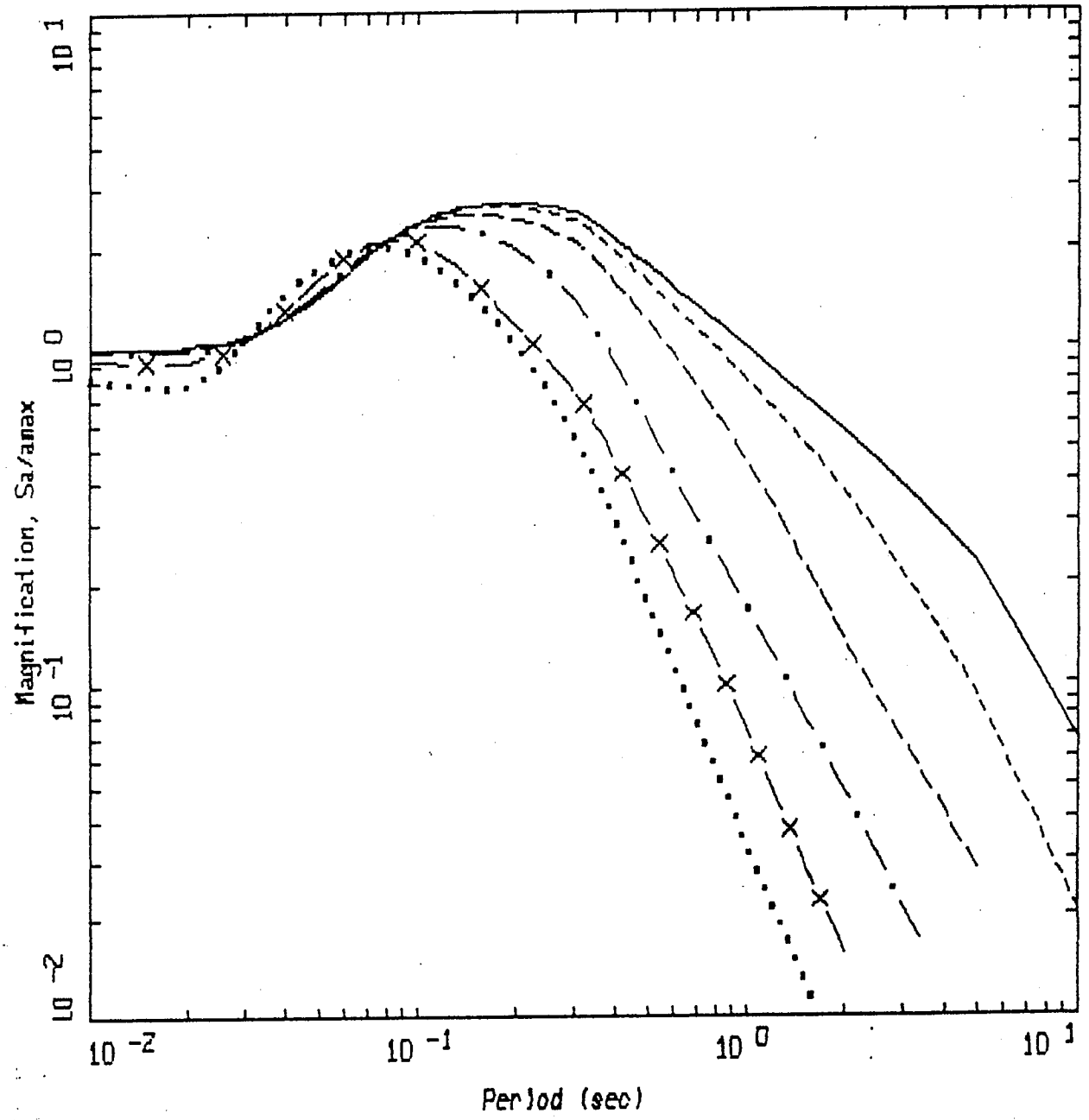

Figure 9. Comparison of 5%-damped response spectral shapes (Sa/a) computed for WNA parameters. Note the shift in peak response to longer period with increasing moment magnitude. Starting with the lowest curve, M = 2.5, 3.5, 4.5, 5.5, 6.5 and 7.5.

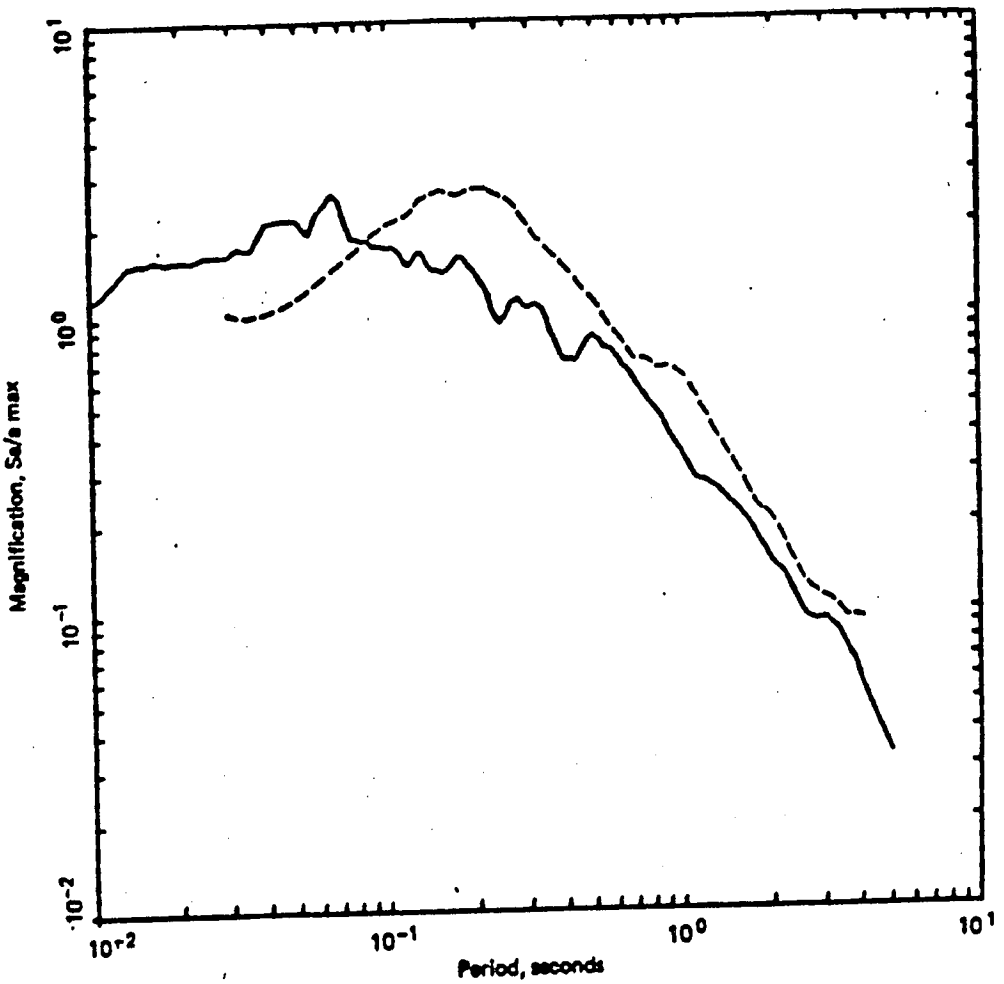

LEGEND

——— 5%, Nahanni mb = 6.4 rock readings

– – – – 5%, San Fernando ML = 6.4, Imperial Valley 79 ML = 6.6 rock recordings

Figure 10. Comparison of average 5% damped response spectral shapes (Sa/a_{max}) computed from strong motion data recorded at rock sites in ENA (solid line) and WNA (dashed line). ENA average shape is from recordings of the m_b = 6.4 Nahanni aftershock. The WNA average shape is from recordings of the San Fernando M_L = 6.4 and Imperial Valley M_L = 6.6 events.

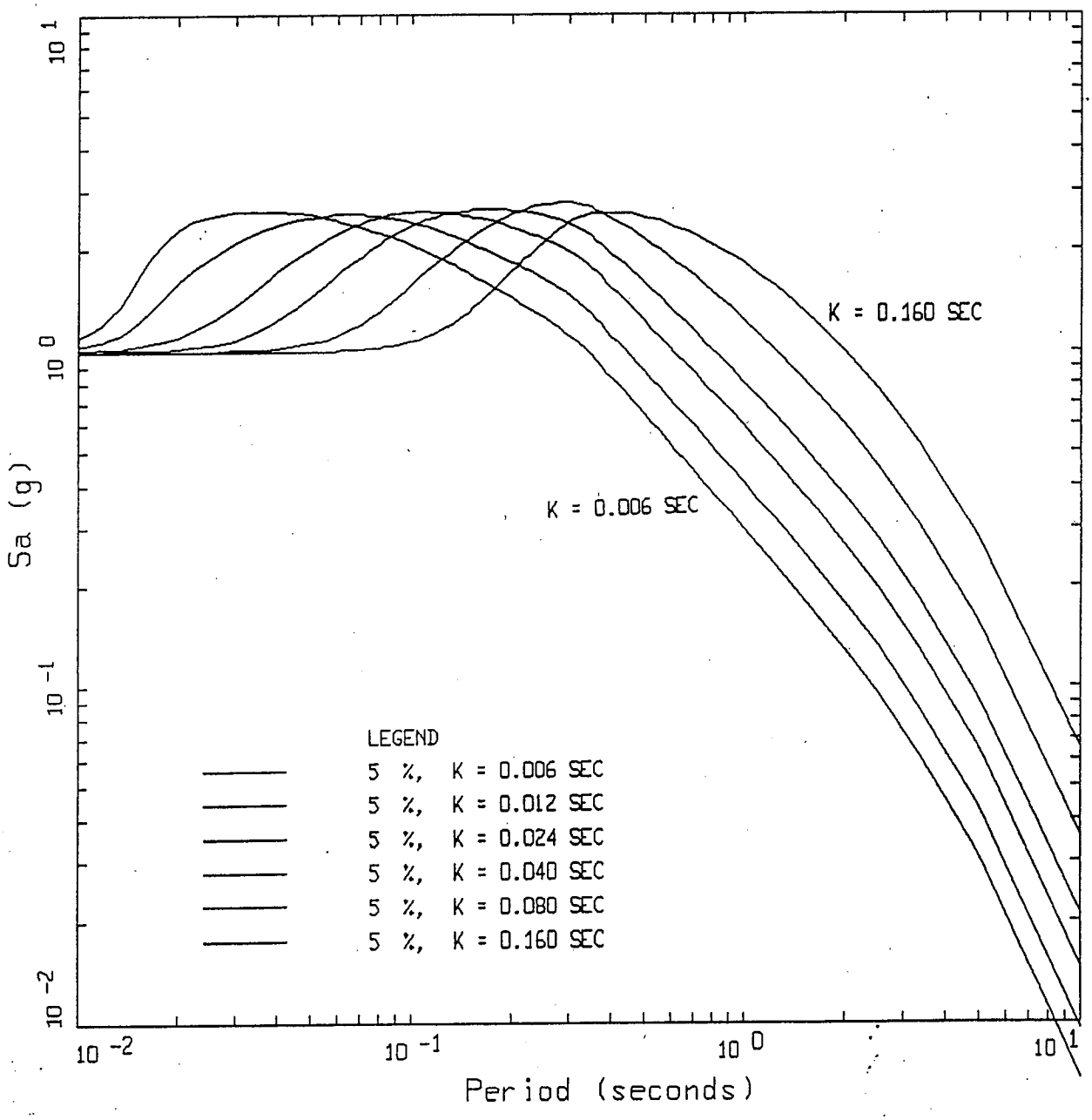

Figure 11. The effects of kappa on 5% damped response spectral shapes computed for a M 6.5 earthquake at 10 km using WNA parameters. As kappa increases, the peak shifts to longer periods and remains essentially constant in amplitude.

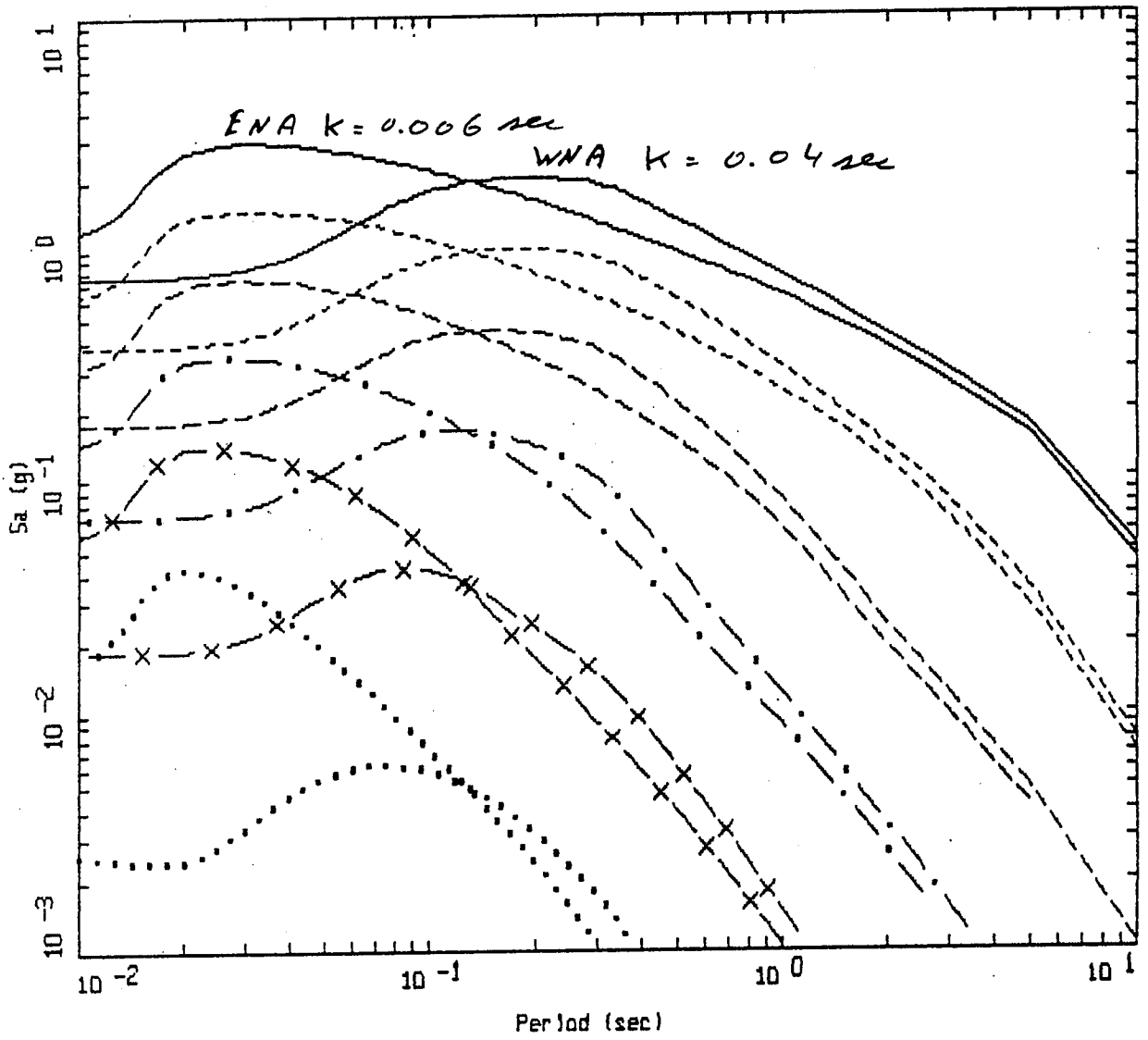

WNA AND ENA SPECTRA
ROCK, R= 10 KM

LEGEND

ENA M=7.5
ENA M=6.5
ENA M=5.5
ENA M=4.5
ENA M=3.5
ENA M=2.5
WNA M=7.5
WNA M=6.5
WNA M=5.5
WNA M=4.5
WNA M=3.5
WNA M=2.5

Figure 12.

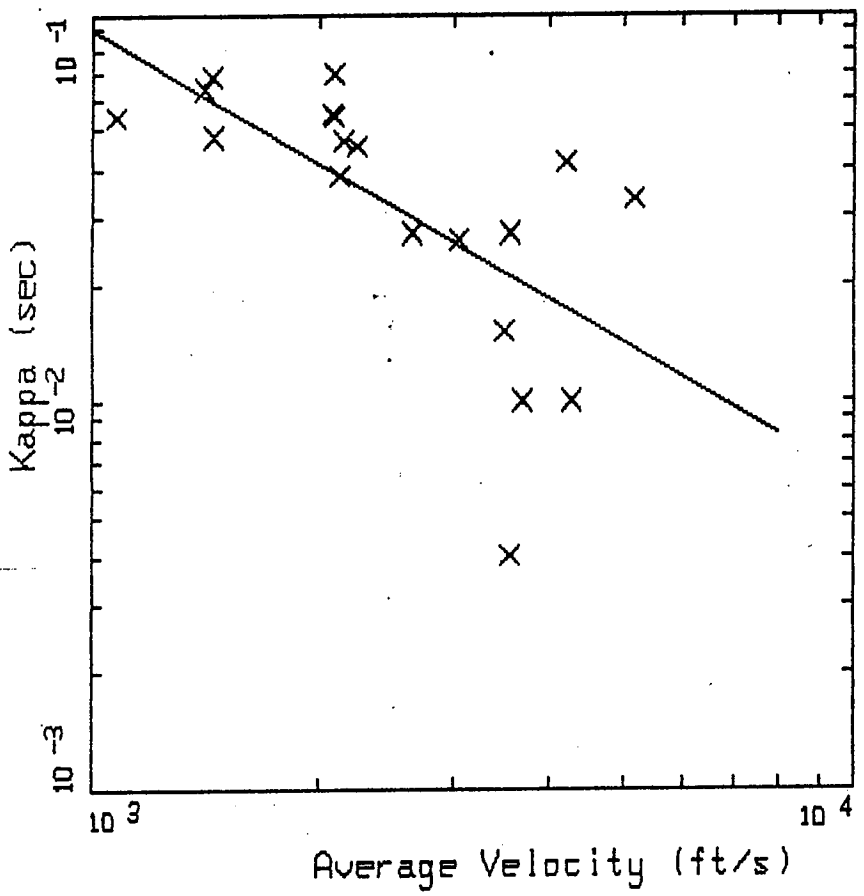

ROCK SITES (WNA)

KAPPA VS AVERAGE (OVER 100 FT) VELOCITY

LEGEND

X DATA

——— . LOG(KAPPA) = 2.40939 - 1.15099 * LOG(VELOCITY IN FT/S)

Figure 13.

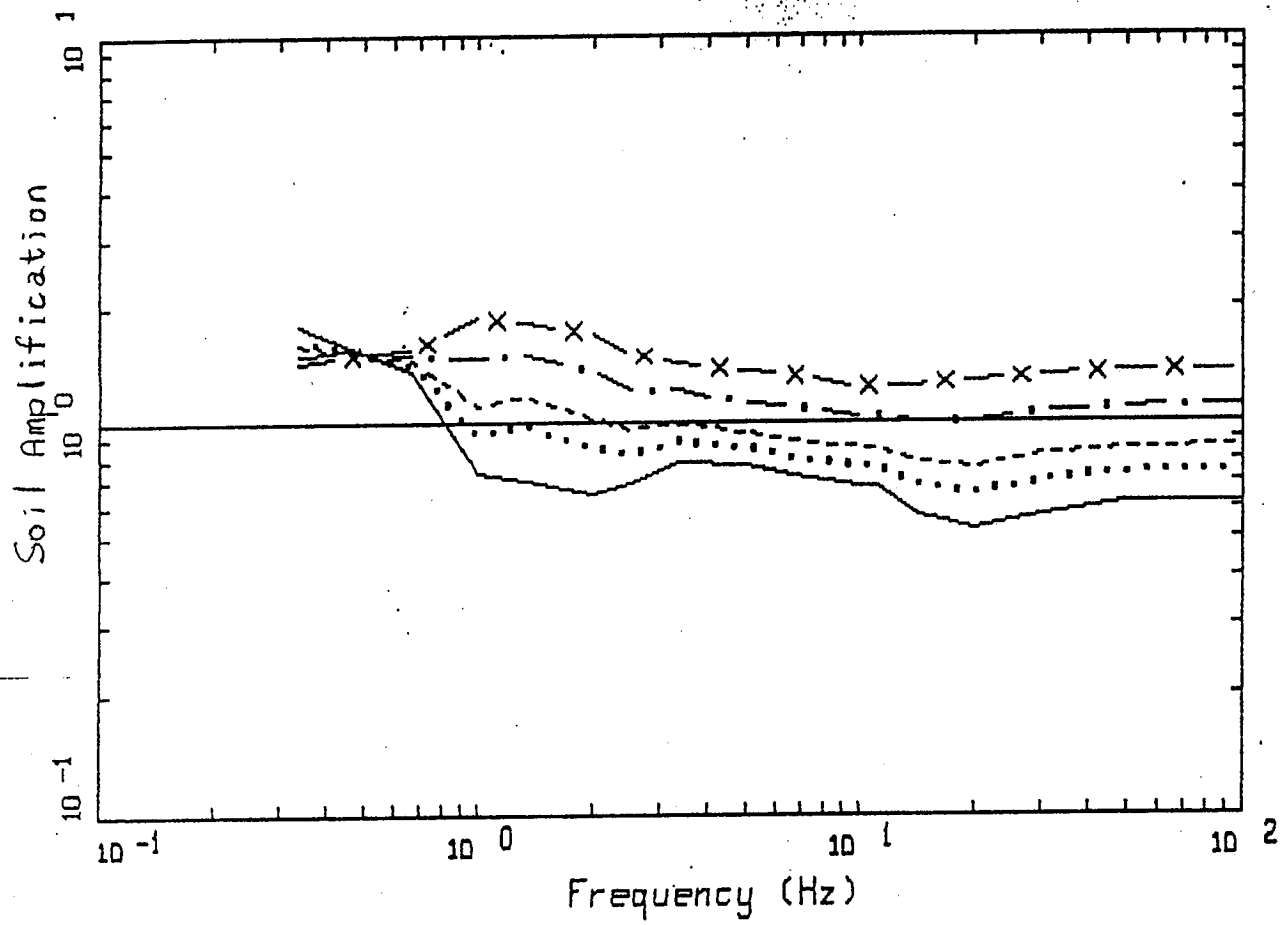

WNA EMPIRICAL M 6.5
DEEP, FIRM

LEGEND

———	R = 1.0 KM, ROCK PGA = 0.73 g
. . . .	R = 5.0 KM, ROCK PGA = 0.40 g
- - - - -	R = 10.0 KM, ROCK PGA = 0.25 g
— · —	R = 25.0 KM, ROCK PGA = 0.11 g
—×—	R = 50.0 KM, ROCK PGA = 0.06 g

Figure 14.

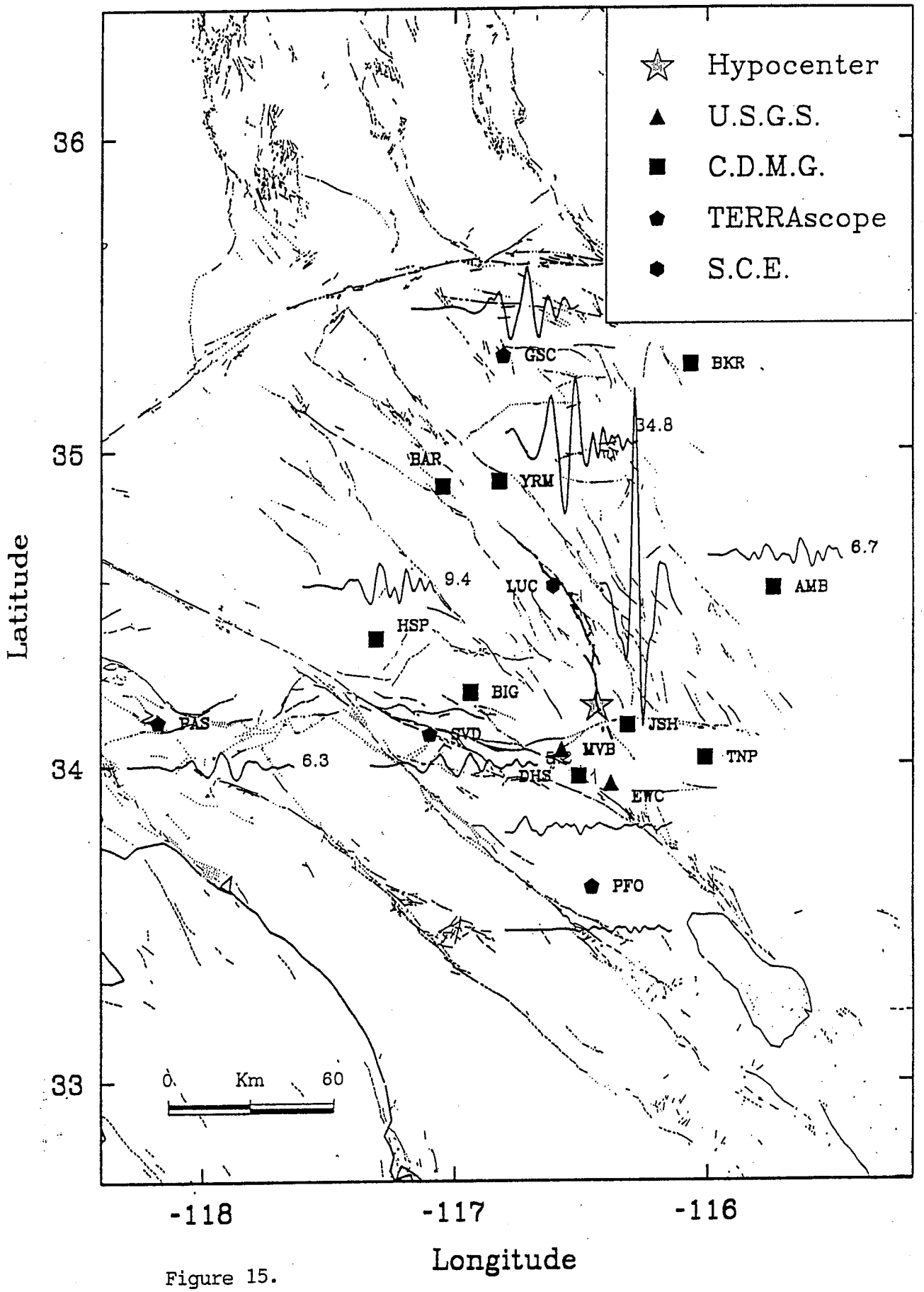
Hypocenter
U.S.G.S.
C.D.M.G.
TERRAscope
S.C.E.
GSC
BKR
34.8
BAR
YRM
6.7
AMB
9.4
LUC
HSP
BIG
PAS
SVD
JSH
MVB
TNP
6.3
DHS
EWC
PFO
0
Km
60
36
35
34
33
-118
-117
-116
Latitude
Longitude

Figure 15.

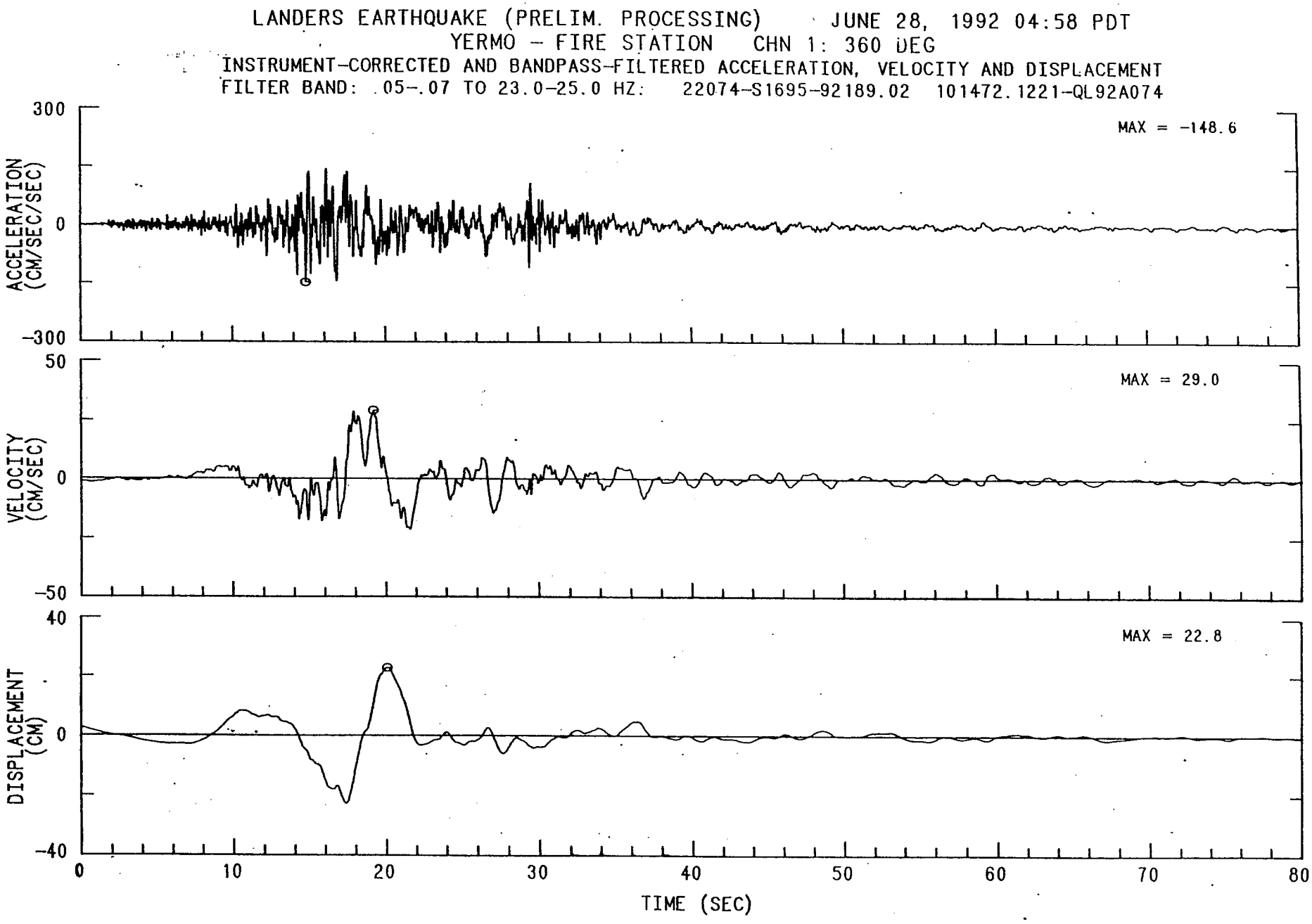
LANDERS EARTHQUAKE (PRELIM. PROCESSING) JUNE 28, 1992 04:58 PDT
YERMO - FIRE STATION CHN 1: 360 DEG
INSTRUMENT-CORRECTED AND BANDPASS-FILTERED ACCELERATION, VELOCITY AND DISPLACEMENT
FILTER BAND: .05-.07 TO 23.0-25.0 HZ: 22074-S1695-92189.02 101472.1221-QL92A074
ACCELERATION (CM/SEC/SEC)
MAX = -148.6
VELOCITY (CM/SEC)
MAX = 29.0
DISPLACEMENT (CM)
MAX = 22.8
TIME (SEC)

Figure 16.

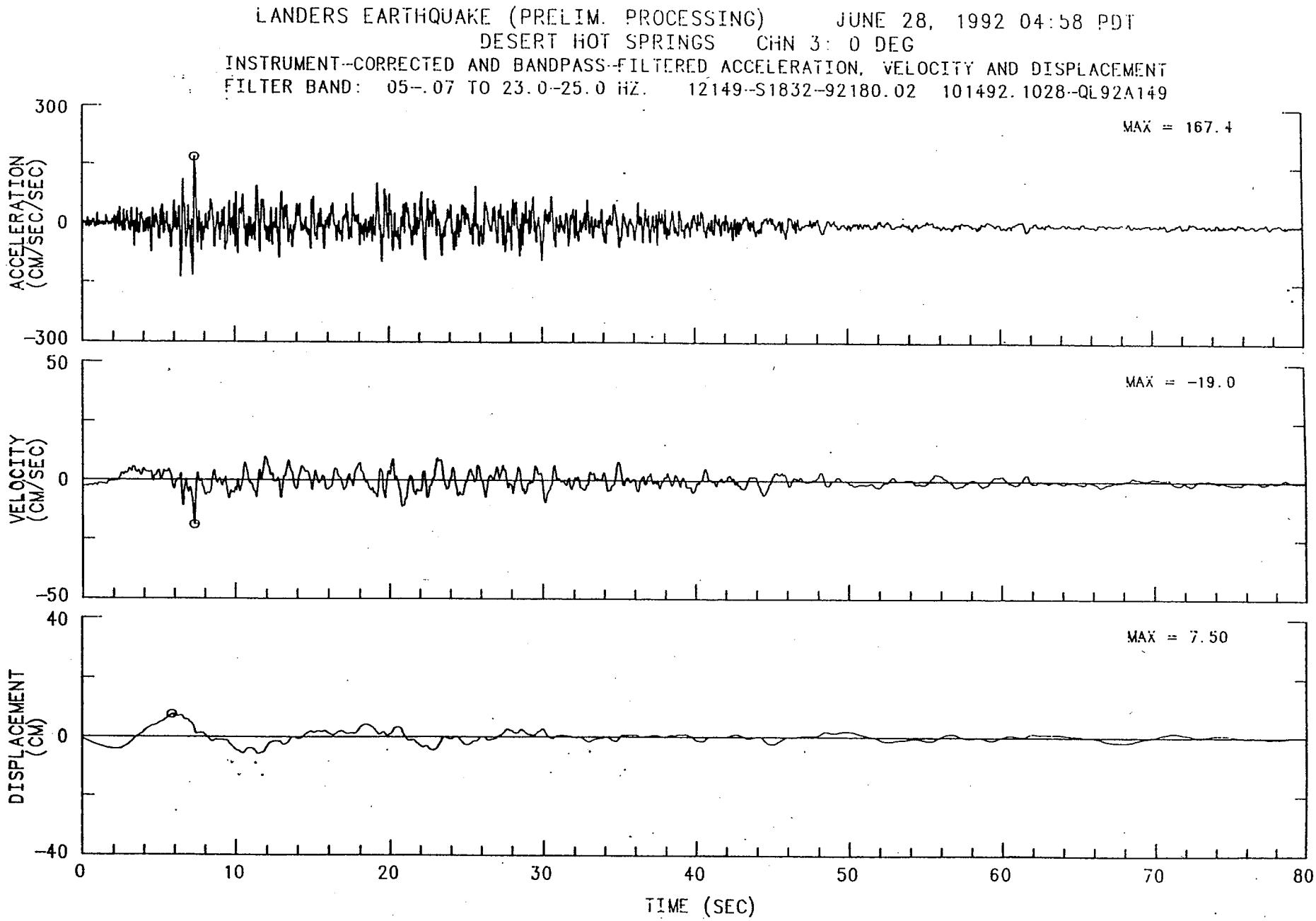
LANDERS EARTHQUAKE (PRELIM. PROCESSING) JUNE 28, 1992 04:58 PDT
DESERT HOT SPRINGS CHN 3: 0 DEG
INSTRUMENT-CORRECTED AND BANDPASS-FILTERED ACCELERATION, VELOCITY AND DISPLACEMENT
FILTER BAND: 05-.07 TO 23.0-25.0 HZ. 12149-S1832-92180.02 101492.1028-QL92A149
ACCELERATION (CM/SEC/SEC)
MAX = 167.4
VELOCITY (CM/SEC)
MAX = -19.0
DISPLACEMENT (CM)
MAX = 7.50
TIME (SEC)

Figure 17.

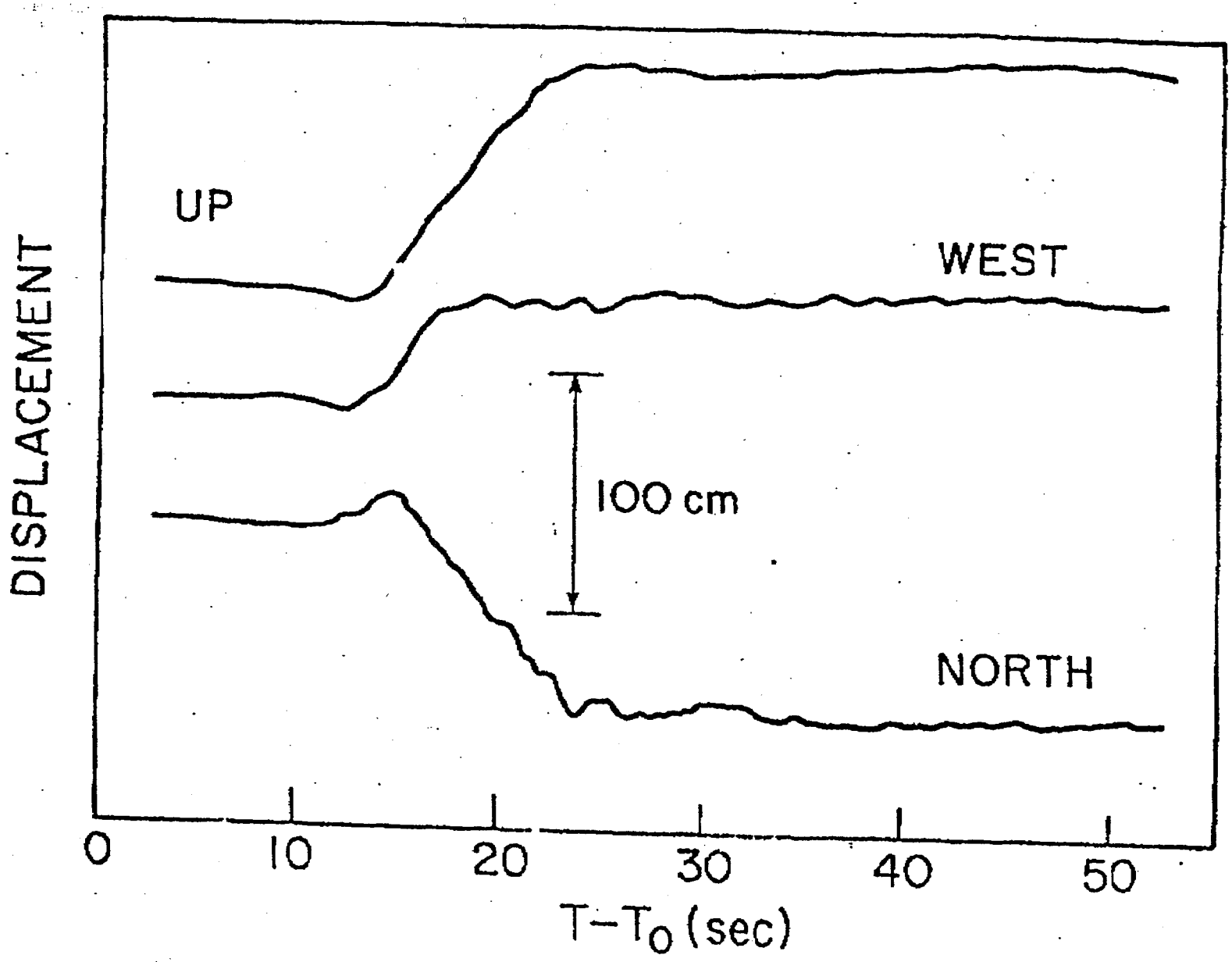

Figure 18.

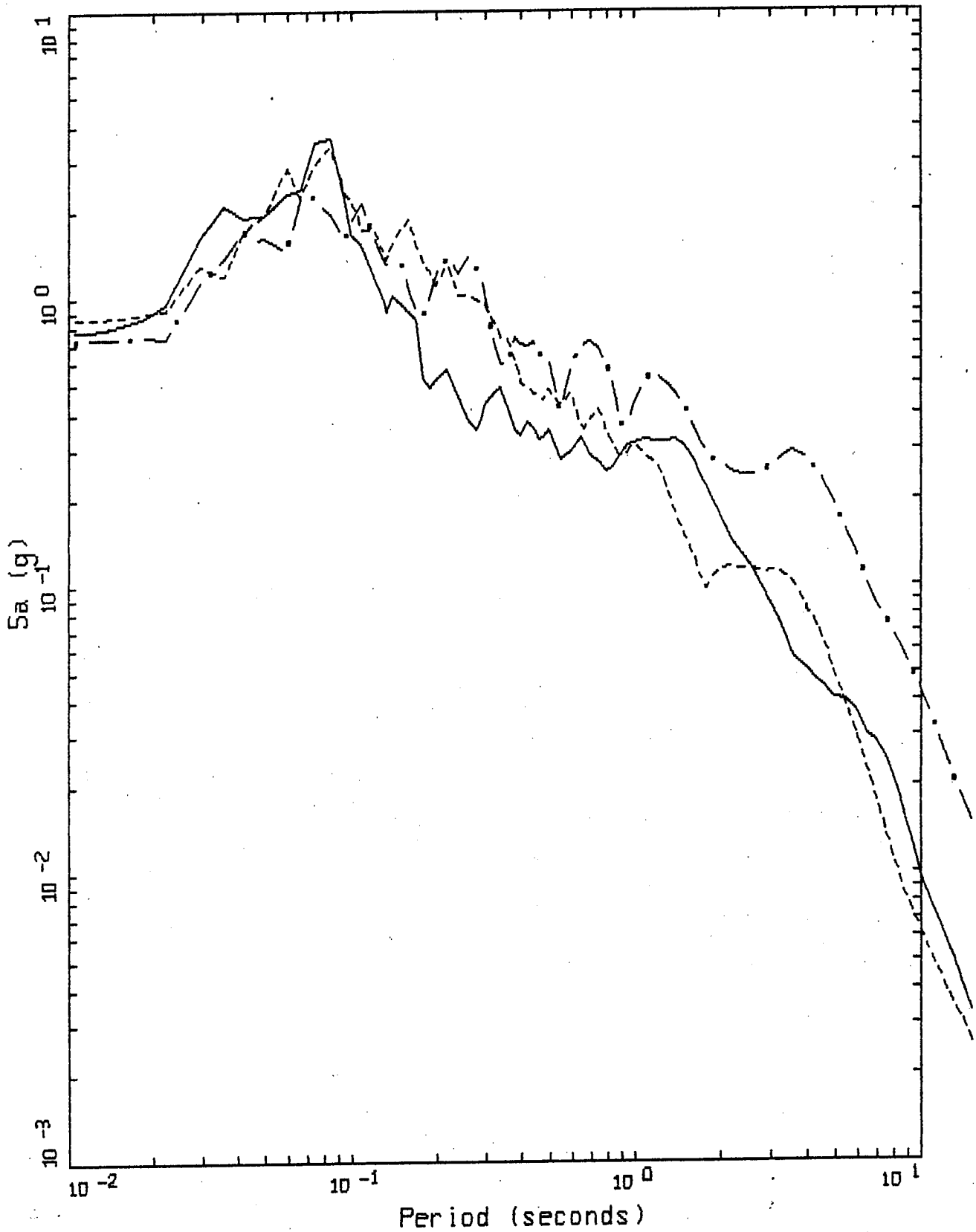

Figure 19. LANDERS 06/28/92 1158
LUCERNE

LEGEND

——— 5 %, PE&A-CORRECTED DATA, COMP VRT

- - - - - 5 %, PE&A-CORRECTED DATA, COMP LONGITUDINAL

— · — 5 %, PE&A-CORRECTED DATA, COMP TRANSVERSE

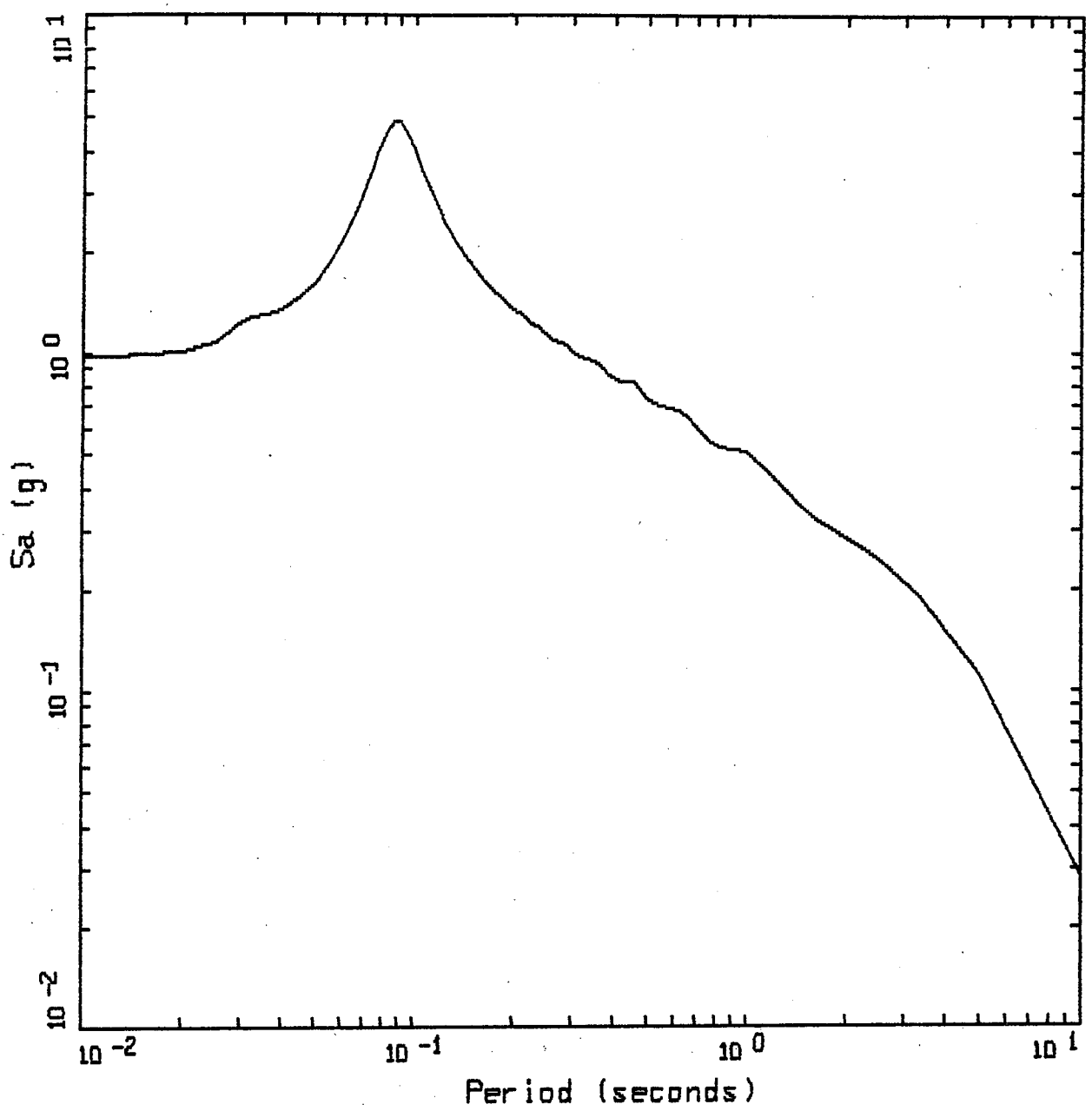

LANDERS EARTHQUAKE 06/28/92
MODELED AT LUCERNE

LEGEND

5 %, RVT: 20FT ENA PROFILE, PGA = 0.970 G

Figure 20.

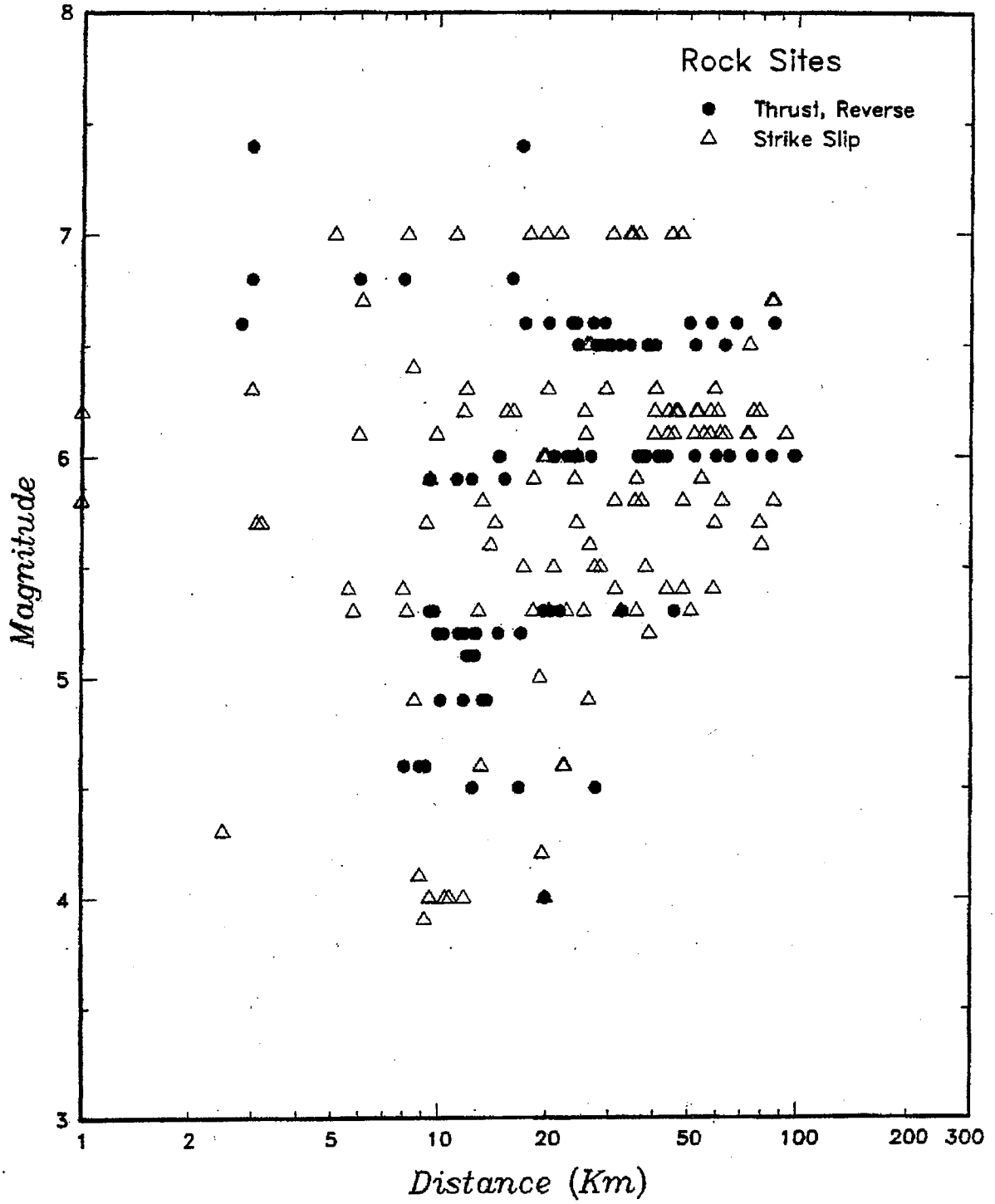
Rock Sites
Thrust, Reverse
Strike Slip
Magnitude
Distance (Km)
8
7
6
5
4
3
1
2
5
10
20
50
100
200
300

Figure 21.

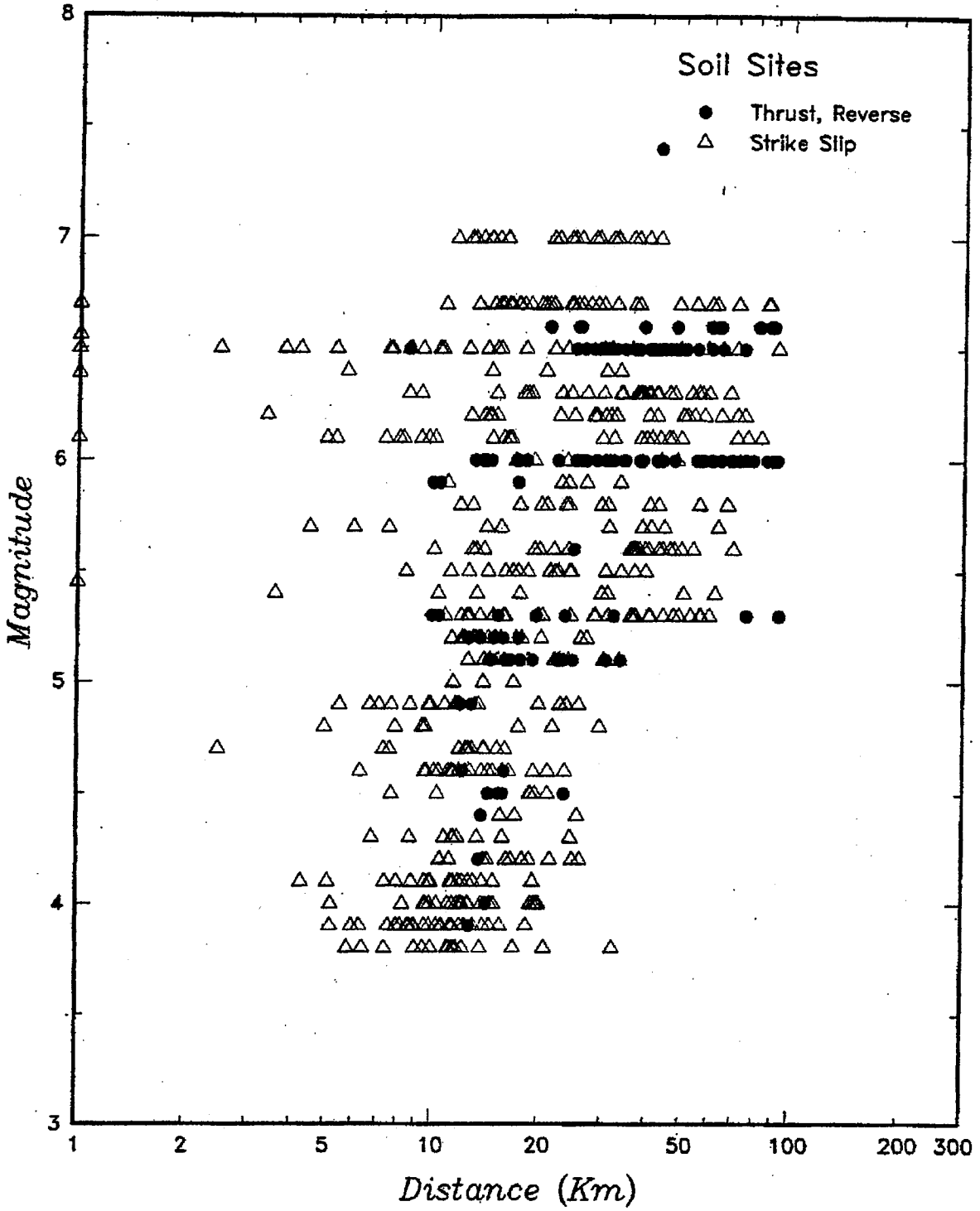
Soil Sites
Thrust, Reverse
Strike Slip
Magnitude
Distance (Km)
8
7
6
5
4
3
1
2
5
10
20
50
100
200
300

Figure 22.

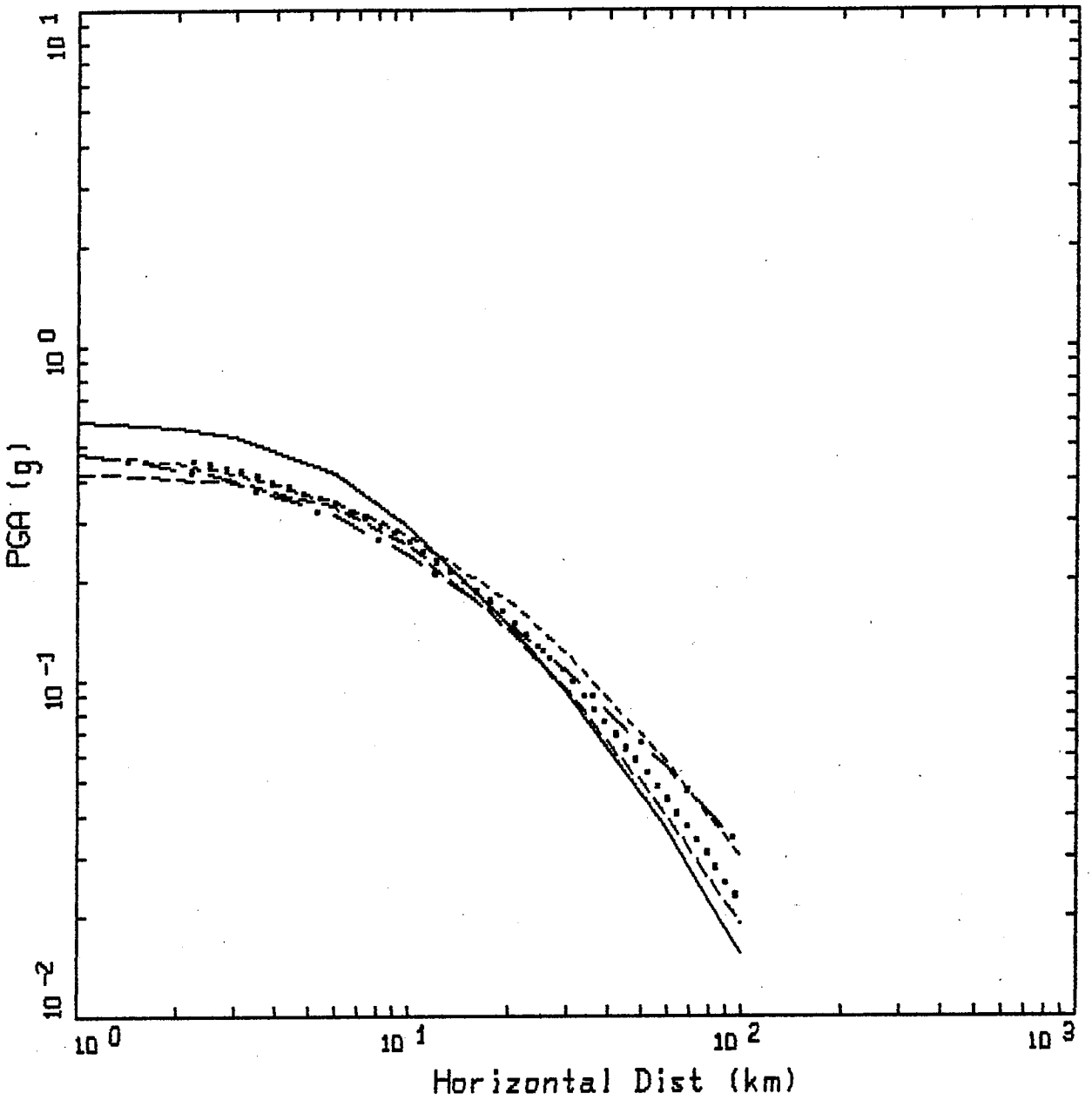

PGA ATTENUATION
M=6.5, SOIL, STRIKE SLIP

LEGEND

——— CAMPBELL, 1993 (D=1.0 KM)

• • • • SADIGH ET AL., 1986

- - - - - IDRISS, 1991 (DEEP SOIL)

— — — — JOYNER-BOORE, 1988 (SOIL OR ROCK)

— • — ABRAHAMSON-SILVA, 1993

Figure 23.

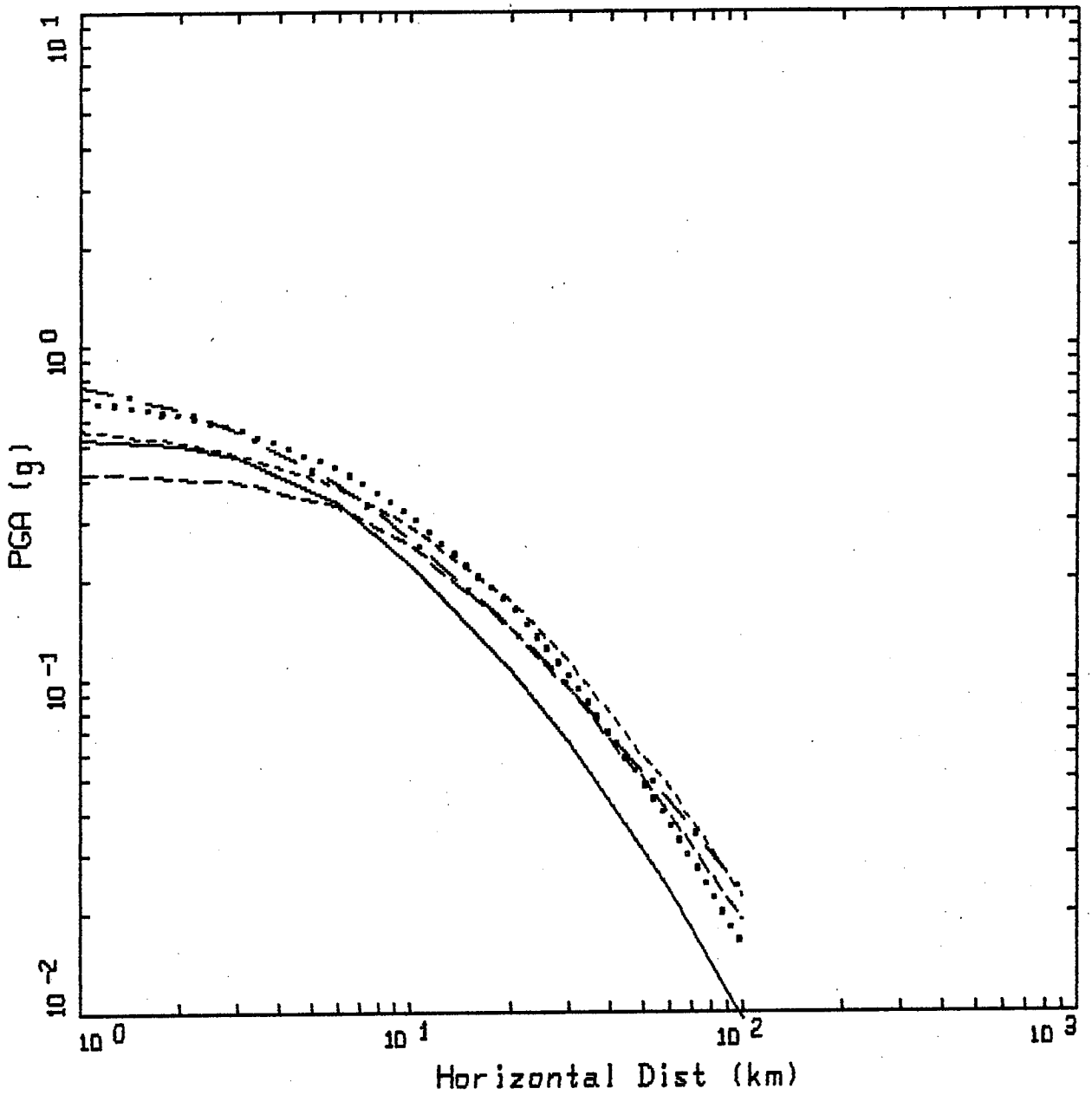

PGA ATTENUATION
M=6.5, ROCK, STRIKE SLIP

LEGEND

——— CAMPBELL, 1993 (D=1.0 KM)

• • • • SADIGH ET AL., 1993

- - - - - IDRISS, 1991 (ROCK & STIFF SOIL)

— — — — JOYNER-BOORE, 1988 (SOIL OR ROCK)

— • — ABRAHAMSON-SILVA, 1993

Figure 24.

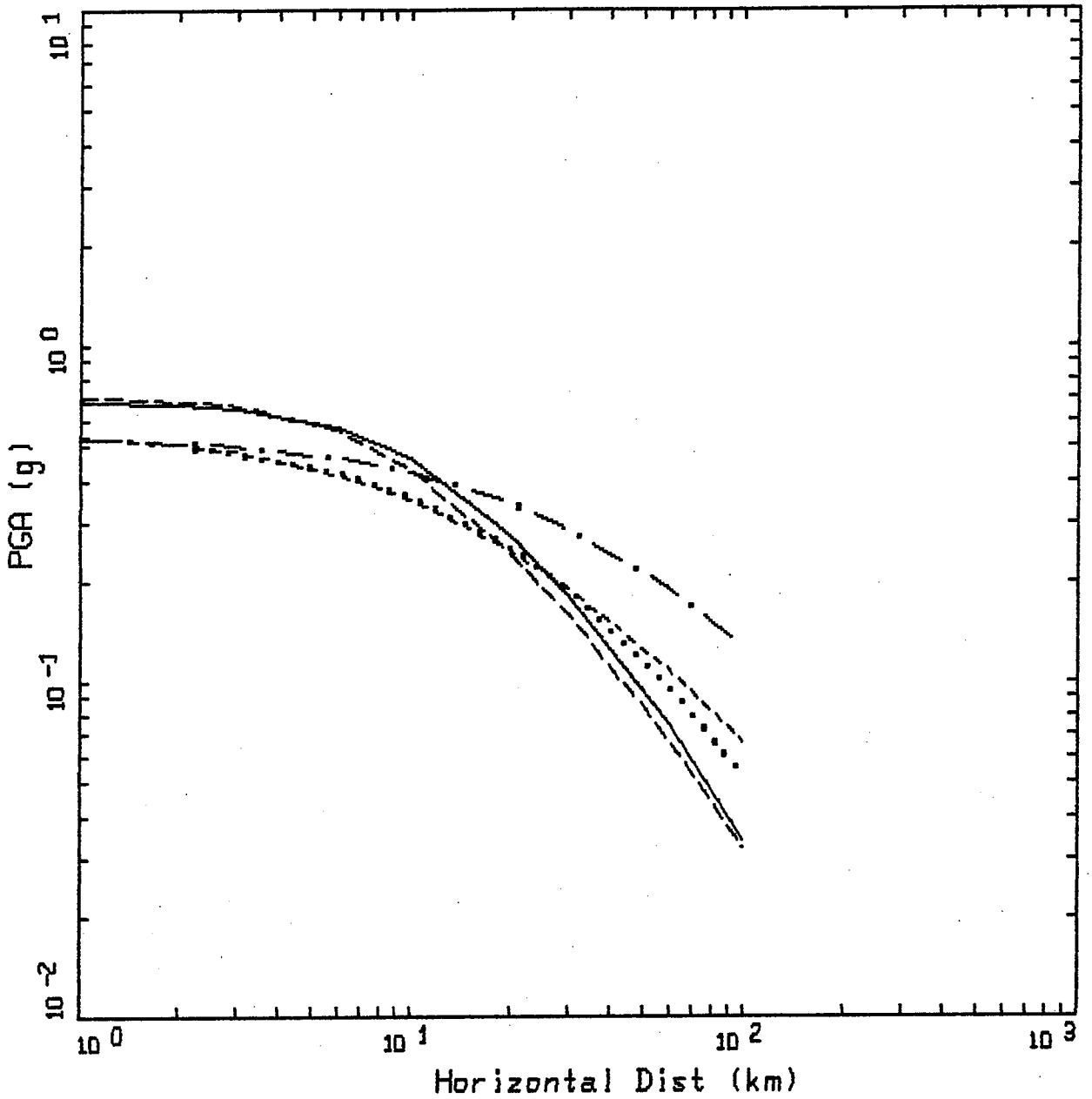

PGA ATTENUATION
M=7.5, SOIL, STRIKE SLIP

LEGEND

CAMPBELL, 1993 (D=1.0 KM)

SADIGH ET AL., 1986

IDRISS, 1991 (DEEP SOIL)

JOYNER-BOORE, 1988 (SOIL OR ROCK)

ABRAHAMSON-SILVA, 1993

Figure 25.

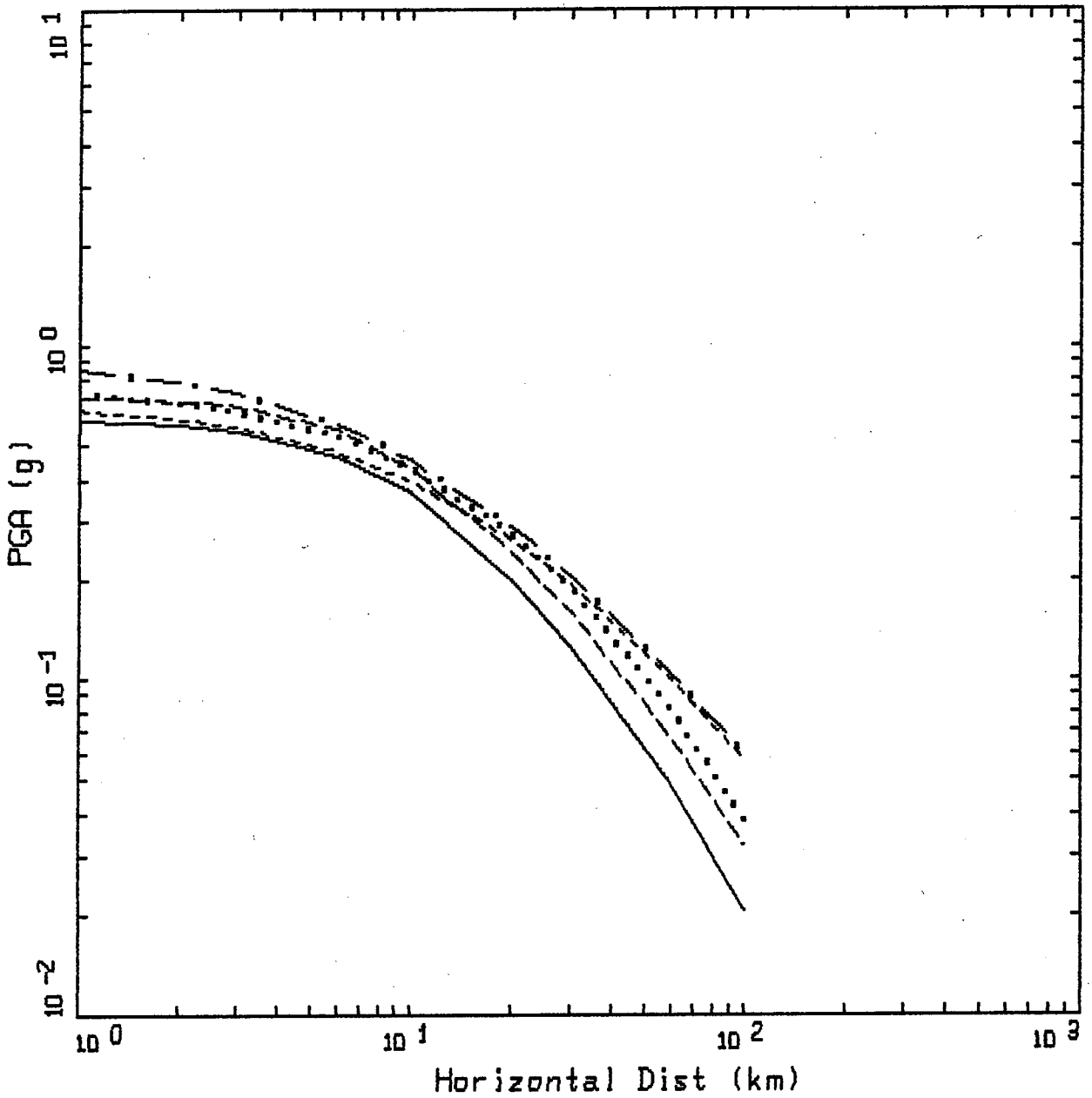

PGA ATTENUATION
M=7.5, ROCK, STRIKE SLIP

LEGEND

CAMPBELL, 1993 (D=1.0 KM)

SADIGH ET AL., 1993

IDRISS, 1991 (ROCK & STIFF SOIL)

JOYNER-BOORE, 1988 (SOIL OR ROCK)

ABRAHAMSON-SILVA, 1993

Figure 26.

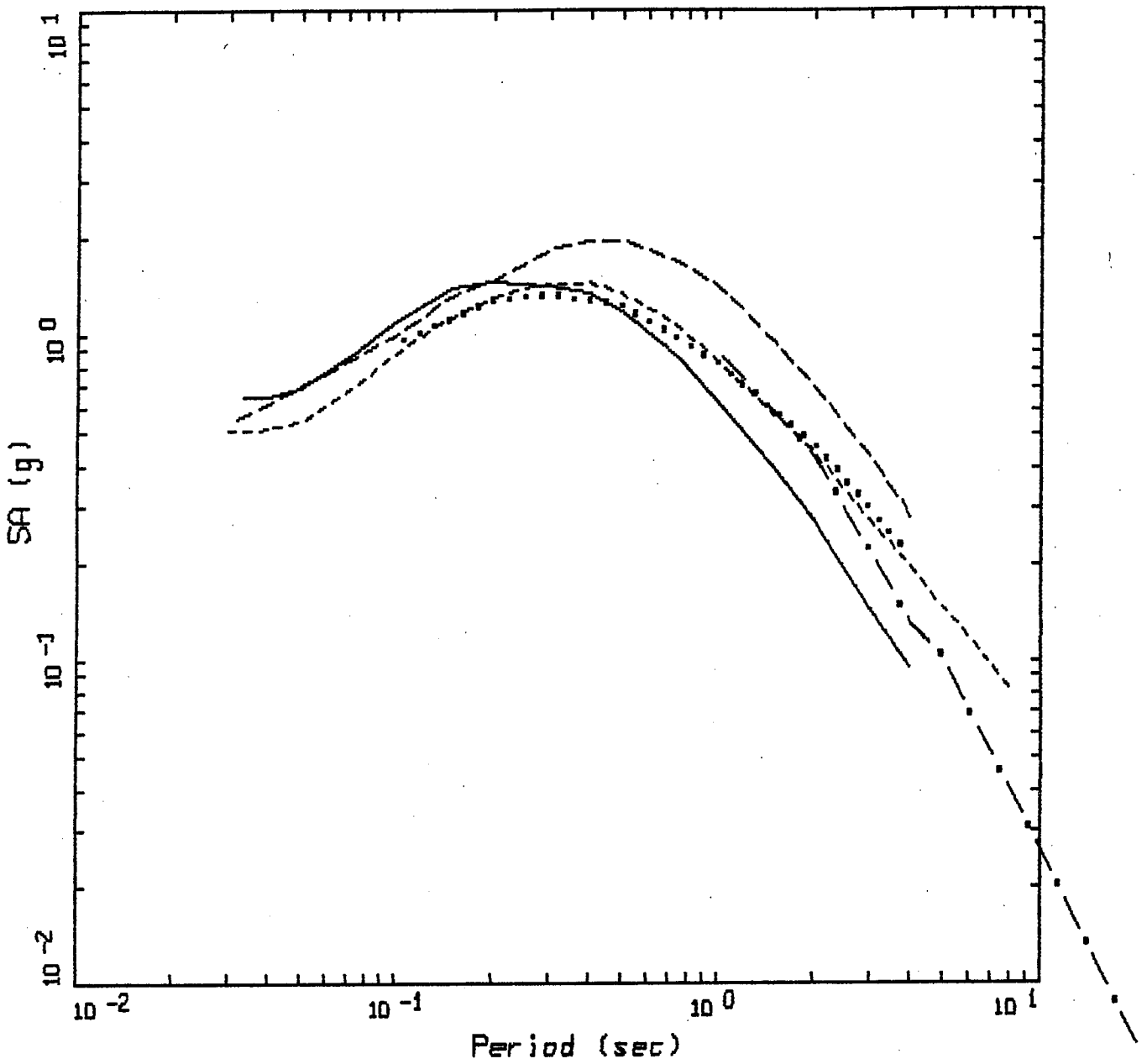

EMPIRICAL RESPONSE SPECTRA
M=7.0, SOIL, STRIKE SLIP, R=1

LEGEND

CAMPBELL, 1993 (D=1.0 KM)

SADIGH ET AL., 1986

IDRISS, 1985 (DEEP SOIL)

JOYNER-BOORE, 1988

ABRAHAMSON-SILVA, 1993

Figure 27.

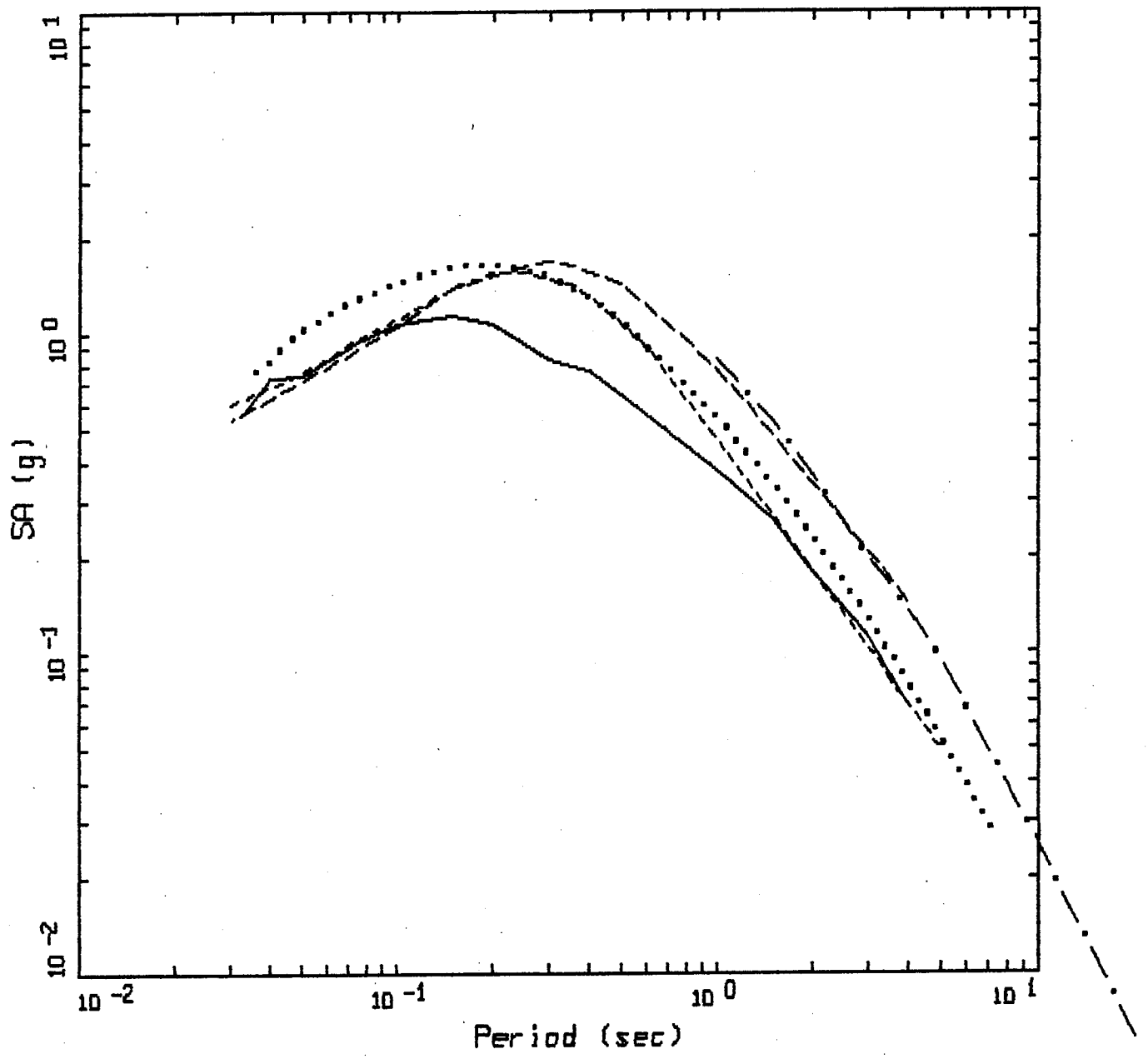

EMPIRICAL RESPONSE SPECTRA
M=7.0, ROCK, STRIKE SLIP, R=1

LEGEND

CAMPBELL, 1993 (D=1.0 KM)

SADIGH ET AL., 1993

IDRISS, 1991

JOYNER-BOORE, 1988

ABRAHAMSON-SILVA, 1993

Figure 28.

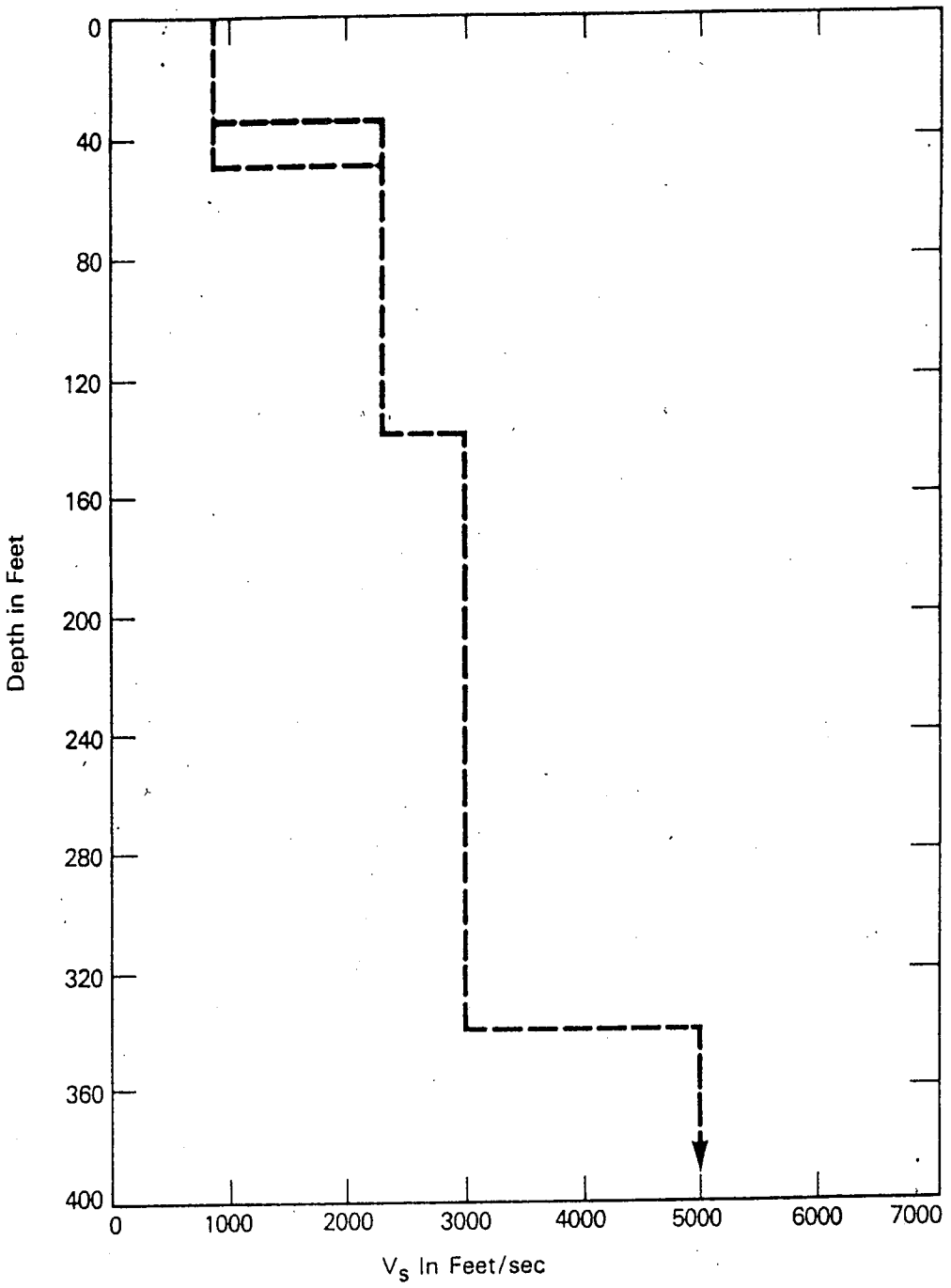

Figure 29. Shear wave (V_S) velocity profile of soil site in Michigan.

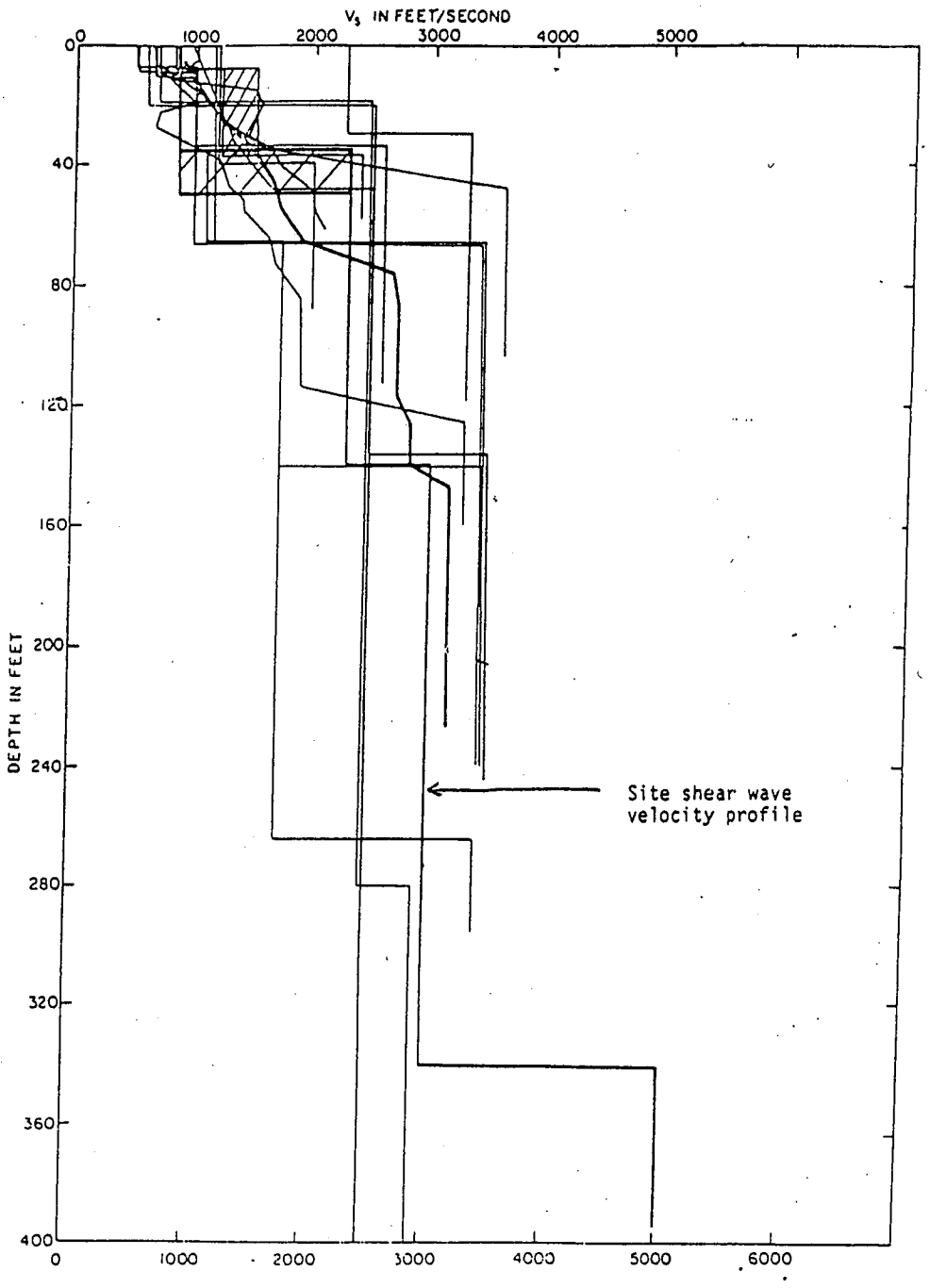

Figure 30. Shear wave velocity profiles of strong motion recording stations.

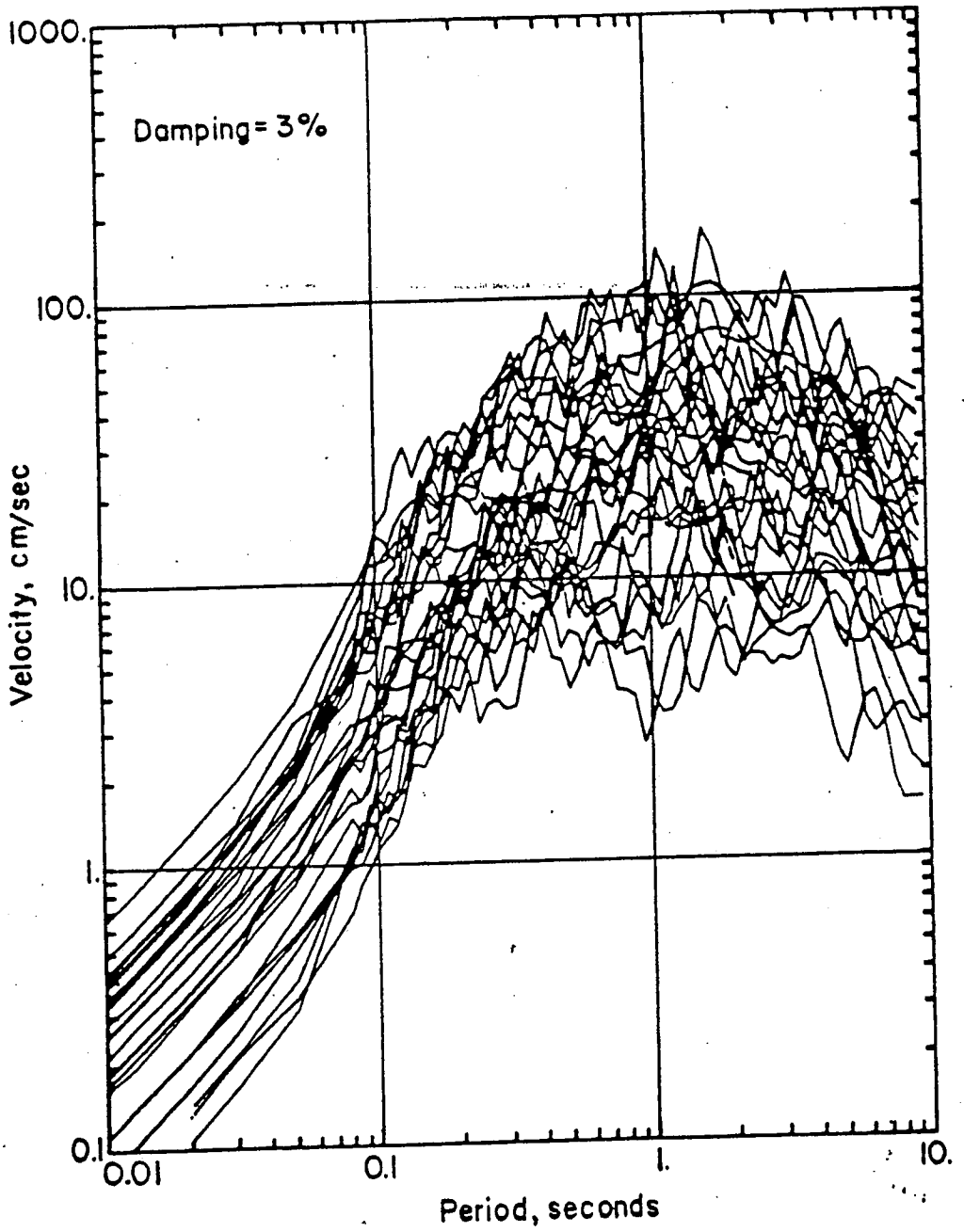
1000.
Damping = 3%
100.
10.
1.
0.1
Velocity, cm/sec
0.01
0.1
1.
10.
Period, seconds

Figure 31.

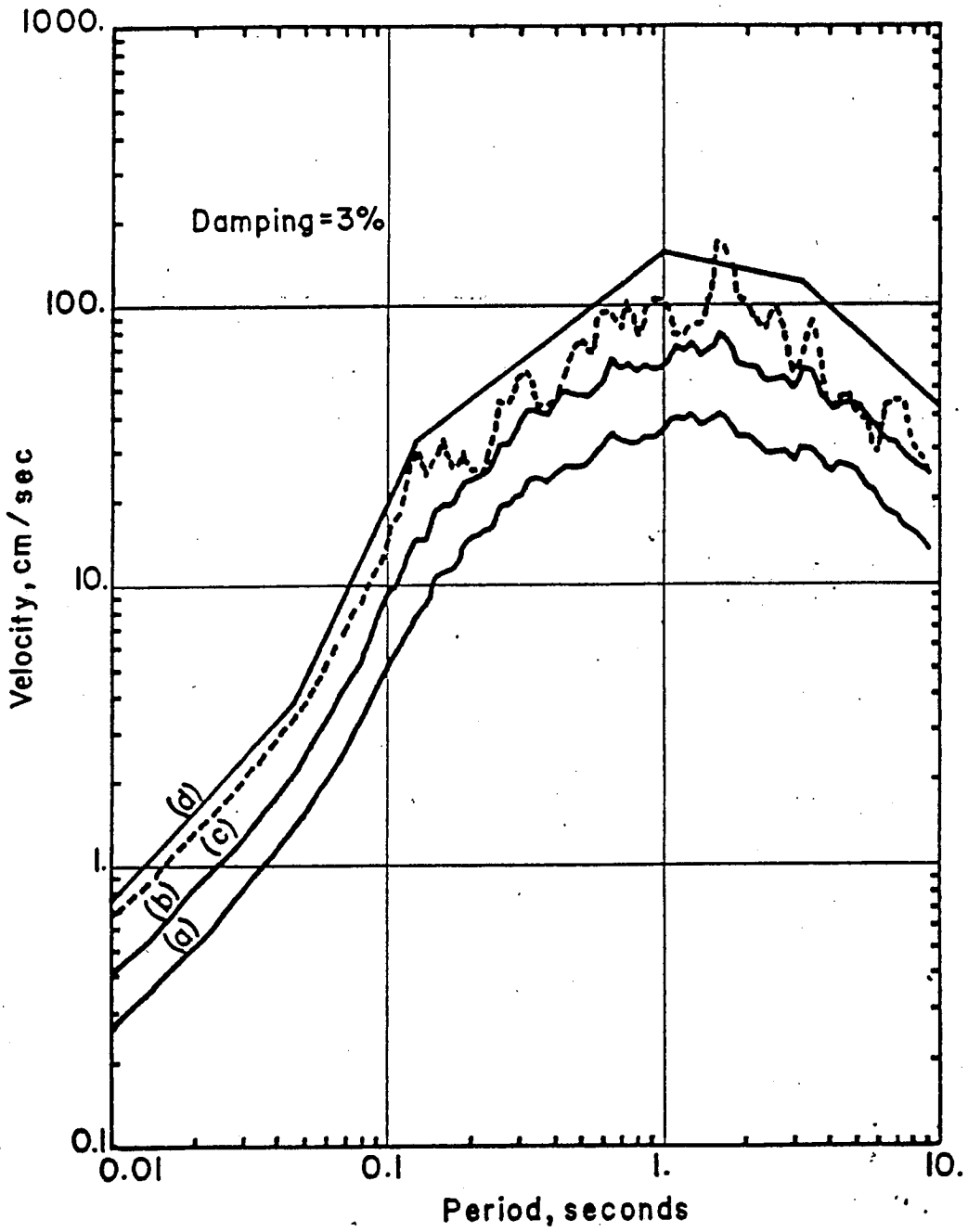
1000.
100.
10.
1.
0.1
Damping=3%
Velocity, cm/sec
(d)
(c)
(b)
(a)
0.01
0.1
1.
10.
Period, seconds

Figure 32.

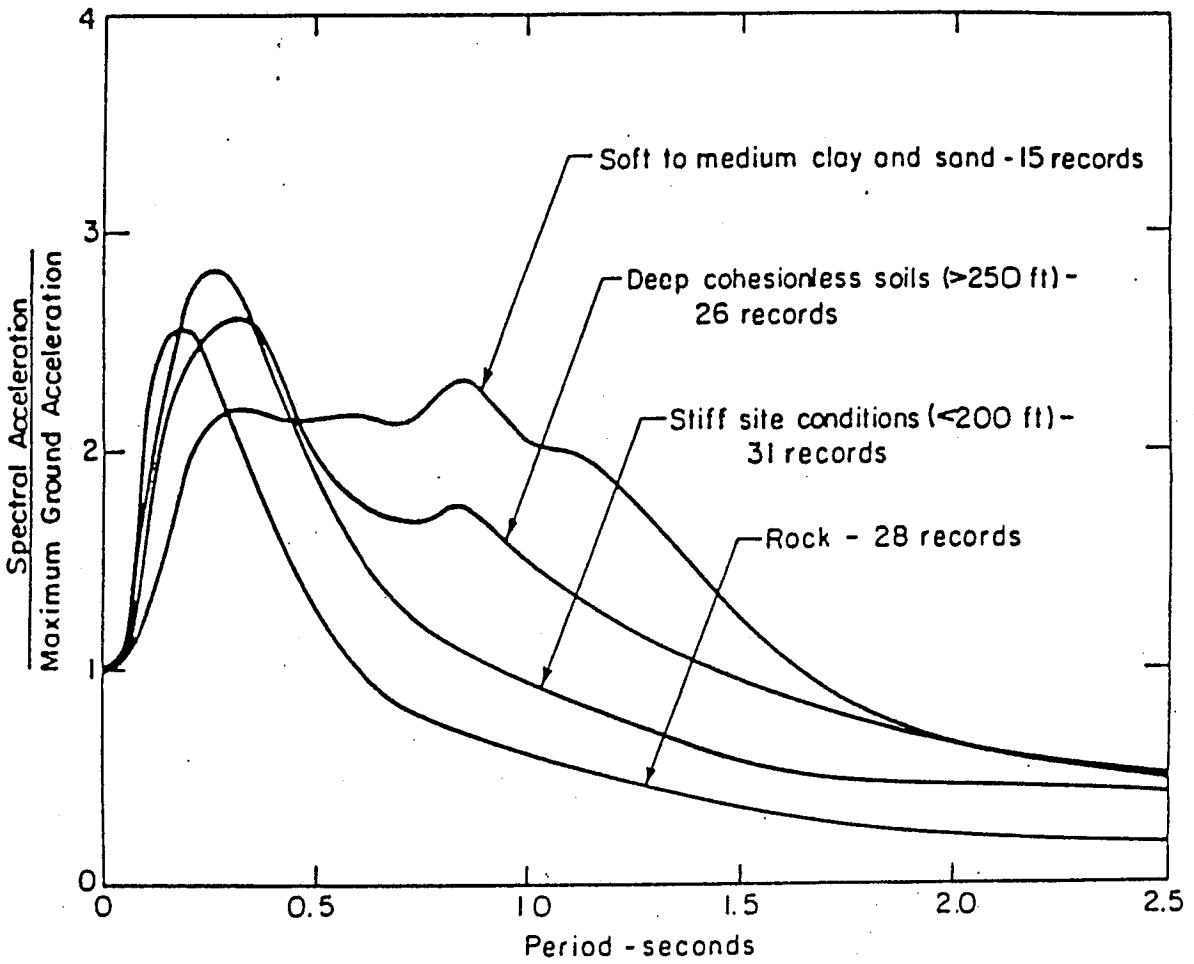

Figure 33. Average 5% damping response spectral shapes (Sa/a) computed from motions recorded on different soil conditions (after Seed, et al., 1976).

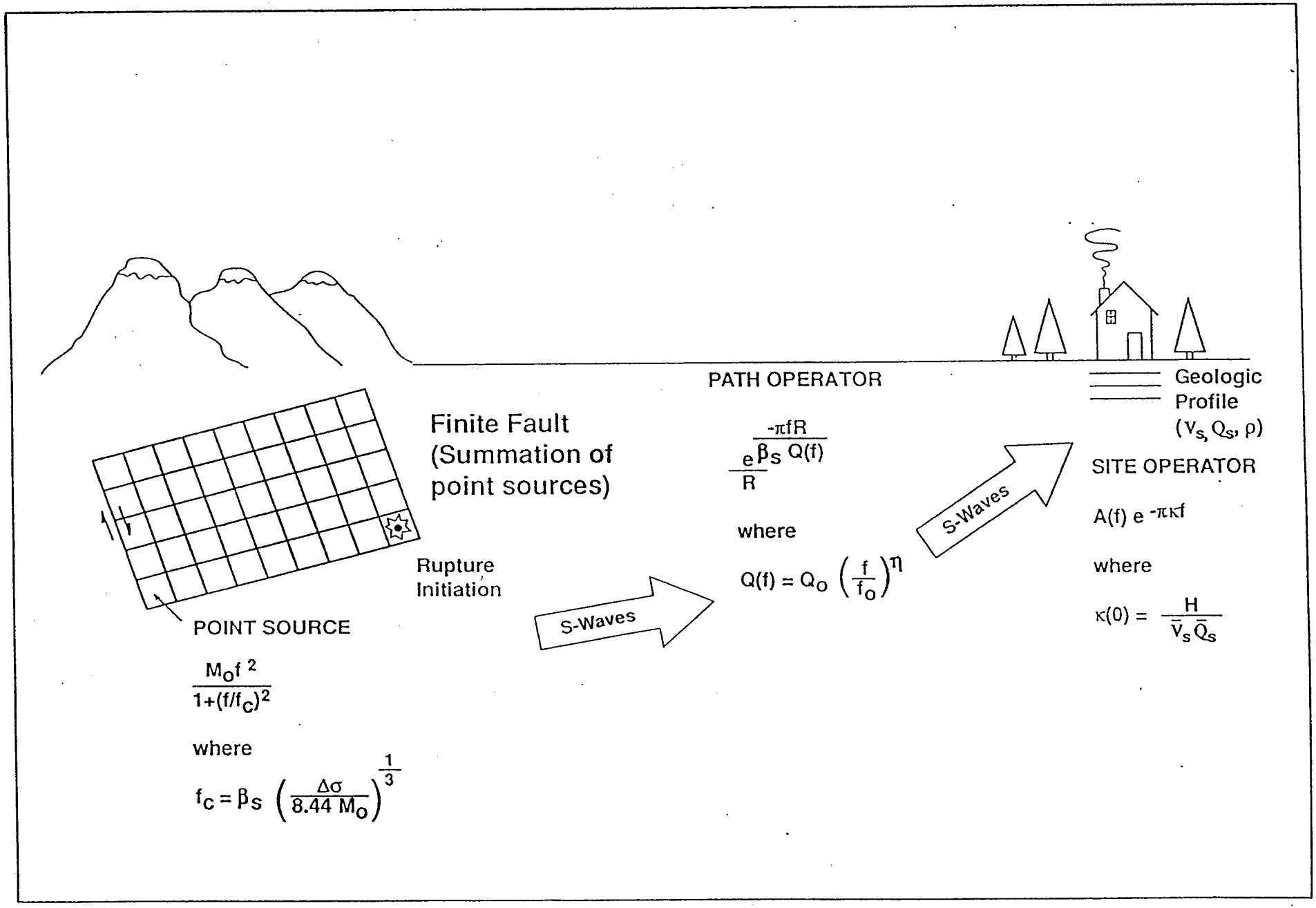

Figure 34. SCHEMATIC OF GROUND MOTION MODEL.

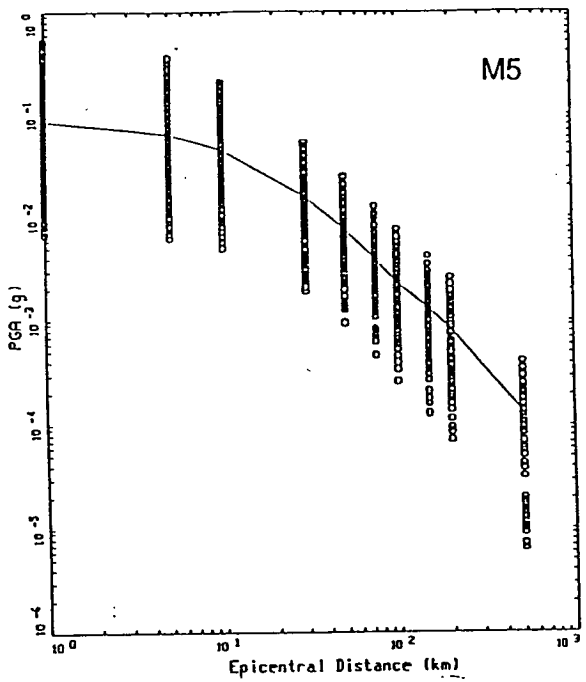

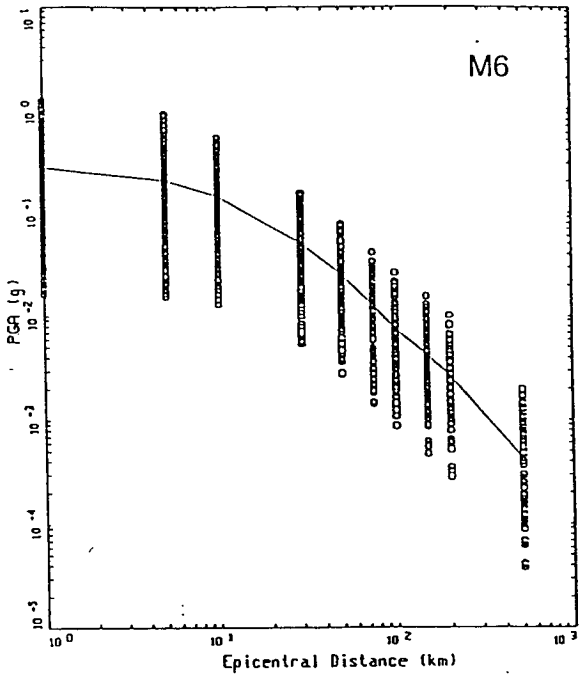

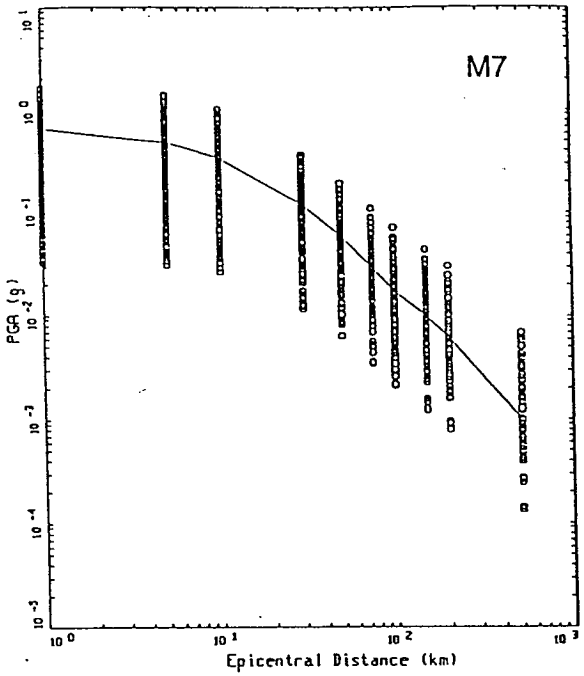

LEGEND

o Data: PGA Predictions

——— Regression on Data for M5, M6, and M7

Figure 35.	STOCHASTIC PEAK ACCELERATION

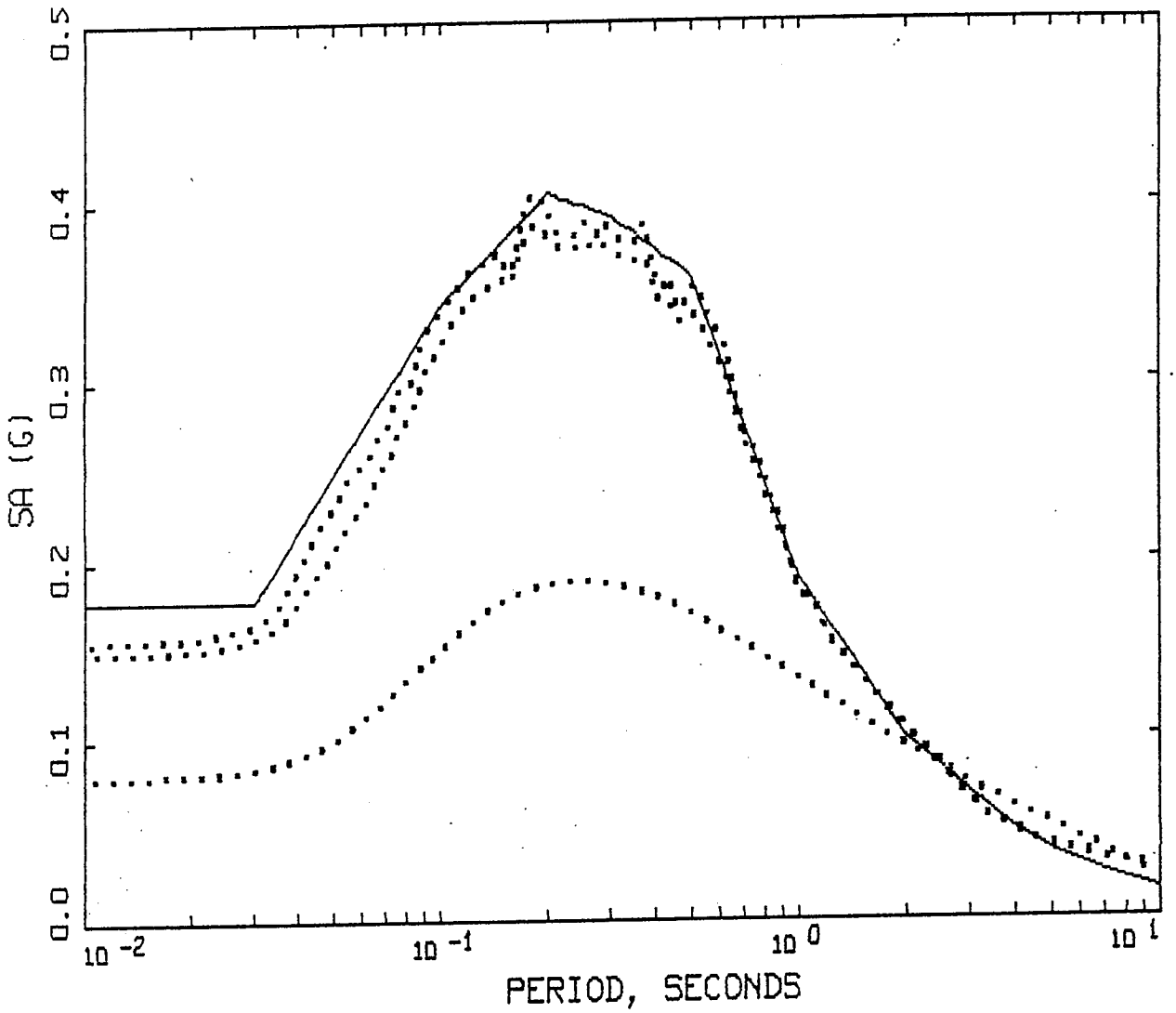

SPECTRAL MATCHING: SPRING CRK
CASCADIA RVT ITERATIONS

LEGEND

——— 5 %, 5% TARGET SPECTRUM
. . . . 5 %, RASCAL MATCH, 5%. ITERATION #0
. . . . 5 %, RASCAL MATCH, 5%. ITERATION #1
. . . . 5 %, RASCAL MATCH, 5%. ITERATION #2

Figure 36.

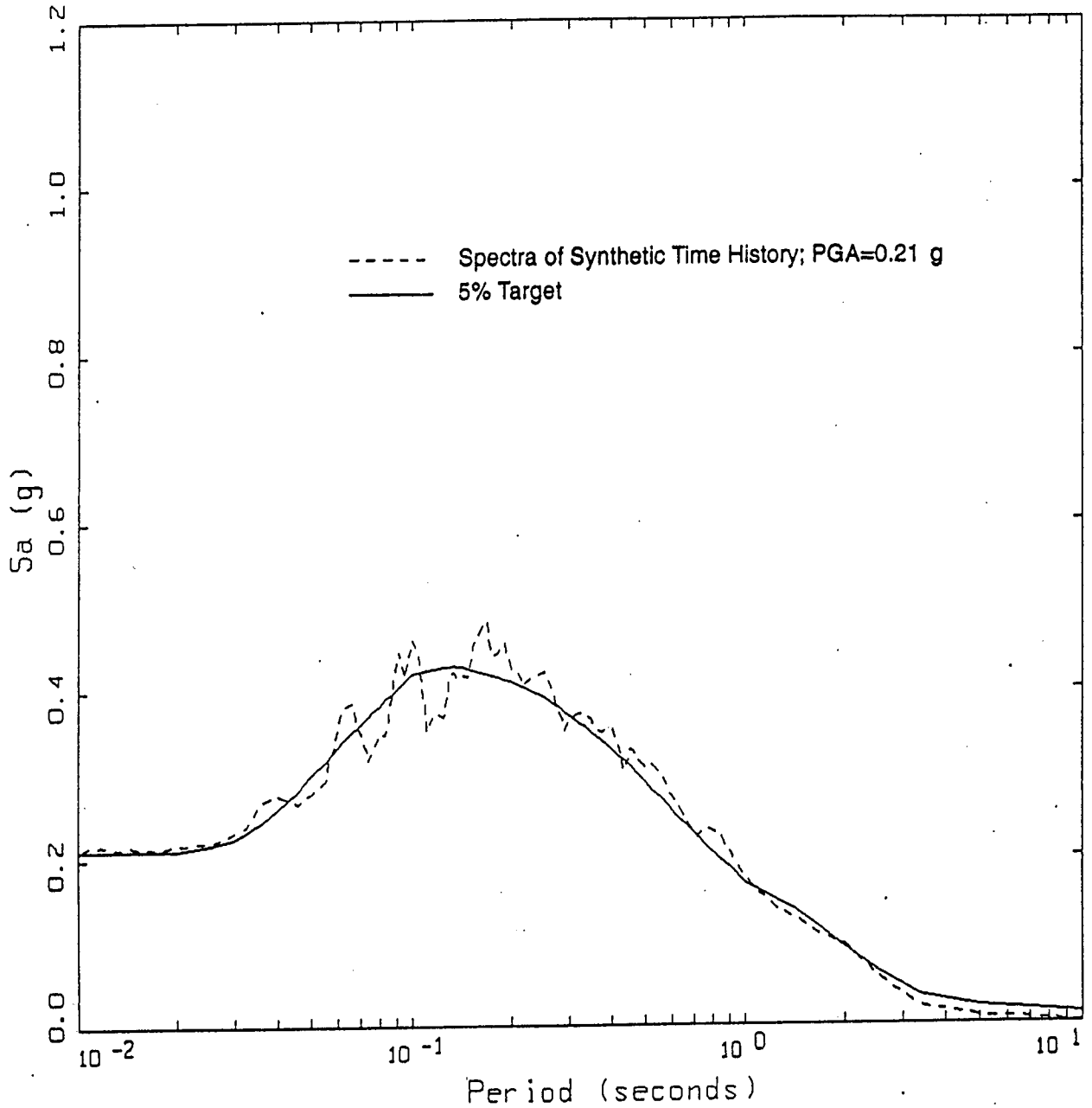

Figure 37. SEE ACCELERATION RESPONSE SPECTRUM AND SPECTRAL MATCH FOR BOISE RIVER DIVERSION DAM

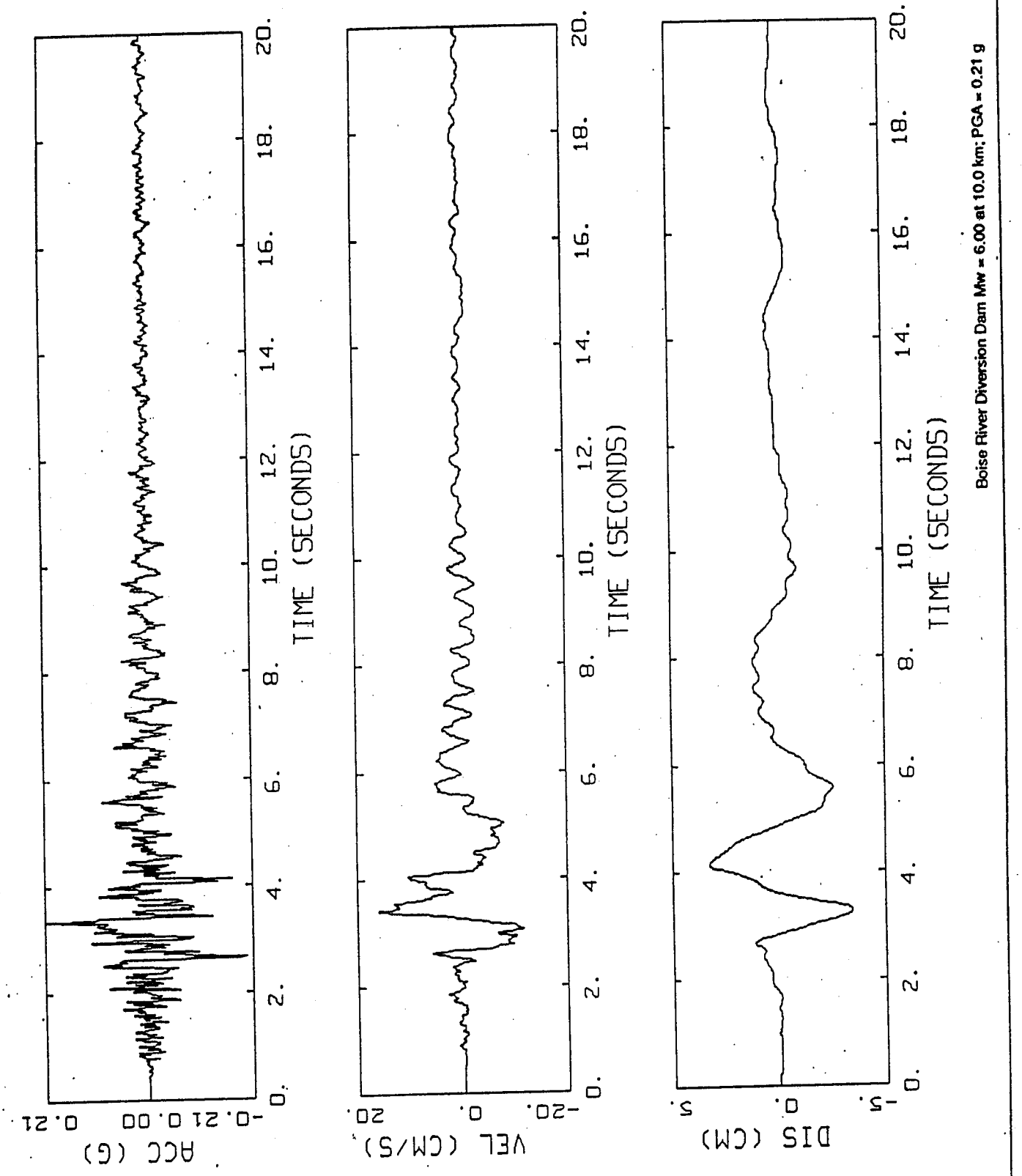

Figure 38. SEE ACCELERATION, VELOCITY AND DISPLACEMENT TIME HISTORIES FOR BOISE RIVER DIVERSION DAM

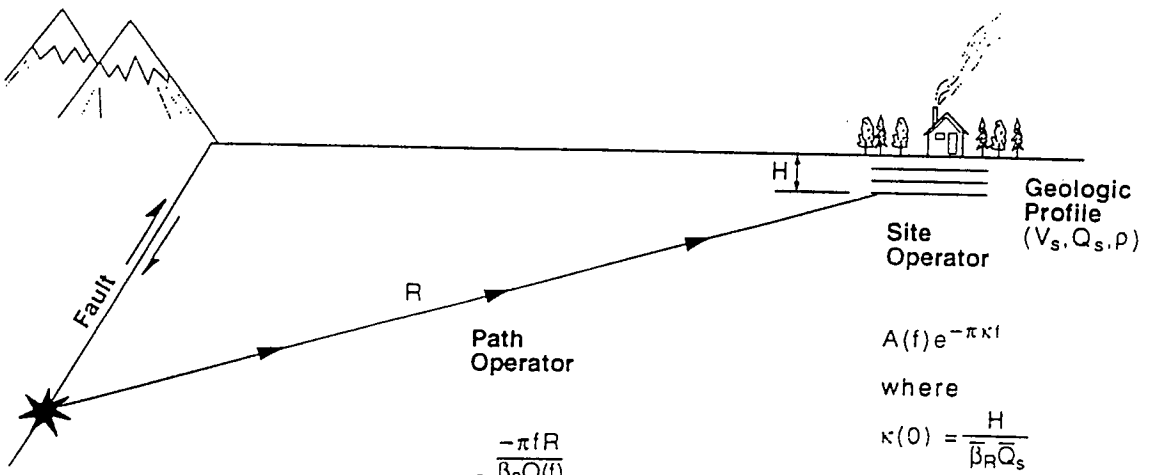

Figure 39. SCHEMATIC OF BAND-LIMITED-WHITE-NOISE GROUND MOTION MODEL

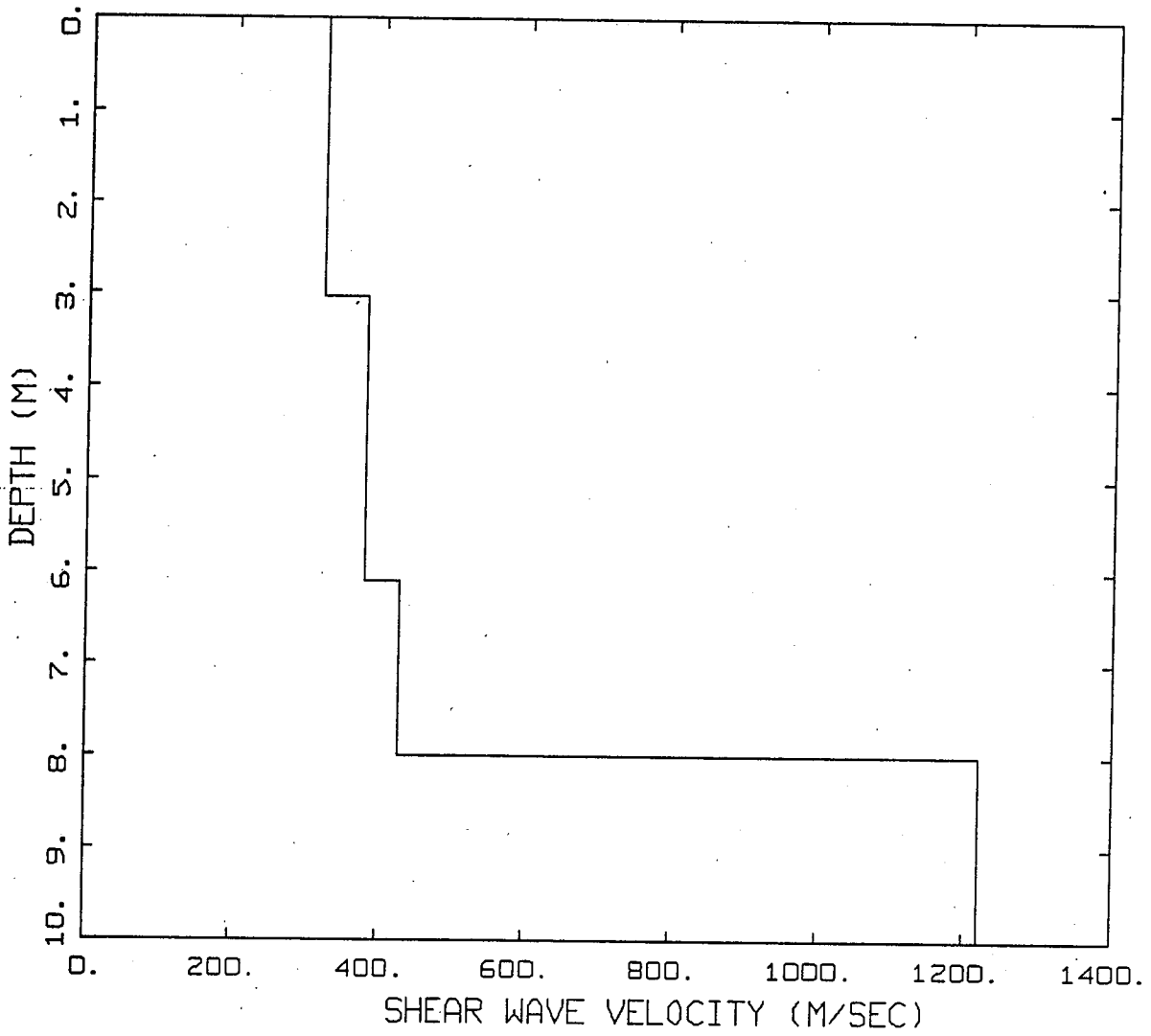

UNITY DAM
MEDIAN PROFILE

Figure 40.

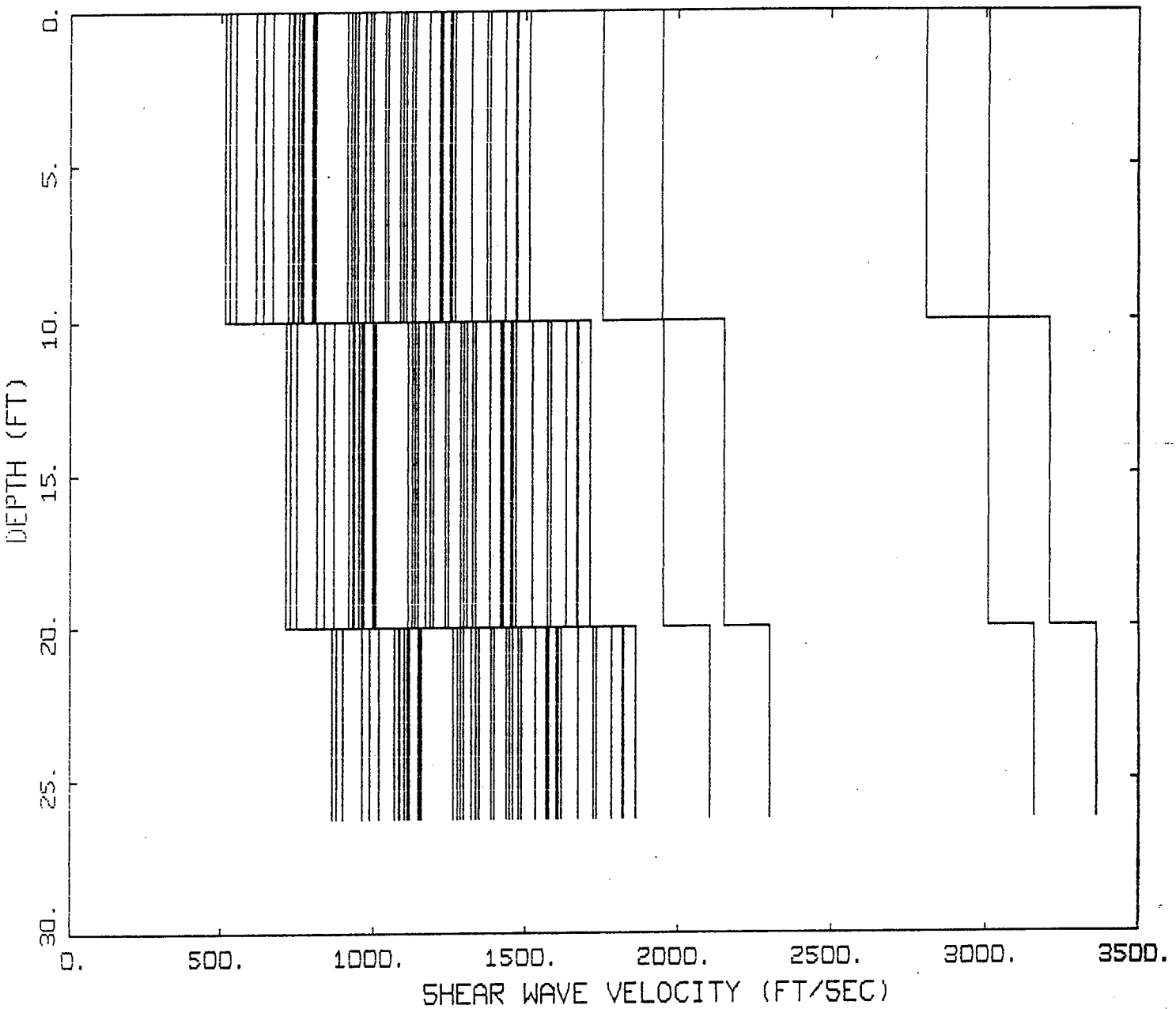

UNITY DAM
VARIATION OF VELOCITY

Figure 41.

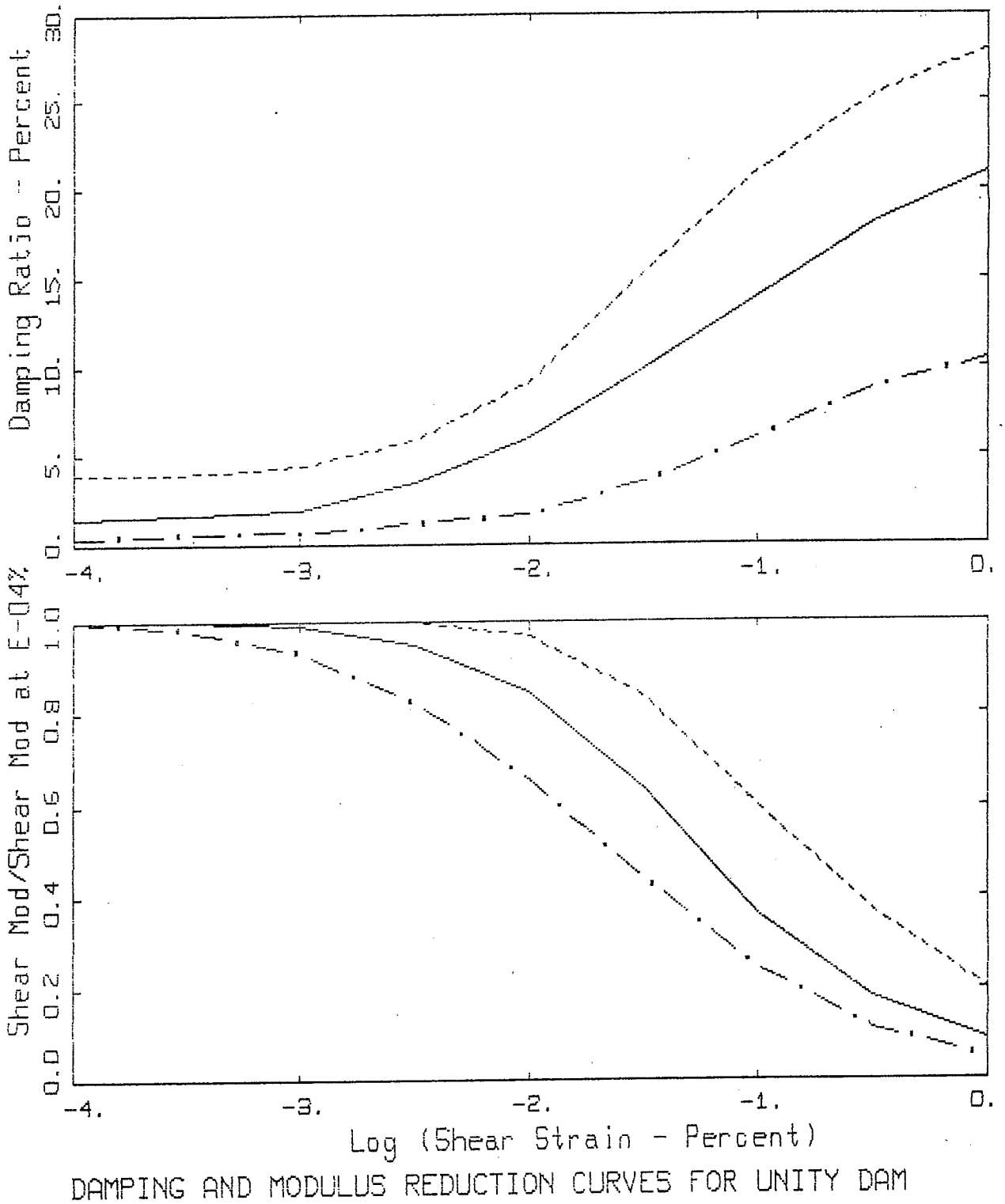

DAMPING AND MODULUS REDUCTION CURVES FOR UNITY DAM

LEGEND

----- UPPER BOUND

——— STANDARD CURVE

—·— LOWER BOUND

Figure 42.

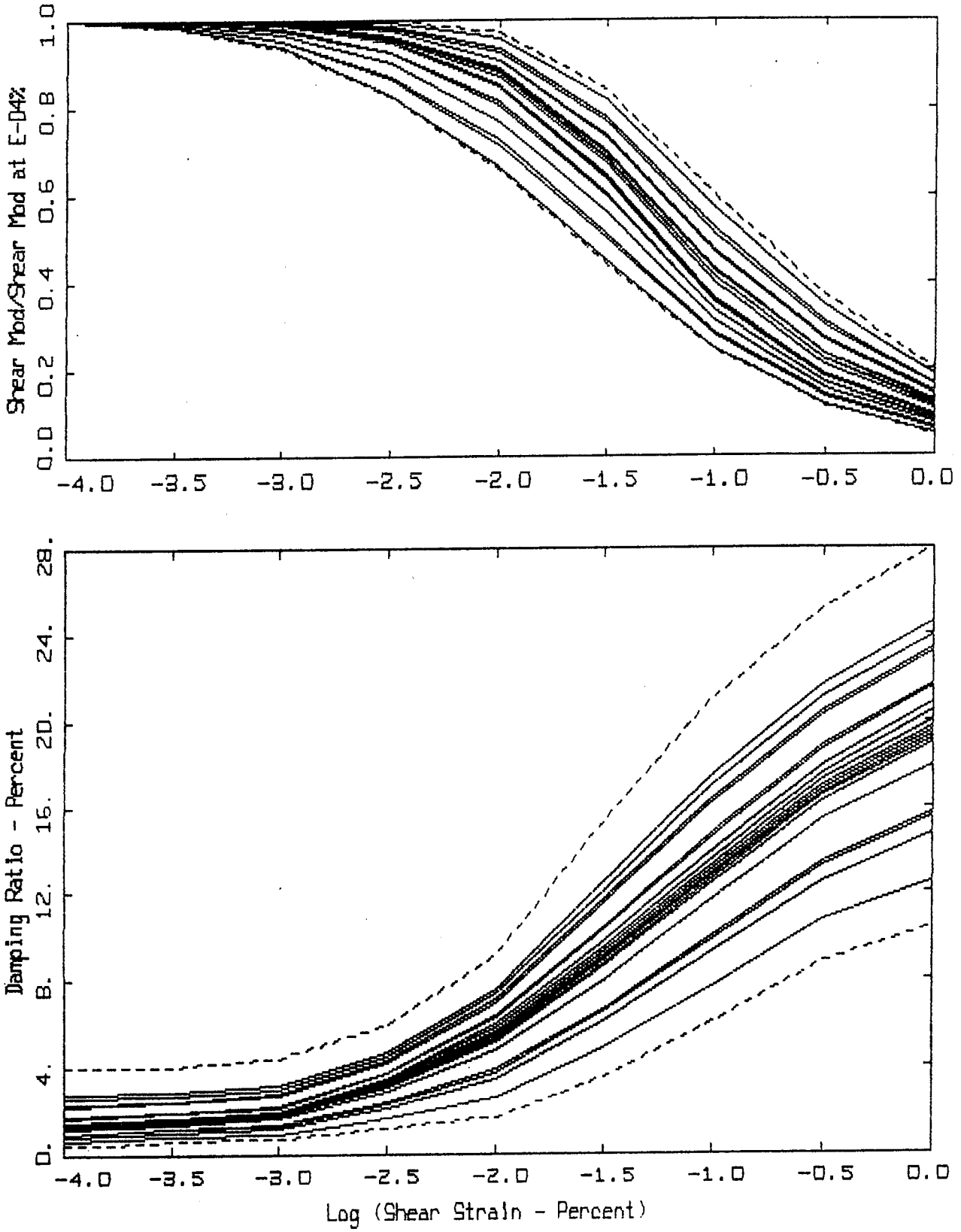

20 RANDOMIZED DAMPING AND MODULUS REDUCTION CURVES FOR UNITY DAM

Figure 43.

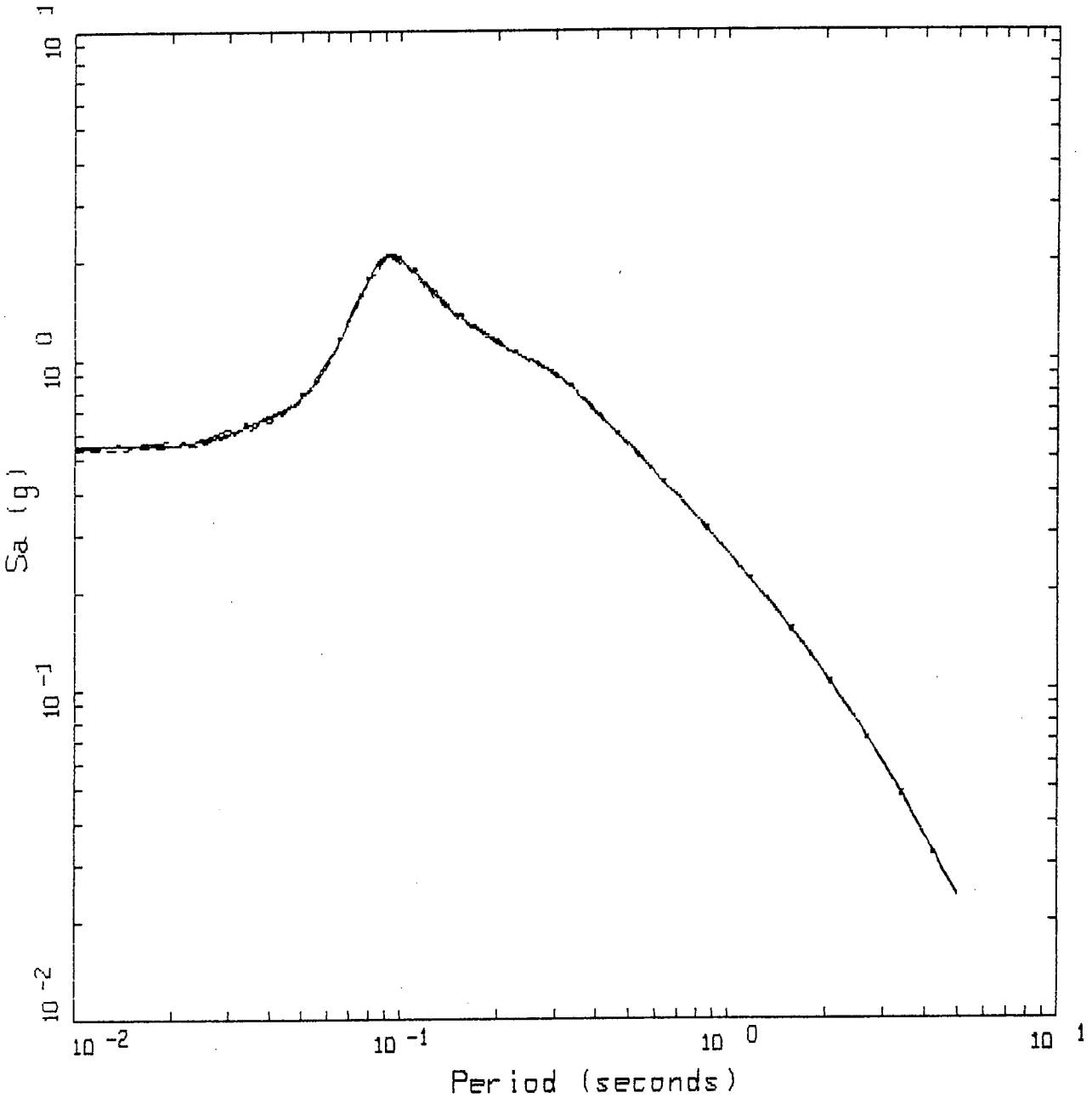

UNITY DAM, M=6.24
VARIATION OF QO

LEGEND

— • — 5 %, 84TH PERCENTILE, PARAMETRIC UNCERTAINTY; AMAX = 0.551 G

——— 5 %, 50TH PERCENTILE, PARAMETRIC UNCERTAINTY; AMAX = 0.542 G

- - - - - 5 %, 16TH PERCENTILE, PARAMETRIC UNCERTAINTY; AMAX = 0.533 G

Figure 44.

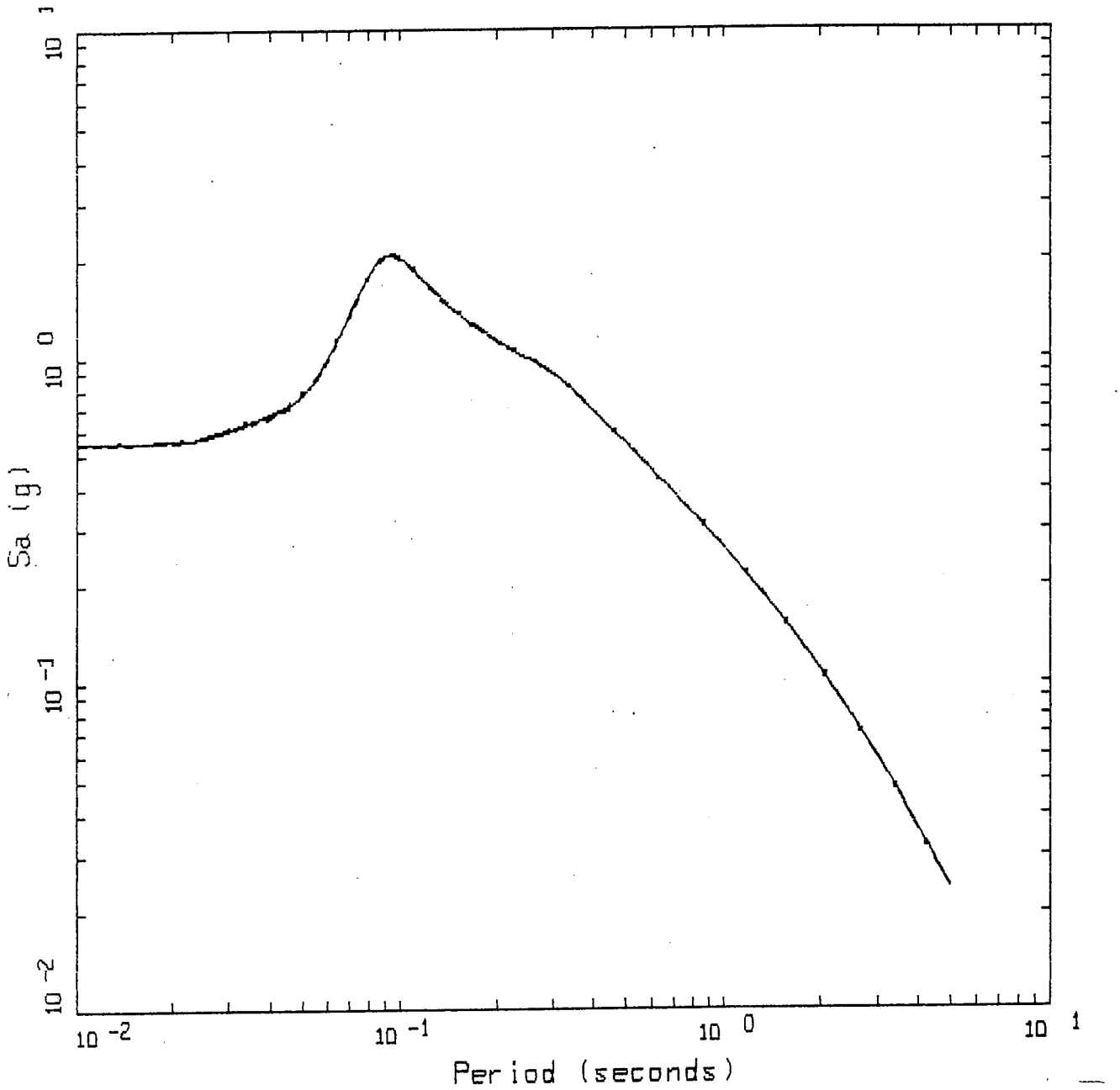

UNITY DAM, M=6.24
VARIATION OF ETA

LEGEND

— • — 5 %, 84TH PERCENTILE, PARAMETRIC UNCERTAINTY; AMAX = 0.548 G

——— 5 %, 50TH PERCENTILE, PARAMETRIC UNCERTAINTY; AMAX = 0.543 G

----- 5 %, 16TH PERCENTILE, PARAMETRIC UNCERTAINTY; AMAX = 0.539 G

Figure 45.

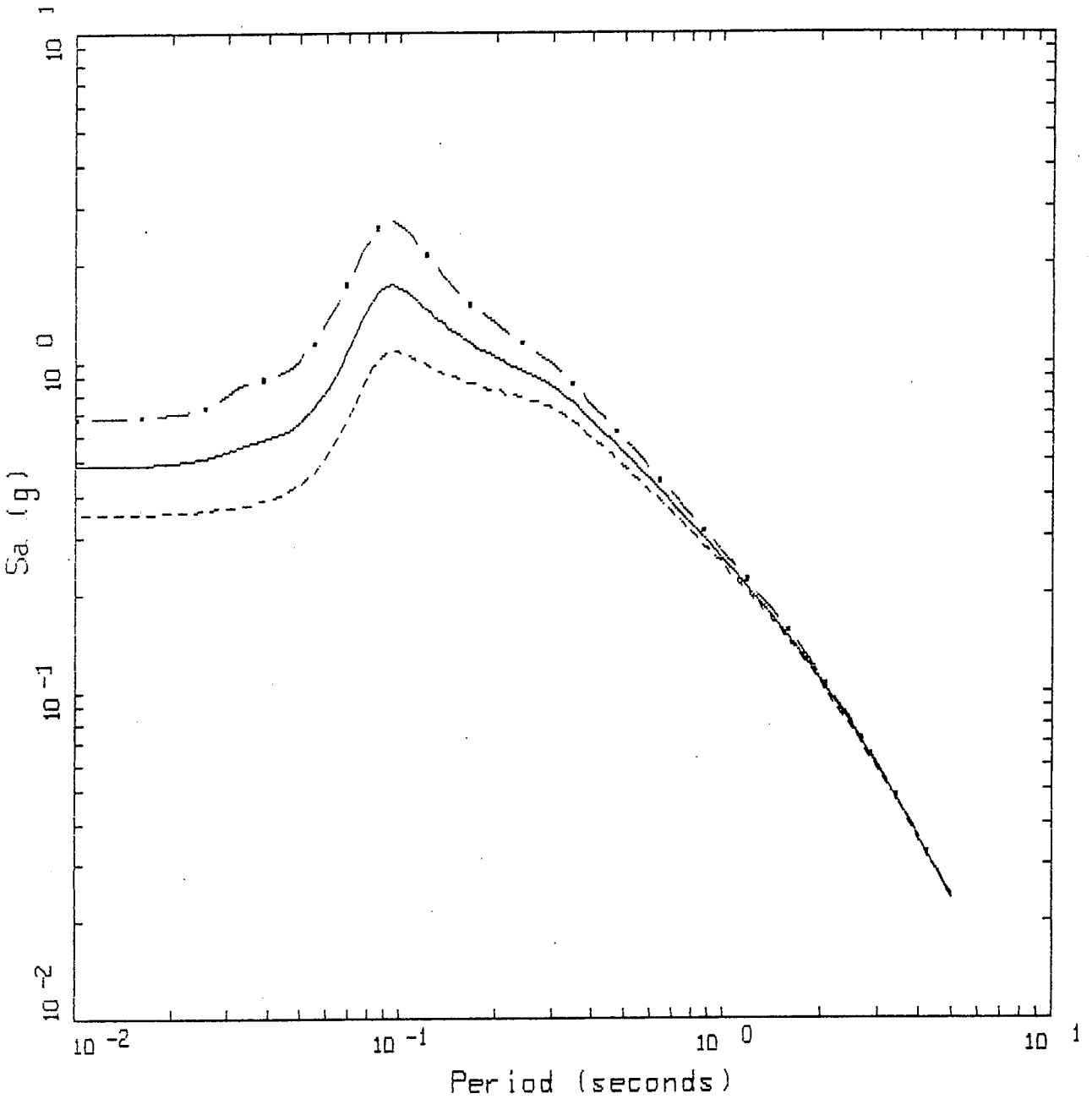

UNITY DAM, M=6.24
VARIATION OF KAPPA

LEGEND

— · — 5 %, 84TH PERCENTILE, PARAMETRIC UNCERTAINTY; AMAX = 0.669 G

——— 5 %, 50TH PERCENTILE, PARAMETRIC UNCERTAINTY; AMAX = 0.483 G

- - - - - 5 %, 16TH PERCENTILE, PARAMETRIC UNCERTAINTY; AMAX = 0.349 G

Figure 46.

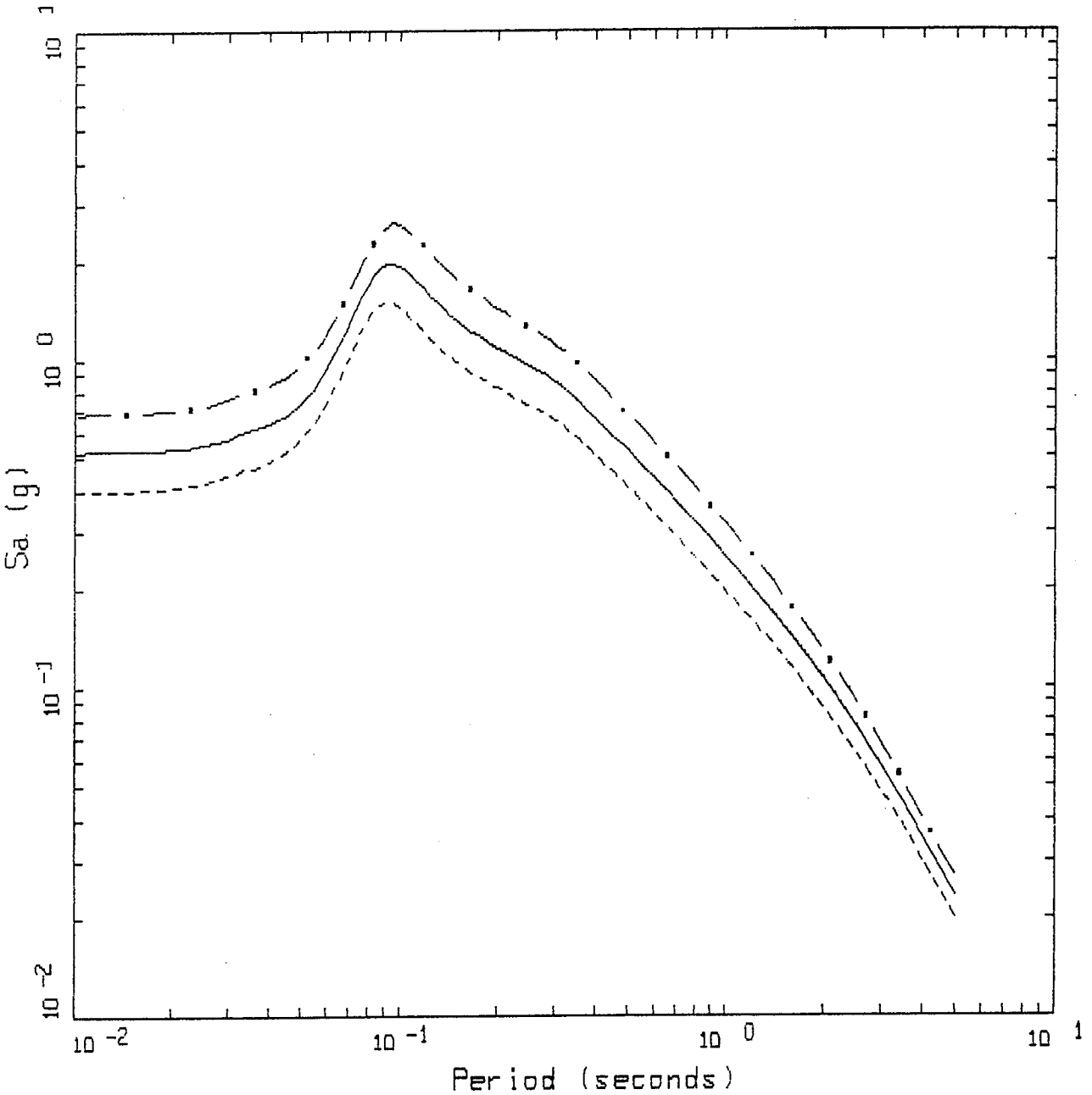

UNITY DAM, M=6.24
VARIATION OF STRESS DROP

LEGEND

— · — 5 %, 84TH PERCENTILE, PARAMETRIC UNCERTAINTY; AMAX = 0.684 G

——— 5 %, 50TH PERCENTILE, PARAMETRIC UNCERTAINTY; AMAX = 0.519 G

- - - - - 5 %, 16TH PERCENTILE, PARAMETRIC UNCERTAINTY; AMAX = 0.393 G

Figure 47.

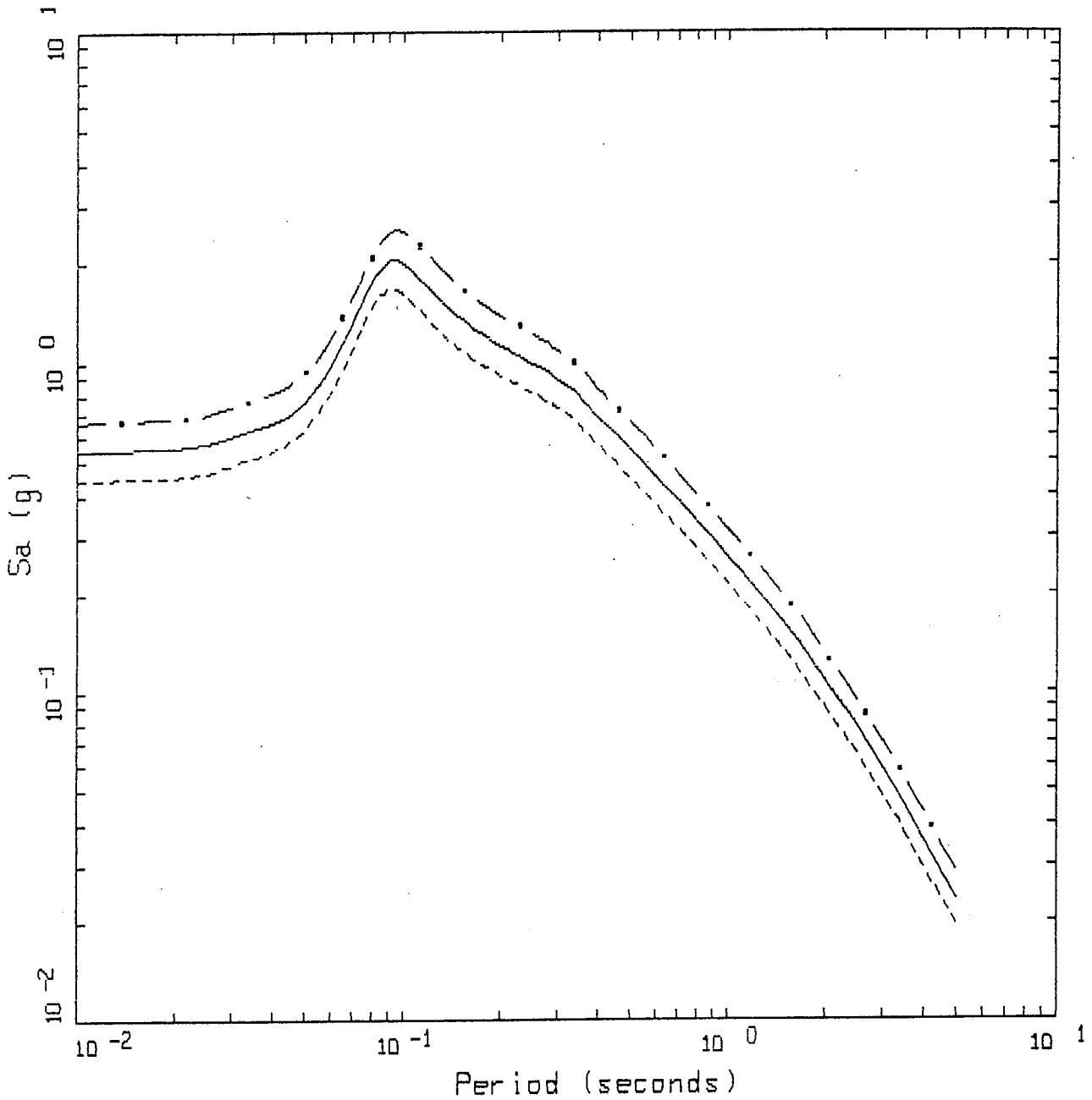

UNITY DAM, M=6.24
VARIATION OF SOURCE DEPTH

LEGEND

— · — 5 %, 84TH PERCENTILE, PARAMETRIC UNCERTAINTY; AMAX = 0.661 G

——— 5 %, 50TH PERCENTILE, PARAMETRIC UNCERTAINTY; AMAX = 0.539 G

- - - - - 5 %, 16TH PERCENTILE, PARAMETRIC UNCERTAINTY; AMAX = 0.440 G

Figure 48.

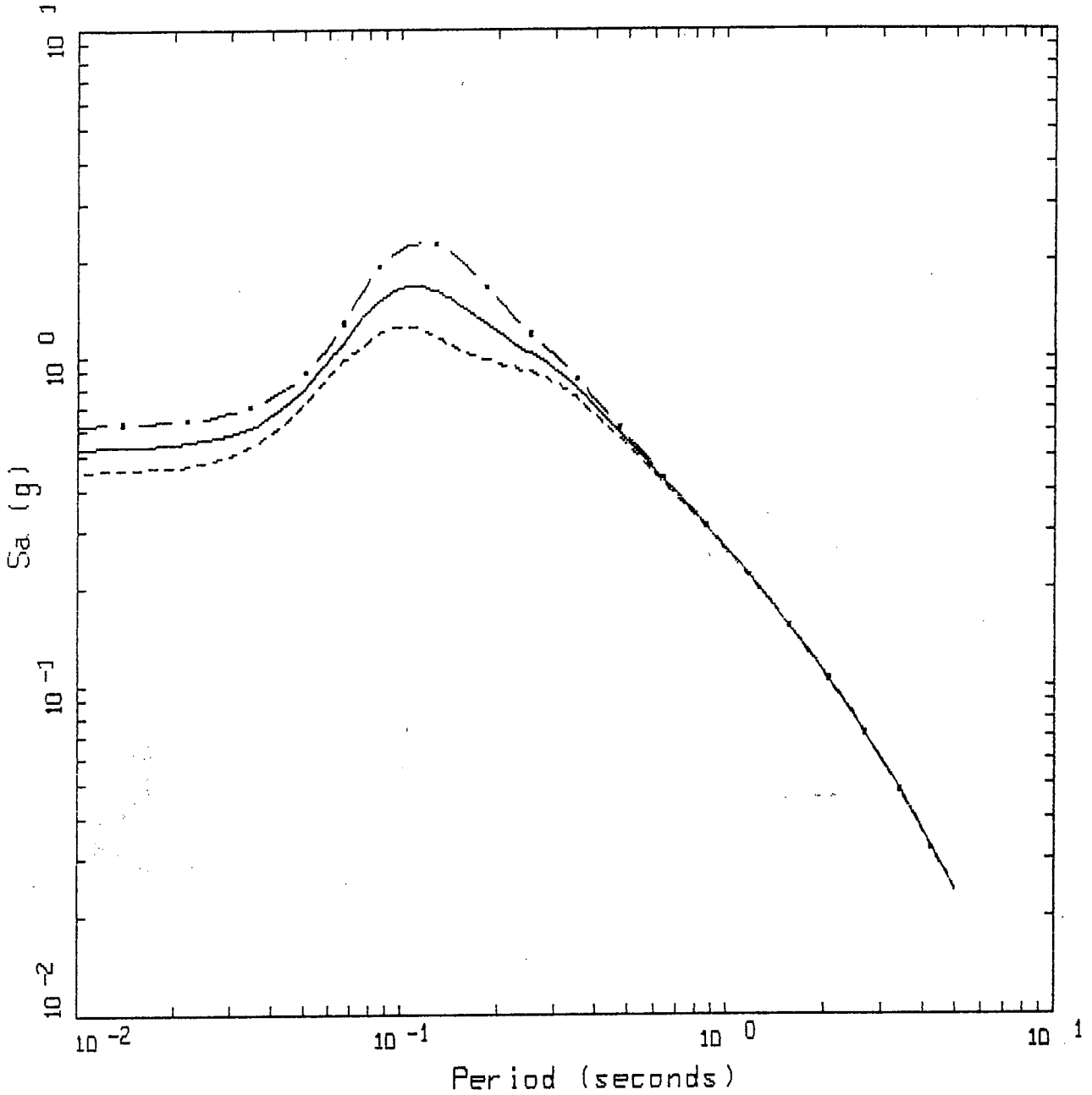

UNITY DAM, M=6.24
VARIATION OF VELOCITY

LEGEND

— • — 5 %, 84TH PERCENTILE, PARAMETRIC UNCERTAINTY; AMAX = 0.624 G

——— 5 %, 50TH PERCENTILE, PARAMETRIC UNCERTAINTY; AMAX = 0.531 G

- - - - - 5 %, 16TH PERCENTILE, PARAMETRIC UNCERTAINTY; AMAX = 0.451 G

Figure 49.

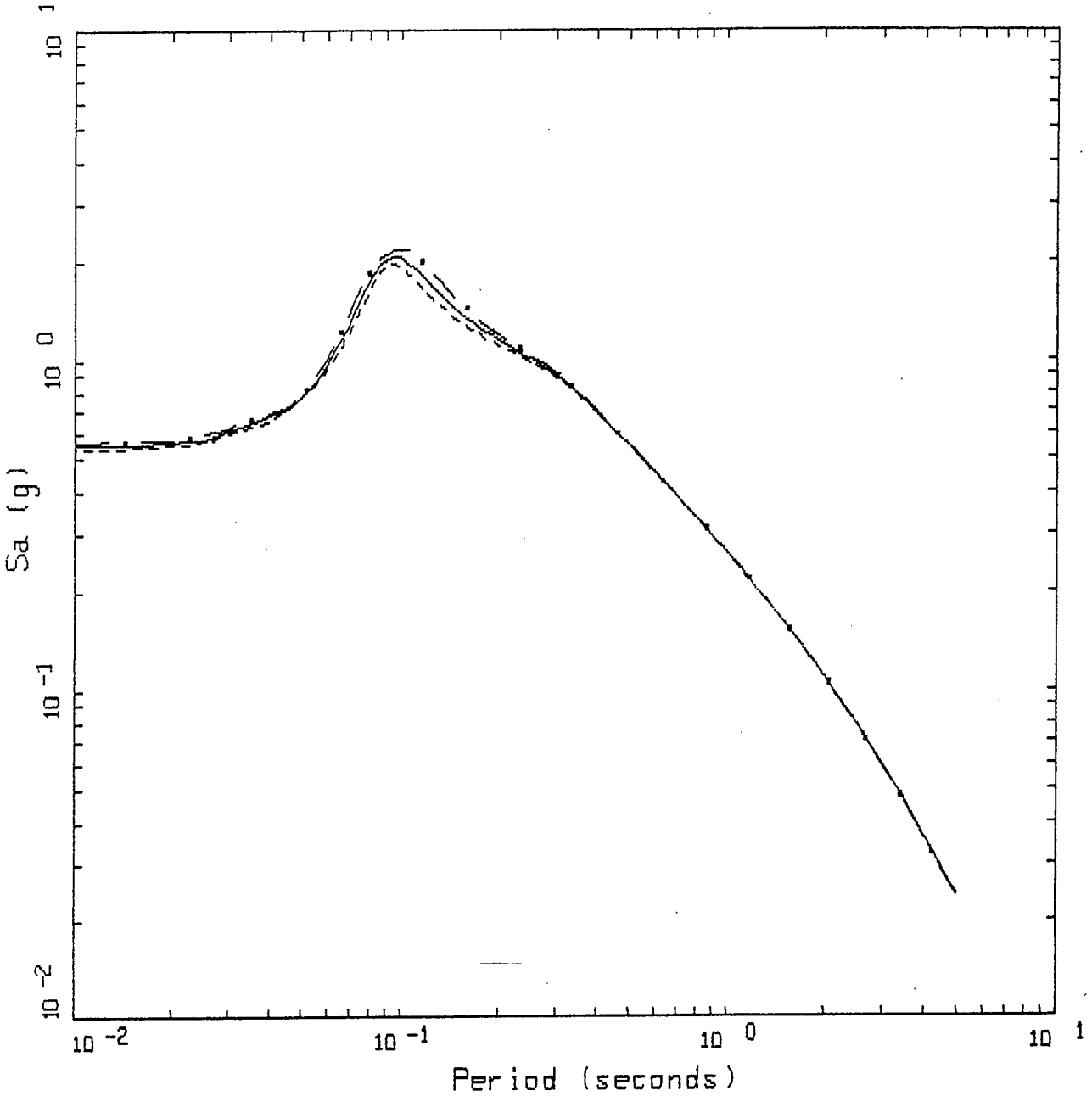

UNITY DAM, M=6.24
VARIATION OF MODULUS REDUCTION

LEGEND

— • — 5 %, 84TH PERCENTILE, PARAMETRIC UNCERTAINTY; AMAX = 0.562 G

——— 5 %, 50TH PERCENTILE, PARAMETRIC UNCERTAINTY; AMAX = 0.547 G

----- 5 %, 16TH PERCENTILE, PARAMETRIC UNCERTAINTY; AMAX = 0.533 G

Figure 50.

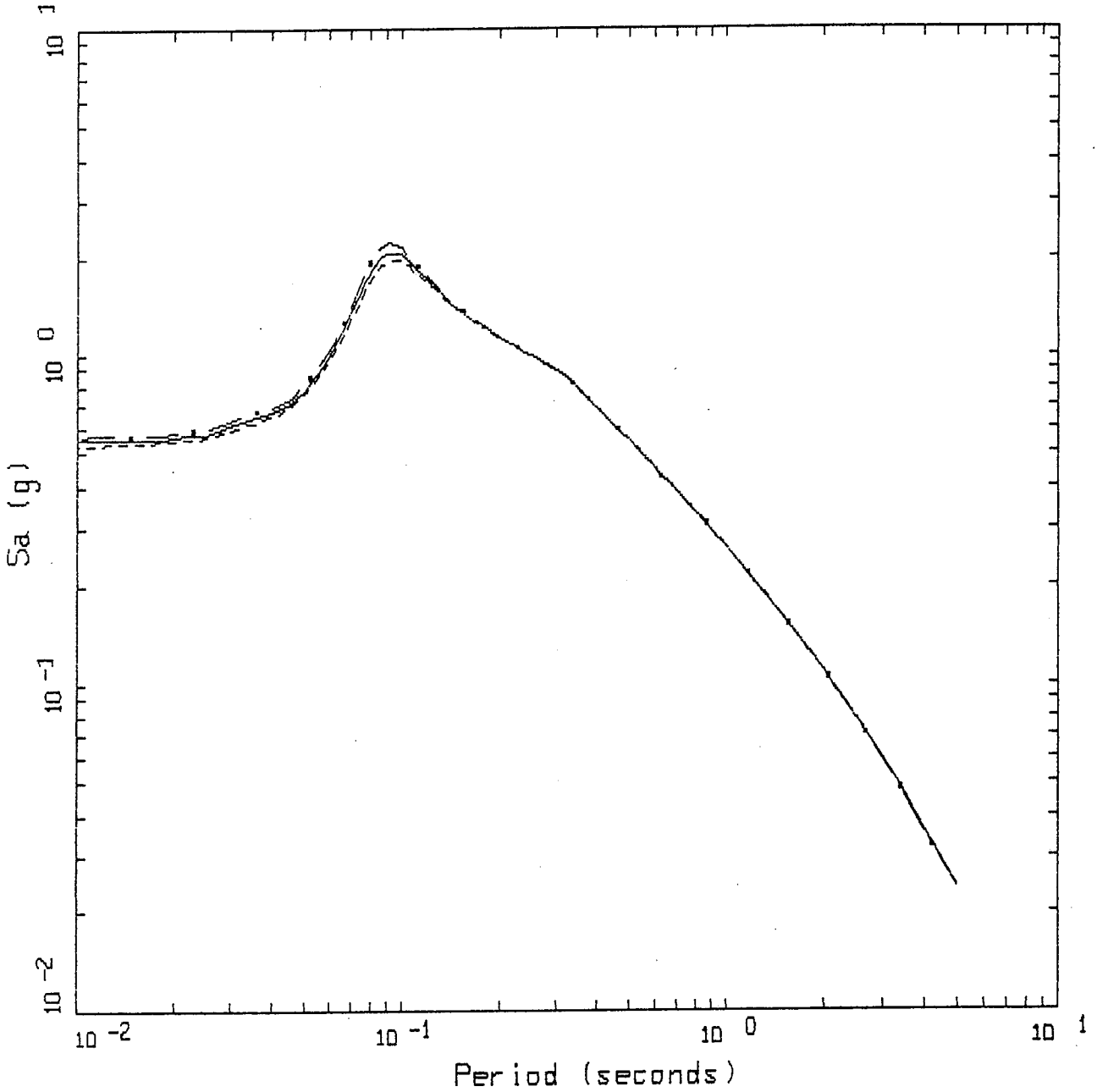

UNITY DAM, M=6.24
VARIATION OF NONLIN DAMPING

LEGEND

— · — 5 %, 84TH PERCENTILE, PARAMETRIC UNCERTAINTY; AMAX = 0.562 G

——— 5 %, 50TH PERCENTILE, PARAMETRIC UNCERTAINTY; AMAX = 0.546 G

----- 5 %, 16TH PERCENTILE, PARAMETRIC UNCERTAINTY; AMAX = 0.530 G

Figure 51.

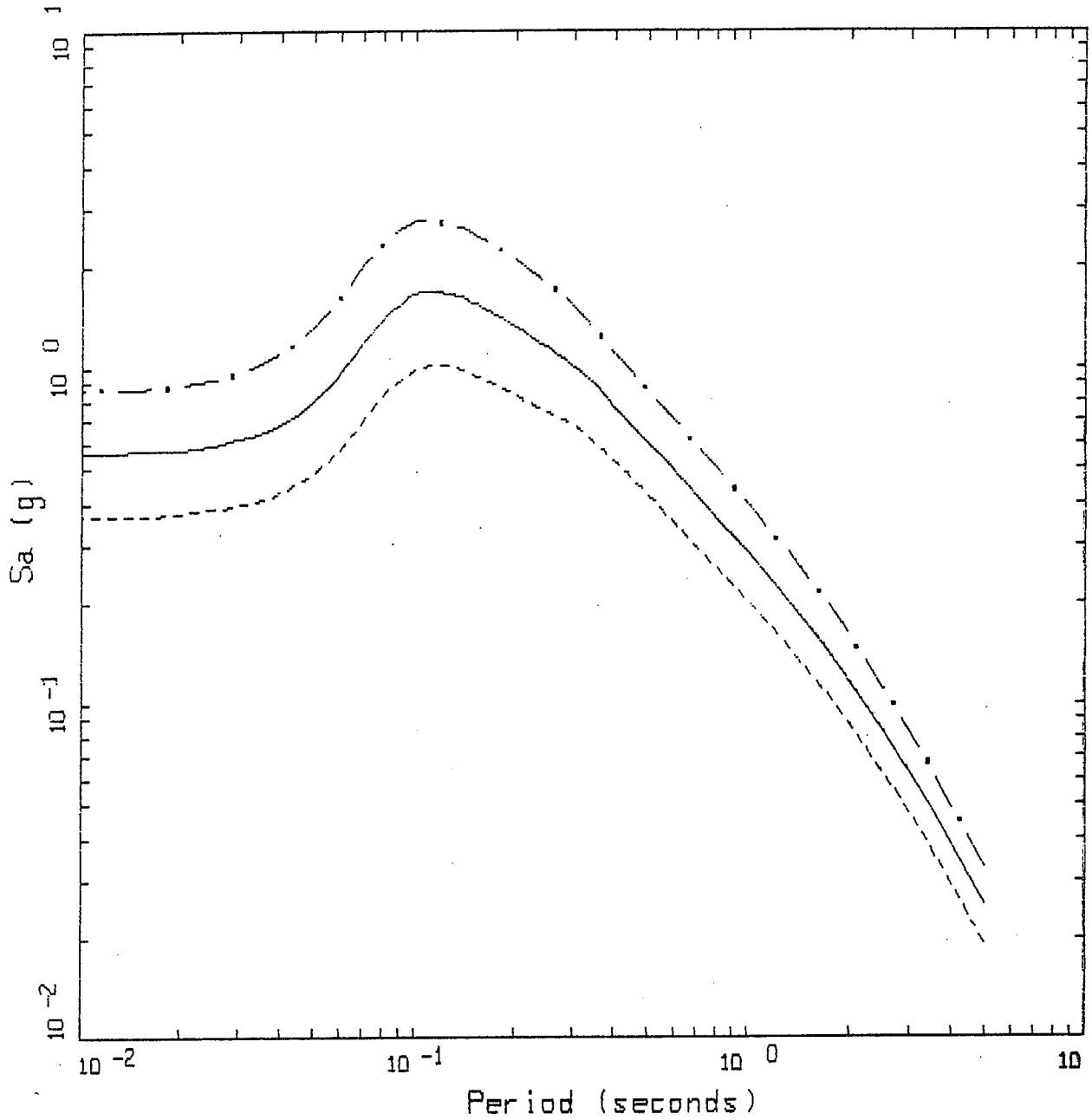

UNITY DAM, M=6.24
VARIATION OF ALL PARAMETERS

LEGEND

— · — 5 %, 84TH PERCENTILE, PARAMETRIC UNCERTAINTY; AMAX = 0.863 G

——— 5 %, 50TH PERCENTILE, PARAMETRIC UNCERTAINTY; AMAX = 0.560 G

----- 5 %, 16TH PERCENTILE, PARAMETRIC UNCERTAINTY; AMAX = 0.364 G

Figure 52.

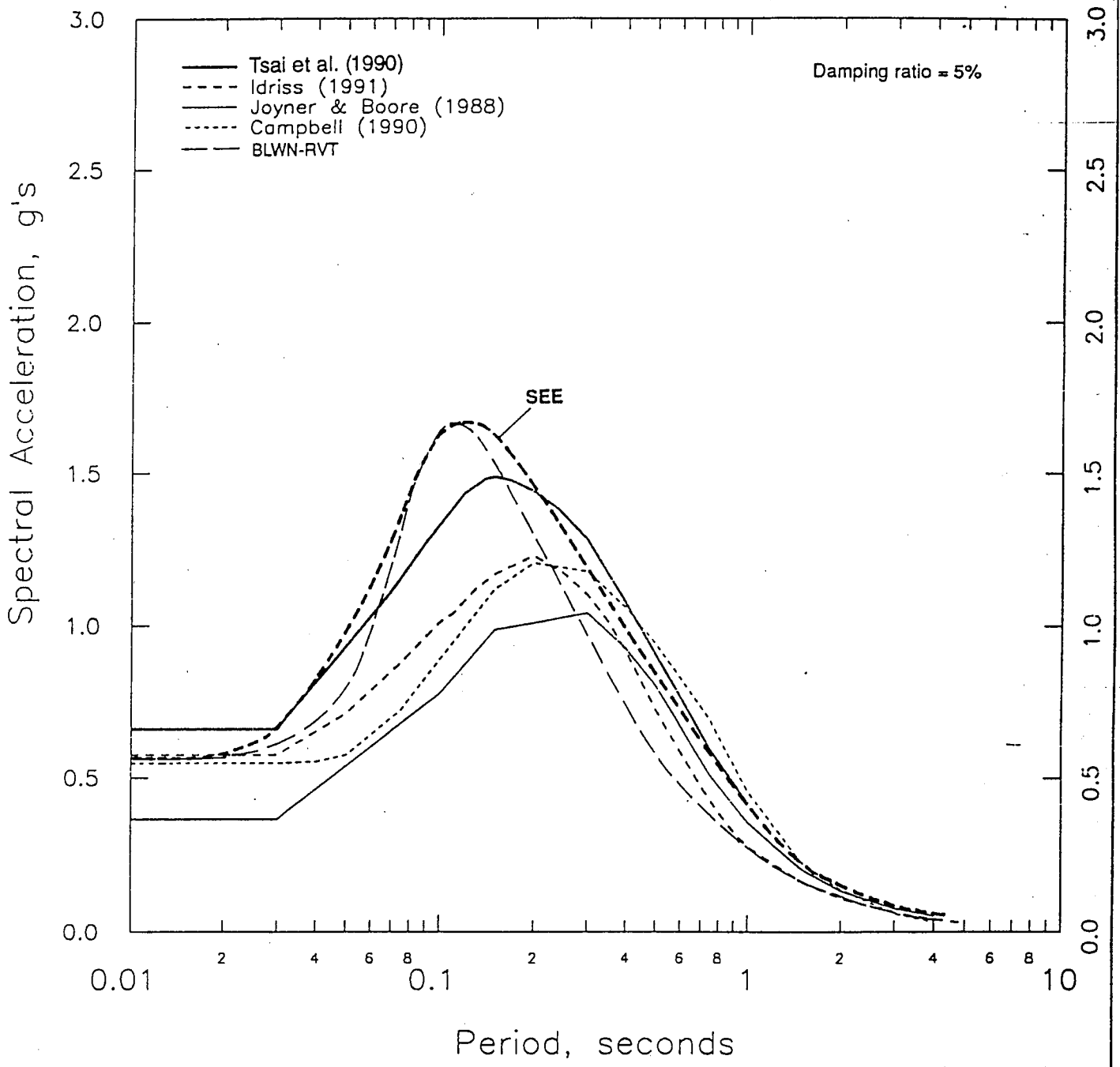

Figure 53. COMPARISON OF EMPIRICAL AND BLWN-RVT MEDIAN RESPONSE SPECTRA AND RECOMMENDED SEE SPECTRUM FOR UNITY DAM

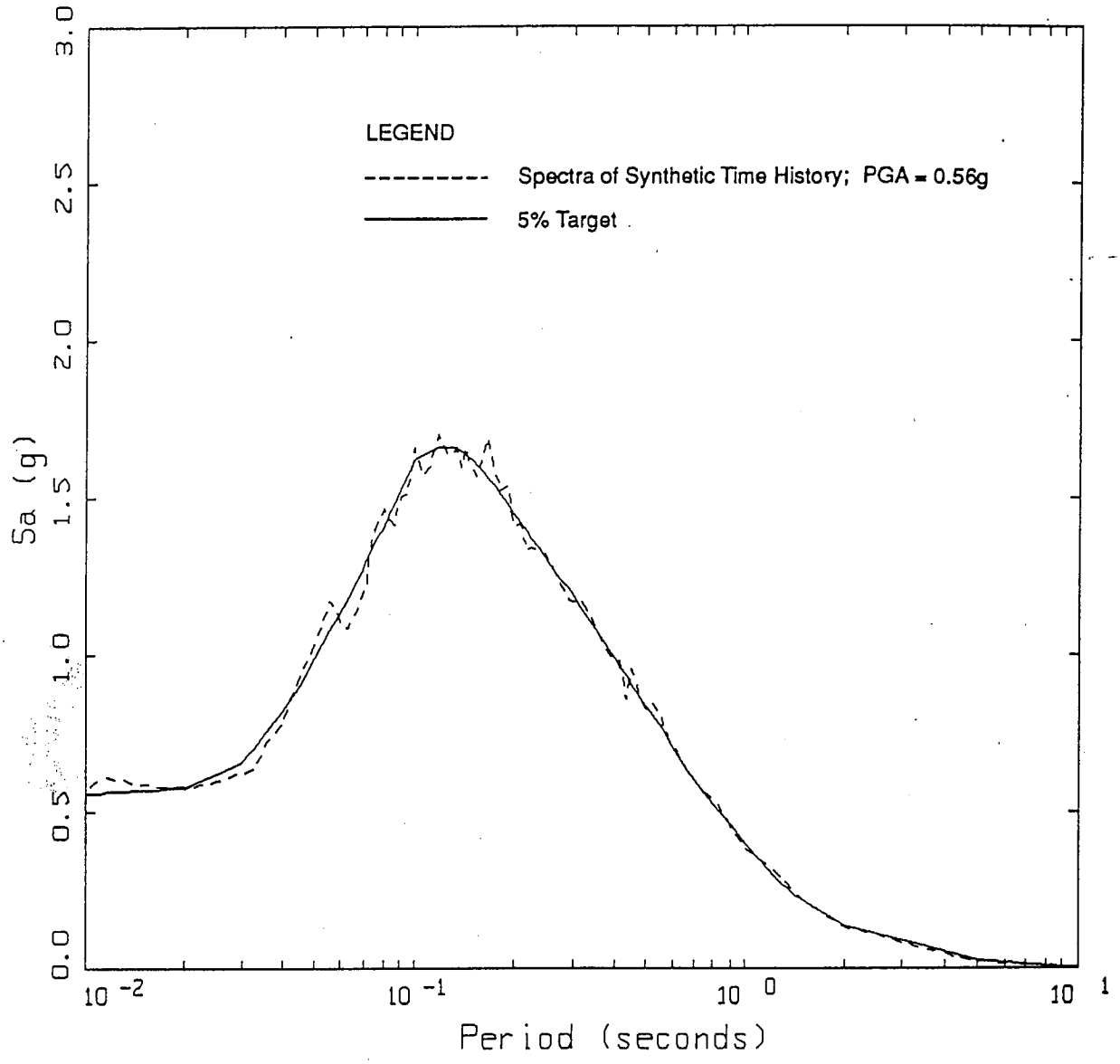

Figure 54.

SEE ACCELERATION RESPONSE SPECTRUM AND SPECTRAL MATCH FOR UNITY DAM

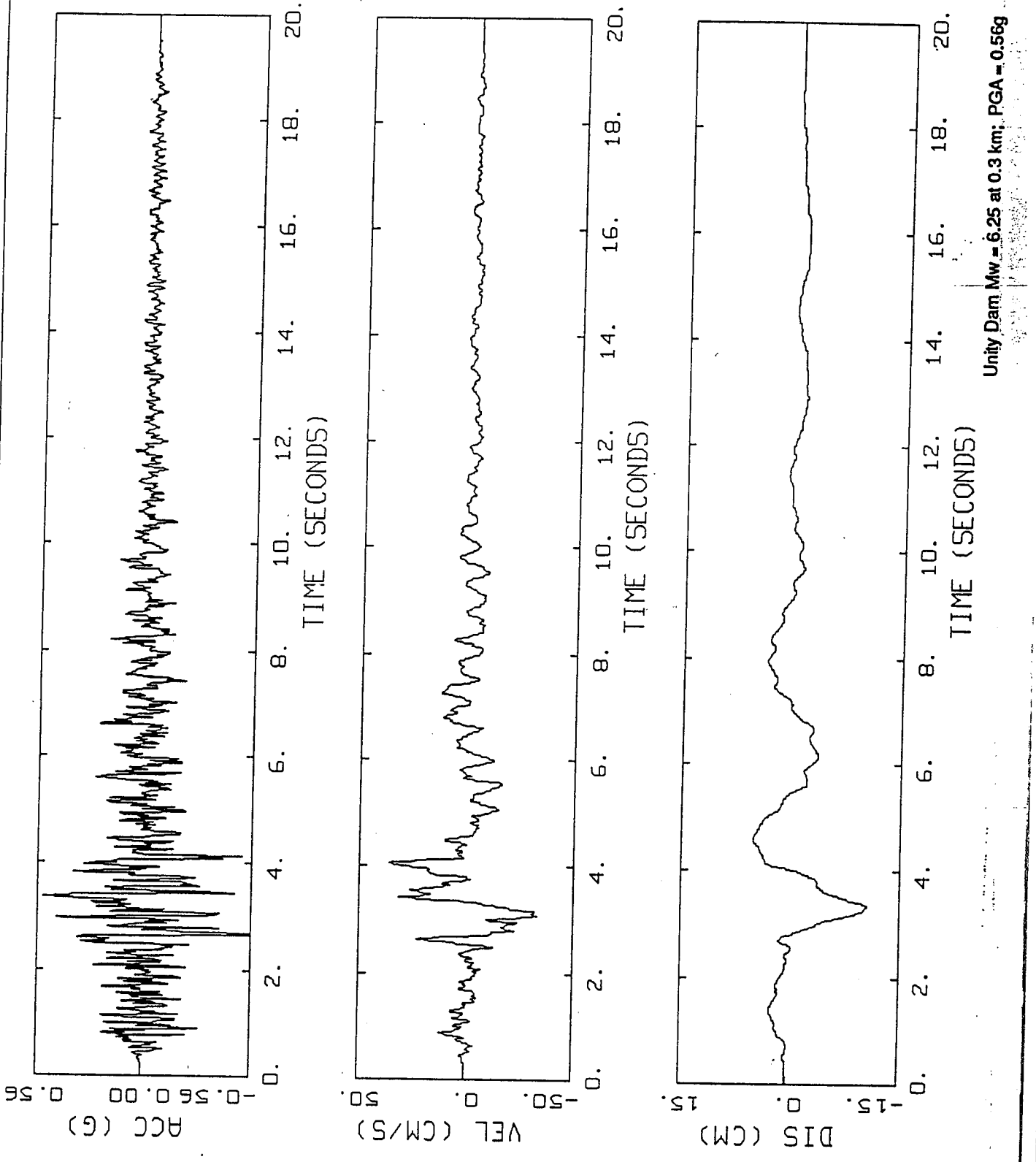

Figure 55.

SEE ACCELERATION, VELOCITY AND DISPLACEMENT TIME HISTORIES FOR UNITY DAM

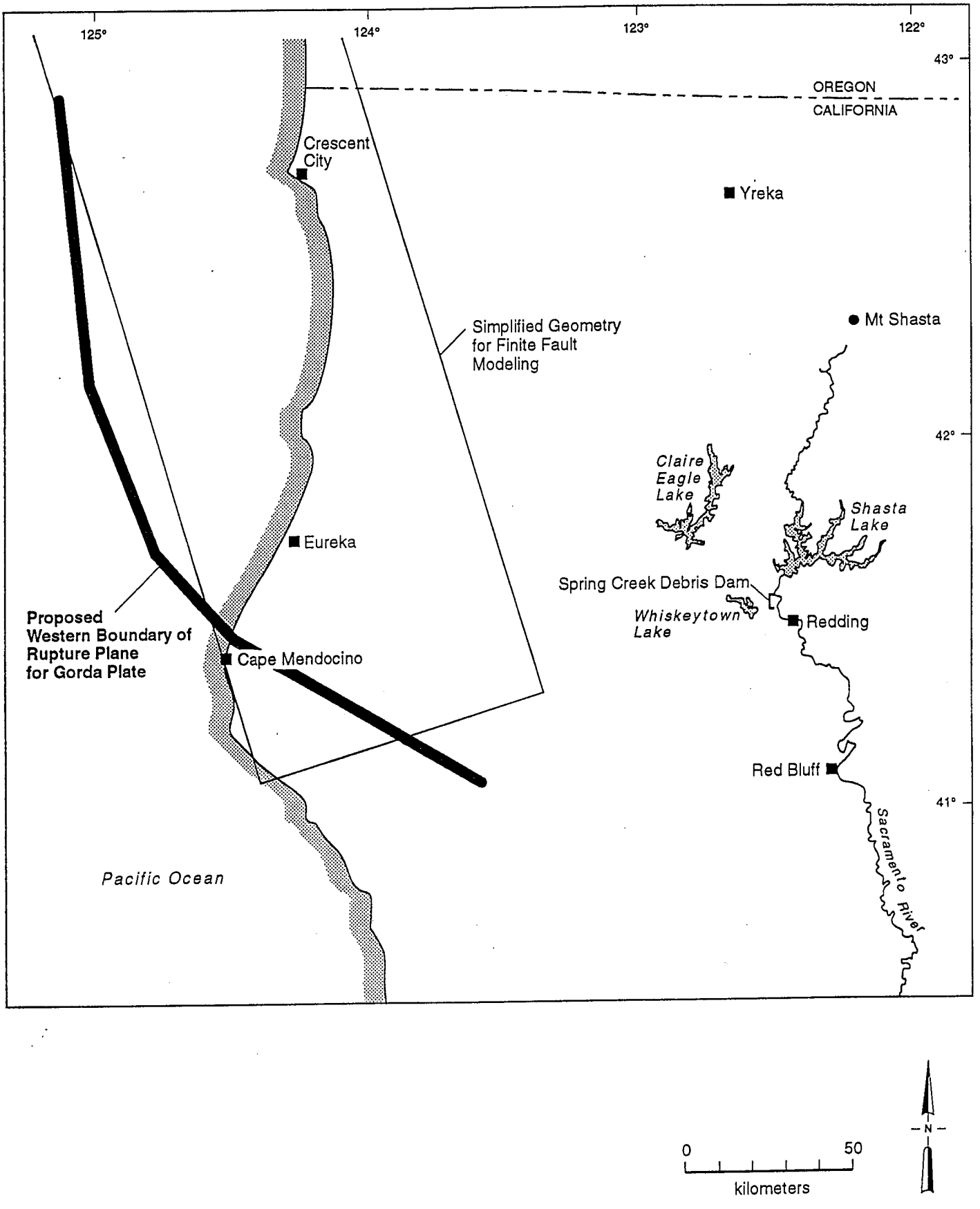

Figure 56. LOCATION MAP AND SOUTHERN CASCADIA SUBDUCTION ZONE EARTHQUAKE RUPTURE GEOMETRY

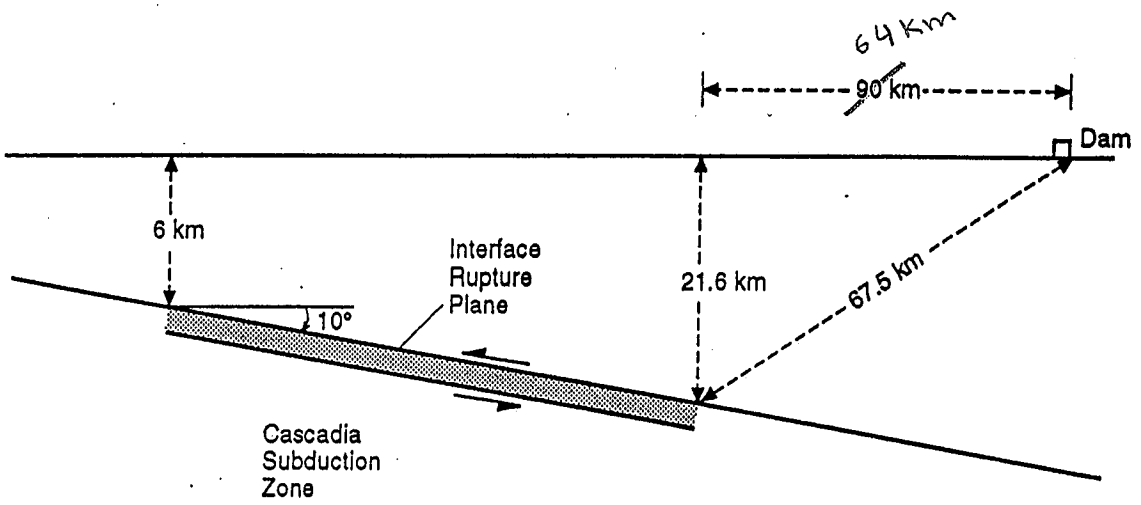

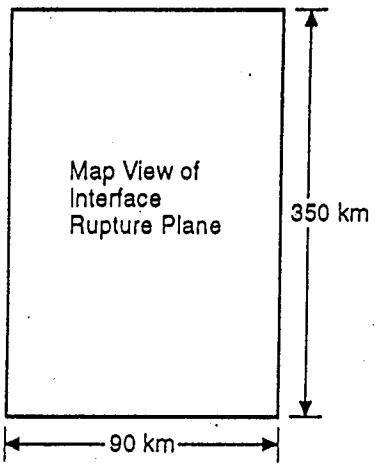

Figure 57. RUPTURE PLANE GEOMETRY FOR THE M_w 8 1/2 CASCADIA SUDDUCTION ZONE INTERFACE MCE

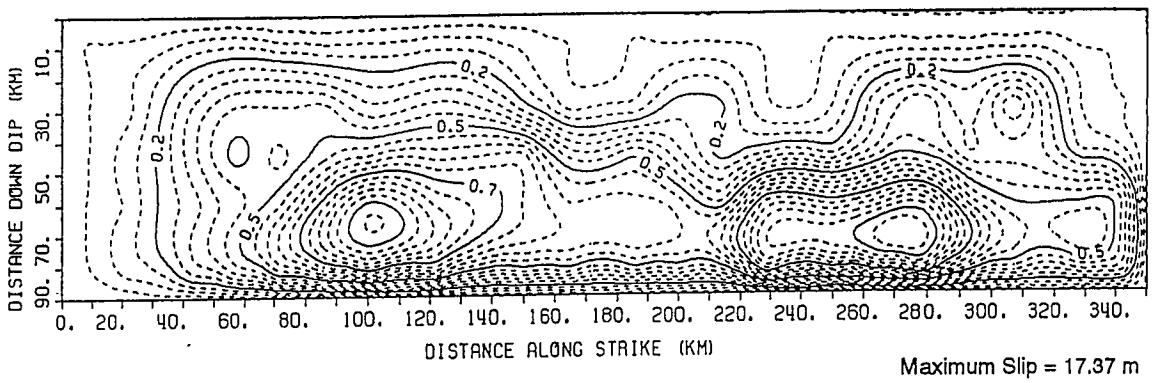

Maximum Slip = 17.37 m

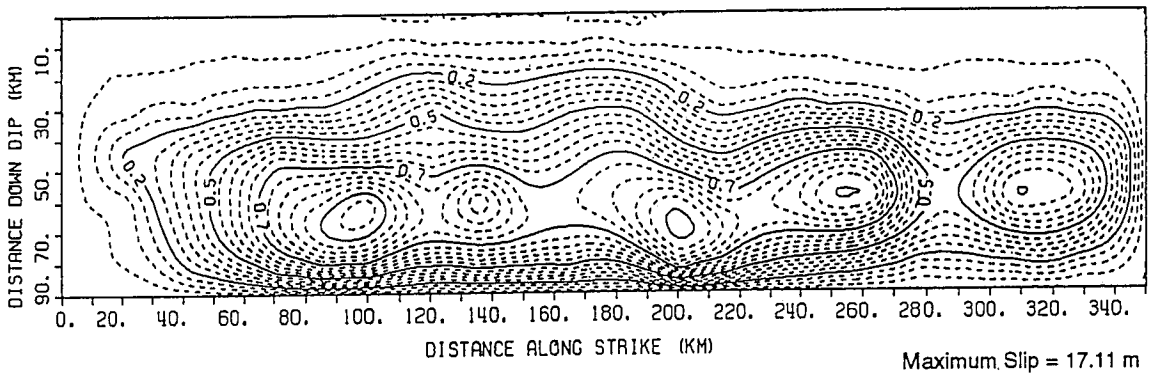

Maximum Slip = 17.11 m

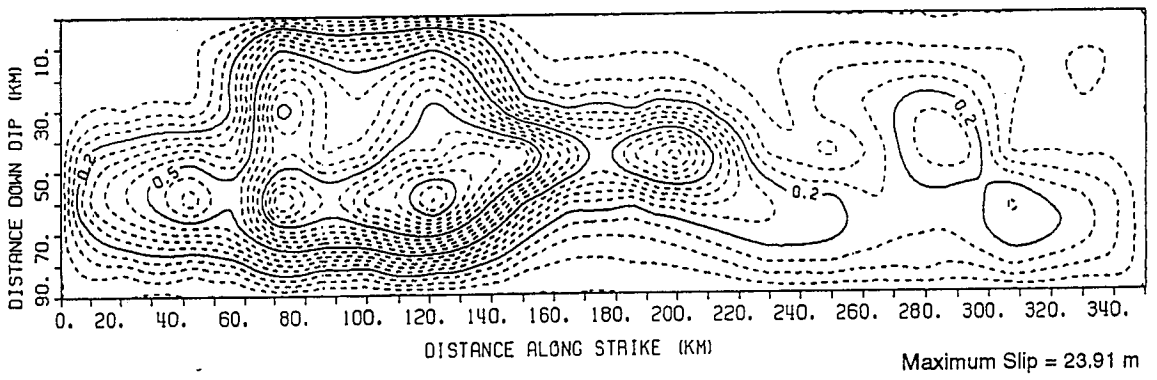

Maximum Slip = 23.91 m

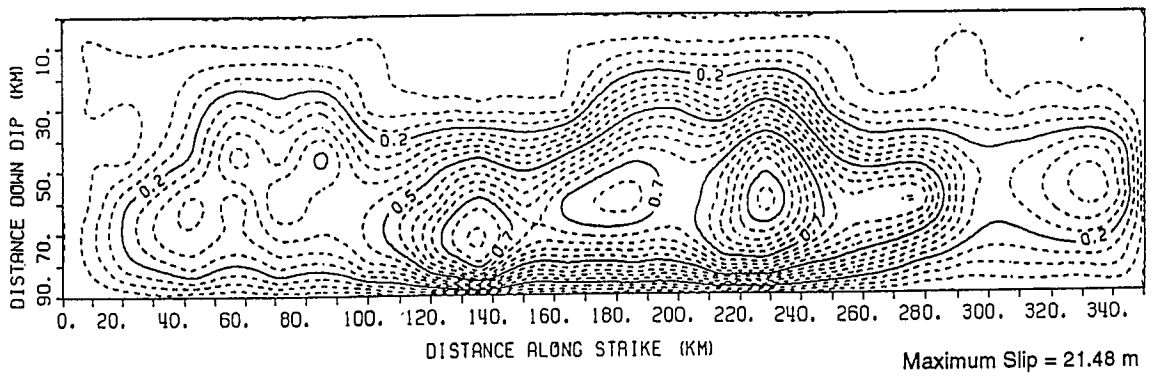

Maximum Slip = 21.48 m

Note: Slip contours are normalized to the maximum slip.

Figure 58. EXAMPLES OF SOUTHERN CASCADIA SUBDUCTION ZONE INTERFACE EARTHQUAKE RANDOMIZED SLIP MODELS

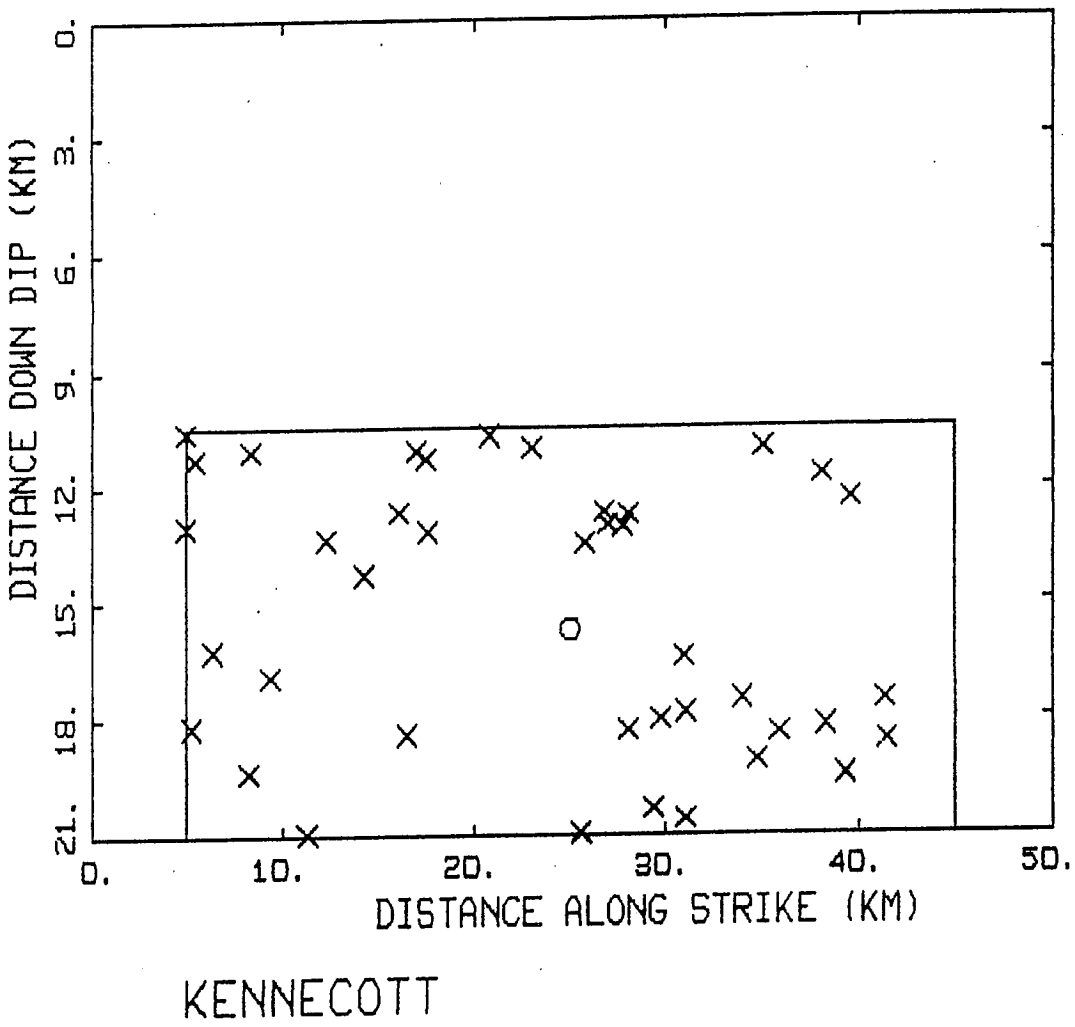
DISTANCE DOWN DIP (KM)
0.
3.
6.
9.
12.
15.
18.
21.
0.
10.
20.
30.
40.
50.
DISTANCE ALONG STRIKE (KM)
KENNECOTT
LEGEND
NUCLEATION POINTS
NUCLEATION ZONE
ACTUAL NUCLEATION POINT

Figure 59.

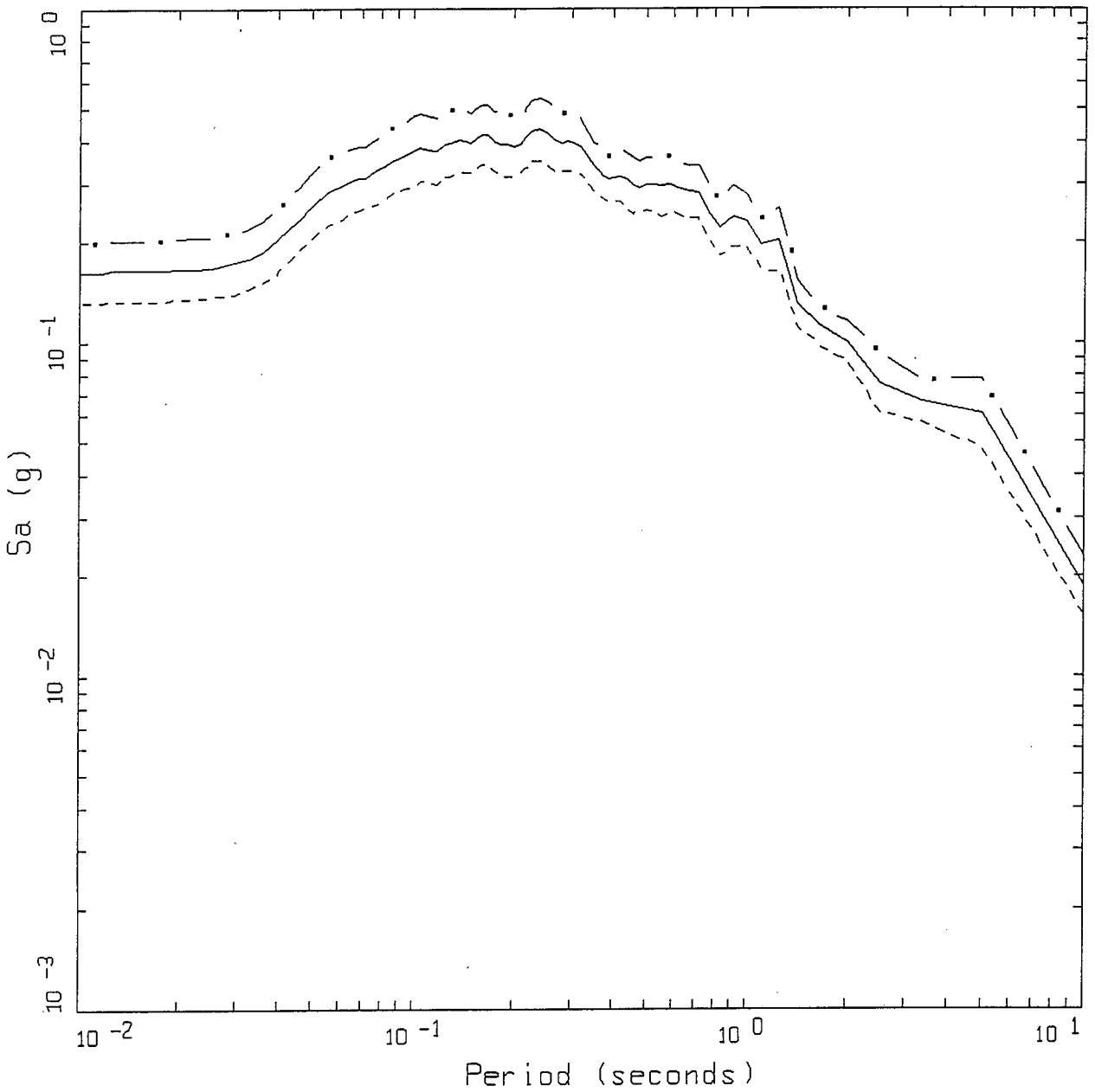

SPRING CREEK DAM, M 8.5 CASCADIA SOURCE
VARIATION OF SLIP.

LEGEND

— • — 84TH PERCENTILE; PGA = 0.199 G

——— 50TH PERCENTILE; PGA = 0.162 G

----- 16TH PERCENTILE; PGA = 0.132 G

Figure 60.

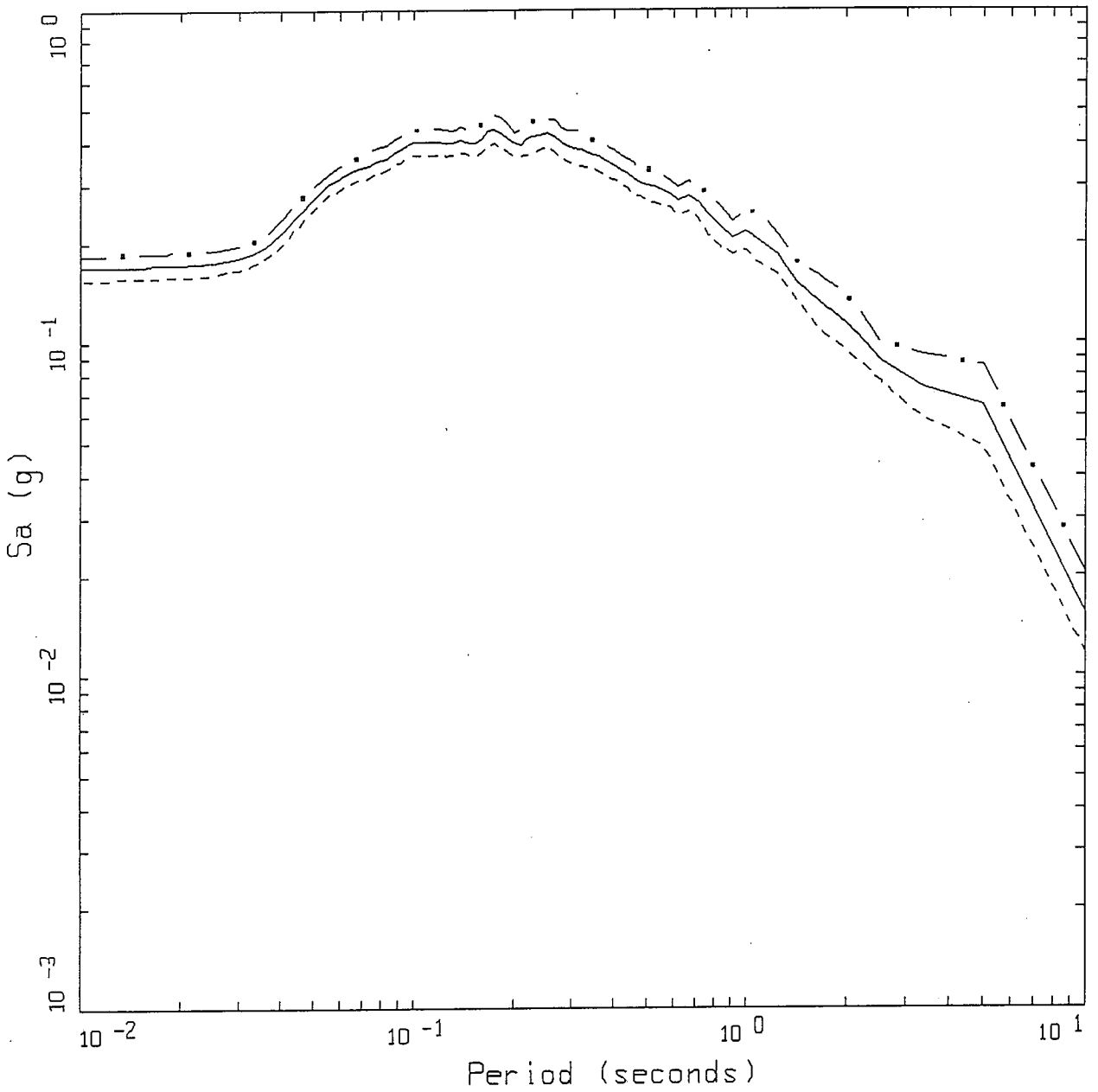

SPRING CREEK DAM, M 8.5 CASCADIA SOURCE
VARIATION OF FOCUS.

LEGEND

— • — 84TH PERCENTILE; PGA = 0.184 G

——— 50TH PERCENTILE; PGA = 0.168 G

- - - - - 16TH PERCENTILE; PGA = 0.154 G

Figure 61.

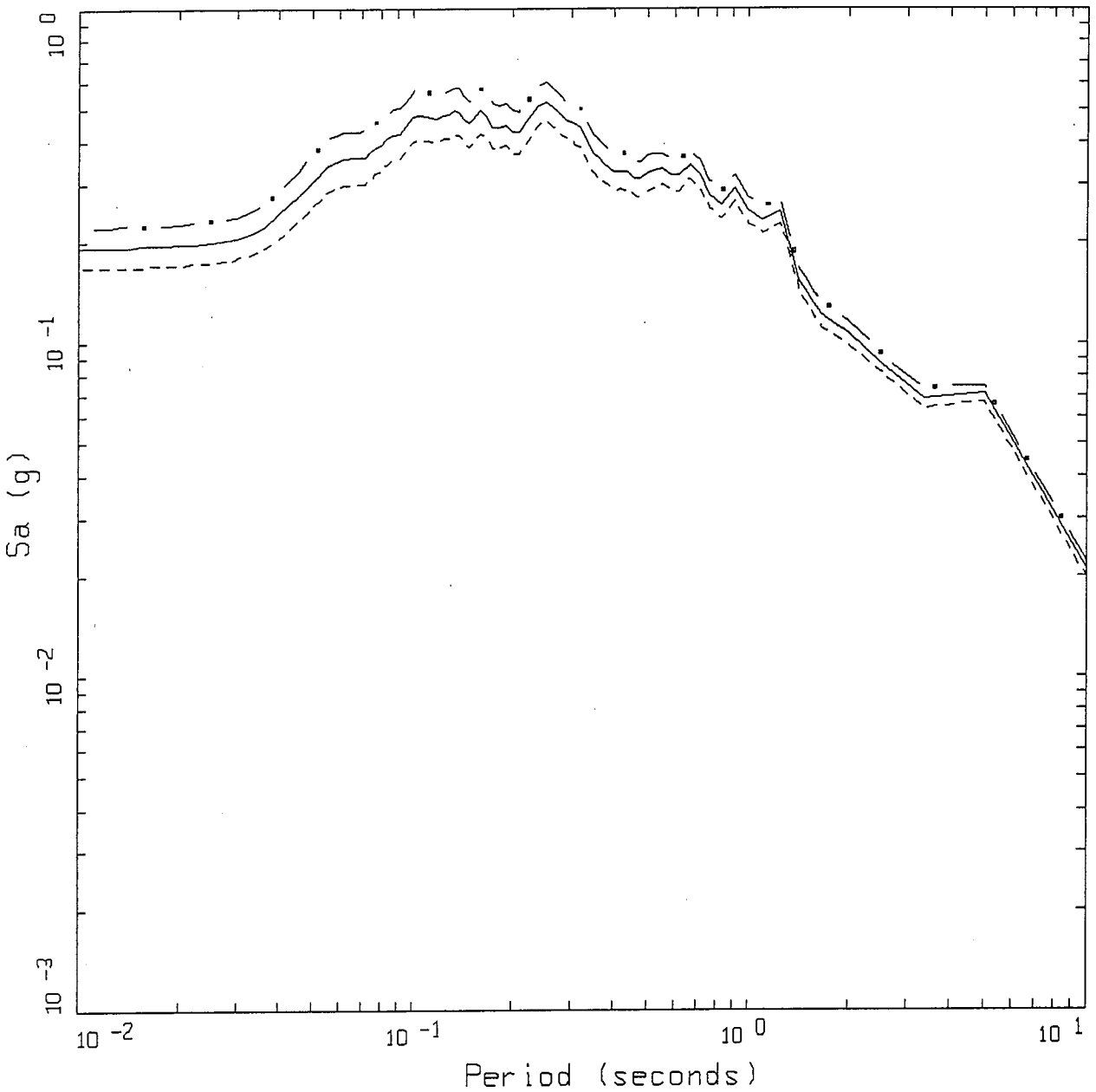

SPRING CREEK DAM, M 8.5 CASCADIA SOURCE
VARIATION OF Q.

LEGEND

— · — 84TH PERCENTILE, PARAMETRIC UNCERTAINTY; PGA = 0.220 G

——— 50TH PERCENTILE, PARAMETRIC UNCERTAINTY; PGA = 0.192 G

- - - - - 16TH PERCENTILE, PARAMETRIC UNCERTAINTY; PGA = 0.167 G

Figure 62.

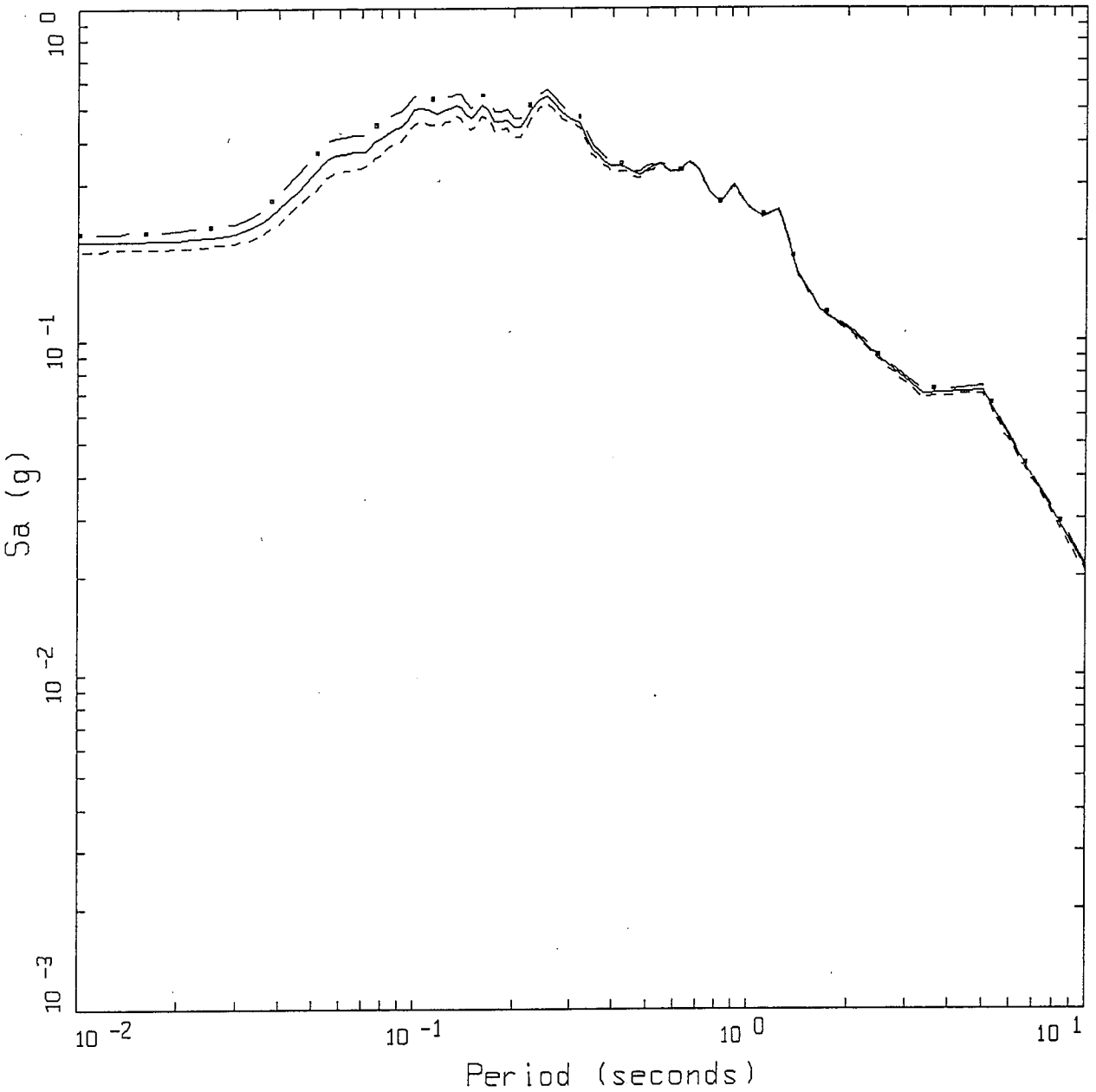

SPRING CREEK DAM, M 8.5 CASCADIA SOURCE
VARIATION OF ETA.

LEGEND

— • — 84TH PERCENTILE, PARAMETRIC UNCERTAINTY; PGA = 0.210 G

——— 50TH PERCENTILE, PARAMETRIC UNCERTAINTY; PGA = 0.198 G

- - - - - 16TH PERCENTILE, PARAMETRIC UNCERTAINTY; PGA = 0.186 G

Figure 63.

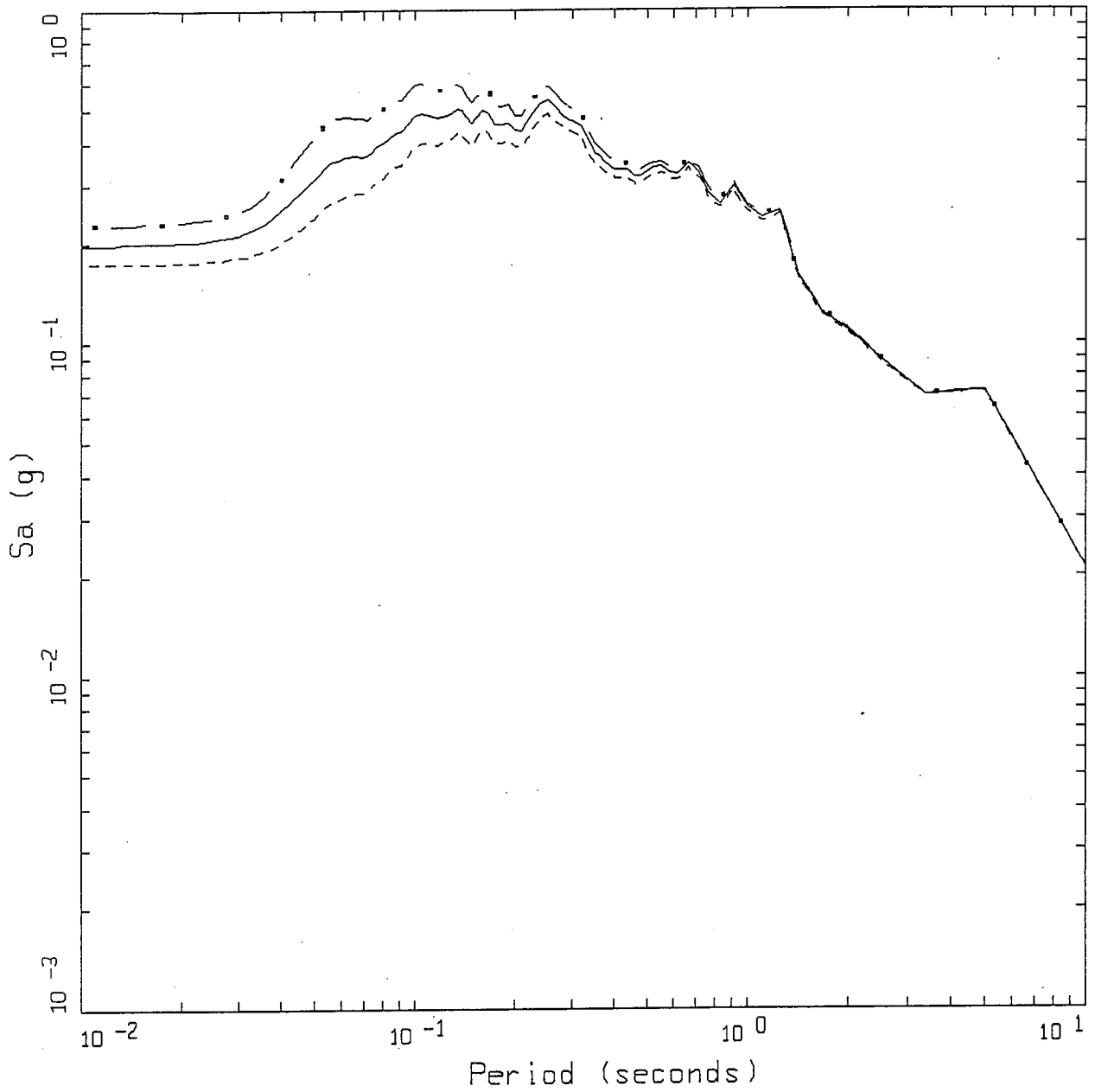

SPRING CREEK DAM, M 8.5 CASCADIA SOURCE
VARIATION OF KAPPA.

LEGEND

— • — 84TH PERCENTILE, PARAMETRIC UNCERTAINTY; PGA = 0.224 G

——— 50TH PERCENTILE, PARAMETRIC UNCERTAINTY; PGA = 0.196 G

- - - - - 16TH PERCENTILE, PARAMETRIC UNCERTAINTY; PGA = 0.172 G

Figure 64.

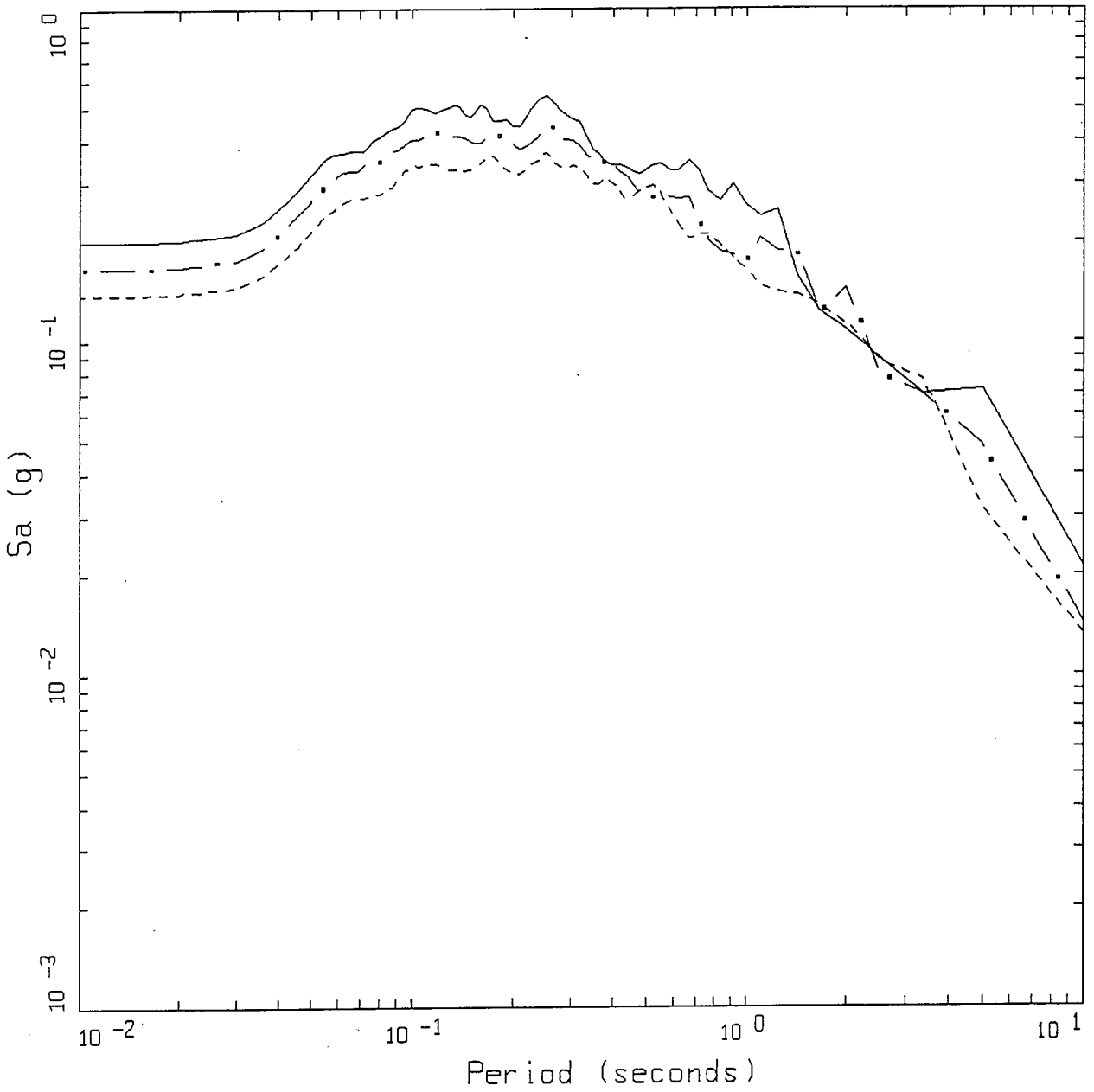

SPRING CREEK DAM, M 8.5 CASCADIA SOURCE DIRECTIVITY.

LEGEND

— • — NORTH FOCUS; PGA = 0.164 G

——— MIDDLE FOCUS; PGA = 0.196 G

- - - - - SOUTH FOCUS; PGA = 0.137 G

Figure 65.

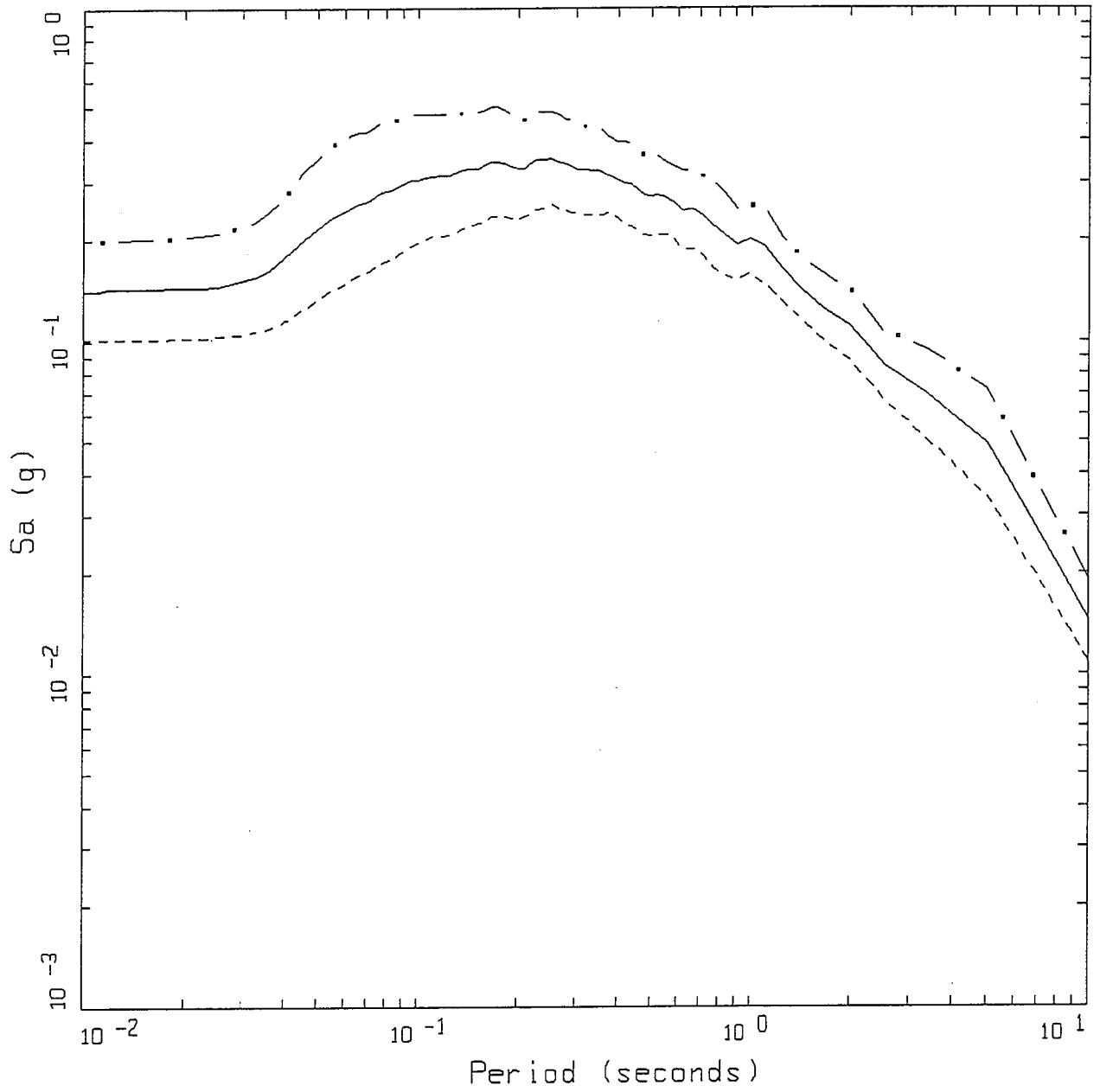

SPRING CREEK DAM, M 8.5 CASCADIA SOURCE
VARIATION OF ALL PARAMETERS.

LEGEND

—— • —— 84TH PERCENTILE, PARAMETRIC UNCERTAINTY; PGA = 0.198 G

———— 50TH PERCENTILE, PARAMETRIC UNCERTAINTY; PGA = 0.141 G

- - - - - 16TH PERCENTILE, PARAMETRIC UNCERTAINTY; PGA = 0.101 G

Figure 66.

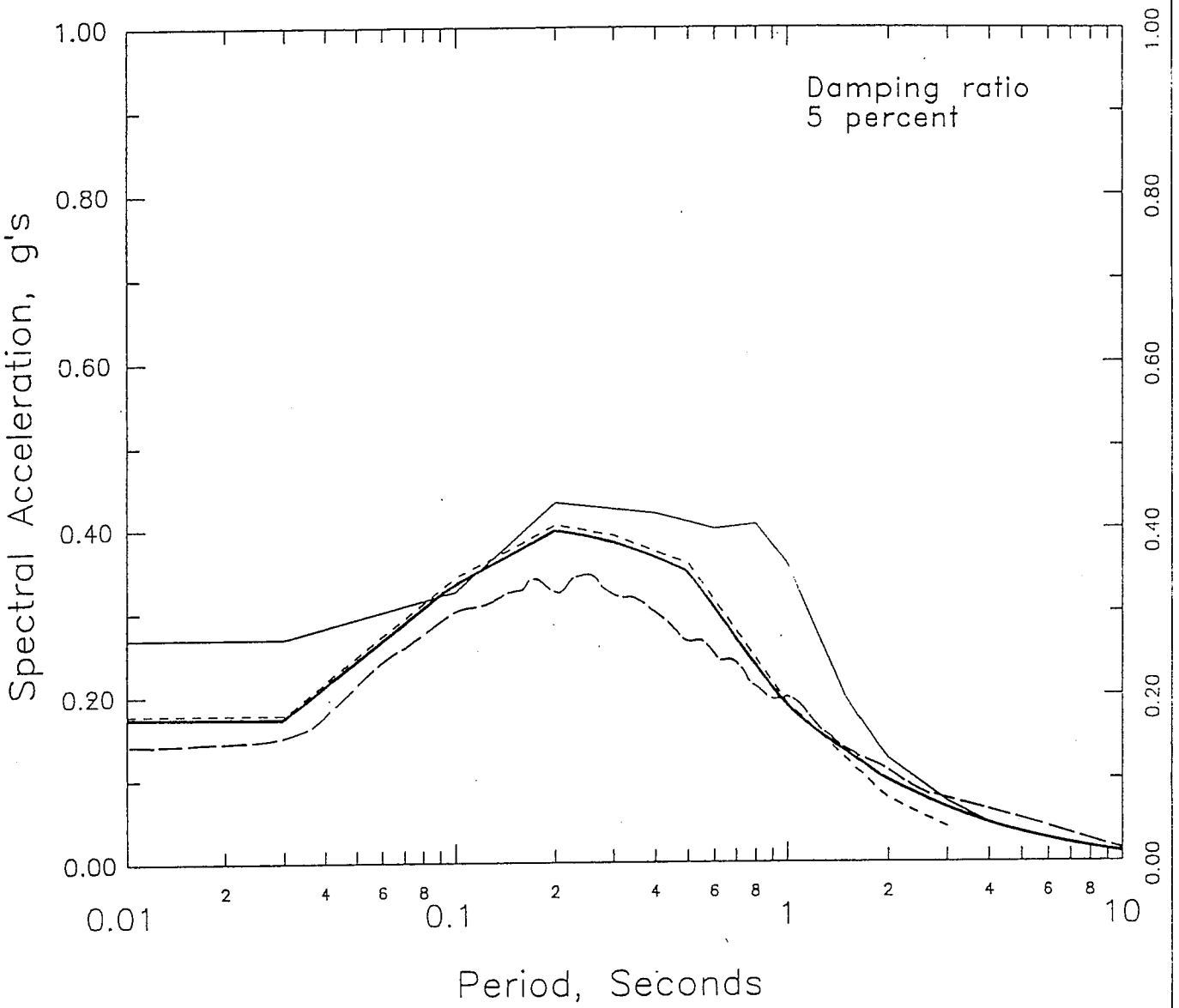

LEGEND

——— Crouse, 1991

------- Youngs et al., 1988

— — — Stochastic

——— Recommended SEE

Figure 67. COMPARISON OF EMPIRICAL AND BLWN-RVT MEDIAN RESPONSE SPECTRA AND RECOMMENDED SPECTRUM FOR THE INTERFACE EARTHQUAKE FOR SPRING CREEK DEBRIS DAM

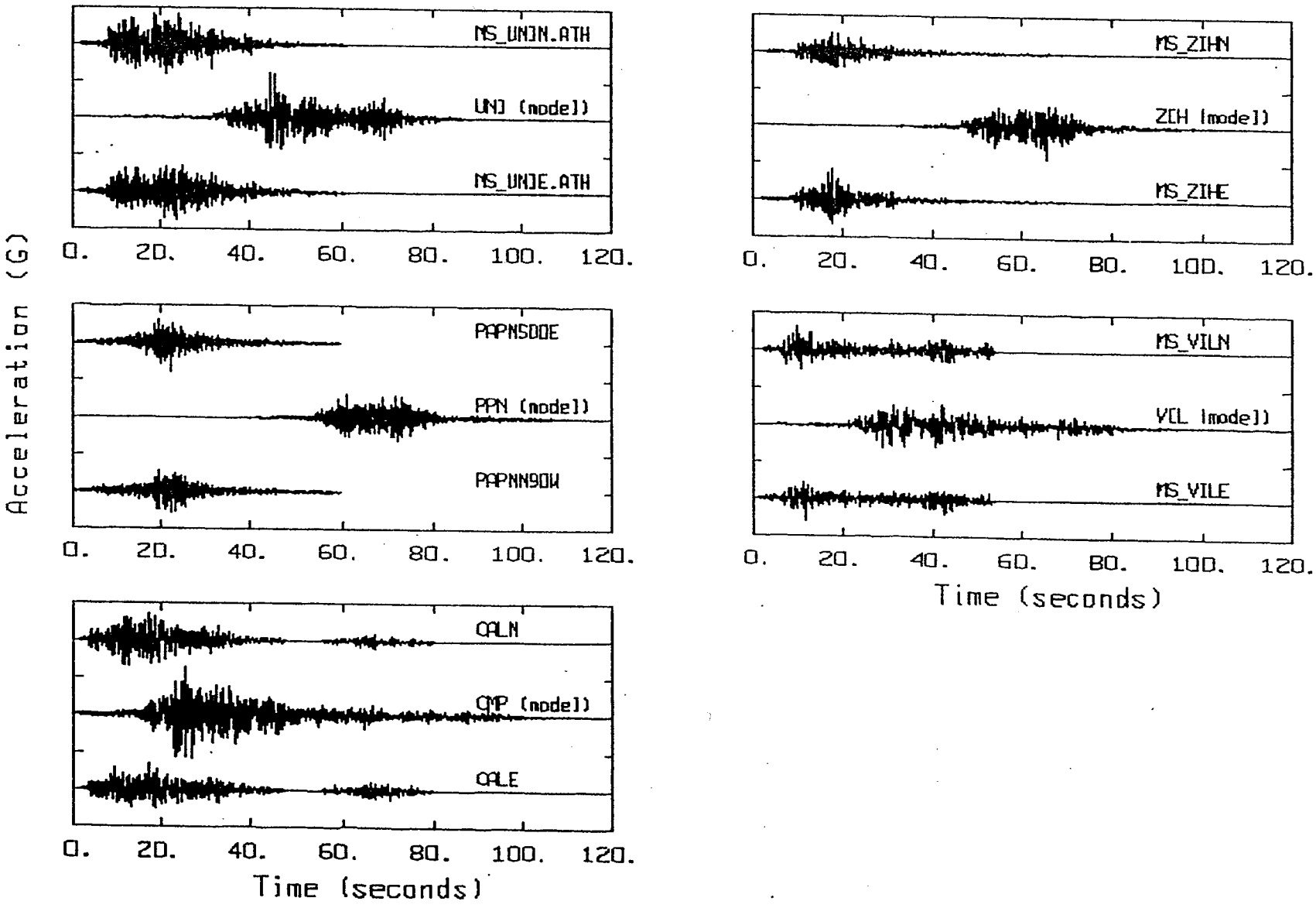
MS_UNIN.ATH
UNI (mode))
MS_UNIE.ATH
MS_ZIHN
ZIH (mode))
MS_ZIHE
PAPNSOOE
PPN (mode))
PAPNN9OW
MS_VILN
VIL (mode))
MS_VILE
CALN
CMP (mode))
CALE
0. 20. 40. 60. 80. 100. 120.
Acceleration (G)
Time (seconds)
MICHOACAN EARTHQUAKE

Figure 68.

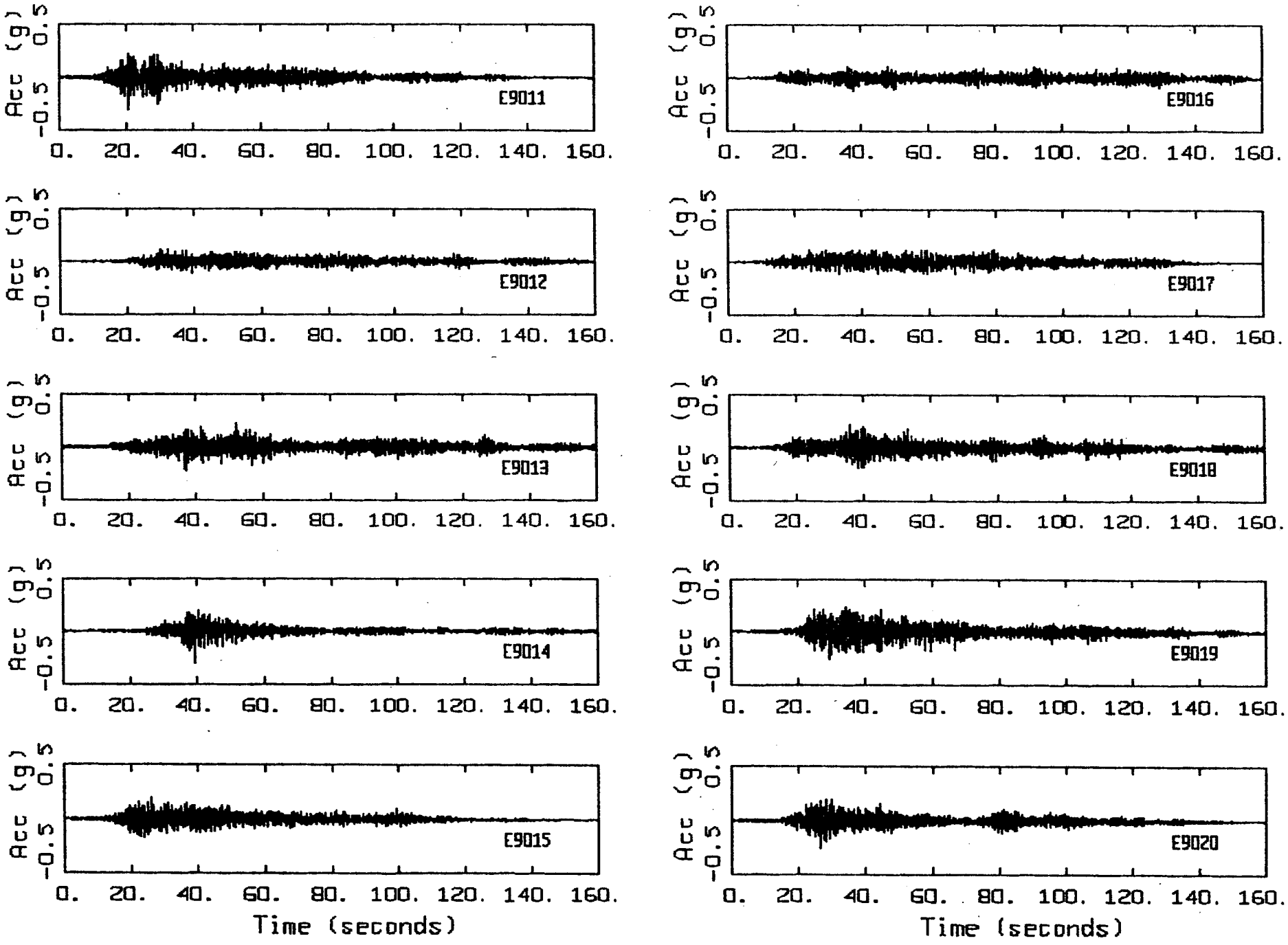

Figure 69. USGSREI, M 8.5, ROCK, LIMB E9, D=50km

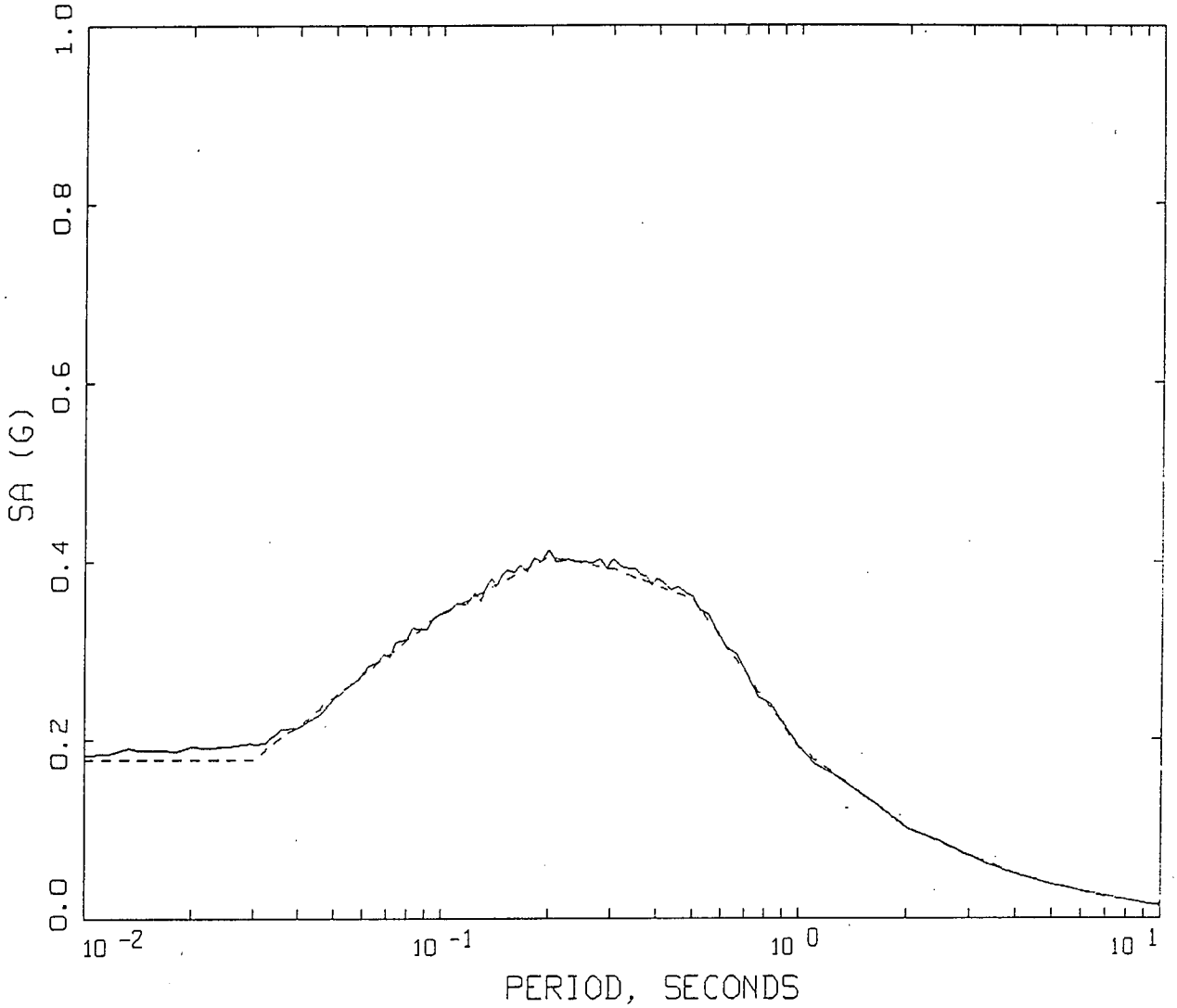

LEGEND

------ 5% Target Spectrum

——— 5% Spectrum of Synthetic Seismogram

Figure 70.	SPECTRAL MATCH FOR CASCADIA SUBDUCTION ZONE INTERFACE EARTHQUAKE RESPONSE SPECTRUM	

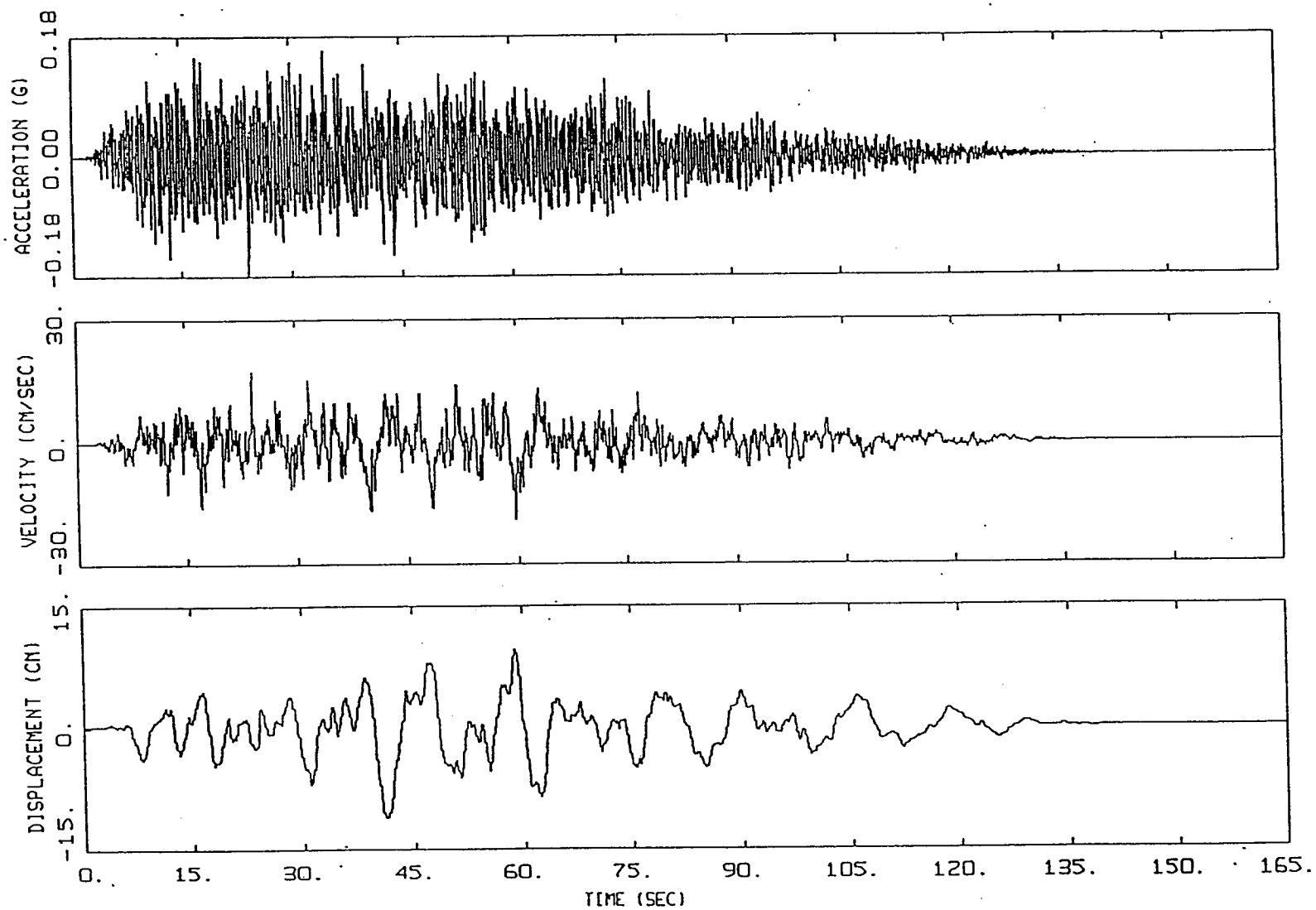

Figure 71. CASCADIA SUBDUCTION ZONE INTERFACE EARTHQUAKE HORIZONTAL TIME HISTORIES

Evaluation and Implementation of an Improved Methodology for Earthquake Ground Response Analysis

Uniform Treatment of Source, Path and Site Effects

Seminar 3

(8/4/94, 51 p.)

Instrumentation and Data Processing

a) General References
b) Review: Approaches to Specify Strong Ground Motions
c) Introductory Comments
d) The Seismograph
e) System Function
f) Filters
g) Noise

CALTRANS

SEMINAR ON STRONG GROUND MOTION

Seminar 3; August 4, 1994

Instrumentation and Data Processing

a) General References:

1980 Aki and Richards: Quantative Seismology. W. H. Freeman and Co.

1971 Bollinger: Blast Vibration Analysis. Southern Illinois University Press.

1979 Hudson, D.E. (1979). Reading and Interpreting Strong Motion Accelerograms. EERI.

1959 Brune, J. N. and J. Oliver. The Seismic Noise of the Earth's Surface. *Bull. Seism. Soc. Am.*, 49(4), 349-353.

1990 Gurrola et al.: Analysis of High Frequency Seismic Noise... SSA., pp 951-970.

1983 Hodder: Computer Processing of New Zealand Strong Motion Accelerograms. *Bull. New Zealand Nat. Soc. for Earthq. Engin.*, 16(3).

b) Review: Approaches To Specify Strong Ground Motions

1) Empirical: Functional form

$$\text{amplitude} = c_1 + c_2 M + c_3 \ln(D + c_4 e^{c_5 M}) + c_6 D + c_7 S + \ldots + c_8 m$$

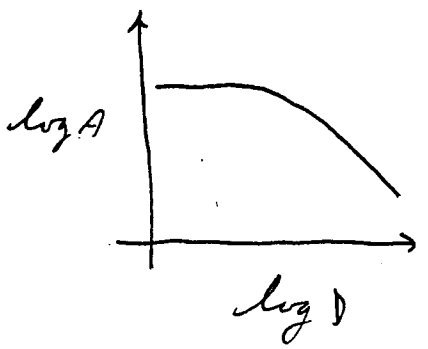

S: site switch

m: mechanism switch.

Advantages: constrained by data

Disadvantages: constrained by data

(unconstrained for **M**, R pairs with few recordings).

2) Statistical: choose recordings with similar **M**, R, and site conditions, scale to design **M** and R, compute fractiles.

Similar advantages/disadvantages as empirical plus scaling.

3) Numerical Modeling: uses a simple (point) or complicated (finite) representation of the source coupled to path and site models (path and/or site components could be empirical).

Advantages: can, in principle be used where data are sparse

Disadvantages: a) must show the model works but need data to do so, b) must evaluate model parameters:

Point: source depth, $\Delta\sigma$, Q(f), A(f), κ

Finite: slip model, hypocenter, mechanism, Q(f), A(f), κ

4) Combined Approach: using both empirical and well calibrated modeling to develop design ground motions where data are sparse.

c) Introductory Comments

Strong motion instrumentation has a long history. Figure 1 shows what is probably the first "strong motion" instrument dating back to 136 A.D. It was developed by a Chinese philosopher/scientist and is most properly termed a seismoscope. It registers the direction of the earthquake by actuating a pendulum which caused a ball to drop from the dragon's mouth into the frog's mouth. The azimuth of the source lies opposite the frog. Around 1800 years later (the repeat time of some major earthquakes, e.g. a **M** 7.5 earthquake on a blind thrust beneath Los Angeles is about 3,000 years (SCEC, 1994)) we have the modern digital accelerograph (Figure 2). The purpose of an accelerograph is to provide an accurate record of ground acceleration in three dimensions. This implies a number of steps or components:

1) Sensor which translates ground acceleration in three original directions into signals (voltage) in a non-distorted manner,

2) Trigger to begin recording (0.01g, 100m sec start up time),

3) An accurate clock for timing,

4) Digitizer to convert sensor analogue signal to digital data (min 12 bit, 66 db)

5) Recording system to store several events at high sample rates (100-200 SPS) and of sufficient duration (10-60 sec),

6) Power supply for each component,

7) Operate unattended and over a temperature range of about 0-50° c,

8) Be reliable, small, compact, and inexpensive.

These are all severe demands on instrumentation and, as we'll see, the modern accelerograph is a very remarkable instrument.

d) The Seismograph

In general, a seismograph is a device to detect and record earth motions. The following are some vibrating systems which might be candidates.

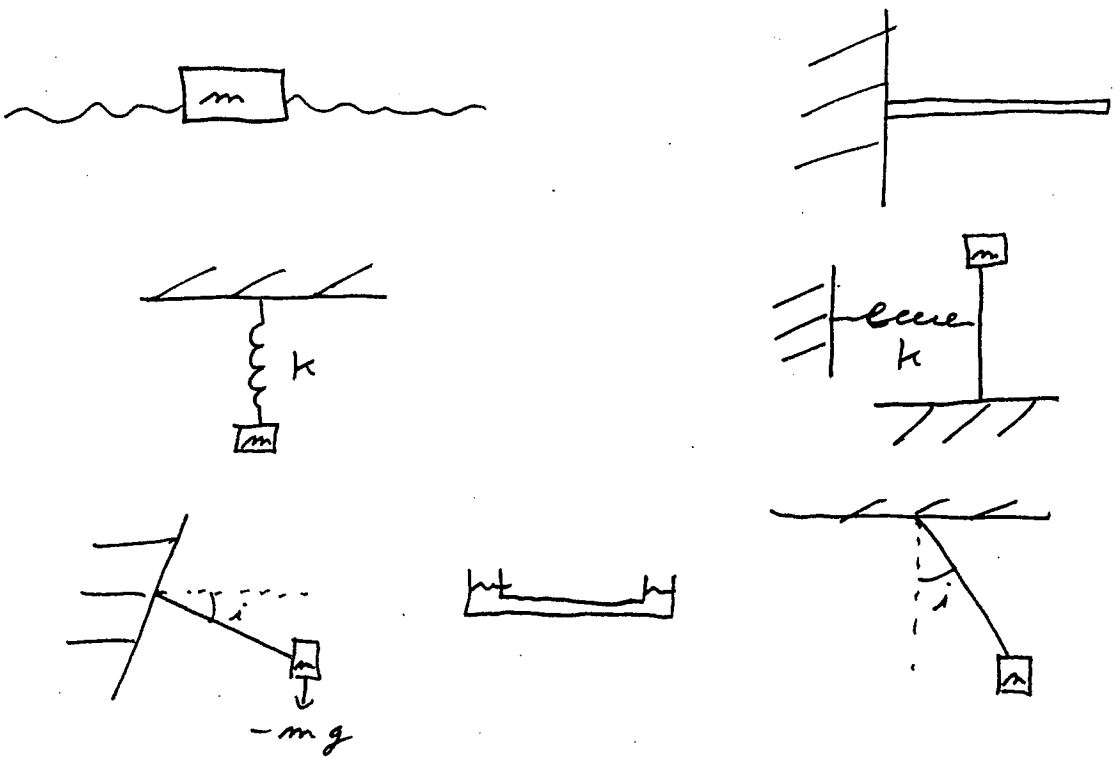

A seismoscope is a device to detect and record earth motions without time (particle motions).

1) System requirements

a) Dynamic range: $db = 20 \log \frac{A}{A_o}$. The range between the largest signal (A) and smallest (A_0). For an accelerograph considering peak acceleration, a nominal maximum could be 2g and background noise at 10 Hz at an average site might be 10^{-6} g. Then

$$db = 20 \log \frac{2}{10^{-6}} = 126$$

or over 6 orders of magnitude. This is an enormous range and is generally not met by recording systems as it implies nearly 24 bit sampling (20 log $2^{\text{bits}-1}$ = db).

b) Bandwidth: Range in frequency between lowest and highest frequencies of interest. For strong ground motions, we are generally interested in about 0.05 Hz (20 sec) to about 100 Hz. To prevent aliasing the analogue signal should extend up to about 200 Hz.

c) System Linearity: System response must be independent of the level of input motion (126 db, over 6 orders of magnitude).

d) Stability and Time Invariance: This generally refers to a very low drift rate.

e) Sensitivity: Adequate amplification with low noise in the frequency range of interest: 10^6 for sensitive seismograph to about 1-10 for strong motion accelerograph.

f) Degrees of Freedom: Generally 1 with minimum cross axis sensitivity (< 1%).

g) Time Accuracy: Within about 0.1 sec UTC.

2) Fundamental Problems

a) Linearity; physical systems are inherently nonlinear

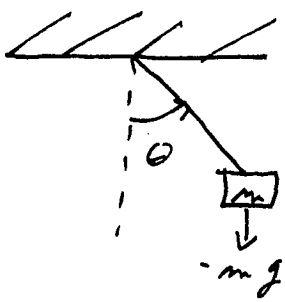

$$\tau = mgl \sin\theta$$

$$\approx mgl\left(\theta - \frac{\theta^3}{3} + \ldots+\right)$$

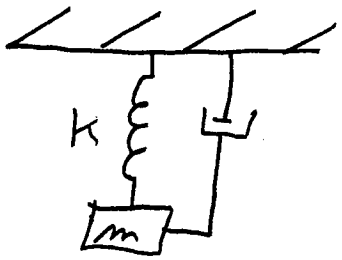

$$F = \kappa x$$

$$\approx \kappa(x + a\,x^2\,D + \ldots+)$$

and creep $\dot{X} = \frac{F}{\eta}$ (viscosity)

b) Parasitic Vibrations: Associated with higher modes of the system. Generally unavoidable, engineer then out of the bandwidth of interest.

c) External magnetic and electric fields introduce noise and drift into electromagnetic systems.

d) Recording systems: Required to produce distortion free recording or perturb the sensor signal in a predictable way (later apply correction).

3) Seismometer Design: 2 basic types

a) Inertial: Senses motion in a mechanical system due to earth acceleration. Generally a mass-spring or pendulous system. Resolution is about 1 Å.

b) Strain: Senses length change over some baseline using quartz rod and capacitors or light (laser) over m's to km's. Resolution is about 1-10 Å.

4) Sensing Devices

a) Mechanical: lever system to mechanically amplify ground motion of inertial reference mass and frame (ground); Wiechert at U.C. Berkeley.

b) Optical: minor rotated by relative motion on a pendulum boom; Wood-Anderson.

c) Electrical: device to convert relative motion between frame (ground) and inertial reference to electrical signal. Two basic types:

1) Velocity transducer: output directly proportional to relative velocity of moving mass; moving coil in magnetic field (self powered),

2) Displacement transducer: output directly proportional to relative displacement. Typical accelerometer: force balance

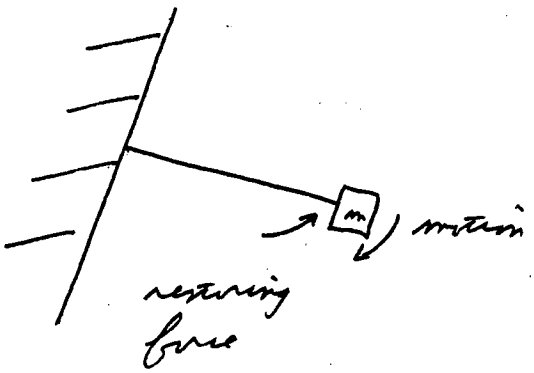

5) Amplifiers: Amplify sensor signal in db range from 0 to about 120 (120 db is a gain of 10^6 or 1 million). Since signals from sensors can be small, about 2.5 μv from a accelerometer sensing earth noise, amplifier noise must be below this level. Typical values are about 1 μv over the frequency range of interest (0.05-200 Hz). Noise levels increase with increasing bandwidth.

6) Recorders: Record amplified signal with a wide dynamic range and bandwidth

a) Analogue

1) film 40 db

2) tape 46 db

b) Digital

1) 12 bit 66 db

2) 16 bit 90 db

e) **System Function:**

1) Displacement Transducer

Simple harmonic oscillator (Damped)

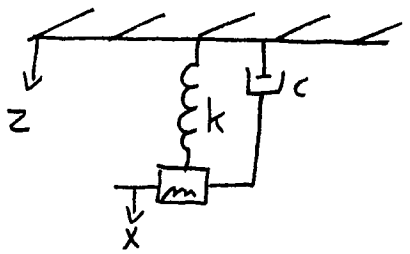

z = absolute motion of earth

x = absolute motion of mass

y = x - z relative motion of mass

$$m\ddot{x} + c\dot{y} + \kappa y = 0$$

$$\ddot{x} = \ddot{y} + \ddot{z}$$

$$\ddot{y} + 2\eta\ \omega_s\ \dot{y} + \omega_s^2\ y = -\ \ddot{z}$$

where y is the record amplitude, $\ddot{z}$ is ground acceleration, and ω_s is the sensor natural frequency. Taking Fourier transforms, rearranging, and taking modulus (neglecting 2 π factors)

$$\tilde{y}(f_e) = \frac{f_e^2}{[(f_s^2 - f_e^2)^2 + (2\eta\ f_s\ f_e)^2]^{1/2}}\ (-\ \tilde{z}\ (f_e))$$

where f_e is the earth or ground frequency.

The system magnification is defined as

$$M = \frac{record\ amplitude}{ground\ displacement} = \frac{|Y|}{|Z|}$$

$$= \frac{f_e^2}{[(f_s^2 - f_e^2)^2 + (2\eta\ f_s\ f_e)^2]^{1/2}}$$

Assumptions:

1) Displacement transducer; force = κy, y relative displacement,

2) Ignored any gain in transducer.

The velocity sensitivity is defined as

$$V.\ S. = \frac{record\ amplitude}{ground\ velocity} = \frac{|Y|}{\omega_e\ |Z|}$$

$$= \frac{f_e}{[(f_s^2 - f_e^2)^2 + (2\eta\ f_s\ f_e)^2]^{1/2}} \quad (neglecting\ 2\pi)$$

and the acceleration sensitivity is given by

$$A.\ S. = \frac{record\ amplitude}{ground\ acceleration} = \frac{|Y|}{\omega_e^2\ |Z|}$$

$$= \frac{1}{[(f_s^2 - f_e^2)^2 + (2\eta\ f_s\ f_e)^2]^{1/2}} \quad (neglecting\ 2\pi)$$

Look closely at magnification:

$$M = \frac{f_e^2}{[(f_s^2 - f_e^2)^2 + (2\eta\ f_s\ f_e)^2]^{1/2}}$$

$$= \frac{|Y|}{|Z|}$$

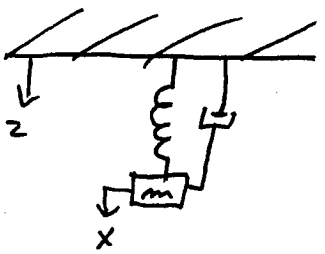

$Y = X - Z$

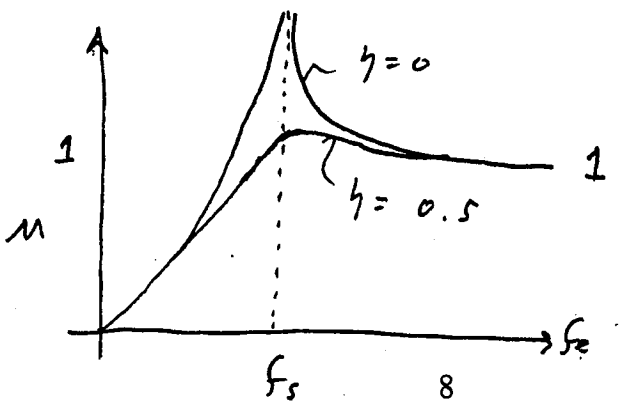

Region 1: f_e near zero

$\mathbf{M} \approx 0$, move z (frame) very slowly, mass rides with frame ($y = x - z \approx 0$, no relative displacement).

Region 2: f_e near f_s

M large, move z at resonant frequency. For low damping amplitude (**M**) becomes very large.

Region 3: $f_e >> f_s$

$\mathbf{M} \approx 1$, move z very rapidly, m (mass) cannot respond and $x = 0$.

Basically we can design an instrument (sensor) to meet our needs by specifying damping (η) and corner frequency (inverse of free period). To see the shapes of **M**, VS, and AS more easily, it is convenient to use log-log axes (powers in f_e are simply straight lines) and work with asymptotes. Also differentiation and integration (times ω or ω^{-1}) are simple slope changes:

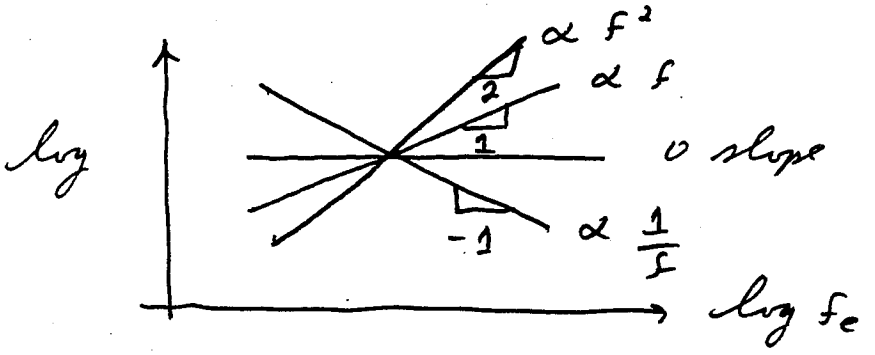

Useful relations $\quad db = 20 \log \frac{A}{A_0}$

slope 1 = 6 db/octave = 20 db/decade

2 = 12 db/octave = 40 db/decade

octave = factor of 2 in frequency

decade = factor of 10 in frequency

On log-log axes the magnification curve for a displacement transducer takes the form:

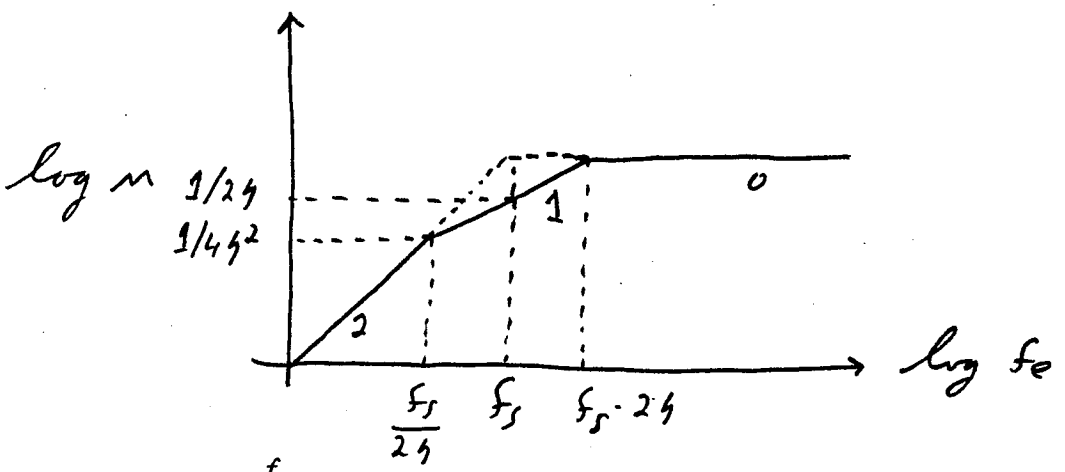

where $\frac{f_s}{2\eta} \le f_s \le f_s \cdot 2\eta$ is the transition region whose width is proportional to the damping (note region exists if $\eta > 0.5$).

If a sensor was desired to for ground displacement, we can see that for frequencies above 2η f_s, the sensor output is proportional to ground displacement (no distortion). If the interest then is displacement for frequencies exceeding about 1 Hz, an f_s of $\le$ 1 Hz would be appropriate and η should be small enough to have a small transition range but not have too much overshoot (0.6 - 0.7 is a good compromise).

Why not make f_s = 0.1 Hz with higher damping? Horizontal motion sensors tilt sensitivity is proportional to $1/f_s$ and noise (earth and instrument) are also proportional to 1/f (discussed later). By putting f_s close to 1 Hz, we can use the instrument as a natural filter: prevent long period noise from entering the output. Fundamental considerations in instrument (sensor) design: know the characteristics (approximate Fourier amplitude spectra) of the signal you are interested in measuring (recording) as well as the ambient earth and instrument noise characteristics!

The velocity sensitivity

$$V.\ S. = \frac{|Y|}{\omega_e\ |Z|}$$

on log-log axes becomes

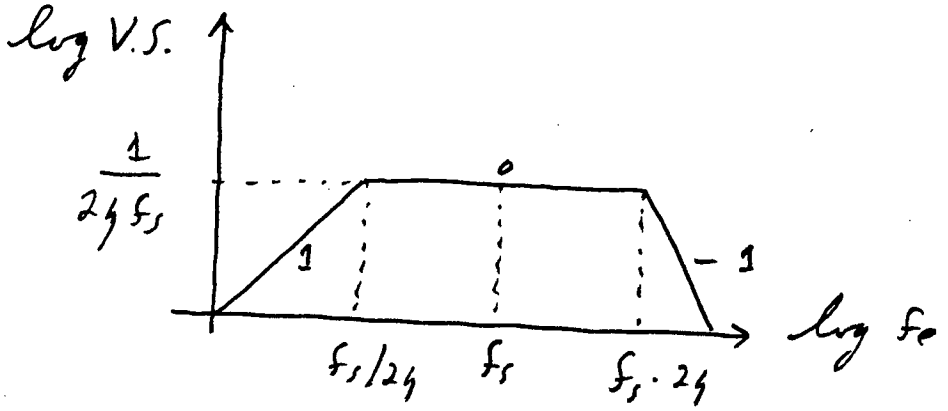

or -1 slope change from **M**

$$V.\ S. = \frac{M}{\omega_e}$$

Similarly the acceleration sensitivity

$$A.\ S. = \frac{|Y|}{\omega_e^2\ |Z|} = \frac{V.\ S.}{\omega_e} = \frac{M}{\omega_e^2}$$

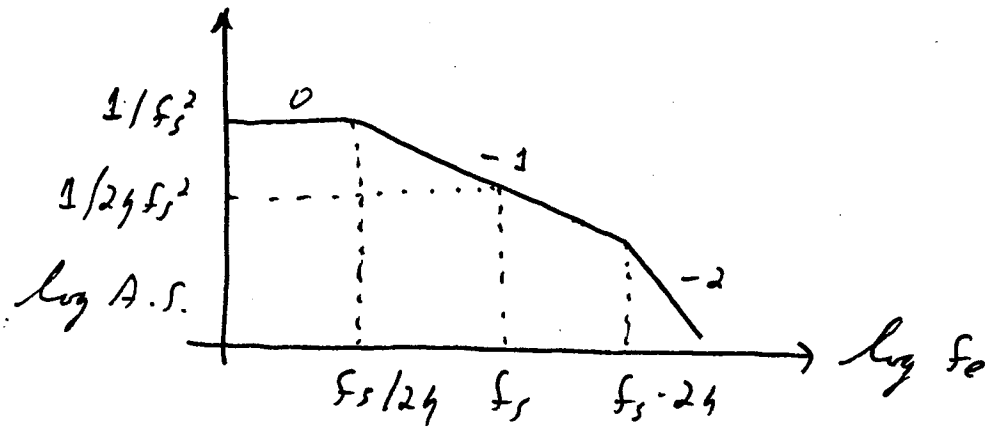

Looking at the acceleration sensitivity, the sensor is "flat" to ground acceleration from D.C. ($f_e = 0$) to about f_s. A good accelerometer then should have f_s higher than any frequency of interest (i.e. > 30 Hz). For a f_s of 50 Hz and damping of 0.7, the acceleration sensitivity is down $1/2\eta$ below the D.C. level ($1/f_s^2$) and the transition region starts at $f_s/2\eta \approx 38$ Hz. Our sensor then has an output directly proportional to ground acceleration from D.C. to about 40 Hz with a "gain" of $1/50^2 = 0.004$ output/ground acceleration. The output (relative mass displacement) for ground acceleration input ($\ddot{z}$) may be in pen deflection or in volts. An amplifier would provide any gain (amplification) desired. For a typical SMA (Strong Motion Accelerometer) the acceleration sensitivity is about 2.5 v/g with a $f_s = 25$ Hz and damping of 0.7 critical. The A.S. would look like

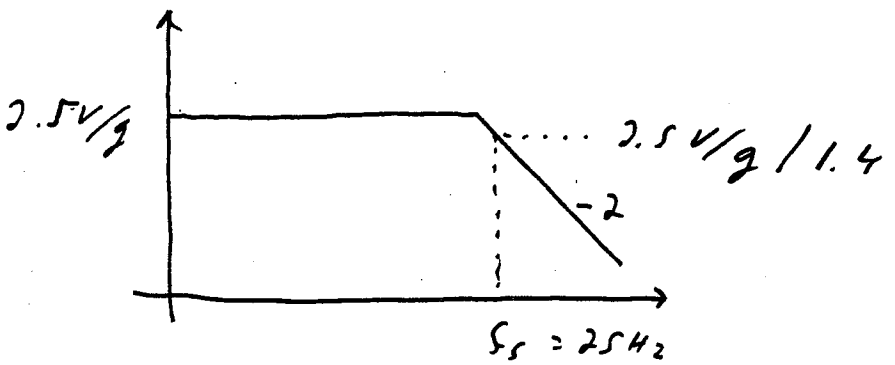

Figure 3 shows the acceleration sensitivity computed for several values of damping (0.1-0.9 critical). The value of 0.7 is a good compromise for no overshoot yet minimizing the transition band. Figure 4 shows the magnification, velocity sensitivity, and acceleration sensitivity for the same instrument. The sensor is a good displacement instrument for $f_e > f_s$, a good acceleration instrument for $f_e < f_s$, and a good velocity instrument for $f_e \approx f_s$.

2) Velocity Transducer

In the displacement transducer the record amplitude was proportional to y, the relative displacement of the mass. If a moving coil is used as a sensor

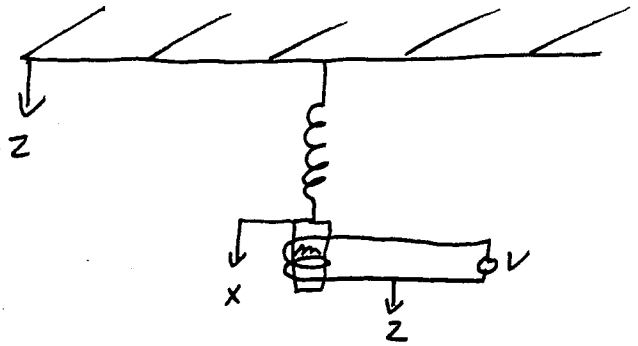

then the output (voltage) is proportional to the relative velocity $\dot{y} = \dot{x} - \dot{z}$ from Lenz's Law

$$\bar{e} = \bar{\dot{Y}} \times \bar{B}$$

$\bar{e}$: *volts/unit length*

$\bar{B}$: *magnate field flux density.*

For the velocity transducer, the magnification, velocity sensitivity, and acceleration sensitivity become

$$M_{VT} = \frac{|Y|}{|Z|} = \frac{\omega_e |Y|}{|Z|} = \omega_e M_{DT}$$

$$V.\ S._{VT} = \frac{|\dot{Y}|}{|\dot{Z}|} = \frac{|Y|}{|Z|} = M_{DT}$$

$$A.\ S._{VT} = \frac{|\dot{Y}|}{|\ddot{Z}|} = \frac{|Y|}{\omega_e |Z|} = V.\ S._{DT}$$

or graphically

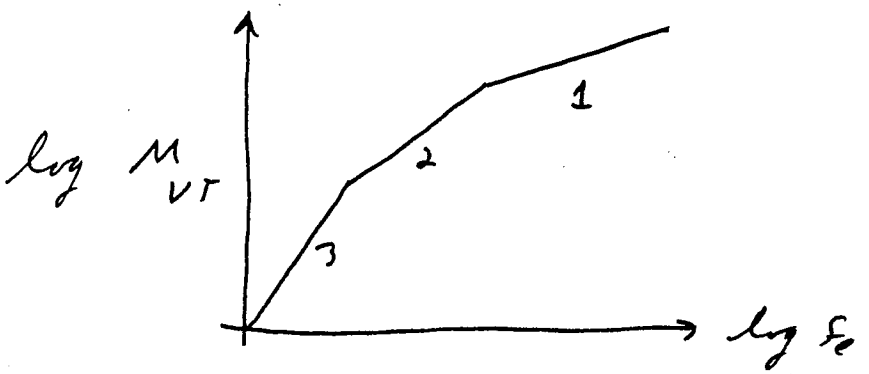

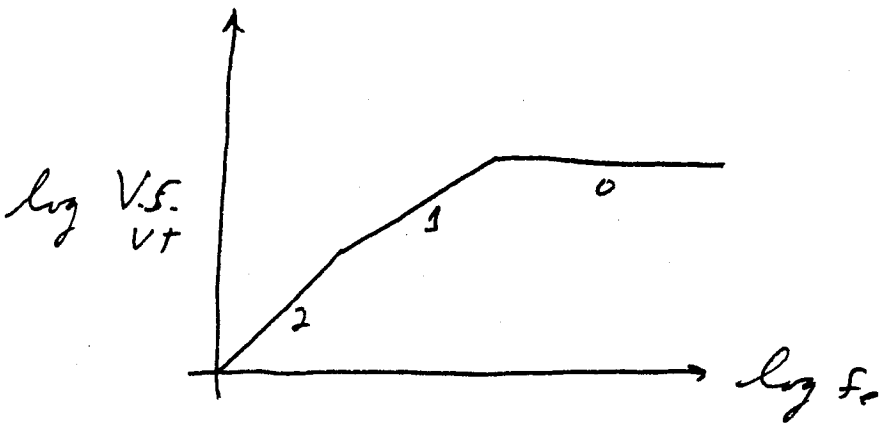

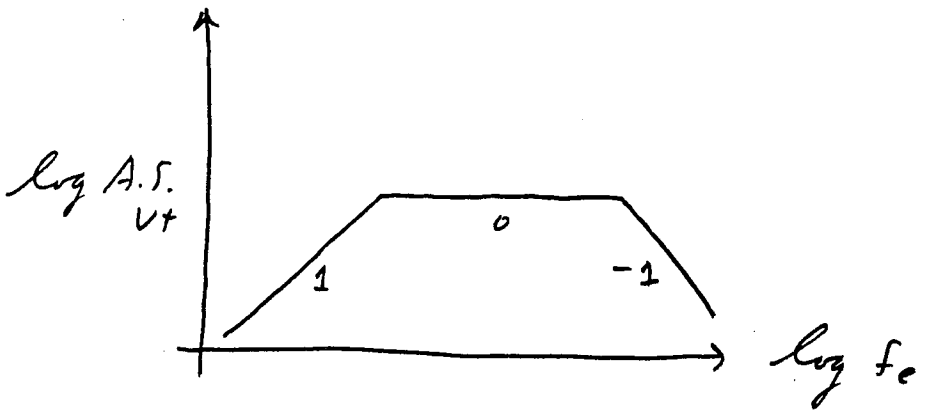

The velocity transducer is the other common instrument used in seismology and, in analogy with the displacement transducer, it is approximately flat to ground velocity (ż) for frequencies beyond the corner f_s. Figure 5 shows the magnification, velocity sensitivity, and acceleration sensitivity computed for the very popular Mark Products L4-C seismometer with a corner frequency of 1 Hz and damping of 0.7 critical. The V.S. is flat for frequencies at nearly 1 Hz and higher with a nominal output (depending an coil resistance) of about 180 V/m/sec. This sensor, and ones similar to it are used extensively in seismological studies of earthquake source, path, and site features for frequencies above about 1 Hz. For lower frequencies (< 1 Hz), the distortion introduced by the sensor must be removed; a procedure called processing in general or more specifically, performing an instrument correction. A similar exercise must be done to accelerograph data if there is interest in frequencies beyond the corner (f_s). This will be discussed in the section on data processing.

As a example of instrument design, the acceleration sensitivity of the velocity transducer shown in Figure 5 has an interesting feature. The peak which occurs at $f_e = f_s$ suggests that if the transition zone could be flattened out the sensor would be, in effect, an accelerometer over the frequency range of flat acceleration sensitivity. Recall that the 2 corners which describe the transition zone are

$$f_e = f_s/2\eta \quad , \qquad f_\eta = f_s \cdot 2\eta$$

the flat region Δf can be defined as

$$\Delta f = f_h - f_e = f_s \cdot (4\,\frac{\eta^2 - 1}{2\eta}) \quad ,$$

then for $\eta > 1$ increasing η increases Δf. If $\eta = 10$ critical then $\Delta f \approx 20$ Hz and with $f_s = 1$, the velocity transducer can be made into an accelerometer over the frequency range of about 0.05-20 Hz. The computed acceleration sensitivity for such a system is shown in Figure 6 along with the standard L4-C seismometer curves. Appendix 1 shows some specifications for 2 moving coil transducers (seismometers), a hydrophone, and a state-of-the-practice accelerograph.

f) Filters

The purpose of filters, either analogous or digital, is to shape the system response. They are used as integrators (add -N slope) or differentiators (add +N slope) as well as to eliminate or reduce unwanted signals or noise over some frequency range. In applications to strong ground motion this generally means to eliminate or reduce the amplitude of noise contamination. Apart from high frequency noise, another reason for low-pass filtering is to prevent aliasing. For sampled data with a sample interval Δt, the highest frequency represented in the data is termed the Nyquist frequency and is given by

$$f_N = 1/2\ \Delta t.$$

If analogue data are sampled or sampled data are decimated (Δt increased), all spectral components with frequencies greater than f_N must be eliminated prior to sampling (or resampling). If they are not, the energy at frequencies exceeding the Nyquist can contaminate frequencies lower than the Nyquist in the sampled data. This process is termed aliasing: higher frequency energy is aliased to lower frequencies. A good rule of thumb for anti-alias filters is to be down at least a factor of 10 at the Nyquist. For a Butterworth, this can be done by applying a 4-pole at $f_N/2$. This will result in 24 db/octave and is down 24 db at $f = f_N$.

1) Filter Theory:

One of the most common filters is termed the Butterworth filter. It is popular because it has very desirable properties, it is easy to create analogous circuits with Butterworth properties, and it is very simple in digital form. It's basic properties are that it remains very flat (maximum flat) to very near its corner frequency and it falls off fairly rapidly beyond. There is a tradeoff in filter theory between flatness (ripple free) and rate-of-fall-off: you can't be ripple free and have maximum fall-off.

For example two low-pass filters: one Butterworth and one an elliptical.

The Butterworth flat (ripple free) but falls off slower, it is simply a good compromise.

The system function for the Fourier amplitude spectrum of the Butterworth filter is

$$\frac{1}{\sqrt{1 + (\frac{f}{f_c})^{2N}}}$$ *Low Pass*

$$\frac{1}{\sqrt{1 + (\frac{f_c}{f})^{2N}}}$$ *High Pass*

where N is the order number or slope on a log-log plot. Low-pass means all frequencies less than f_c (filter corner) are passed and similarly for high-pass.

Since N (pole or order number) is a slope of N, the fall-off is N · 6 db/octave. For example, a low-pass filter with a corner frequency of 30 Hz and with N = 4 falls off at 24 db/octave. At 60 Hz then the signal amplitude would be down 24 = 20 log $\frac{A}{A_0}$ or

$\frac{A}{A_0} = 10^{-1.2} = 0.06$.

This would be a good filter to eliminate 60 Hz power line noise. Unfortunately there is signal fall-off starting from the corner frequency: down by $\frac{1}{\sqrt{2}} = -3\ db$

The Butterworth filter characteristics are:

a) Easy to apply low-, high-, and band-pass (combine low- and high-pass through multiplication)

b) down 3 db ($1/\sqrt{2}$) at corner

c) fall-off of 6 db/octave/pole.

Figure 7 shows band-pass Butterworth filters with corners at 0.1 Hz (high-pass) and 50 Hz (low-pass) for orders 2, 4, and 6. The change in fall-off is apparent (note the jump in doubling the order decreases with increasing order), the flat zone increases with increasing order, and the -3 db points are common to all orders. This bandwidth (0.1-50 Hz) is not bad for strong motion recordings of small to moderate earthquakes. Simply multiplying the filters (4-pole)

$$\frac{1}{\sqrt{1 + (\frac{0.1}{f_e})^8}} \times \frac{1}{\sqrt{1 + (\frac{f_e}{50})^8}}$$ *(plotted in Figure 6)*

High-pass times Low-pass

times the acceleration sensitivity (accelerometer with a corner at 50 Hz or beyond) (adding an amplifier, digitizer, and recorder) produces a strong motion seismograph to record motions from

0.1-50 Hz.

g) Noise

In general noise sources arise from the earth (see Seminar 1, Table 1), the system, and from processing. For strong motion recording, the principal sources of noise are:

1) digitizer noise for film and analogous tape records (processing),

2) accelerometer noise (system), and ground noise (earth) due to natural phenomena and cultural activity. Figure 8 shows these noise models along with our ground motion spectra computed at R = 10 km for **M** 2.5-7.5. The dots are the approximate source corner periods. Figure 9 is an analogous plot for R = 50 km. If, for example, we do not have a digital system, the digitizer noise controls. With a digital system, sensor noise controls. A good rule of thumb is that the S/N ratio $\geq$ 6 db or at least a factor of 2.

If we wished to design an accelerograph with film recording, we have the following constraints:

1) Noise limited by digitizer,

2) Dynamic range of 40 db.

What can we expect to see and where should we expect to have to filter?

R = 10 km	R = 50 km
M > 3.5	**M** > 4.5
$\Delta f \approx$ 0.05 - 30 Hz	$\Delta f \approx$ 0.1-20 Hz

0.05 Hz: should resolve

all source corners **M** 3.5-7.5

However we have only 40 db dynamic range or factor of 100 between smallest and largest signal. Since a factor of 10 is about one unit in magnitude, we are limited to 2 magnitude units for on-scale recording above noise. This is dismal and a significant factor in

limiting the number of useful recordings.

If, on the other hand, we have a digital system, the advantage is twofold: processing noise is eliminated, the sensor is now the noise floor and the dynamic range is greatly increased. For example 16 bit (90 db) would easily accommodate a magnitude range of about 4. Coupled with the lower noise, our window becomes

R = 10 km	R = 50 km
M > 2.5 (to about 6.5)	M > 3.5 (to about 7.5)
Δf = 0.01-50 Hz	Δf = 0.05-30 Hz

Digital systems represent a tremendous improvement in our ability to record useable data.

System Filters, magnitude range

Film Recorder	**Digital Recorder**
0.05 Hz high-pass	0.01 Hz high-pass
20 Hz low-pass	50 Hz low-pass
2 magnitude units	4 magnitude units

Figure 10 shows the two system responses and their respective dynamic ranges assuming a maximum recorder voltage of 2.5v.

h) Data Processing

The art of data processing with particular reference to strong ground motion refers to 1) instrument removal (correction) and 2) elimination of noise (earth, system, and processing) through filtering.

1) Instrument Removal: This aspect of data processing is probably the most straightforward and involves removing (deconvolving) the instrument response (Figure 3) from the record. The approach generally taken to remove the instrument is to divide its response out of the Fourier amplitude spectrum of the recorded motions. To illustrate this process, Figure

11 shows whole record Fourier amplitude spectra computed from a film recording of an aftershock of the 1979 Empirical Valley earthquake (M $\approx$ 5.2, R $\approx$ 10 km). This spectrum is unfiltered and includes the instrument response (Figure 3). Figure 12 shows the spectrum after removing (dividing out) the instrument response. Note the turnaround in the spectrum at high frequency ($\geq$ 35 Hz) resulting from dividing out the instrument response which decreases rapidly (f^{-2}) beyond the corner (25 Hz). From our model of earthquake spectra and noise (Figure 8), this increase is likely due to noise introduced in digitizing the film record and should be filtered out.

To examine possible noise contamination at low frequency (long periods) Figure 13 shows the instrument corrected Fourier amplitude spectrum integrated twice (times f^{-2}). The spectrum continues to increase with decreasing frequency out to nearly 0.05 Hz (20 sec), the length of the record. This spectrum does not resemble the earthquake for field source spectrum

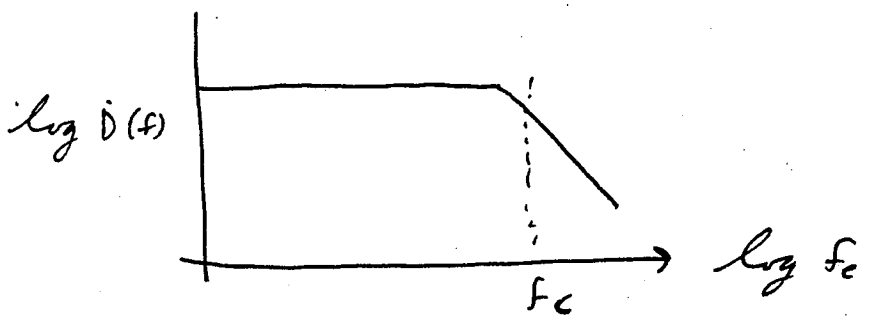

and suggests the presence of low frequency noise. From Figure 8, the corner frequency should be near 0.8 Hz ($f_c \approx 300\ e^{-1.15M}$) so the spectrum should begin to flatten out near 1 Hz. To illustrate the effects of low frequency noise in the time domain, Figure 14 shows acceleration, velocity, and displacement time histories produced from the unprocessed record. While the velocity record appears reasonable, the displacement shows a very long period drift or a baseline problem. This is a typical feature of long period noise in strong motion recordings. The best way to eliminate or minimize this contamination is to apply a high-pass filter to reduce the spectrum for frequencies lower than the corner frequency.

For this record, as for most strong motion data, noise contamination is present at both high and low frequencies. The low pass filter design for the high frequency noise is rather straightforward. From Figure 12, the filter should be applied just before where the spectrum turns around (near 30 Hz) recalling that at the corner the filter is already down $1/\sqrt{2} = 0.707$. The order number must be high enough to roll off the turnaround (about an f^2 dependence) so a 4-5 pole would force the spectrum to decrease at a net fall-off of f^2 or f^3 beyond 30 Hz.

For the high-pass filter at the low frequency end, the situation is much more subtle and the process approaches that of an art if one wishes to maximize the low frequency signal. The process I use is to view the instrument corrected spectrum (Figure 12) from the perspective of having the basic properties of an approximate Brune source accommodating differences due to site and path effects as well as departures from the simple source spectrum due to finite source effects (directivity). With this in mind, the spectrum in Figure 12 should increase with increasing frequency to a flat portion somewhere near 1 Hz. At R = 10 km, from Figure 8, we should resolve the corner ($\approx$ 0.8 Hz) (note this may not be the case at R = 50 km, Figure 9) and the high-pass filter corner should be somewhat lower than this. Based on experience and trial and error (filtering and integrating to displacement), the corner was chosen at 0.35 Hz with order 5. Figure 15 shows the instrument corrected and filtered acceleration Fourier amplitude spectrum and Figure 16 shows the corresponding displacement spectrum. Note the absence of the high frequency turnaround in Figure 15 and the roll off at low frequency in the displacement spectrum (Figure 16). The resulting time histories are shown in Figure 17. Comparing unprocessed time histories (Figure 14) to processed (Figure 17) the processing has increased the accelerations, reduced the velocities, and eliminated the long period baseline problem revealing a clean displacement pulse.

Another approach to baseline correction is polynomial fitting (Appendix 2). While this method does remove long period trends it suffers from not using any understanding of the physical processes involved and can remove important signal.

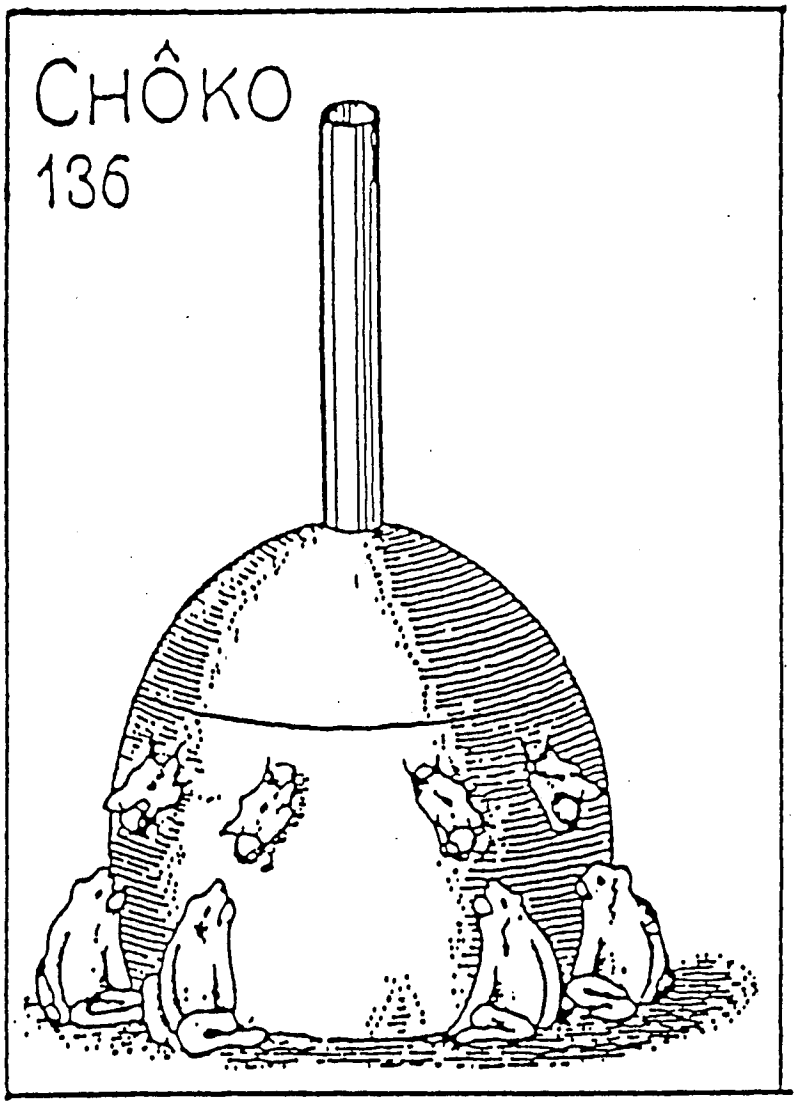

Figure 1 Dragon seismoscope

KINEMETRICS

EARTHQUAKE ENGINEERING INSTRUMENTS

SSA-1

Solid State Accelerograph

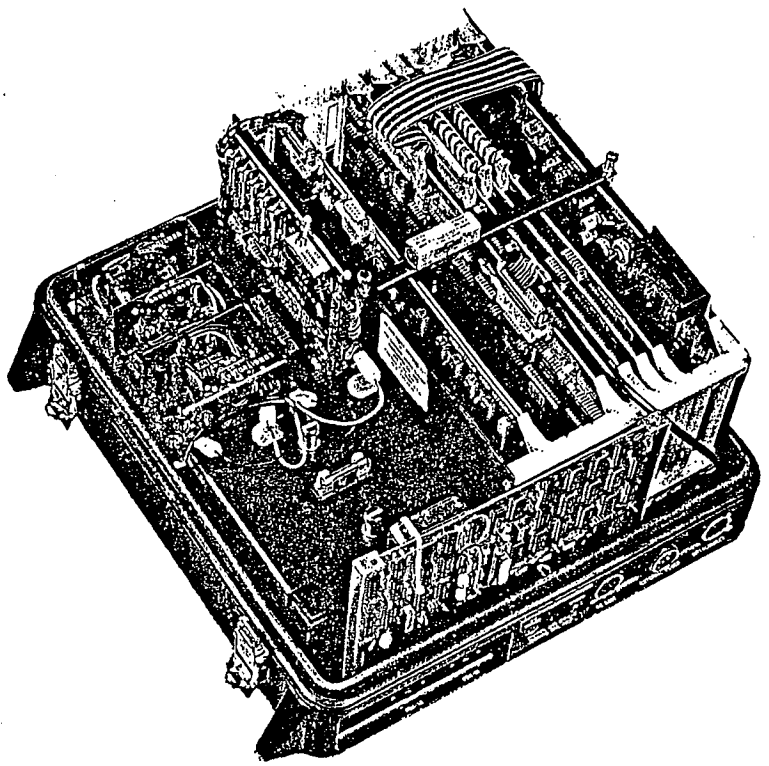

Figure 2.

The standard system includes Kinemetrics Force Balance Accelerometers, CMOS static RAM based, triggered event recording system, environmental enclosure, and battery backup for up to 7 days. Also provided are both QuickLook® and QuickTalk®: user friendly, menu-oriented software for retrieving and displaying earthquake data over the standard RS-232C link.

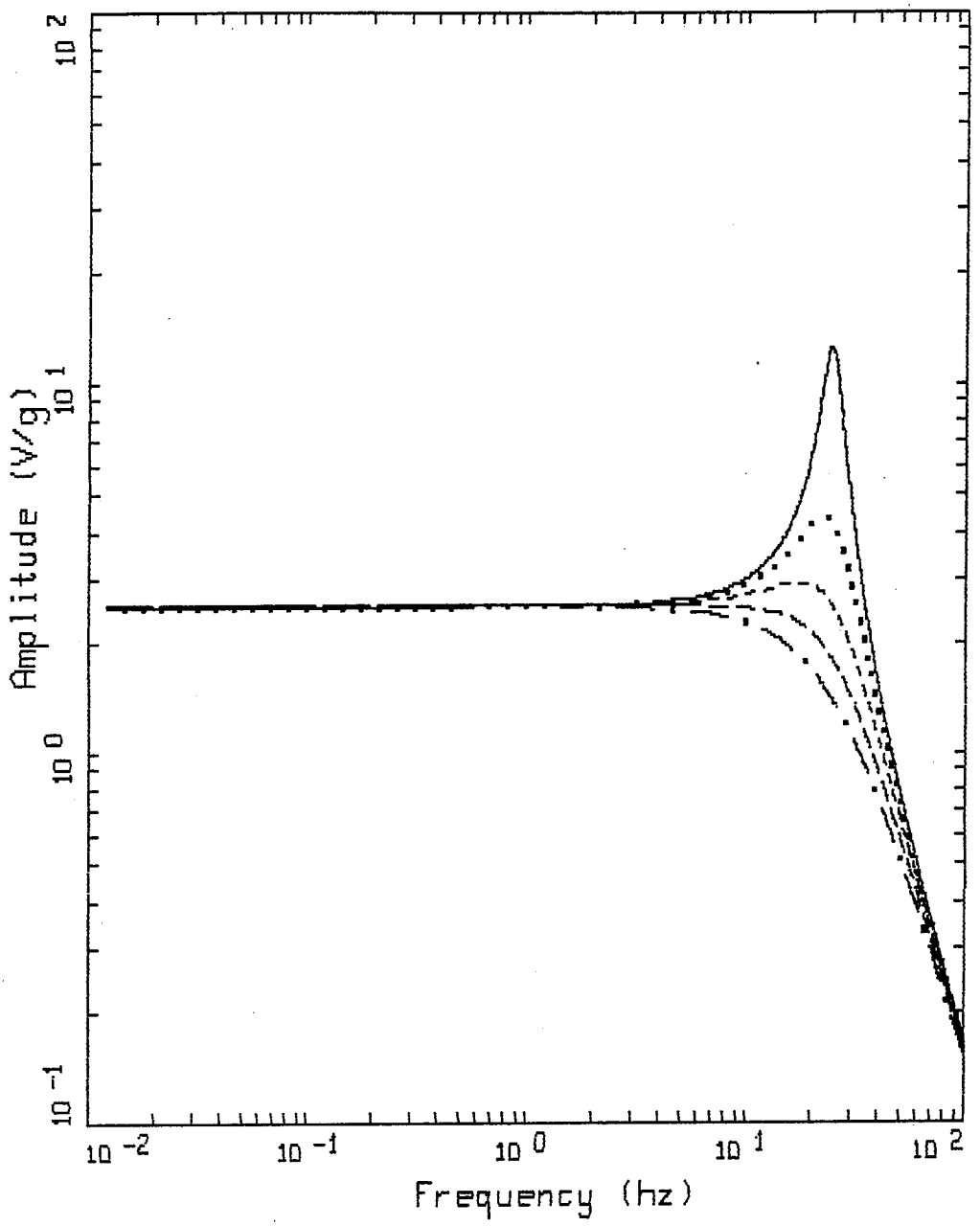

SMA INSTRUMENT RESPONSE (FC = 25 HZ)
ACCELERATION SENSITIVITY

LEGEND

——— DAMPING = 0.1 CRITICAL

• • • • DAMPING = 0.3 CRITICAL

- - - - - DAMPING = 0.5 CRITICAL

— — — — DAMPING = 0.7 CRITICAL

— • — DAMPING = 0.9 CRITICAL

Figure 3.

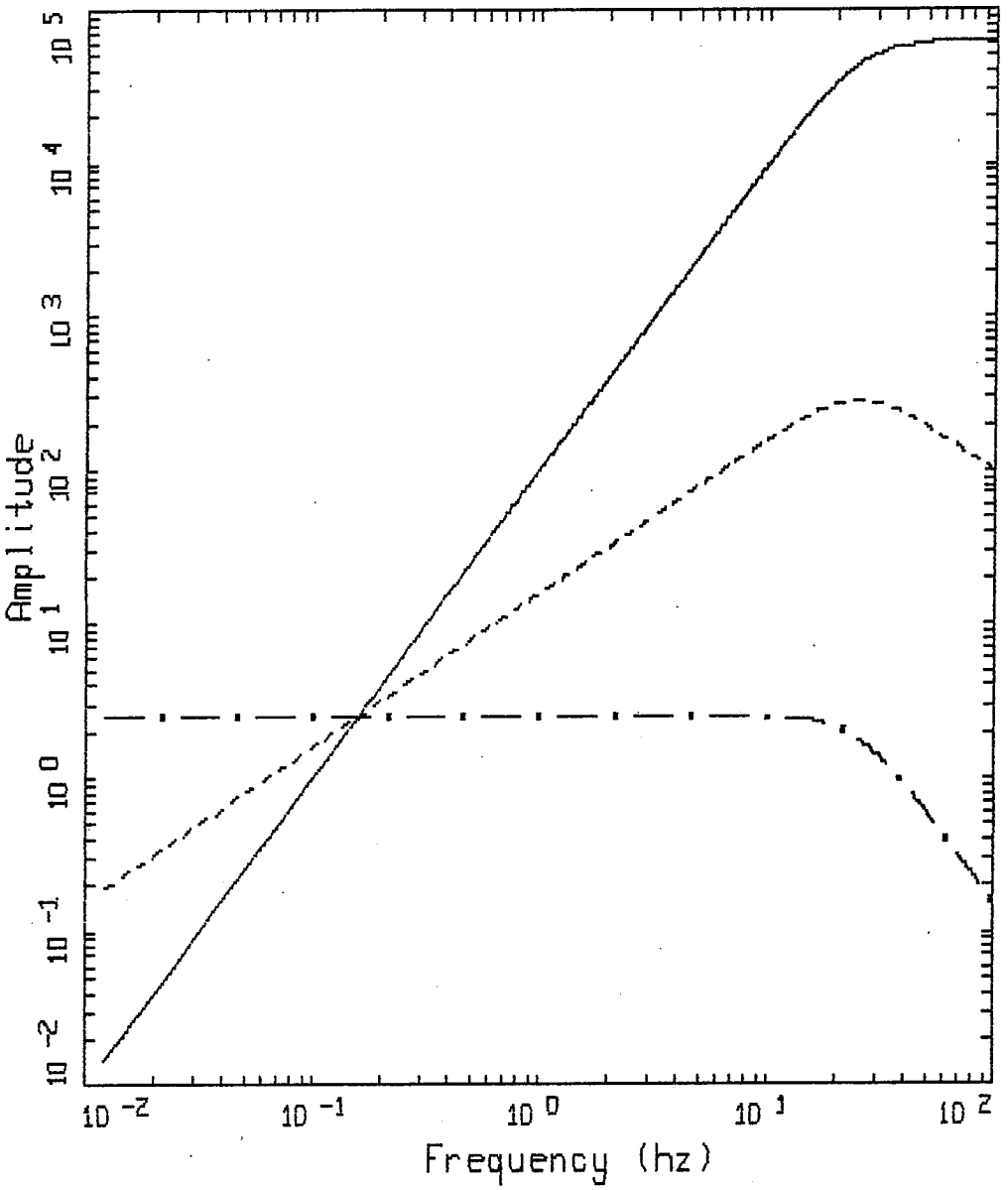

SMA INSTRUMENT RESPONSE (FC = 25 HZ)
DAMPING = 0.7 CRITICAL

LEGEND
MAGNIFICATION
VELOCITY SENSITIVITY
ACCELERATION SENSITIVITY

Figure 4.

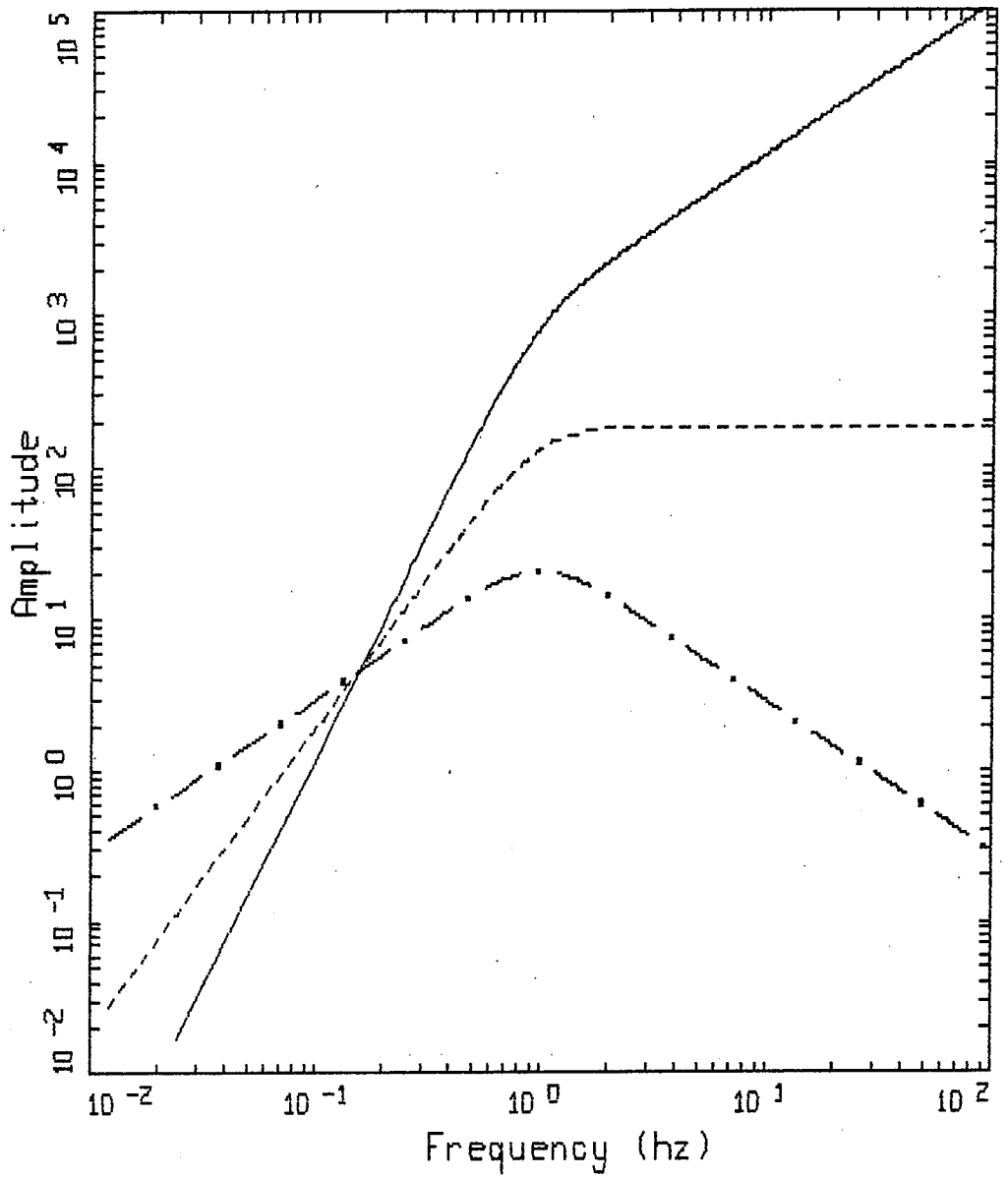

L4C INSTRUMENT RESPONSE (FC = 1 HZ)
DAMPING = 0.7 CRITICAL

LEGEND
——— MAGNIFICATION
----- VELOCITY SENSITIVITY (180 V/M/SEC)
— • — ACCELERATION SENSITIVITY

Figure 5.

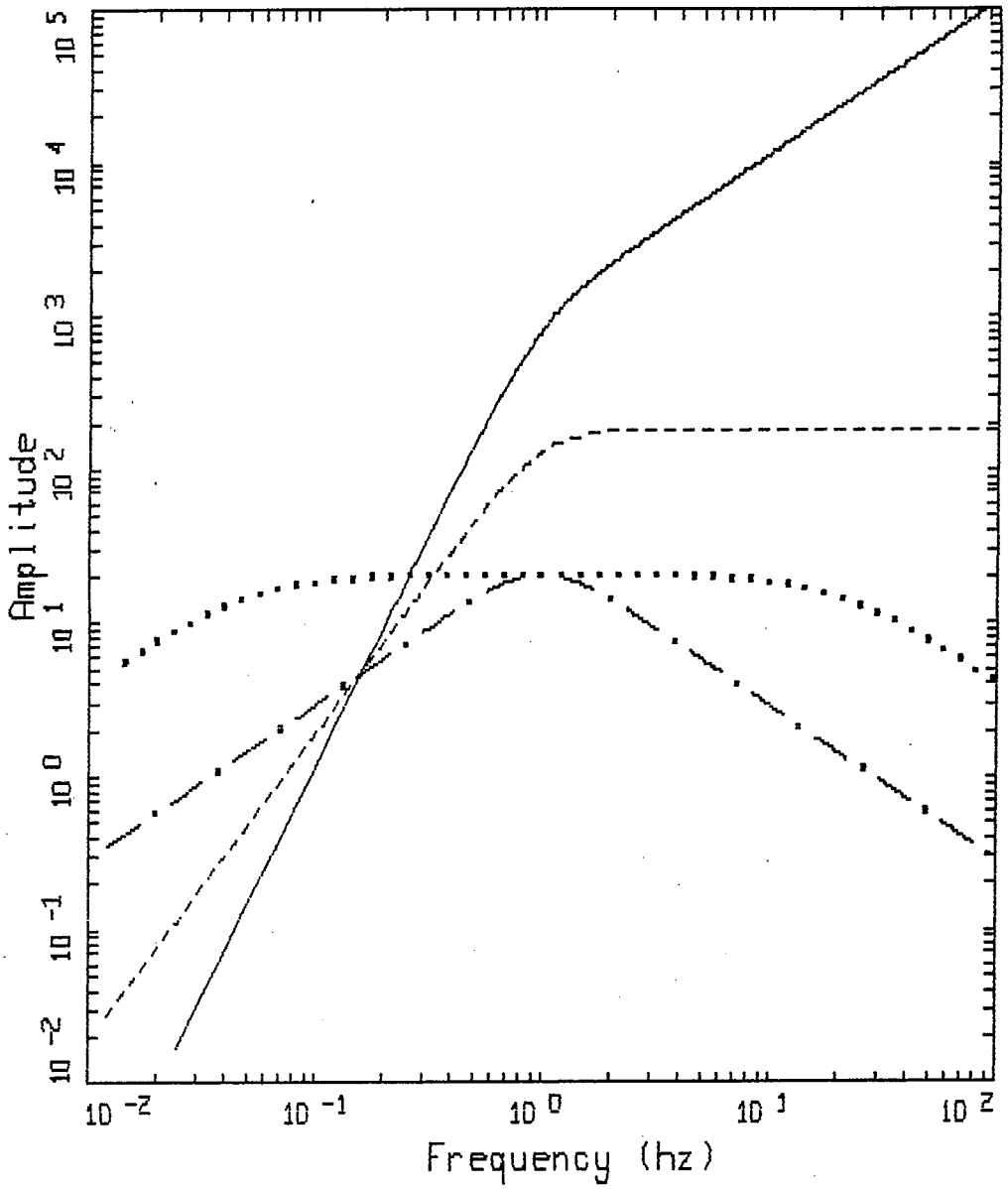

L4C INSTRUMENT RESPONSE (FC = 1 HZ)
DAMPING = 0.7 CRITICAL

LEGEND

——— MAGNIFICATION

- - - - - VELOCITY SENSITIVITY

— • — ACCELERATION SENSITIVITY

• • • • ACCELERATION SENSITIVITY, DAMPING = 10 * CRITICAL

Figure 6.

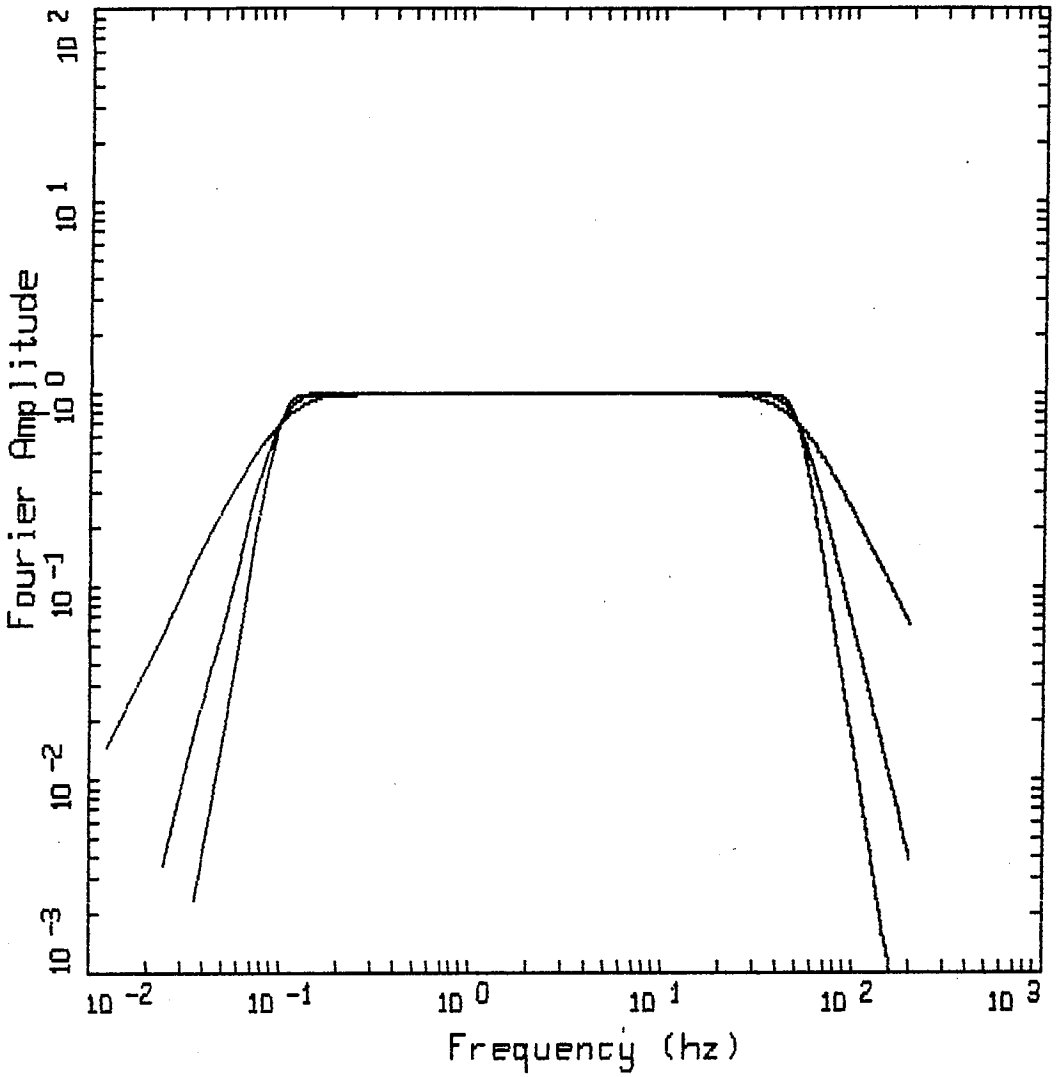
Fourier Amplitude
10 2
10 1
10 0
10 -1
10 -2
10 -3
10 -2
10 -1
10 0
10 1
10 2
10 3
Frequency (hz)
CAUSAL FILTERS(BUTTERWORTH)
FC = 0.1, 50 HZ
LEGEND
2-POLE
4-POLE
6-POLE

Figure 7.

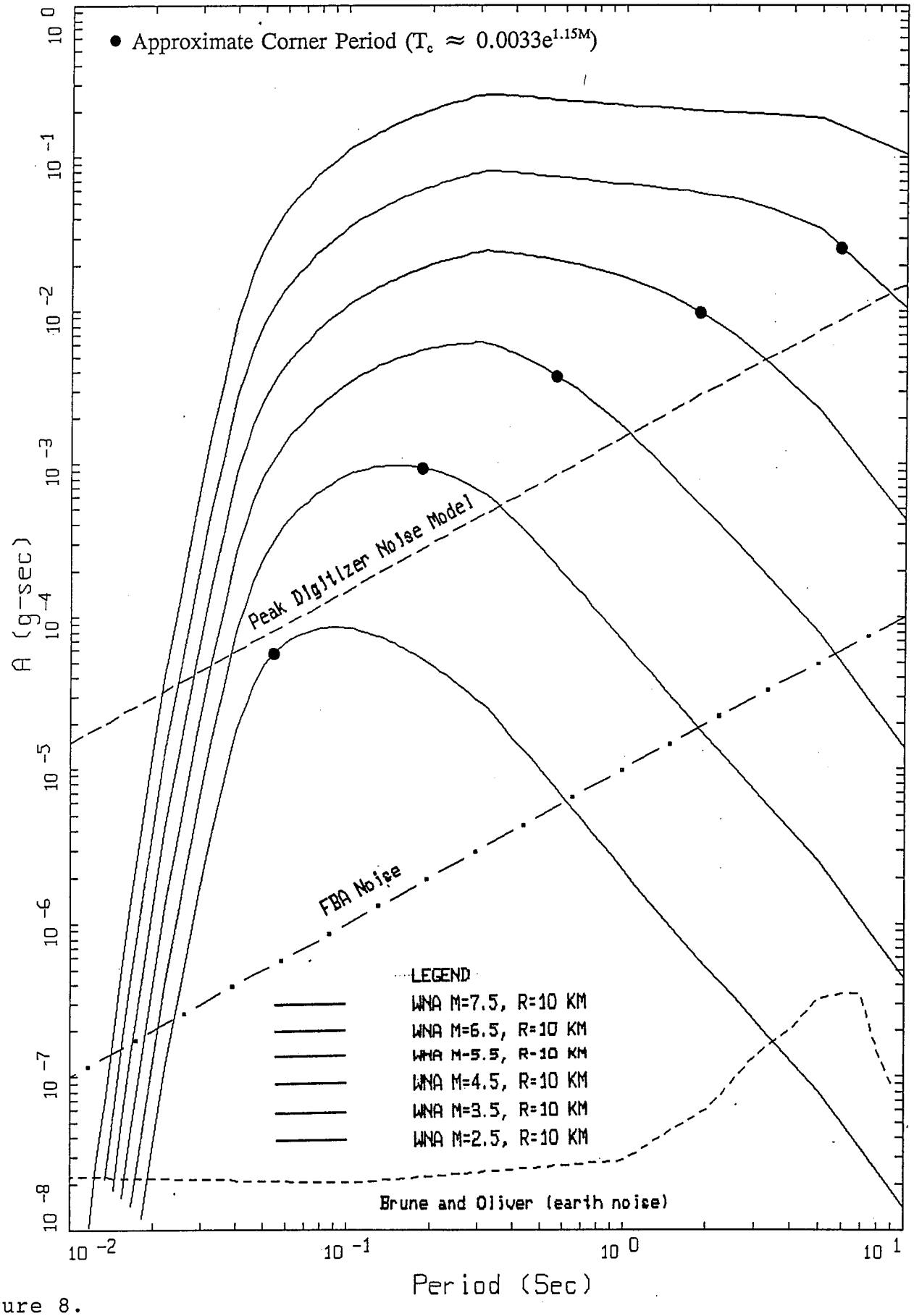

Figure 8.

Signal-Noise Characteristics
Source at 10 km

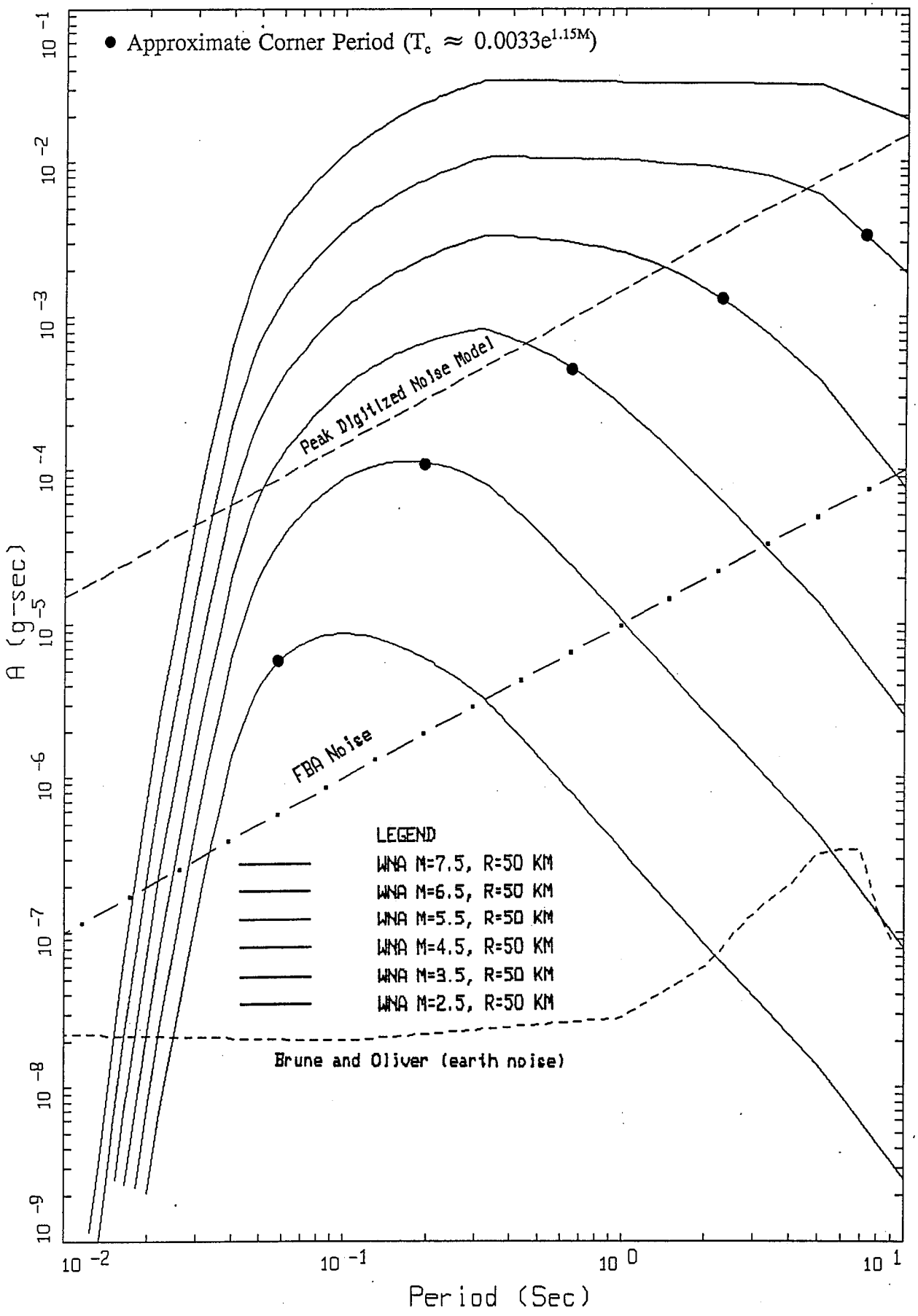

Figure 9. Signal-Noise Characteristics Source at 50 km

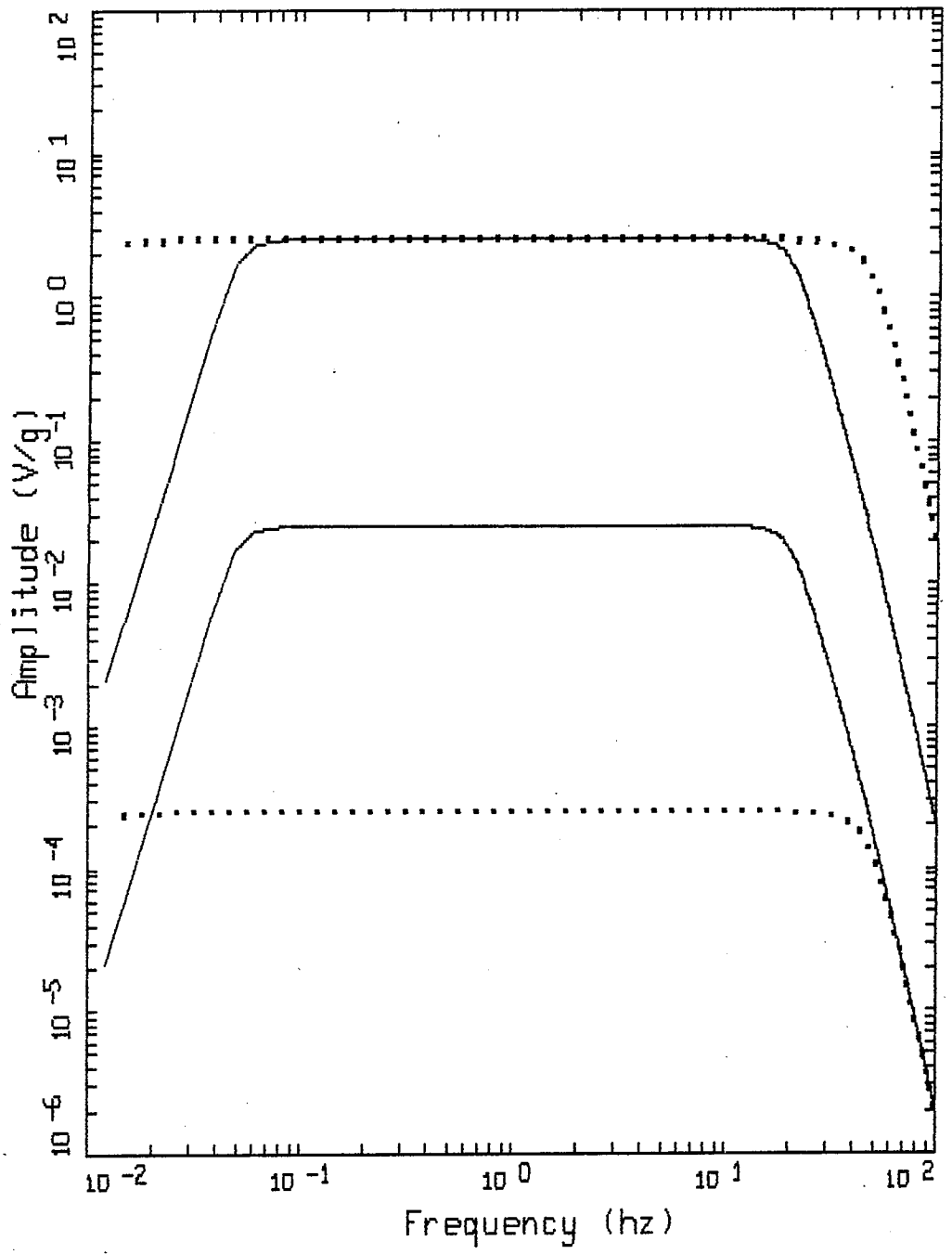

INSTRUMENT RESPONSE (FC = 50 HZ)
ACCELERATION SENSITIVITY

LEGEND

——— DAMPING = 0.7 CRITICAL, FILM RECORDER

• • • • DAMPING = 0.7 CRITICAL, DIGITAL RECORDER

——— DAMPING = 0.7 CRITICAL, FILM RECORDER / 100

• • • • DAMPING = 0.7 CRITICAL, DIGITAL RECORDER / 10,000

Figure 10.

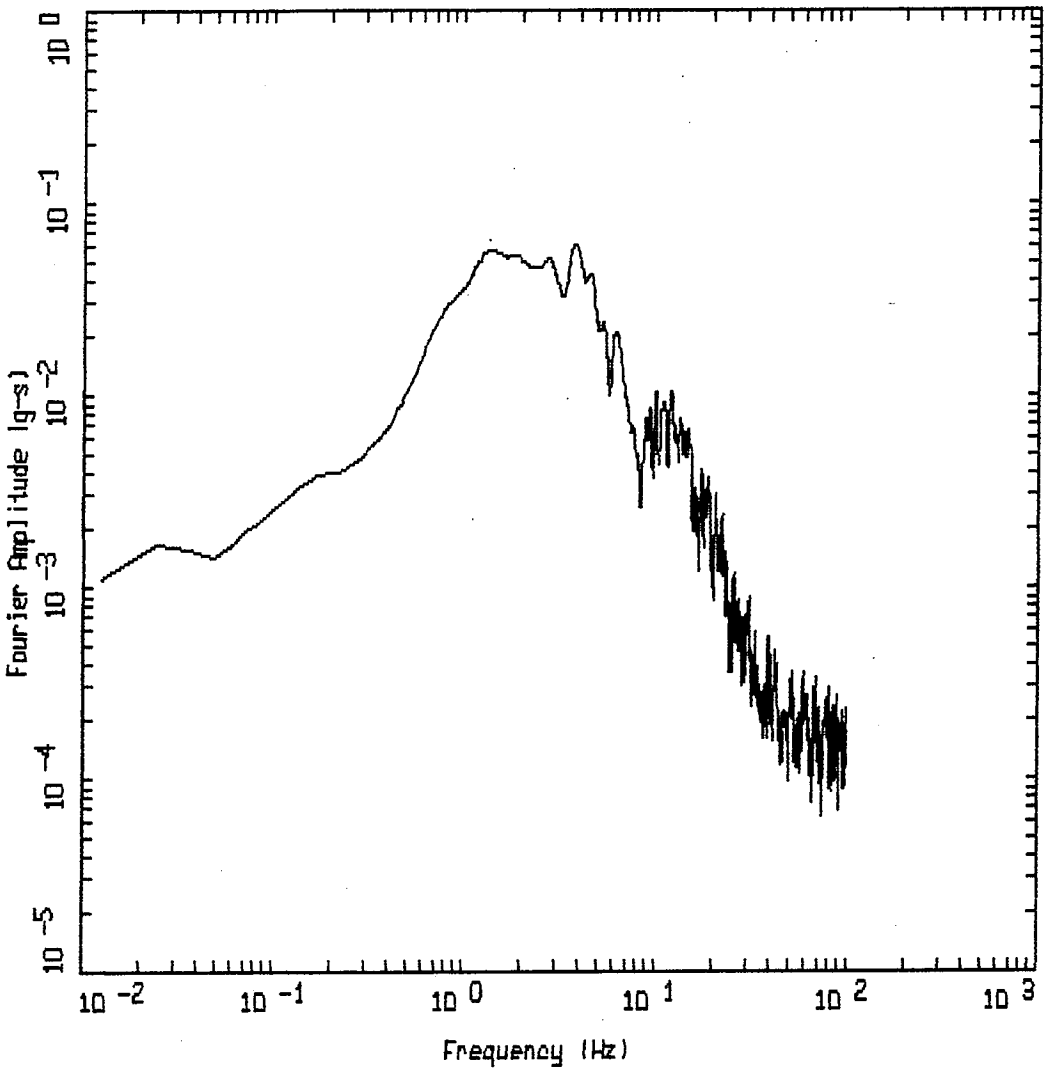

IMPERIAL VALLEY AFTERSHOCK, EL CENTRO 6, 230 DEG COMPONENT
FOURIER SPECTRUM FROM RAW ACCELERATIONS

LEGEND

Figure 11.

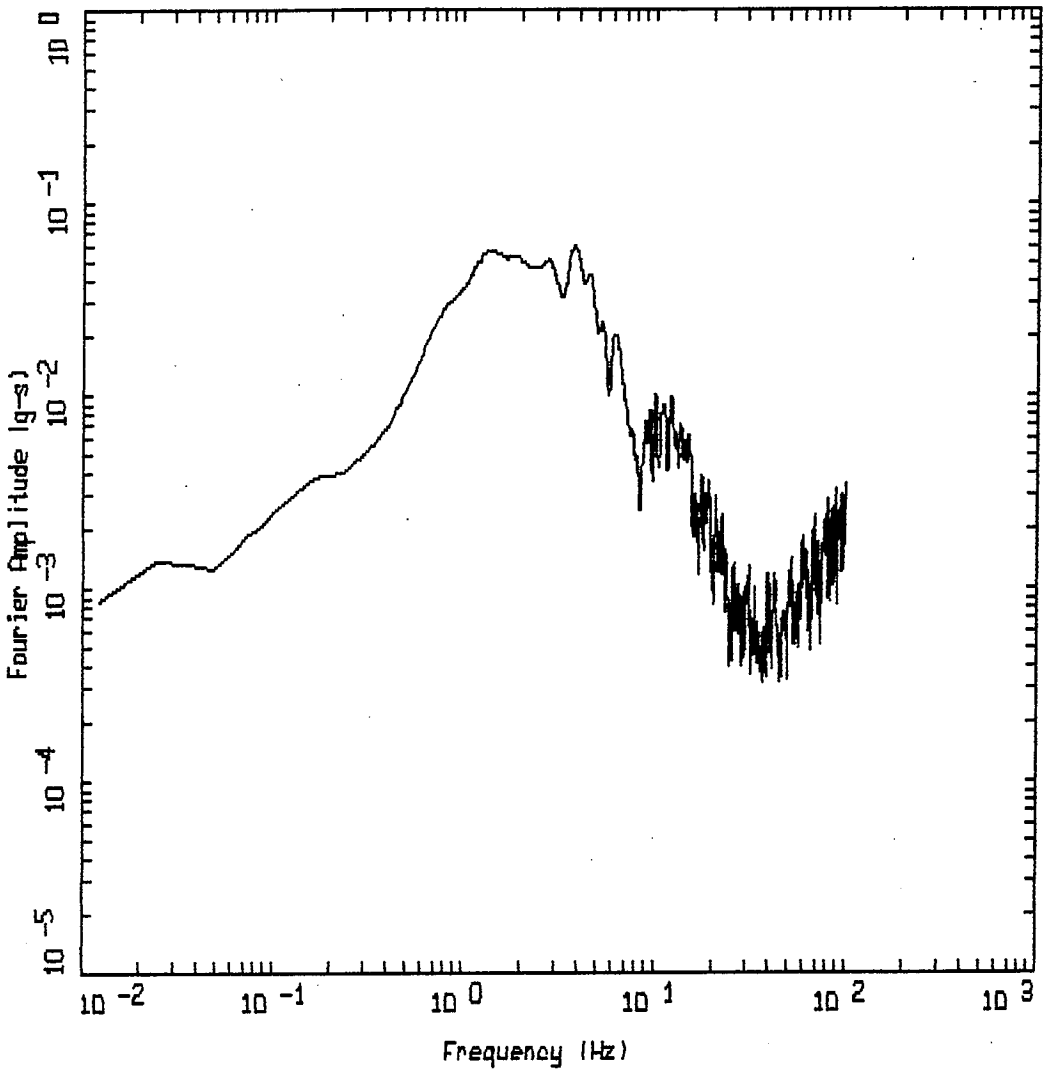

IMPERIAL VALLEY AFTERSHOCK, EL CENTRO 6, Z30 DEG COMPONENT
FOURIER SPECTRUM FROM INSTRUMENT-CORRECTED ACCELERATIONS

LEGEND

Figure 12.

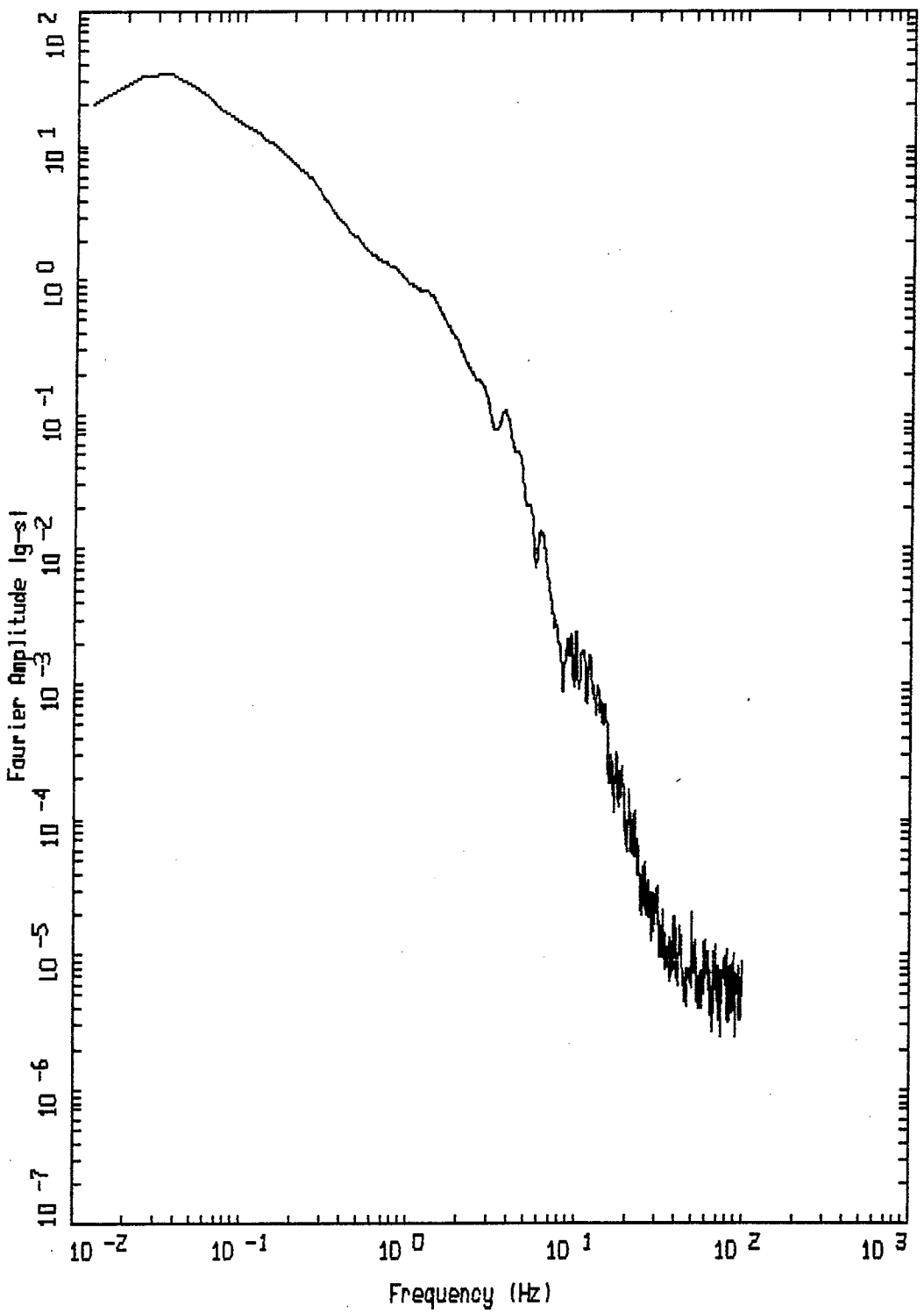

IMPERIAL VALLEY AFTERSHOCK, EL CENTRO 6, 230 DEG COMPONENT
FOURIER SPECTRUM FROM INSTRUMENT-CORRECTED DISPLACEMENTS

LEGEND

Figure 13.

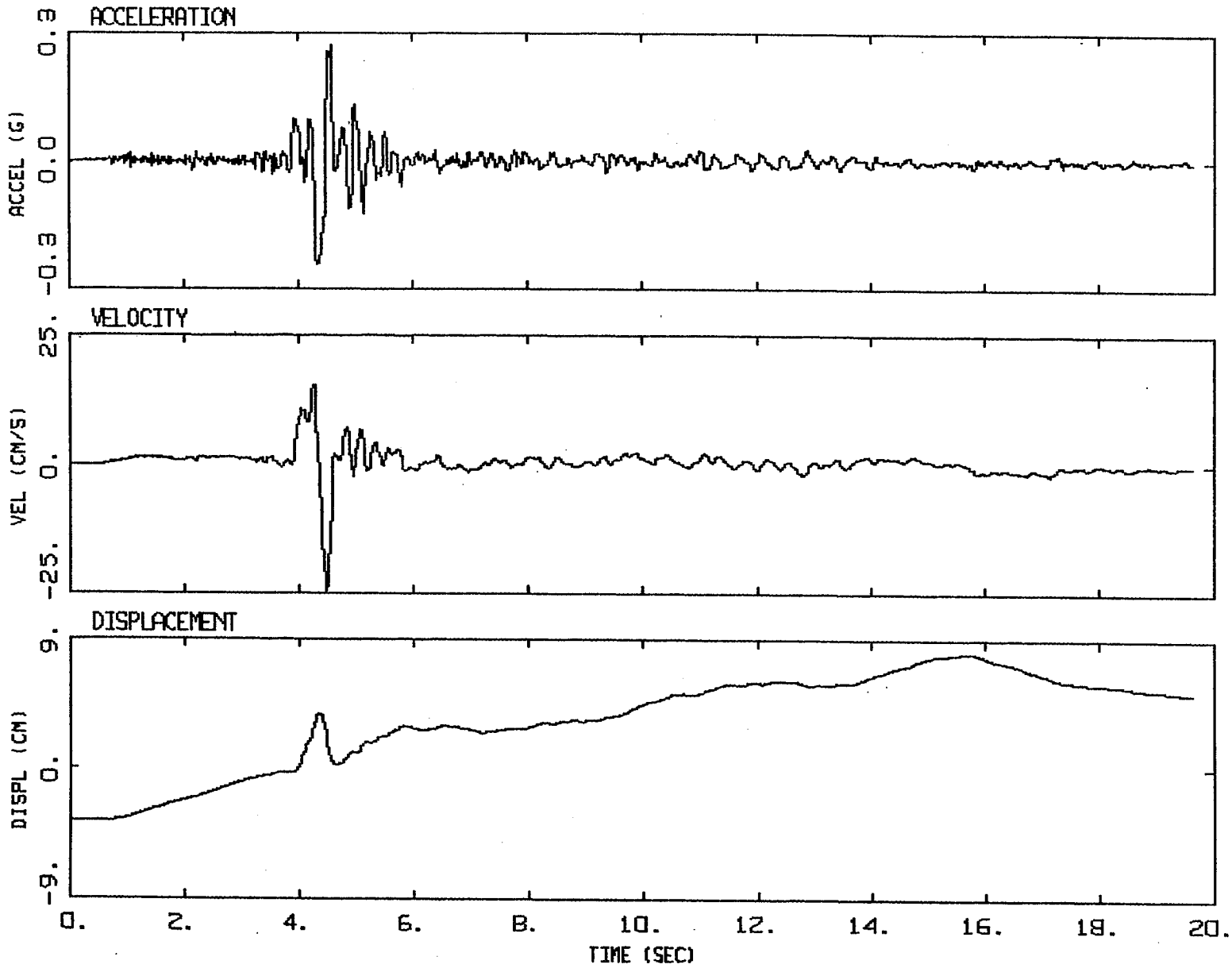

Figure 14.

IMPERIAL VALLEY 10/15/79 23:19, EL CENTRO 6, 230 DEG
INTEGRATED FROM RAW ACCELERATIONS

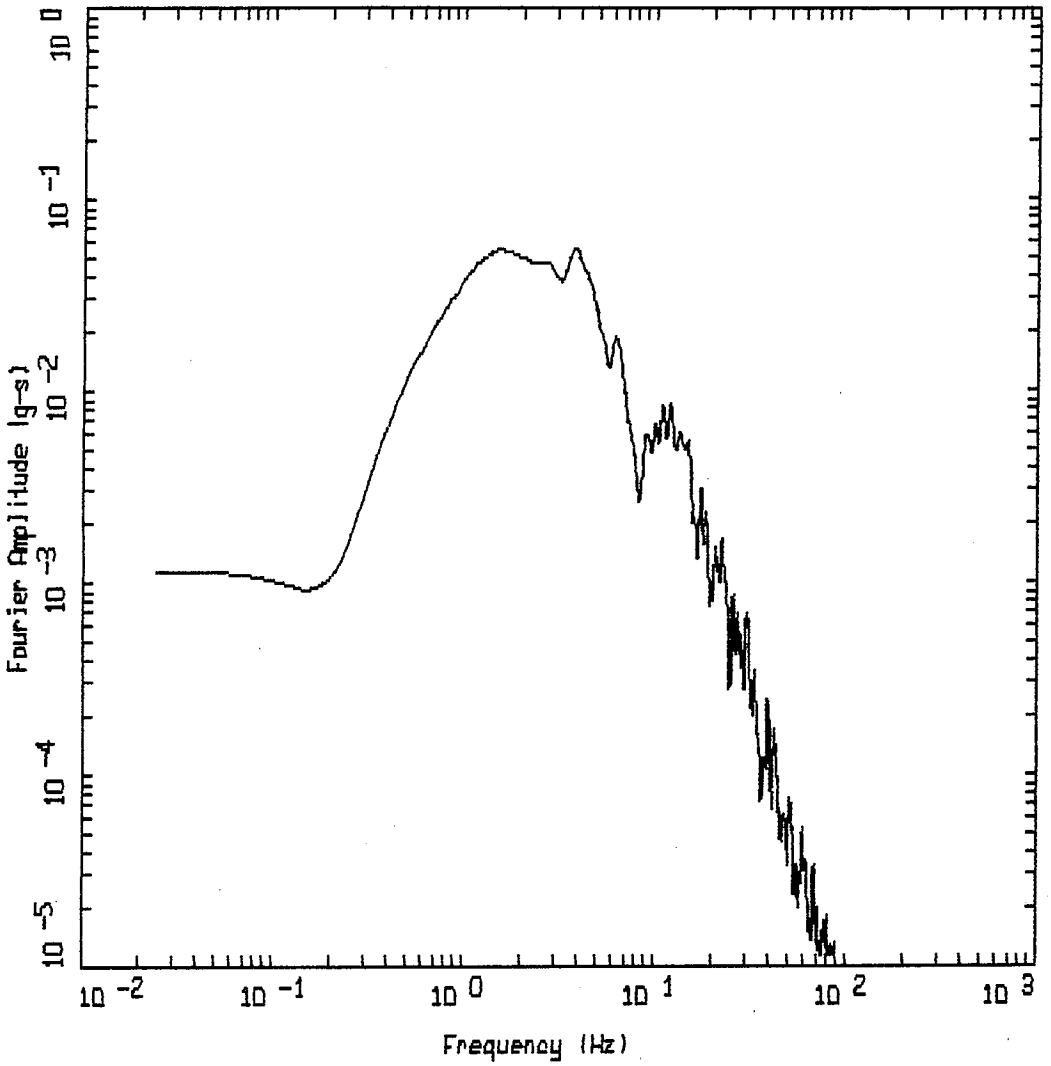

IMPERIAL VALLEY AFTERSHOCK, EL CENTRO 6, 230 DEG COMPONENT
FOURIER SPECTRUM FROM PROCESSED ACCELERATIONS

LEGEND

——— LP 5-POLE AT 30 HZ, HP 5-POLE AT 0.35 HZ

Figure 15.

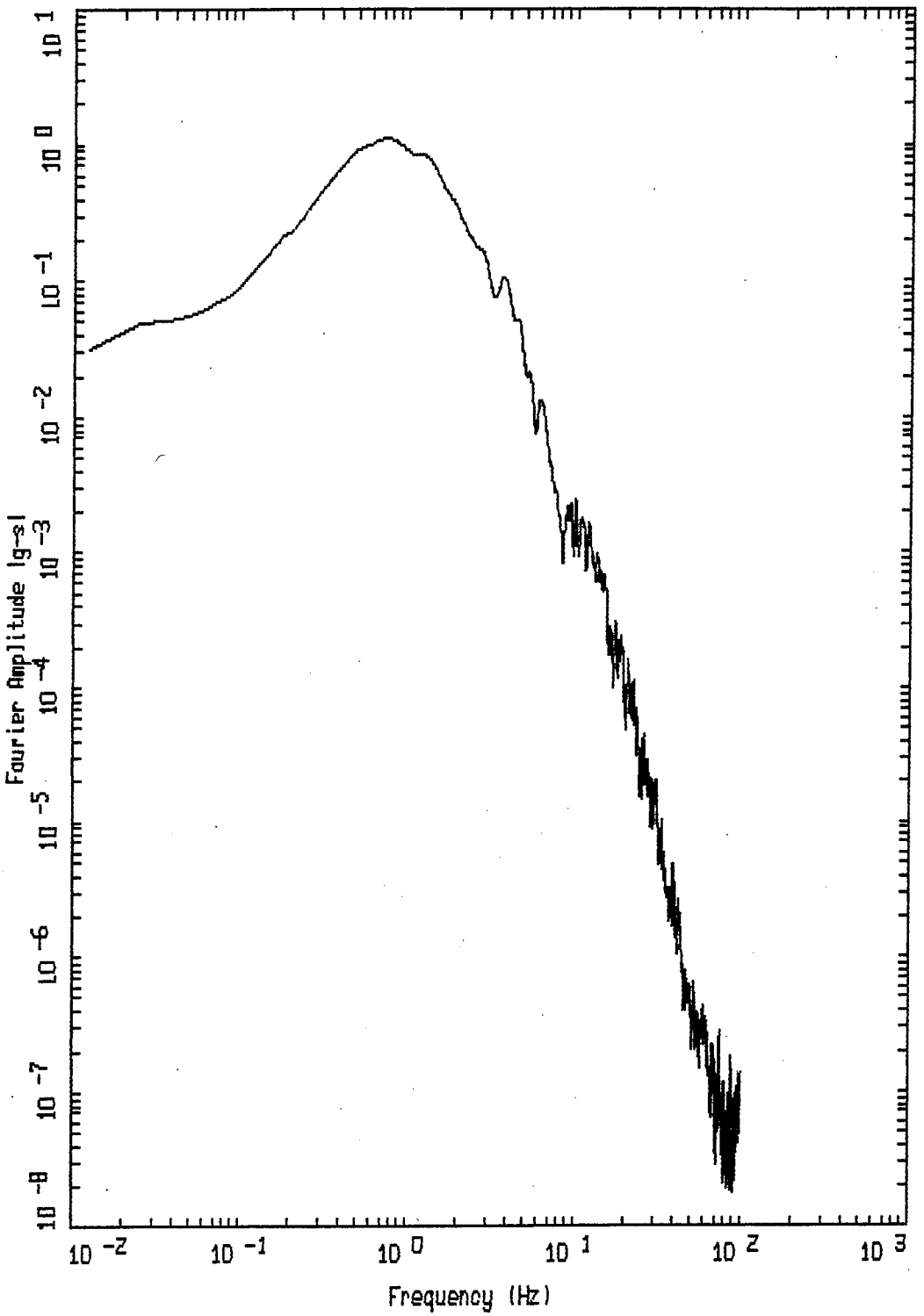

IMPERIAL VALLEY AFTERSHOCK, EL CENTRO 6, 230 DEG COMPONENT
FOURIER SPECTRUM FROM PROCESSED DISPLACEMENTS

LEGEND

Figure 16.

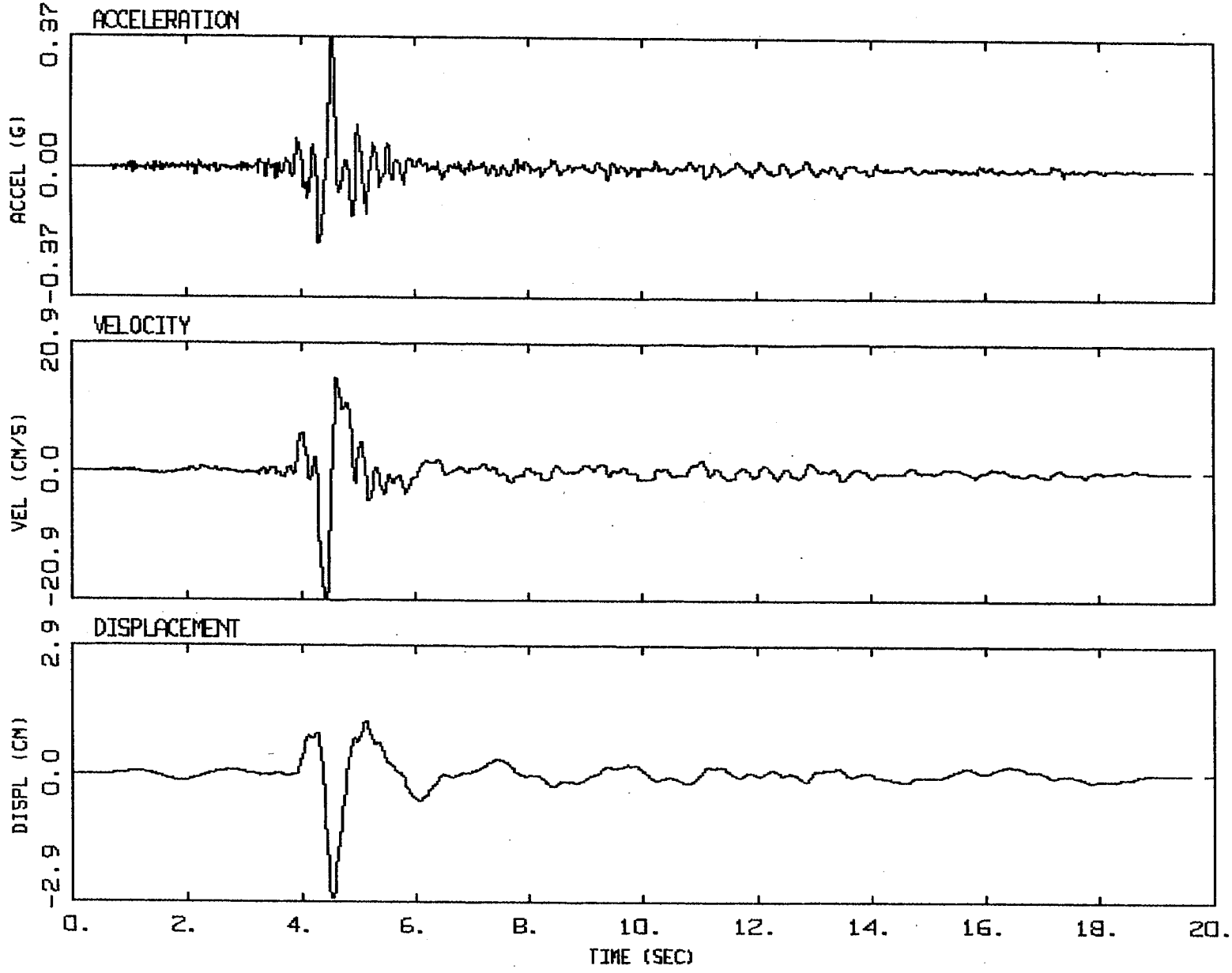

Figure 17.

IMPERIAL VALLEY 10/15/79 2319, EL CENTRO 6, 230 DEG
INTEGRATED FROM CORRECTED AND BASE-CORRECTED ACCELERATIONS

APPENDIX 1

Sensor and System Specifications

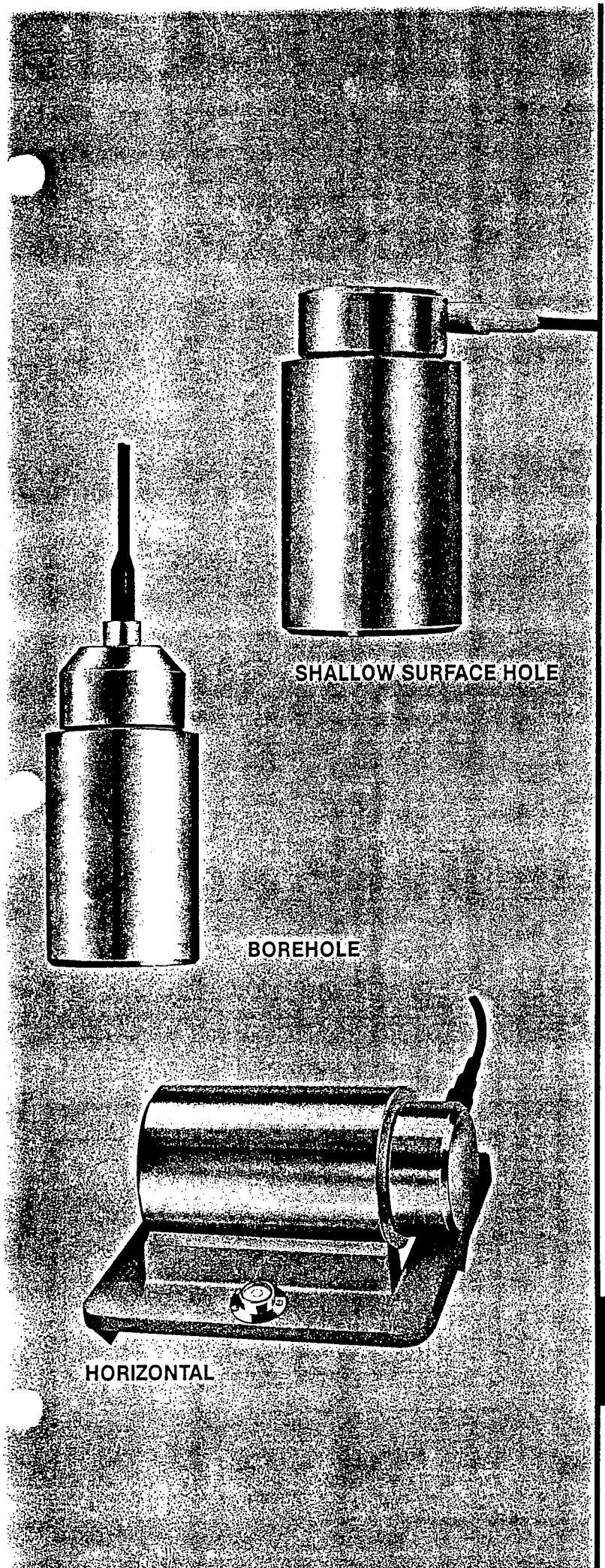

The L-4 is an INSTRUMENT QUALITY ONE Hz or TWO Hz multi-purpose geophone, that is small, light, and economical. It is designed to yield the performance needed for scientific studies, yet has the ruggedness required for petroleum exploration work.

The L-4 design ELIMINATES the usual causes of FAILURE in VERY LOW FREQUENCY geophones, such as SPRING FATIGUE, OVER-STRESS and INSTABILITY. This geophone maintains a close frequency tolerance with tilt and temperature, and is TRANSPORTED WITHOUT CLAMPING the moving element.

The L-4 is available with or without calibration coils and may be obtained as VERTICAL OR HORIZONTAL elements. A variety of fittings are available for custom application.

FEATURES

STABLE NATURAL FREQUENCY

LOWEST DISTORTION

INSTRUMENT QUALITY

HUMBUCK CONSTRUCTION

VERY HIGH OUTPUT

NO SPRING SAG

U.S. PATENT 3,451,040
FRENCH PATENT 1,598,454

1.0 Hz AND 2.0 Hz LAND OR BOREHOLE GEOPHONE

L-4

Basic unit is guaranteed for six months, external voltage and highline damage not included on warranty.

Warranty is subject to the terms and conditions listed on our General Warranty page in this catalog.

	L-4C 1.0 Hz GEOPHONE	L-4A 2.0 Hz GEOPHONE
TYPE	Moving dual coil, humbuck wound	Moving dual coil, humbuck wound
FREQUENCY	1.0 ± 0.05 Hz measured on 200 pound weight at 0.09 inches/second	2.0 ± 0.25 Hz measured on 200 pound weight at 0.09 inches/second
FREQUENCY CHANGE WITH TILT	Less than 0.05 Hz at 5° from vertical	less than 0.10 Hz at 10° from vertical
FREQUENCY CHANGE WITH EXCITATION	Less than 0.05 Hz from 0 to 0.09 inches/second	Less than 0.10 Hz from 0 to 0.18 inches/second
SUSPENDED MASS	1000 grams	500 grams
STANDARD COIL RESISTANCES	500, 2000, 5500	500, 2000, 5500
LEAKAGE TO CASE	100 megohm minimum at 500 volts	100 megohm minimum at 500 volts
TRANSDUCTION POWER	$8.8\ 10^{-3}$ watts/inch/second or 13.6 watts/meter/second	$8.8\ 10^{-3}$ watts/inch/second or 13.6 watts/meter/second
OPEN CIRCUIT DAMPING	(bo) = 0.28 critical	(bo) = 0.28 critical
CURRENT DAMPING	$(bc) = \frac{1.1\ Rc}{Rs + Rc}$	$(bc) = \frac{1.1\ Rc}{Rs + Rc}$
COIL INDUCTANCE	Lc = 0.0011 Rc Lc in henries	Lc = 0.0011 Rc Lc in henries
CASE TO COIL MOTION	PP 0.250 inches	PP 0.250 inches
ELECTRIC ANALOG OF CAPACITY	$Cc = \frac{73{,}500}{Rc}$ (microfarads)	$Cc = \frac{36{,}500}{Rc}$ (microfarads)
ELECTRIC ANALOG OF INDUCTANCE	Lm = 0.345Rc (henries)	Lm = 0.17Rc (henries)
CASE HEIGHT	5⅛ inches—13 cm.	5⅛ inches—13 cm.
CASE DIAMETER	3 inches—7.6 cm.	3 inches—7.6 cm.
TOTAL DENSITY	3.7 grams/cm^3	2.9 grams/cm^3
TOTAL WEIGHT	4¾ pounds—2.15 kilograms	3¾ pounds—1.7 kilograms
OPERATING TEMPERATURE	Range: −20° to 140°F or −29° to 60°C	Range: −20° to 140°F or −29° to 60°C

	L-4C 1.0 Hz GEOPHONE			L-4A 2.0 Hz GEOPHONE		
COIL RESISTANCE, OHMS	**500**	**2000**	**5500**	**500**	**2000**	**5500**
TRANSDUCTION, VOLTS/IN/SEC	2.12	4.23	7.02	2.12	4.23	7.02
COIL INDUCTANCE, HENRIES	0.55	2.20	6.05	0.55	2.20	6.05
ANALOG CAPACITANCE, MICROFARADS	147	36.8	13.4	73.0	18.3	6.64
ANALOG INDUCTANCE, HENRIES	173	690	1900	85.0	340	935
SHUNT FOR 0.70 DAMPING, OHM	810	3238	8905	810	3238	8905

Open Circuit Damping (b_o) = 0.28 Critical Coil Current Damping (b_c) = $\frac{1.1\ Rc}{Rc + Rs}$ Total Damping (b_t) = $b_o + b_c$

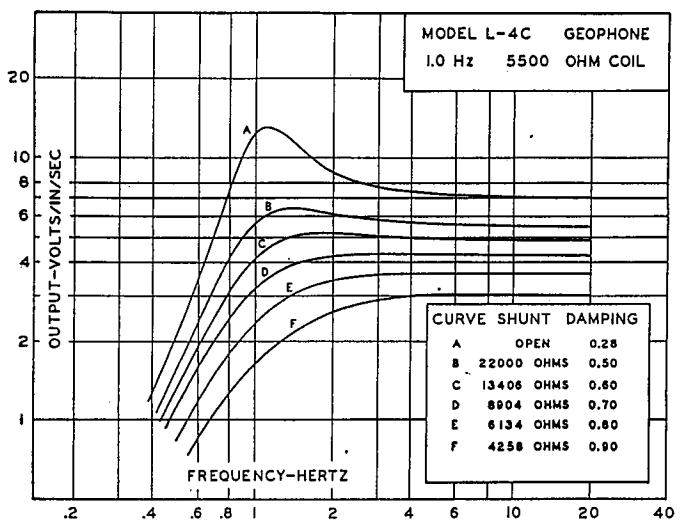

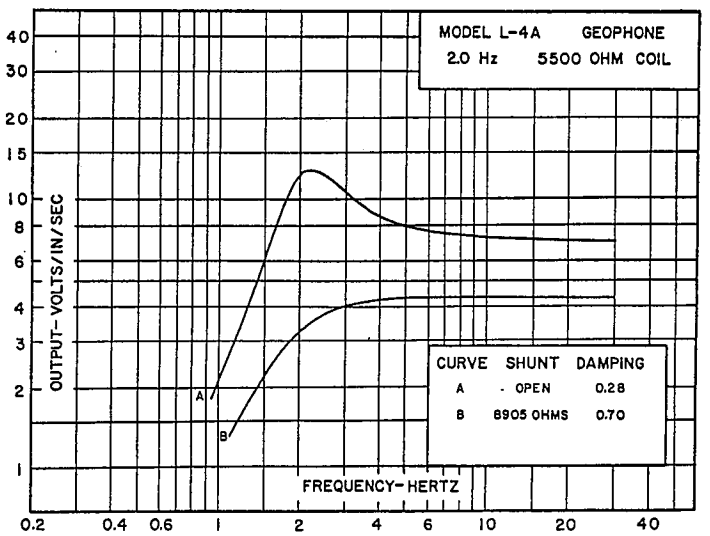

MARK PRODUCTS, U.S. INC.
Area 713/498-0600
10507 Kinghurst Dr.
Houston, Texas 77099
Telex 76-2069

MARK PRODUCTS, LTD.
Area 403/275-3544
1108 55th Ave. N.E.
P.O. Box 73
Calgary, Alberta, Canada T2P 2G9

5M1184

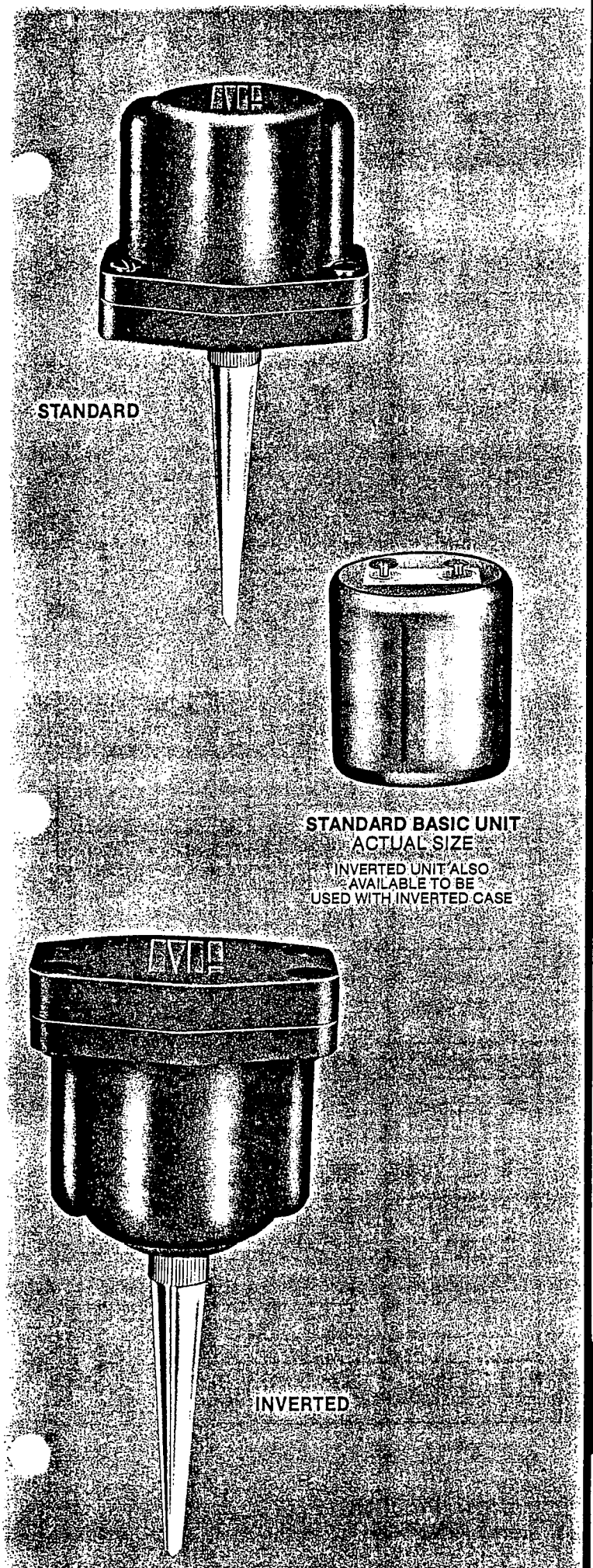

The L-10 Digital Grade Subminiature geophone is a small, lightweight reliable unit. This geophone incorporates engineering techniques, developed and perfected by Mark engineers, that provide long life at original, new specifications — for low frequency as well as the higher frequency units. Each L-10 is individually checked for phase and damping.

This instrument quality geophone is designed for field durability. Its high strength Super-Tuf Nylon case and sealing compound permits a field repairable cable take-out without special tools. Other cases are available for land and marsh applications.

The Standard Case provides for the cable to exit near the bottom of the case. A Standard Basic Unit must be used in this assembly.

In the Inverted Case the cable exits from the top, and an Inverted Basic Unit must be used.

FEATURES

SUBMINIATURE
DIGITAL GRADE
DUAL COIL
HIGH OUTPUT
LOW DISTORTION
STABLE
LOW PROFILE
WATERPROOF
ECONOMICAL
4.5 Hz TO 30 Hz

SUBMINIATURE DIGITAL GRADE LAND GEOPHONE

L-10

Basic unit guaranteed for two years on prorated basis, external voltage and highline damage not included in warranty.

	L-10A	L-10B
Standard Frequency Range, Hz	10-30	4.5-10
Frequency Tolerance	± 5%	± 0.5 Hz
Standard Coil Resistance, Ohms Resistance Tolerance, %	138/215/374 5 5 6.5	138/215/374 5 5 6.5
Maximum Distortion @ 0.7 in/s @ 12 Hz or Resonance	0.2%	0.2%
Transduction Constant, V/in/s ± 10%	$0.041\sqrt{Rc}$	$0.041\sqrt{Rc}$
Open Circuit Damping, ± 10%	$\frac{4.289}{f}$	$\frac{1.908}{f}$
Coil Current Damping	$\frac{16.93\ Rc}{f(Rc+Rs)}$	$\frac{12.15\ Rc}{f(Rc+Rs)}$
Suspended Mass, Grams	12.20	17.00
Power Sensitivity, mW/in/s	1.67	1.67
Case-to-Coil, Motion, in. p-p	0.080	0.080
Basic Unit Diameter, in.	1.25	1.25
Basic Unit Height, in.	1.4	1.4
Basic Unit Weight, oz.	5.0	5.0

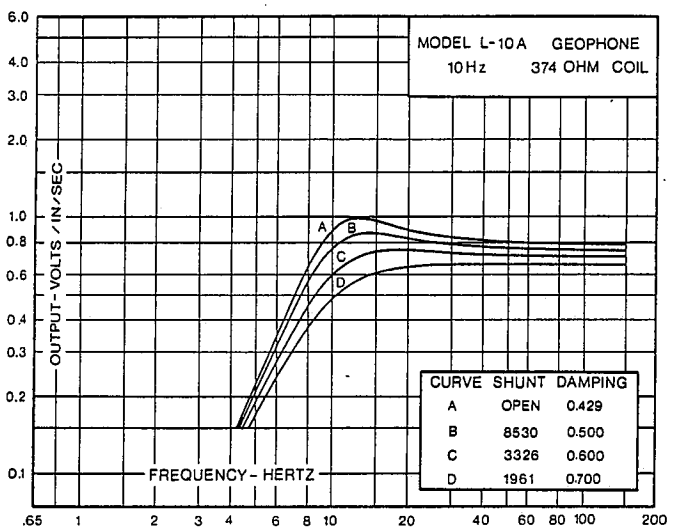

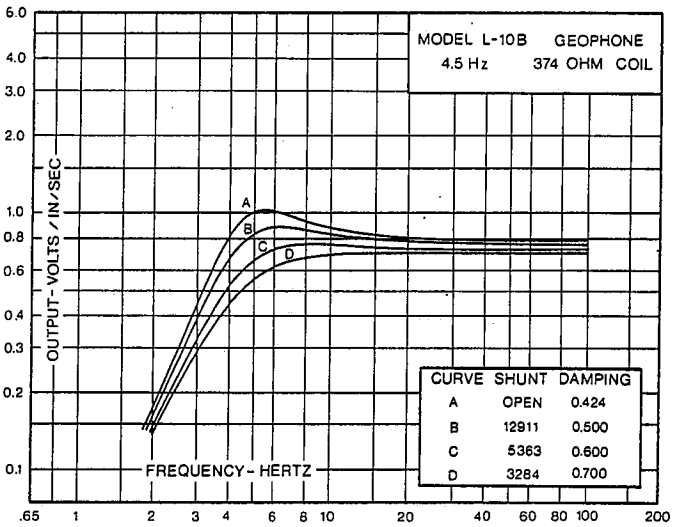

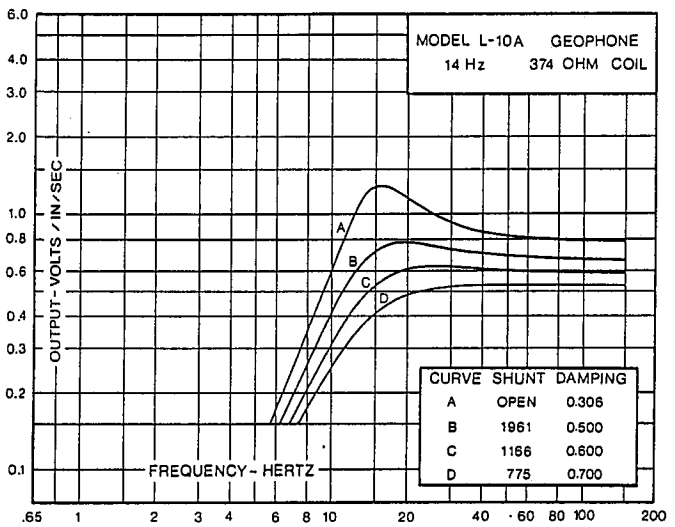

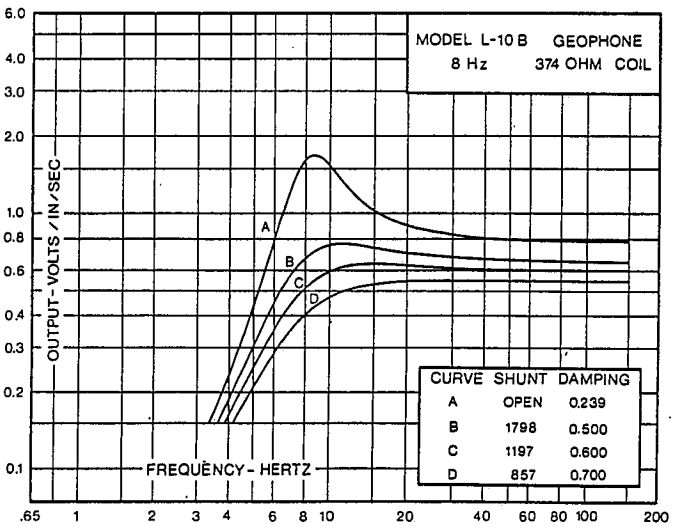

MARK PRODUCTS, U.S. INC.
Area 713/498-0600
10507 Kinghurst Dr.
Houston, Texas 77099
Telex 76-2069

MARK PRODUCTS, LTD.
Area 403/275-3544
1108 55th Ave. N.E.
P.O. Box 73
Calgary, Alberta, Canada T2P 2G9

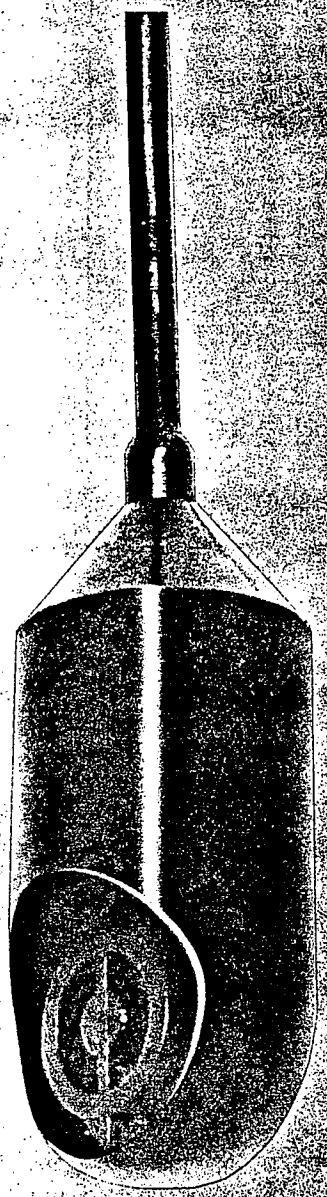

P-44 HYDROPHONE

FEATURES

HIGH OUTPUT
LOW SENSITIVITY LOSS
TO DEPTHS OF 250 FT
ECONOMICAL
RESONANT FREQUENCY
8 HZ or 10 HZ
ACCELERATION CANCELLING
EASY POLARITY CHECK

The P-44 Hydrophone is a 100% molded polyurethane unit that eliminates case type water leakage and offers to the industry an economical unit for multiple usage.

It is designed to spill any air entrapped around the unit, thereby increasing its high frequency response without parasitic resonances.

The P-44 is transformer coupled. It has an acceleration cancelling piezoelectric crystal arrangement and an easy method for polarity test.

GENERAL SPECIFICATIONS

Natural Frequency	± 15%	8 Hz	10 Hz
Voltage Sensitivity	± 1.5 dB	7.5 volts/bar	14 volts/bar
Amplitude Response	± 1 dB	8 to 800 Hz	10 to 800 Hz

Impedance	250 ohms
D.C. Resistance	140 ohms
Maximum Working Depth	250 ft.
Depth at which permanent changes in character-istics occur	500 ft.
Operating Temperatures	0 to 35° C.
Cable Size	0.310 in.

Case Dimensions

Diameter	2 in.
Length	4⅜ in.
Weight	0.5 lbs.

HYDROPHONE P-44

Basic unit guaranteed for one year on prorated basis.

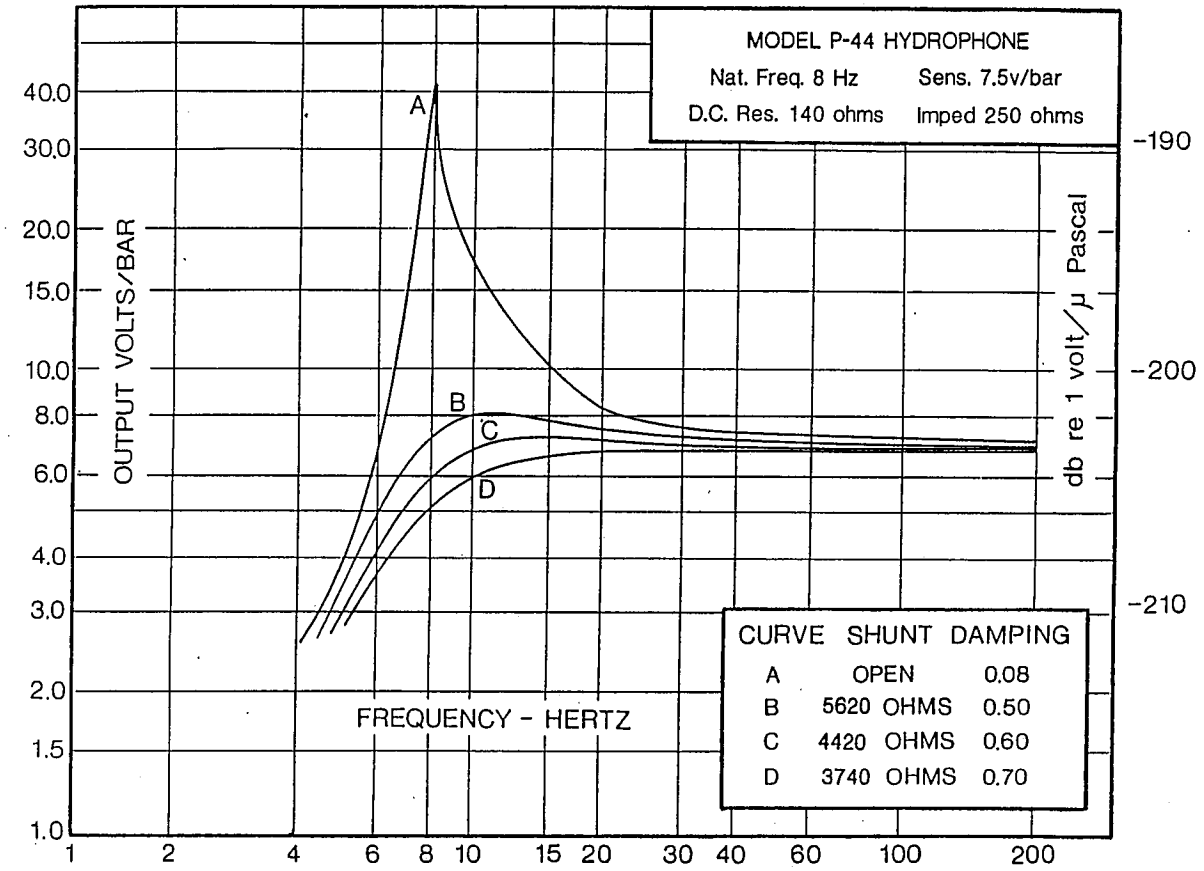

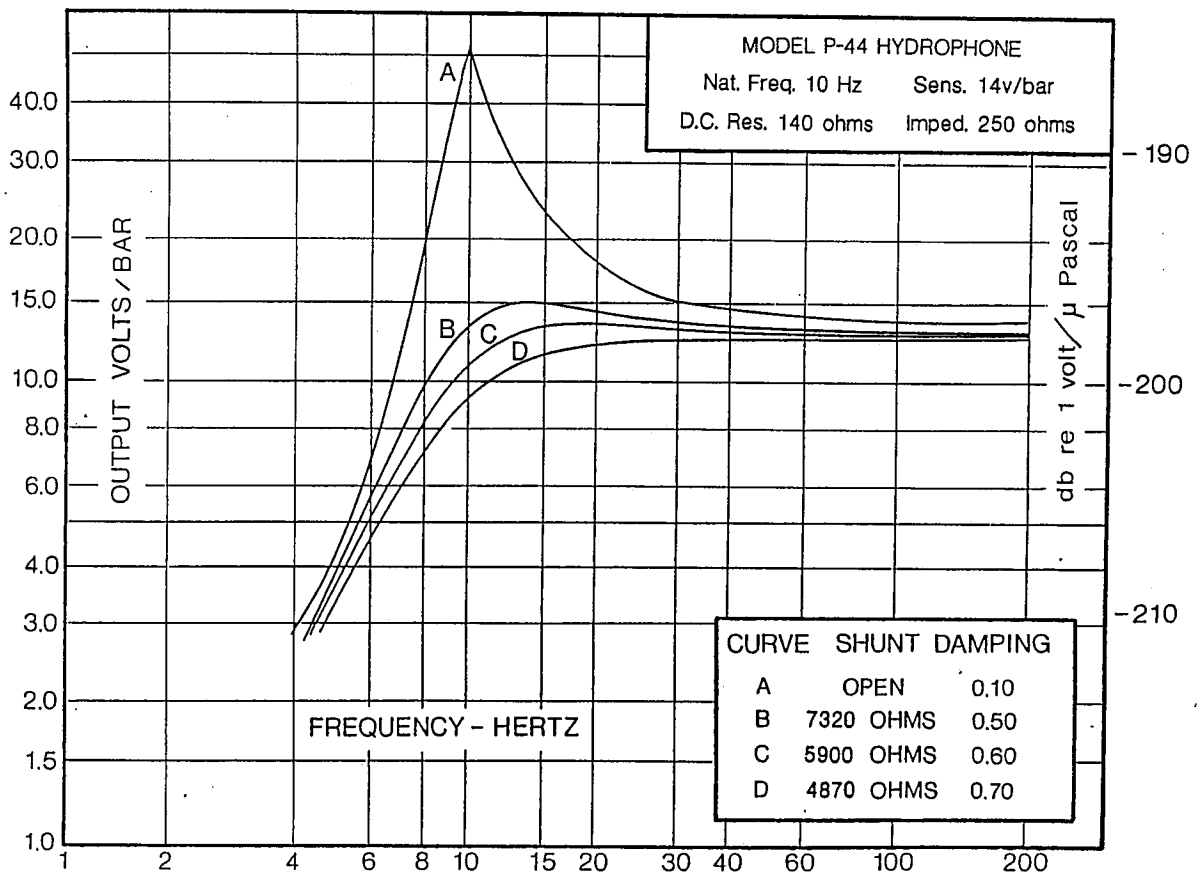

MARK PRODUCTS, U.S. INC.
Area 713/498-0600
10507 Kinghurst Dr.
Houston, Texas 77099
Telex 76-2069

MARK PRODUCTS, LTD.
Area 403/275-3544
1108 55th Ave. N.E.
P.O. Box 73
Calgary; Alberta, Canada T2P 2G9

KINEMETRICS

EARTHQUAKE ENGINEERING INSTRUMENTS

SSA-1

Solid State Accelerograph

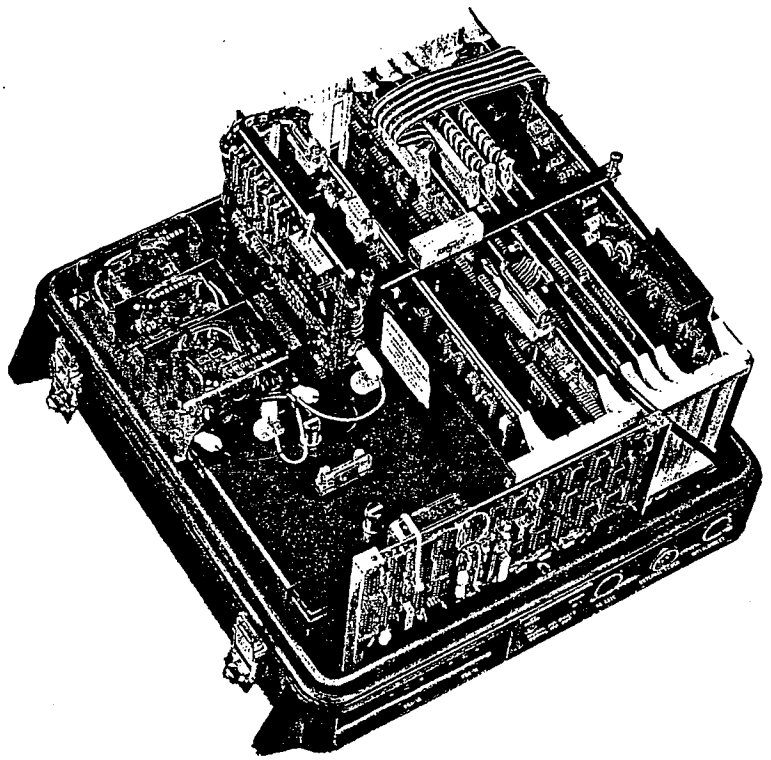

The SSA-1 Solid State Accelerograph has earned a world wide reputation for quality and reliability in digital strong motion recording. Designed specifically for data integrity and ease of playback, the SSA-1 pioneered the use of PCs for rapid access to data, and simple retrieval, both directly and remotely using standard modems.

The standard system includes Kinemetrics Force Balance Accelerometers, CMOS static RAM based, triggered event recording system, environmental enclosure, and battery backup for up to 7 days. Also provided are both QuickLook® and QuickTalk®: user friendly, menu-oriented software for retrieving and displaying earthquake data over the standard RS-232C link.

Key benefits of the SSA-1 include:

- versatility with four channel recording,
- ease of maintenance through plug-in boards,
- seismically qualified design tested to IEEE 344-1987 "Recommended Practices for Seismic Qualification of IE Equipment for Nuclear Power Stations",
- networkable with other units through local or extended interconnect option,
- remote annunciation with output relay option.

USA – 222 VISTA AVE., PASADENA, CA 91107 – TEL. (818) 795-2220; FAX (818) 795-0868; TLX 67-5402 • SWITZERLAND – Z.I. LE TRÉSI 3, 1028 PRÉVERENGES – TEL. – (21) 8032829 FAX (21) 8032895

GENERAL DESCRIPTION

The SSA-1 is a digital strong motion accelerograph designed to monitor ground motion, and trigger and record earthquakes which exceed a predetermined threshold. Data is recorded in CMOS static RAM, and played back through an RS-232C interface. The system is designed to operate from internal batteries which are normally trickle charged. The CMOS solid-state memory is 512K bytes on a plug-in card, and is expandable to nearly eight megabytes. Standard recording time is approximately 18 minutes, 288 minutes with the larger memory. The sample rate is 200 samples per second per channel.

With a resolution of 1 part in 2000, the SSA-1 can record a full scale of 1000 gals as well as perturbations as small as .5 gals in the same record. The frequency response from zero to 50 Hertz enables the SSA-1 to be used on a wide variety of applications. The simple RS-232C serial interface facilitates connection to telephone lines for remote interrogation. Event time, duration and peak acceleration are recorded in each event header for rapid retrieval and evaluation.

SSA-1 SPECIFICATIONS

Sensor

Type:	Internal, orthogonally oriented triaxial FBA
Full Scale:	Standard unit: 2g.
Natural Frequency:	50 Hz nominal
Damping:	70% critical
Bandwidth:	DC to 50 Hz

Data Acquisition Characteristics

Sample rate:	200 samples per second (sps) per channel
Number of channels:	Three. Longitudinal, vertical and transverse (L,V,T). Optional: four.
Anti-alias filter:	2 pole, 50Hz, Butterworth
Frequency response:	DC to anti-alias filter cutoff
Sensitivity:	±2.5 volts full scale (Full scale sensitivity is adjustable with preamp settings of 1, 2, 4 or 8)
Resolution:	12 bits, offset binary coding
Noise:	Approximately 1 lsb in 12 bit system

Pre-event Memory
Selectable in steps from 0 to 15 seconds

Trigger
Programmable threshold trigger, 0.1 to 10% of full scale, bandwidth .1 Hz to 12 Hz.

Post-event Hold Time
10, 15, 30, 60 and 90 seconds

Recording Characteristics

Recording medium:	512 kilobytes of CMOS static RAM standard (with battery back-up)
Recording capacity:	Approximately 18 minutes of 3 channel 200 sps data using linear-predictor type data compression algorithm.
Playback system:	Direct or remote RS-232C connection of SSA-1 to IBM-PC (or 100% compatible) at standard baud rates to 38.4 kilobaud. File transfer uses standard Xmodem protocol. Includes Kinemetrics QuickLook® and QuickTalk® programs as well as an ever-expanding assortment of other support software.

Environmental

Operating Temperature:	-20°C to +65°C (-4°F to +149°F)
Humidity:	100%

Batteries

Primary Power Source:	Single supply operation. Two internal 12 volt 6.5 Ah battery. Primary batteries provide approx 7 days of operation without charging. External battery connection fully protected, e.g., polarity, fuse, Tranzorb®, etc.
Backup batteries:	3.6 volt lithium batteries for clock and RAM backup.

Battery Charger
Wall mounted unit supplied. 110/220 Vac, 47-63 Hz operation.

Power Consumption

Operating Voltage:	11 to 14 Vdc
Current Drain:	Approximately 75 mA

Dimensions

Length:	400mm (15.5")
Width:	410mm (16")
Height:	200mm (8")
Weight:	17.5 kg (38.5 lbs)
Mounting:	Single hole for (1/4") stud

Controls
Internal power ON-OFF switch.
Internal DIP switch for baud rate setting, access to password and special diagnostic functions.
All other functions initiated from SSA-1 monitor program.

Indicators
EVENT and AC CHARGE (LEDs)

Standard I/O Connectors
RS-232C Command Port
DCE Interface, 8 bits with no parity. Baud rates of 300, 600, 1200, 2400, 4800, 9600, 19200, 38400 baud. DIP switch selectable. XON-XOFF protocol used for ASCII communication. Xmodem checksum and CRC protocol used for data transfer.
External Power
Connection to charger (and optional external battery).
Interconnect
Local interconnect for common start, common sampling, and common time.

Timing System
Internal clock standard. Records time of event in header. (Accuracy approx. $\pm 5 \times 10^{-5}$ from 0-50°C). Optional higher accuracy time code generators and time code receivers available for precise timing. Recommended for interconnected units.

ORDERING INFORMATION

SSA-1	P/N 107200
Options	
Provision for 4th channel input	P/N 107310
Provision for External FBA-23	P/N 107315
Additional 3-pole filter board	P/N 107305
External FBA Force Balance Accelerometers, replacing standard internal sensors, specify full scale 1/4, 1/2, or 1g	
FBA-11 Uniaxial Surface	P/N 105000
FBA-23 Triaxial Surface	P/N 105610
FBA-23DH Triaxial Downhole	P/N 108350
Expansion Memory (in place of standard 512 Kbytes)	
Specify 1, 2, 3, 4, 6, or 8 Mbytes	Consult Factory
OMEGA Synchronized Clock, includes cable, preamp and antenna	P/N 107335
GPS	Consult Factory
TCG-2 Time Code Generator (high accuracy)	P/N 107210
WWVB Time Broadcast Receiver	P/N 107220-04
A60-FS Antenna for WWVB, incl. cable	P/N 790011
Accessories	
Cable, SSA-1/2 to modem, RS-232C	P/N 107393
Cable, SSA-1/2 to PC, RS-232C	P/N 107392-01
Cable, local interconnect, SSA-1/2, 3 ft.	P/N 500305-02
Extended Interconnect System Consists of transient protection box, cable, accessory parts. Specify w/ or w/o SMA-1 option	P/N 107213
Interconnect cable, Box to Box	P/N 700302
Interconnect cable, Box to SMA-1	P/N 700245
Extender Board	P/N 107375
External Mounting Kit	P/N 107395
TCG-2PR w/accessory cables Time Code Generator Portable Reference	P/N 107205
Supplies	
Battery, rechargeable, set	P/N 103413
Battery, backup clock	P/N 700300
Battery, RAM backup	P/N 700300
Desiccant	P/N 700049

KINEMETRICS

EARTHQUAKE ENGINEERING INSTRUMENTS

FBA-3

Force Balance Accelerometer

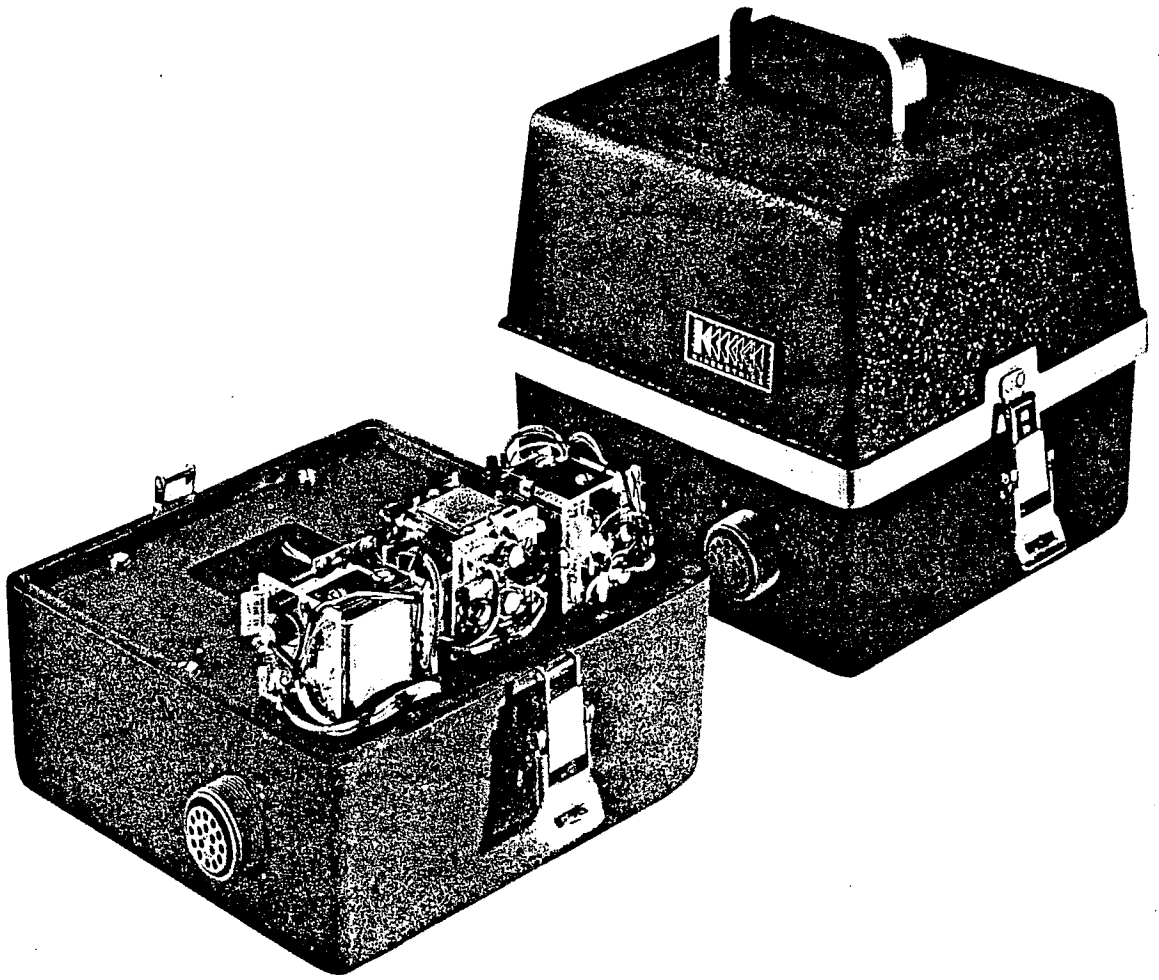

The FBA-3 Force Balance Accelerometer is a high-sensitivity, low-frequency triaxial device suitable for a variety of seismic and structural applications. It is an economical instrument characterized by high reliability, ruggedness and low current drain.

Designed to meet the stringent requirements of USNRC Regulatory Guide 1.12 for nuclear power plants, the FBA-3 is deployed in over 100 nuclear power plants in the United States and abroad. Frequency response is flat from dc to 50 Hz. Nominal full-scale range is ±1 g, but optional full-scale ranges are available.

The FBA-3 is packaged in a cast aluminum base and cover, sealed to prevent the entrance of moisture and dirt. The three accelerometers are orthogonally mounted on an internal deck plate.

KINEMETRICS INC., TWO TWENTY TWO VISTA AVENUE, PASADENA, CA. 91107 (213) 795-2220 - TELEX 67-5402 KMETRICS PSD

KINEMETRICS

EARTHQUAKE ENGINEERING INSTRUMENTS

TECHNICAL DESCRIPTION

The FBA-3 is a spring-mass device which uses variable capacitance transduction, as shown in the schematic below. The output is fed back to the parallel

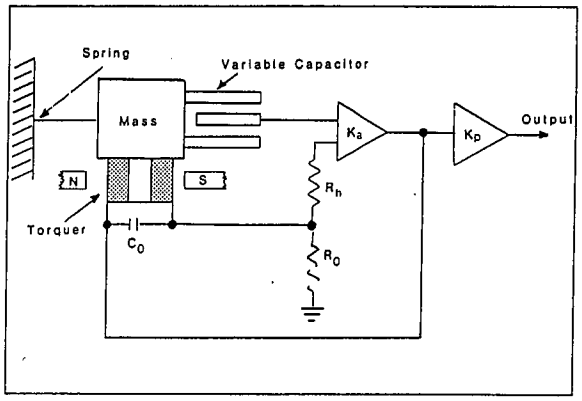

combination of capacitor C_0 and the torquer coil, which is an integral part of the mass. From the coil the feedback loop is completed through resistors R_0 and R_h. This has the effect of stiffening the system, thus increasing the natural frequency to 50 Hz. Resistor R_0 (with C_0) controls the damping, which normally is adjusted to 70% critical. The acceleration sensitivity is controlled by the gain K_p of the post-amplifier.

TECHNICAL SPECIFICATIONS

Full-scale range
± 1.0g, (¼, ½ & 2 g optional)
Natural frequency
50 Hz*
Bandwidth
DC to 50 Hz (3dB point)
Damping
70% critical*
Operating temperature range
– 20° to 70°C (0° to 160°F)
Output (full-scale)
± 2.5V* into 50,000 ohms
Zero offset
Less than 25 mV*
Cross-axis sensitivity
Less than .03 g/g*
Linearity
Less than 1% of full-scale
Noise (0 to 50 Hz)
Less than ± 25 μV
Noise (0 to 10,000 Hz)
Less than ± 2.5 mV*
Dynamic Range (0 to 50 Hz)
100 dB
Temperature effects (zero drift and sensitivity)
Less than 2% of full-scale
Supply voltage
+/– 12 Vdc
Turn-on time
Operational within 0.1 second after power applied
Calibration
Electrical commands can be applied to produce damping and natural frequency outputs

*Measured values furnished with each sensor.

SEISMIC QUALIFICATION

Kinemetrics/Systems has provided strong motion accelerograph systems to over 100 nuclear power plants throughout the world for over 10 years. Kinemetrics products have been carefully tested for generic qualification to meet most existing and future requirements.

Kinemetrics seismic test characteristics for the FBA-3 accelerometer have the following general characteristics:

1. Biaxial: horizontal and vertical rotated, and repeated at 90 degrees.
2. Five OBE's (Operating Base Earthquake) followed by one SSE (Safe Shutdown Earthquake) in each direction.
3. Random excitation controlled at ⅓ octave intervals with incoherent phasing between axes, over the range 1 to 40 Hz.
4. Test duration of thirty seconds minimum.
5. Minimum SSE RRS ZPA (Required Response Spectrum Zero Period Acceleration) of 2 g with 3% damped response accelerations exceeding 6 g in the range 2 to 20 Hz.
6. Sensor SSE RRS ZPA of 6 g with 1% damped response accelerations exceeding 14 g in the range 2 to 30 Hz.
7. Functional testing conducted on devices prior to, during and following seismic tests.

In addition, Kinemetrics has performed RIM (Required Input Motion) testing of pipe-mounted sensors. The FBA-3 accelerometer has been qualified as follows:

1. Biaxial: horizontal and vertical rotated, and repeated at 50 degrees.
2. Steady-state sinusoidal dwell tests at ½ octave intervals from 1 to 45 Hz.
3. Dwell duration of 30 seconds at each frequency.
4. 0-Peak input acceleration at each frequency of 4.5 g except limited by displacement (below 5 Hz).
5. Functional tests conducted on devices prior to, during and following seismic tests.

PHYSICAL CHARACTERISTICS

Dimensions
200mm × 200mm × 200mm water tight enclosure (8" cube)
Weight
7 kg (15 pounds)

APPENDIX 2

Polynomial Baseline Correction

Another way of removing the baseline or low frequency problem is to fit a polynomial to the displacement time history and remove it from the acceleration time history. Assume

$$a(t) = a'(t) + a_0 + a_1 t + a_2 t^2$$

where a(t) is acceleration time history with low frequency noise and $a'(t)$ is the noise-free record. Then

$$d(t) = d'(t) + \frac{a_0 t^2}{2} + \frac{a_1 t^3}{6} + \frac{a_2 t^4}{12}$$

and the coefficients a_j are determined by a fit to d(t) because the long period noise is amplified in d(t).

The noise free record $a'(t)$ is obtained by subtraction of the polynomial from a(t). Note, do not start with a quadratic in displacement because the constant and linear terms will be lost in going to acceleration:

$$d(t) = d'(t) + a_0 + a_1 t + a_2 t^2$$

$$a(t) = a'(t) + a_2 .$$

Evaluation and Implementation of an Improved Methodology for Earthquake Ground Response Analysis

Uniform Treatment of Source, Path and Site Effects

Seminar 4

(9/29/94, 49 p.)

Empirical Attenuation Models

a) General References
b) Review: Instrumentation and Data Processing
c) Introductory Comments
d) Development of Predictive Equations
e) Summary of Predictive Relations
f) Comparisons of Predictive Relations
g) Future Trends

CALTRANS

SEMINAR ON STRONG GROUND MOTION

Seminar 4; September 29, 1994

Empirical Attenuation Models

a) General References:

1994 Boore et al.: Estimation of response spectra and peak accelerations from western North American earthquakes: and interim report. *U.S. Geological Survey Open-File Rept.* 94-127.

1994 Campbell and Bozorgnia: Near-source attenuation of peak horizontal acceleration from worldwide accelerograms recorded from 1957 to 1993. *Fifth U.S. Nat'l Conf. on Earthquake Engineering*. Chicago, Illinois.

1993 Boore et al.: Estimation of response spectra and peak acceleration from western North American earthquakes: An interim report." *USGS* Open-File Rept. 93-509.

1993 Idriss: Procedures for selecting earthquake ground motions at rock sites. *National Institute of Standards and Technology*. NIST GCR 93-625.

1993 Campbell: Empirical prediction of near-source ground motion from large earthquakes. in V.K. Gaur, ed., *Proceedings, Intern'l Workshop on Earthquake Hazard and Large Dams in the Himalya.* INTACH, New Delhi, p. 93-103.

1993 Sadigh et al.: Specification of Long period ground motions. Proceedings ATC-17-1, Seismic Isolation Systems, vol. 1.

1989 Campbell: Empirical prediction of near-source ground motion for the Diablo Canyon Power Plant Site, San Luis Obispo County, California. *U.S. Geological Survey Open-File Rept.* 89-484.

1988 Joyner and Boore: Measurement, characterization, and prediction of strong ground motion. *Earthquake Engineering and Soil Dynamics II,*

Recent Advances in Ground-Motion Evaluation, Proc. of the Specialty Conf. Sponsored by the Geotechnical Engineering Div. of the ASCE 1, 43-102.

1987 Idirss: Earthquake ground motions. Lecture presented at the EERI course on Strong ground motion, in Pasadena, California.

1985 Idriss: Evaluating seismic risk in engineering practice. *Proc. Eleventh Internat. Conf. on Soil Mech. and Foundation Eng.*, San Francisco, edited by A.A. Balkema, Rotterdam, 1, 255-320.

1981 Joyner and Boore: Peak horizontal acceleration and velocity from strong-motion records including records from the 1979 Imperial Valley, California, earthquake. *Bull. Seism. Soc. Am.*, 71, 2011-2038.

b) Review: Instrumentation and Data Processing

Seismograph: device to detect and record earth motions

1) System Requirements

a) Dynamic range: $db = 20 \log \frac{A}{A_0}$. The range between the largest signal (A) and smallest (A_0). For an accelerograph considering peak acceleration, a nominal maximum could be 2g and background noise at 10 Hz at an average site might be 10^{-6} g. Then

$$db = 20 \log \frac{2}{10^{-6}} = 126$$

or over 6 orders of magnitude. This is an enormous range and is generally not met by recording systems as it implies nearly 24 bit sampling ($20 \log 2^{\text{bits}-1} =$ db).

b) Bandwidth: Range in frequency between lowest and highest frequencies of interest. For strong ground motions, we are generally interested in about 0.05 Hz (20 sec) to about 100 Hz. To prevent aliasing the analogue signal should

extend up to about 200 Hz.

c) System Linearity: System response must be independent of the level of input motion (126 db, over 6 orders of magnitude).

d) Stability and Time In Variance: This generally refers to a very low drift rate.

c) Sensitivity: Adequate amplification with low noise in the frequency range of interest: 10^6 for sensitive seismograph to about 1-10 for strong motion accelerograph.

f) Degrees of Freedom: Generally 1 with minimum cross axis sensitivity ($< 1\%$).

g) Time Accuracy: Within about 0.1 sec UTC.

2) Sensing Device (inertial seismometer)

a) Mechanical

b) Optical

c) Electrical

1) Velocity transducer

2) Displacement transducer

3) Amplifier: db 0-120, noise levels $\approx$ 1 μV (0.05 - 200 Hz). Signals as low as 2.5 μV (accelerometer sensing earth noise).

4) Recorders: Dynamic Range

a) Analogue: film 40 db
tape 46 db

b) Digital: 12 bit 66 db
16 bit 90 db

5) Filters: Remove noise (earth and system) and shape instrument response.

Figure 4: Accelerometer (displacement transduce) response curves

Figure 5: Velocity (velocity transducer) response curves

Figure 7: Butterworth bandpass filters

Figure 8: Signal-noise characteristics

Figure 10: Instrument window

6) Processing

a) Instrument removal

b) Filter out low- and high-frequency noise

1) High-frequency noise, easy to select cut-off frequency

2) Low-frequency noise, difficult to select cut-off frequency, use $T_c \approx 0.0033\ e^{1.15M}$ to estimate source corner period. Should recover periods to at least T_c.

c) Introductory Comments

Empirical ground motion models may be broadly defined as predictive relationships based predominately upon recordings of strong ground motions or explosions (e.g. UNE's at Yucca Mountain). Results from numerical modeling may be used to guide in the selection of values or range of permissible values for coefficients and (or) to supplement the empirical data base. By definition, however, the empirical models must be largely constrained (coefficients determined by) recordings of strong ground motions. In order to gain some insights into the functional forms used as empirical models, it is instructive to return to the simple point-source model and examine the source, path, and site terms. These terms can be directly related to the terms in the empirical relations and the physical basis for the empirical relations established.

1) Physical Basis for Empirical Models

From our point-source ground motion model for Fourier amplitude spectra

$$\tilde{a}(f) = \frac{c}{1+(\frac{f}{f_c})^2} M_o \quad x \quad \frac{1}{R} e^{-\frac{\pi f R}{VQ(f)}} \quad x \quad A(f)\ e^{-\pi \kappa f}$$

source x *path* x *site*

Taking logs (strong ground motion peak values are approximately log normally distributed random variables)

$$\log \tilde{a}(f) = \log \left(\frac{c}{1+(\frac{f}{f_c})^2}\right) + \log M_o \qquad \textit{source term}$$

$$+ \log (1/R) - \frac{\pi f R}{V Q (f)} \qquad \textit{path term}$$

$$+ \log (A(f)) - \pi \kappa f \qquad \textit{site term}$$

and from $\mathbf{M_o}$ - **M** relation $\log \mathbf{M_o} = 1.5\ \mathbf{M} + 16.1$,

then

$$\log (\tilde{a}(f)) = \log\left(\frac{c^1}{1+(\frac{f}{f_c})^2}\right) + 1.5\ M \qquad \textit{source term}$$

$$+ \log (1/R) - \frac{\pi f R}{V Q(f)} \qquad \textit{path term}$$

$$+ \log (A(f)) - \pi\ \kappa\ f \qquad \textit{site term}$$

where $\log c^1 = \log c + 16.1$.

Source Terms:

a) Constant term.

b) Magnitude scaling term; **M**, f_c. Note $\log \tilde{a}(f) \propto \mathbf{M}$ in this model. As a result, $\tilde{a}(f)$ is unbounded as **M** increases. This is an consequence of all the moment being released from a point and suggests the point-source model should break down (overpredict) beyond some **M**. For a finite source, as **M** increases so does the area ($\log A = -3.49 + 0.91\ \mathbf{M}$; Wells and Coppersmith, 1994). As a result, more moment is released at greater distances so $\tilde{a}(f)$ saturates

or reaches a limit as **M** increases.

Path Terms:

a) (1/R) term: geometrical attenuation for a body wave. Appropriate for R < 70-100 km; beyond dealing with surface waves $\propto 1/\sqrt{R}$.

b) $\frac{\pi f R}{V Q(f)}$: term $\propto$ to R and reflects attenuation due to crustal damping.

Site Terms:

a) log (A(f)): rock or soil amplification term.

b) $\pi\kappa f$: rock or soil damping term.

2) General Functional Form of Empirical Attenuation Relations:

$$\log y = c_1 + c_2 M + c_3 M^{c_4} + S\,(mechanism) + \quad source$$

$$c_5 \log (r + c_6 \exp (c_7 M)) + c_8 r + \quad path\ and\ source$$

$$s(site) \quad site$$

where y is a peak ground motion value PGA, PGV, RSA (T, η), FAS (T) and c_j, S is determined by regressions on data and r is some distance measure to a finite source.

3) Term Comparison: Physical model to empirical model

	POINT-SOURCE	EMPIRICAL
source terms	$\log\left(\frac{c^1}{1 + (\frac{f}{f_c})^2}\right) + 1.5\ M$	$c_1 + c_2\ M + c_3\ M^4 + S\ (mechanism)$

with source parameters **M**, f_c. The radiation pattern coefficient $R(\theta, \phi)$ is included in c^1 (radiation pattern affects $\hat{a}(f)$ through mechanism).

path terms	$\log(1/R^n)$	$c_5 \log\ (r + c_6\ exp\ (c_7\ M)) + c_8\ r.$
	$\frac{\pi f R}{V Q(f)}$	

The term c_6 exp (c_7 **M**) mimics an increase in distance as **M** increases and results in ground motion saturation for small r. For $c_6 = 0$, c_5 is the effective geometrical attenuation power. C_8 is the crustal damping term.

site terms	log (A(f))	S
	$\pi \kappa f$	

There is a direct correspondence between the physical parameters in the simple ground motion model and functional form for empirical models: i.e. the empirical models are driven by source, path, and site physics with coefficients rather than model parameters determined by data. The importance in having physically based functional forms lies in increased confidence in extrapolations to distances and magnitudes which are poorly represented in the empirical data base.

d) Development of Predictive Equations

Empirical predictive relations have a long history in ground motion specification and date back to the early 1970's (See Idriss (1979) for a comprehensive review of relationships developed prior to 1979). Naturally the earlier predictive relationships were based upon

intensity due to the paucity of instrumental data. While very useful in semi-quantitative appraisals of ground motion and assessment of size for pre-instrumental earthquakes, the large uncertainties associated with intensity data make this approach unsuitable for quantative estimation of strong ground motions.

In areas of relative high seismicity and population density such as urban California, instrumental strong motion data of sufficient quantity and quality (supplemented by world-wide recordings) to reasonably constrain empirical regressions became available in the late 60's and early 70's. The **M** 6.5 1971 San Fernando earthquake provided the first data set for a large earthquake comprising a variety of site conditions and distance ranges. Eight years later, the **M** 6.5 1979 Imperial Valley earthquake provided both a good check for the existing relationships (particularly for deep soil sites) and (with the nuclear power industry) the impetus for development of the modern predictive relations based largely on strong motion data recorded in California. While there are a number of empirical relationships (see Joyner and Boore, (1988) for an excellent review and discussion of extant empirical predictive relations) we will concentrate on four which are identified alphabetically by their originators: Campbell, Idriss, Joyner and Boore, and Sadigh. For these relationships, the predictive equations for both soil and rock will be presented to get a feel for the variations implicit in the use different functional forms, subsets of the data, and site definitions. Following these presentations, we'll look at some emerging developments on effects of fault type, near source effects, and differences between hanging wall and foot wall site locations for dipping faults.

It should be emphasized that, by definition, predictive relations for strong ground motions are transitory and, under the best circumstances, are updated subsequent to well recorded large earthquakes (**M** $\geq$ 6.5) or at least every several years. As a result, the originators of any set of relations used should be contacted at least annually for updates and implementation information.

1) Campbell:

To implement his current relationship, Campbell (personal communication, 8/15/1994) recommends the use of peak ground acceleration found in Campbell and Bozorgnia (1994) for

alluvium, soft rock, and hard rock. For response spectral ordinates, Campbell recommends using the response spectral shapes (PSA/PGA) for alluvium and soft rock found in Campbell (1989) and for hard rock found in Campbell (1993) combined with the PGA from Campbell and Bozorgnia (1994).

a) Predictive relation for an average horizontal component PGA at stiff soil, soft, and hard rock sites.

$$\ln(PGA) = 3.512 + 0.904\,M - 1.328 \ln\left(R_S^2 + (0.149\,EXP\,(0.647\,M))^2\right)^{1/2} + (1.125 - 0.112 \ln(R_S) - 0.0957\,M)\,F + (0.440 - 0.171 \ln(R_S))\,S_{SR} + (0.405 - 0.222 \ln(R_S))\,S_{HR} + \epsilon$$

R_S = closest distance ($\leq$ 60 km) to seismogenic rupture (min 3 km) and is magnitude dependent.

M	min R_S (km)
5.0	7.3
5.5	5.8
6.0	3.5
6.57	3.0

M = moment magnitude

F = 0 SS, NS

0.5 unknown

1 RS, OB

S_{SR} = 1 soft rock sedimentary (Tertiary);

S_{HR} = 1 hard rock crystalline, metaporyphic;

S_{SR} = S_{AR} = 0 alluvium.

$\sigma_{\ln PGA}$ = 0.889 - 0.691 **M** $M < 7.4$

0.38 $M > 7.4$

b) Predictive relation for 5% damped an average horizontal component PSV at hard rock sites. Compute PSV/PGA and scale with PGA from (a) above for currently recommended PSV.

$$\ln(y) = \beta_o + 0.683\,M\,\beta_1 \tanh(0.647\,(M - 4.7)) - 1.01 \ln(r) - \propto R_s + 0.27\,F + ((\beta_2 - 0.105 \ln(R_s)))\,S + ((\beta_2 \text{ tank } (0.620\,D) + \epsilon$$

$$r = (R_s^2 + (0.0586 \text{ EXP } (0.683\,M))^2)^{1/2}$$

$$\propto = \beta_4 + \beta_5\,M$$

S = 0 soil

1 hard rock

R_s = closest distance to seismogenic rupture

For hard rock S = 1, D = 0

Table 1 contains the model coefficients and uncertainties.

c) Predictive relation for PSV at firm soil sites and at soft rock sites. Compute PSV/PGA and scale with PGA from (a) above for currently recommended PSV. Firm soil sites include sands, gravels, and low plasticity clays with depths exceeding about 30 ft. Bay mud and old bay clay sites are excluded. Table 2 shows the model and Tables 3, 4, 5 contain model coefficients for PGA, PGV, and 5% damped PSV for an average horizontal component and for the vertical component as well as uncertainties.

d) Features of interest:

1) Saturation: $\ln (R_s^2 + (0.149 \text{ EXP } (0.67\,M)^2)^{1/2}$ terms in PGA relation.

2) Mechanism factor is magnitude and distance dependent: F term in PGA relation.

3) Site term is distance dependent: S terms is PGA relation.

4) Parameter D: depth to basement rock. Defined as seismogenic basement or top of crystalline or metamorphic basement rocks. For sedimentary basements D is characterized as the depth of high in-situ velocities, low velocity gradients, and small impedance contrasts. If some doubt exists for the appropriate value of D, the uncertainty of Sadigh (1991) should be substituted.

5) Building effects: κ_i factors in soil/soft rock relation.

6) Uncertainties are not magnitude dependent.

e) Examples: Figure 1 shows the effects of mechanism verses distance for M 5.0, 6.5, and 8.0 as well as the soft rock/hard rock amplification factors verses distance for PGA. Earthquakes with reverse mechanisms are predicted to have generally higher PGA values than strike slip mechanisms particularly at close-in distances. Also seen in Figure 1 (top) is the effect of saturation showing weaker magnitude scaling for PGA at larger magnitudes and at closer distances.

Also shown in Figure 1 (bottom) are the soft rock/hard rock amplifications for PGA. Soft rock sites are predicted to have higher PGA values than hard rock sites at all distances with the difference (about 15%) increasing with distance.

2) Idriss

The predictive relation of Idriss is in equation form for PGA for rock, stiff, deep, and soft soil and 5% damped PSA for rock (Idriss, 1993). The rock PGA relation has been recently updated (personal communication, 9/11/1994) and the soil PGA relation is referred to as Idriss (1991) and appears in Idriss (1992), a presentation at the Fall seminar on "Earthquake Ground Motions and Foundation Design" in San Francisco on October 15, 1992. For soil PSA charts (Tables) are given for PSA/PGA at M_s 6.75 for stiff, deep, and soft soils. The stiff and deep soil categories are deposits of sands, gravels, and low PI clays generally less than about 200 ft for stiff and beyond for the deep category. Soft profiles are predominately cohesive soils with low shear-wave velocities.

To scale the soil PSA to magnitudes other than M_s 6.75 Idriss (1987) has additional charts which are site and distance independent for M 4.5-9.2 normalized to M_s 6.75 at periods 0.2, 0.5, 2, and 8 seconds. For intermediate periods, interpolation must be used.

a) The predictive equation for median PGA at all sites and 5% damped PSA at rock sites is given by:

$$\ln (y) = [\alpha_o + EXP\ (\alpha_1 + \alpha_2\ M)] +$$

$$[\beta_o - EXP\ (\beta_1 + \beta_2\ M)] \ln (R + h) +$$

$$F\ \phi + \epsilon$$

where

M is M_L for $M \leq 6$ and M_s for $M > 6$,

R = closest distance to rupture surface for $M \geq 6$ and hypocentral distance for $M < 6$.

F = 0 SS

0.5 OS

1.0 RS.

The coefficients are listed in Table 6 for PGA for all site conditions and in Table 7 for PSA at rock sites. To evaluate PSA at stiff, deep, and soft soil sites, 5% damped response spectral shapes for M 6.75 are listed in Table 8. Table 9 lists factors to scale the M 6.75 shapes to other magnitudes ranging from 4.5 to 9.25.

b) Features of interest:

1) No saturation term.

2) Mechanism factor is magnitude and distance independent.

3) Charts for response spectral shapes for soil sites.

4) Uncertainties are magnitude dependent.

c) Examples: Figure 2 shows 5% damped response spectral shapes (PSA/PGA) for M_s 6.75 for rock stiff and deep soils. The figure shows higher magnification at short periods for stiffer sites (rock > stiff soil > deep soil) and the converse at long periods.

Figure 3 shows the magnitude scaling for spectral shapes at distinct periods ranging from 0.2 sec to 8.0 sec. The curves are normalized to $M_s = 6.75$ and pass through 1 and that point. The curves show a strong dependence of shape on magnitude reflecting and increase in long period spectral content as magnitude increases (Silva and Darragh, 1994).

3) Joyner and Boore

This relationship was first published in a complete form in 1981 (Joyner and Boore, 1981). It has been recently revised and now exists as Boore et al. (1993, 1994).

a) The predictive equation for PGA, PGV, and PSV for site classes A, B, and C is given as

$$\log (y) = b_1 + b_2 (M - 6) + b_3 (M - 6)^2 +$$

$$b_4 + b_5 \log r +$$

$$b_6 G_B + b_7 G_c + \varepsilon_r + \varepsilon_e$$

where

$$r = (d^2 + h^2)^{1/2},$$

d = closest distance to the surface projection of the fault,

$G_B = 0, \quad G_c = 0$ *site class A,*

$G_B = 1, \quad G_c = 0$ *site class B,*

$G_B = 0, \quad G_c = 1$ *site class C.*

The relationship is valid for M 5.0-7.7, d $\leq$ 100 km and for PGA and PSV over the period range of 0.1-2.0 sec. Site categories are based on the average shear-wave velocity over the top 30m and are defined as follows:

Class	$\overline{V_S}$ *(m/sec) over top 30m*
A	> 750
B	360-750
C	180-360
D	< 180

Site class D was poorly represented in the data and is not considered in the regressions. The 1981 edition of the predictive relationship (Joyner and Boore, 1988) used only a soil and rock classification with most of the rock sites falling into class B and soil sites into class C. Class A corresponds to relatively hard rock profiles. Tables 10 and 11 list the coefficients and uncertainties.

b) Features of interest:

1) No saturation,

2) No mechanism factor,

3) Site classification based on shear-wave velocity.

c) Examples: Figure 4 shows PGA and 5% damped PSV (0.3 and 1.0 sec) for M 6.5 verses distance for site classes B and C. For comparison the earlier relation (1981) for soil sites is also shown. At close distances, site class C has values similar to the soil site but at large distances ($\geq$ 30 km) the new relation (Boore et al., 1993, 1994) is consistently higher.

Figure 5 shows a similar plot for site class C with magnitudes 5.5, 6.5, and 7.5. For PGA, the absence of magnitude scaling is apparent, showing the same increase in level for each jump in magnitude.

4) Sadigh

The relationship of Sadigh is best described by Joyner and Boore (1988) which contains the PGA and 5% damped PSA relation as well as uncertainties for rock and soil. Recently the relation for rock has been updated (Sadigh et al., 1993) and is generally referred to as the CALTRANS relation.

a) For soil sites, the predictive relation for PGA and PSA is given by

$$\ln (y) = a + b\,M + C_1\,(8.5 - M)^{C\,2} +$$

$$d \ln (r + h_1\,EXP\,(h_2\,M))$$

where

M is moment magnitude,

r is the closest distance to the rupture surface.

The relationship is appropriate for strike-slip earthquakes and should be increased by 20% for reverse-slip events. Table 12 lists the coefficients and uncertainties for both soil and rock sites. The rock relation has been superseded and should not be used.

b) For rock sites, the predictive relation for PGA and 5% damped PSA for an average horizontal component is shown in Table 13 along with the coefficients. As with the soil relation, the values are appropriate for strike-slip earthquakes. For reverse/thrust and oblique-slip mechanisms, the relation is to be multiplied by 1.2 and 1.09 respectively. Table 14 lists the uncertainties and Table 15 shows the relation and coefficients for vertical motions.

For the rock relation, numerical modeling was used to guide extrapolations of long period (> 2 sec) spectral ordinates for large magnitudes up to M 8.0. This is the only relation which has used modeling as constraints beyond the range of data.

c) Features of interest:

1) Saturation term: ln ($r + h_1$ EXP (h_2 M)).

2) Uncertainties are magnitude dependent.

3) For the rock relation, the upper limit in magnitude is 8.0.

4) Mechanism factor is magnitude and distance independent.

d) Examples: Figure 6 shows 5% damped PSV for **M** 6.75 at a distance of 3 km along with numerical simulations. Figure 7 shows a similar plot for **M** 8.0 at 10 km. The **M** 6.75 empirical relation was used as a calibration for the simulations. The **M** 8.0 simulations were there used to guide the extrapolation of the empirical relation to **M** 8.0.

e) Examples of Distance Measures

To illustrate the different definitions of distance used in the predictive relations, Figure 8 shows examples for vertical and dipping faults respectively. For the vertical fault, the definitions are clear but some care must be taken in applications to dipping faults, particularly for the Boore et al. (1993, 1994) relation.

f) Summary of Predictive Relations

Relation	M Range*	Distance Range (km)	Period Range (sec)	Verticals
Campbell	4.7-8.0**	3-60	0.04-4.0	soft rock/soil
Idriss	4.6-7.4	1-100	0.03-5.0	-----
Boore	5.0-7.7	0-100	0.10-2.0	-----
Sadigh	4.5-8.0***	0-100***	0.05-7.5***	rock

*The magnitude range is that covered by data except for Sadigh where numerical simulations were used to extrapolate at larger magnitudes and long periods.

**M 8.1 1985 Michoacan, Mexico subduction zone earthquake included.

***For rock relation. For soil, upper limits are **M** 7.7, 50 km, and the period range is 0.1-4.0 sec.

g) **Comparisons of Predictive Relations**

1) PGA and PSA: Figures 9 and 10 show PGA verses horizontal fault distance for rock and soil sites respectively. Magnitudes 5.5 and 7.5 are shown to illustrate similarities and differences at the lower and upper ranges of interest for engineering applications (**M** 5.5 contributions are important in probabilistic seismic hazard evaluations). At rock sites (Figure 9) the relations are very similar for **M** 7.5 and show differences for **M** 5.5 particularly at close distances. At large distances, Boore et al. (1993) show significantly higher motions particularly for **M** 5.5. At soil sites (Figure 10) similar trends are seen except for the very high motions at close distances predicted by Boore et al. (1994) for **M** 7.5. This may be an artifact of the simple functional form not accommodating effects of nonlinear soil response as a component of the saturation term.

To compare 5% damped spectral shapes, Figures 11 and 12 show PSA/PGA for **M** 6.75 at a distance of 10 km for rock and soil sites respectively. The shapes have been extended at short periods by assuming saturation to PGA at 0.03 sec and linearly extrapolating from the shortest period each relation is defined to 1 at 0.03 sec. The spectral shapes are very similar for this magnitude except for the Campbell rock relation showing higher long period and lower short period amplifications. The similarity in shapes may lead one to infer that the shapes are better defined than the absolute levels. However, around **M** 6.5-6.75 is the magnitude range of a majority of the data (Seminar 2, Figure 22) and the relations are expected to be similar. Near the edges of the data base, however, is where differences due to functional forms, site definitions, and subsets of the data base used in the regressions are expected to manifest themselves in differences in predicted motions (Seminar 2). To illustrate these differences, spectral shapes are presented for **M** 7.75 at the same distance as in Figures 13 and 14. For both rock and soil sites, the shapes for **M** 7.75 show higher variability among the relations than at **M** 6.75.

To compare uncertainties for the predictive relations, Figure 15 shows the natural log of the standard errors verses frequency. In general, they have similar shapes and values, being

higher at low frequencies and decreasing with increasing frequency. The exception is Campbell which only moderately shows this trend and is significantly lower at low frequencies. This is the result of the inclusion of the depth to basement term D. The reduction in uncertainty at low frequencies by including a single term D reflecting sediment or soft rock depth suggests that a significant amount of the low frequency variability may be due to simple 1-dimensional effects.

h) Future Trends

1) Magnitude dependence of variability: uncertainty is lower for larger magnitudes or higher levels of motion.

a) Source and/or site effect?

2) Mechanism dependence of amplitudes: reverse-slip mechanisms have higher ($\approx$ 20-30%) PGA values than strike-slip (normal-slip about the same as strike slip) at the same fault distance,

a) Are the differences period and distance dependent?

b) Are higher stress drops associated with reverse slip earthquakes?

3) Hanging-wall verses foot-wall analyses suggest higher motions on the foot-wall ($\approx$ 20%)

a) Geometric effect?

4) Near-source effects

a) Saturation of PGA: source and/or site effect?

b) directivity/mechanism: for strike-slip earthquakes fault normal component larger than fault parallel ($\approx$ 20-40%) (see Seminar 1; Section d, Features of Strong Ground Motion).

TABLE 1

MODEL COEFFICIENTS

Y*	β_0	β_1	β_2	β_3	β_4	β_5	σ
PGA	-3.15	0	0	0	0.0150	-0.000995	0.50
Sa (0.04 s)	-3.14	0	0.22	0	0.0158	-0.00105	0.53
Sa (0.05 s)	-3.09	0	0.18	0	0.0161	-0.00105	0.57
Sa (0.075 s)	-2.83	0	0.18	0	0.0174	-0.00109	0.56
Sa (0.1 s)	-2.61	0	0.08	0	0.0174	-0.000988	0.58
Sa (0.15 s)	-2.37	0	-0.09	0	0.0160	-0.000730	0.60
Sa (0.2 s)	-2.32	0	-0.21	0	0.0139	-0.000470	0.64
Sa (0.3 s)	-2.36	0	-0.42	0	0.0115	-0.000273	0.61
Sa (0.4 s)	-3.02	0.60	-0.46	0.12	0.0103	-0.000212	0.65
Sa (0.5 s)	-3.36	0.75	-0.50	0.25	0.00825	0	0.67
Sa (0.75 s)	-4.03	1.06	-0.49	0.37	0.00734	0	0.69
Sa (1 s)	-4.73	1.37	-0.41	0.57	0.00655	0	0.72
Sa (1.5 sec)	-5.61	1.73	-0.29	0.72	0.00557	0	0.55
Sa (2 sec)	-6.24	1.96	-0.32	0.83	0.00496	0	0.52
Sa (3 sec)	-7.12	2.19	-0.13	0.86	0.00422	0	0.51
Sa (4 sec)	-7.47	2.00	-0.20	1.05	0.00376	0	0.56

* All units are in fractions of gravity (g)

Table 2
Equations Derived by Campbell (1989)
for Spectral Ordinates at Firm Soil Sites and at Soft Rock Sites

$$Ln(Y) = a + bM + dLn[R + c_1 \exp(c_2 M)] + eF + f_1 \tanh[f_2(M + f_3)]$$
$$+ g_1 \tanh(g_2 D) + h_1 K_1 + h_2 K_2 + h_3 K_3 + \varepsilon$$

Ln: natural logarithm
exp: exponential function
tanh: hyperbolic tangent function; *tanh*(x) = [*exp*(x) - *exp*(-x)]/[*exp*(x) + *exp*(-x)]
Y = ground motion parameter (peak acceleration, a, peak velocity, v, and pseudo relative spectral velocity, PRV, at 5% damping);
M = earthquake magnitude (M_L for $M < 6$ and M_S for $M \geq 6$);
R = distance to seismogenic rupture in km;
F = parameter representing style of faulting; $F = 0$ for strike slip faults and $F = 1$ for reverse faults;
D = depth to basement rock (sediment depth) in km;
K_i = parameter representing building effects; $K_1 = 1$ for embedded buildings three to 11 stories; $K_2 = 1$ for embedded buildings with more than 11 stories; $K_3 = 1$ for non embedded buildings greater than two stories in height; $K_1 = K_2 = K_3 = 0$ for all other sites;
ε = standard error term (natural logarithm);

Note: the pseudo absolute spectral acceleration, PAA, can be obtained from pseudo relative spectral velocity, PRV, using the following equations:

$$PAA = \omega PRV / 981 \qquad or \qquad PAA = 2\pi PRV / (981T)$$

in which PAA is in g's, PRV is in cm/sec, ω is circular frequency in radians per second and T is period in seconds.

Table 3
Regression Coefficients: Horizontal Components

Parameter, Y	Period (sec)	No. Eq.	No. Rec.	a	b	c_1	c_2	d	e	f_1	f_2	f_3	g_1	g_2	σ
PHA, g		25	200	-2.470	1.08	0.311	0.597	-1.81	0.382						0.421
PHV, cm/sec		21	152	-1.974	1.34	0.00935	1.01	-1.32	0.327				1.16	0.0776	0.395
PSRVH, cm/sec	0.04	15	86	-0.648	1.08	0.311	0.597	-1.81	0.382						0.42
	0.05	20	142	-0.379	1.08	0.311	0.597	-1.81	0.382						0.44
	0.075	21	144	0.251	1.08	0.311	0.597	-1.81	0.382						0.46
	0.10	21	144	0.754	1.08	0.311	0.597	-1.81	0.382						0.48
	0.15	21	144	1.424	1.08	0.311	0.597	-1.81	0.382						0.50
	0.20	21	144	1.788	1.08	0.311	0.597	-1.81	0.382						0.50
	0.30	21	144	2.170	1.08	0.311	0.597	-1.81	0.382						0.50
	0.40	21	144	2.009	1.08	0.311	0.597	-1.81	0.382	0.425	0.570	-4.7			0.50
	0.50	21	144	1.930	1.08	0.311	0.597	-1.81	0.382	0.685	0.570	-4.7			0.50
	0.75	21	144	1.612	1.08	0.311	0.597	-1.81	0.382	1.27	0.570	-4.7			0.50
	1.0	21	144	1.268	1.08	0.311	0.597	-1.81	0.382	1.74	0.570	-4.7			0.50
	1.5	21	144	0.487	1.08	0.311	0.597	-1.81	0.382	2.43	0.570	-4.7	0.344	0.553	0.50
	2.0	21	144	0.040	1.08	0.311	0.597	-1.81	0.382	2.83	0.570	-4.7	0.469	0.553	0.50
	3.0	21	144	-0.576	1.08	0.311	0.597	-1.81	0.382	3.17	0.570	-4.7	0.623	0.553	0.50
	4.0	20	127	-0.766	1.08	0.311	0.597	-1.81	0.382	3.08	0.570	-4.7	0.857	0.553	0.50

Table 4
Regression Coefficients: Vertical Components

Parameter, Y	Period (sec)	No. Eq.	No. Rec.	a	b	c_1	c_2	d	e	f_1	f_2	f_3	g_1	g_2	σ
PVA, g		24	197	-4.003	0.978	0.0536	0.674	-1.45	0.239						0.569
PVV, cm/sec		21	150	-4.336	1.72	0.00594	1.14	-1.51	0.337						0.520
PSRVV, cm/sec	0.04	15	85	-2.082	0.978	0.0536	0.674	-1.45	0.239						0.62
	0.05	20	141	-1.634	0.978	0.0536	0.674	-1.45	0.239						0.62
	0.075	21	142	-0.903	0.978	0.0536	0.674	-1.45	0.239						0.62
	0.10	21	142	-0.488	0.978	0.0536	0.674	-1.45	0.239						0.62
	0.15	21	142	-0.125	0.978	0.0536	0.674	-1.45	0.239						0.62
	0.20	21	142	0.157	0.978	0.0536	0.674	-1.45	0.239						0.62
	0.30	21	142	0.356	0.978	0.0536	0.674	-1.45	0.239						0.62
	0.40	21	142	0.188	0.978	0.0536	0.674	-1.45	0.239	0.214	0.546	-4.7			0.62
	0.50	21	142	0.038	0.978	0.0536	0.674	-1.45	0.239	0.435	0.546	-4.7			0.62
	0.75	21	142	-0.035	0.978	0.0536	0.674	-1.45	0.239	0.719	0.546	-4.7			0.62
	1.0	21	142	-0.448	0.978	0.0536	0.674	-1.45	0.239	1.37	0.546	-4.7			0.62
	1.5	21	141	-1.287	0.978	0.0536	0.674	-1.45	0.239	2.18	0.546	-4.7	0.344	0.553	0.62
	2.0	21	141	-1.580	0.978	0.0536	0.674	-1.45	0.239	2.36	0.546	-4.7	0.469	0.553	0.62
	3.0	20	125	-1.741	0.978	0.0536	0.674	-1.45	0.239	2.24	0.546	-4.7	0.623	0.553	0.62
	4.0	17	119	-1.975	0.978	0.0536	0.674	-1.45	0.239	2.46	0.546	-4.7	0.857	0.553	0.62

Table 5

Regression Coefficients: Building Effects

Horizontal Components					Vertical Components				
Parameter, Y	Period (sec)	h_1	h_2	h_3	Parameter, Y	Period (sec)	h_1	h_2	h_3
PHA, g		-0.180	-0.489		PVA, g			-0.392	
PHV, cm/sec					PVV, cm/sec		0.366		0.388
PSRVH, cm/sec	0.04	-0.180	-0.489		PSRVV, cm/sec	0.04		-0.392	-0.103
	0.05	-0.180	-0.489			0.05	-0.083	-0.712	-0.264
	0.075	-0.180	-0.489			0.075	-0.206	-0.582	-0.371
	0.10	-0.180	-0.489			0.10	-0.197	-0.650	-0.370
	0.15	-0.180	-0.489			0.15		-0.392	
	0.20	-0.180	-0.489			0.20		-0.392	
	0.30	-0.180	-0.489			0.30		-0.392	
	0.40	-0.180	-0.489			0.40		-0.347	
	0.50	-0.180	-0.489			0.50		-0.153	
	0.75	-0.180	-0.489			0.75		-0.347	
	1.0	-0.180	-0.219			1.0		-0.278	
	1.5	-0.180	0.074			1.5		0.284	0.619
	2.0	-0.180	0.072			2.0		0.437	0.992
	3.0	0.218	0.391	0.663		3.0	0.291	0.691	1.15
	4.0	0.330	0.503	0.759		4.0	0.085	0.722	1.10

Table 6

COEFFICIENTS FOR IDRISS RELATION FOR PGA AT ROCK, STIFF, DEEP, AND SOFT SOIL SITES

	α_0	α_1	α_2	β_0	β_1	β_2	ϕ	h
$M \leq 6$								
rock sites	0	1.127	0.011	0	1.126	-0.106	0.28	10.0
stiff soil sites	-1.15	2.261	-0.083	0	1.602	-0.142	0.20	20.0
deep soil sites	0	2.089	-0.089	0	1.458	-0.143	0.20	20.0
soft soil sites	0	1.673	-0.137	0	1.285	-0.206	0.20	20.0
$M > 6$								
rock sites	0	2.763	-0.262	0	2.215	-0.288	0.28	10.0
stiff soil sites	-0.05	3.477	-0.284	0	2.475	-0.286	0.20	20.0
deep soil sites	0	3.418	-0.308	0	2.319	-0.285	0.20	20.0
soft soil sites	0	2.952	-0.350	0	2.015	-0.328	0.20	20.0

The standard error terms σ_{ln} are

ϵ = 1.29 - 0.12 M, $M \leq 7.25$; 0.42 $M > 7.25$ *rock sites*

= 1.39 - 0.14 M, $M \leq 7.25$; 0.38 $M > 7.25$ *soil sites*

Table 7

COEFFICIENTS FOR IDRISS RELATION FOR 5% DAMPED PSA AT ROCK SITES

FOR MAGNITUDE, $M \leq 6$

$\beta_1 = 1.602$, $\beta_2 = -0.142$, $h = 20.0$, $\phi = 0.2$

Period-sec	$\propto_0$	$\propto_1$	$\propto_2$	β_0	*Standard Error Term,* ϵ
0.030	-0.150	2.261	-0.083	0	1.29-0.12*M
0.050	-0.278	2.365	-0.092	0.066	1.29-0.12*M
0.075	-0.308	2.334	-0.081	0.070	1.29-0.12*M
0.100	-0.318	2.319	-0.075	0.072	1.32-0.12*M
0.110	-0.328	2.294	-0.070	0.073	1.33-0.12*M
0.130	-0.338	2.255	-0.062	0.075	1.34-0.12*M
0.15	-0.348	2.219	-0.055	0.076	1.35-0.12*M
0.20	-0.358	2.146	-0.042	0.078	1.37-0.12*M
0.25	-0.429	2.073	-0.030	0.080	1.38-0.12*M
0.30	-0.486	2.010	-0.020	0.082	1.39-0.12*M
0.35	-0.535	1.977	-0.016	0.087	1.40-0.12*M
0.40	-0.577	1.921	-0.009	0.092	1.41-0.12*M
0.50	-0.648	1.818	0.003	0.099	1.42-0.12*M
0.60	-0.705	1.704	0.017	0.105	1.43-0.12*M
0.70	-0.754	1.644	0.022	0.111	1.44-0.12*M
0.80	-0.796	1.593	0.025	0.115	1.45-0.12*M
0.90	-0.834	1.482	0.039	0.119	1.46-0.12*M
1	-0.867	1.432	0.043	0.123	1.47-0.12*M
1.5	-0.970	1.072	0.084	0.136	1.47-0.12*M
2	-1.046	0.762	0.121	0.146	1.47-0.12*M
3	-1.143	0.194	0.191	0.160	1.47-0.12*M
4	1.177	-0.466	0.280	0.169	1.47-0.12*M
5	-1.214	-1.361	0.410	0.177	1.47-0.12*M

Table 7 (cont'd)

COEFFICIENTS FOR IDRISS RELATION FOR 5% DAMPED PSA AT ROCK SITES

FOR MAGNITUDE, $M > 6$

$\beta_1 = 2.475$, $\beta_2 = -0.286$, $h = 20.0$, $\phi = 0.2$

Period-sec	α_0	α_1	α_2	β_0	*Standard Error Term,* ϵ, $M < 7\frac{1}{4}$	*Standard Error Term,* ϵ, $M \geq 7\frac{1}{4}$
0.030	-0.050	3.477	-0.284	0	1.29-0.12*M	0.42
0.050	-0.278	3.426	-0.269	0.066	1.29-0.12*M	0.42
0.075	-0.308	3.359	-0.252	0.070	1.29-0.12*M	0.42
0.100	-0.318	3.327	-0.243	0.072	1.32-0.12*M	0.45
0.110	-0.328	3.289	-0.236	0.073	1.33-0.12*M	0.46
0.130	-0.338	3.233	-0.225	0.075	1.34-0.12*M	0.47
0.15	-0.348	3.185	-0.216	0.076	1.35-0.12*M	0.48
0.20	-0.358	3.100	-0.201	0.078	1.37-0.12*M	0.50
0.25	-0.429	3.034	-0.190	0.080	1.38-0.12*M	0.51
0.30	-0.486	2.982	-0.182	0.082	1.39-0.12*M	0.52
0.35	-0.535	2.943	-0.177	0.087	1.40-0.12*M	0.53
0.40	-0.577	2.906	-0.173	0.092	1.41-0.12*M	0.54
0.50	-0.648	2.850	-0.169	0.099	1.42-0.12*M	0.55
0.60	-0.705	2.803	-0.166	0.105	1.43-0.12*M	0.56
0.70	-0.754	2.765	-0.165	0.111	1.44-0.12*M	0.57
0.80	-0.796	2.728	-0.164	0.115	1.45-0.12*M	0.58
0.90	-0.834	2.694	-0.163	0.119	1.46-0.12*M	0.59
1	-0.867	2.662	-0.162	0.123	1.47-0.12*M	0.60
1.5	-0.970	2.536	-0.160	0.136	1.47-0.12*M	0.60
2	-1.046	2.447	-0.160	0.146	1.47-0.12*M	0.60
3	-1.143	2.295	-0.159	0.160	1.47-0.12*M	0.60
4	-1.177	2.169	-0.159	0.169	1.47-0.12*M	0.60
5	-1.214	2.042	-0.157	0.177	1.47-0.12*M	0.60

Table 8

SPECTRAL MAGNIFICATION FACTORS FOR IDRISS ATTENUATION FOR MAGNITUDE 6-3/4

Period (sec)	Spectral Magnification Factor		
	Stiff Soil	Deep Soil	Soft Soil
0.03	1.0000	1.0000	1.0000
0.05	1.1500	1.0700	1.0700
0.08	1.5000	1.4100	1.2700
0.10	1.8200	1.7000	1.4800
0.15	2.4000	2.1700	1.7800
0.20	2.7200	2.4400	1.9600
0.25	2.8500	2.6000	2.1000
0.30	2.8900	2.6800	2.2000
0.35	2.8300	2.6900	2.2500
0.40	2.6000	2.7000	2.2900
0.50	2.2100	2.5000	2.3400
0.60	1.9000	2.2700	2.3400
0.70	1.6300	2.0300	2.2700
0.80	1.4200	1.8300	2.1800
0.90	1.2600	1.6600	2.0600
1.00	1.1300	1.5100	1.9500
1.50	0.7200	1.0100	1.4100
2.00	0.5200	0.7300	1.0500
2.50	0.4000	0.5560	0.8190
3.00	0.3200	0.4481	0.6620
3.50	0.2650	0.3695	0.5490
4.00	0.2240	0.3153	0.4640
4.50	0.1930	0.2720	0.4010
5.00	0.1690	0.2394	0.3510
6.00	0.1345	0.1915	0.2770
8.00	0.0928	0.1320	0.1860
10.00	0.0691	0.0986	0.1380

Table 9.

Dependence of Spectral Ordinates on Magnitude,
Normalized to a Magnitude of 6-3/4
For Idriss Attenuation

Magnitude	Spectral Ordinates Normalized to M=6-3/4					
	T=0.1 sec	T=0.2 sec	T=0.5 sec	T=2 sec	T=8 sec	T=10 sec
4.50	1	0.860	0.350	0.120	0.039	0.033
4.75	1	0.700	0.400	0.157	0.059	0.050
5.00	1	0.740	0.455	0.205	0.089	0.077
5.25	1	0.780	0.520	0.265	0.131	0.116
5.50	1	0.810	0.590	0.340	0.193	0.172
5.75	1	0.860	0.660	0.430	0.281	0.255
6.00	1	0.900	0.740	0.540	0.400	0.370
6.25	1	0.930	0.820	0.680	0.560	0.530
6.50	1	0.960	0.910	0.820	0.770	0.740
6.75	1	1	1	1	1	1
7.00	1	1.050	1.100	1.200	1.300	1.310
7.25	1	1.100	1.220	1.400	1.590	1.680
7.50	1	1.130	1.330	1.600	1.900	2.000
7.75	1	1.190	1.420	1.800	2.150	2.220
8.00	1	1.220	1.520	1.960	2.350	2.400
8.25	1	1.220	1.520	1.960	2.350	2.400
8.50	1	1.220	1.520	1.960	2.350	2.400
8.75	1	1.220	1.520	1.960	2.350	2.400
9.00	1	1.220	1.520	1.960	2.350	2.400
9.25	1	1.220	1.520	1.960	2.350	2.400

Table 10

Coefficients of equations for the random and larger horizontal components of peak acceleration (in g; distance in km).

Component	B1	B2	B3	B4	B5	B6	B7	H	S1	SC	SR	SE	SLOGY
random	-.105	.229	0.0	0.0	-.778	.162	.251	5.57	.186	.098	.210	.093	.230
larger	-.038	.216	0.0	0.0	-.777	.158	.254	5.48	.193	.000	.193	.068	.205

The equations are to be used for 5.0 <= M <= 7.7 and d <= 100.0 km.

Table 11

Smoothed coefficients of equations for the random horizontal component of 5 percent damped PSV (cm/s; distance in km).

T(s)	B1	B2	B3	B4	B5	B6	B7	H	S1	SC	SR	SE	SLOGY
.10	1.653	.327	-.098	.00000	-.934	.046	.136	6.27	.191	.083	.208	.003	.208
.11	1.725	.318	-.100	.00000	-.937	.071	.156	6.65	.189	.087	.208	.005	.208
.12	1.782	.313	-.101	.00000	-.939	.093	.174	6.91	.187	.091	.208	.008	.208
.13	1.828	.309	-.101	.00000	-.939	.111	.191	7.08	.186	.094	.208	.010	.209
.14	1.864	.307	-.100	.00000	-.938	.127	.206	7.18	.185	.097	.209	.012	.209
.15	1.892	.305	-.099	.00000	-.937	.140	.221	7.23	.185	.100	.210	.015	.211
.16	1.915	.305	-.098	.00000	-.935	.153	.234	7.24	.184	.102	.210	.017	.211
.17	1.933	.305	-.096	.00000	-.933	.163	.246	7.21	.184	.104	.211	.019	.212
.18	1.948	.306	-.094	.00000	-.930	.173	.258	7.16	.184	.106	.212	.021	.213
.19	1.959	.308	-.092	.00000	-.927	.182	.269	7.10	.184	.108	.213	.023	.215
.20	1.967	.309	-.090	.00000	-.924	.190	.279	7.02	.184	.109	.214	.025	.215
.22	1.978	.313	-.086	.00000	-.918	.203	.297	6.83	.185	.112	.216	.029	.218
.24	1.982	.318	-.082	.00000	-.912	.214	.314	6.62	.185	.114	.217	.033	.220
.26	1.982	.323	-.078	.00000	-.906	.224	.329	6.39	.186	.116	.219	.036	.222
.28	1.979	.329	-.073	.00000	-.899	.232	.343	6.17	.187	.118	.221	.040	.225
.30	1.974	.334	-.070	.00000	-.893	.239	.356	5.94	.187	.120	.222	.043	.226
.32	1.967	.340	-.066	.00000	-.888	.245	.367	5.72	.188	.121	.224	.046	.228
.34	1.959	.345	-.062	.00000	-.882	.251	.378	5.50	.189	.122	.225	.048	.230
.36	1.950	.350	-.059	.00000	-.877	.256	.387	5.30	.190	.123	.226	.051	.232
.38	1.940	.356	-.055	.00000	-.872	.260	.396	5.10	.191	.125	.228	.054	.235
.40	1.930	.361	-.052	.00000	-.867	.264	.405	4.91	.192	.125	.229	.056	.236
.42	1.920	.365	-.049	.00000	-.862	.267	.413	4.74	.193	.126	.230	.058	.238
.44	1.910	.370	-.047	.00000	-.858	.271	.420	4.57	.193	.127	.231	.061	.239
.46	1.900	.375	-.044	.00000	-.854	.273	.427	4.41	.194	.128	.232	.063	.241
.48	1.890	.379	-.042	.00000	-.850	.276	.433	4.26	.195	.129	.234	.065	.243
.50	1.881	.384	-.039	.00000	-.846	.279	.439	4.13	.196	.129	.235	.067	.244
.55	1.857	.394	-.034	.00000	-.837	.284	.452	3.82	.198	.131	.237	.071	.248
.60	1.835	.403	-.030	.00000	-.830	.289	.464	3.57	.199	.133	.239	.076	.251
.65	1.815	.411	-.026	.00000	-.823	.293	.474	3.36	.201	.134	.242	.079	.254
.70	1.797	.418	-.023	.00000	-.818	.297	.483	3.20	.202	.135	.243	.083	.257
.75	1.781	.425	-.020	.00000	-.813	.300	.490	3.07	.203	.136	.244	.086	.259
.80	1.766	.431	-.018	.00000	-.809	.303	.497	2.98	.204	.137	.246	.089	.261
.85	1.753	.437	-.016	.00000	-.805	.306	.503	2.92	.205	.138	.247	.092	.264
.90	1.742	.442	-.015	.00000	-.802	.309	.508	2.89	.206	.139	.249	.095	.266
.95	1.732	.446	-.014	.00000	-.800	.312	.513	2.88	.207	.140	.250	.097	.268
1.00	1.724	.450	-.014	.00000	-.798	.314	.517	2.90	.208	.141	.251	.100	.270
1.10	1.710	.457	-.013	.00000	-.795	.319	.523	2.99	.209	.143	.253	.104	.274
1.20	1.701	.462	-.014	.00000	-.794	.324	.528	3.14	.210	.145	.255	.108	.277
1.30	1.696	.466	-.015	.00000	-.793	.328	.532	3.36	.211	.146	.257	.111	.280
1.40	1.695	.469	-.017	.00000	-.794	.333	.535	3.62	.212	.148	.259	.114	.283
1.50	1.696	.471	-.019	.00000	-.796	.338	.537	3.92	.212	.150	.260	.117	.285
1.60	1.700	.472	-.022	.00000	-.798	.342	.538	4.26	.212	.151	.260	.119	.286
1.70	1.706	.473	-.025	.00000	-.801	.347	.539	4.62	.212	.153	.261	.122	.289
1.80	1.715	.472	-.029	.00000	-.804	.351	.539	5.01	.212	.154	.262	.124	.290
1.90	1.725	.472	-.032	.00000	-.808	.356	.538	5.42	.212	.156	.263	.126	.292
2.00	1.737	.471	-.037	.00000	-.812	.360	.537	5.85	.212	.157	.264	.128	.293

The equations are to be used for 5.0 <= M <= 7.7 and d <= 100.0 km.

Table 12

GROUND MOTION PREDICTION

TABLE 5. PARAMETERS IN THE PREDICTIVE EQUATIONS OF SADIGH (WRITTEN COMMUNICATION, 1987) FOR THE RANDOMLY ORIENTED HORIZONTAL COMPONENT OF PSEUDOACCELERATION RESPONSE (g) AT 5 PERCENT DAMPING AND OF PEAK ACCELERATION (g)

								M < 6.5	M ≥ 6.5		
Period (s)	a	b	c_1	c_2	d	h_1	h_2	$\sigma_{\ln y}$	h_1	h_2	$\sigma_{\ln y}$
Pseudoacceleration response at soil sites											
0.1	-2.024	1.1	0.007	2.5	-1.75	0.8217	0.4814	1.332 – 0.148M	0.3157	0.6286	0.37
0.2	-1.696	1.1	.0	2.5	-1.75	.8217	.4814	1.453 – 0.162M	.3157	.6286	.40
0.3	-1.638	1.1	- .008	2.5	-1.75	.8217	.4814	1.486 – 0.164M	.3157	.6286	.42
0.5	-1.659	1.1	- .025	2.5	-1.75	.8217	.4814	1.584 – 0.176M	.3157	.6286	.44
1.0	-1.975	1.1	- .060	2.5	-1.75	.8217	.4814	1.62 – 0.18M	.3157	.6286	.45
2.0	-2.414	1.1	- .105	2.5	-1.75	.8217	.4814	1.62 – 0.18M	.3157	.6286	.45
4.0	-3.068	1.1	-0.160	2.5	-1.75	0.8217	0.4814	1.62 – 0.18M	0.3157	0.6286	0.45
Peak acceleration at soil sites											
	-2.611	1.1	0.0	2.5	-1.75	0.8217	0.4814	1.26 – 0.14M	0.3157	0.6286	0.35
Pseudoacceleration response at rock sites											
0.1	-0.688	1.1	0.007	2.5	-2.05	1.353	0.406	1.332 – 0.148M	0.579	0.537	0.37
0.2	-0.479	1.1	- .008	2.5	-2.05	1.353	.406	1.453 – 0.162M	.579	.537	.40
0.3	-0.543	1.1	- .018	2.5	-2.05	1.353	.406	1.486 – 0.164M	.579	.537	.42
0.5	-0.793	1.1	- .036	2.5	-2.05	1.353	.406	1.584 – 0.176M	.579	.537	.44
1.0	-1.376	1.1	- .065	2.5	-2.05	1.353	.406	1.62 – 0.18M	.579	.537	.45
2.0	-2.142	1.1	- .100	2.5	-2.05	1.353	.406	1.62 – 0.18M	.579	.537	.45
4.0	-3.177	1.1	-0.150	2.5	-2.05	1.353	0.406	1.62 – 0.18M	0.579	0.537	0.45
Peak acceleration at rock sites											
	-1.406	1.1	0.0	2.5	-2.05	1.353	0.406	1.26 – 0.14M	0.579	0.537	0.35

Table 13

ATTENUATION RELATIONSHIPS FOR HORIZONTAL ROCK MOTION
(PEAK GROUND ACCELERATION AND 5% - DAMPED RESPONSE SPECTRAL ACCELERATIONS FOR STRIKE-SLIP FAULTING)

M_w = or < 6½

Period(s)	C_1	C_2	C_3	C_4	C_5	C_6	C_7
PGA	-0.624	1.0	0.000	-2.100	1.29649	0.250	0.0
0.05	-0.090	1.0	0.006	-2.128	1.29649	0.250	-0.082
0.07	0.110	1.0	0.006	-2.128	1.29649	0.250	-0.082
0.09	0.212	1.0	0.006	-2.140	1.29649	0.250	-0.052
0.10	0.275	1.0	0.006	-2.148	1.29649	0.250	-0.041
0.12	0.348	1.0	0.005	-2.162	1.29649	0.250	-0.014
0.14	0.307	1.0	0.004	-2.144	1.29649	0.250	0.0
0.15	0.285	1.0	0.002	-2.130	1.29649	0.250	0.0
0.17	0.239	1.0	0.0	-2.110	1.29649	0.250	0.0
0.20	0.153	1.0	-0.004	-2.080	1.29649	0.250	0.0
0.24	0.060	1.0	-0.011	-2.053	1.29649	0.250	0.0
0.30	-0.057	1.0	-0.017	-2.028	1.29649	0.250	0.0
0.40	-0.298	1.0	-0.028	-1.990	1.29649	0.250	0.0
0.50	-0.588	1.0	-0.040	-1.945	1.29649	0.250	0.0
0.75	-1.208	1.0	-0.050	-1.865	1.29649	0.250	0.0
1.00	-1.705	1.0	-0.055	-1.800	1.29649	0.250	0.0
1.50	-2.407	1.0	-0.065	-1.725	1.29649	0.250	0.0
2.00	-2.945	1.0	-0.070	-1.670	1.29649	0.250	0.0
3.00	-3.700	1.0	-0.080	-1.615	1.29649	0.250	0.0
4.00	-4.230	1.0	-0.100	-1.570	1.29649	0.250	0.0
5.00	-4.714	1.0	-0.100	-1.540	1.29649	0.250	0.0
7.50	-5.530	1.0	-0.110	-1.510	1.29649	0.250	0.0

Notes: Relationships for reverse/thrust faulting are obtained by multiplying the strike-slip amplitudes by 1.2. Relationships for oblique faulting are obtained by multiplying the strike-slip amplitudes by 1.09.

Attenuation relationships:

$\ln PGA = C_1 + C_2 * M + C_4 * \ln(R + \exp(C_5 + C_6 * M))$

$\ln S_a(T) = C_1 + C_2 * M + C_3 * (8.5 - M)^{2.5} + C_4 * \ln(R + \exp(C_5 + C_6 * M)) + C_7 * \ln(R + 2)$

In the above equations, PGA is peak ground acceleration in g's, $S_a(T)$ is acceleration response spectral ordinate at period T in g's, M is moment magnitude, and R is the closest distance to fault rupture surface in km.

M_w = or > 6½

Period(s)	C_1	C_2	C_3	C_4	C_5	C_6	C_7
PGA	-1.274	1.1	0.000	-2.100	-0.48451	0.524	0.0
0.05	-0.740	1.1	0.006	-2.128	-0.48451	0.524	-0.082
0.07	-0.540	1.1	0.006	-2.128	-0.48451	0.524	-0.082
0.09	-0.438	1.1	0.006	-2.140	-0.48451	0.524	-0.052
0.10	-0.375	1.1	0.006	-2.148	-0.48451	0.524	-0.041
0.12	-0.302	1.1	0.005	-2.162	-0.48451	0.524	-0.014
0.14	-0.343	1.1	0.004	-2.144	-0.48451	0.524	0.0
0.15	-0.365	1.1	0.002	-2.130	-0.48451	0.524	0.0
0.17	-0.411	1.1	0.0	-2.110	-0.48451	0.524	0.0
0.20	-0.497	1.1	-0.004	-2.080	-0.48451	0.524	0.0
0.24	-0.590	1.1	-0.011	-2.053	-0.48451	0.524	0.0
0.30	-0.707	1.1	-0.017	-2.028	-0.48451	0.524	0.0
0.40	-0.948	1.1	-0.028	-1.990	-0.48451	0.524	0.0
0.50	-1.238	1.1	-0.040	-1.945	-0.48451	0.524	0.0
0.75	-1.858	1.1	-0.050	-1.865	-0.48451	0.524	0.0
1.00	-2.355	1.1	-0.055	-1.800	-0.48451	0.524	0.0
1.50	-3.057	1.1	-0.065	-1.725	-0.48451	0.524	0.0
2.00	-3.595	1.1	-0.070	-1.670	-0.48451	0.524	0.0
3.00	-4.350	1.1	-0.080	-1.610	-0.48451	0.524	0.0
4.00	-4.880	1.1	-0.100	-1.570	-0.48451	0.524	0.0
5.00	-5.364	1.1	-0.100	-1.540	-0.48451	0.524	0.0
7.50	-6.180	1.1	-0.110	-1.510	-0.48451	0.524	0.0

Notes: Relationships for reverse/thrust faulting are obtained by multiplying the strike-slip amplitudes by 1.2. Relationships for oblique faulting are obtained by multiplying the strike-slip amplitudes by 1.09.

Attenuation relationships:

$\ln PGA = C_1 + C_2 * M + C_4 * \ln(R + \exp(C_5 + C_6 * M))$

$\ln S_a(T) = C_1 + C_2 * M + C_3 * (8.5 - M)^{2.5} + C_4 * \ln(R + \exp(C_5 + C_6 * M)) + C_7 * \ln(R + 2)$

In the above equations, PGA is peak ground acceleration in g's, $S_a(T)$ is acceleration response spectral ordinate at period T in g's, M is moment magnitude, and R is the closest distance to fault rupture surface in km.

Table 14

DISPERSION RELATIONSHIPS FOR HORIZONTAL ROCK MOTION

Ground Motion Parameter	Period	Sigma (lny)
Peak Ground Acceleration	–	1.39 - 0.14*M; 0.38 for M> = 7.25
Response Spectra Accel.	0.05	1.39 - 0.14*M; 0.38 for M> = 7.25
Response Spectra Accel.	0.07	1.40 - 0.14*M; 0.39 for M> = 7.25
Response Spectra Accel.	0.09	1.40 - 0.14*M; 0.39 for M> = 7.25
Response Spectra Accel.	0.10	1.41 - 0.14*M; 0.40 for M> = 7.25
Response Spectra Accel.	0.12	1.41 - 0.14*M; 0.40 for M> = 7.25
Response Spectra Accel.	0.14	1.42 - 0.14*M; 0.41 for M> = 7.25
Response Spectra Accel.	0.15	1.42 - 0.14*M; 0.41 for M> = 7.25
Response Spectra Accel.	0.17	1.42 - 0.14*M; 0.41 for M> = 7.25
Response Spectra Accel.	0.20	1.43 - 0.14*M; 0.42 for M> = 7.25
Response Spectra Accel.	0.24	1.44 - 0.14*M; 0.43 for M> = 7.25
Response Spectra Accel.	0.30	1.45 - 0.14*M; 0.44 for M> = 7.25
Response Spectra Accel.	0.40	1.48 - 0.14*M; 0.47 for M> = 7.25
Response Spectra Accel.	0.50	1.50 - 0.14*M; 0.49 for M> = 7.25
Response Spectra Accel.	0.75	1.52 - 0.14*M; 0.51 for M> = 7.25
Response Spectra Accel.	1.00	1.53 - 0.14*M; 0.52 for M> = 7.25
	>1.00	1.53 - 0.14*M; 0.52 for M> = 7.25

Table 15

ATTENUATION RELATIONSHIPS FOR VERTICAL ROCK MOTION
(PEAK GROUND ACCELERATION AND 5% - DAMPED RESPONSE SPECTRAL ACCELERATIONS FOR STRIKE-SLIP FAULTING)

M_w = or < 6½

Period(s)	C_1	C_2	C_3	C_4	C_5	C_6
PGA	-0.430	1.0	0.000	-2.300	1.2726	0.228
0.04	0.3379	1.0	0.000	-2.450	1.2726	0.228
0.05	0.5041	1.0	0.000	-2.450	1.2726	0.228
0.06	0.6095	1.0	0.000	-2.450	1.2726	0.228
0.07	0.6896	1.0	0.000	-2.450	1.2726	0.228
0.09	0.6718	1.0	-0.00330	-2.420	1.2726	0.228
0.10	0.6252	1.0	-0.00468	-2.400	1.2726	0.228
0.12	0.5535	1.0	-0.00707	-2.380	1.2726	0.228
0.14	0.3813	1.0	-0.00909	-2.333	1.2726	0.228
0.15	0.2524	1.0	-0.01000	-2.300	1.2726	0.228
0.17	0.0122	1.0	-0.01462	-2.241	1.2726	0.228
0.20	-0.3005	1.0	-0.02061	-2.164	1.2726	0.228
0.24	-0.6678	1.0	-0.02734	-2.077	1.2726	0.228
0.30	-1.1392	1.0	-0.03558	-1.971	1.2726	0.228
0.40	-1.7656	1.0	-0.04619	-1.835	1.2726	0.228
0.50	-2.2748	1.0	-0.05442	-1.729	1.2726	0.228
0.75	-3.2062	1.0	-0.06939	-1.536	1.2726	0.228
1.00	-3.8818	1.0	-0.08000	-1.400	1.2726	0.228
1.50	-4.2618	1.0	-0.08554	-1.400	1.2726	0.228
2.00	-4.5719	1.0	-0.08946	-1.400	1.2726	0.228
2.50	-4.8167	1.0	-0.09251	-1.400	1.2726	0.228
3.00	-5.0364	1.0	-0.09500	-1.400	1.2726	0.228

Notes: Relationships for reverse/thrust faulting are obtained by multiplying the strike-slip amplitudes by 1.1. Relationships for oblique faulting are obtained by multiplying the strike-slip amplitudes by 1.048.

Attenuation relationships:

$\ln PGA = C_1+C_2*M+C_4*\ln(R+\exp(C_5+C_6*M))$

$\ln S_a(T) = C_1+C_2*M+C_3*(8.5 - M)^2.5+C_4*\ln(R+\exp(C_5+C_6*M))$

In the above equations, PGA is peak ground acceleration in g's, $S_a(T)$ is acceleration response spectral ordinate at period T in g's, M is moment magnitude, and R is the closest distance to fault rupture surface in km.

M_w = or > 6½

Period(s)	C_1	C_2	C_3	C_4	C_5	C_6
PGA	-1.080	1.1	0.000	-2.300	-0.3524	0.478
0.04	-0.3121	1.1	0.000	-2.450	-0.3524	0.478
0.05	-0.1459	1.1	0.000	-2.450	-0.3524	0.478
0.06	-0.0405	1.1	0.000	-2.450	-0.3524	0.478
0.07	0.03956	1.1	0.000	-2.450	-0.3524	0.478
0.09	0.0218	1.1	-0.00330	-2.420	-0.3524	0.478
0.10	-0.0248	1.1	-0.00468	-2.400	-0.3524	0.478
0.12	-0.0965	1.1	-0.00707	-2.380	-0.3524	0.478
0.14	-0.2687	1.1	-0.00909	-2.333	-0.3524	0.478
0.15	-0.3976	1.1	-0.01000	-2.300	-0.3524	0.478
0.17	-0.6378	1.1	-0.01462	-2.241	-0.3524	0.478
0.20	-0.9505	1.1	-0.02061	-2.164	-0.3524	0.478
0.24	-1.3178	1.1	-0.02734	-2.077	-0.3524	0.478
0.30	-1.7893	1.1	-0.03558	-1.971	-0.3524	0.478
0.40	-2.4157	1.1	-0.04619	-1.835	-0.3524	0.478
0.50	-2.9248	1.1	-0.05442	-1.729	-0.3524	0.478
0.75	-3.8562	1.1	-0.06939	-1.536	-0.3524	0.478
1.00	-4.5318	1.1	-0.08000	-1.400	-0.3524	0.478
1.50	-4.9118	1.1	-0.08554	-1.400	-0.3524	0.478
2.00	-5.2219	1.1	-0.08946	-1.400	-0.3524	0.478
2.50	-5.4667	1.1	-0.09251	-1.400	-0.3524	0.478
3.00	-5.6864	1.1	-0.09500	-1.400	-0.3524	0.478

Notes: Relationships for reverse/thrust faulting are obtained by multiplying the strike-slip amplitudes by 1.1. Relationships for oblique faulting are obtained by multiplying the strike-slip amplitudes by 1.048.

Attenuation relationships:

$\ln PGA = C_1+C_2*M+C_4*\ln(R+\exp(C_5+C_6*M))$

$\ln S_a(T) = C_1+C_2*M+C_3*(8.5 - M)^2.5+C_4*\ln(R+\exp(C_5+C_6*M))$

In the above equations, PGA is peak ground acceleration in g's, $S_a(T)$ is acceleration response spectral ordinate at period T in g's, M is moment magnitude, and R is the closest distance to fault rupture surface in km.

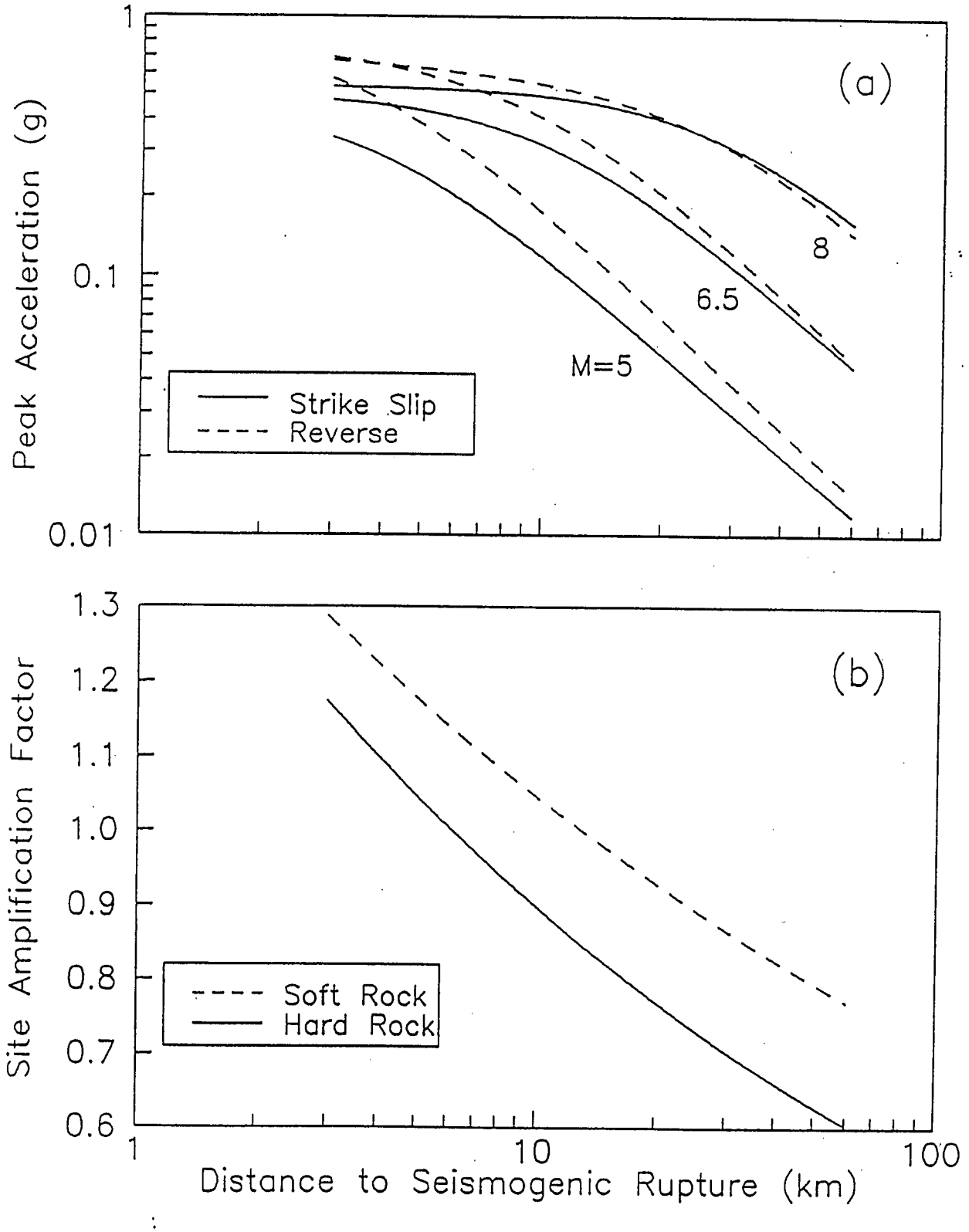

Figure 1. Attenuation relationship developed in this study for alluvium showing the scaling of peak horizontal acceleration with (a) magnitude and style of faulting and (b) site geological conditions. (Source; Campbell and Bozorgnia, 1994)

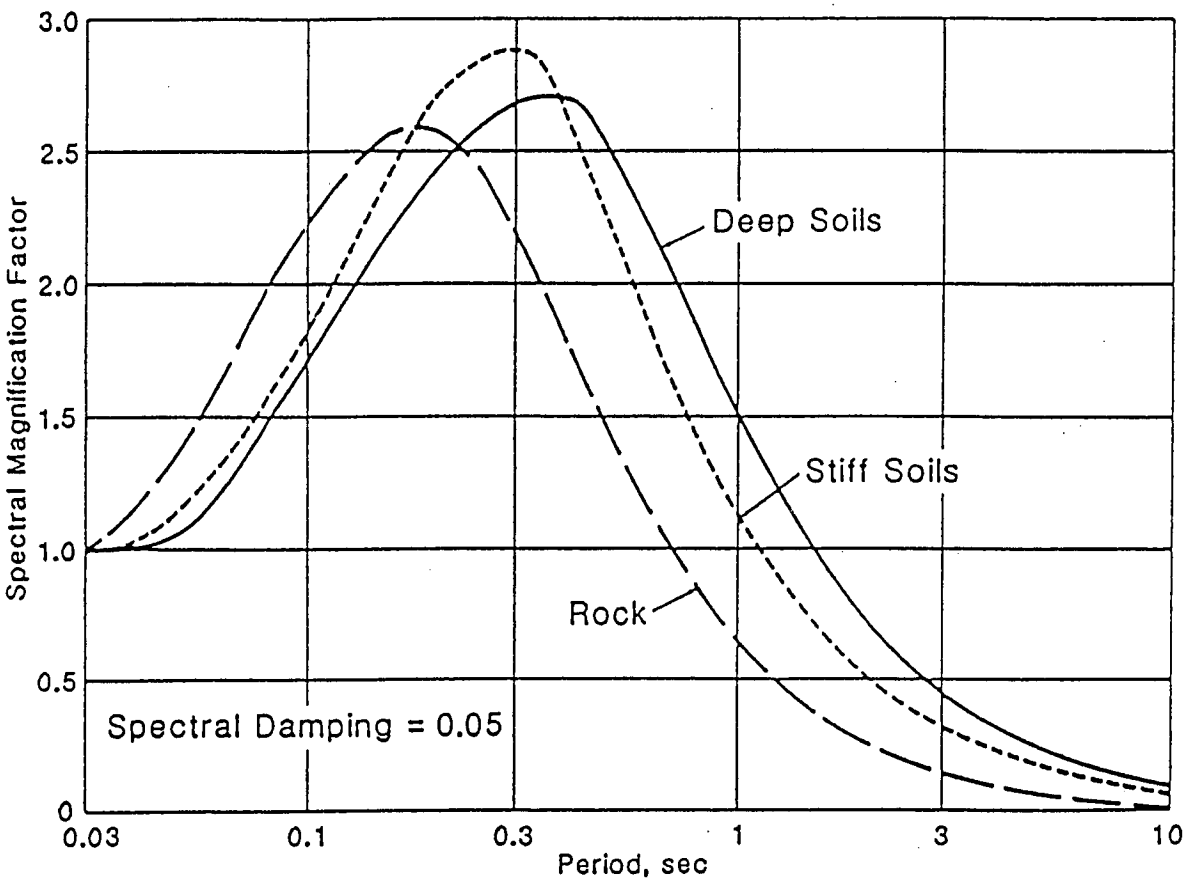

Figure 2. Average spectral shapes for three different subsurface conditions (Source; Idriss, 1985).

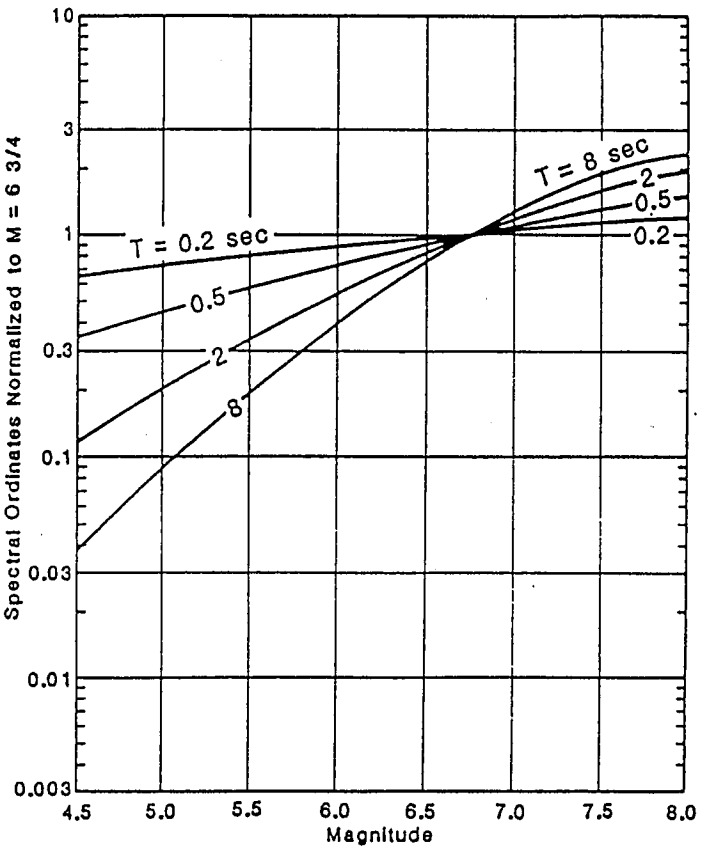

Figure 3. Approximate dependence of spectral ordinates on magnitude -- Results normalized with respect to M_s = 6-3/4 (Source; Idriss, 1987).

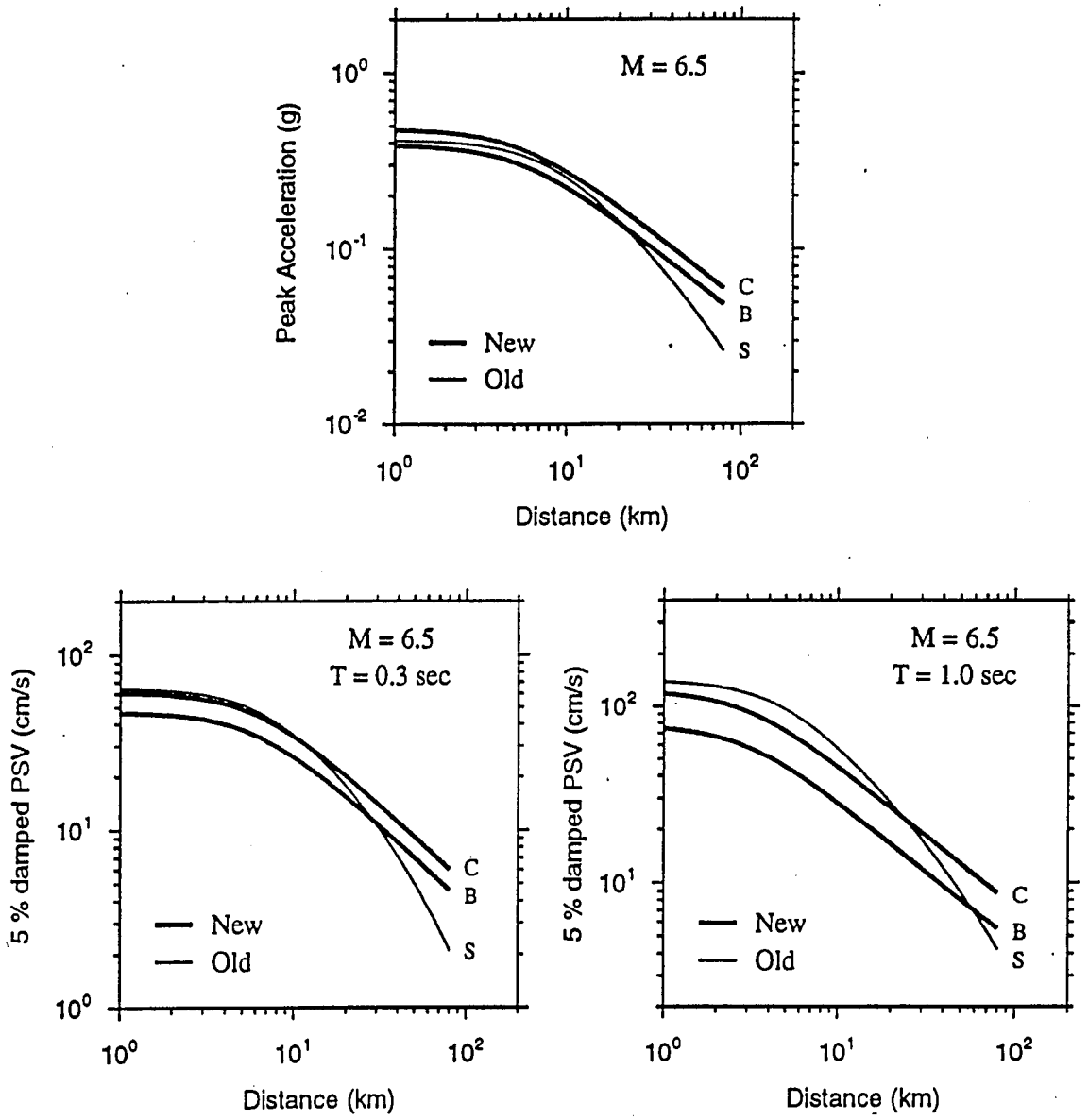

Figure 4. Comparison of ground motions computed from the old and new equations as a function of distance for magnitude 6.5 and soil site classes (Source; Boore et al., 1993).

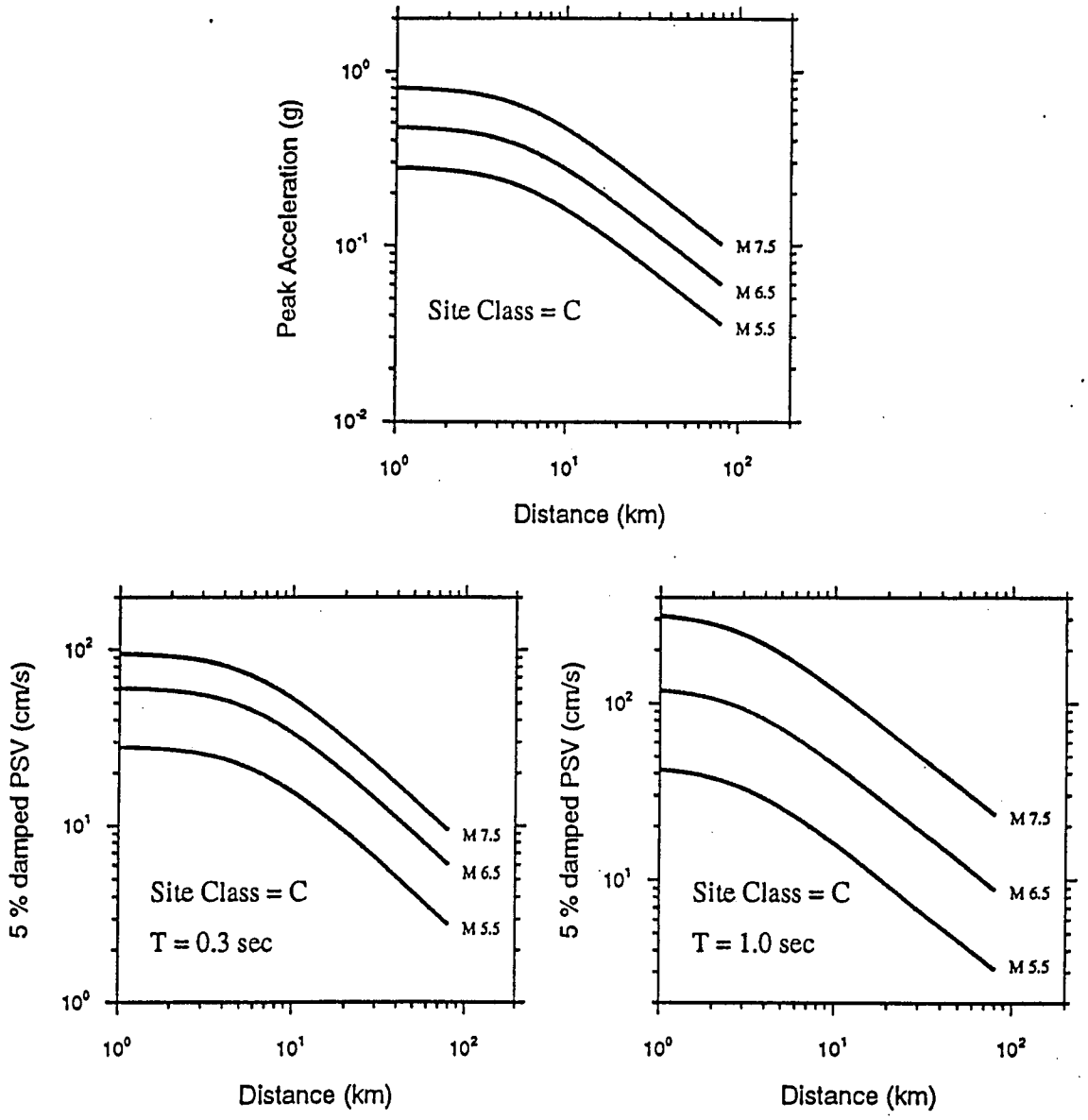

Figure 5. Attenuation with distance of peak acceleration and response spectra for the random horizontal component (Source; Boore et al., 1993).

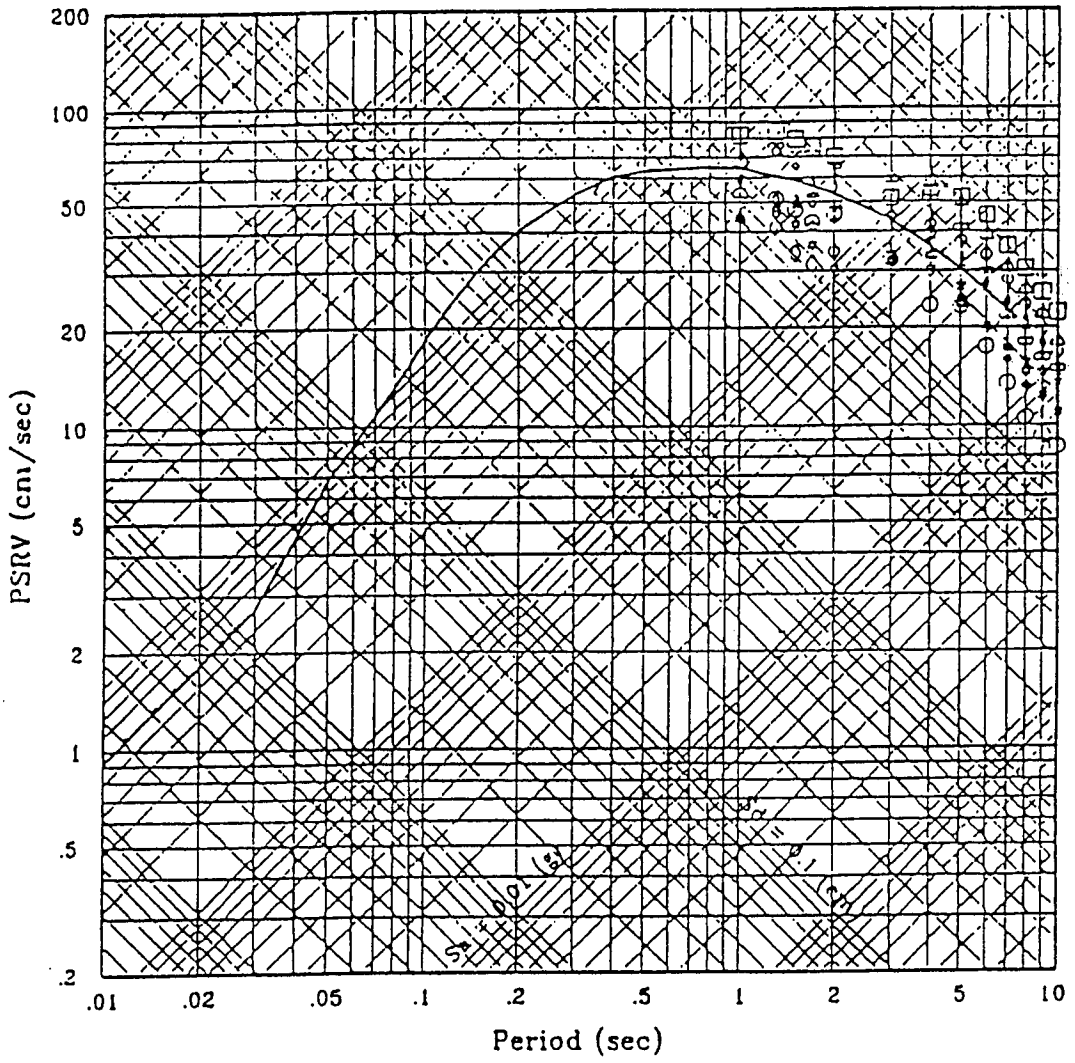

Figure 6. Comparison of the numerically simulated long period motions with the empirical median spectrum for M 6¾ at R = 3 km (Source; Sadigh et al., 1993).

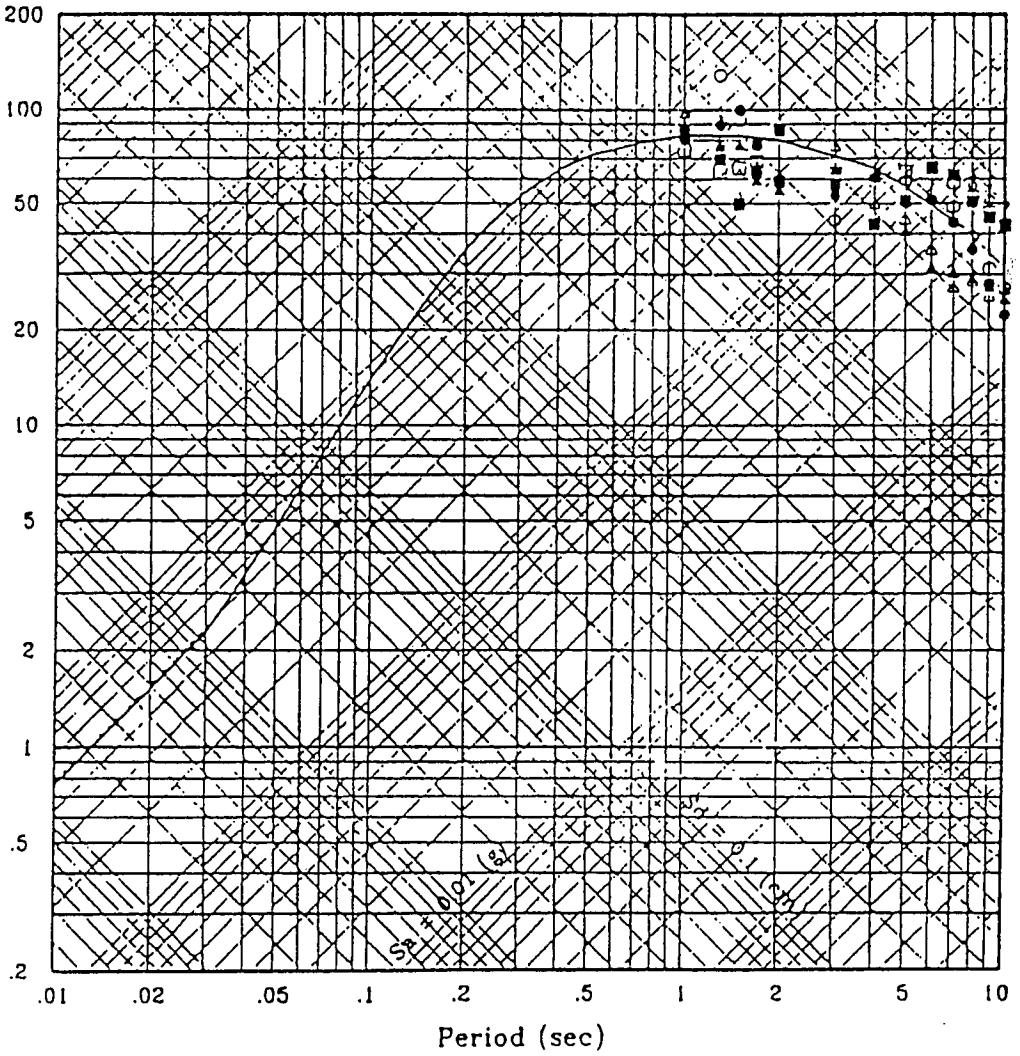

Figure 7. Comparison of the numerically simulated long period motions with the empirical median spectrum for M 8 at R = 10 km (Source; Sadigh et al., 1993).

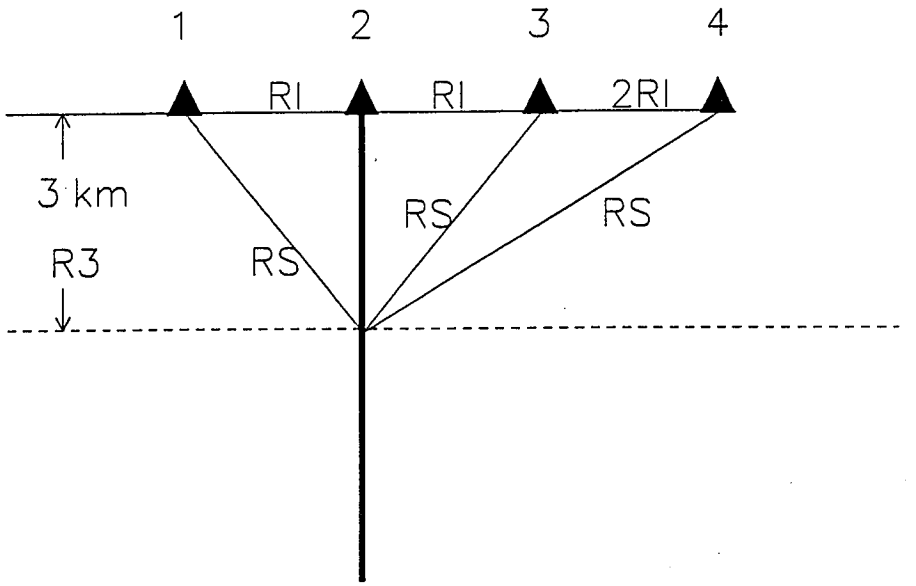

Relation\Site	1	2	3	4
Campbell	RS (M)	R3 (M)	RS (M)	RS (M)
Idriss and Sadigh	RI (M)	O (M)	RI (M)	2 RI (M)
Joyner and Boore	RI	O (M)	RI	2 RI

Figure 8. Distance measure schematic for a vertical fault.

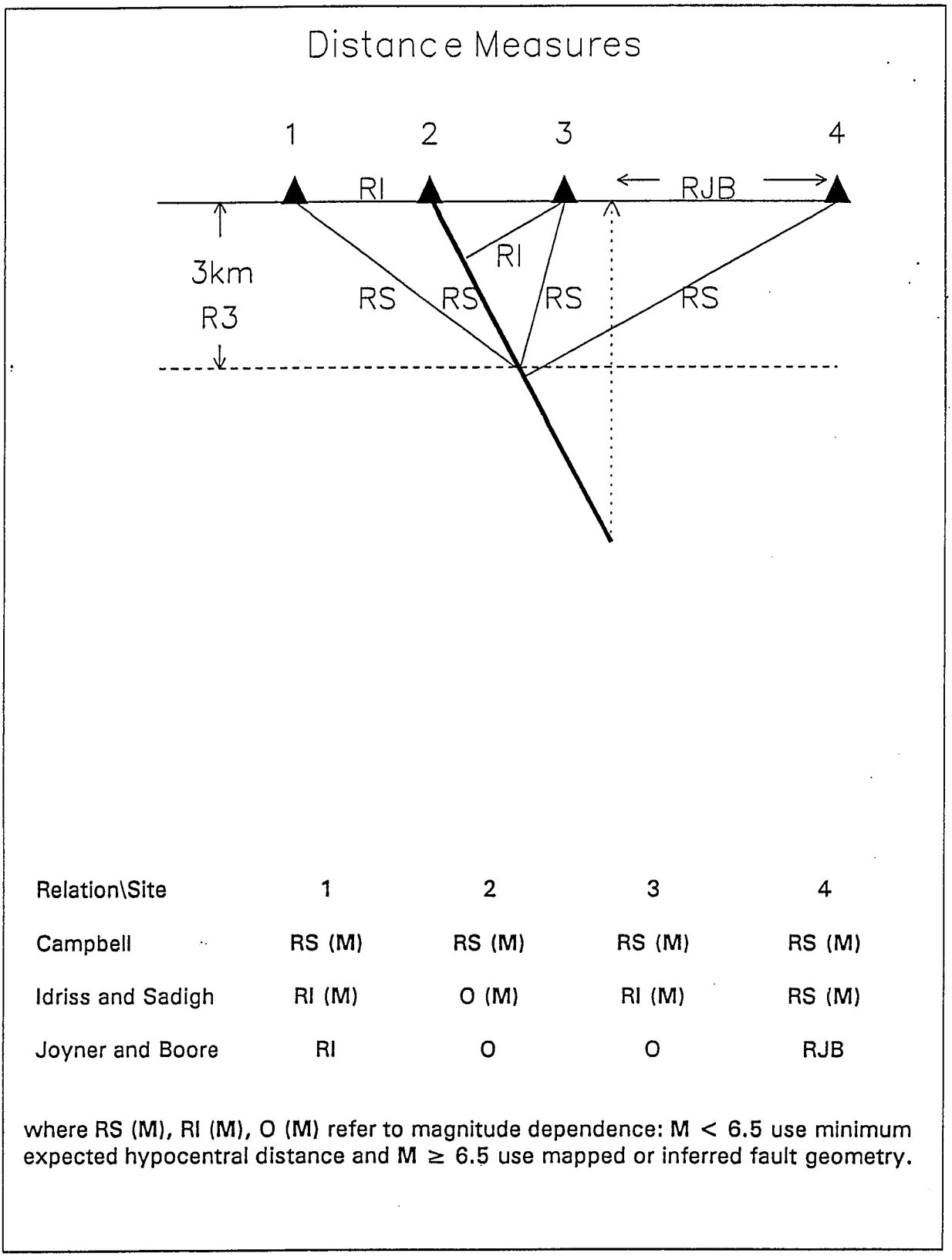

Relation\Site	1	2	3	4
Campbell	RS (M)	RS (M)	RS (M)	RS (M)
Idriss and Sadigh	RI (M)	O (M)	RI (M)	RS (M)
Joyner and Boore	RI	O	O	RJB

where RS (M), RI (M), O (M) refer to magnitude dependence: $M < 6.5$ use minimum expected hypocentral distance and $M \geq 6.5$ use mapped or inferred fault geometry.

Figure 8 continued. Distance measure schematic for a dipping fault.

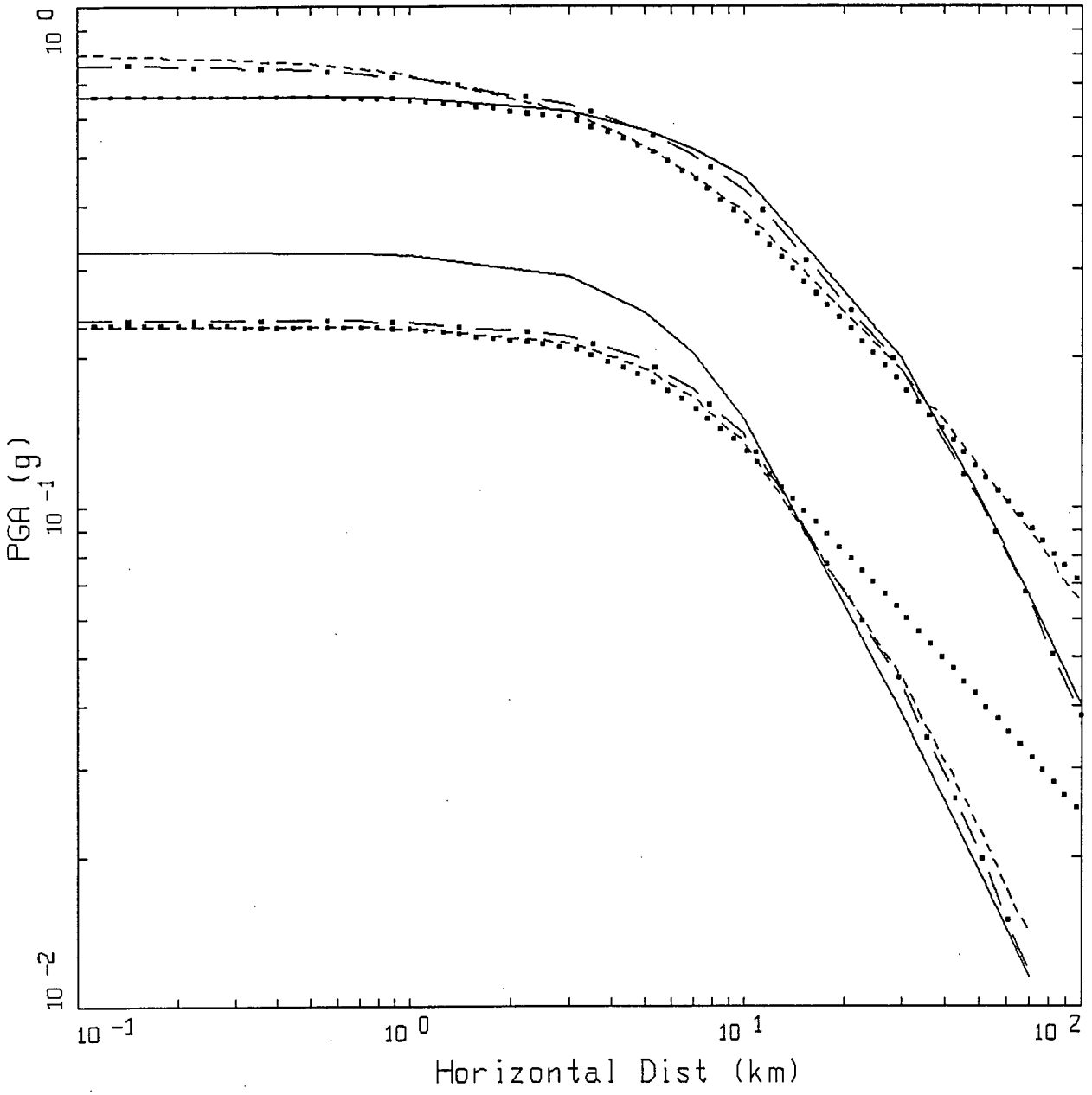

COMPARISON OF ROCK PGA RELATIONS
M 5.5 AND 7.5 (STRIKE SLIP)

LEGEND

——— CAMPBELL, 1994 (SOFT ROCK)

- - - - - IDRISS, 1994 (ROCK)

• • • • BOORE, JOYNER & FUMAL, 1993 (CLASS B)

— • — SADIGH, 1991 (ROCK)

Figure 9.

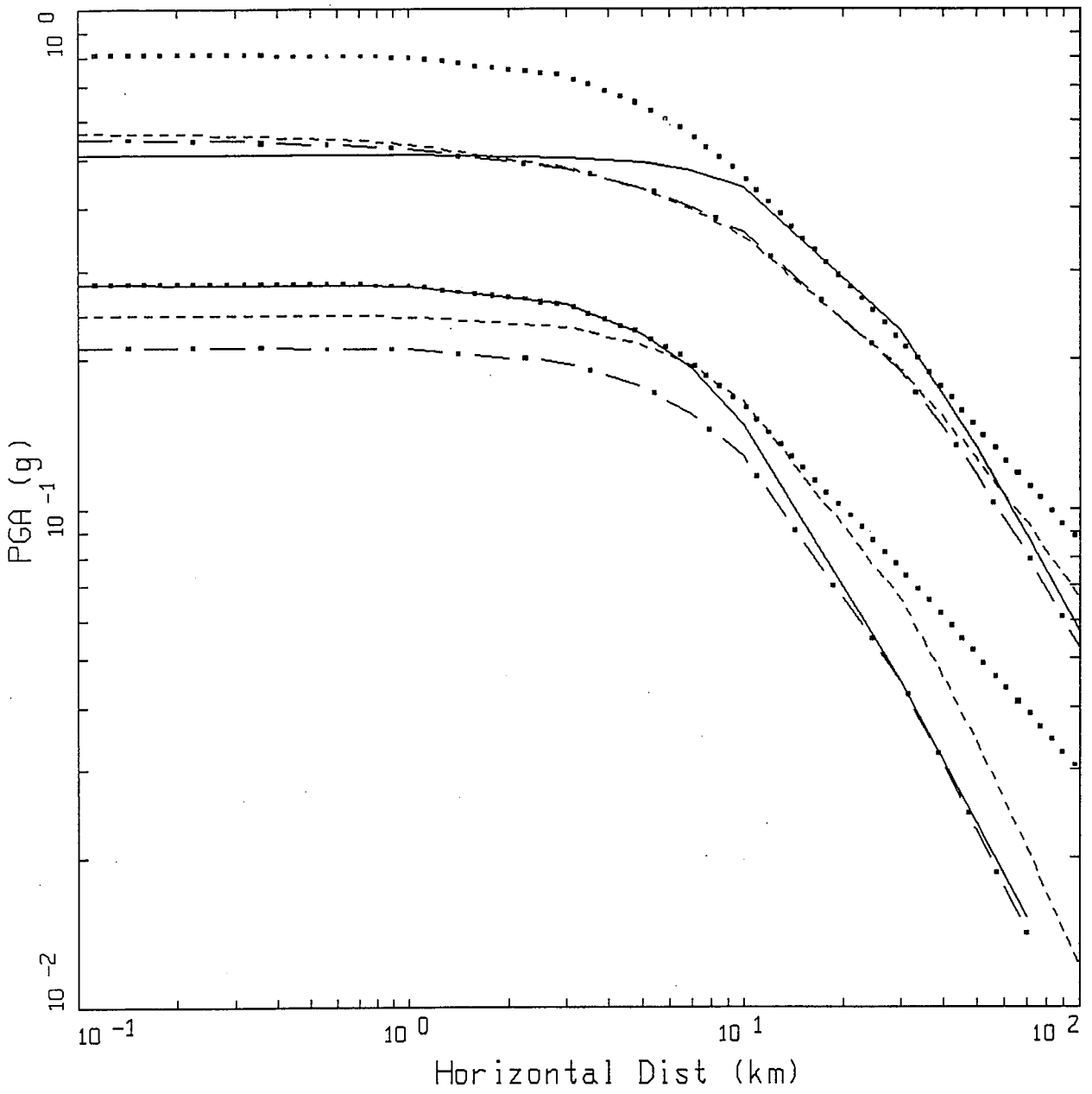

COMPARISON OF SOIL PGA RELATIONS
M 5.5 AND 7.5 (STRIKE SLIP)

LEGEND

——— CAMPBELL, 1994 (SOIL)

- - - - - IDRISS, 1991 (DEEP SOIL)

• • • • BOORE, JOYNER & FUMAL, 1993 (CLASS C)

—— • — SADIGH, 1987 (SOIL)

Figure 10.

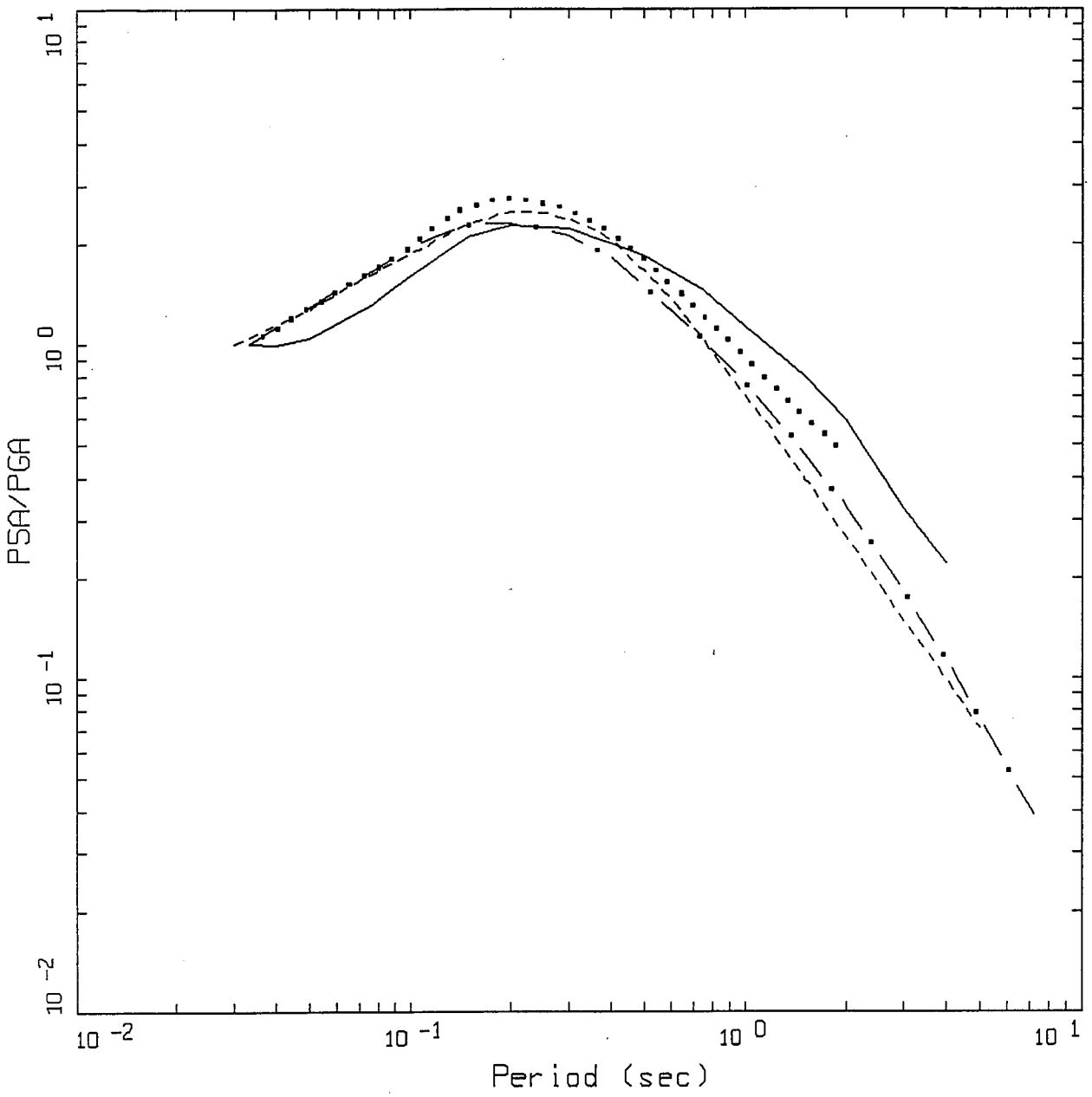

COMPARISON OF ROCK PSA/PGA RELATIONS
M 6.75 (STRIKE SLIP), R = 10 KM

LEGEND

——— CAMPBELL, 1989 (SOFT ROCK)

- - - - - IDRISS, 1991 (ROCK)

• • • • BOORE, JOYNER & FUMAL, 1993 (CLASS B)

— • — SADIGH, 1991 (ROCK)

Figure 11.

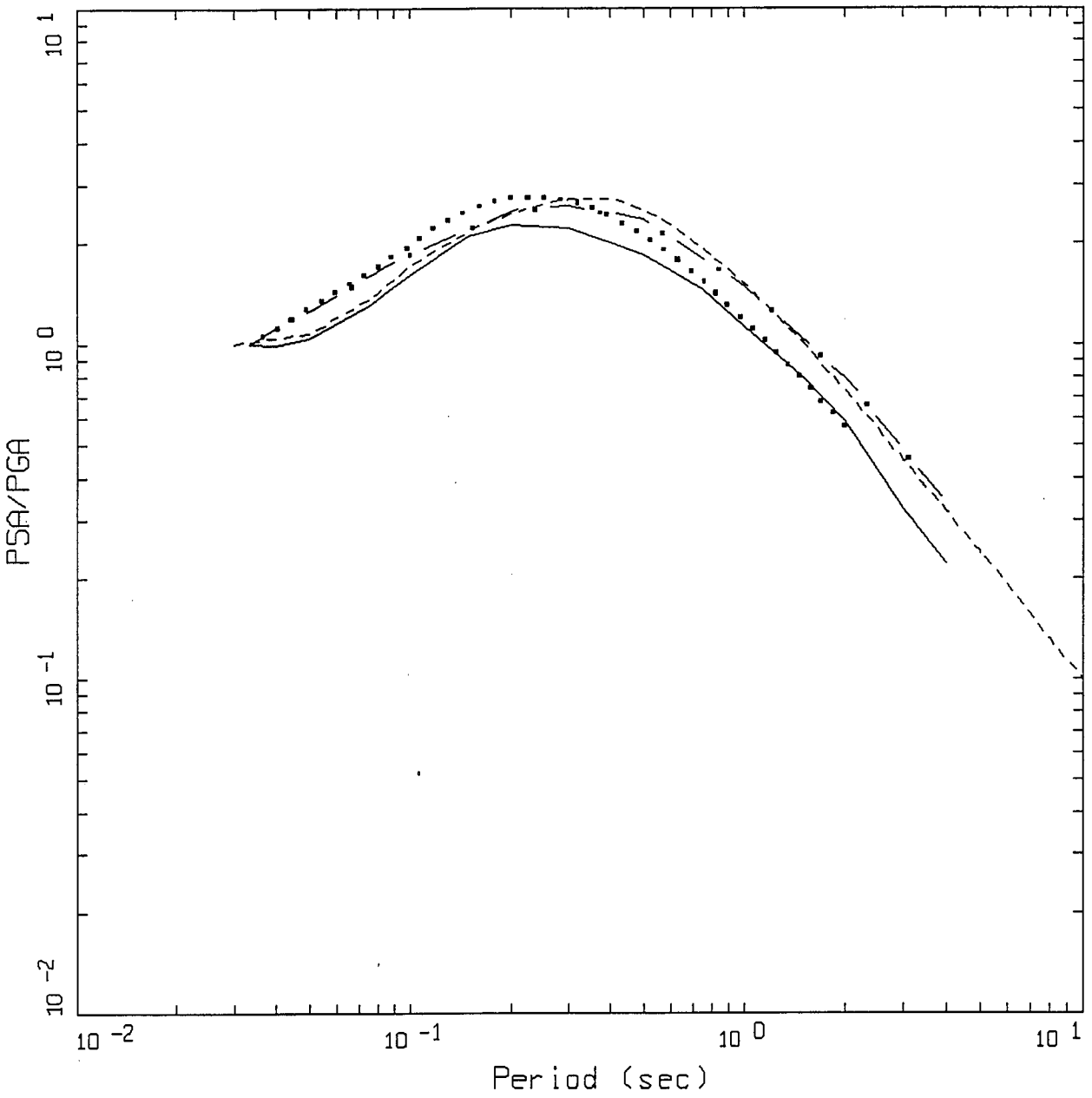

COMPARISON OF SOIL PSA/PGA RELATIONS
M 6.75 (STRIKE SLIP), R = 10 KM

LEGEND

——— CAMPBELL, 1989 (SOIL)

- - - - - IDRISS, 1994 (DEEP SOIL)

• • • • BOORE, JOYNER & FUMAL, 1993 (CLASS C)

— • — SADIGH, 1987 (SOIL)

Figure 12.

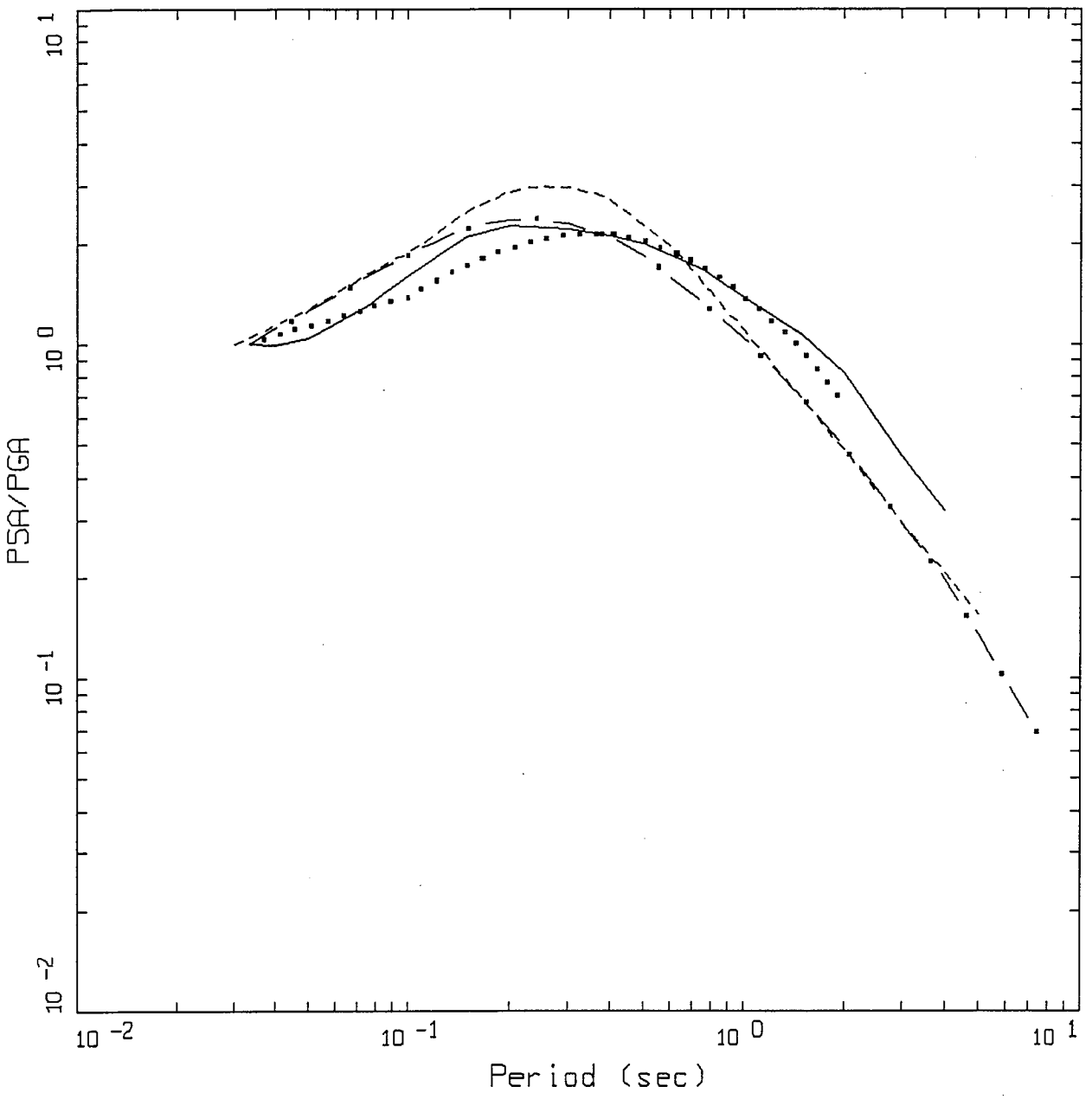

COMPARISON OF ROCK PSA/PGA RELATIONS
M 7.75 (STRIKE SLIP), R = 10 KM

LEGEND

——— CAMPBELL, 1989 (SOFT ROCK)

- - - - - IDRISS, 1991 (ROCK)

• • • • BOORE, JOYNER & FUMAL, 1993 (CLASS B)

— • — SADIGH, 1991 (ROCK)

Figure 13.

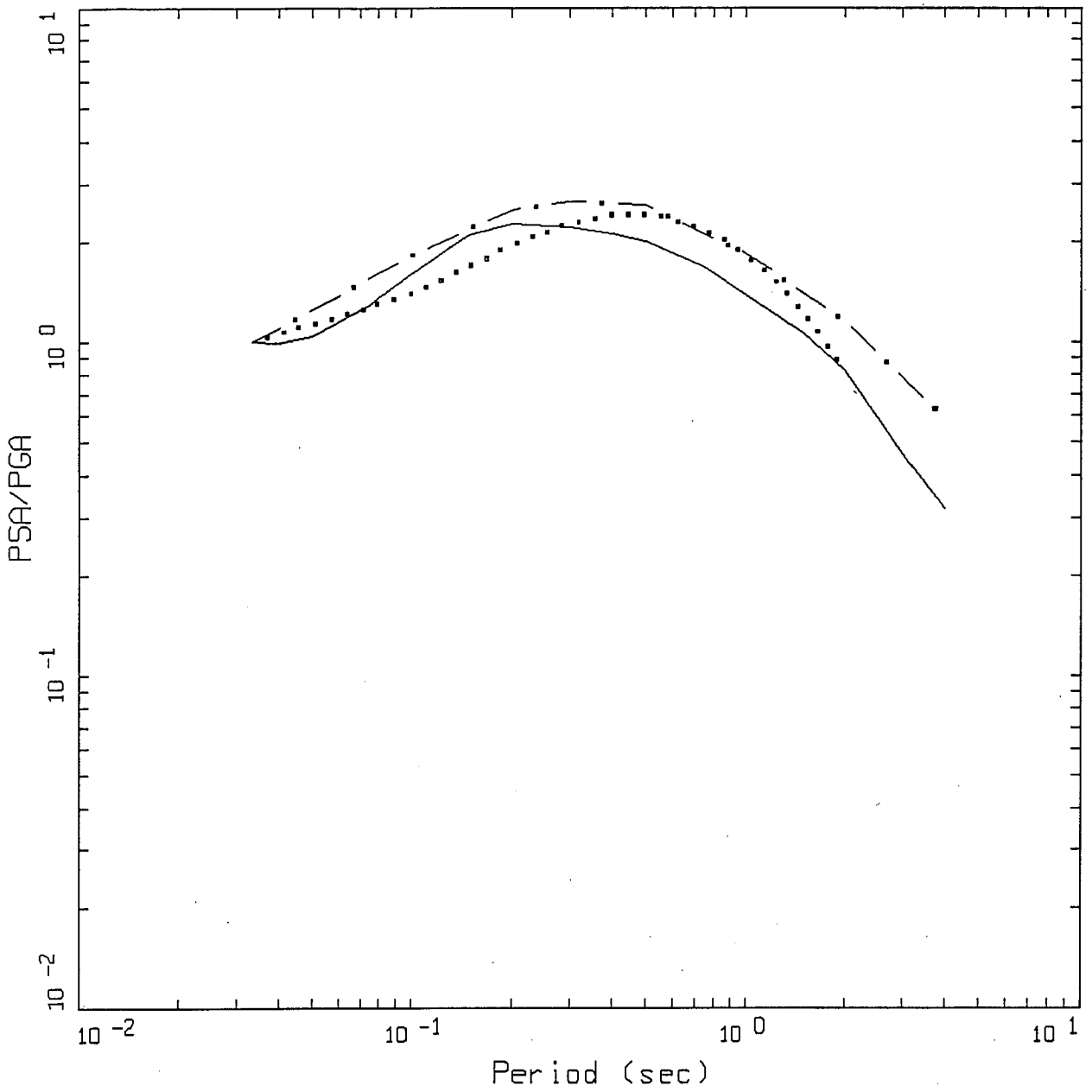

COMPARISON OF SOIL PSA/PGA RELATIONS
M 7.75 (STRIKE SLIP), R = 10 KM

LEGEND

——— CAMPBELL, 1989 (SOIL)

• • • • BOORE, JOYNER & FUMAL, 1993 (CLASS C)

— • — SADIGH, 1987 (SOIL)

Figure 14.

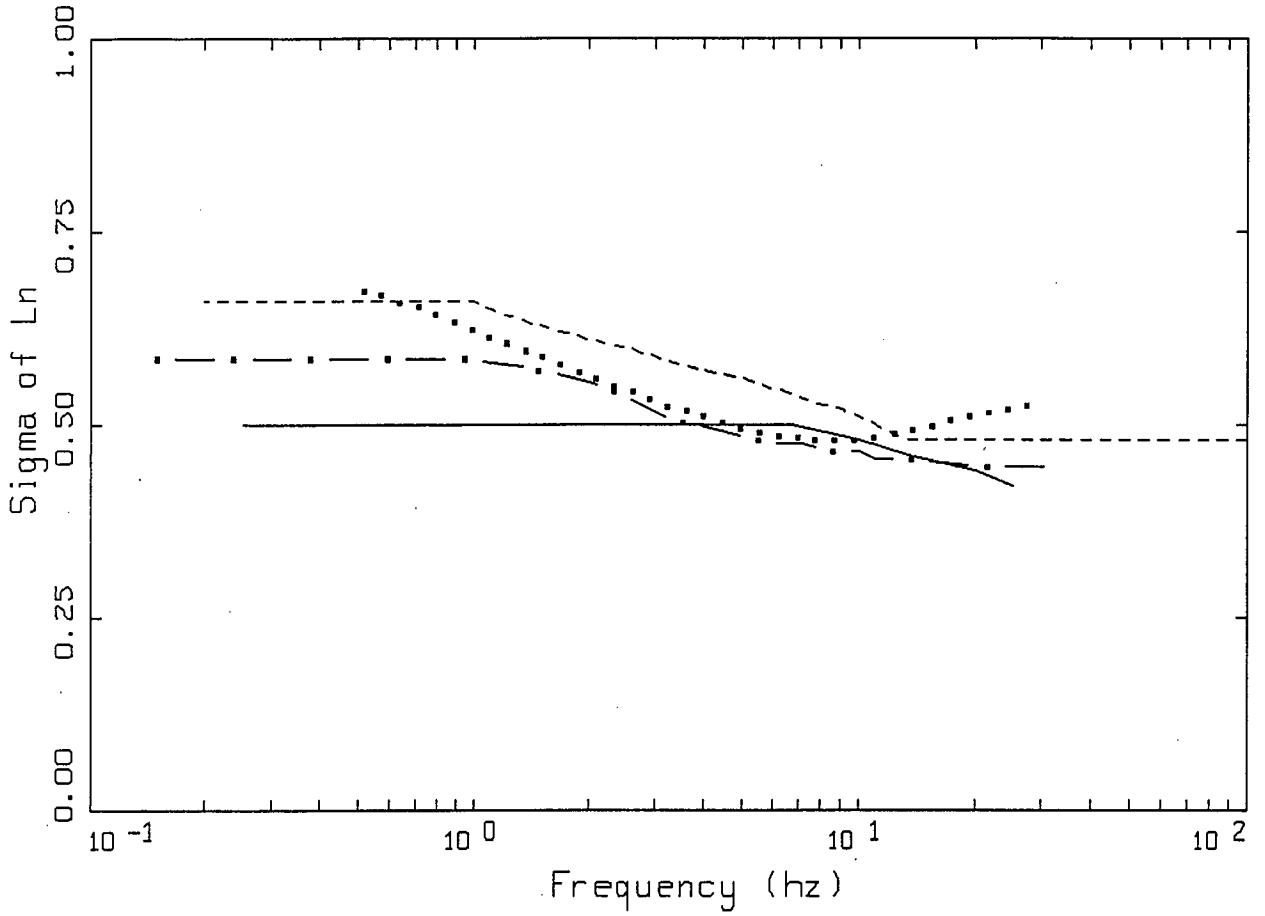

COMPARISON OF UNCERTAINTY
IN ATTENUATION RELATIONS FOR M=6.75

LEGEND

——— CAMPBELL, 1989 (SOFT ROCK/SOIL)

- - - - - IDRISS, 1994 (ROCK, STIFF AND DEEP SOIL)

• • • • BOORE, JOYNER & FUMAL, 1993 (CLASS A, B, AND C)

— • — SADIGH, 1991 (ROCK)

Figure 15.

Evaluation and Implementation of an Improved Methodology for Earthquake Ground Response Analysis

Uniform Treatment of Source, Path and Site Effects

Seminar 5

(10/27/94, 37 p.)

Numerical Ground Motion Models

a) General References
b) Review: Empirical Attenuation Models
c) Introductory Comments
d) Background
    1) Purely Theoretical Method
    2) Empirical Green Function Method
    3) Empirical Source Function Method
    4) Stochastic Finite Fault Method
e) Empirical Green/Source Function Method
f) Stochastic Finite Fault Model
    1) Point Source Model
    2) Finite Fault Model
    3) Uncertainty in Model Parameters

CALTRANS

SEMINAR ON STRONG GROUND MOTION

Seminar 5; October 27, 1994 NBW

Numerical Ground Motion Models

a) General References:

See REFERENCES

b) Review: Empirical Attenuation Models

1) General Functional Form

$$\log y = C_1 + C_2 M + C_3 M^{C_4} + S\,(mechanism) \qquad \textit{source}$$

$$C_5 \log (r + C_6 EXP (C_7 M)) + C_8 r + \qquad \textit{path and source}$$

$$s\,(site) \qquad \textit{site}$$

2) Procedure: regress on data to determine C_j, S, s

a) Data set may be entirely recordings or supplemented with simulations,

b) Simulations may guide in selecting functional form and/or constraining coefficients.

3) Data Density

Data density (M, r) determines high and low confidence areas in M, r space: Where the relations are well constrained the difference between relations is small. For M and r where the data are sparse the differences are much greater and largely controlled by particular functional forms and constraints placed on coefficients (particularly C_6 and C_7; saturation terms)

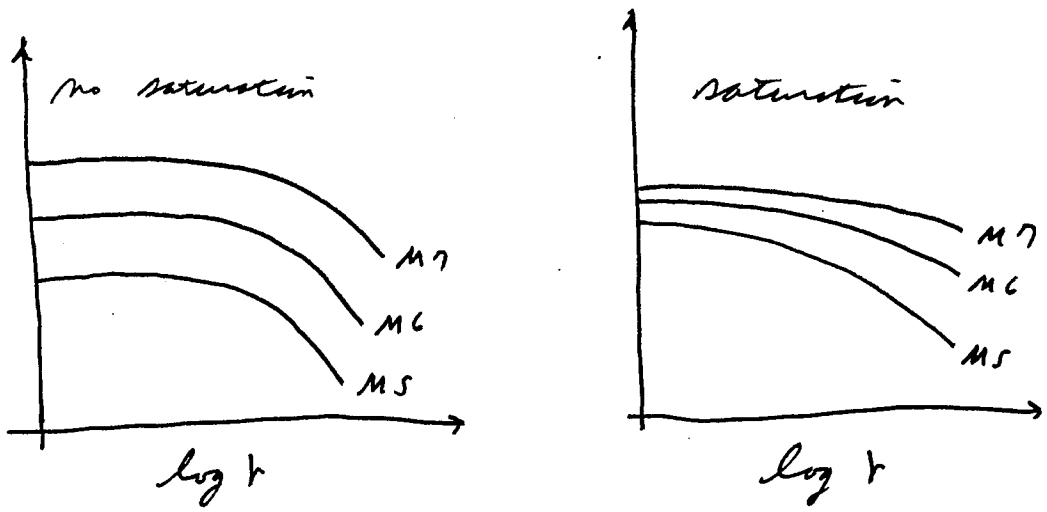

4) $M > 6.5$, $r < 10$ km data still sparse particularly $M \geq 7$ and for rock sites, best to average 3-4 relations.

5) Four Relations Introduced

a) Campbell

2) Idriss

3) Boore et al 1993, 1994

4) Sadigh.

Each had particular features!

6) Future Trends:

a) Uncertainty is magnitude (amplitude) dependent

b) Effects of mechanism: reverse slip 20-30% higher PGA than strike and normal slip earthquakes

c) Hanging-wall 20% higher PGA than foot-wall

d) Near source:

1) Saturation

2) Directivity: fault normal component 20-40% larger than fault parallel.

c) Introductory Comments

In this and subsequent seminars, the emphasis will be on the stochastic finite fault numerical modeling approach to provide sufficient background for routine implementation by CALTRANS. In this seminar, the various approaches to modeling strong ground motions will be introduced and references cited. The concentration will be on the stochastic point and finite source models with detailed presentations of both. Particular emphasis will be placed on the RVT aspect, model parameters, and uncertainties. Only rock sites will be considered as site effects will be addressed in detail in the next 3 seminars.

d) Background

In general there are two basic forms of the theoretical approach to computing synthetic motions: purely theoretical and semi-empirical. As implied by the descriptive classifications, the semi-empirical incorporates some aspect of actual recordings into the simulation process. The motivating desire behind this approach is to accommodate some natural aspects of source, path, and/or site processes into the motions. The trade-off being in a method which is less transportable: records representing the source, path, and site conditions under consideration are required or assumed to be applicable.

1) Purely Theoretical Method

Methods that rely totally on mathematical models may be separated into kinematic (fault slip is specified) or dynamic (stresses acting upon the fault surface are specified). The kinematic models are, by far, the most straight-forward in terms of mathematical representation, physical interpretation, and use. As a result, kinematic models are in more widespread use than dynamic models and are the usual method employed for synthetic strong motion computations. This method requires specification of the time and spatial distribution of slip on a fault surface combined with the computation of Green functions for the particular propagation path. The Green function represents the medium response, at the location of the site, to a point source (in space and time) located on the source fault surface (Helmberger and Malone, 1975; Helmberger and Harkrider, 1978; Aki and Richards, 1980). The heart of this method is the calculation of Green functions for realistic earth models.

The application of kinematic ground motion modeling dates to the work of Aki

(1968) and Haskell (1969) in which a smooth temporal and spatial distribution of slip was assumed. While appropriate for simulations of teleseismic and long period strong ground motions (Bouchon, 1981), accurate simulation of higher frequencies (1-35 Hz) requires nonuniform spatial distributions of slip. Early applications of kinematic modeling that revealed the importance of heterogeneities in slip include: the 1968 Borego Mountain earthquake by Heaton and Helmberger (1977); the 1971 San Fernando earthquake by Trifunac (1974), Heaton and Helmberger (1979), and the 1979 Imperial Valley earthquake by Hartzell and Helmberger (1982) and Olson and Absel (1982). More recent developments feature greater accuracy (and speed) in computing Green functions for vertically heterogeneous earth models (Luco and Apsel, 1983; Apsel and Luco, 1983; Spudich and Ascher, 1983; Ascher and Spudich, 1986) as well as laterally heterogeneous structure (Spudich and Frazer, 1984).

In application of the kinematic modeling, it is generally found that nonuniform slip, in terms of one or more patches of relatively large slip, or asperities, are necessary to explain essential features of strong ground motions (Hartzell and Heaton, 1986). The location and size of these asperities generally controls short period aspects of strong motion, consequently their distribution (location, size, and amount of slip) is an essential element of deterministic modeling. Because the character of asperities is generally not known for future earthquakes, it is desirable to model suites of "reasonable", or perhaps random, asperity distributions and then use an average result.

Dynamic models of faulting, in which the stresses are specified, are significantly less tractable than kinematic models. Das (1980) has developed a 3-D boundary integral approach to dynamic rupture problems. Das and Kostrov (1983) have modeled the breaking of a single asperity and Andrews (1985) has modeled rupture propagation controlled by a slip-dependent friction law. Boatwright and Quin (1986) have developed a dynamic model in which initial conditions are randomized and rupture initiation is spontaneous for any point on the fault surface.

While these dynamic models are quite useful in studying the physics of rupture

initiation and propagation (dislocation dynamics), they are currently of limited use in modeling strong ground motions because of difficulties in determining the required input parameters.

2) Empirical Green Function Method

Introduced by Hartzell (1978) this method has as its basis the use of observed records from small earthquakes as Green functions. To simulate a large earthquake, the observed Green functions earthquakes are scaled for distance and radiation pattern differences between the source and recorded motion sites and that of the simulated earthquake (Hartzell, 1978). The large event to be simulated is then treated as a linear combination of smaller events with site specific wave propagation (path and site) naturally incorporated through the observed empirical Green functions (Heaton and Hartzell, 1986). Implicit in applications of this technique is the assumption of similarity in that source spectral characteristics of smaller events are the same as those from the larger earthquake. This appears to be valid at least for earthquakes having moment magnitude less than about $8^{1/4}$. An important aspect of the method is the direct incorporation of the effects of dynamic rupture over the source dimension of the small event. The source of the smaller event has rupture properties that are likely similar to that of a postulated larger event. Therefore, the effects due to statistical irregularity of the rupture process are present in the modeled motions. Descriptions and applications of the technique are given by Hartzell (1978, 1985), Kanamori (1979), Hadley and Helmberger, (1980), Irikura (1983), Munguiá and Brune (1984), Houston and Kanamori (1986) and Heaton and Hartzell, (1986).

While the empirical Green function approach has many attractive features, simplicity in concept being among them, there are important details in the summation process that control both the low and high frequency levels of the radiated spectrum. In order for the simulated event to have the correct moment, N smaller events must be summed, with N specified by an integral ratio of the moment of the larger event to the smaller (Hartzell, 1985; Heaton and Hartzell, 1986). If uniform rupture is assumed, the Fourier amplitude spectrum of the simulated earthquake will underestimate the high

frequency content of the larger source, showing too rapid a decay with frequency (ω-cube instead of ω-square) (Hartzell, 1985). To remedy this artifact of smooth rupture propagation, randomness must be added to the process. Typically this is done by adding a random element to the rupture velocity, rise time, radiation pattern, or slip distribution to create asperties (Hartzell, 1985). The elements of randomness may be added to one or more of these faulting parameters; the shape of the computed spectrum at high frequencies is sensitive to the degree of randomness and to which parameters are affected.

Joyner and Boore (1986) address the consequences of source scaling laws and the constraints they place upon summation techniques in general. It is essential to carefully calibrate or validate the method with ground motion data over a wide period range or bandwidth for earthquakes that must be modeled as extended sources, that is, for earthquakes where rupture propagation characteristics are apparent in the strong motion recordings.

3) Empirical Source Function Method

A shortcoming of the empirical Green function method is the lack of a sufficient number of recorded small earthquakes on the source of interest (Hadley et al., 1982). To circumvent this problem, an elegant augmentation to the empirical Green function technique was introduced by Hadley et al., (1982) in which Green functions are computed for the particular crustal model pertinent to the area of interest. The observed small earthquake is then used as an empirical source and site function that describes, in a realistic nature, the stochastic elements in the dislocation time history (Wald et al., 1988).

This approach faces the same issues as the empirical Green function method regarding long period constraints (moment) in terms of number of small sources to sum. In addition, similar questions regarding appropriate degrees and types of randomness to introduce into details of rupture to produce the proper high frequency behavior must also be resolved. The main advantage naturally is that the source/site function need not be recorded in the area of interest. It is important however, to deconvolve the propagation path effects appropriate to the region in which the source function was recorded (Barker et al., 1988). The method has been validated in both Western North America and Eastern North America tectonic

environments (Barker et al., 1988; Wald et al., 1988) by comparing recorded and simulated motions.

The uncertainty and bias in the empirical source function method has recently been evaluated (Abrahamson et al., 1990). For peak acceleration, the total uncertainty is represented by a scale factor of approximately 1.6 for the one sigma level. The bias indicates that the methodology is most appropriate at frequencies exceeding about 3 Hz (Abrahamson et al., 1990).

Another, perhaps, limiting aspect of the empirical source function method is the lack of site specificity. The empirical source function is assumed to represent site effects as well as the source specific dislocation time history (Wald et al., 1988). Strictly, the technique is appropriate for site conditions upon which the small earthquake used for the source function was recorded. To treat varying site conditions, the appropriate response of the site from which the source function was extracted must be deconvolved and the response of the near site convolved into the motions. This imposes two sources of uncertainty onto the process.

For short period (3-35 Hz) simulations of strong ground motions close to extended sources the empirical source function technique is well calibrated for applications to Western North America. It represents a very powerful tool for applications where appropriate source-site functions are available or where site specific effects are not essential, desired, nor warranted.

4) Stochastic Finite Fault Method

The stochastic Finite Fault model (Schneider et al., 1993) is a purely theoretical kinematic model and may be considered a relative of the empirical source function method. The stochastic finite fault model follows the same procedures as the empirical source or Green function methods but substitutes a theoretical source model compared to the empirical source function method and theoretical source, path, and site models (Green functions) in comparison to the empirical Green function method. In short it uses theoretical green functions with region and site specific source, path, and site parameters.

e) Empirical Green/Source Function Method

This method was first introduced by Hartzell (1978) where he used aftershock records of the 1940 Imperial Valley, California earthquake recorded at El Centro to model the El Centro mainshock displacement record. Since that time the technique has been implemented and expanded by many workers including the Japanese (Irikura, 1983).

1) Fundamental Assumptions:

a) Similarity: Source parameters for small and large earthquakes are related.

All of the kinematic simulation methods which add small earthquakes to model a large earthquake rely on the following similarity conditions (Kanamori and Anderson, 1975)

$$\frac{W}{L} = \textit{constant, aspect ratio}$$

$$\frac{\overline{D}}{L} = \textit{constant, strain drop}$$

$$\frac{\tau}{\tau_D} = \frac{\tau\, V_R}{L} = \textit{constant, dynamic similarity;}$$

where

W = *fault width*

$\overline{D}$ = *average slip*

L = *fault length*

τ = *rise time*

V_R = *rupture velocity*

τ_D = *faulting duration* = L/V_R

These similarity conditions can be deduced from the relations shown in Figure 1:

$$L \alpha W \alpha \overline{D} \alpha \tau \alpha M_0^{\frac{1}{3}}, \quad \textit{or alternatively}$$

$$M_0 \alpha L^3$$

and

$$V_R \approx \textit{constant}$$

With the similarity conditions we can write relationships of fault parameters between a large and a small earthquake

$$\frac{L_l}{L_s} = \frac{W_l}{W_s} = \frac{\overline{D_l}}{\overline{D_s}} = \frac{\tau_l}{\tau_s} = (\frac{M_{0\,l}}{M_{0\,s}})^{\frac{1}{3}} = N^{\frac{1}{3}} \qquad (1)$$

where subscripts l and s refer to large and small respectively and N represents the number of small earthquakes to add to match the moment of the large earthquake.

b) Linearity: motion (hard rock outcrop) due to a large earthquake may be written as a sum over small earthquakes.

In general, the motion $U(t)$ due to slip velocity $\dot{D}\ (x, y, t)$ distributed on a fault surface with length L and width W may be written as

$$U(t) = \int_0^W \int_0^L \dot{D}(x, y, t,) * G(x, y, t,)\ \ d\,y\,d\,x \qquad (2)$$

where * denotes time convolution, G (x, y, t) is the double-couple motion due to a fault displacement of unity (impulse in space) and is termed the Green function.

If the system is linear, U(t) can be decomposed into contributions from individual patches (subfaults) on the rupture surface

$$U(t) = \sum_{i}^{NW} \sum_{j}^{NL} U_{ij}(t) \tag{3}$$

where

$$U_{ij}(t) = \int_{(i-1)\Delta W}^{i\Delta W} \int_{(j-1)\Delta l}^{j\Delta l} \dot{D}(x, y, t,) * G(x, y, t,) \; d\,y\,d\,x \tag{4}$$

and $\Delta W = W/NW \qquad \Delta l = l/NL.$

Assume have recordings of motions due to a small earthquake on the i, j^{th} subfault

$$U^{s}_{ij}(t) = \int_{(i-1)\Delta W}^{i\Delta W} \int_{(j-1)\Delta l}^{j\Delta l} \dot{D}^{s}_{ij}(x,y,t) * G(x,y,t)\; dydx \tag{5}$$

where

$\dot{D}^{s}_{ij}(x, y, t)$ is the slip velocity distribution for the small earthquake.

If a function can be defined to relate the subevent slip distribution (D^{s}_{ij}) to that of the large earthquake (D)

$$D(x, y, t) = F_{ij}(t) * D^{s}_{ij}(x, y, t) \tag{6}$$

then

$$U(t) = \sum_{i}^{NW} \sum_{j}^{NL} F_{ij}(t) * U^{s}_{ij}(t) \tag{7}$$

and $F_{ij}(t)$ is taken as a series of impulses of average delay given by the subevent rise time τ_s and of duration given by the rise time of the large earthquake τ_l. F_{ij} then distributes

the subevent rise time over the duration of the slip duration of the large earthquake to build up the total slip.

$$F_{ij} = S_{ij} \sum_{k=1}^{NF} \delta (t - T_{ij} - \tau_k) \qquad (8)$$

where

$T_{ij} = T_{Rupt} + \epsilon_1$

T_{Rupt} = *time for rupture front to reach subfault*

ϵ_1 = *random term to accelerate/decellerate rupture front, non circular rupture front*

$\tau_\kappa = k\ \tau_s + \epsilon_2$

τ_s = *subevent rise time*

ϵ_2 = *random term*: log *normal with* $\sigma_{ln} = 0.8$*

NF = number of subevents to fire to build up large earthquake rise time

S_{ij} = relative slip weights scaled to give correct moment (asperity distribution) and δ is the Dirac delta function: $\delta\ (0) = 1$

The motion (Equation 3) can then be written as a triple sum

*Stochastic finite fault

$$U(t) = \sum_{i}^{NW} \sum_{j}^{NL} S_{ij} \sum_{k}^{NF} U_{ij}^{s}(t) * \delta(t - T_{ij} - \tau_k) \qquad (9)$$

The process is depicted in Figure 2.

For application to the stochastic finite fault, the Brune point-source model is substituted for the recordings of small earthquakes $U^s_{ij}(t)$.

c) Parameter Selection

The selection of the correct parameter values is based partly on theory and partly on validation exercises. In general, we require the following parameters:

NW, number of subfault along width

NL, number of subfault along length

NF, number of subevents to fire in each subfault

τ_s and τ_l, rise times.

From Equation (1) the similarity conditions give us

$$\frac{M_{0l}}{M_{0s}} = NW \cdot NL \cdot NF$$

$$= \frac{\mu A_l \overline{D_l}}{\mu A_s \overline{D_s}} \qquad (10)$$

then

$$\frac{A_l}{A_s}\frac{\overline{D_l}}{\overline{D_s}} = NW \cdot NL \cdot NF$$

and from (1) $$\frac{\overline{D_l}}{\overline{D_s}} = \frac{\tau_l}{\tau_s}$$

$$\frac{A_l}{A_s}\frac{\tau_l}{\tau_s} = NW \cdot NL \cdot NF$$

which we can break up into

$$\frac{A_l}{A_s} = NW \cdot NL \quad , \quad \frac{\tau_l}{\tau_s} = NF \quad . \tag{11}$$

At this point, we simply require a rule to fix rupture area based on M_0 or **M**. Using the Wells and Coppersmith (1994) relation,

$$\log A = -3.49 + 0.91\,\mathbf{M} \tag{12}$$

fixes the area of the large earthquake.

For applications of the stochastic finite fault method to crustal earthquakes, the subevent magnitude is taken to be M5* (for large subduction zone earthquakes with **M** $\geq$ 7.5, M_s = 6.4) and the area is taken to be about 10 km^{2*}. Since such small sources are thought to be approximately square (or circular)
L = W $\approx \sqrt{10} \approx$ 3 km.

To fix rise time, another empirical relation is used

$$\log \tau = 0.33 \log M_0 - 8.62 \; . \tag{13}$$

This is based on measured rise times for a number ($\approx$ 15) of earthquakes with well

*Based on validation exercises

determined moments. In the current implementation Equation (13) is used for τ_s and τ_1 and NF computed from Equation (11), $NF = \tau_1/\tau_s$.

To fix L and W for the earthquake, the subsurface rupture length from Wells and Coppersmith (1994) can be used

$$\log RLD = -2.44 + 0.59M, \tag{14}$$

along with their relation for rupture width

$$\log RW = -1.01 + 0.32M . \tag{15}$$

The width should be truncated such that the fault depth does not exceed the seismogenic crust or about 15-17 km. At this point as M increases, the rupture width is fixed and rupture length is computed by dividing rupture width out of the estimated rupture area.

To model an earthquake of moment magnitude M_1 the following process is used to develop the fault parameters:

1) Assume (for the stochastic finite fault) M_s fixed at M5 with an area of $\approx$ 10 km^2 and $\Delta l \approx \Delta W \approx 3\ km$,

2) Compute A_1 using $\log A_1 = -3.49 + 0.91\ M_1$

3) Compute/determine L and W

4) $NL \cdot NW = A_l / A_s$

5) Choose final Δl and ΔW so that

   a) $NL \cdot \Delta l \approx L, \quad NW \cdot \Delta W \approx W$

   b) $\Delta l \cdot \Delta W \approx 10\ km^2$

   c) $NL \cdot NW \approx A_1/A_s$

6) $NF = 10^{0.5(M_l - M_s)}$

Example: $M_l = 7.0$, $W = 10$ km as constraints.

$$M_s = 5.0 \quad , \qquad A_s \approx 10\ km^2$$

$$A_l = 759\ km^2$$

$$L = 759\ km^2/10\ km \approx 76\ km$$

$$NL \cdot NW = A_l/A_s \approx 76$$

$$\Delta W = W/NW = 10\ km/3 \quad = 3.33\ km$$

$$\Delta l = 10\ km^2/3.33\ km \approx 3.00\ km$$

$$NW = 3 \quad , \quad NL = 76\ km/3.00 \approx 25$$

$$NW \cdot NL = 75 \approx A_l/A_s$$

$$NF = 10^{0.5(M_l - M_s)} = 10$$

f) Stochastic Finite Fault Model

The preceding development on the empirical Green/source function method has been general with the exception of fixing M_s to 5 and A_s to about 10 km^2. This restriction is for the stochastic finite fault and is based on validation exercises using these subevent parameters. Changing them would require revalidation and some adjustment on the distributions of random variables rupture time and rise time (see Equation 8).

The following development will be on the stochastic finite fault in particular. The essential difference between it and the empirical Green/source function approach is the substitution of a Brune single-corner-frequency ω-square point source model for the Green/source function. In addition, random vibration theory RVT is used to estimate peak time domain values for PGA, PGV, and response spectra. Time histories may be generated by

simply adding the phase spectrum for a M5 earthquake recorded at close distances and on rock (CF. see Seminar 1, Figures 32-35). To illustrate the entire set of model parameters, the Brune point source model will be reviewed followed by the stochastic finite source model.

1) Point Source Model

From Seminar 1 Equation (14), the Fourier amplitude spectrum for the point source model for rock sites is given by

$$\hat{a}(f) = C \frac{M_0 f^2}{1 + (\frac{f}{f_c})^2} \cdot \frac{e^{-\frac{\pi f R}{\beta Q(f)}}}{R} \cdot A(f) e^{-\pi \kappa f} \qquad (16)$$

$$and\ C = \frac{1}{\rho \beta^3} \cdot 2 \cdot 0.63 \cdot \frac{1}{\sqrt{2}} \quad ,$$

$$f_c^3 = \frac{\beta^3}{8.44} \frac{\Delta \sigma}{M_0} \quad ,$$

with parameters

M_0 = seismic moment, $\log M_0 = 1.5\,M + 16.1$,

$\Delta\sigma$ = stress drop,

ρ = source region mass density,

β = source region shear-wave velocity,

$Q(f) = Q_0(\frac{f}{f_0})^{\eta}$ = crustal path damping,

A(f) = amplification factors or crustal model,

κ = damping in shallow crustal rocks.

The numerical constants in the term C represent

2 = free surface effect

0.63 = average radiation pattern coefficient (Boore and Boatwright, 1984)
$1/\sqrt{2}$ = vectorial partition into a random horizontal component.

In applications to the finite-fault model $\tilde{a}(f)$ is used as a Green function and point sources are distributed on the fault surface at specified locations. As a result, R becomes the subfault to site distance; ρ, β, and A(f) are taken appropriate for mid-fault depths, and the 0.63 and $1/\sqrt{2}$ terms are set to 1.

2) Finite Fault Model

The stochastic finite-fault model is depicted in Figure 3 (Figure 34, Seminar 2) where point source models are shown distributed on the fault surface. As discussed in Section (e), the stochastic finite-fault is a subset of the empirical Green/source function method simply summing point sources with Brune spectra as Green functions. In the implementation of the method the spike seismogram (porcupine) given by Equation (8) is computed for subfaults closest to each Green function and scaled by the slip, subfault-to-site distance, and radiation pattern (optional). After the sum has been computed for the nearest subfaults, the porcupine is transformed into the frequency domain and multiplied by the complex source spectrum including the Q(f) and kappa operators. The next Green function is considered and the porcupine computed for its nearest subfaults (no double counting), transformed into the frequency domain, and multiplied by the appropriate complex source spectrum. The spectrum is added to the first and the process repeated for each Green function. The result is a complex spectrum reflecting source finiteness and directivity. The summed spectrum is then propagated through a crustal model (or amplification factors added) and finally an equivalent-linear site model. At this point, a time history may be produced if a phase spectrum for the M_s earthquake was added to the Brune source spectrum (by default an analytical Brune phase spectrum is used). To provide statistical stability over the different phase spectra which could be associated with the M_s subevent and, consequently, the large earthquake phase spectrum, RVT is used to estimate PGA, PGV, and response spectra from the summed power spectrum (Appendix A).

To provide an appropriate duration for use in the RVT estimates, the summed complex spectrum is transformed into the time domain and the 5-75% Arias intensity computed (Ou and Herrmann, 1990). As a result, effects of source finiteness such as asperity distribution and directivity are reflected in the duration as well as in the summed power spectral density.

a) Finite Fault Geometry

Figure 4 shows the finite fault geometry and coordinate systems. It is adopted from Aki and Richards (1980) Figure 4.20. We have added fault zone coordinates (XFC, YFC) to ease inputting suites of nucleation points. Global coordinates are right handed with axes x, y, z and z positive down. The slip vector $\overline{D}$ is taken relative to the x-y plane and is taken as the direction of the hanging wall. The rake angle ϕ is the angle between the strike direction and slip vector and varies between $-\pi$ and π. ϕ = 0, π for strike slip earthquakes and for $0<\phi<\pi$ there is some vertical component of slip. To accommodate nonuniform slip angles, rake must be specified for each subfault in the finite code.

Fault strike is controlled by the angle λ and dip by the angle δ. A vertical fault has $\delta = \pi/2$ and $\phi = 0$ *or* π while a dip-slip fault has $\delta = \pi/2$ but $\phi = \pi/2$ or $-\pi/2$. By convention the foot wall is taken to lie in the down dropped block, then $\phi = \frac{\pi}{2}$

b) Finite Fault Model Parameters

For rock sites, the specific model parameters for the finite fault are:

General Parameters

ρ = source region mass density,

β = source region shear-wave velocity,

$Q(f) = Q_0(\frac{f}{f_0})^{\eta}$ = crustal path damping,

κ = damping in shallow crustal rocks.

A(f) = amplification factors or crustal model

Subevent Parameters

M_s = 5.0 magnitude

L_s, W_s; $A_s \approx 10$ km^2; source area

NL, NW = number of subfaults along length and width

$$\Delta\sigma = \frac{7}{16}\frac{M_0^s}{r_s^5}, \qquad r_s = \sqrt{A_s/\pi}\ ; \qquad \text{point source stress drop}$$

Finite Fault Parameters

M_1 = magnitude

S_{ij} = relative slip for each subfault

λ = fault strike

δ = fault strike dip

ϕ_{ij} = fault rake for each subfault

$V_R = 0.8\,\beta$, rupture velocity

XFC, YFC = nucleation point

τ_1 = rise time

xs, ys, zs = site location

3) Uncertainty In Model Parameters

There are two sources of variability associated with using a numerical model to predict strong ground motions: modeling variability and parametric variability. Modeling variability is a measure of how well the model works (how accurately it predicts ground motions) when specific parameter values are known. The modeling variability is measured by misfits of model

predictions to recorded motions and is due to model defects or unaccounted for components in the source, path, and site models (i.e. a point-source cannot model the effects of directivity).

Parametric variability results from variability in model parameters (i.e. slip distribution, soil profile, etc). Both the modeling and parametric variabilities may have components of randomness and uncertainty. Randomness represents the component of variability which is intrinsic or irreducible for a given model. The uncertainty component reflects a lack of knowledge and may be reduced as more data are analyzed. For example, in the point-source model, stress drop is generally taken to be independent of source mechanism and region and is found to vary substantially with a standard error of about 0.7 (natural log) (EPRI, 1993). This variation or uncertainty in $\Delta\sigma$ results in a variability in ground motion predictions for future earthquakes. If, however, seismologists find that normal faulting earthquakes have generally lower stress drops than strike-slip which are lower than reverse mechanism earthquakes, perhaps much of the scatter in $\Delta\sigma$ is due to the grouping. In extensional regimes, where normal faulting earthquakes are most likely to occur, this new information may result in a reduction in uncertainty for stress drop, say to 0.3 or 0.4 resulting in less ground motion variation due to stress drop uncertainty. There is, however, a component of this stress drop variability which can never be reduced in the context of the Brune model. This is simply due to the heterogeneity of the earthquake dynamics which is not accounted for in the model and results in the randomness component of parametric variability in stress drop. A more sophisticated model may be able to accommodate or model more accurately source dynamics but, perhaps, at the expense of a larger number of parameters and increased parametric uncertainty (i.e. the finite fault with slip model and nucleation point as unknown parameters for future earthquakes).

The distinction of randomness and uncertainty is model driven and somewhat arbitrary. The apportion is only important in the context of probabilistic seismic hazard analyses as uncertainty is treated as alternative hypotheses in logic trees while randomness is integrated over. That is, the uncertainty component in stress drop is treated by using an N point approximation to the stress drop distribution and assigning a branch in the logic tree for each stress drop and associated weight. For example, a reasonable three point approximation to a normal distribution is given by weights of 0.2, 0.6, 0.2 for expected 5%, mean, and 95% values of stress drop

respectively. If the distribution of uncertainty in stress drop was such that the 5%, mean, and 95% values were 50, 100, and 20 bars respectively, the stress drop branch on a logic tree would have 50, and 200 bars with weights of 0.2 and 100 bars with a weight of 0.6. The randomness component in stress drop variability would then be formally integrated over in the hazard calculation.

a) Total Variability

For deterministic seismic hazard evaluations, the essential element in a good estimate of 1-sigma motions is the total variability: modeling plus parametric.

1) Modeling Variability: Modeling variability (uncertainty plus randomness) is usually evaluated by comparing response spectra computed from recordings to predicted spectra. The modeling variability is defined as the standard error of the residuals of the log of the average horizontal component (or vertical component) response spectra. The residual is defined as the difference of the logarithms of the observed average 5% damped acceleration response spectra and the predicted response spectra. At each period, the residuals are squared, and summed over the total number of sites for all earthquakes modeled. Dividing the resultant sum by the number of sites results in an estimate of the model variance. Any model bias (average offset) that exists may be estimated in the process (Abrahamson et al., 1990) and used to correct (lower) the variance and to adjust the median as well. In this approach, the modeling variability can be separated into randomness and uncertainty where the bias corrected variability represents randomness and the total variability represents randomness plus uncertainty. The uncertainty is captured in the model bias as this may be reduced in the future by refining the model. The remaining variability (randomness) remains irreducible for this model.

2) Parametric Variability: Parametric variability or the variability in ground motions predictions due to uncertainty and randomness in model parameters is difficult to assess. Formally, it is straight forward in that a Monte Carlo approach may be used with each parameter randomly sampled about its mean (median) value either individually for sensitivity analyses or combined to estimate the total parametric variability (see Seminar

2). In reality, however, there are two complicating factors.

The first factor involves the specific parameters kept fixed with all earthquakes, paths, and sites when computing the modeling variability. These parameters are then implicity included in modeling variability provided the data sample a range in source path and site conditions. The parameters which are varied during the assessment of modeling variation should have a degree of uncertainty and randomness associated with them for the next earthquake. Any ground motion prediction should then have a variation reflecting this lack of knowledge and randomness in the free parameters.

An important adjunct to fixed and free parameters is the issue of parameters which may vary but by fixed rules. For example, rise time is magnitude dependent with its dependency fixed by an empirical relation (Equation 13). In evaluating, the modeling variability with different magnitude earthquakes, rise time is varied, but because it follows a strict rule, any variability associated with rise time variation is counted in modeling variability. This is strictly true, if in the assessment of modeling variation, the sample of earthquakes has adequately spanned the space of magnitude and mechanism and other factors which may affect rise time and the modeled next earthquake is within that space. As a result, the validation or assessment of model variation should be done on as large a number of earthquakes of varying size and mechanism as possible.

The second more obvious factor in assessing parametric variability is a knowledge of the appropriate distributions for the parameters (assuming correct values for median or mean estimates). In general, for the stochastic model, median parameter values and uncertainties are based, to the extent possible, an evaluating the parameters derived from previous earthquakes (EPRI, 1993). Seminar 9 will treat the finite- and point-source model parameters and their uncertainties as well as model sensitivity to individual parameters and. In additions, Seminar 2 presented a limited example of parametric variations for both source models.

The parametric variability is site, path, and source dependent and must be evaluated for

each application. For example, a distant source may show a large variation in ground motion due to path damping while a nearly source may have the site dominate (Seminar 2). The same source and path may have different sites (rock and soil) with very different parametric variability simply due to different uncertainties in the two sites.

In combining the modeling and parametric variations, they are assumed independent (covariance is zero) and the variances are simply added

$$_{\ln}\sigma_T = \text{SQRT}\ (_{\ln}\sigma^2_M + {}_{\ln}\sigma^2_P) \qquad (17).$$

$_{\ln}\sigma^2_M$ = modeling variation

$_{\ln}\sigma^2_P$ = parametric variation

The results for an application to a M 7 normal faulting earthquake at a distance of 20 km for a rock site are shown in Figures 5 and 6 for the point- and finite-source models respectively. For frequencies from about 0.4 Hz to 3 Hz modeling variability dominates while above 3 Hz, the contribution is about equal between modeling and parametric. Interestingly, the variabilities are nearly the same for both sources above 0.4 Hz. The increase in the finite parametric variation at low frequency is likely due to slip model and nucleation point variation.

REFERENCES

Abrahamson, N.A., Somerville, P.G., Cornell, C.A. (1990). "Uncertainty in numerical strong motion predictions" *Proc. Fourth U.S. Nat. Conf. Earth. Engin.*, Palm Springs, CA., 1, 407-416.

Aki, K., and Richards, P.G. (1980). *Quantitative Seismology, Theory and Methods.* W.H. Freeman and Company, 1.

Aki, K. (1968). "Seismic displacements near a fault." *J. Geophys. Res.*, 73, 5359-5376.

Andrews, D.J. (1985). "Dynamic plane-strain shear rupture with a slip-weakening friction law calculated by a boundary integral method." *Bull. Seism. Soc. Am.*, 75, 1-21.

Apsel, R.J., and Luco, J.E. (1983). "On the Green's functions for a layered half-space." *Bull. Seism. Soc. Am.*, 73, 931-951.

Ascher, U., and Spudich, P. (1986). "A hybrid collocation method for calculating complete theoretical seismograms in vertically varying media." *Geophys. J. R. Astron. Soc.* 86, 19-40.

Barker, J.S., Somerville, P.G., and McLaren, J.P. (1988). "Modeling ground-motion attenuation in eastern North America," *Proc. Symp. on Seismic Hazards, Ground Motions, Soil-Liquifaction and Engineering Practice in Eastern North America*, edited by K.H. Jacob, Nat. Center for Earthq. Engin. Res. Tech. Rept. NCEER-87-0025, 339-352.

Boatwright, J., and Quin, H. (1986). "The complex radiation from a 3-D dynamic model of a complex rupture process. Part I: confined ruptures." *Earthquake Source Mechanics.* Maurice Ewing Series, edited by S. Das et al., Am. Geophys. Union., Wash. D.C., 6(37), 97-109.

Boore, D.M. and J. Boatwright (1984) "Average body-wave radiation coefficients." *Bull. Seism. Soc. Am.*, 74, 1615-1621.

Bouchon, M. (1981). "A simple method to calculate Green's functions for elastic layered media." *Bull. Seism. Soc. Am.*, 71, 959-971.

Das, S. (1980). "A numerical method for determination of source time functions for general three-dimensional rupture propagation." *Geophys. J. R. Astron. Soc.*, 62, 591-604.

Das, S., and Kostrov, B.V. (1983). "Breaking of a single asperity: rupture process and seismic radiation." *J. Geophys. Res.*, 88, 4277-4288.

Electric Power Research Institute (1993). *Guidelines for determining design basis ground motions.* Palo Alto, Calif: Electric Power Research Institute, vol. 1-5, EPRI TR-102293.
vol. 1: Methodology and guidelines for estimating earthquake ground motion in eastern

North America.
vol. 2: Appendices for ground motion estimation.
vol. 3: Appendices for field investigations.
vol. 4: Appendices for laboratory investigations.
vol. 5: Quantification of seismic source effects.

Hadley, D.M., and Helmberger, D.V. (1980). "Simulation of strong ground motions." *Bull. Seism. Soc. Am.*, 70(2), 617-630.

Hadley, D.M., Helmberger, D.V., and Orcutt, J.A. (1982). "Peak acceleration scaling studies." *Bull. Seism. Soc. Am.*, 72, 959-979.

Hartzell, S.H. (1978). "Earthquake aftershocks as Green's functions." *Geophys. Res. Letters*, 5, 1-4.

Hartzell, S.H., and Helmberger, D.V. (1982). "Strong-motion modeling of the Imperial Valley earthquake of 1979." *Bull. Seism. Soc. Am.*, 72, 571-596.

Hartzell, S. (1985). "The use of small earthquakes as Green's functions." *Strong Ground Motion Simulation and Earthquake Engineering Applications,* edited by R.E. Scholl and J.L. King, Earthq. Engin. Res. Inst., Publ. 85-02, 22-1 - 22-8.

Hartzell, S.H., and Heaton, T.H. (1986). "Rupture history of the 1984 Morgan Hill, California, earthquake from the inversion of strong motion records." *Bull. Seism. Soc. Am.*, 76, 649-674.

Haskell, N.A. (1969). "Elastic displacements in the near field of a propagating fault." *Bull. Seism. Soc. Am.*, 59, 865-908.

Heaton, T.H., and Helmberger, D.V. (1977). "A study of the strong ground motion of the Borrego Mountain, California, earthquake." *Bull. Seism. Soc. Am.*, 67, 315-330.

Heaton, T.H., and Helmberger, D.V. (1979). "Generalized ray models of the San Fernando earthquake." *Bull. Seism. Soc. Am.*, 69, 1311-1341.

Heaton, T.H., and Hartzell, S.H. (1986). *Estimation of Strong Ground Motions from Hypothetical Earthquakes on the Cascadia Subduction Zone, Pacific Northwest.* USGS Open-File Rept. 86-328.

Helmberger, D.V., and Malone, S.D. (1975). "Modeling local earthquakes as shear dislocations in a layered half space." *J. Geophys. Res.*, 80, 4881-4888.

Helmberger, D.V., and Harkrider, D.G. (1978). "Modeling earthquakes with generalized ray theory." *Modern Problems in Elastic Wave Propagation,* edited by J. Miklowitz and Achenbash, John Wiley and Sons, New York.

Houston, H., and Kanamori H. (1986). "Source spectra of great earthquakes: teleseismic constraints on rupture processes and strong motion." *Bull. Seism. Soc. Am.*, 76, 19-42.

Irikura, K. (1983). "Semi-empirical estimation of strong ground motions during large earthquakes." *Bull. Disaster Prevention Res. Inst.*, Kyoto Univ., 33, 63-104.

Joyner, W.B., and Boore, D.M. (1986). "On simulating large earthquakes by Green's-function addition of smaller earthquakes." *Earthquake Source Mechanics,* Maurice Ewing Ser. 6, edited by S. Das et al., Am. Geophys. Union. 269-274.

Kanamori, H., D.L. Anderson (1975). "Theoretical basis of some empirical relations in seismology." *Bull. Seismol. Soc. Am.*, 65, 1073-1095.

Kanamori, H. (1979). "A semi-empirical approach to prediction of long-period ground motions from great earthquakes." *Bull. Seism. Soc. Am.*, 69(6), 1645-1670.

Luco, J.E., and Apsel, R.J. (1983). "On the Green's functions for a layered half-space. Part I." *Bull. Seism. Soc. Am.*, 73, 909-929.

Munguiá, L., and Brune, J.N. (1984). "Simulations of strong ground motions for earthquakes in the Mexicali-Imperial Valley." *Proc. Workshop on Strong Ground Motion Simulation and Earthquake Engin. Applications,* Earthq. Engin. Res. Inst., Pub. 85-02 21-1 - 21-19.

Muramatu, I. and K. Irikura (1982). "Synthesis of strong earthquake motions over a wide frequency range." *Natural Disaster Science,* 4(2), 55-78.

Olson, A.H., Absel, R.J. (1982). "Finite faults and inverse theory with application to the 1979 Imperial Valley earthquake." *Bull. Seism. Soc. Am.*, 72, 1969-2001.

Ou, G.B., and Herrmann, R.B. (1990). "Estimation theory for strong ground motion." *Seism. Res. Letters.* 61.

Schneider, J.F., W.J. Silva, and C.L. Stark (1993). Ground motion model for the 1989 **M** 6.9 Loma Prieta earthquake including effects of source, path and site. *Earthquake Spectra,* 9(2), 251-287.

Spudich, P., and Ascher, U. (1983). "Calculation of complete theoretical seismograms in vertically varying media using collocation methods." *Geophys. J. R. Astron. Soc.* 75, 101-124.

Spudich, P., and Frazer, L.N. (1984). "Use of ray theory to calculate high-frequency radiation from earthquake sources having spatially variable rupture velocity and stress drop." *Bull. Seism. Soc. Am.*, 74, 2061-2082.

Trifunac, M.D. (1974). "A three dimensional dislocation model for the San Fernando, California, earthquake of February 9, 1971." *Bull. Seism. Soc. Am.*, 64, 149-172.

Wald, D.J., Burdick, L.J., and Somerville, P.G. (1988). "Simulation of acceleration time histories close to large earthquakes." *Earthquake Engineering and Soil Dynamics II-Recent Advances in Ground-Motion Evaluation,* Proc. Am. Soc. Civil Engin., Specialty Conf., Park City, Utah, 20, 430-444.

Wells, D.L., Coppersmith, K.J. (1994). "New empirical relationships among magnitude, rupture length, rupture width, rupture area, and surface displacement." *Bull. Seism. Soc. Am.* 84(4), 974-1002.

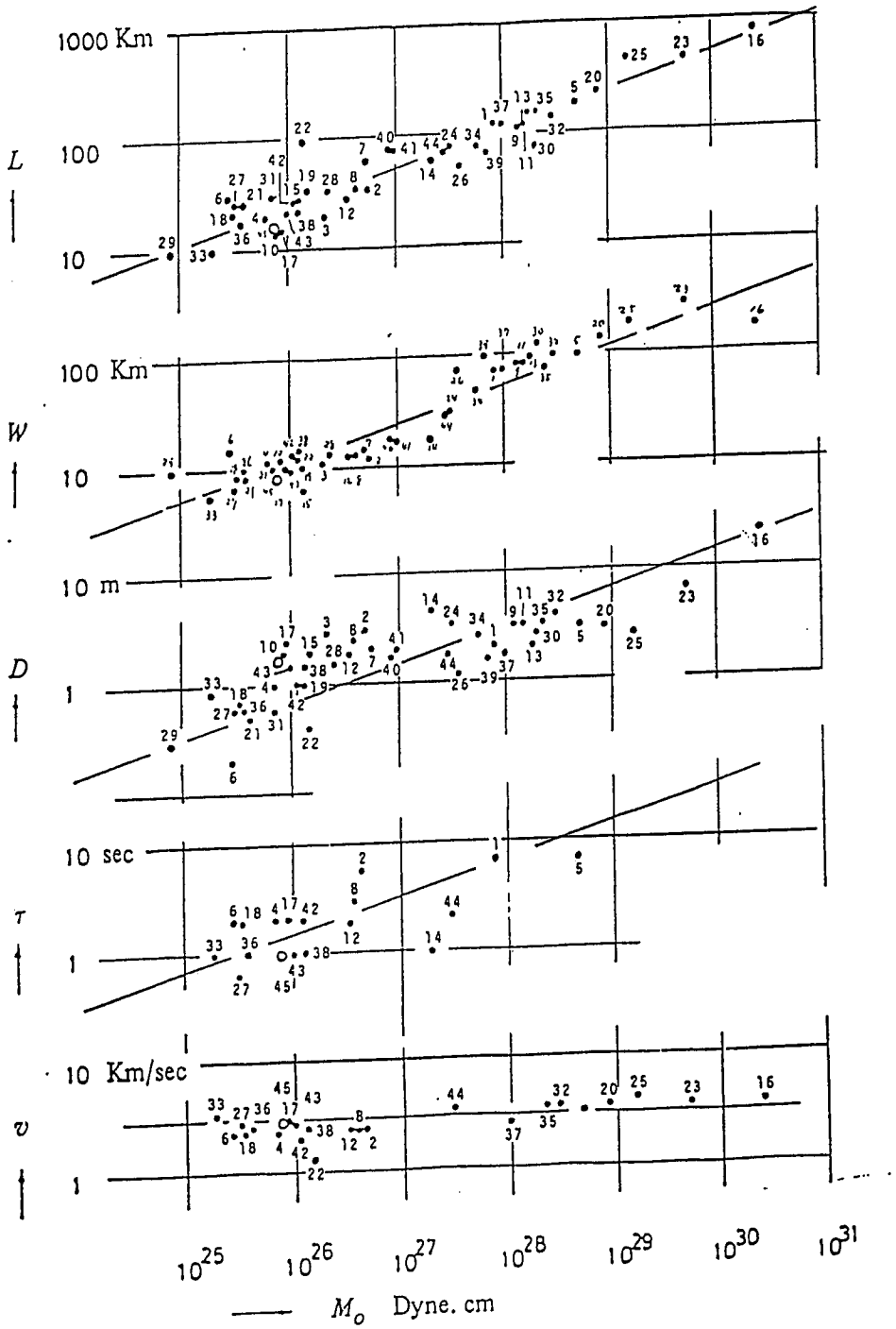

Figure 1.

Relation between the source parameters and the seismic moment on 45 large earthquakes. Abscissa: seismic moment (M_0), ordinate: fault length (L), fault width (W), final displacement (D), rise time (τ) and rupture velocity (v). No. 1–41, from the Geller's table; No. 42, the Izu-Hanto-Oki Earthquake of 1974 [13], No. 43, the Izu-Oshima-Kinkai Earthquake of 1978 [14]; No. 44, the Miyagi-Ken-Oki Earthquake of 1978[15]; No. 45, the Izu-Hanto-Toho-Oki Earthquake of 1980[16].

Source: Muramatu and Irikura (1982)

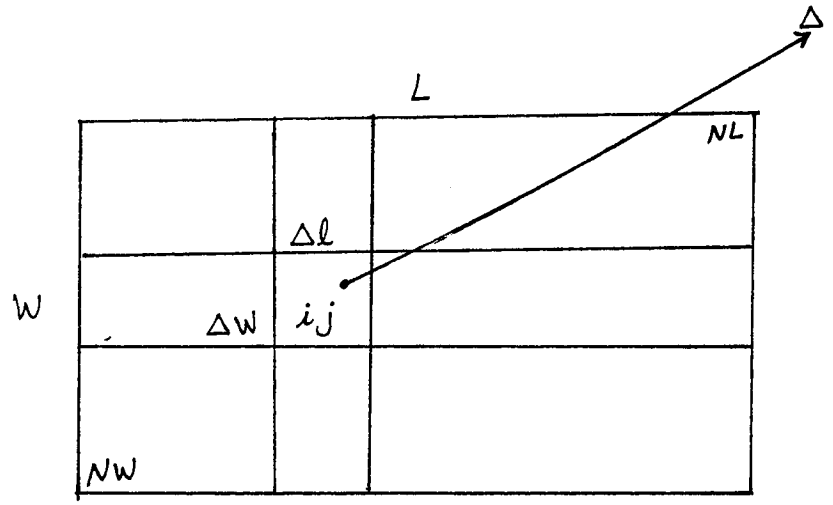

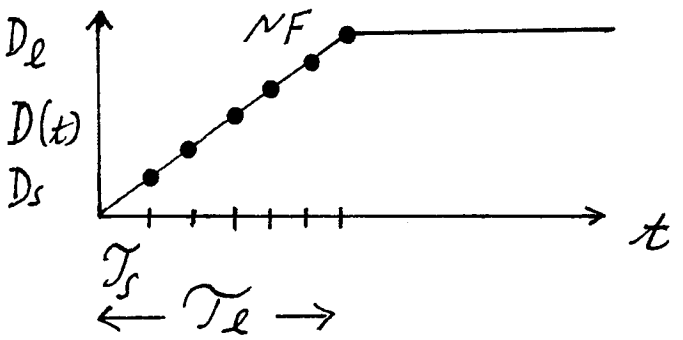

$$T_\ell = NF\, T_s$$

Figure 2. Top: fault geometry depicting subfault ij. Bottom: build up of final slip for each subfault over the duration of the rise time of the large earthquake.

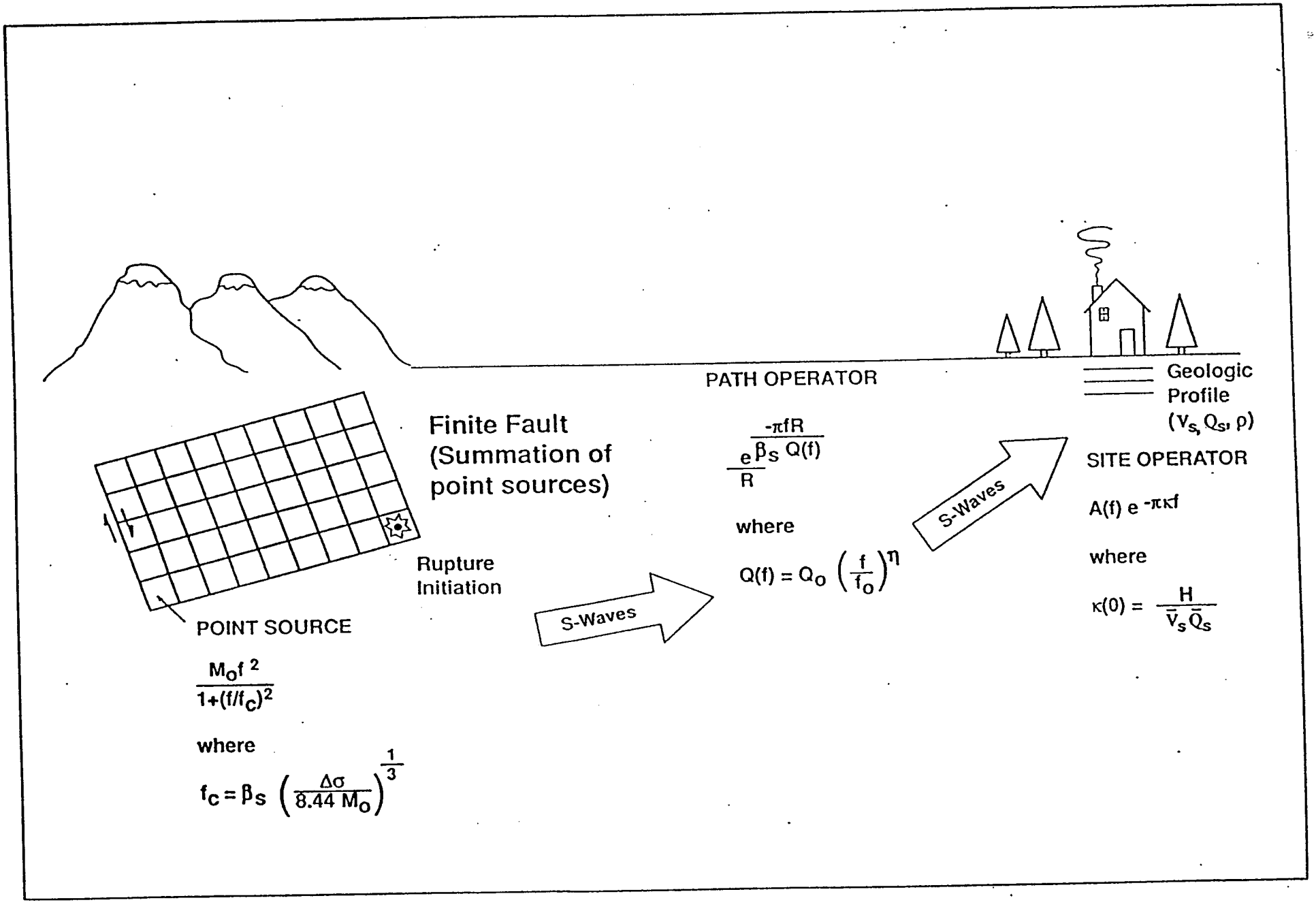

Figure 3. SCHEMATIC OF GROUND MOTION MODEL.

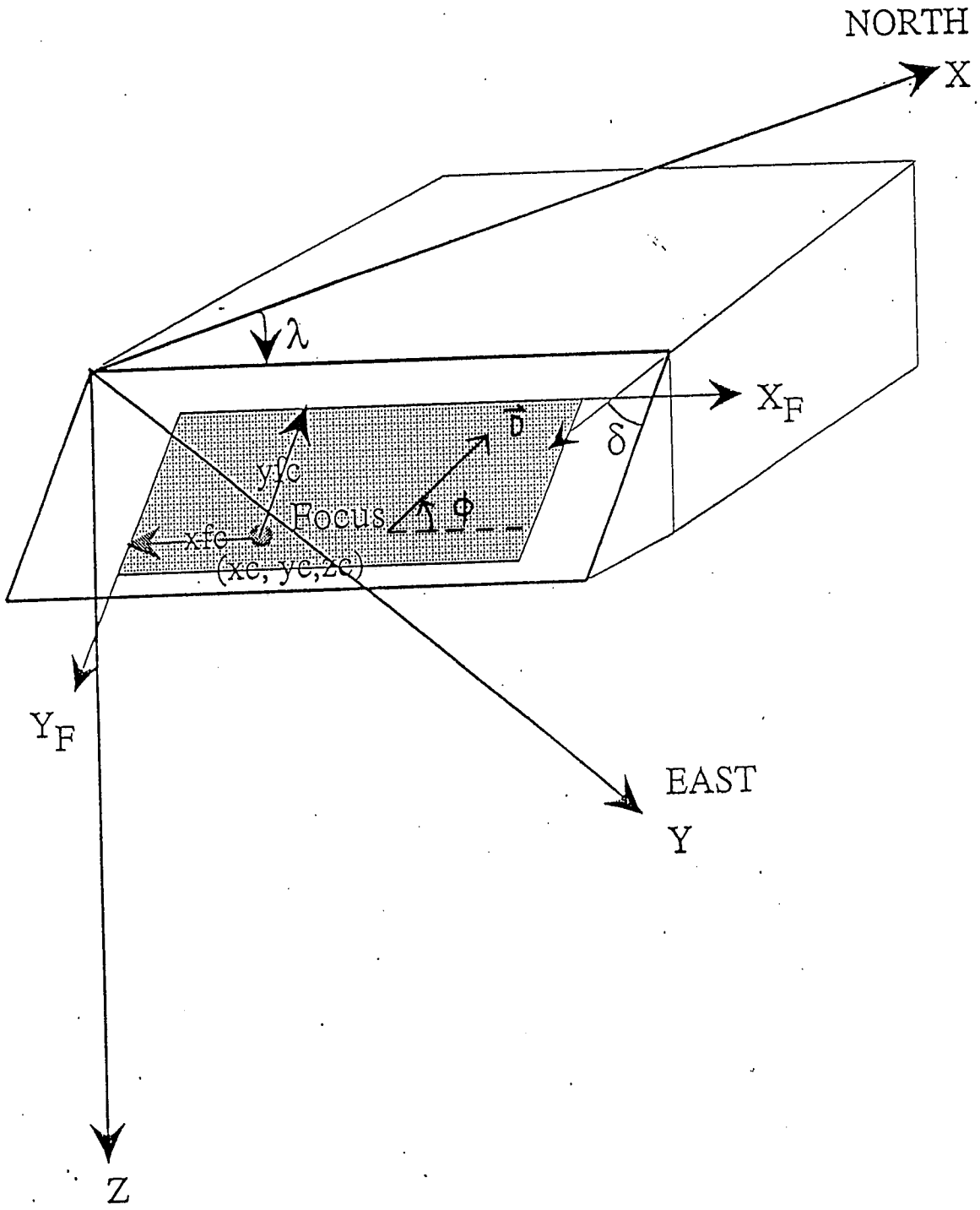

Figure 4. Finite fault geometry adopted from Figure 4.20 of Aki and Richards (1980).

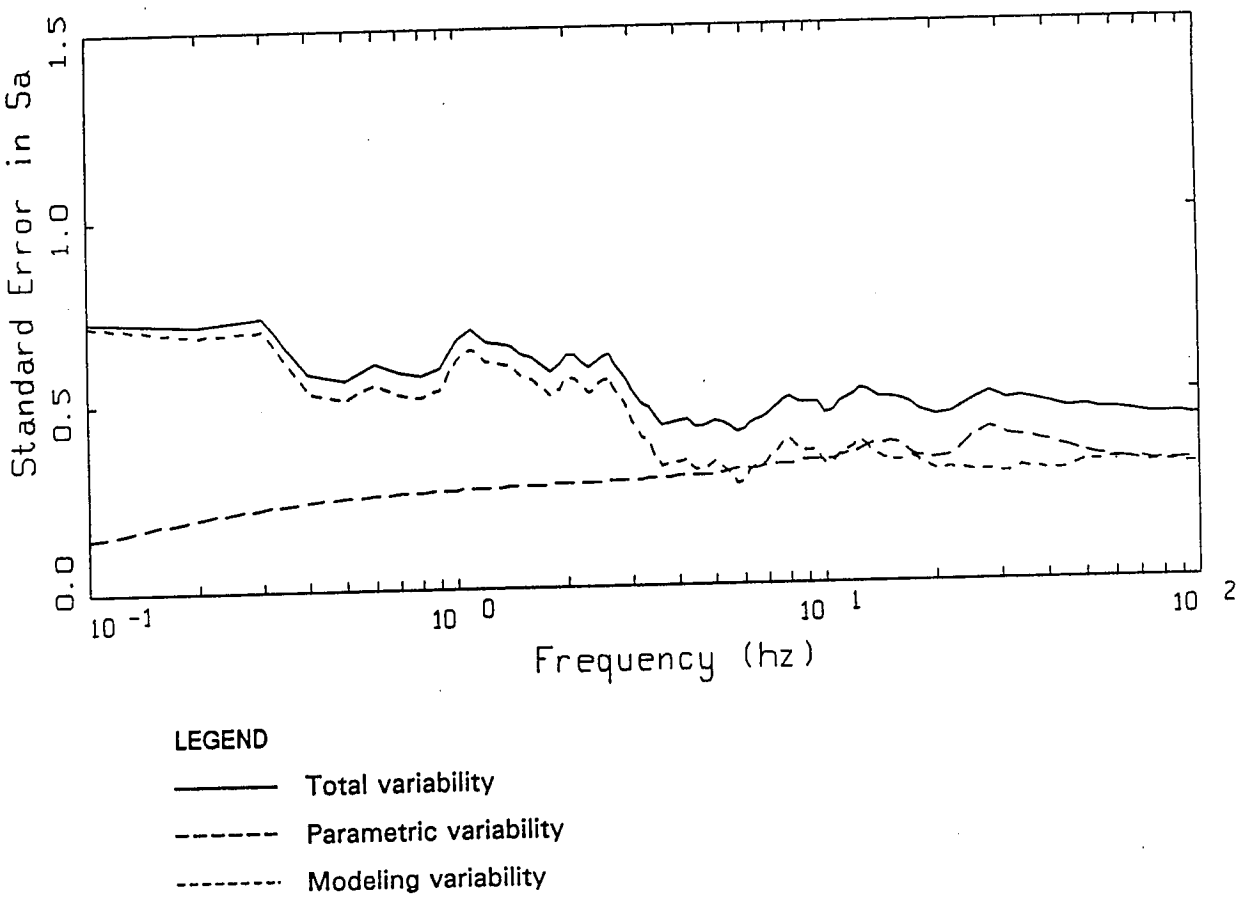

Figure 5. Variability estimates for a **M** 7 earthquake at a distance of 20 km and at a rock site: point source.

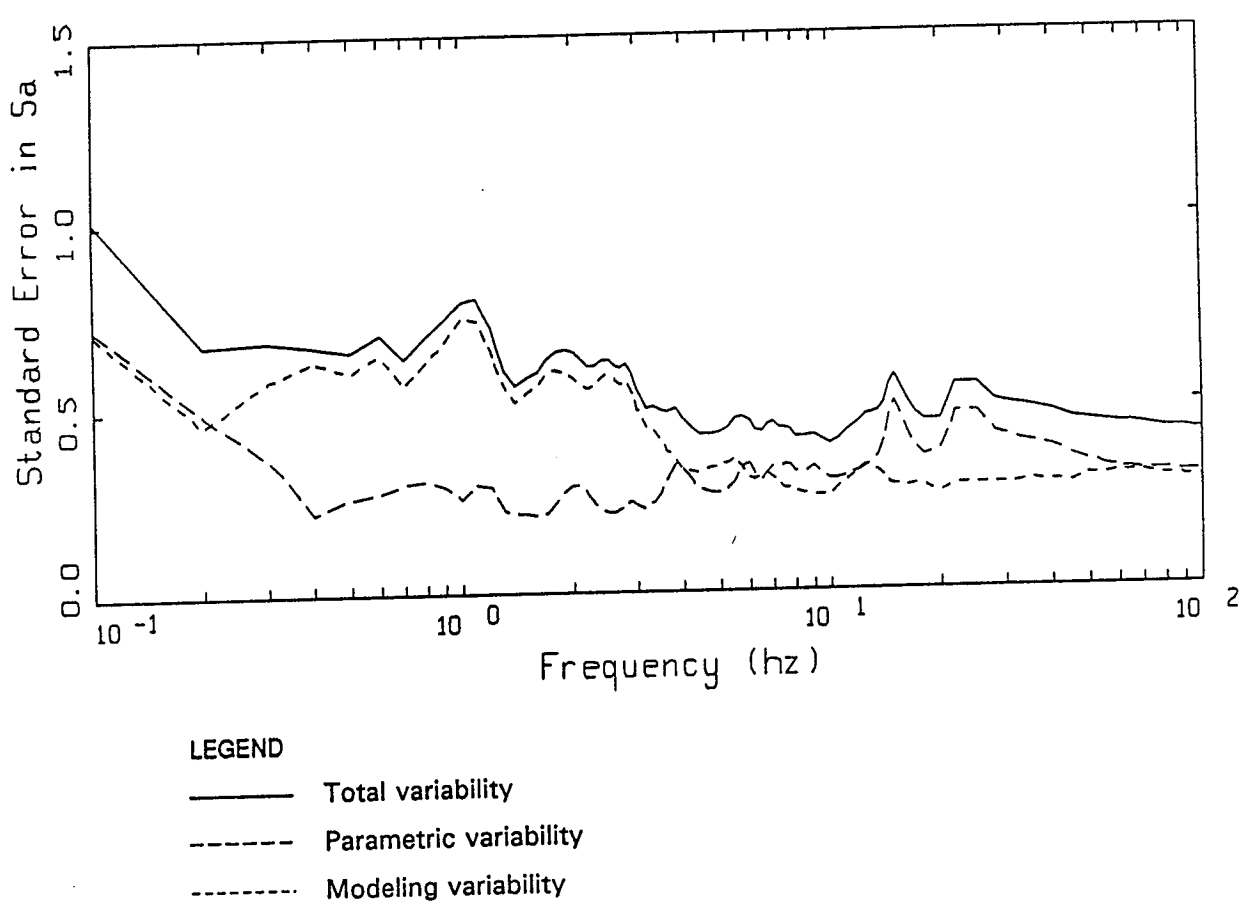

Figure 6. Variability estimates for a M 7 earthquake at a distance of 20 km and at a rock site: finite source.

APPENDIX A

Random Vibration Theory

RVT in its implementation to strong ground motion in simply a probabilistic approach to predicting the expected value of the peak to RMS ratio. The RMS may be computed in the frequency domain from Parseval's theorem:

$$\frac{1}{N\Delta t} \sum_{j}^{N} a_j \, \Delta t = 2 \sum_{i}^{N/2} P_i \, \Delta f \qquad \text{(A1)}$$

where

a_j discrete time history of N points,

Δt sample interval (sec),

Δf sample interval (Hz) = $1/N\Delta t$,

P power spectral density given by,

$$P_i = \frac{\tilde{a}_i \cdot \tilde{a}_i^*}{N\Delta t} ,$$

$\tilde{a}_i$ or $\tilde{a}(f_i)$ is the discrete Fourier transform of the time series a_j.

The left hand side of Equation (A1) is the RMS^2 of the time sequence a_j and Parseval's theorem shows that it is equal to the sum over all frequencies of the power spectral density. The RMS is then given by

$$RMS = \left(\frac{2 \sum_{j}^{N/2} \tilde{a}_j \, \tilde{a}_j^*}{(N\Delta t)^2} \right)^{\frac{1}{2}} \qquad \text{(A2)}$$

or, rewritten in our notation as

$$a_{RMS} = \frac{2}{T} \int_0^\infty |\tilde{a}\ (f)|^2\ df \qquad \text{(A3)}$$

where $\tilde{a}(f)$ is the summed complex Fourier spectral density and T is the duration of the time history. For a point source, the duration is simply $1/f_c$ and for the finite source the 5-75% Arias intensity of the transformed $\tilde{a}(f)$ is used.

To apply RVT, we define the spectral moments (Boore, 1983; Silva and Lee, 1987)

$$m_k = 2 \int_0^\infty (\omega)^k\ |A(f)|\ df, \qquad \text{(A4)}$$

and the expected value of the peak to RMS ratio is given by

$$\frac{a_p}{a_{RMS}} = (2 \ln N)^{\frac{1}{2}} + \frac{\gamma}{(2 \ln N)^{1/2}} \qquad \text{(A5)}$$

where

$\gamma = 0.5772$ Euler's constant

$N = 2 \tilde{f}\ T$ Number of zero crossings

$$\tilde{f} = \frac{1}{2\pi} \left(\frac{m_2}{m_0}\right)^{\frac{1}{2}} \quad \text{Predominant frequency} \qquad \text{(A6)}$$

$$a_{RMS} = \left(\frac{m_0}{T}\right)^{\frac{1}{2}} . \qquad \text{(A7)}$$

Then given $\tilde{a}(f)$ and T and the assumption that a(t) is random noise over a duration T

with a Fourier amplitude spectrum defined by $\tilde{a}(f)$, RVT can be used to give stable mean estimates of peak time domain values. The estimates are over the population of phase spectra which are associated with the Fourier amplitude spectrum $\tilde{a}(f)$.

To estimate oscillator response, the squared oscillator transfer function given on p. 25 of Seminar 1

$$\frac{f^4}{[(f_j^2 - f_4^2)^2 + (2\eta f_j f)^2]} \tag{A8}$$

is simply added to the integrand of Equation (A4) as a product. The resulting a_p will be the estimate of the oscillator peak pseudo absolute acceleration for a damping of η and oscillator frequency f_j.

For response spectra calculations, a modification is needed to the duration T used in Equation (A7). This arises because for short duration time histories, the longer period oscillators do not have sufficient time to build up their RMS response. Boore and Joyner (1984) have developed an empirical correction factor which employs an equivalent duration T_{RMS} which is greater than T and is given by

$$T_{RMS} = T + D_0 \frac{\gamma^3}{\gamma^3 + 1/3} \tag{A9}$$

where

$$D_0 = (2\pi\eta f_j)^{-1}, \qquad \gamma = \frac{T}{D_0} \tag{A10}$$

This extended duration is then used in Equation (A7) for the RMS calculation only.

REFERENCES

Boore, D.M. (1983). "Stochastic simulation of high-frequency ground motions based on seismological models of the radiated spectra." *Bull. Seism. Soc. Am.*, 73(6), 1865-1894.

Boore, D.M. and Joyner, W.B. (1984). "A note on the use of random vibration theory to predict peak amplitudes of transient signals." *Bull. Seism. Soc. Am.*, 74, 2035-2039.

Silva, W.J., Lee, K. (1987) *"WES RASCAL code for synthesizing earthquake ground motions"* State-of-the-Art for Assessing Earthquake Hazards in the United States, Report 24, U.S. Army Engineers Waterways Experiment Station, Misc. Paper S-73-1.

Silva, W.J. (1988). *"Estimated Ground Motions for a New Madrid Event."* Report prepared for U.S. Army Engineer Waterways Experiment Station by Woodward-Clyde Consultants.

Evaluation and Implementation of an Improved Methodology for Earthquake Ground Response Analysis

Uniform Treatment of Source, Path and Site Effects

Seminar 6

(12/1/94, 49 p.)

Source, Path, and Site Effects in Strong Ground Motion

a) General References
b) Introductory Comments
c) Source Effects
    1) Directivity
    2) Site Location
    3) Slip Distribution
    4) Fault Dip
    5) Stress Drop
d) Propagation Path Effects
    1) Crustal Damping
    2) Geometric Attenuation
e) Site Effects
    1) Rock Sites
    2) Soil Sites

CALTRANS

SEMINAR ON STRONG GROUND MOTION

Seminar 6; December 1, 1994

Source, Path, and Site Effects in Strong Ground Motion

a) General References:

1988 Aki: Local site effects on ground motion. *Earthquake Engineering and Soil Dynamics II-Recent Advances in Ground-Motion Evaluation, Proc. Am. Soc. Civil. Engin. Specialty Conf.*, J. Lawrence Von Thun, ed., Park City, Utah, Pub. 20, 103-155.

1991 Silva: Global characteristics and site geometry. Chapter 6 in *Proceedings: NSF/EPRI Workshop on Dynamic Soil Properties and Site Characterization.* Palo Alto, Calif.: Electric Power Research Institute, NP-7337.

1993 Silva: Factors controlling strong ground motions and their associated uncertainties. *ASCE Symposium On High Level Nuclear Waste Repositories,* 132-161.

b) Introductory Comments

The subject of this seminar is to examine the effects of source, path, and site processes on strong ground motions. As stated in Seminar 5, the concentration will be on the stochastic model (for implementation by CALTRANS) so much of the illustrations and explanations will be in that context. This should not be overly restrictive however as the stochastic model shares many elements in common with other ground motion models (Seminar 5). Many of the effects due to such parameters as point source stress drop, finite source slip model, nucleation point (directivity), crustal damping, site velocity profile, and site damping were briefly presented in Seminar 1 using a combination of observations and modeling. The intent here is to go into more detail regarding causes of these effects from the perspective of the stochastic model. The specific issues to be addressed are:

1) Source effects

   a) Directivity

b) Site location

c) Slip distribution

d) Fault dip

e) Stress drop

1) finite source

2) point source,

2) Propagation path effects

a) Crustal damping

b) Radiation damping,

3) Site effects

a) Rock site

1) crustal amplification

2) kappa

b) Soil site

1) velocity profile

2) nonlinearity.

For all of these effects, model calculations will be used to illustrate degrees and frequency ranges of influence on response spectra. For some assessment regarding these effects on time histories, a review of Seminar 1 is recommended for illustrative examples. Time and scope constraints preclude presenting both time histories and response spectra for the analyses. In general, the parametric effects will be assessed by assuming a base case scenario (magnitude, fault type, site location, and path and site properties, etc) and parameters changed or site location varied. Comparisons will then be made between base case response spectra and the parametric variation.

c) Source Effects

For source effects, specific issues addressed include: directivity, site location, slip distribution, fault dip, and stress drop (finite- and point-source). For the finite fault, the base case source

model (Table 1) is taken as a **M** 7 earthquake with a length and width of 75 km and 10 km respectively (Figure 1). Two sites are considered, one just off the north end (0.6 km) and a middle site, 4 km east of the surface projection of the top of the rupture surface. The fault/site geometry is depicted in Figure 1. The scenario with the end site represents a most likely earthquake on the Newport-Inglewood Fracture Zone at the La Cinenega site and was specified by CALTRANS. The middle site was chosen to illustrate the effects of dip (hanging wall verses foot wall) with the distance increased to 4 km to show more of an effect.

1) Directivity: As developed in Seminar 1 (Equation 11), directivity results in a change in the apparent source corner frequency (inverse of rupture duration) for a site located near a long extended fault when the rupture propagates toward or away from the site. Recall there are 2 source corner frequencies: one due to rise time and one due to finiteness with each contributing a f^{-1} fall off for an omega-square source. Our discussion here pertains to just the finiteness corner. As a result of the presence of 2 corners (as well as nonuniform slip) the illustrations of directivity using finite fault simulations are somewhat subtle. In addition, we are looking at an average horizontal component which tends to reduce the effects of directivity as it is much stronger on the fault normal component compared to the fault parallel component (C.F. Figures 61-76 of Seminar 1).

From Seminar 1

$$\tau_c = \tau_R - \frac{L}{C}\cos(\phi), \quad C = \alpha, \beta$$

where τ_c is an apparent corner period due to rupture finiteness and τ_R is the rupture time (L/V_R).

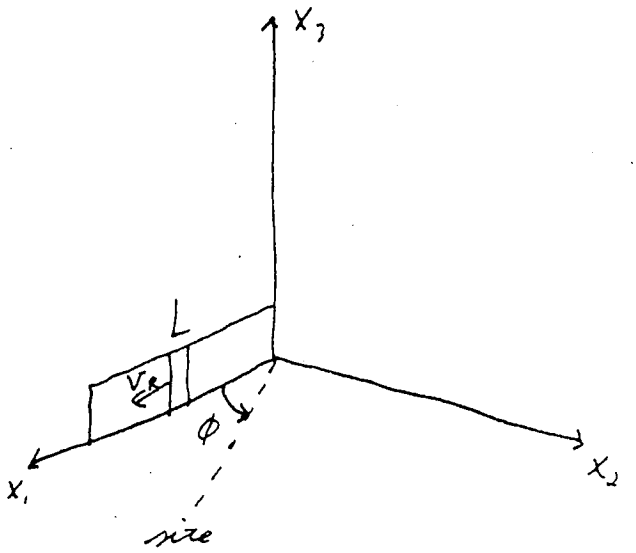

For a site along x_1, $\phi = 0$ and rupture propagates toward the site. In this case $\tau_c < \tau_R$ and $f_c > f_R$, the corner frequency shifts to higher frequency (more high frequency energy in the ground motion, looks like a higher stress drop event). For $\phi = \pi$, rupture is away from the site, $f_c < f_R$, and there is less energy in the ground motion (looks like a lower stress drop

event).

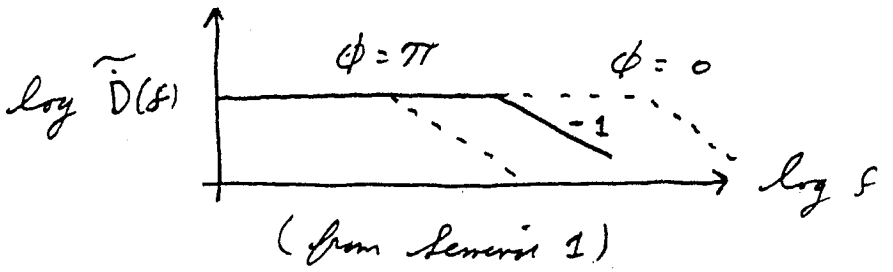

To illustrate how directivity enters the stochastic finite fault model, we need to examine Equation (7) from Seminar 5 in detail:

$$U(t) = \sum_{i}^{NW} \sum_{j}^{NL} F_{ij}(t) * U_{ij}^{s}(t)$$

where U(t) is the simulated ground motion for a large earthquake U_{ij}^{s} (t) are recordings of small earthquakes on the fault (Green functions) and F_{ij} (t) is a spike seismogram (porcupine) reflecting the effects of rupture finiteness. Each spike adds a scaled Green function to U (t) so F_{ij} (t) represents the number of subevents fired in each subfault with a delay given by the subevent rise time as well as delays for all subfaults. The scaling in F_{ij} (t) is for subfault to site distance (corrected for Green function location) and slip weight. The duration of F_{ij} (t) is the rise time of the simulated earthquake while the total duration of F(t) is the rupture duration. Because F(t) defines the finite rupture characteristics through scaling and delays of the Green functions (or source functions), it carries the directivity information predominately through its duration.

To illustrate how the porcupine or spike seismogram conveys directivity information to U(t), it is useful to first look at same examples of spikes of uniform amplitudes and their Fourier amplitude spectra. Figure 2 shows three spike seismograms comprising 1, 2, and 3 spikes as well as their Fourier amplitude spectra. The single spike has a constant spectrum as expected (spike of amplitude 1/sample interval should have a Fourier amplitude spectral density of 1). The multiple spikes, separated by 0.2 sec for plotting resolution (sample interval is 0.01 sec) show notched spectra with the first minima moving to lower frequency going from 2 to 3 spikes. As the duration of spikes increases then, the notches shift to lower frequency reflecting the trend

shown in the sketch of D(f) for $\phi = 0, \pi$.

In order to see what the Fourier amplitude spectrum of the porcupine (F(f)) should look like and how directivity manifests itself, it is instructive to sketch an idealized spectrum or transfer function. If F(f) is designed to transfer a **M** 5 Brune omega-square source (or Green function) into a **M** 7 Brune omega-square earthquake, F(f) is easy to sketch. Figure 3 shows the expected shape of F(f) with the simplified assumption that both the modeled and Green function earthquakes are Brunce omega-square single corner frequency sources. In this idealized example, the modeled earthquake is **M** 7 and the Green function is **M** 5. At low frequency (below the corner frequency of the modeled event) F(f) is constant with an amplitude given by the moment ratios. At the corner frequency of the modeled event, about 0.1 Hz, F(f) falls off with a 2 slope (12 db/octave) until about 1 Hz, the corner frequency of the **M** 5 subevent. Beyond that F(f) has a value of the moment ratio to the 1/3 power. In this context, the effects of directivity are reflected in a shift of the **M** 7 corner frequency: higher for rupture toward the site, lower for rupture away. Since stress drop, measured in the frequency domain, is proportional to the corner frequency (Table 1) radiation toward the site results in a shorter duration time history, higher corner frequency, and a higher stress drop.

To demonstrate the porcupine and transfer function for the base case model (Figure 1, Table 1) Figure 4 shows the time and frequency domain representations of F(t) at the end site (north) for north, middle, and south nucleation points. As the focus progresses from north to south (rupture away then to toward the site), the porcupine decreases in duration. The Fourier amplitude spectra show approximately the expected shape (Figure 3) but are complicated by the slip distribution and distance scaling and randomization in subevent rupture and rise times (Seminar 5). In general, although the low frequency plateau is not clear, there is an increase in low frequency energy from north focus to south focus. The north focus spectrum has a low frequency corner near 0.03 Hz (33 sec) and this shifts to about 0.06-0.07 Hz for the south focus reflecting the 12-15 sec duration of the porcupine (Figure 4, bottom).

Of special interest is the double peak in the south focus spectra near 0.5 Hz. This peak is reflected in the response spectra computed for the three nucleation points and shows up in

Figure 5 (dashed line) as a substantial peak at about 1.3 sec. In Figure 5, the south focus response spectrum is generally slightly higher than the north focus for periods shorter than about 3 sec with the 1.3 sec peak representing the largest difference. The peak particle velocities also reflect the differences in low frequency levels being about 39 cm/sec for the north focus and 46 cm/sec for the south focus. Interestingly, the spectral peak due to directivity in Figure 5 near 1.3 sec for the south focus is not unlike that observed from the M 7.2 Landers earthquake recorded at the closest (1.8 km) site Lucerne. Figure 6 shows 5% damped response spectra computed for the average horizontal component from the Lucerne recordings. Near 3 sec there is a peak or shoulder in the response spectrum which is attributed to directivity (See Seminar 1). These long period peaks occur in the spectrum at the Yermo fire station, located in the direction of rupture propagation but are absent at Desert Hot Springs, located at the opposite end of the fault and at the same fault distance (Seminar 1). Apparently the finite fault model, through the porcupine, is capturing the observed features of rupture directivity. The differences between the Lucerne spectra and the base case are likely due to differences in source size, slip model, and site location.

An additional interesting feature shown in Figure 4 is the Fourier amplitude spectrum computed for the south focus with a constant subevent rise time (dashed line). The figure shows a spectral deficiency from about 0.5 to 2-3 Hz. This spectral hole is expected and is a result of summing many small events to make a single large earthquake. Figure 7 shows the resulting response spectra compared to that with a randomized subevent rise time. The differences are dramatic and filling the spectral hole in the Green function summation method has received considerable deserved attention of late.

2) Site Location: To examine the effects of site location median and 1-sigma estimates of 5% damped response spectra were computed for the end and middle sites (Figure 1, Table 1). In order to average out the effects of nucleation point (directivity) and slip model, these parameters were randomized (30 realizations) and median spectra computed. Figure 8 shows the spectra computed for the end and middle sites. At short periods, the spectrum for the middle site exceeds that for the end site by a factor of about 2, somewhat less for long periods. A large difference is expected as the end site has more of the fault at a larger distance than the middle

site. The difference in motions is then due to geometrical attenuation which is independent of period in this model and to crustal damping. The later should result in a larger short period difference in motions between the end and middle sites. However the high median PGA value of 1.144G for the middle site seems unreasonable. A linear analysis was done with a kappa value of 0.04 sec (Table 1) and, in reality, some nonlinear response would be expected for a typical soft rock site increasing kappa possibly to about 0.05-0.06 sec. This would reduce short period spectral amplitudes by 20-30% but even these values may still be larger than one would expect. Interestingly, increasing the fault width to 13 km, closer to a more reasonable value for a M 7.0 earthquake (keeping the length at 75 km) reduced the PGA about 30% to 0.872G. The spectrum is shown in Figure 9. An increase in kappa value to 0.05-0.06 see would bring the PGA down to about 70% G.

3) Slip Distribution: A convenient way of assessing the effects of slip distribution is to examine the standard error (natural log) in the computed response spectrum for a suite of random slip models (Seminar 1). In this analysis, the nucleation point is fixed at the center of the nucleation zone (Figure 1) and all other parameters held fixed at base case values. The resulting variability in response spectra computed at the end and middle sites represents a statistically significant estimate of the effects of slip or asperity distribution on ground motions at these sites for the selected base case parameters. Figure 10 shows the resulting uncertainty plots for both the end and middle sites. For periods shorter than about 0.1 sec, the effects of asperity distribution are similar for both end and middle sites. At intermediate periods, however, 0.1-3 sec, the ground motions at the end site are slightly more sensitive to slip model than at the middle site. In this period range, the uncertainties (natural log) are 0.35 for the end site and about 0.25 for the middle site. These represent multiplicative 1-sigma factors of about 1.4 and 1.3 respectively, which are moderately large.

4) Fault Dip: To assess the effects of fault dip (hanging wall verses foot wall), both end and middle (4 km east) sites were run randomizing over focus and slip model. Figure 11 shows the resulting median spectra for the end site. In this case, motions for the vertical fault are about 10% larger then either the east 45° or west 45° dipping faults which are nearly the same. Apparently, changing the dip from 90° has the simple effect of increasing the distance for end

sites.

For the middle site, Figure 12, there is a difference of about 20% between the hanging wall (east dip) and foot wall (west dip) with the hanging wall the larger. Interestingly, the hanging wall motions are nearly the same as the vertical fault (about 5% larger). Recordings of earthquakes from reverse faults however, suggest a much larger differences between the hanging wall and foot wall and with vertical strike slip faults. Another factor which may be contributing to the differences seen in recordings is the change in aspect ratio between vertical and dipping faults. In dipping faults, the width is generally greater than for vertical faults which would have the effect of bringing more of the fault closer to the site (keeping the area fixed). The Wells and Coppersmith (1994) empirical relation for reverse fault width is given by

$$\log (RW) = -1.61 + 0.41\,\mathbf{M}$$

which gives about 18 km for a **M** 7 earthquake. To assess the effects of an increased fault width on sensitivity to dip, analyses were done for both the middle and end sites (keeping the area constant). Figure 13 shows median spectra computed at the end site with the 18 km width (length is 42 km). As with the 10 km width (Figure 11), there is very little difference between east and west dip (hanging wall and foot wall). In Figure 14, however, for the middle site, the effects are large and period dependent. Short period (less than about 1 sec) hanging wall motions (east dip) are about 35% higher than foot wall motions and are nearly the same at longer periods. Comparing hanging wall and vertical fault motions at the middle site (10 km width, Figure 12) shows about a 30% difference at all periods with the hanging wall motions being the larger. The increased fault width appears to be a factor in the differences between hanging wall and foot wall motions and vertical faults as well.

5) Stress Drop: To assess the effects of stress drop, both the point- and finite-source models are considered. As discussed in Seminar 1, both source models use a difference interpretation of stress drop. For the finite fault, stress drop is proportional to fault slip over a fault dimension such as length. For a circular fault, the relation for stress drop is

$$\Delta\sigma = \frac{7}{16} \frac{M_o}{(\frac{A}{\pi})^{\frac{3}{2}}}$$

where A is the fault area. For fixed magnitude (moment M_o), a change in stress drop for a finite fault is simply a change in area. For the base case fault, with an area of 750 km^2, the stress drop is 48 bars (Table 1). To assess the effects on median response spectra, analyses were done for fault areas reflecting a factor of 2 in stress drop, 24 and 96 bars with areas of 1,100 km^2 and 44 km^2 respectively. Figure 15 shows the resulting median spectra from randomizing over slip and nucleation point for the end site. To obtain a more reliable estimate, a large number of sites (average over azimuth) should be considered but these results are interesting and suggest a strong dependence on area which is largely period independent.

For the point source, stress drop is a scaling parameter for high frequencies or frequencies higher than the corner frequency and is given by

$$\Delta\sigma = 8.44\ M_o \left(\frac{f_c}{\beta}\right)^3.$$

Changing stress drop in this model then changes the corner frequency (Seminar 1), resulting in more high frequency energy for higher stress drop. For western North America, the median stress drop is about 100 bars (Seminar 1) and single point source runs were made for stress drops of 100, 50, and 200 bars, factors of 2 about the median. The results are shown in Figure 16 and the spectra show a strong dependence on stress drop, nearly as strong as the finite fault for the end site. As expected, the dependence is period dependent decreasing with increasing period.

d) Propagation Path Effects

In the context of the stochastic model, the propagation path refers to crustal damping and geometrical attenuation (radiation damping). Both components of the model are presented and discussed in Seminar 1. Since local sources generally control design in California, the primary focus of CALTRANS is the prediction of near-source ground motions. As a result, path effects

are generally small and will be demonstrated for two fault distances, 0.6 km and 20 km, using the same source model as used in the source effects presentation of the last section. The close site (0.6 km) is off the north end (Figure 1) and the 20 km site is 20 km from the north end. The use of end sites maximizes path effects giving a maximum path length of about 90 km. Because the path lengths are relatively short, the effects of crustal reflections and surface waves are neglected. For distances beyond about 50-100 km these effects can be important and may be accommodated by incorporating past-critical reflections (Ou and Herrmann, 1990) or by changing the geometrical attenuation from 1/R to $1/\sqrt{R}$ (body waves to surface-waves) and increasing the duration (to accommodate build up of multiple reflections/transmissions) (Herrmann, 1985).

1) Crustal damping: The crustal damping term in both the point and finite source models is of the form

$$e^{-\frac{\pi f R}{2 V_s Q(f)}}$$

where $Q(f) = 150\ f^{0.60}$ WNA

$= 670\ f^{0.33}$ ENA.

The western North America Q(f) model is appropriate for tectonically active regions such as California while the ENA model, with significantly higher Q(f) (lower damping, $\eta \approx$ 1/2 Q), is appropriate for stable regions such as continental interiors (central and eastern North America). The higher damping WNA model is responsible for the distance dependency of response spectral shapes for distances exceeding about 40-50 km (Silva and Green, 1989). For the higher Q(f) ENA model, the distance dependency of spectral shapes doesn't become large until source to site distances exceed about 80-100 km.

The two Q(f) models are plotted in Figure 17 and show constant slopes on log axes. The higher damping (lower Q(f)) WNA model has a much stronger frequency dependence than the ENA model, possibly reflecting a different mechanism or combination of intrinsic and scattering crustal damping than for ENA.

Figure 18 shows the computed response spectra at 0.6 and 20 km for the base case scenario (Table 1). The spectra are log averages over slip model and nucleation point variation to produce stable and smooth estimates. At 0.6 km, the maximum effect of damping is about 10% while at 20 km, it rises to about 30%. The effect is most pronounced for periods shorter than about 1 sec. On average, the effects would be less as the end site maximizes the path damping effect. Also the range in Q(f) models is extreme and not likely to occur within a tectonic region.

2) Geometrical attenuation: Sometimes referred to as radiation damping is demonstrated in Figure 19 using the base case scenario. The short period motions (PGA) are down by about 300% in going from 0.6 km to 20 km fault distance. The longer period motions are down somewhat less due to the frequency dependence of the crustal damping (Figure 17). The factor of these reduction is less than 0.6/20 change in fault distance because most of the contribution to the surface motion comes from areas of high slip (asperities) which generally occur at depths between about 5 and 10 km for vertical strike slip faults in tectonically active regions. To demonstrate this, Figure 20 shows a sample of 4 slip models from the suite of 30 realizations. The zones of high slip are generally concentrated between about 5-10 km. If a slant range is used from 8 km depth to the site, the change in or average asperity distance is about 8/21, close to the factor of about 3 change in spectral ordinates in going from 0.6 to 20 km fault distance.

e) Site Effects

In the stochastic model (Seminar 1), site effects are separated into rock and soil foundation conditions. For rock sites, crustal amplification, due to a decrease in shear-wave velocity from the source to the site, as well as shallow crustal damping are considered site effects. To accommodate soil effects, a 1-D soil column is simply placed on the rock site.

1) Rock sites: Site effects for rock sites are modeled

$$A(f)\ e^{-\pi\kappa f} \qquad \text{(Seminar 1)}$$

where A(f) represents crustal amplification and κ (kappa) represents frequency

independent damping which occurs in the upper 1-2 km beneath the site (Seminar 1). The A(f) factors are computed for the crustal model appropriate to the region of interest from a depth of about 8 km to the top crustal layer assuming normally incident shear-waves.

Kappa appears to be related to rock strength and varies inversely with shear-wave velocity. Kappa values may be measured using earthquake recordings at the site (or similar sites) or are based on rock type (Silva and Darragh, 1994) or average velocity over the top 100 ft (Seminar 1).

To demonstrate the effects of A(f) and kappa on response spectral ordinates, three California crustal models were selected representing northern California soft rock (Wald et al., 1991), southern California soft rock (Saikia, 1993), and southern California hard rock (Landers crust, Wald and Heaton, 1994). The three crustal models are shown in Figure 21. The Landers crustal model was used by Wald and Heaton (1994) in their study of long period ($>$ 2 sec) ground motions from the **M** 7.2 1992 Landers earthquake. Kappa values associated with the crustal models are 0.04 sec for the soft rock profiles (Silva and Darragh, 1994) and 0.02 sec for the hard rock profile. The hard rock kappa value 0.02 sec is based upon analyses of recordings of the Landers earthquake at the closest site Lucern. The site is a shallow ($\approx$ 20 ft) stiff soil with a total (soil plus rock) kappa of 0.02 sec. Site response analyses using an equivalent-linear 1-D model (Seminar 1) showed a strain compatible soil kappa of about 0.004 sec. As a result of the small contribution of the soil to the total kappa, a value of 0.02 sec is taken as a reasonable approximation for this California hard rock site.

To examine the effects of crustal velocity profile and damping on the rock site term

$$A(f)\ e^{-\pi\kappa f}$$

Figure 22 shows a plot of smoothed crustal transfer functions for the three crustal models for a source at 8 km depth. The transfer functions, rock surface-to-elastic half space Fourier amplitude spectral ratios, are the product of A(f) and $e^{-\pi\kappa f}$ and reflect the net

crustal amplification. For the soft rock crusts, Wald and Saikia, the net amplifications are very similar for periods shorter than about 0.5 sec with the Saikia crust showing slightly larger amplification at longer periods. This is due to the generally lower velocities in the top 6-7 km. The lower velocities in the southern California crust (appropriate for the Los Angeles area) probably reflect the effects of the deep basin and result in an amplification of intermediate period strong ground motions. The hard rock Landers crustal amplification is the lowest out to nearly 0.2 sec where, because of the lower kappa value of 0.02 sec, it crosses the soft rock factors. To isolate the effects of kappa, the hard rock transfer function was also computed with a value of 0.04 sec and is shown as the dashed line in Figure 22. This set of factors is the lowest showing that, in general, the greater the crustal velocity gradient, the larger the amplification factors. However, it is the net factors which are important and because hard rock sites, although having smaller velocity gradients and lower amplifications than soft rock sites, usually show higher short period net amplifications simply due to lower kappa values (Silva and Darragh, 1994).

To illustrate the effects of the net amplifications on ground motions, Figure 23 shows median 5% damped spectral accelerations for the three crustal models at fault distances of 0.6 and 20 km. As expected results for the soft rock sites are nearly the same with both higher than the hard rock spectra at periods longer than about 0.1-0.2 sec. At shorter periods, the hard rock spectra exceed the soft rock spectra with the differences weakly dependent on distance. Interestingly, the PGA values at each distance are close, apparently because PGA is controlled by the Fourier spectra at periods where they are nearly the same for each crustal model (0.1-0.2 sec).

To show the effect of kappa on the hard rock site, Figure 24 compares motions computed for values of 0.02 and 0.04 sec at the fault distance of 0.6 km. Doubling kappa, for high kappa values, reduces short period spectral ordinates ($\leq$ 0.2 sec) by about 50%. For short periods, kappa is a significant ground motion parameter (Silva, 1991).

2) Soil sites: To examine the effects of a 1-D soil column on computed ground motions,

RVT based equivalent-linear response analyses are computed for shallow (20 ft), intermediate (120 ft), and deep (500 ft) generic soil profiles. The generic profiles are intended to represent generally stiff sandy soil conditions in WNA and are taken from a single gradient based on an eyeball fit to a large number of measured profiles. The gradient is simply truncated at the appropriate depths (20, 120, and 500 ft) with a typical WNA bedrock velocity of 3000 ft/sec (EPRI, 1993). This velocity is compatible with the top layer of the northern California soft rock crust (Figure 21) on which it is placed. Figure 25 shows the WNA soil profiles along with a stiffer 20 ft deep ENA profile used to model the motions at the Lucern site, about 1 km fault distance from the **M** 7.2 Landers earthquake. Site investigations suggested the presence of a shallow stiff soil layer which is approximated by Category 1 of the EPRI generic ENA soil profiles used to model site response for nuclear power sites in the eastern United States (EPRI, 1993).

To accommodate nonlinear response, a random vibration theory (RVT) equivalent linear approach is used which is compatible with the point- and finite-source stochastic models (EPRI, 1993). Depth (confining pressure) dependent modulus reduction and damping curves appropriate for soils consisting of sands, gravels, and low PI clays are used to model the material nonlinearities (EPRI, 1993).

To evaluate the effects of the soil column and nonlinear response, median response spectra computed for the three profiles are compared to the northern California soft rock median spectra at the two fault distances, 0.6 and 20 km using the soft rock simulations as control motions. To produce stable and smooth estimates of site response, the soil profiles are randomized about the median values (Figure 25) using an algorithm which preserves the velocity correlations between layers (EPRI, 1993). In addition, as with the subsequent analyses, both slip model and nucleation point are randomized as well (30 realizations).

Figure 26 shows the results for a fault distance of 0.6 km. The rock spectrum generally shows higher motions at short periods with period dependent cross over points for each profile. For periods longer than about 0.6-0.7 sec, the median spectra form a family

with higher motions for deeper profiles reflecting amplification due to the velocity gradients.

At 20 km fault distance, Figure 27, the soil response is much more linear and the motions for the soil profiles exceeds those of the rock throughout most of the bandwidth. At the closer distance, the larger control motions result in higher strain compatible damping in the profiles, reducing the short period motions.

To see whether or not the response computed for each of the profiles (20, 120, and 500 ft) is similar to that of motions recorded at soil sites which are similar to the three profiles, response spectral shapes (5% damped spectral acceleration divided by peak acceleration) are compared for predicted and recorded motions. Spectral shapes are used rather than absolute spectra because the particular earthquakes and sites are not modeled. The base case parameters and source model is used (Table 1, Figure 1) at a distance of 20 km (end of fault). The use of spectral shapes approximately cancels distance (out to about 50 km) and radiation pattern effects; Silva and Darragh (1994). Randomizing over slip model, nucleation point, and profile results in a confidence band in spectral shape which should include the particular source and site conditions.

For the shallow site, Figure 28 shows spectral shapes compared to the motions recorded at the Tarzana site from the **M** 6.7 1994 Northridge earthquake at a fault distance of about 18 km. The site is a shallow soil and the spectral shape is generally within the $\pm$ 1-sigma confidence band for the 20 ft generic profile. At long periods, the recorded motions are low relative to the simulations because the magnitude, **M** 6.7, is significantly below the **M** 7.0 simulations.

Figure 29 shows results of similar quality with the peak motion shifted to longer periods for the intermediate profile (120 ft). The site is the Palo Alto Veterans Memorial Hospital, a soil profile about 200 ft deep (Schneider et al., 1993). The earthquake is the 1989 **M** 6.9 Loma Prieta at a fault distance of about 24 km.

For the deep profile, Figure 30 shows model (500 ft profile) results compared to motions recorded at the Gilroy Array No. 2 site from the **M** 6.9, 1989 Loma Prieta earthquake. The fault distance is about 16 km and both predictions and recording show a shift of the peak to longer periods and elevated long period spectral levels compared to the site of intermediate depth (Figure 29).

A final comparison illustrating the dramatic difference a shallow soil can have on ground motions is shown in Figure 31. In this case, the stochastic point source is used to model the motions recorded at the Lucern site from the 1992 **M** 7.2 Landers earthquake. The site is located about 1 km fault distance and consists of stiff shallow soil over hard granitic rock. A generic 20 stiff soil column (Figure 25) is used over the Landers crust (Figure 21). Inversions of strong motion data at a number of sites resulted a point source stress drop of 47 bars using a source depth of 8 km. The site kappa value is about 0.02 sec (from template fits; Silva and Darragh, 1994) resulting in a rock kappa of about 0.016 sec as previously discussed. Figure 31 shows the average (log) spectra of the two horizontal components (solid line) computed from the recorded motions compared to point source simulations for the Landers crust with and without the 20 ft profile. The simulations are for a **M** 7.2 earthquake at a depth of 8 km and epicentral distance of 1 km. The effect of the soil column is dramatic for periods shorter than about 0.2 sec and provides a much closer match to the data. The ability of the simple point source model combined with a generic soil column to provide such a favorable comparison at such a close distance to a **M** 7.2 earthquake is remarkable and suggests the large role of site conditions in the variability of strong ground motions.

REFERENCE

1993 Electric Power Research Institute: *Guidelines for determining design basis ground motions.* Palo Alto, Calif: Electric Power Research Institute, vol. 1-5, EPRI TR-102293. vol. 1: Methodology and guidelines for estimating earthquake ground motion in eastern North America.

vol. 2: Appendices for ground motion estimation.
vol. 3: Appendices for field investigations.
vol. 4: Appendices for laboratory investigations.
vol. 5: Quantification of seismic source effects.

1985 Herrmann: An extension of random vibration theory estimates of strong ground motion to large distance. *Bull. Seism. Soc. Am.*, 75, 1447-1453.

1990 Ou and Herrmann: A statistical model for ground motion produced by earthquakes at local and regional distances. *Bull. Seism. Soc. Am.*, 80, 1397-1417.

1993 Saikia: Estimated ground motions in Los Angeles due to $M_W = 7$ earthquake on the Elysian Thrust fault. *Bull. Seism. Soc. Amer.*, 83(3), 780-810.

1993 Schneider et al.: Ground motion model for the 1989 **M** 6.9 Loma Prieta earthquake including effects of source, path and site. *Earthquake Spectra,* 9(2), 251-287.

1994 Silva and Darragh: Engineering characterization of strong ground motion recorded at rock sites." Palo Alto, Calif.: Electric Power Research Institute, Final Report RP 2556-48.

1989 Silva and Green: Magnitude and distance scaling of response spectral shapes for rock sites with applications to North American tectonic environment. *Earthquake Spectra,* 5(3):591-624.

1991 Silva: Global characteristies and site geometry. *Proceedings: NSF/EPRI Workshop on Dynamic Soil Properties and Site Characterization.* Electric Power Res. Inst., EPRI NP-7337.

1994 Wald and Heaton: Spatial and temporal distribution of slip for the 1992 Landers, California, earthquake. *Bull. Seism. Soc. Amer.*, 84(3), 668-691.

1991 Wald et al.: Rupture model of the 1989 Loma Prieta Earthquake from the inversion of strong motion and broadband teleseismic data. *Bull. Seism. Soc. Amer.*, 81(5), 1540-1572.

1994 Wells and Coppersmith: New empirical relationships among magnitude, rupture length, rupture width, rupture area, and surface displacement. *Bull. Seism. Soc. Am.* 84(4), 974-1002.

Table 1

Base Case Parameters

Parameter	Value
kappa	0.04 sec
β source region shear-wave velocity	3.2 km/sec
ρ mass density	2.7 cgs
Q_o	150 (WNA), 670 (ENA)
η	0.60 (WNA), 0.33 (ENA)
M	7.0
M_o	3.98 x 10^{26} dyne-cm
$\Delta\sigma = 8.44\ M_o \left(\frac{f_c}{\beta}\right)^3 = 100$ *bars, point source* $= \frac{7}{16}\ \frac{M_o}{(\frac{A}{\pi})^{\frac{3}{2}}} = 48$ *bars, finite source*	
A fault area	75 km x 10 km
mechanism*	vertical, strike slip (N-S)
h source depth	8 km, point source
D site distance	0.6 km; epicentral, point source 0.6 km; surface projection of top of rupture surface, end site (north) 4.0 km; surface projection of top of rupture surface, middle site
site condition	soft rock with average shear wave velocity over the top 300 ft of about 3,000 ft/sec
crustal model	Wald et al. (1991) Loma Prieta

*For vertical and dipping faults top of fault is at a depth of 2 km and for dipping faults (45° E and W) top of fault is hinge line.

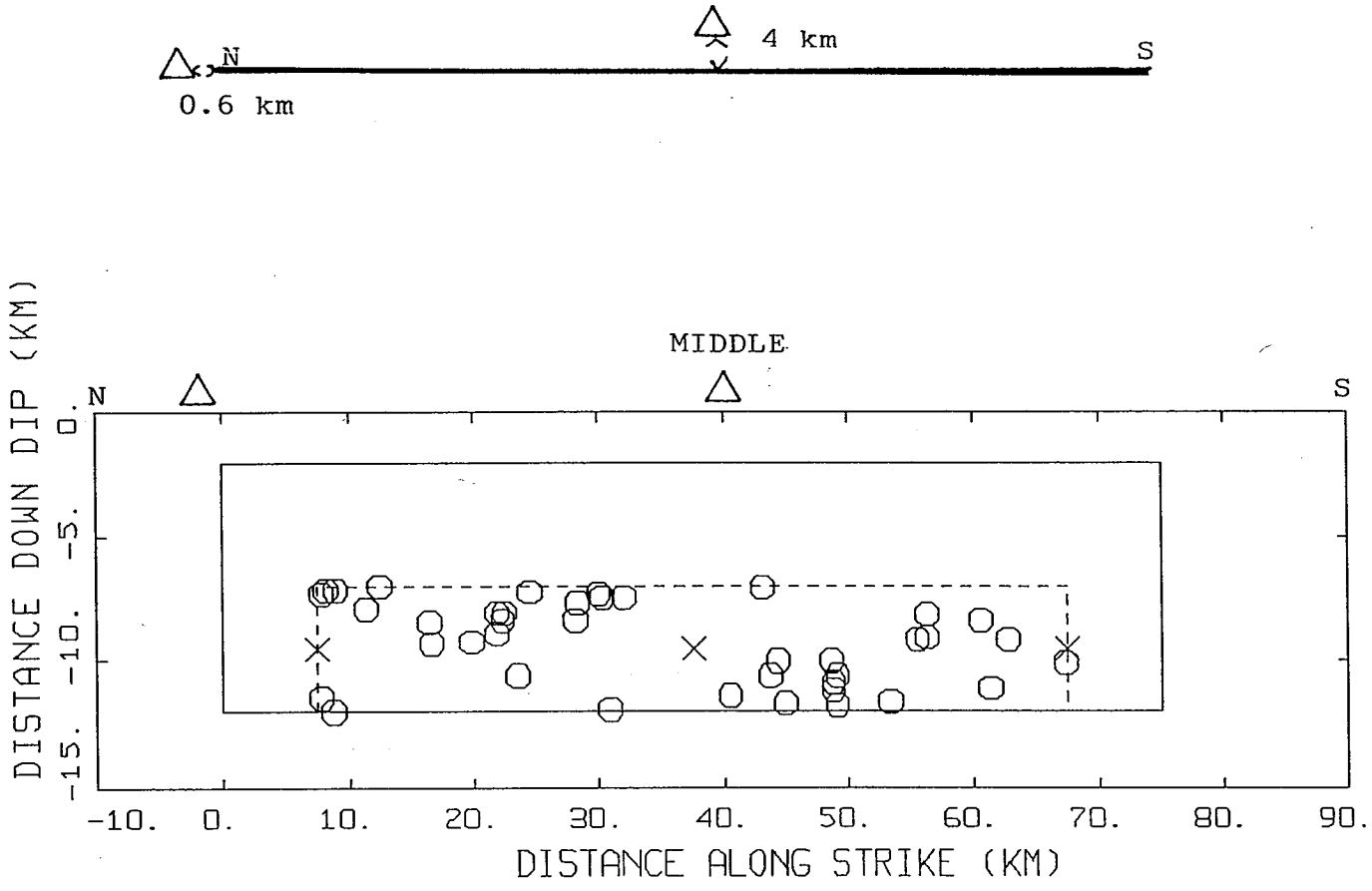

Figure 1. Base case fault/site geometry plan view (top), side view (lower). Fault is vertical strike-slip. For dipping faults, 45° east and 45° west, top of fault is hinge line. Open circles are random nucleation points within the nucleation zone. X's are north, middle (base case), and south nucleation points.

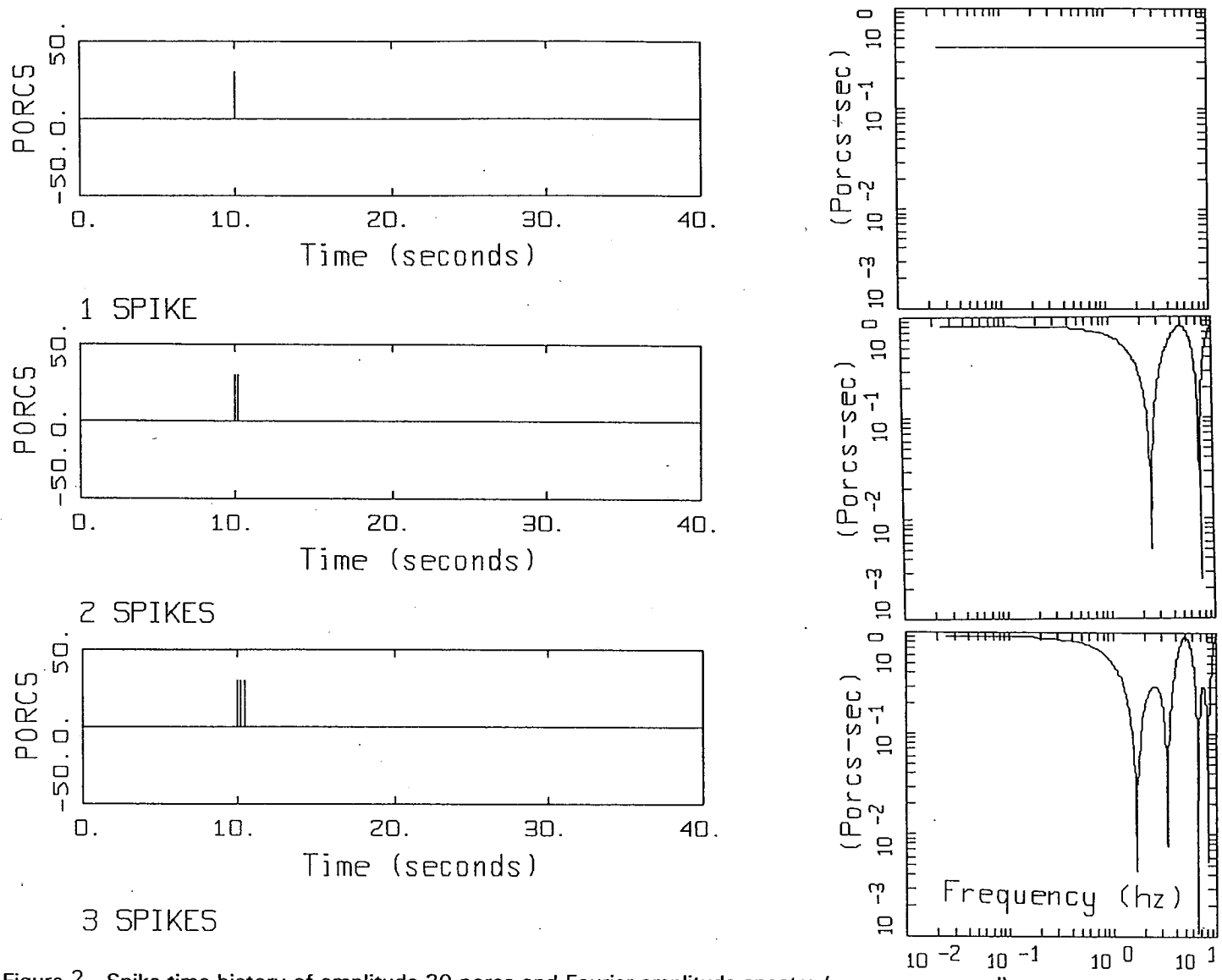

Figure 2 . Spike time history of amplitude 30 porcs and Fourier amplitude spectra (no mean removal).

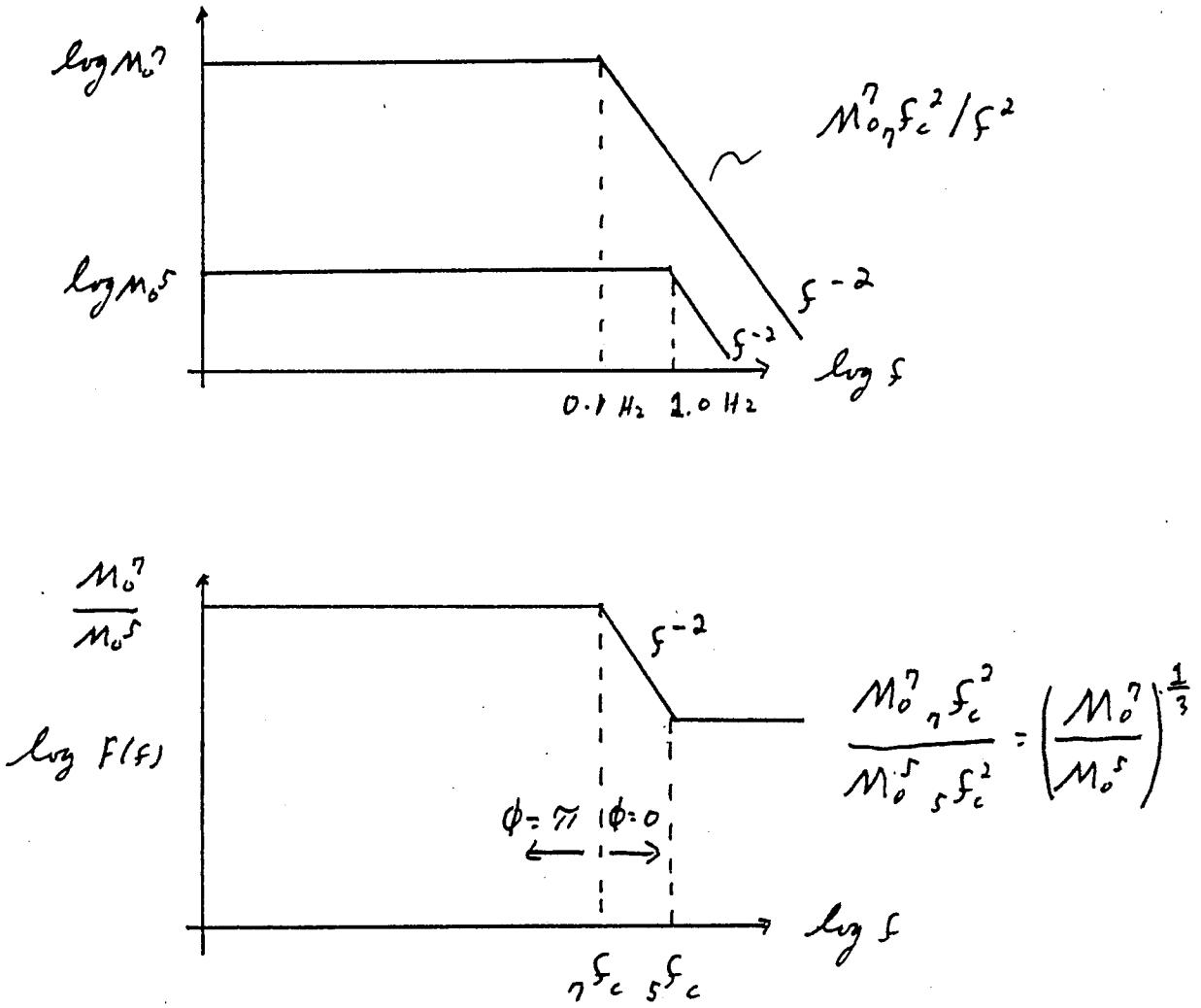

$$ {}_7f_c \propto \frac{1}{\tau_R - \frac{L}{c}\phi} $$

$\phi = 0$, rupture toward site, ${}_7f_c$ increases

$\phi = \pi$, rupture away from site, ${}_7f_c$ decreases

Figure 3. Source spectra for subevent M 5 earthquake and modeled M 7 earthquake assuming a single-corner-frequency omega-square source model (top). Transfer function required to transform M 5 to M 7 retaining omega-square properties and a single corner frequency (lower). ${}_7f_c$ represents the M 7 source corner frequency which shifts with site location. τ_R is the rupture duration.

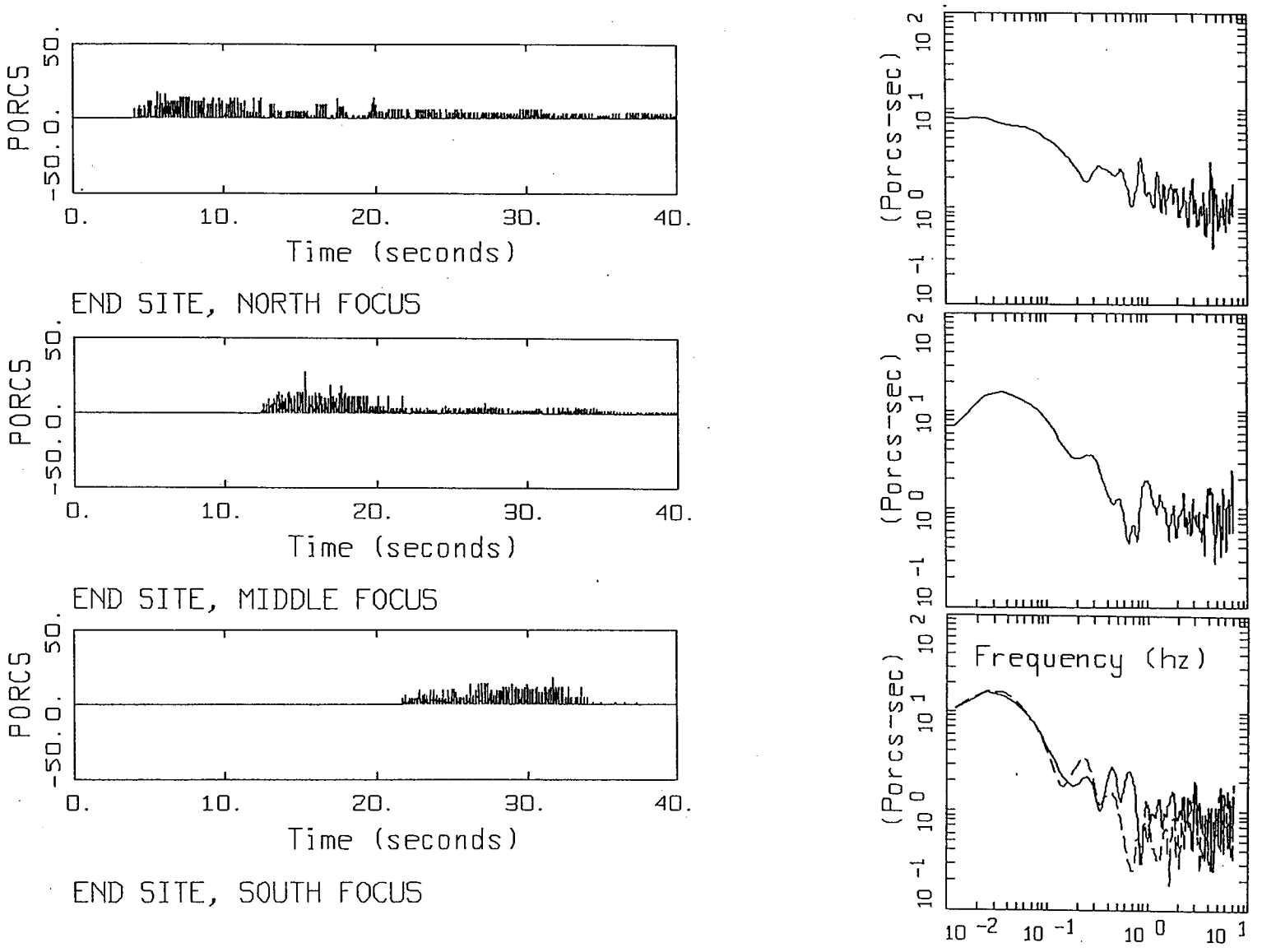

Figure 4. Porcupine time history and Fourier amplitude spectra (0.3 Hz smoothing) at the end site (north) for north, middle, and south foci using base case parameters (Table 1). Dashed line for south focus Fourier amplitude spectra is for constant subevent rise time and reveals a spectral hole from about 0.4 Hz to 3 Hz.

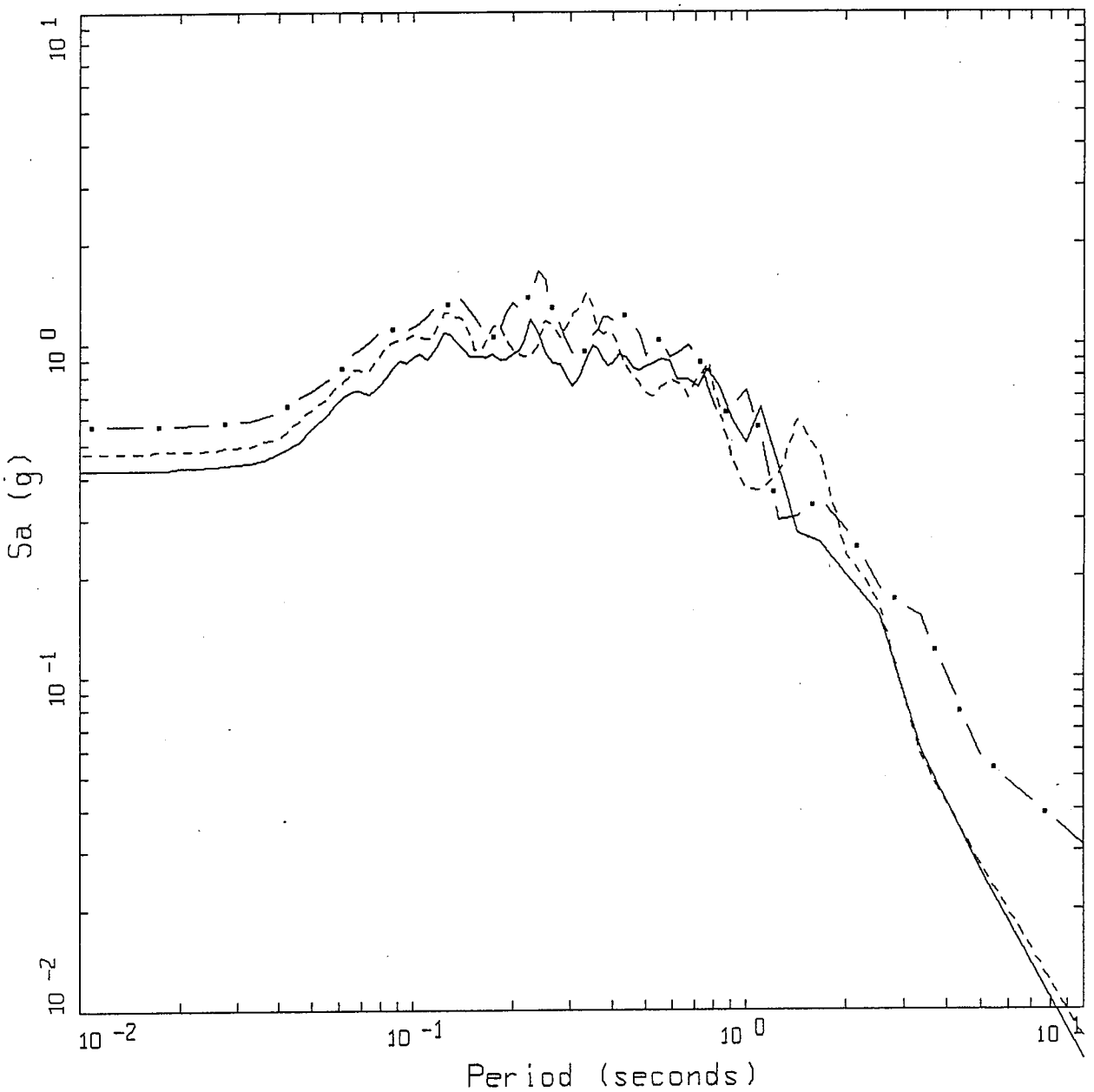

Figure 5. Response spectra (5% damping) computed for the base case fault model at the end site (Figure 1, Table 1) for north (solid line), middle (dashed-dotted line) and south (dotted line) nucleation points.

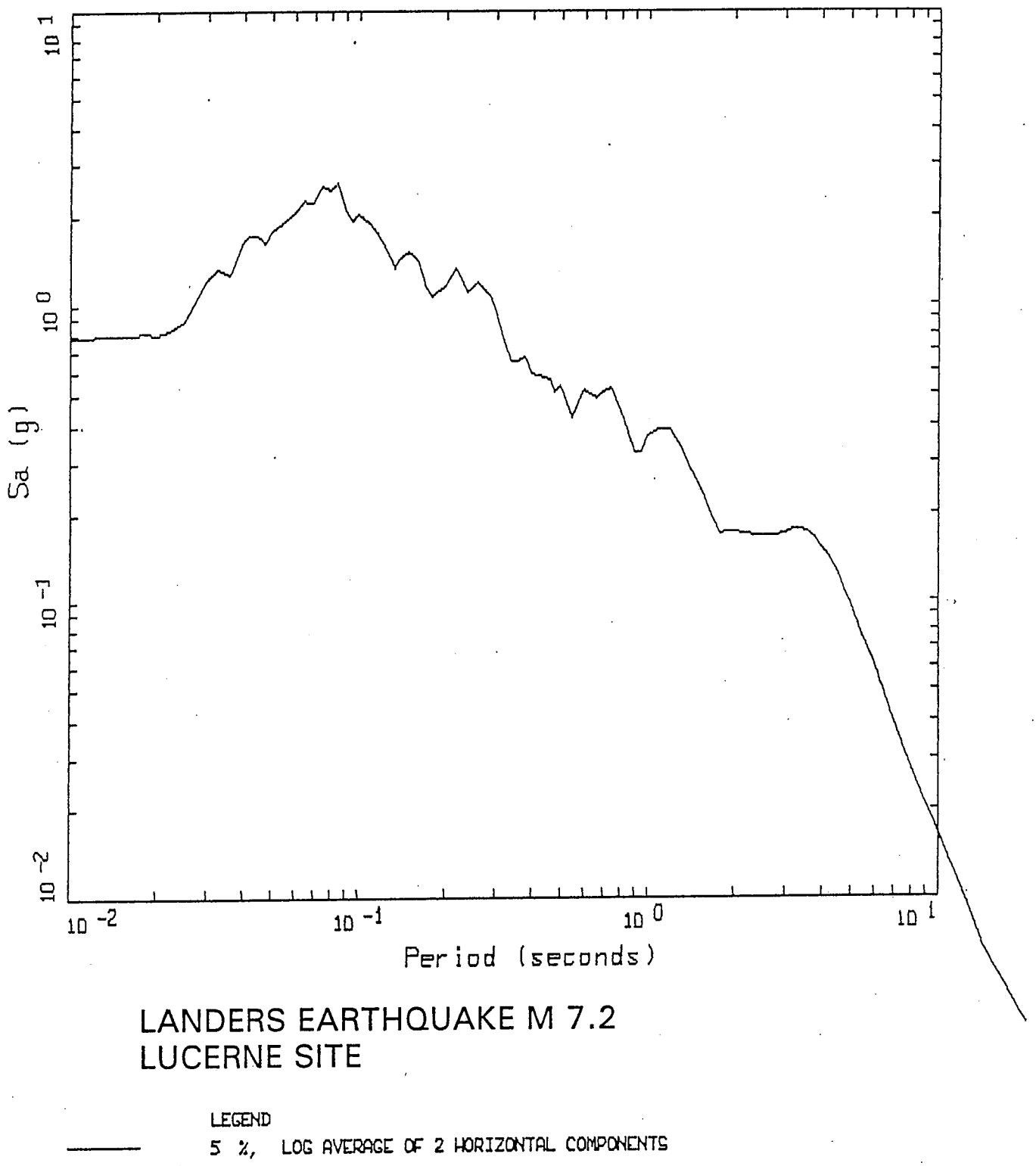

Figure 6. Average horizontal component response spectra (5% damping) computed from recordings of the Landers earthquake at the Lucerne site. Rupture distance is 1.8 km.

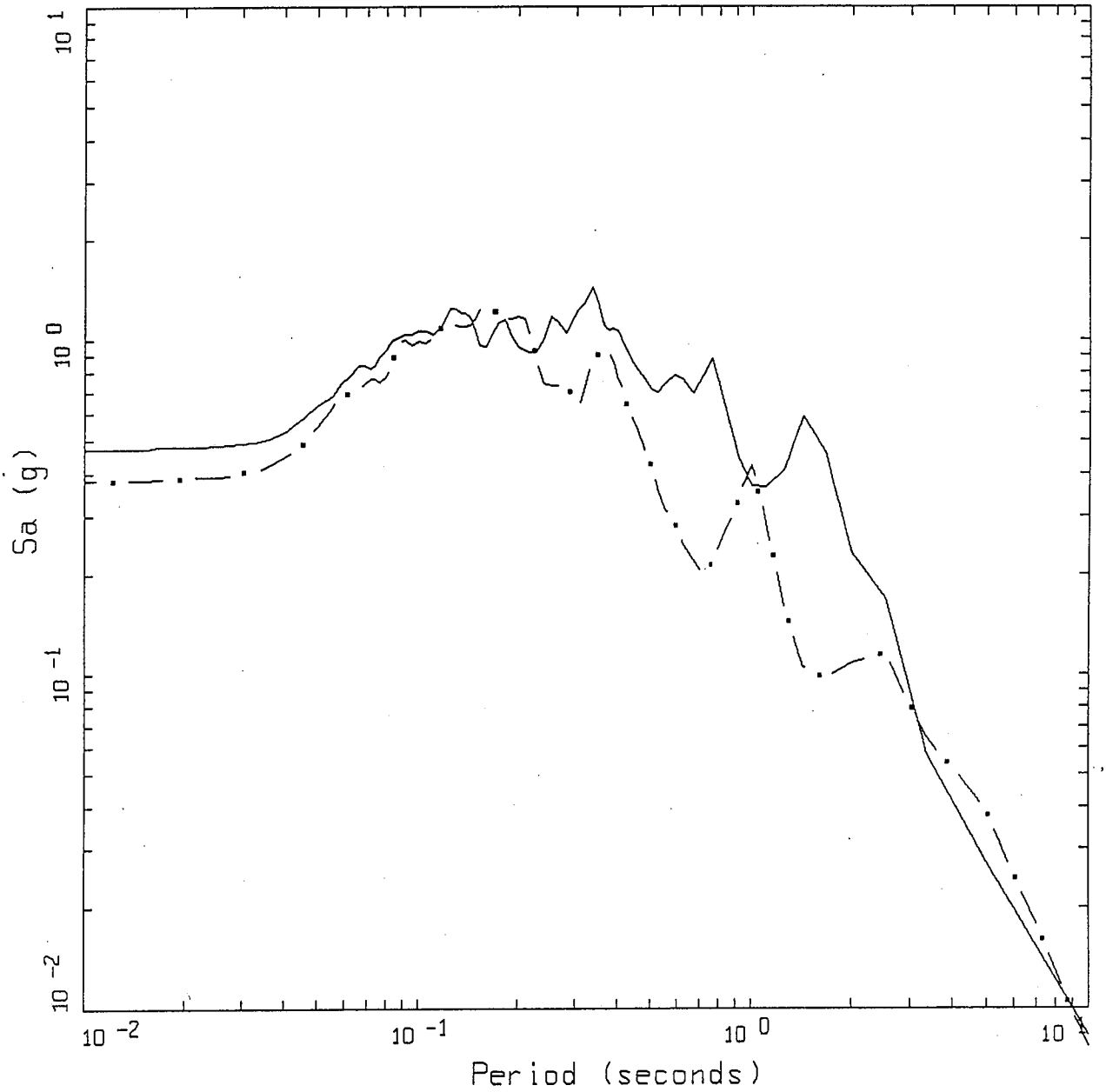

LEGEND

SOUTH FOCUS, PGA = 0.472 G

SOUTH FOCUS, CONSTANT SUBEVENT RISE TIME, PGA = 0.377 G

Figure 7. Response spectra (5% damping) computed for the base case (Figure 1, Table 1) fault model at the end (north) site for south focus with randomized subevent rise time (solid line) and constant subevent rise time (dash-dotted line).

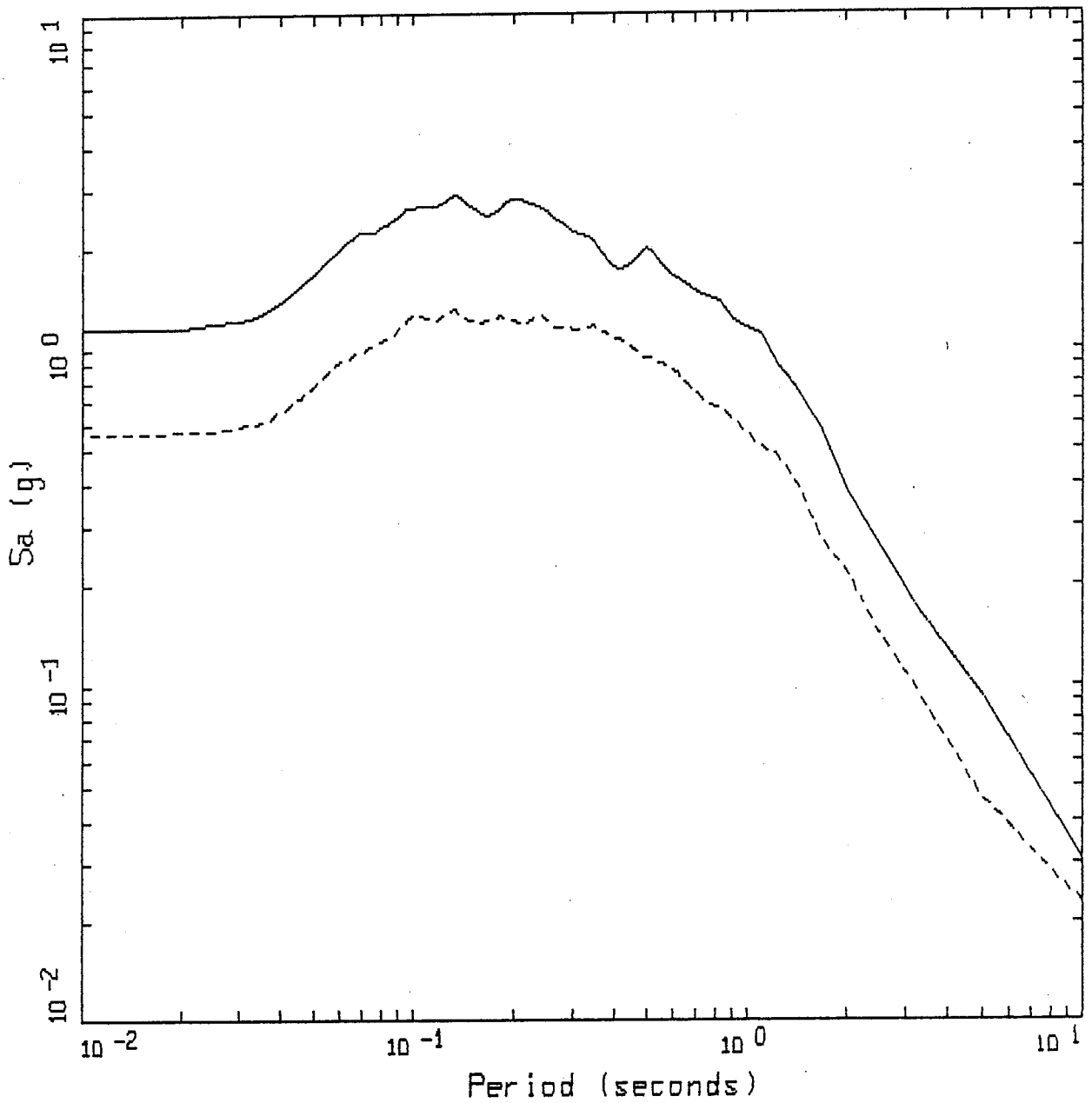

Figure 8. Median response spectra (5% damping) computed for the base case fault model at the end and middle sites (Figure 1, Table 1). Slip model and nucleation point have been randomized (30 realizations).

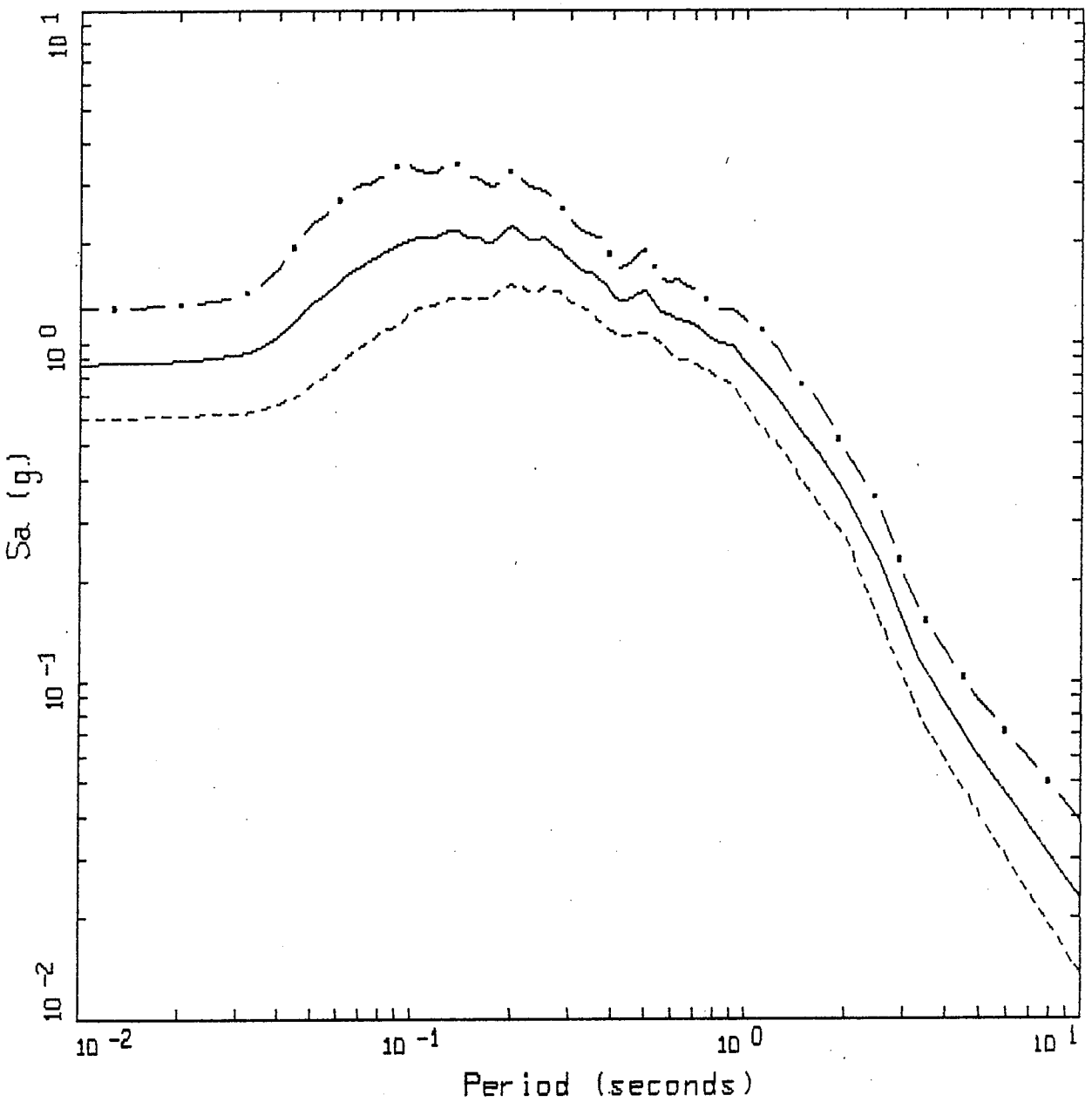

Figure 9. Median and ± 1-sigma response spectra (5% damping) computed for the base case fault model at the middle site (Figure 1, Table 1) with the fault width increased to 13 km (fault length kept at 75 km). Slip model and nucleation point have been randomized (30 realizations).

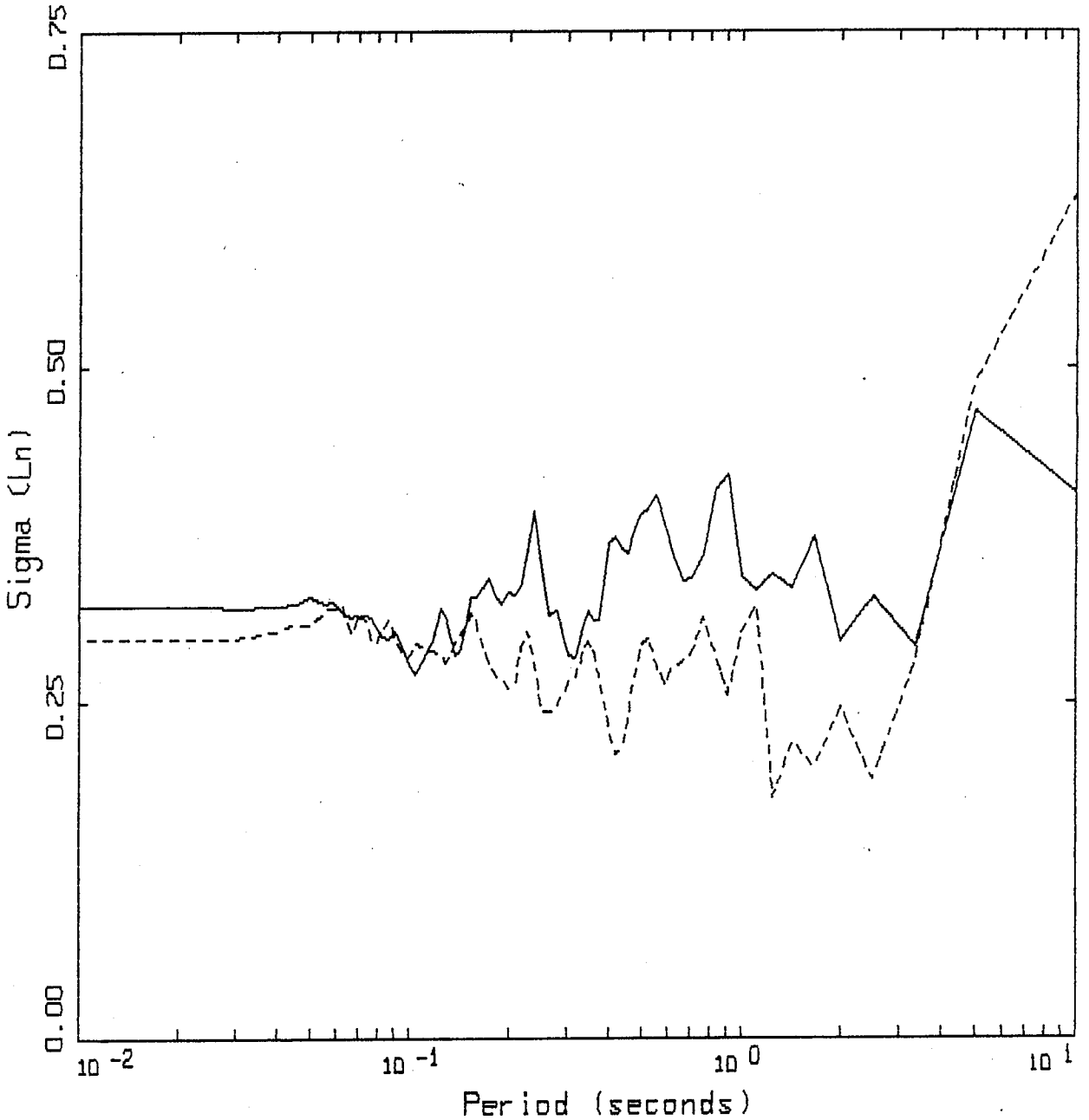

Figure 10. Variation of 5% damped response spectra computed for the base case fault model (Figure 1, Table 1) for 30 randomized slip models (end site, solid line; middle site, dashed line).

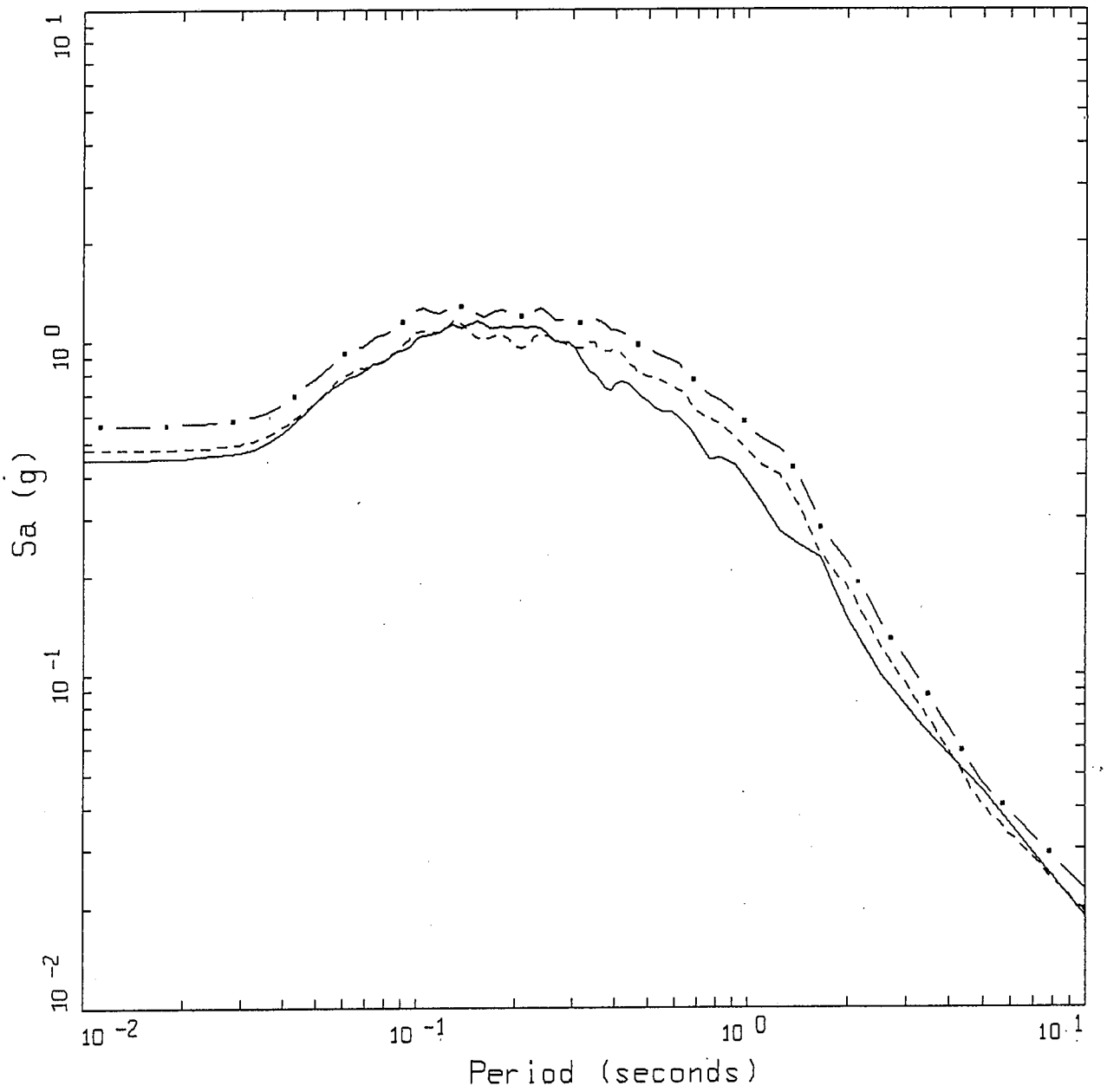

M 7.0 FINITE SOURCE, D=0.6 KM
VARIATION OF ALL PARAMETERS, END SITE

LEGEND

———— 50TH PERCENTILE, EAST 45 DEGREE DIP, PGA = 0.445 G

- - - - - 50TH PERCENTILE, WEST 45 DEGREE DIP, PGA = 0.476 G

—·— 50TH PERCENTILE, 90 DEGREE DIP; PGA = 0.561 G

Figure 11. Median response spectra (5% damping) computed for the base case fault model at the end site (Figure 1, Table 1) for 3 dip angles 45° E (solid line), 45° W (dashed line), 90° (dashed-dotted line). Slip model and nucleation point have been randomized (30 realizations).

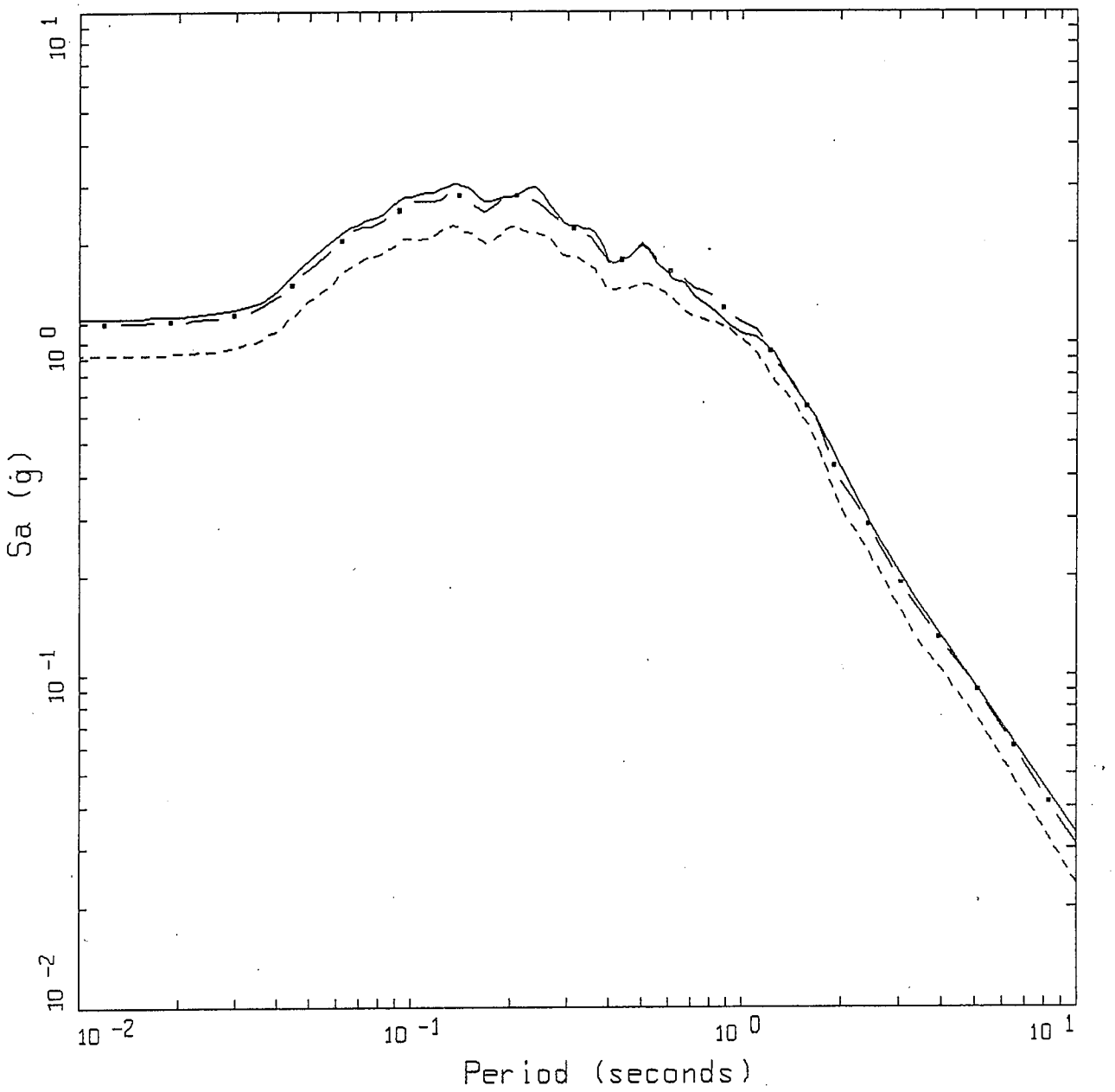

Figure 12. Median response spectra (5% damping) computed for the base case fault model at the middle site (Figure 1, Table 1) for 3 dip angles 45° E (solid line), 45° W (dashed line), 90° (dashed-dotted line). Slip model and nucleation point have been randomized (30 realizations).

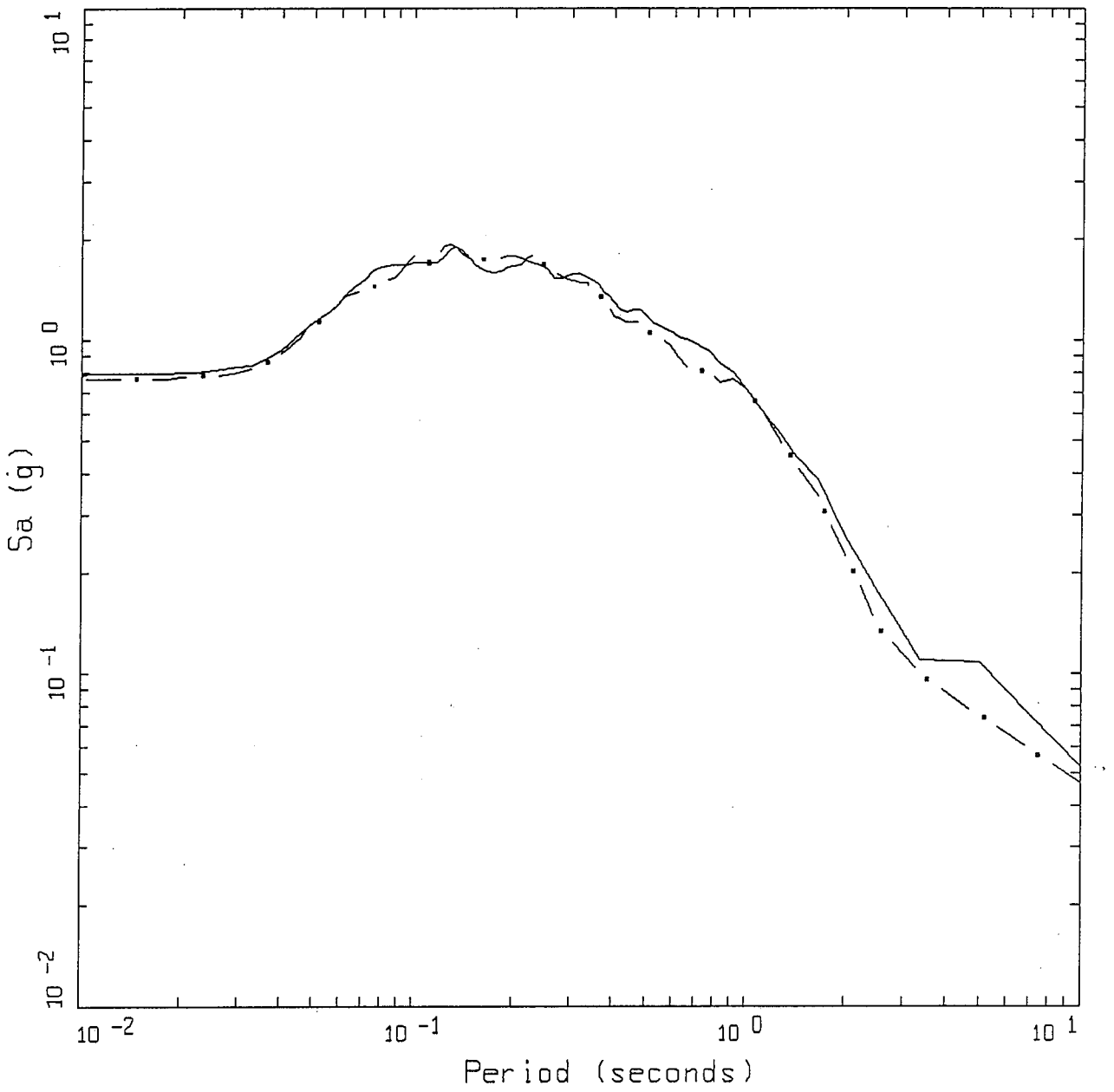

Figure 13. Median response spectra (5% damping) computed for the base case fault model at the end site (Figure 1, Table 1) for 2 dip angles 45° E (solid line) and 45° W (dashed-dotted line). Fault width has been increased to 18 km with the area held constant. Slip model and nucleation point have been randomized (30 realizations).

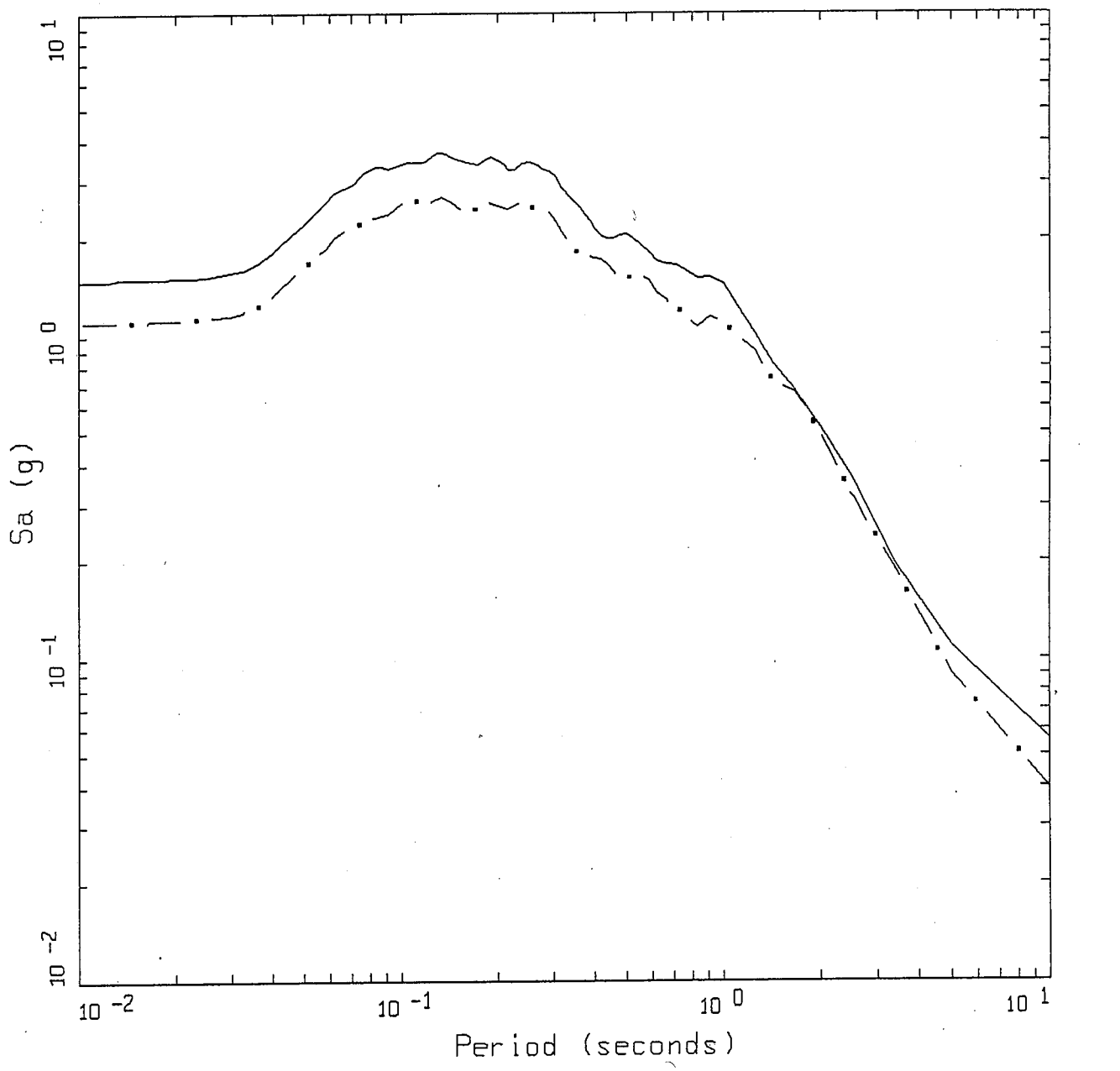

Figure 14. Median response spectra (5% damping) computed for the base case fault model at the middle site (Figure 1, Table 1) for 2 dip angles 45° E (solid line) and 45° W (dashed-dotted line). Fault width has been increased to 18 km with the area held constant. Slip model and nucleation point have been randomized (30 realizations).

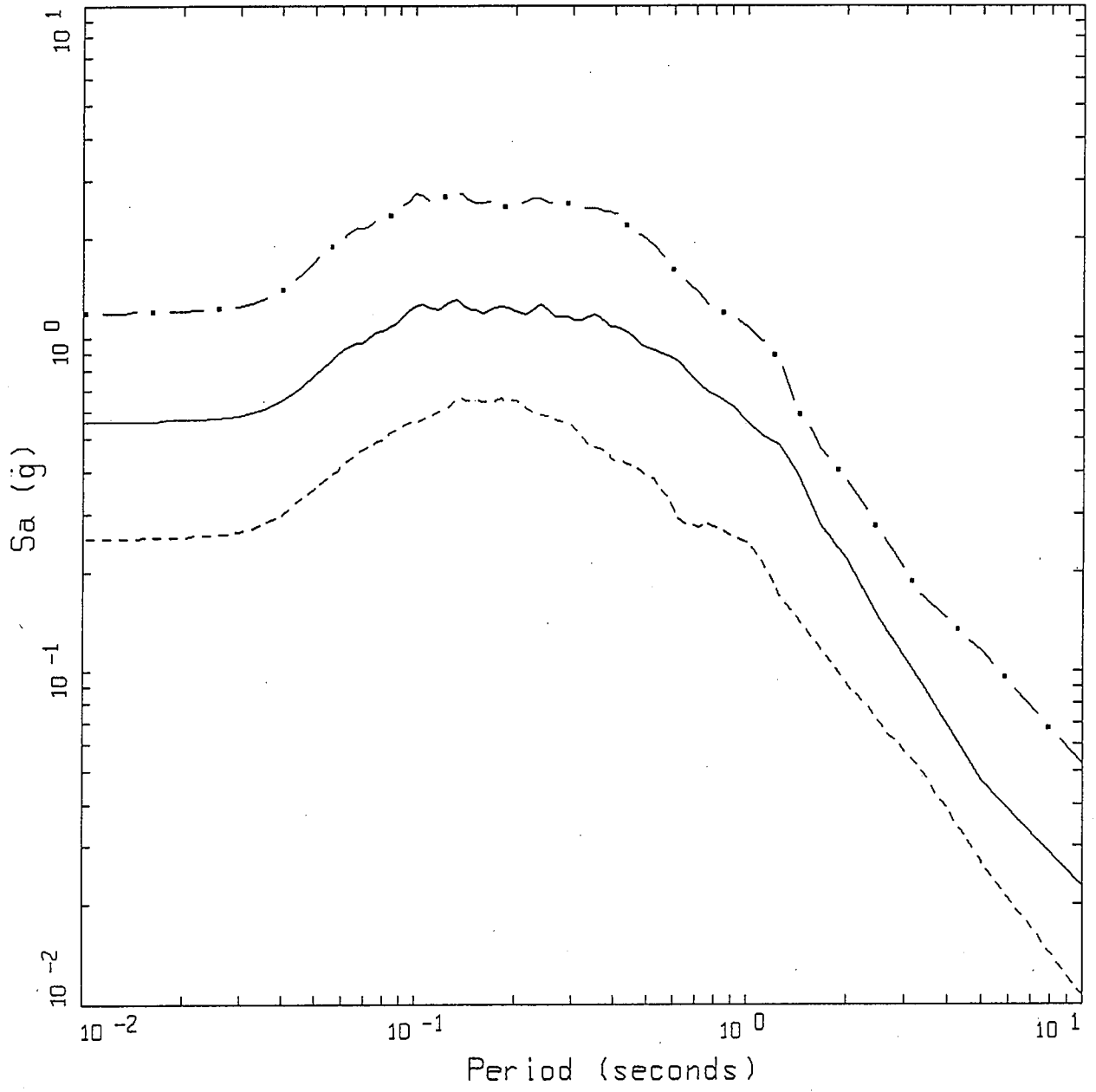

Figure 15. Median response spectra (5% damping) computed for the base case fault model at the end site (Figure 1, Table 1) for different stress drops (areas). Solid line, 48 bars, base case; dash-dotted line, 96 bars; dotted line, 24 bars. Slip model and nucleation point have been randomized (30 realizations).

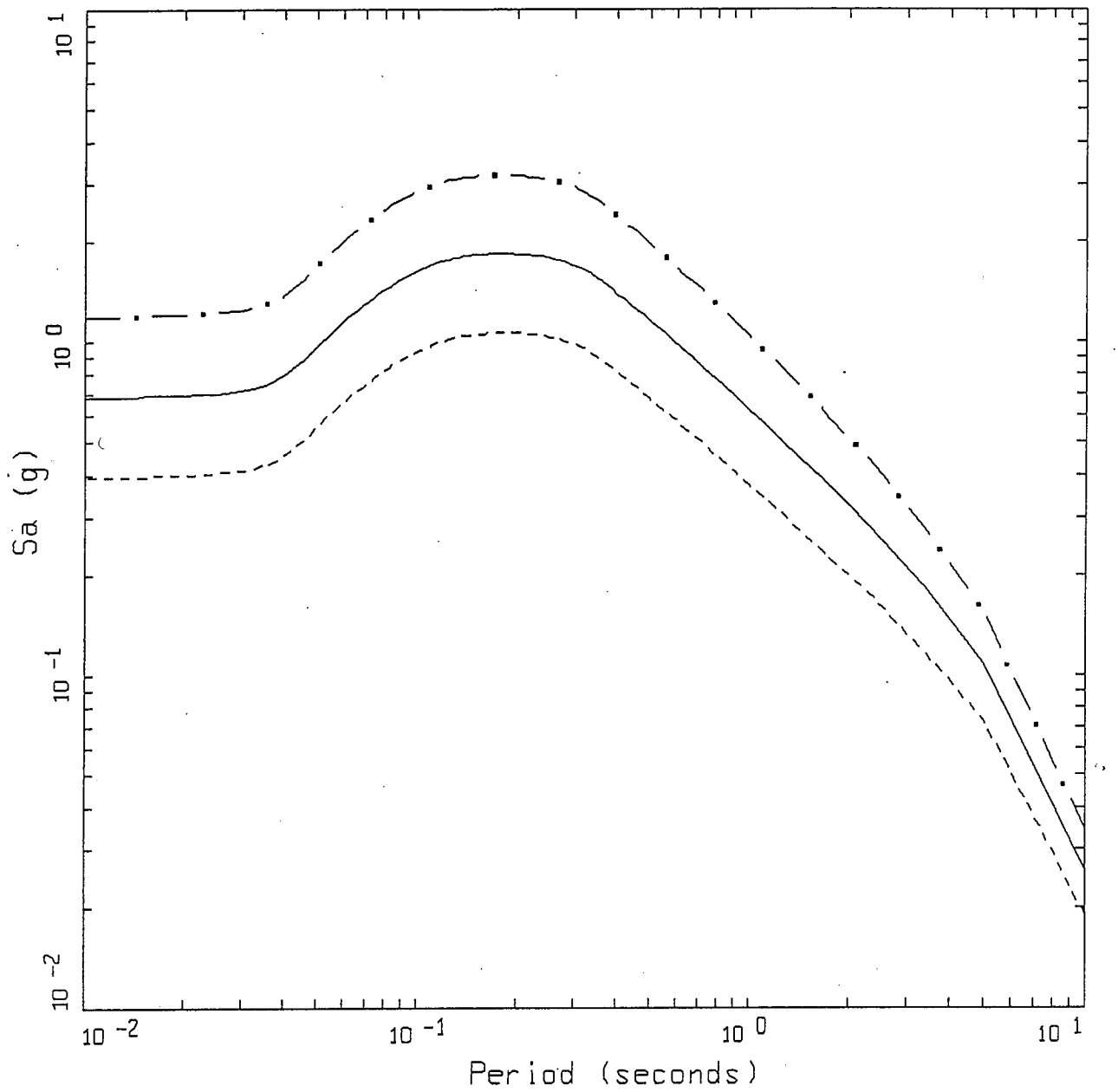

Figure 16. Response spectra (5% damping) computed for the base case point source model at an epicentral distant of 0.6 km and a depth of 8 km (Table 1) for different stress drops. Solid line, 100 bars, base case; dash-dotted line, 200 bars; dashed line, 50 bars.

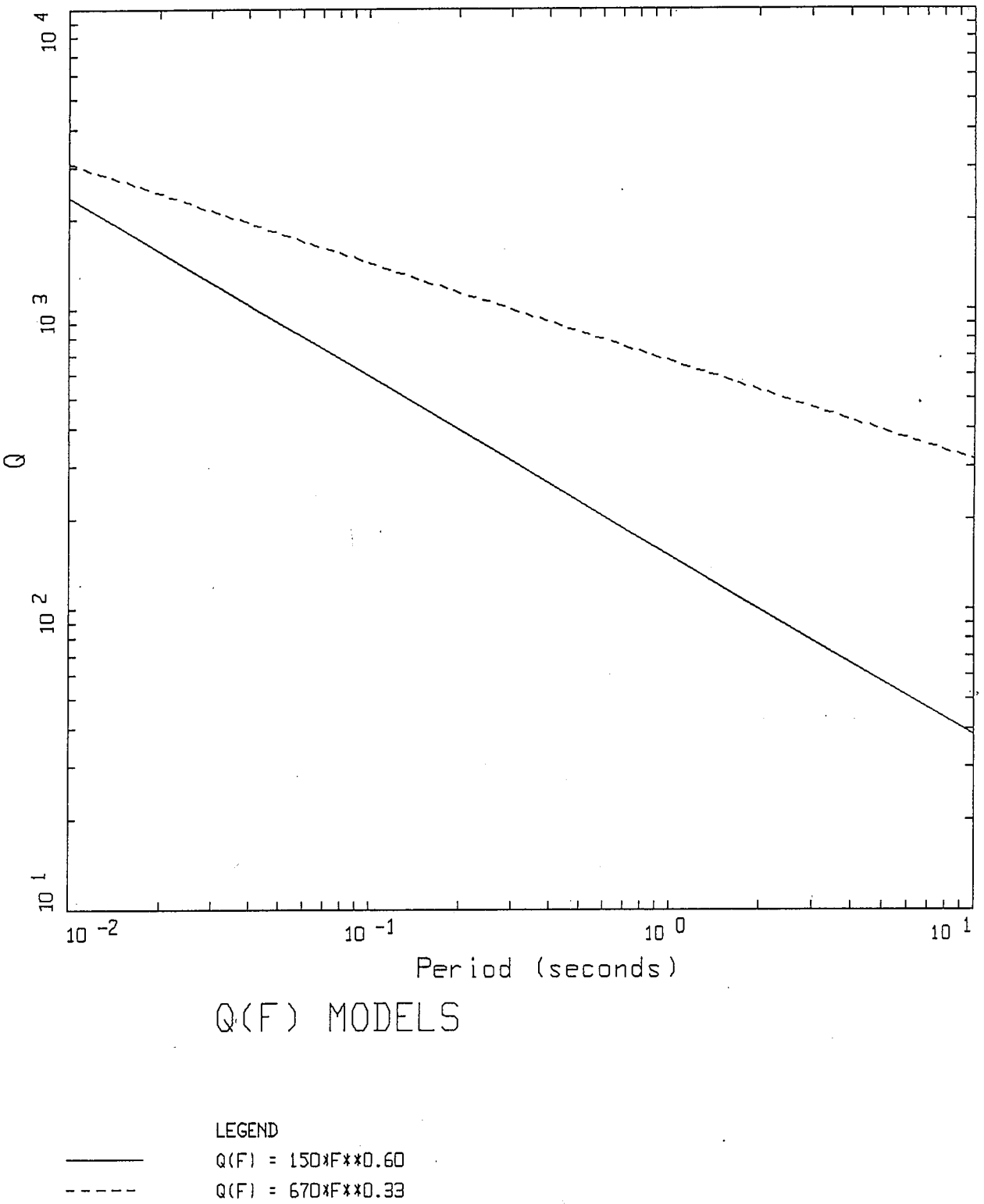

Figure 17. Q(f) models plotted verses period. Damping (fractional) is given approximately by 1/(2 Q(f)).

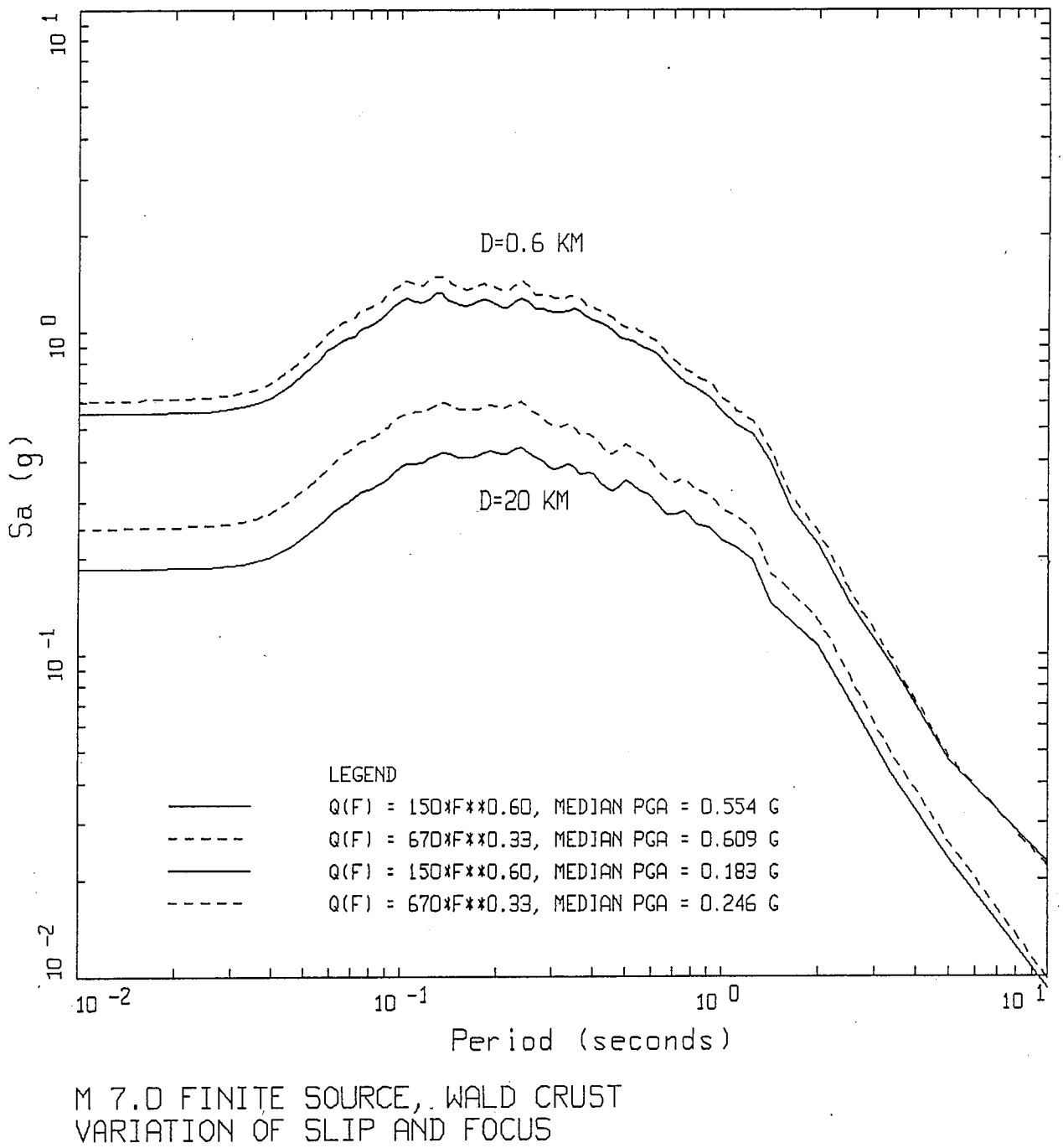

Figure 18. Effects of propagation path damping (Q(f)) on 5% damped spectral acceleration for fault distances 0.6 km (upper set) and 20 (lower set) km (Figure 1). Q(f) models represent typical WNA 150 $f^{0.60}$ and ENA 670 $f^{0.33}$ values. Slip model and nucleation point have been randomized (30 realizations).

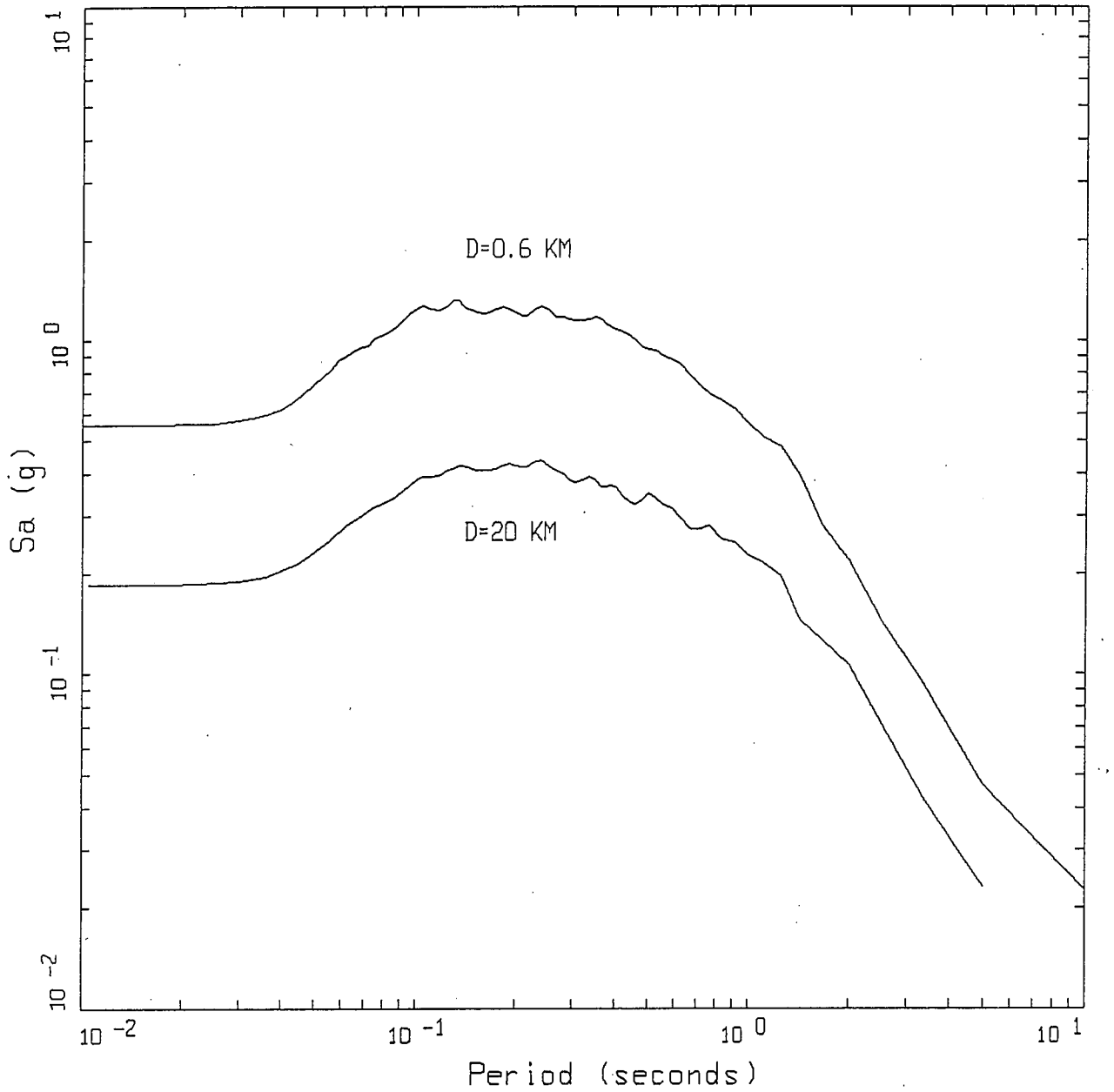

M 7.0 FINITE SOURCE, WALD CRUST
VARIATION OF SLIP AND FOCUS

LEGEND

D=0.6 KM, MEDIAN PGA = 0.554 G

D=20 KM, MEDIAN PGA = 0.183 G

Figure 19. Effects of distance on 5% damped spectral acceleration for fault distances 0.6 km (upper) and 20 (lower) km (Figure 1). Slip model and nucleation point have been randomized (30 realizations).

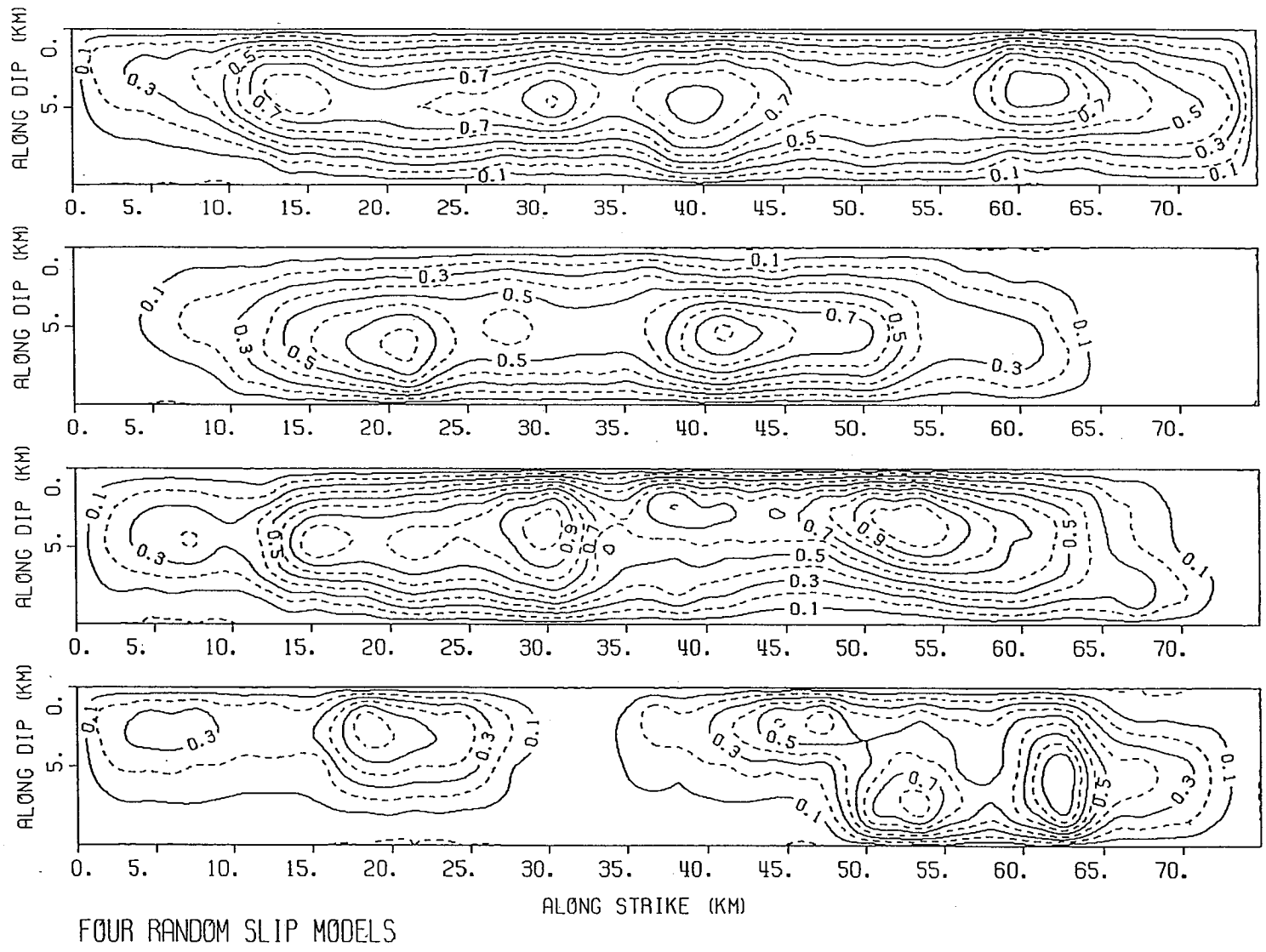

Figure 20. Example subset of the 30 random slip models. Slip model generation preserves the size, number, shape, and general location of asperities found in slip models derived from recordings of large (M ≥ 6.5) earthquakes (note, top of fault is at a depth of 2 km).

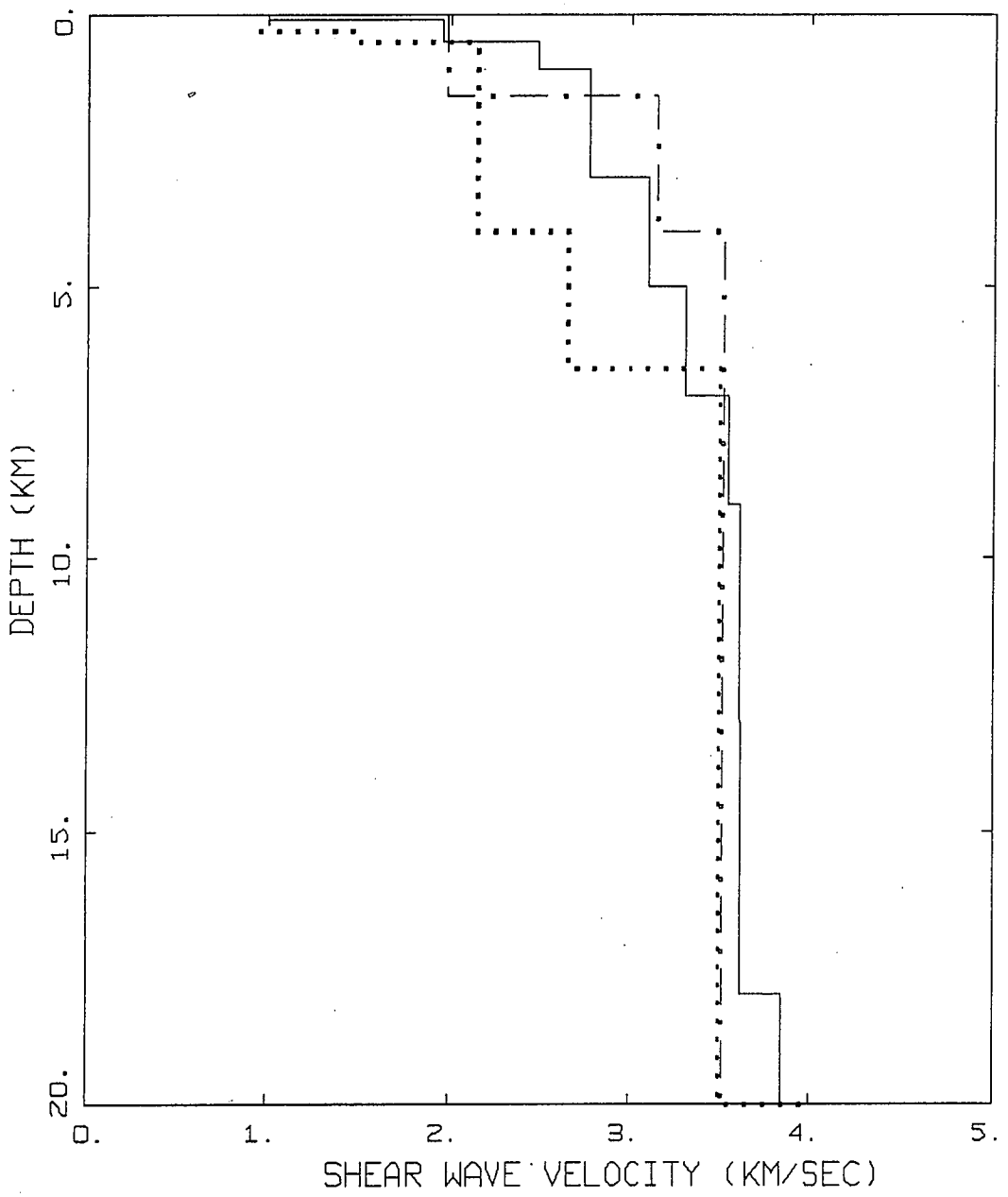

Figure 21. Crustal models used in assessing the effects of crustal amplification on response spectral ordinates. Northern California soft rock (Wald et al., 1991) southern California Los Angeles area soft rock (Saikia, 1993), and southern California hard rock (Landers; Wald and Heaton, 1994).

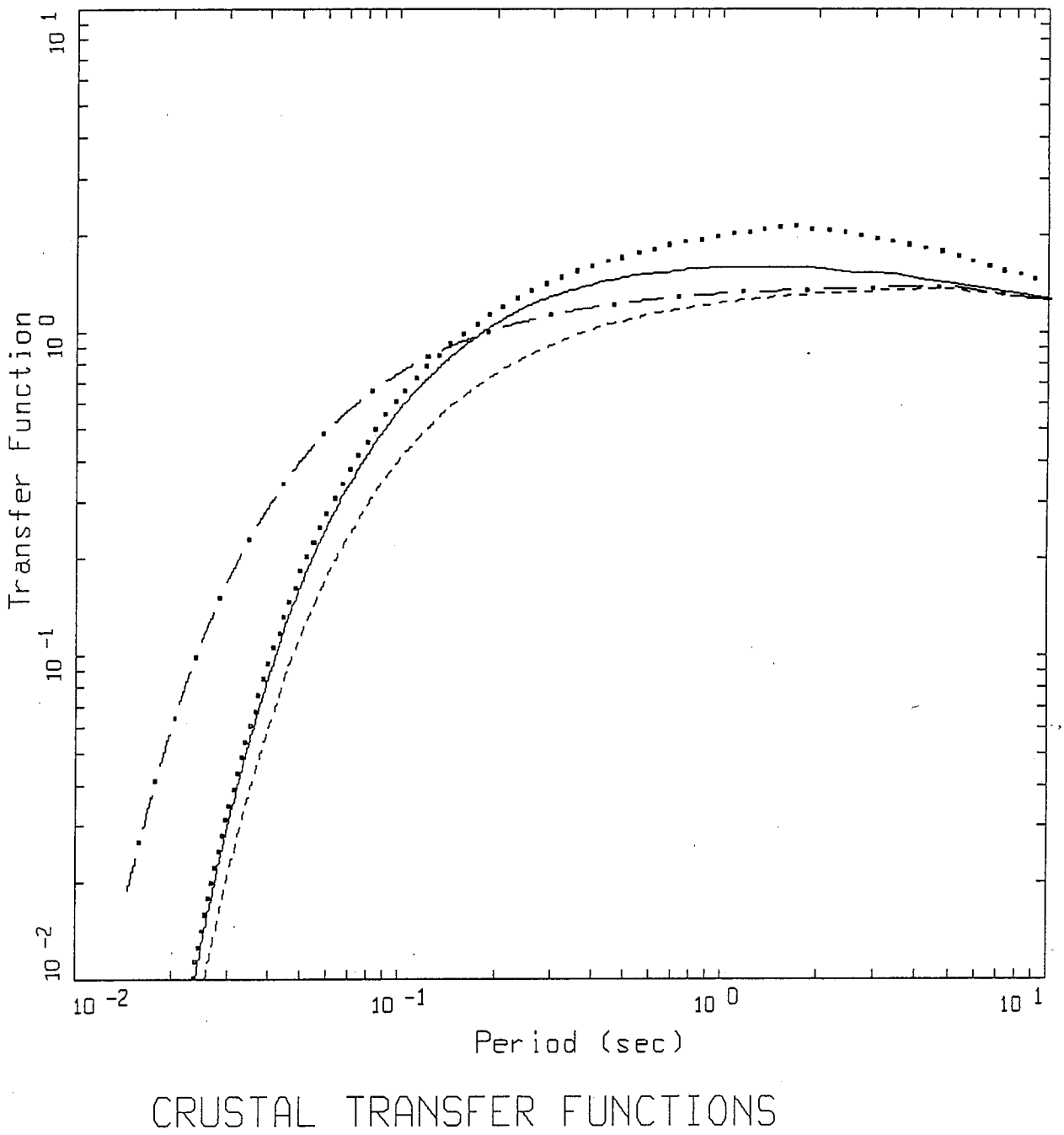

Figure 22. Net crustal amplification factors for northern California soft rock (Wald et al., 1991) southern California Los Angeles area soft rock (Saikia, 1993), and southern California hard rock (Landers; Wald and Heaton, 1994). The Landers crustal model was run with both hard rock and soft rock kappa values of 0.02 and 0.04 sec respectively.

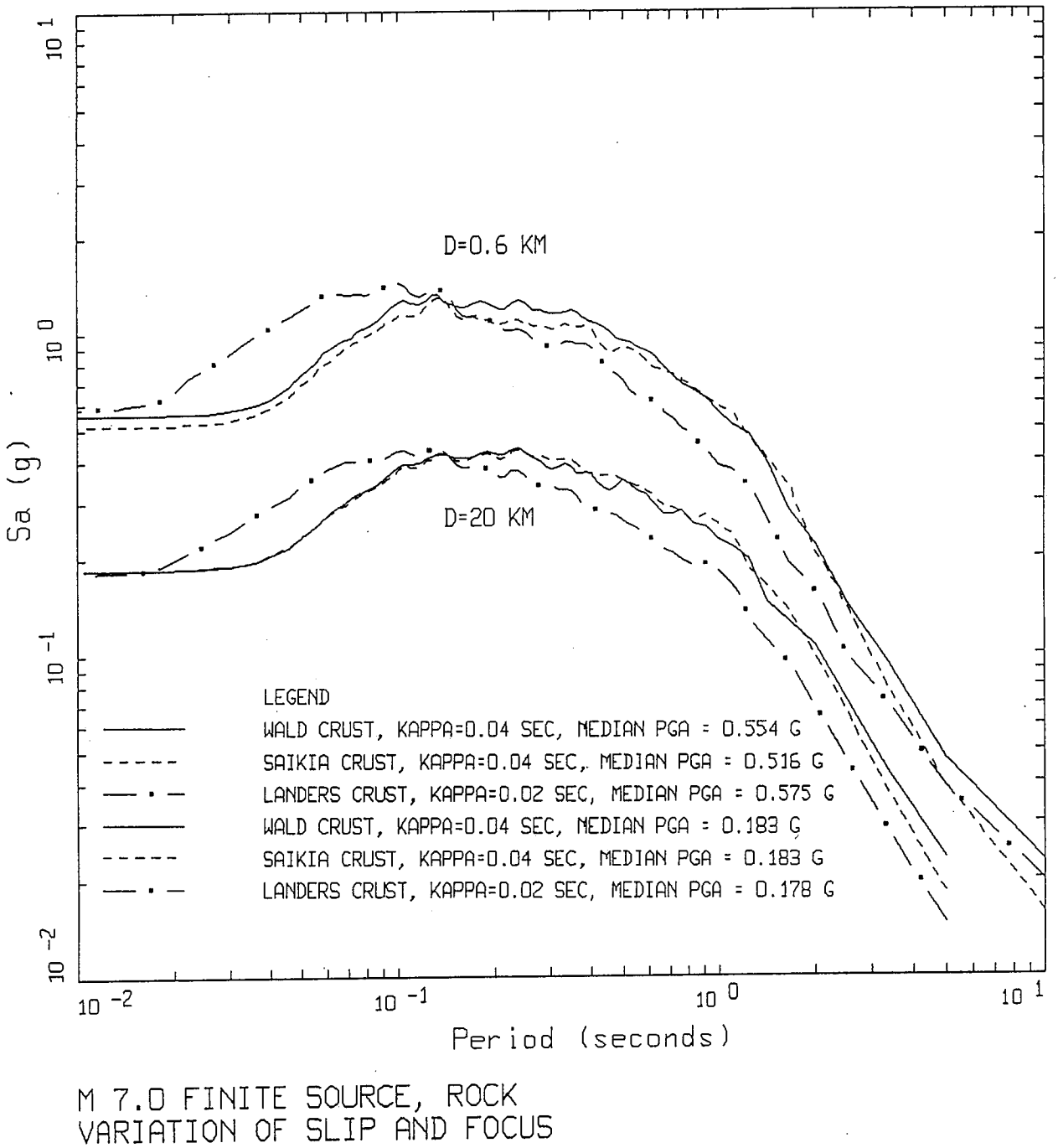

Figure 23. Rock site effects on 5% damped spectral acceleration for fault distances 0.6 km (upper set) and 20 (lower set) km (Figure 1). Crustal models (see Figure 21) represent northern and southern California soft rock (Wald et al., 1991 and Saikia, 1993) and southern California hard rock (Landers; Wald and Heaton, 1994). Soft and hard rock kappa values are 0.04 and 0.02 sec respectively. Slip model and nucleation point have been randomized (30 realizations).

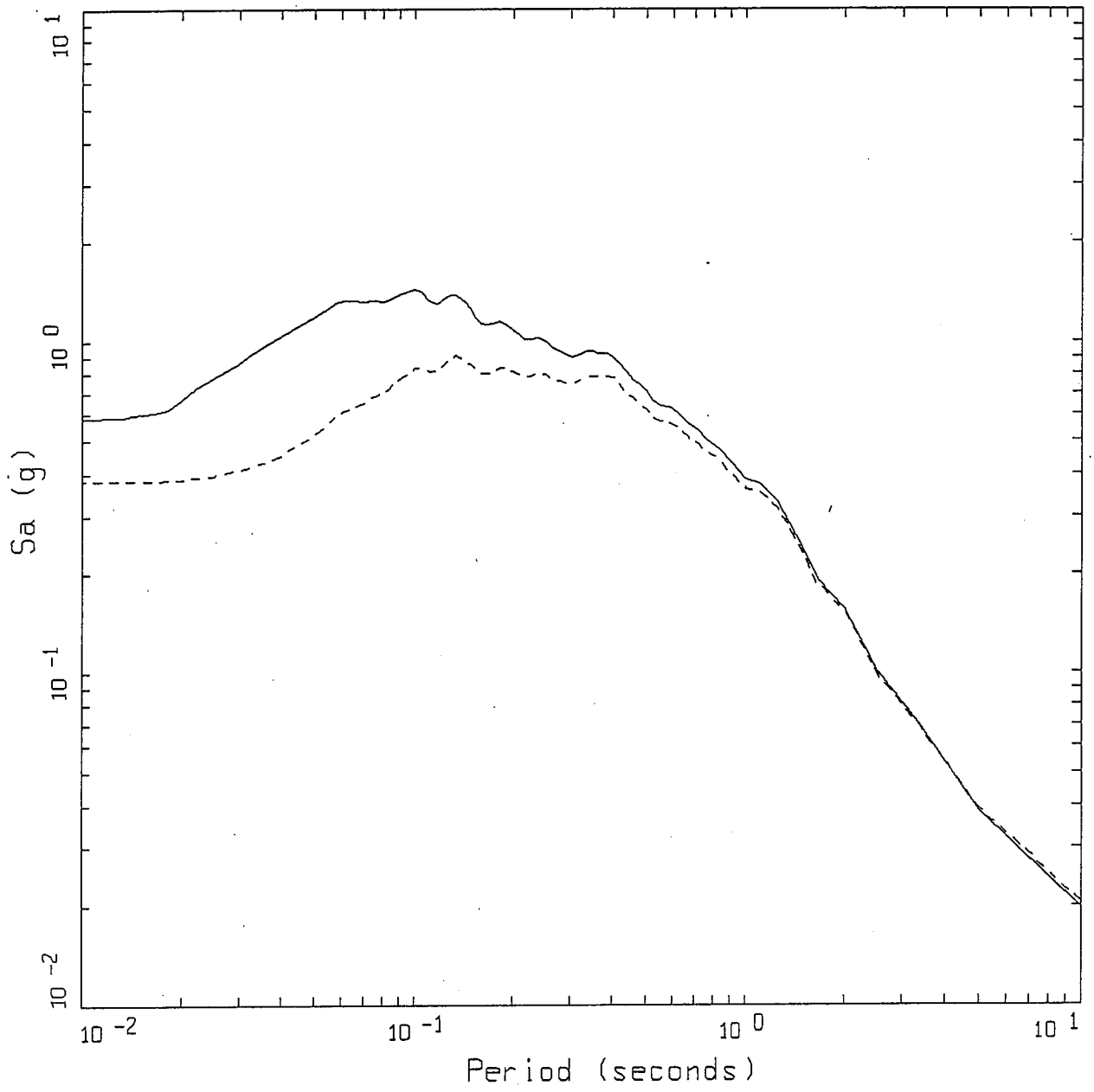

Figure 24. Effects of kappa on 5% damped spectral acceleration for the Landers hard rock crustal model (Figure 21). Solid line, base case hard rock kappa of 0.02 sec; dashed line, base case soft rock kappa of 0.04 sec.

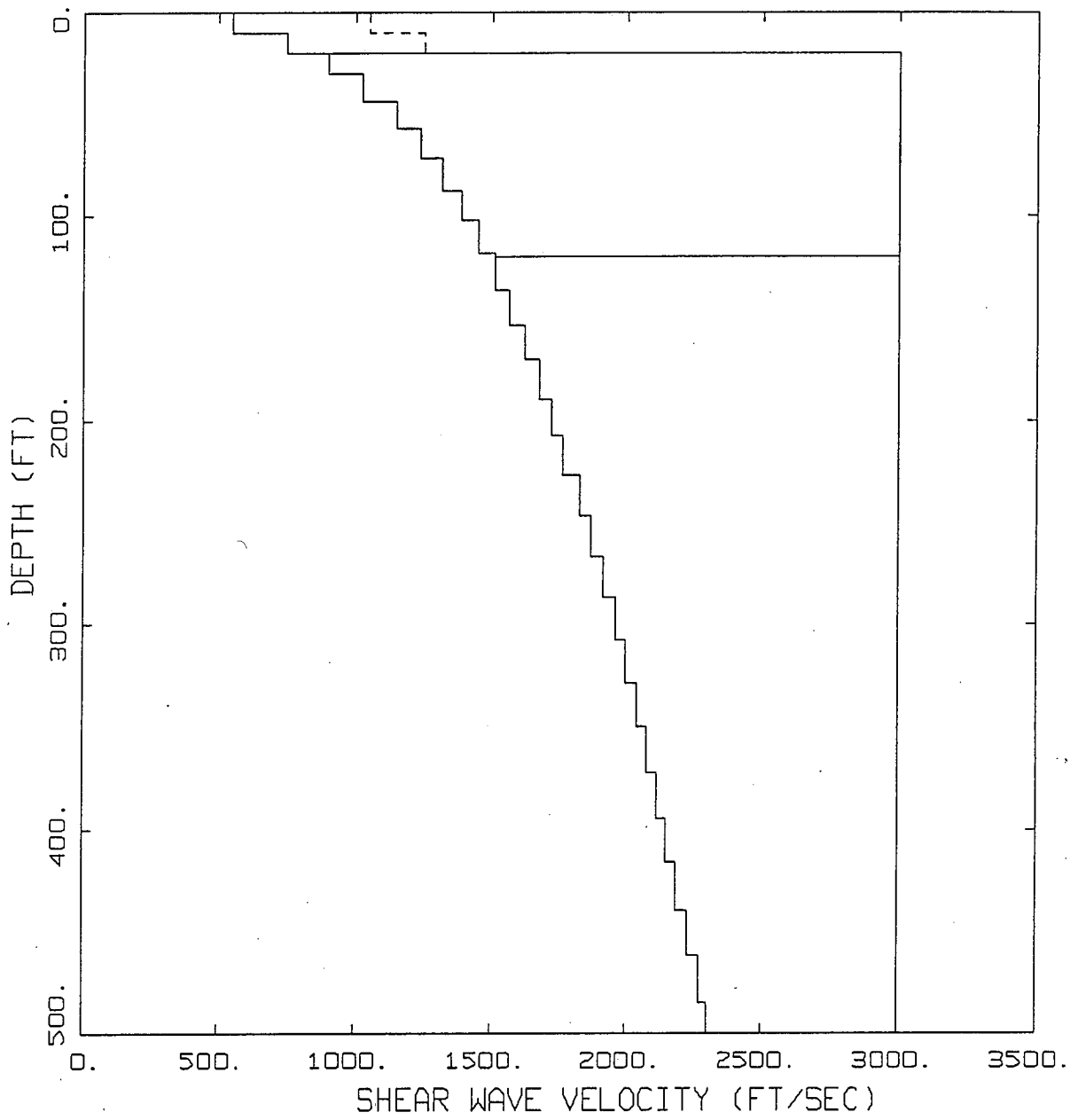

Figure 25. Soil profile used in assessing the effects of a soil column on response spectral ordinates. WNA stiff is appropriate for sandy soils in western North America. ENA soil is Category 1 of the EPRI generic profiles appropriate for sandy soils at nuclear power plants in the central and eastern United States.

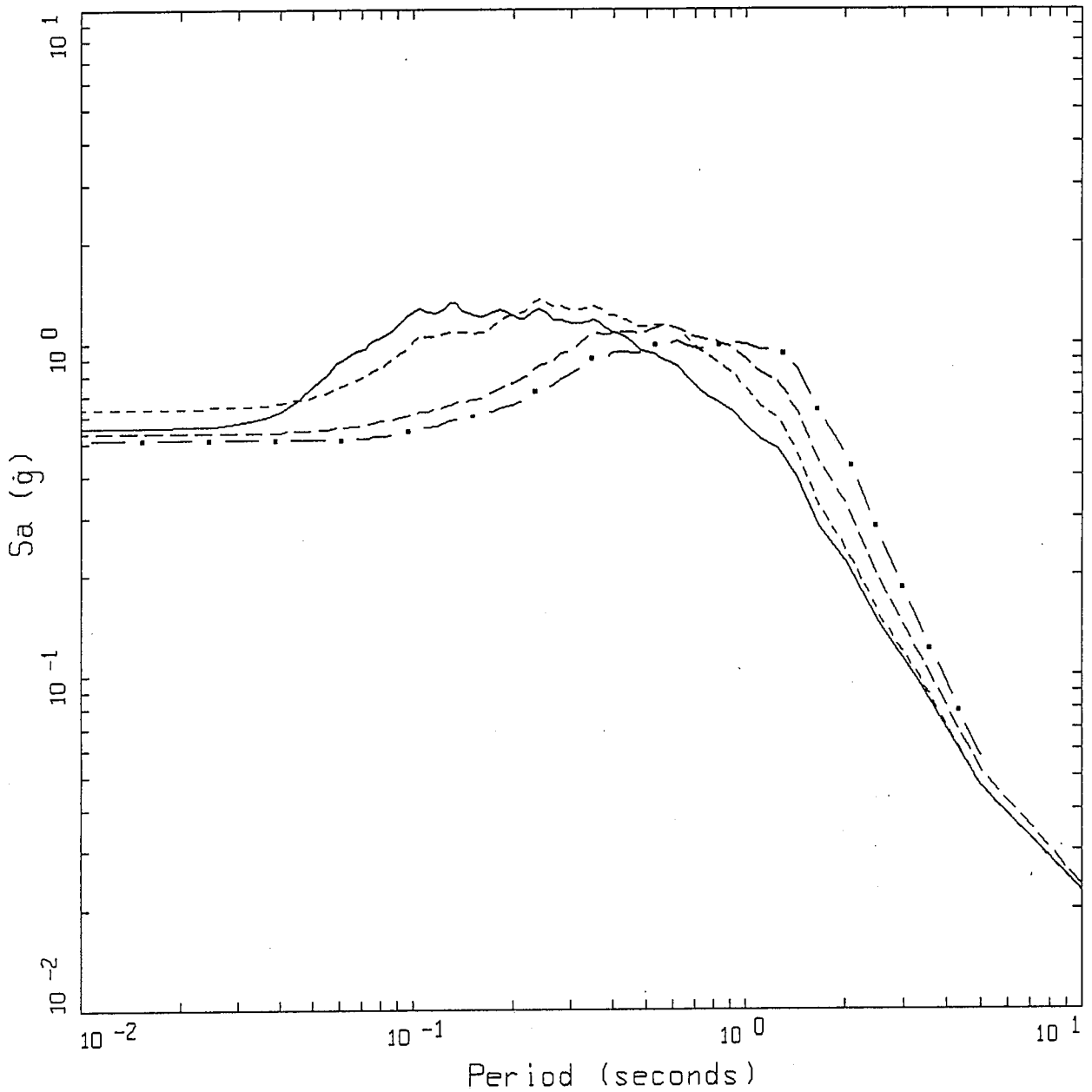

Figure 26. Soil site effects on 5% damped spectral acceleration for a fault distance of 0.6 km.

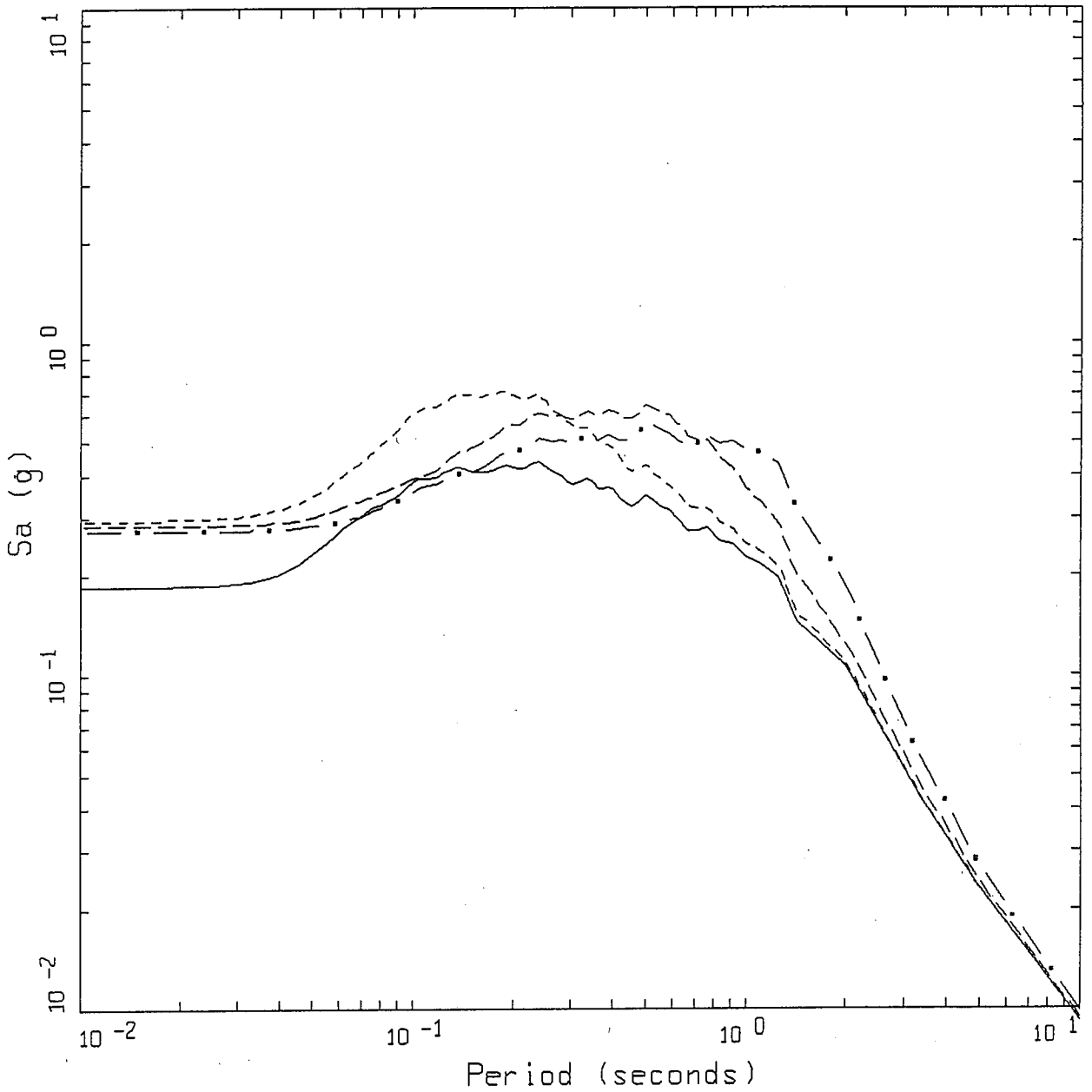

M 7.0 FINITE SOURCE, D=20 KM, WALD CRUST
VARIATION OF SLIP AND FOCUS

LEGEND

———— ROCK, MEDIAN PGA = 0.183 G

- - - - - 20 FT WNA STIFF SOIL, PROFILE VARIATION, MEDIAN PGA = 0.291 G

— — — — 120 FT WNA STIFF SOIL, PROFILE VARIATION, MEDIAN PGA = 0.282 G

— • — 500 FT WNA STIFF SOIL, PROFILE VARIATION, MEDIAN PGA = 0.273 G

Figure 27. Soil site effects on 5% damped spectral acceleration for a fault distance of 20 km.

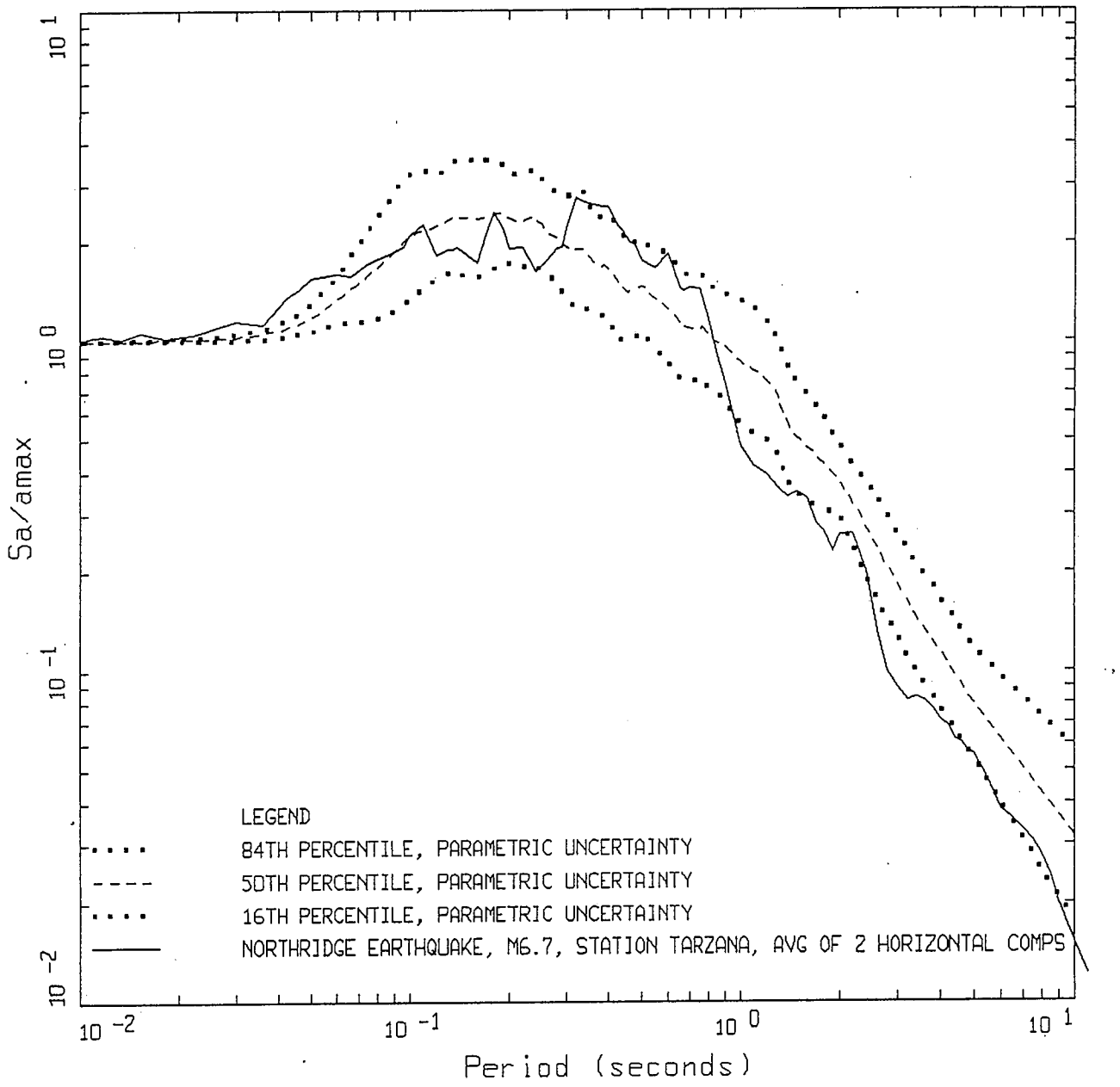

Figure 28. Comparison of 5% damped response spectral shapes: 1994 M 6.7 Northridge earthquake recordings at the shallow soil site Tarzana (solid line) with motions computed for a 20 ft thick generic soil profile (Figure 25) over a soft rock northern California crust (Figure 21). The simulations are for a M 7.0 vertical strike slip earthquake at a site 20 km from one end (Figure 1). Slip model, nucleation point, and profile are randomized (30 realizations).

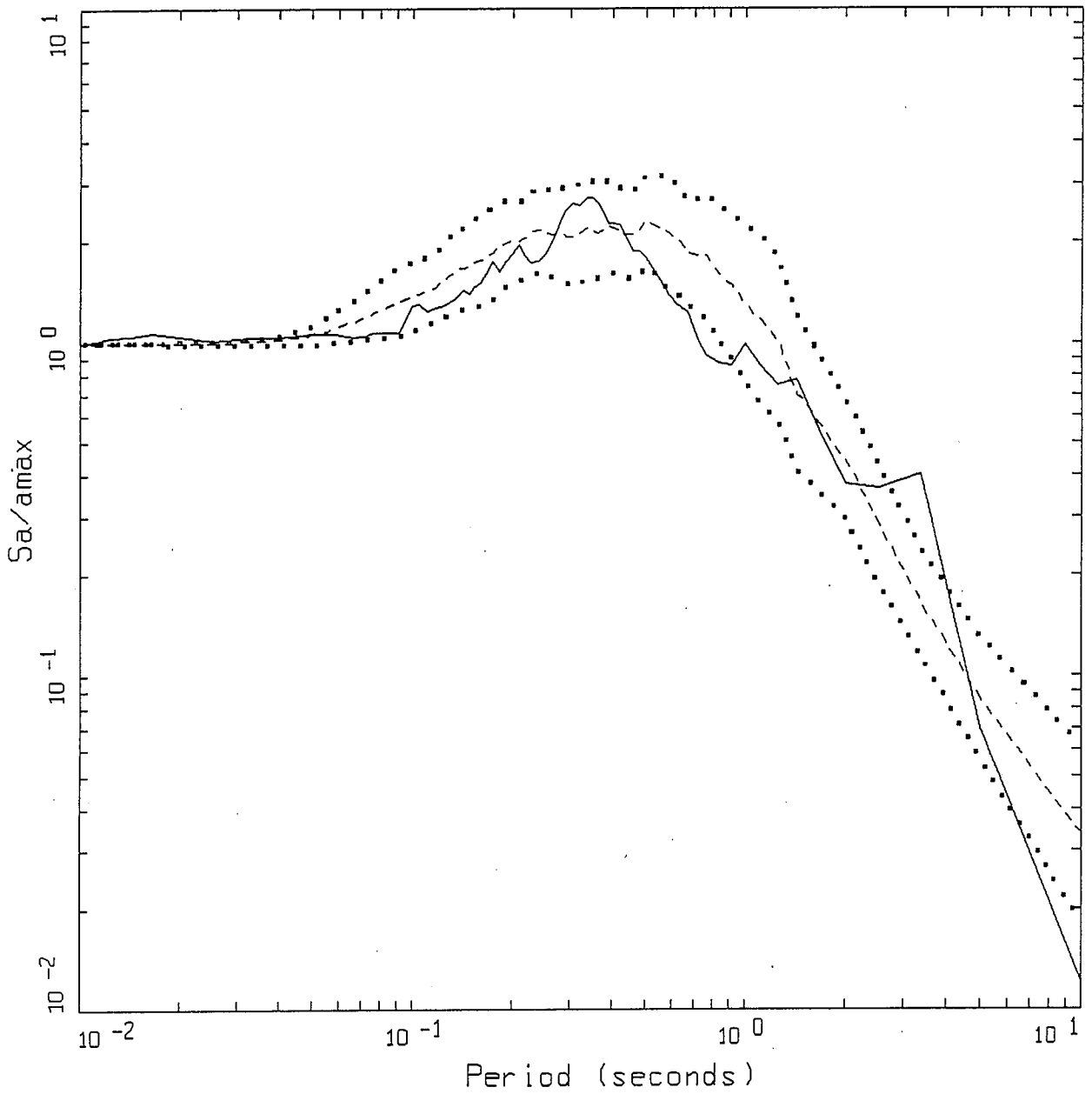

M 7.0 FINITE SOURCE, D=20 KM, 120 FT SOIL, WALD CRUST
VARIATION OF SLIP, FOCUS, AND PROFILE

LEGEND

- 84TH PERCENTILE, PARAMETRIC UNCERTAINTY
- 50TH PERCENTILE, PARAMETRIC UNCERTAINTY
- 16TH PERCENTILE, PARAMETRIC UNCERTAINTY
- LOMA PRIETA EARTHQUAKE, M6.9, STATION PALO ALTO VET, AVG OF 2 HORIZONTAL COMPS

Figure 29. Comparison of 5% depth damped response spectral shapes: 1989 **M** 6.0 Loma Prieta earthquake recordings at the intermediate depth soil site Palo Alto Veterans Hospital (solid line) with motions computed for a 120 ft thick generic soil profile (Figure 25) over a soft rock northern California crust (Figure 21). The simulations are for a M 7.0 vertical strike slip earthquake at a site 20 km from one end (Figure 1). Slip model, nucleation point, and profile are randomized (30 realizations).

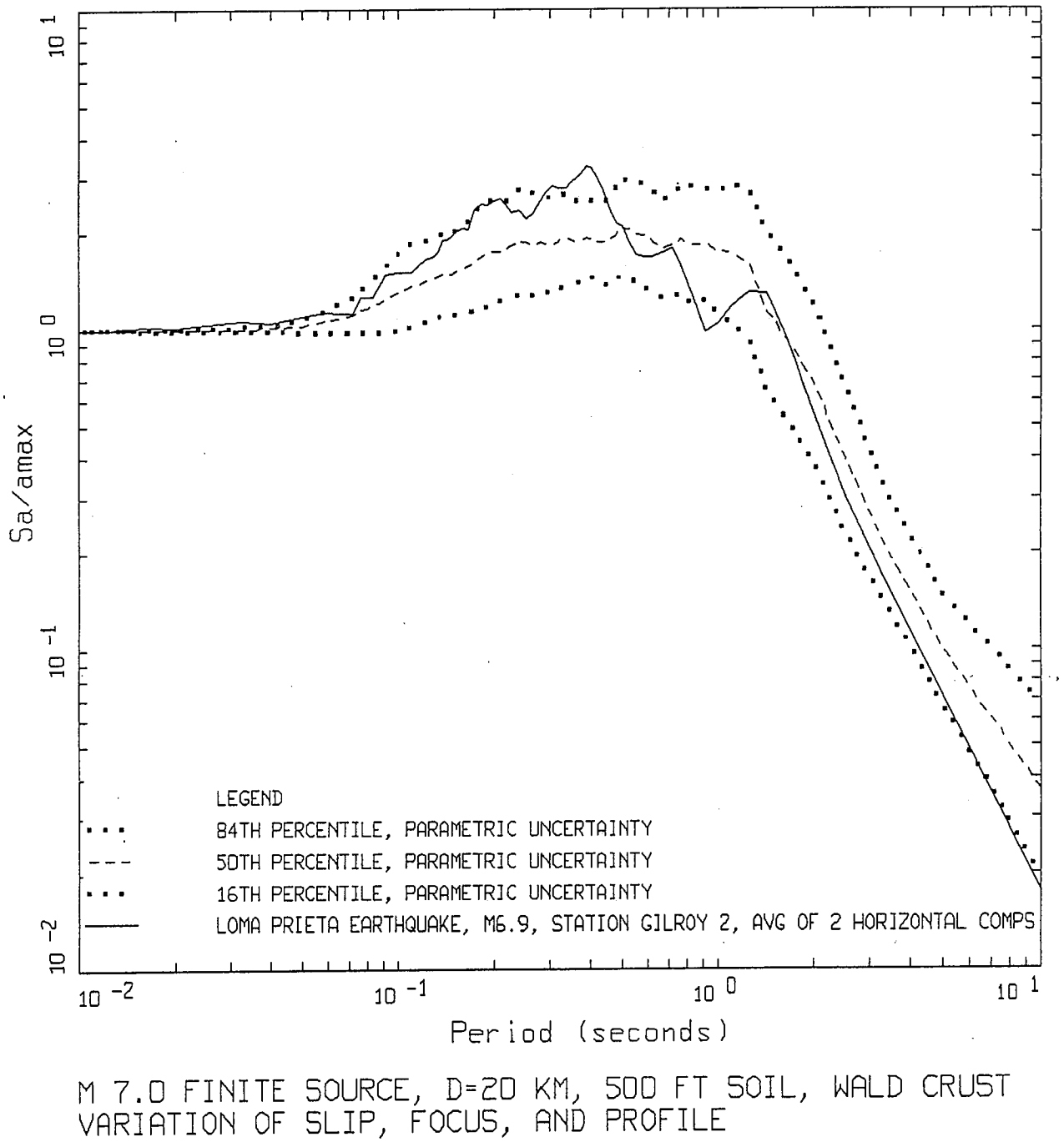

Figure 30. Comparison of 5% damped response spectral shapes: 1989 M 6.9 Loma Prieta earthquake recordings at the deep soil site Gilroy Array No. 2 (solid line) with motions computed for a 500 ft thick generic soil profile (Figure 25) over a soft rock northern California crust (Figure 21). The simulations are for a M 7.0 vertical strike slip earthquake at a site 20 km from one end (Figure 1). Slip model, nucleation point, and profile are randomized (30 realizations).

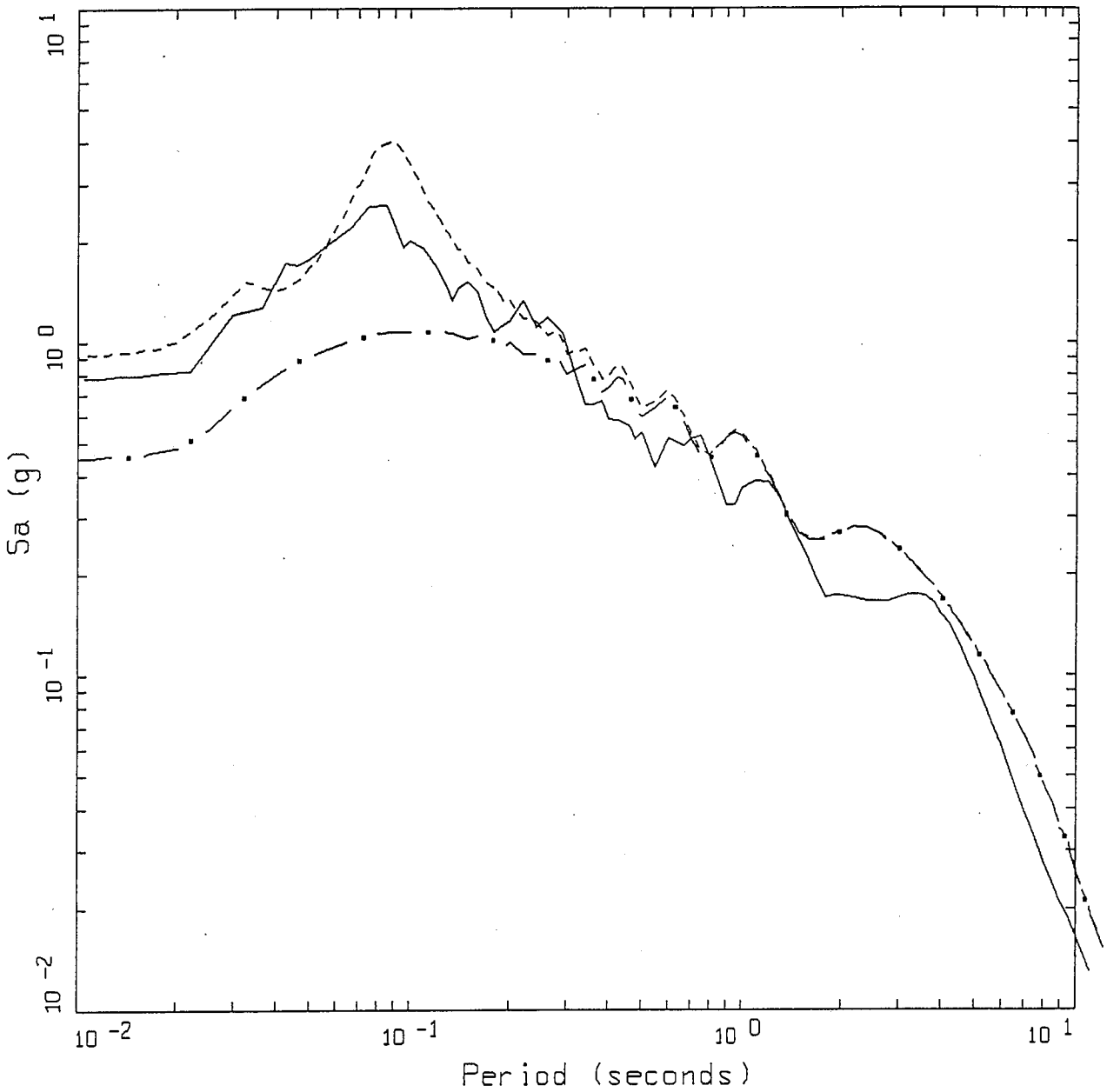

Figure 31. Comparison of 5% damped spectral acceleration: 1992 M 7.2 Landers earthquake recordings at the shallow stiff soil site Lucern (solid line) with motion computed using a point source at a depth of 8 km and epicentral distance of 1 km. The point source stress drop is 47 bars (based on multiple site inversions). Dash-dotted line: Landers hard rock crust (Figure 21) with a kappa of 0.02 sec. Dashed line: 20 ft stiff generic ENA soil (Figure 25) on Landers crust with a rock kappa of 0.016 sec.

Evaluation and Implementation of an Improved Methodology for Earthquake Ground Response Analysis

Uniform Treatment of Source, Path and Site Effects

Seminar 7

(1/26/95, 59 p.)

Global Site Effects

a) General References
b) Introduction
c) Global or Non 1-D Site Effects
    1) Topographic Effects
    2) Alluvial Valley Effects
    3) Variability of Observed 2-Dimensional Site Effects
d) 1-D Site Effects
    1) Site Classification
    2) Soil Versus Rock
    3) Mechanism of 1-D Site Effects
    4) Approaches to Modeling Nonlinear 1-D Site Effects

CALTRANS

SEMINAR ON STRONG GROUND MOTION

Seminar 7; January 26, 1995

Global Site Effects

a) General References

1988 Aki: Local site effects on ground motion. *Earthquake Engineering and Soil Dynamics II-Recent Advances in Ground-Motion Evaluation, Proc. Am. Soc. Civil. Engin. Specialty Conf.*, J. Lawrence Von Thun, ed., Park City, Utah, Pub. 20, 103-155.

1991 Silva: Global characteristics and site geometry. Chapter 6 in *Proceedings: NSF/EPRI Workshop on Dynamic Soil Properties and Site Characterization.* Palo Alto, Calif.: Electric Power Research Institute, NP-7337.

b) Introduction

Local geologic conditions have long been recognized to have a predominant effect upon strong ground motions (Hayashi et al., 1971; Mohraz, 1976; Seed et al., 1976). For example, Figure 1 shows average spectral amplifications (response spectral acceleration divided by peak acceleration) computed from recordings made on rock and soil sites at close distances to earthquakes in the magnitude range of about 6 to 7. The differences in spectral shapes are significant and depend strongly upon the general site classifications. These variations in spectral content represent average site dependent ground motion characteristics and result from vertical variations in soil material properties (1-D effects). Due primarily to the limited number of records from earthquakes of different magnitudes, spectral content in terms of response spectral shapes, was interpreted not to depend upon magnitude nor distance, being primarily affected by the stiffness and depth of the local soil profile. With an increase in the strong motion data base, it has become apparent that spectral shapes depend strongly upon magnitude as well as site conditions (Joyner and Boore, 1982, Idriss, 1985; Silva and Green, 1989) and that site effects extend to rock sites as well (Boatwright and Astrue, 1983; Campbell 1981, 1985, 1988; Cranswick et al., 1985; Silva and Darragh, 1994).

Examples of differences in spectral content largely attributable to one-dimensional site effects at rock sites can be seen in comparisons of spectral amplifications computed from motions recorded in both active and stable tectonic regions (Silva and Darragh, 1994). Figure 2 shows average spectral shapes computed from recordings made on rock at close distances to large and small earthquakes (Table 1). For both magnitudes (moment magnitude M 6.4 and 4.0), the motions recorded in eastern North America (ENA), a stable tectonic region, show a dramatic shift in the maximum spectral amplifications toward shorter periods compared to the western North American (WNA) motions. These differences in spectral content are significant and are interpreted as primarily resulting from differences in the shear-wave velocity and damping in the rocks directly beneath the site (Boore and Atkison, 1987; Toro and McGuire, 1987; Silva and Green, 1989; Silva and Darragh, 1994). Also evident in Figure 2 is the strong magnitude dependency of the response spectral shapes. The smaller earthquakes show a much narrower bandwidth. This is a consequence of lower corner frequencies for smaller magnitude earthquakes (Boore, 1983; Silva and Green, 1989; Silva and Darragh, 1995).

The difference in spectral content due to soil site effects, as shown in Figure 1, and due to path or rock site effects, as shown in Figure 2, are dramatic and illustrate the degree to which one-dimensional site conditions (vertical variations in dynamic material properties) control strong ground motions.

Superimposed upon these effects, for linear systems, are the effects of lateral heterogeneities upon strong ground motion. Such laterally varying structures as surface topography, dipping interfaces, and changes in material properties contribute two- and three-dimensional aspects to ground motion specification. These non-homogeneous effects, resulting from scattering, focusing, and mode conversions are present at all sites to some extent. In some cases, these global effects can significantly alter the spectral content of ground motions as well as increase the duration of strong shaking.

c) Global or Non 1-D Site Effects

For the purpose of discussion, some very general definitions of non-homogeneous geologic conditions are useful. Figure 3 shows a sketch which outlines idealized two-dimensional structures depicting topographic as well as alluvial valley features. Site 1 illustrates mountain or ridge topographic features recognizing that the effects pertain to sides and bases of elevated structures as well as to the crests. Site 2 represents mountain base or valley rock outcrop

conditions. Sites 3, 4, and 5 represent alluvial valley sites. Site 3 may represent a valley edge site while sites 4 and 5 are intermediate and valley center sites.

1) Topographic Effects: Topographic effects are due to a focusing of energy near ridge crests and the interaction of the primary (incident) wavefield with outgoing scattered surface waves (Bard, 1983). The resulting total wavefield shows broad-band amplifications at ridge crests and is most pronounced for wavelengths which correspond roughly to the width of the structure (21 in Figure 3). Along the slopes and at the bases of elevated geologic structures, the interaction of the primary field with the scattered fields results in complicated patterns of amplification and deamplification. This varying pattern is associated with rapidly varying phase and may be expected to give rise to differential motions which could be of concern to extended structures.

An example of computed ridge effects is shown in Figure 4. The ridge structure shown has a shape ratio (h/l) of 0.4 and the amplifications, relative to a homogeneous half-space, for sites 1-6 moving from crest to base are shown above the feature. In the amplification factors shown, the dimensionless frequency is the ridge width (21) to wavelength ratio. Figure 4 clearly shows broad amplifications occurring at the ridge crest (site 1) with a value near 1.5 for wavelengths comparable to the ridge width. As the site locations move down the slope to the base, the interference patterns appear in the amplification factors and show oscillating patterns ranging from amplification to deamplification.

The computed value of the amplification at the crest is generally less than about 1.5 while the deamplification at the base for the same dimensionless frequency (around 1) is not less than about 0.75. The resulting crest-to-base amplification would then be about 2 and would not exceed 3. While these results are only appropriate for a shape ratio of 0.4 and effects computed for other ratios show somewhat larger amplifications and deamplifications, they do serve to illustrate the general underprediction of observed crest-to-base ratios. Observed amplifications range from about 2 to 20 in the spectral domain (Fourier and response) (Bard, 1983) and can be as high as 30 (Davis and West, 1973).

In the time domain these amplifications generally are observed to range up to about 5 (Griffiths and Bollinger, 1979). Predicted values of ridge-to-base amplifications are generally much less than these and range from 3 to 4 in the spectral domain to less than 2 in the time domain (Geli et al., 1988). The differences, between predicted and observed crest-to-base topographical

effects are up to about 10, which is a factor of 3 higher than the predicted total effect. Causes of this significant underestimate are related to the influence of three dimensional effects as well as ridge-ridge interactions (Geli et al., 1988).

The lateral dimensions of geologic structures which may impact strong motion depends upon frequency through wavelength. If the bandwidth of interest to engineered structures is taken as 0.2 to 25 Hz and assuming the shear-wave velocities near the earth's surface range approximately from 1 to 3 km/sec for soft and hard rocks respectively (Silva and Darragh, 1994), the corresponding range in wavelength is 40m to 5 km and 120m to 15 km, respectively. Topographical irregularities of dimensions near this range may then exert considerable influence upon corresponding ground motions depending upon the shape ratios (Geli et al., 1988).

Examples of computed topographic effects are presented in Appendix A for a mesa structure and in Appendix B for an intrusive (magma) body. The intrusive body is regarded as subsurface topography in this case.

2) Alluvial Valley Effects: Consideration of ground motions in alluvial valleys is fundamentally an assessment of departures in response from the classical vertically propagating plane shear-wave one-dimensional model (Seed and Idriss, 1969; Schnabel et al., 1972). The main effect of the curvature of the sediment-basement interface is the generation of surface waves and trapped body waves which propagate in the alluvium and superpose with the vertically-propagating shear waves. This results in an amplification of motion as well as increased duration over one-dimensional soil effects alone.

Observations suggest that the simple one-dimensional model works well at and near the valley center in predicting the effect of the valley response to outcrop motions (King and Tucker, 1984; EPRI, 1993) (sites 4 and 5 in Figure 3). This observation is also predicted in modeling (Bard and Gariel, 1986) which, as one may expect, is predicted to be more appropriate for shallow and wide valleys than for deep and narrow valleys. Edge effects, associated with rapid changes in soil thickness may give rise to the local generation of short period surface waves which, because of material damping, do not significantly alter the spectral content of motions some distance from the edges (Tucker and King, 1984). Additionally, long period body waves incident at shallow angles to a shallow basin structure may become trapped and propagate across the basin as surface waves until reaching the thinning margin when they scape as body waves (Vidale and Helmburger, 1988). In the basin, these locally generated surface waves can give rise to large amplifications and increased durations not predicted by vertically propagating shear waves.

Figure 5 shows predicted Fourier spectral amplifications (relative to homogeneous half-space) for a shallow and wide valley with damping values of 2.5% for the alluvium. The valley has a shape ratio of 0.1 and spectral amplifications are shown for sites ranging from valley edge (1) to valley center (8). Frequency is normalized by the 1-dimensional resonant frequency for the valley center (β/4h). The dark solid line represents 2-dimensional response including a velocity gradient in the sediments, the light solid site represents a constant velocity alluvium, and the dashed line represents a 1-dimensional response for the gradient profile. Figure 5 shows, in going from the edge to the valley center, the diminishing effects of surface waves due to material damping and the predominance of vertically propagating shear waves. The fluctuations shown in the amplifications as a function of frequency for the 2-dimensional computations are a result of interference between the incident primary wave and scattered surface wavefields. Interestingly, the 1- dimensional results overpredict at the edge, underpredict just off the edge (sites 2 and 3), and then do a very acceptable job out to the valley center generally showing differences less than a factor of 2 from the 2-dimensional results. From an engineering perspective, 1-dimensional results may be adequate for all sites depicted. Near the valley edge (sites 1-3), depending upon the frequency range of interest, the broad-band amplification due to the interference of scattered surface waves and vertically propagating shear-waves can be accommodated by extending some percentage of the 1-dimensional fundamental resonance to higher frequencies. Away from the edge, a 1-dimensional response analysis using a reasonable variation in parameters would likely encompass the differences between 1- and 2-dimensional amplifications shown at the remaining sites. The edge effects, however, may result in significant differential motions perpendicular to the valley edge.

An example of basin effects for a wide valley which shows the trapping of body wave and the generation of long period surface waves is clearly illustrated in the particle velocity records integrated from strong motion recordings of the 1971 San Fernando earthquake.

The earthquake occurred beneath the northern edge of the San Fernando Valley, shown in the left panel of Figure 6, and was recorded along a profile of stations (Figure 6, left panel) extending south of the epicenter across the San Fernando Valley, then across the Santa Monica Mountains, and across the Los Angeles basin. The velocity model used to compute synthetic seismograms is shown in the right panel of Figure 6. Transverse velocity synthetic seismograms computed for a point source at a depth of 10 km show the development of Love waves in the San Fernando Valley, their disappearance at the Santa Monica (where they are converted to SH body waves), and their reappearance at the northern edge of the Los Angeles basin due to the interaction of SH waves with the thickening basin margin.

The same features are seen in the profile of velocity seismograms derived from the recorded accelerograms shown in the center panel of Figure 7. The recorded tangential component velocity seismograms are interspersed with synthetic seismograms in Figure 7, center panel. The development of Love waves in the San Fernando Valley, their disappearance in the Santa Monica Mountains, and their reappearance in the Los Angeles basin are apparent in both the recorded and synthetic seismograms. The observed variation of peak particle velocity with distance along the profile is compared with that of the synthetic profile in Figure 7, right panel. The synthetic amplitudes of the 1-D uniform layered and structure, which cannot trap the waves, are much smaller than the motions recorded at the Los Angeles basin sites. Additional 1-D simulations which use the appropriate 1-D structure for each site (Figure 6, right panel) are shown as open circles. Interestingly, the 1-D results using a local structure does as well as the 2-D simulations except near the edge of the Los Angles basin (site S262) just south of the Santa Monica Mountains (Figure 6). These results are similar to those predicted by Bard and Gariel (1986) for wide valleys with low shape ratios (Figure 5).

For deep and narrow valleys with large shape ratios ($\geq$ 0.25), a change in response occurs which involves a new set of mode shapes affecting the valley as a whole (Bard and Bouchon, 1985; Bard and Gariel, 1986). This class of mode shapes involves in-phase, large amplitude motions of the whole valley. Predicted results for these high aspect ratio valleys are shown in Figure 8 which is analogous to Figure 5 except the shape ratio has been increased from 0.1 to 0.4. The differences in response, from those of the shallow valleys (Figure 5), are seen as much more complicated resonance phenomena and generally higher amplifications away from the valley edge (site 1). The whole valley in-phase resonance is seen beginning at site 2 as a gradual increase in the peak near the dimensionless frequency 1 as the sites progress toward the valley center. For valleys of this class, deep and narrow, the 1-dimensional theory gives a conservative prediction near the edges (sites 1 and 2 in Figure 6) but seriously underpredicts the valley effects at high frequencies (by a factor of 2-4) at sites 3 and 4 and into the valley center. Perhaps the most important aspect of the resonance phenomenon shown for deep valleys is the oscillating nature of the amplifications showing several maxima where the 1-dimensional theory shows only the fundamental and perhaps the first overtone. Additionally, the 2-Dimensional resonances associated with deep and narrow valleys are expected to give rise to significant degrees of differential motions (Bard and Gariel, 1986). From a viewpoint of design ground motions, 2-dimensional computations for a variation in parameters would likely result in a near continuum of resonances and thus a very broad-band amplification of motion. Near the valley center at sites 7 and 8, the 2-dimensional fundamental resonance has an amplitude nearly twice that corresponding to vertically propagating shear-waves and at a slightly higher frequency.

To summarize the effects of non-homogeneous geological structures on strong ground motions, Table 2 shows an influence matrix listing the nature of the effects and the degree to which they may be predicted.

Observed spectral amplifications of alluvial valley sites (Fourier spectra) with respect to outcrop motion generally ranges up to about 10 (King and Tucker, 1984) and are in reasonable accord with predictions. Spectral amplifications as high as 30 have been measured for the lake bed in Mexico City (Lermo et al., 1988). Seed et al.(1988) modeled the amplification effects of the shallow ($\approx$ 60m) clay layer due to the September 19, 1985 M 8.1 earthquake remarkably well using the simple 1-dimensional theory. However, the increased durations compared to outcrop motions at some of the sites is unaccounted for in the simple theory and may be related to lateral changes in thickness in the shallow clay layer and thus local generation of surface waves (Bard et al., 1988) (depicted at site 5 in Figure 3).

3) Variability of Observed 2-Dimensional Site Effects: As a result of the careful observations of both topographical and alluvial valley effects in the Garm region of the USSR, the standard error of variation in amplification has been quantified (Tucker and King, 1984). After careful instrument calibration which quantified the variability of system response, repeated measurements of ridge and valley effects has shown that the observed variability in amplifications is approximately 1.5 (Tucker and King, 1984; Tucker et al., 1984; King and Tucker, 1984) and that ridge and valley effects depend weakly upon source azimuth and incidence angle. Observed topographic and alluvial valley effects, ranging from about 2 to 10 are then resolvable on a repeatable basis and are generally significantly greater than the measurement uncertainty.

To summarize, topographic effects due to rapid and significant changes in elevation over the dimensions of approximately one wavelength generally range from about 2 to 10 and are most pronounced at the ridge or hill crest and for wavelengths comparable to the width of the structure. The sides of topographic highs undergo patterns of amplification and deamplification with associated rapid changes in phase. Alluvial valley effects which result in departures from the vertical propagating shear-wave model, are largest for sites located in high aspect ratio valleys (large thickness to half-width ratios, $\geq$ 0.25) and away from valley edges where the simple 1-dimensional theory may underpredict the effects by factor of 2 to 3 (Bard et al., 1988). For shallow and wide valleys (shape ratio $\leq$ 0.25), such as the lakebed sites in Mexico City and the San Fernando and Los Angeles basins, have demonstrated that short period ($<$ 5 sec) response is dominated by vertically propagating shear-waves, particularly away from the edges.

Although the 1-dimensional theory captures many of the essential features of amplification due to alluvial valleys, it fails to explain the increased durations observed at some sites. The increased durations of significant motion shown by some of the lakebed sites in Mexico City require the effects of local generation of laterally propagating energy, perhaps due to thickness variations in the shallow clay layer (buried valley or depression within a valley).

In addition, the long period response of large basin structures may be dominated by trapped body waves which propagate across the basin as surface waves with large amplifications and increased durations.

Careful observations of topographic as well as alluvial valley effects have quantified the variability of observed amplification to a factor of about 1.5. Additionally, the observations have shown a weak dependence of amplification to source azimuth and incidence angle (Tucker and King, 1984).

d) 1-D Site Effects

As depicted in Figures 1 and 2, 1-D site effects generally are the dominant influence at most sites with the nonhomogeneous factors being a large contribution to the variability in observed motions. Because 1-D effects dominate as figures 1 and 2 suggest, the prediction of strong ground motions, either empirically or analytically, can be considerably improved by incorporating differences in site conditions at both soil and rock sites.

1) Site Classification: A significant issue associated with the reduction in uncertainty in ground motion estimation is a consistent definition of 1-D site conditions. That is, a definition of site characteristics which unambiguously distinguishes resolvable and stable differences in response is clearly needed and must be implemented in both empirical and analytical approaches. For example, it makes little sense to use an empirical attenuation relation to define rock control motions for a site specific response analysis at a 100 ft deep soil site if the definition of rock used in developing the empirical relation included stiff soils (say S1 in Table 3). This also applies to analytical approaches in that modeling results to be used as rock control motions must use a crustal model with shallow properties consistent with either the soil bedrock conditions or the conditions beneath the soil column to be modeled. Whatever the approach to specifying strong ground motions, a consistent definition of site conditions is required.

The definition of rock conditions for classification of accelerograph sites has been rather elusive

and variable. In general, a site is classified as rock if, based mainly on visual examination, materials a geologist would describe as rock either by type or formation is thought to be within about 15-30 ft of the surface (e.g. Table 3, Geomatrix Consultants). More recently a classification based on the average velocity over the top 30m has been proposed (Boore et al., 1994) and the misleading terms rock and soil have been replaced with site classifications A-D (Table 3). For building code purposes, a more general classification has been in existence for some time (Table 3). In this scheme, the distinctions among site characteristics is very coarse and recommendations exist for replacing it with the Boore et al. (1994) site classes along with revised amplification factors. This is certainly a step in the right direction provided the Boore et al. (1994) classification scheme does unambiguously distinguish resolvable and stable differences in site response. However, major issues with using velocities averaged over 30m do exist: 1) is this depth sufficient to capture long period information; a wave with a period of 1 sec has a wavelength of 360m for an average velocity of 360m/sec and ¼ wavelength (the distance over which a change in velocity is sensed by a wave) is 90m and 2) how many sites (recording and structures) have velocity data available? Interestingly, the more information the classification scheme requires, the fewer recording sites are available resulting in more poorly constrained attenuation relations.

In lieu of drilling all strong motion sites to some depth (which should be done), a classification scheme is needed which captures the essential differences in response between classes of site conditions that can be implemented with a site visit by a geologist or with velocity data. Additional necessary requirements for a site classification scheme include universal adoption by code provisions and those developing attenuation relations, recognition and accommodate of conventional site specific response analyses using empirical control motions appropriate for materials either underlying soil deposits, and that site classes can be represented by a specified low-strain shear-wave velocity and damping profile and its uncertainty. Until these conditions are met, further reductions in uncertainty in specification of strong ground motions is not likely.

2) Soil Verses Rock: The conventional view of rock site conditions is materials with shear-wave velocities exceeding about 760 m/sec (2500 ft/sec) which is generally taken to mean that it remains reasonably linear for moderate to high levels of loading (30-50% g). Additionally site effects are thought not to be large at rock sites being much more dominant at soil sites. With the increase in recordings and velocity information at both rock and soil sites, it is becoming clear that the distinction between rock (certainly soft or typical California rock) and soil is not clear and that the motions at rock sites is more highly variable than at soil sites. Additionally, the definition of rock of materials with shear-waves velocities exceeding $\approx$ 760

m/sec is driven largely by response analyses and acturally represents a small percentage of rock sites in tectonically active regions.

To demonstrate the general similarities and differences in sites classified as deep soil (alluvium) and rock (Geomatrix Consultants scheme) Figures 9 and 10 show shear-wave velocity profiles from a number of rock and soil sites respectively. Interestingly, the rock sites appear to show higher variability and a much steeper velocity gradient than the soil sites and some rock sites have very low near surface velocities. Nearly half the rock sites do not reach the 760 m/sec criterion until 7-15m. To look at average properties, Figures 11 and 12 show median and $\pm$ 1-sigma values for the rock and soil profiles. From these Figures, it is apparent that typical rock sites are characterized by low ($\approx$ 300 m/sec) near surface velocities, a steep velocity gradient, and perhaps a larger variation than soil sites.

In general then, average rock sites would be expected to exhibit nonlinear response to depths of 15-20m under moderate to high loading conditions if the materials behaved dynamically similar to unconsolidated soils such as sands, gravels, and low PI clays. Additionally, these sites are typified by a steeper velocity gradient and higher variability than soil sites. These observations suggest that typical rock sites in tectonically active regions such as California should be treated in a manner analogous to soil and that the only clear distinguishing feature between rock and soil is perhaps the velocity gradients. However, this conclusion is based on relatively few rock site velocity data which may be biased toward softer sites near fault zones and does not address any fundamental and stable differences in low-strain damping at rock sites. Clearly more data are needed to resolve the issue but at least there is a strong suggestions that 1-D site effects apply to both rock and soil sites and that they should not be treated separately.

3) Mechanism of 1-D Site Effects: The physical mechanism responsible for site amplification is an increase in wave amplitude as propagation velocity generally decreases toward the surface. If material damping is neglected, the decrease in shear-wave velocity toward the surface results in an increase in motion. This arises because flow of energy per unit time and per unit area (energy flux) $\rho\ V_S\ \dot{u}^2$ (ρ = density, V_S = propagation velocity, $\dot{u}$ = particle velocity) is conserved. Therefore if V_S decreases, $\dot{u}$ must increase in an elastic system. In any profile, however, some material damping is always present and the net amplification (or deamplification) involves an interplay between counteracting effects. This may result in some cases in an amplification of peak particle velocity (and perhaps displacement) and a deamplification of peak acceleration due to the different frequency content of the two measures of ground motion.

The other phenomena which is observed, and is predicted by simple shear-beam theory, is the presence of resonances. These are due simply to the constructive interference of upgoing and downgoing waves in the soil column. Since there are generally stiffness contrasts within a profile, particularly when firm rock is encountered, a fraction of the seismic energy which enters the column can become trapped as upgoing and downgoing wave-fields reflected successively from the free surface and the contrasts. Resonances occur at the surface due to constructive interference at frequencies given by multiples of one-quarter wavelength of the shear- or compressional- waves in the soil column. The spectral amplitudes of the resonances are determined by the stiffness and density contrast at interfaces as well as details of the variation of shear modula and soil density with depth.

The resonance phenomena and the general increase in amplitude with decreasing velocity of propagation are greatly affected by material damping. This causes the multiply-reflected energy to gradually damp out and can be observed as a successive decrease in spectral amplitudes at the higher modes (Silva et al., 1987).

These phenomena, the increase in amplitude due an overall decrease in velocity toward the surface and resonance effects operate on a large scale from the source region at depths of about 5-15 km to the surface. In the last seminar (Seminar 6) the large scale effects or amplifications were presented as the net result of amplification and linear damping through the kappa operator. In this case, the rock had a shear-wave velocity at the surface of about 1 km/sec. Superimposed on these effects is the equivalent-linear or nonlinear site response for materials that are softer than about 1 km/sec whether the site is classified as rock or soil.

4) Approaches To Modeling Nonlinear 1-D Site Effects: In general 1-D site effects are modeled using vertically propagating shear waves and nonlinear (may be approximated through equivalent-linear) material response. The fundamental issues which require validation in this approach are the following: 1) adequacy of the vertically propagating shear-wave model, 2) appropriateness of laboratory derived strain dependencies of dynamic material properties coupled with in-situ velocities to in-situ high strain conditions, and 3) the suitability of nonlinear and equivalent-linear solution schemes. Appendix C presents a summary paper of a recent EPRI (1993) project which was, in part, specifically designed to address these issues in a rigorous and consistent manner.

REFERENCES

Bard, P.Y. and J. Gariel (1986). "The seismic response of two-dimensional sedimentary deposits with lage vertical velocity gradiencts." *Bull. Seism. Soc. Am.*, 76, 343-366.

Bard, P.Y. and Bouchon, M. (1985). "The two-dimensionsl resonance of Sediment-filled Valleys." *Bull. Seism. Soc. Am.*, 75, 519-541.

Bard, P.Y. (1983). *Les Effets de Site d'Origine Structurale en Sismologie, Modelisation et Interpretation, Application au Risque Sismique.* These d'Etat, Universite Scientifique et Medicale de Grenoble, France. (in French)

Boatwright, J., and Astrue, M. (1983). "Analysis of the aftershocks of the New Brunswick earthquake." *Workshop on Site-Specific Effects of Soil and Rock on Ground Motion and the Implications for Earthquake-Resistant Design.* USGS Open-File Rept. 83-245.

Boore, D.M., W.B. Joyner, and T.E. Fumal (1994). "Estimation of response spectra and peak accelerations from western North American earthquakes: and interim report. Part 2. *U.S. Geological Survey Open-File Rept.* 94-127.

Boore, D.M., and Atkinson, G.M. (1987). "Stochastic prediction of ground motion and spectral response parameters at hard-rock sites in eastern North America." *Bull. Seism. Soc. Am.*, 77(2), 440-467.

Campbell, K.W. (1988). "Predicting strong ground motion in Utah." *Evaluation of Regional and Urban Earthquake Hazards and Risk in Utah,* edited by W.W. Hays and P.L. Gori, USGS Prof. Paper.

Campbell, K.W. (1985). "Strong motion attenuation relations: a ten-year perspective." *Earthquake Spectra* 1, 759-804.

Campbell, K.W. (1981). "Near-source attenuation of peak horizontal acceleration." *Bull. Seism. Soc. Am.*, 71(6), 2039-2070.

Cranswick, E., Wetmiller, R., and Boatwright, J. (1985). "High-frequency observations and source parameters of microearthquakes recorded at hard-rock sites." *Bull. Seism. Soc. Am.*, 75(6), 1535-1567.

Davis, L.L., and West, L.R. (1973). "Observed effects of topography on ground motion." *Bull. Seism. Soc. Am.*, (63), 283-298.

Electric Power Research Institute (1993). *Guidelines for determining design basis ground motions.* Palo Alto, Calif: Electric Power Research Institute, vol. 1-5, EPRI TR-102293.

vol. 1: Methodology and guidelines for estimating earthquake ground motion in eastern North America.
vol. 2: Appendices for ground motion estimation.
vol. 3: Appendices for field investigations.
vol. 4: Appendices for laboratory investigations.
vol. 5: Quantification of seismic source effects.

Geli, L., Bard, P.Y., and Jullien, B. (1988). "The effect of topography on earthquake ground motion: a review and new results." *Bull. Seism. Soc. Am.*, 78(1), 42-63.

Griffith D.W. and Bollinger, G.A. (1979). "The effect of Appalachian Mountain topography on seismic waves." *Bull. Seism. Soc. Am.*, (69), 1081-1105.

Hayashi, S., Tsuchida, H., and Kurata, E. (1971). "Average response spectra for various subsoil conditions." *Third Joint Meeting, US-Japan Panel on Wind and Seismic Effects,* UJNR, Tokyo.

Idriss, I.M. (1985). "Evaluating seismic risk in engineering practice." *Proc. Eleventh Internat. Conf. on Soil Mech. and Foundation Eng.*, San Francisco, edited by A.A. Balkema, Rotterdam, 1, 255-320.

Joyner, H.B. and D.M. Boore (1982) "Prediction of earthquake response spectra." *USGS,* Open-File Rept. 82-977.

King, J.L., and Tucker, B.E. (1984). "Observed variations of earthquake motion across a sediment-filled valley." *Bull. Seism. Soc. Am.*, 74, 137-151.

Lermo, J., Rodriguez, M., and Singh, S.K. (1988). "Natural period of sites in the valley of Mexico from microtremor measurements and strong motion data, the Mexico earthquake of September 19, 1985." *Earthquake Spectra,* 4(4).

Mohraz, B. (1976). "A study of earthquake response spectra for different geological conditions." *Bull. Seism. Soc. Am.*, 66(3) 915-935.

Seed, H.B., Romo, M.P., Sun, J.I., Jaime, A. and Lysmer, J. (1988). "The Mexico Earthquake of September 19, 1985--Relationship between soil conditions and earthquake ground motions." *Earthquake Spectra,* 4(4), 687-729.

Seed, H.B., C. Ugas and J. Lysmer. (1976). "Site-dependent spectra for earthquake resistant design." *Bull. Seism. Soc. Am.*, 66, 221-243.

Seed, H.B., and Idriss, I.M. (1969). "The influence of soil conditions on ground motions during earthquake." *J. Soil Mech. Found. Engin. Div.*, Am. Soc. Civil Engin., ASCE, 94, 93-137.

Schnabel, P.B., Lysmer, J., and Seed, H.B. (1972). *SHAKE: a Computer Program for Earthquake Response Analysis of Horizontally Layered Sites.* Earthq. Engin. Res. Center, Univ. of Calif. at Berkeley, EERC 72-12.

Silva, W.J. and R. Darragh (1994). "Engineering characterization of earthquake strong ground motion recorded at rock sites." Palo Alto, Calif:Electric Power Research Institute, RP 2556-48.

Silva, W. J., Turcotte, T., Moriwaki, Y. (1988). "Soil Response to Earthquake Ground Motion," Electric Power Research Institute, Walnut Creek, California, Report No. NP-5747.

Silva, W.J., and Green, R.K. (1989). "Magnitude and distance scaling of response spectral shapes for rock sites with applications to North American tectonic environment." *Earthquake Spectra,* 5(3), 591-624.

Toro, G.R., and McGuire, R.K. (1987). "A investigation into earthquake ground motion characteristics in eastern North America." *Bull. Seism. Soc. Am.*, 77(2),468-489.

Vidale, J.E., and Helmberger, D.V. (1988). "Elastic finite-difference modeling of the 1971 San Fernando, California earthquake." *Bull. Seism. Soc. Am.*, 78(1), 122-141.

Table 1
EARTHQUAKES AND STATIONS USED FOR WNA AND ENA COMPARISONS

Earthquake	Date	Magnitude (M_L)	M	Source Depth(km)	Epicentral Distance(km)	Station	USGS No.	Reprocessed Average Horizontal Peak Acceleration (g)
San Fernando	710209	6.4	6.6	8.4	23.0	Lake Hughes 12	128	0.316
					26.3	Lake Hughes 9	127	0.147
					27.3	Lake Hughes 4	126	0.184
					33.8	Griffith Park	141	0.185
					36.1	Seis. Lab.	266	0.151
					43.2	Santa Anita	104	0.194
Nahanni	851223	6.4(m_b)	6.8*	18.0	8.0	Site #1		1.176
					9.0	Site #2		0.450
					20.0	Site #3		0.202
Coalinga Aftershocks								
A	83050322	3.8		7.64	8.54	LLN		0.0053
D	83050700	3.9		8.92	8.39	LLN		0.0189
K	83051013	3.9		4.79	12.46	LLN		0.0036
K3	83051405	3.9		11.18	5.56	VEW		0.0269
M	83051414	3.9		9.15	4.94	LLN		0.0084
New Brunswick	820331	4.01*		5***	4	Mitchell Road		0.20

* After Choy and Boatwright (1988).
** After Boore and Atkinson (1987).
*** After Toro and McGuire (1987).

Table 2
2-D GEOLOGIC STRUCTURAL EFFECTS INFLUENCE MATRIX

Structure	Conditions	Type	Size	Quantitative Predictability*
Surface Topography	Sensitive to shape ratio, largest for ratio between 0.2 - 0.6. Most pronounced when wavelength ≈ mountain width.	Amplification at top of structure. Amplification and deamplification at base, rapid changes in amplitude phase along slopes.	Ranges up to a factor of 30 but generally from about 2-10.	Poor: generally underpredict size. May be due to ridge-ridge interaction and 3-D effects.
Sediment-Filled Valleys				
1) Shallow and wide (shape ratio ≤ 0.25	Effects most pronounced near edges. Largely vertically propagating shear-waves away from edges.	Broad band amplification near edges due to generation of surface waves.	1-D models may underpredict at higher frequencies by about 2 near edges.	Good: away from edges 1-D works well, near edges extend 1-D amplifications to higher frequencies.
2) Deep and narrow (shape ratio ≥ 0.25)	Effects throughout valley width.	Broad band amplification across valley due to whole valley modes.	1-D models may underpredict for a wide bandwidth by about 2-4 away from edges. Resonant frequencies shifted from 1-D.	Fair: given detailed description of vertical and lateral changes in material properties.
3) General	Local changes in shallow sediment thickness.	Increased duration.	Duration of significant motions can be doubled.	Fair
4) General	Generation of long period surface waves from body waves at shallow incidence angles.	Increased amplification and duration due to trapped surface waves.	Duration and amplification of significant motions may be increased over 1-D predictions.	Good at periods exceeding 1 sec.

*Good (generally within a factor of 2)
Fair (generally within a factor of 2-4)
Poor (qualitative only, can easily be off by an order of magnitude)

Table 3

SITE CLASSIFICATION SCHEMES

Boore et al., 1994	
Class	Average Shear-Wave Velocity Over 30m (m/sec)
A	> 750
B	360 - 750
C	180 - 360
D	<180

Geomatrix Consultants, 1994	
Class	Description
A	Rock. Instrument is founded on rock material (V_s > 600 m/s (1969 ft/sec)) or a very thin veneer (less than 5m (16 ft) of soil overlying rock material.
B	Shallow (stiff) soil. Instrument is founded in/on a soil profile up to 20m (66 ft) thick overlying rock material, typically in a narrow canyon, near a valley edge, or on a hillside.
C	Deep narrow soil. Instrument is founded in/on a soil profile at least 20m (66 ft) thick overlying rock material in a narrow canyon or valley no more than several kilometers wide.
D	Deep broad soil. Instrument is founded in/on a soil profile at least 20m (66 ft) thick overlying rock material in a broad canyon or valley.
E	Soft deep soil. Instrument is founded in/on a deep soil profile that exhibits low average shear-wave velocity (V_s < 150 m/s (492 ft/sec)).

Table 3 (cont.)

SITE CLASSIFICATION SCHEMES

NEHRP, 1991 (similar to UBC, 1991)	
Soil Profile Type	Description
S_1	A soil profile with either: (1) rock of any characteristic, either shale-like or crystalline in nature, that has a shear wave velocity greater than 2,500 feet per second or (2) stiff soil conditions where the soil depth is less than 200 feet and the soil types overlying the rock are stable deposits of sands, gravels, or stiff clays.
S_2	A soil profile with deep cohesionless or stiff clay conditions where the soil depth exceeds 200 feet and the soil types overlying rock are stable deposits of sands, gravels, or stiff clays.
S_3	A soil profile containing 20 to 40 feet in thickness of soft- to medium-stiff clays with or without intervening layers of cohesionless soils.
S_4	A soil profile characterized by a shear wave velocity of less than 500 feet per second containing more than 40 feet of soft clays or silts.

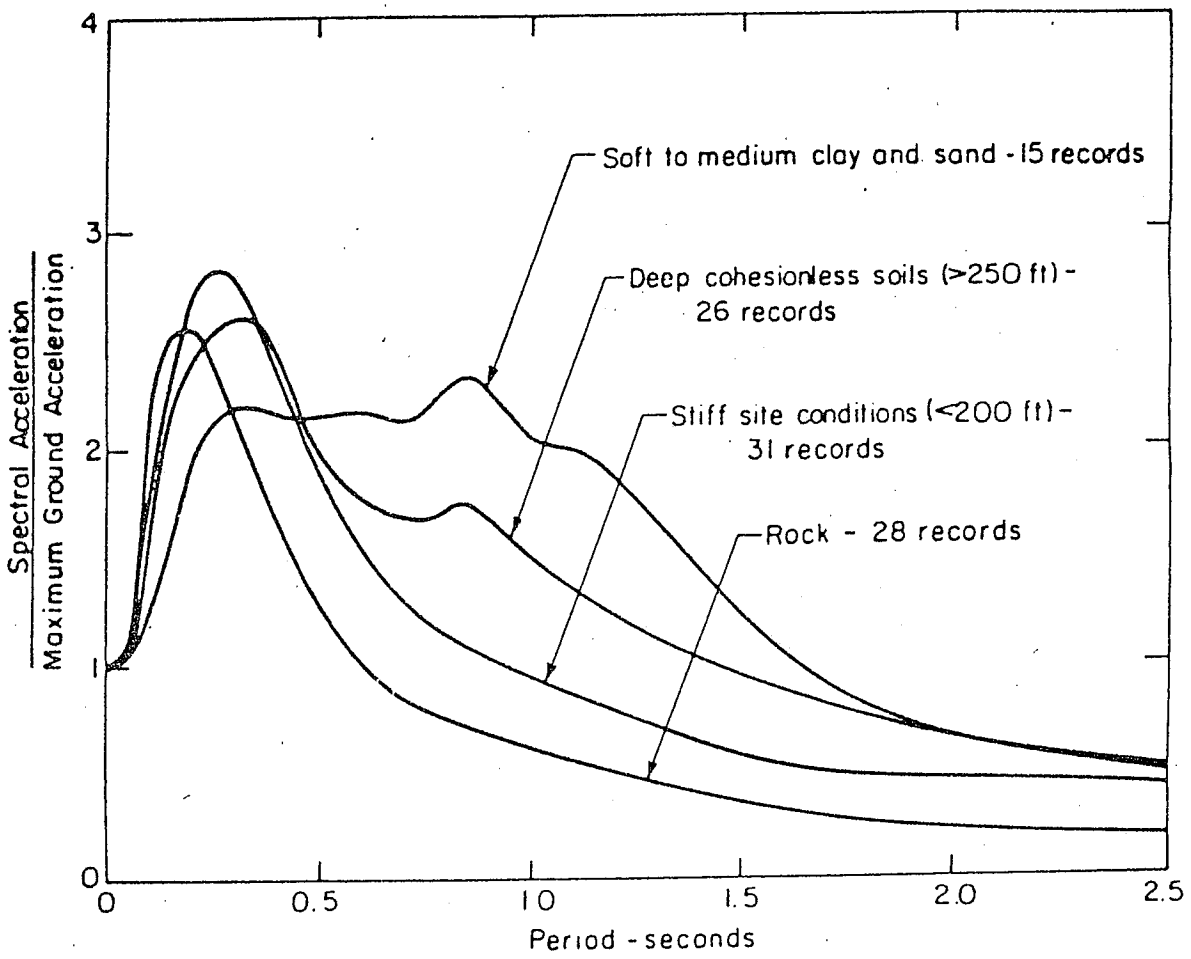

Figure 1. Average 5% damping response spectral shapes (Sa/a) computed from motions recorded on different soil conditions (after Seed, et al., 1976).

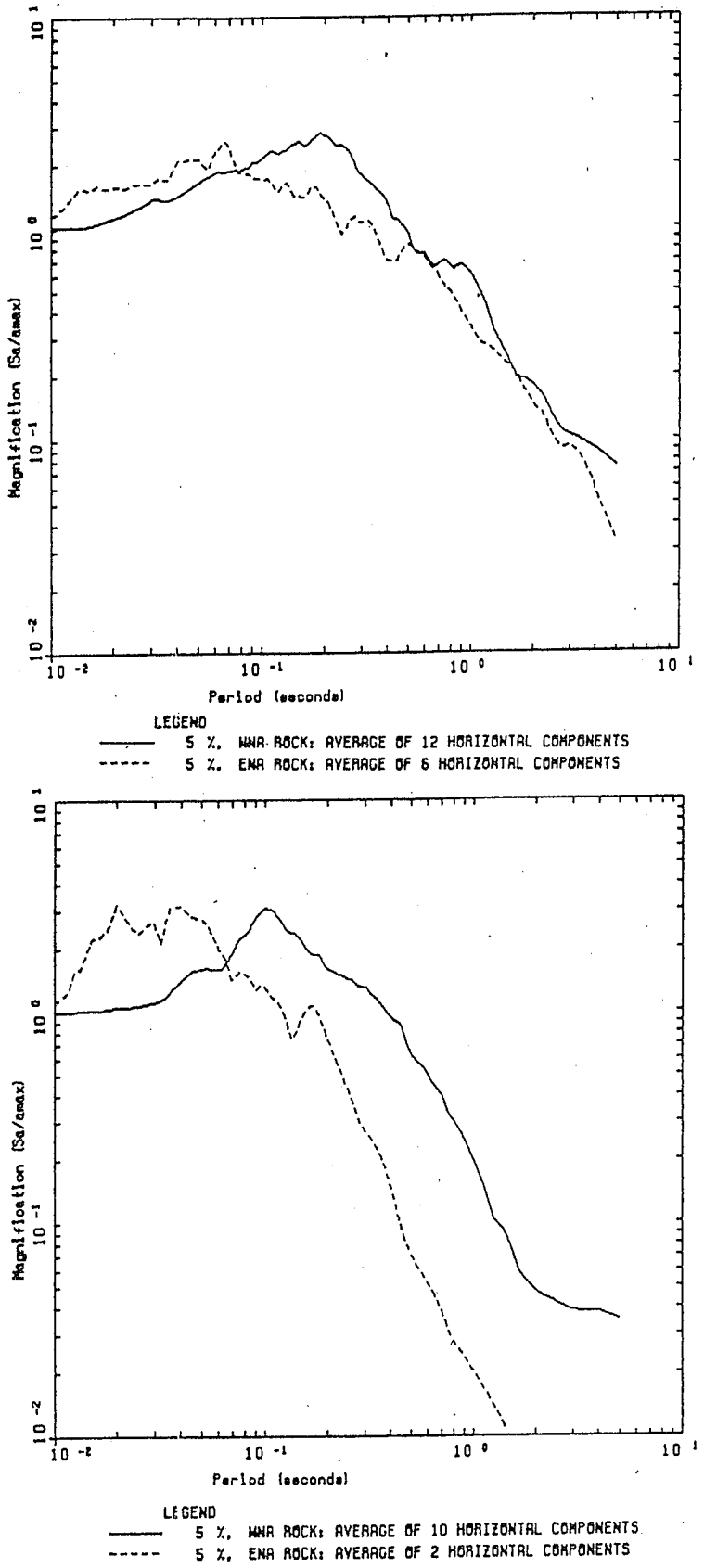

Figure 2. Average 5% damping response spectral shapes (Sa/a) computed from motions recorded on rock sites at close distances to M = 6.4 earthquakes (top figure) and M = 4.0 earthquakes (bottom figure). In each figure the solid line corresponds to motions recorded in WNA, dashed line to motions recorded in ENA. (See Table 1 for a list of earthquakes, sites, distances, and average peak accelerations).

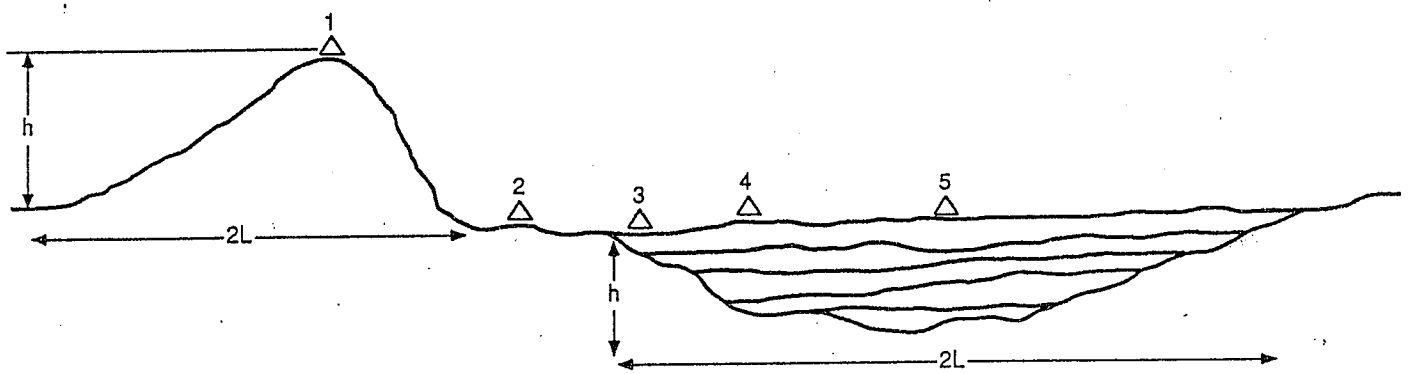

Figure 3. Sketch of idealized two-dimensional features which result in topographical and alluvial valley effects to strong ground motion. Site 1 depicts elevated topography with a shape ratio given by h/l. Site 2 represents mountain base or valley rock outcrop conditions. Sites 3, 4, and 5 are alluvial valley sites representing valley edge, intermediate, and center locations respectively.

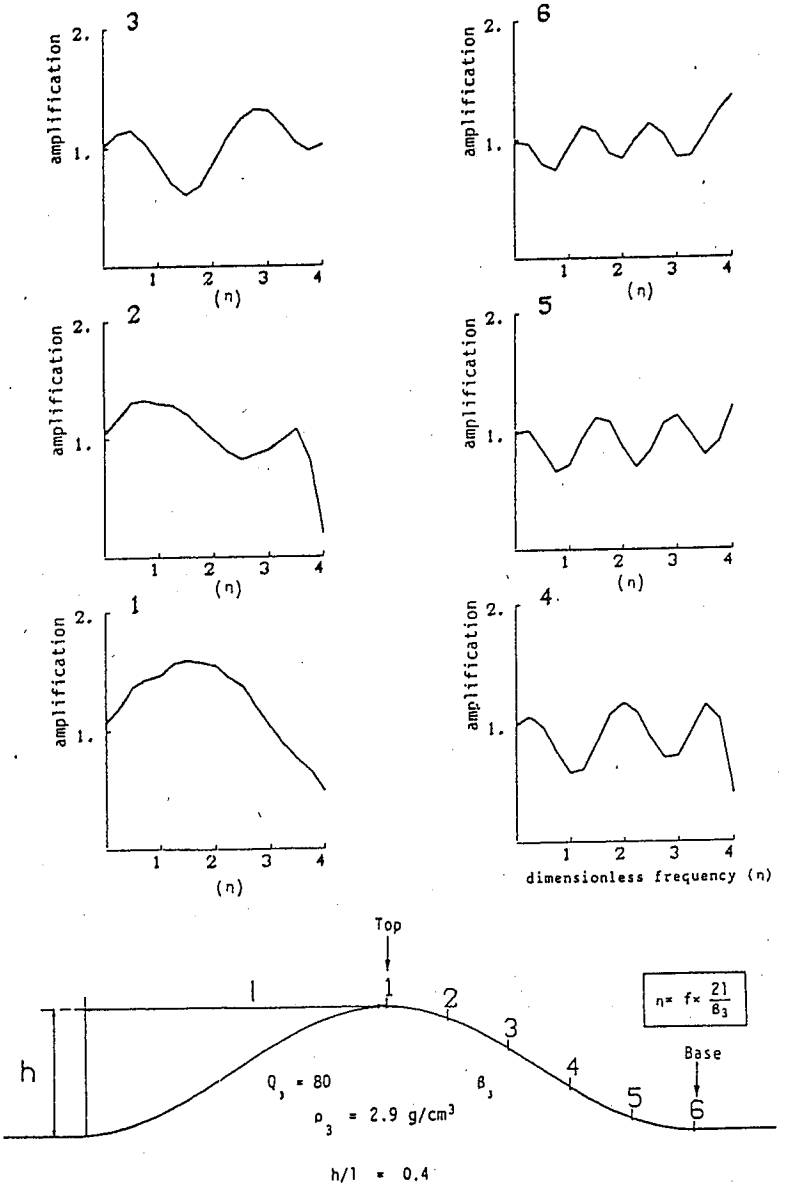

Figure 4. SH Fourier transfer functions to homogeneous halfspace outcrop motions computed at six sites for an isolated, homogeneous ridge. The shape ratio is 0.4 and the dimensionless frequency is the ratio of the structure width (2l) to wavelength (after Geli et al., 1988).

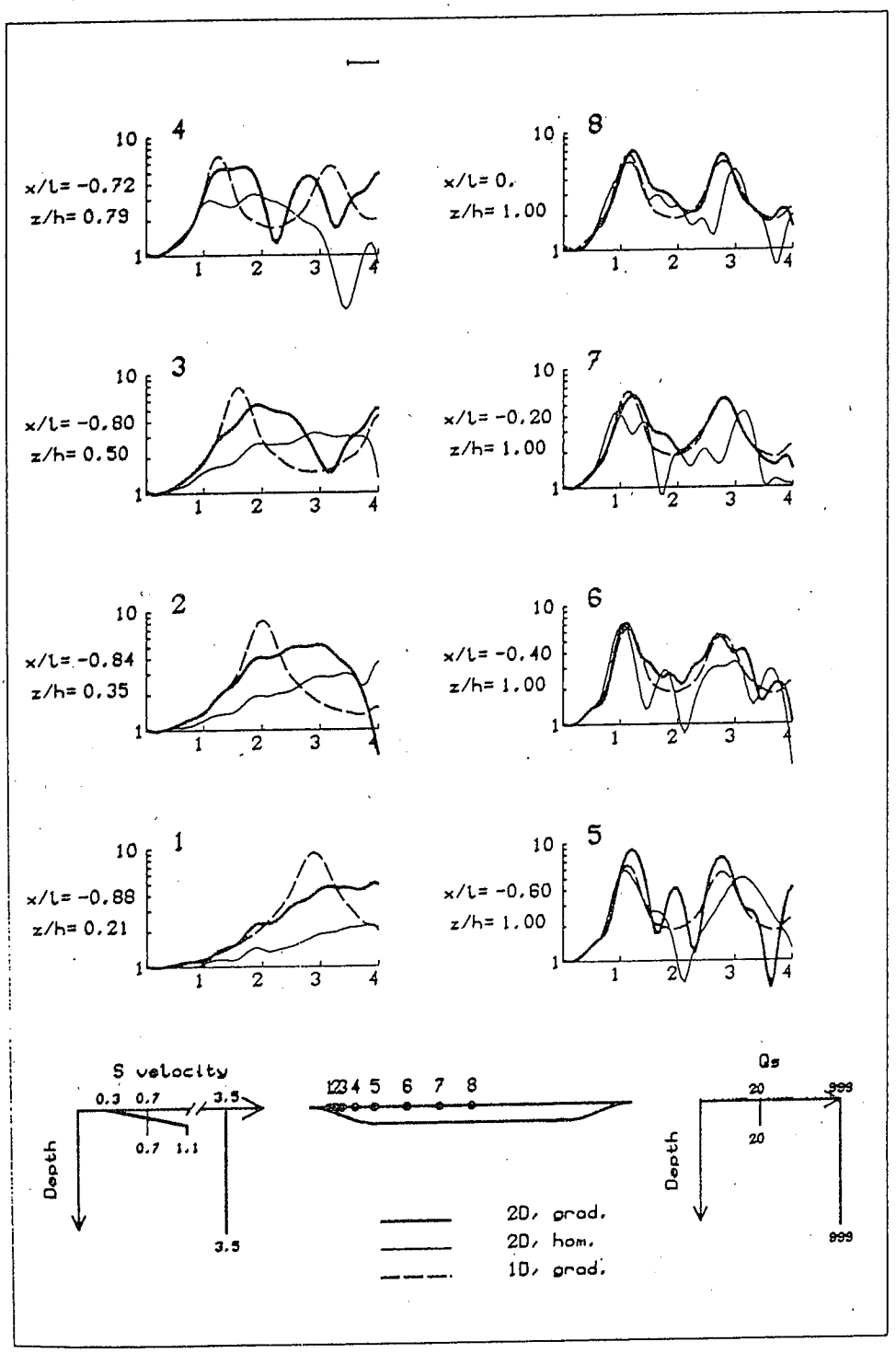

Figure 5. Smoothed SH transfer functions to homogeneous halfspace outcrop motions computed at 8 sites for a wide and shallow alluvial valley with a shape ratio of 0.1. Two-dimensional calculations for a gradient shear-wave velocity profile (heavy solid line) and for a constant velocity alluvium (thin solid line) are shown. Dotted line represents 1-dimensional results. Frequency has been normalized by the frequency of the fundamental resonance for the homogeneous layer at site 8 (after Bard and Gariel, 1986).

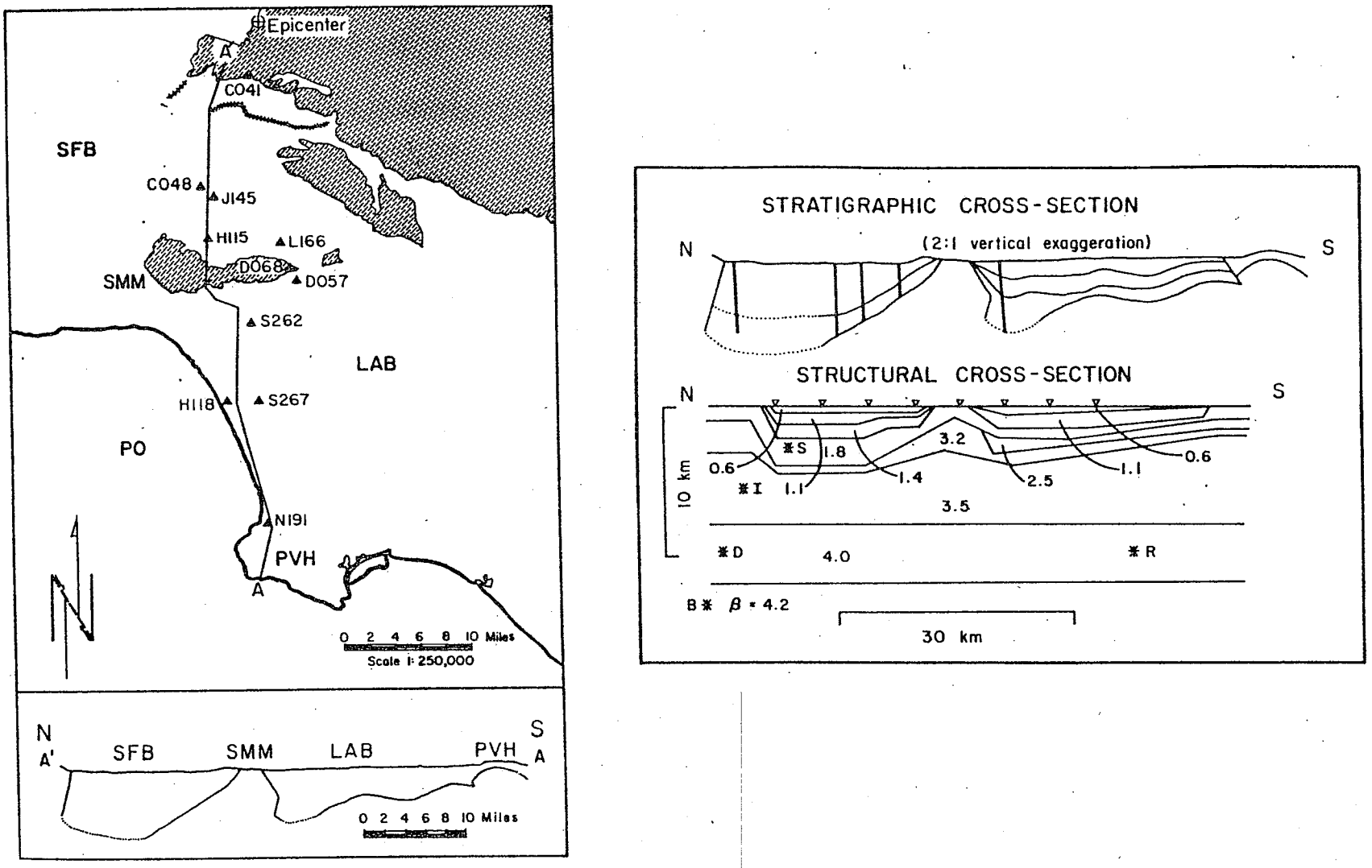

Figure 6. Map and cross-section of the San Fernando region showing the epicenter of the 1971 earthquake and profile of recording stations across the San Fernando Basin, Santa Monica Mountains, and Los Angeles Basin (left panel). Stratigraphic cross-section of the same region showing shear-wave velocities and site locations for the simulated motions (right panel). (After Vidale and Helmberger, 1988).

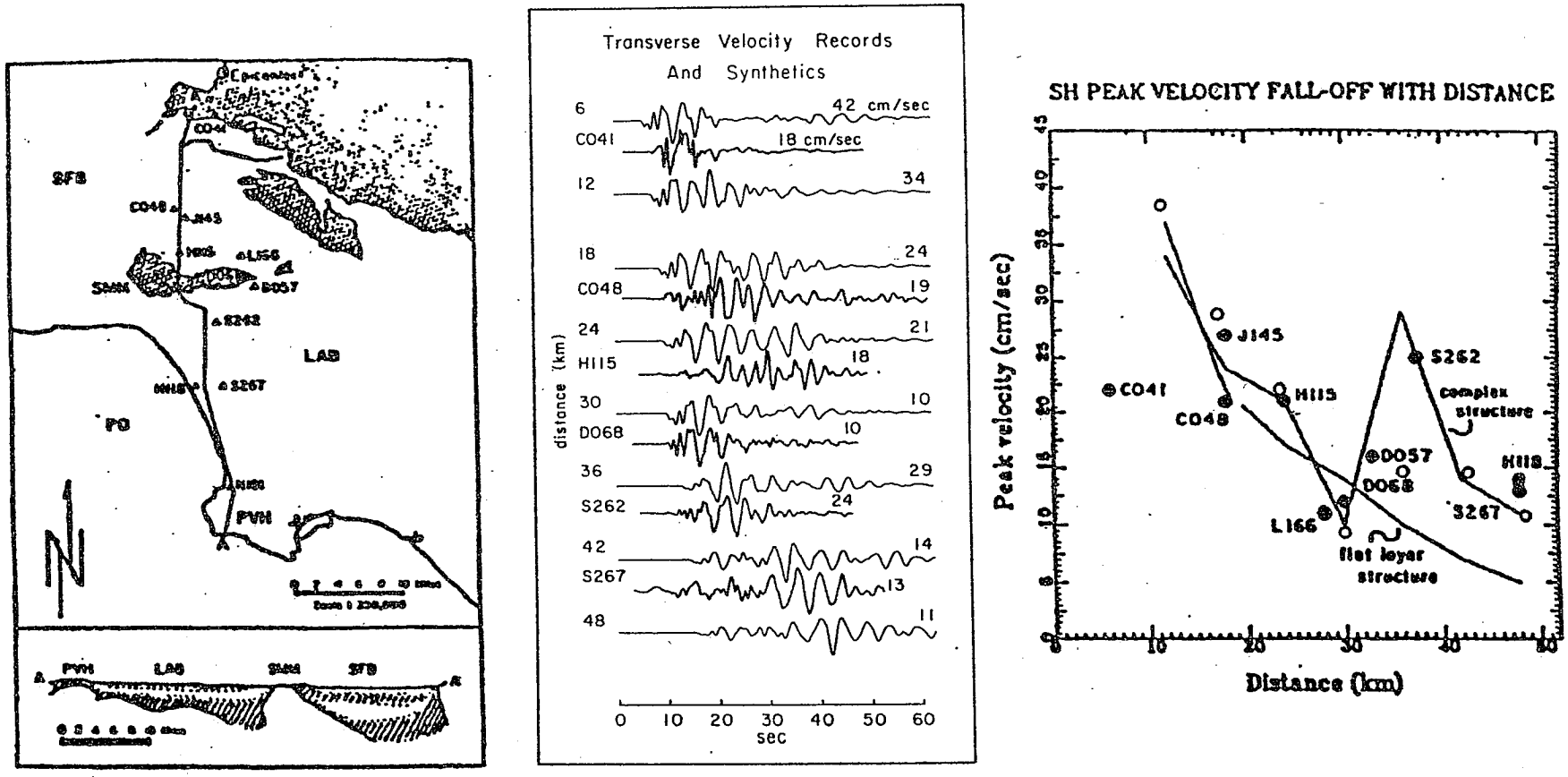

Figure 7. Comparisons in waveform (center panel) and variation of peak particle velocity with distance (right panel) or recorded and synthetic seismograms along the profile shown in the left panel. In the center panel, recorded seismograms are shown labeled with the site names. In the right panel, recorded values are shown as dots, and synthetic values for complex and uniform flat layered structures are shown as lines. Open circles show simulations using appropriate 1-dimensional column at each site location (after Vidale and Helmberger, 1988).

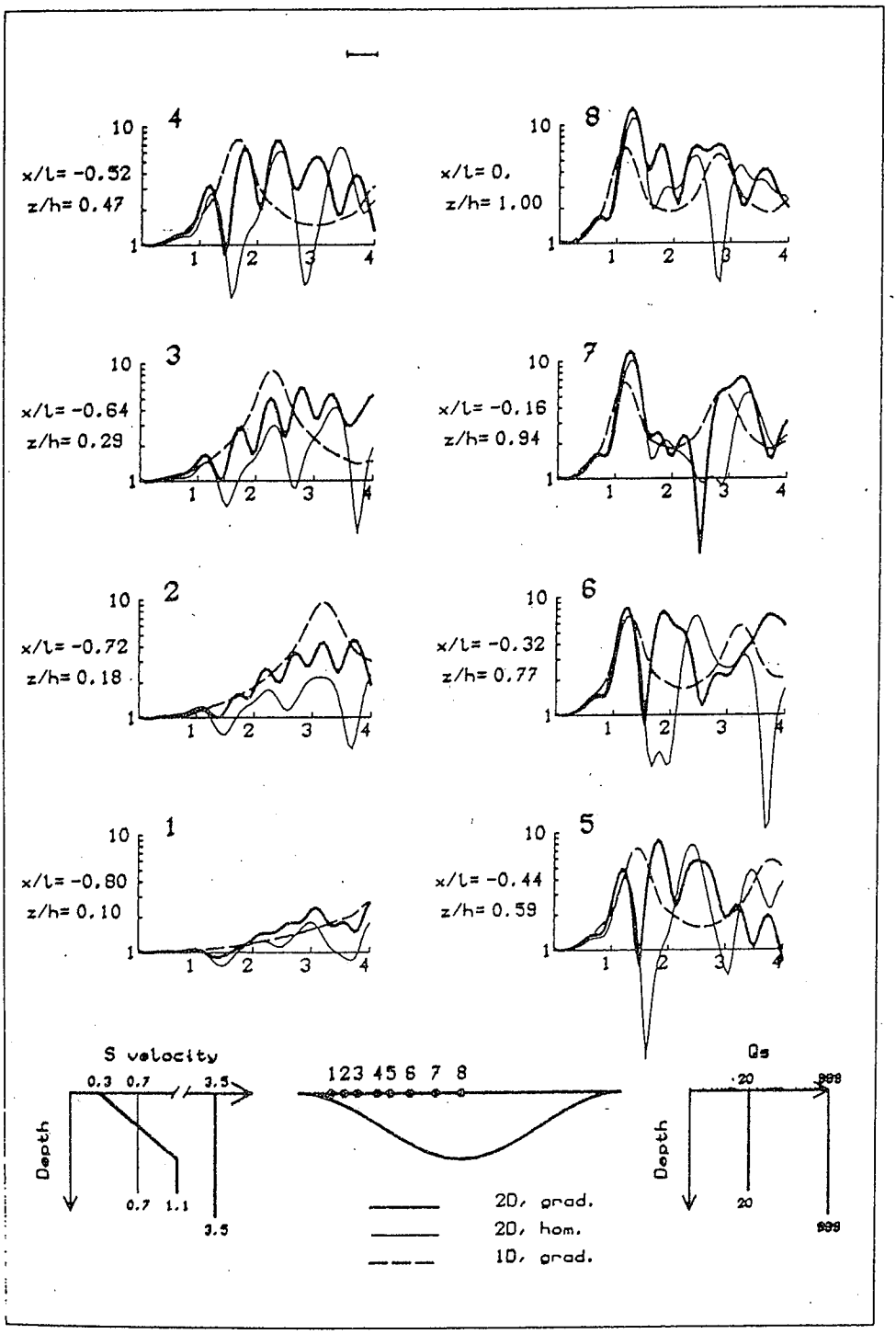

Figure 8. Smoothed SH transfer functions to homogeneous halfspace outcrop motions computed at 8 sites for a wide and shallow alluvial valley with a shape ratio of 0.4. Two-dimensional calculations for a gradient shear-wave velocity profile (heavy solid line) and for a constant velocity alluvium (thin solid line) are shown. Dotted line represents 1-dimensional results. Frequency has been normalized by the frequency of the fundamental resonance for the homogeneous layer at site 8 (after Bard and Gariel, 1986).

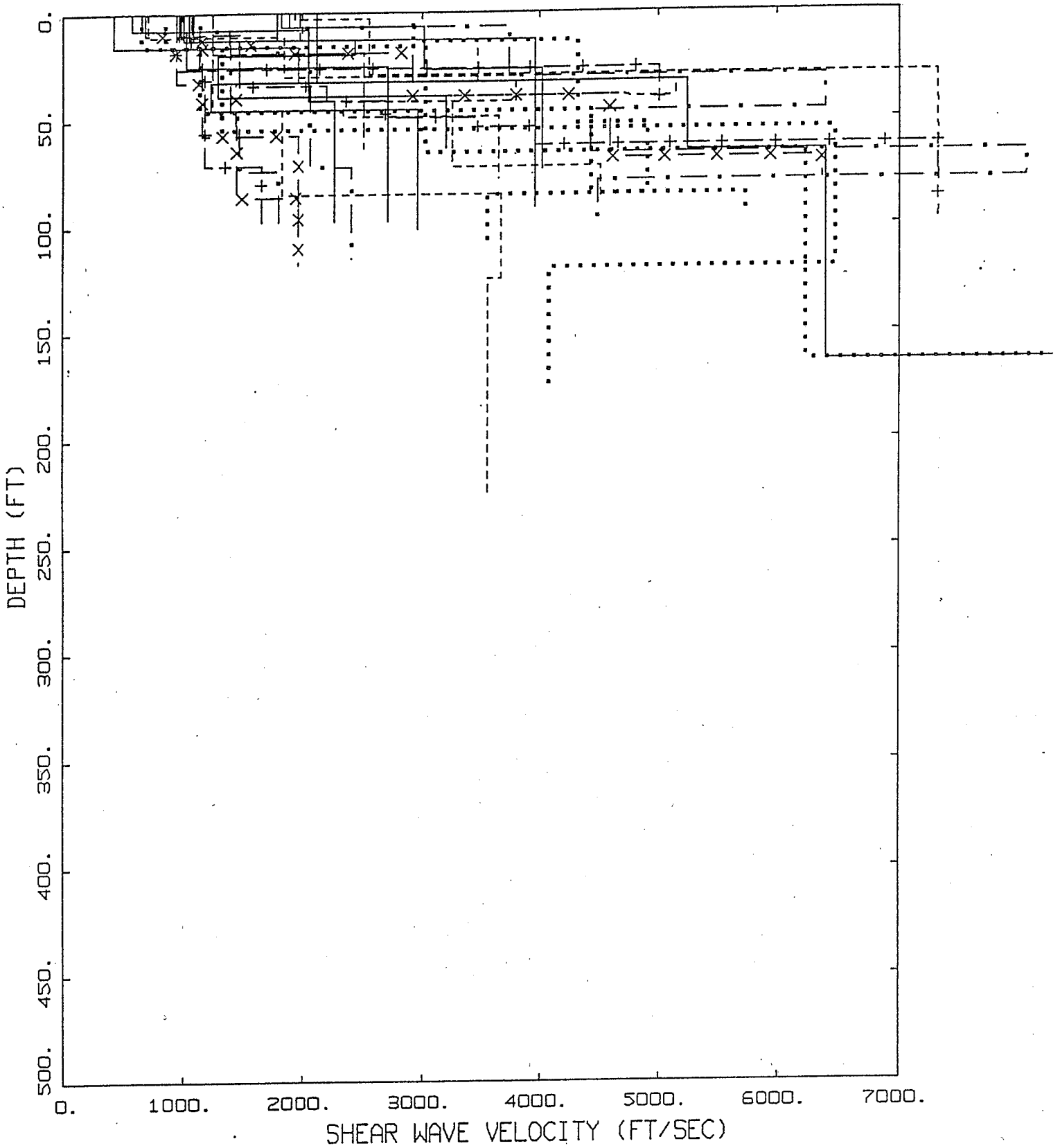

Figure 9. Shear-wave velocity profiles for accelerograph sites classified as rock.

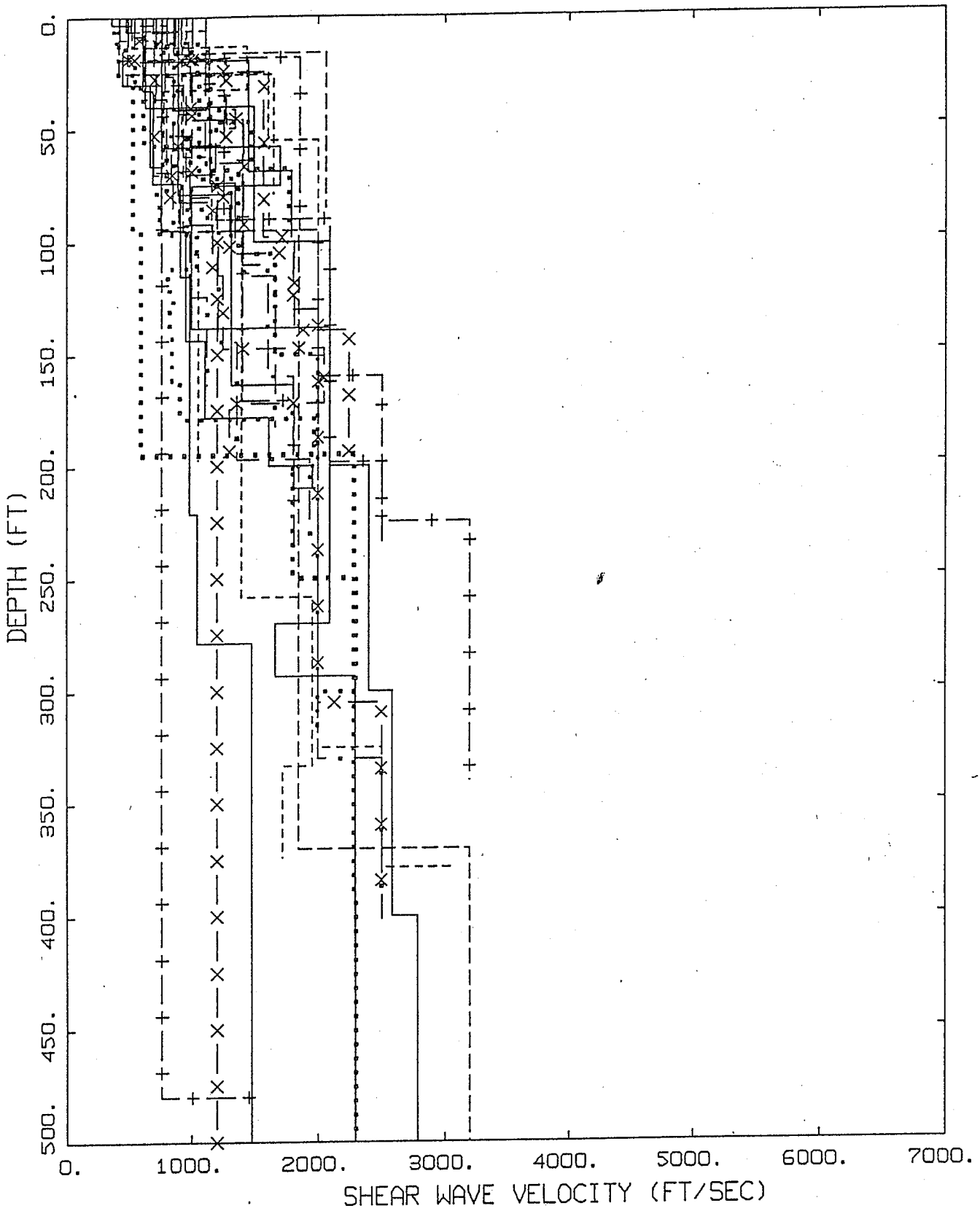

Figure 10. Shear-wave velocity profiles for accelerograph sites classified as soil.

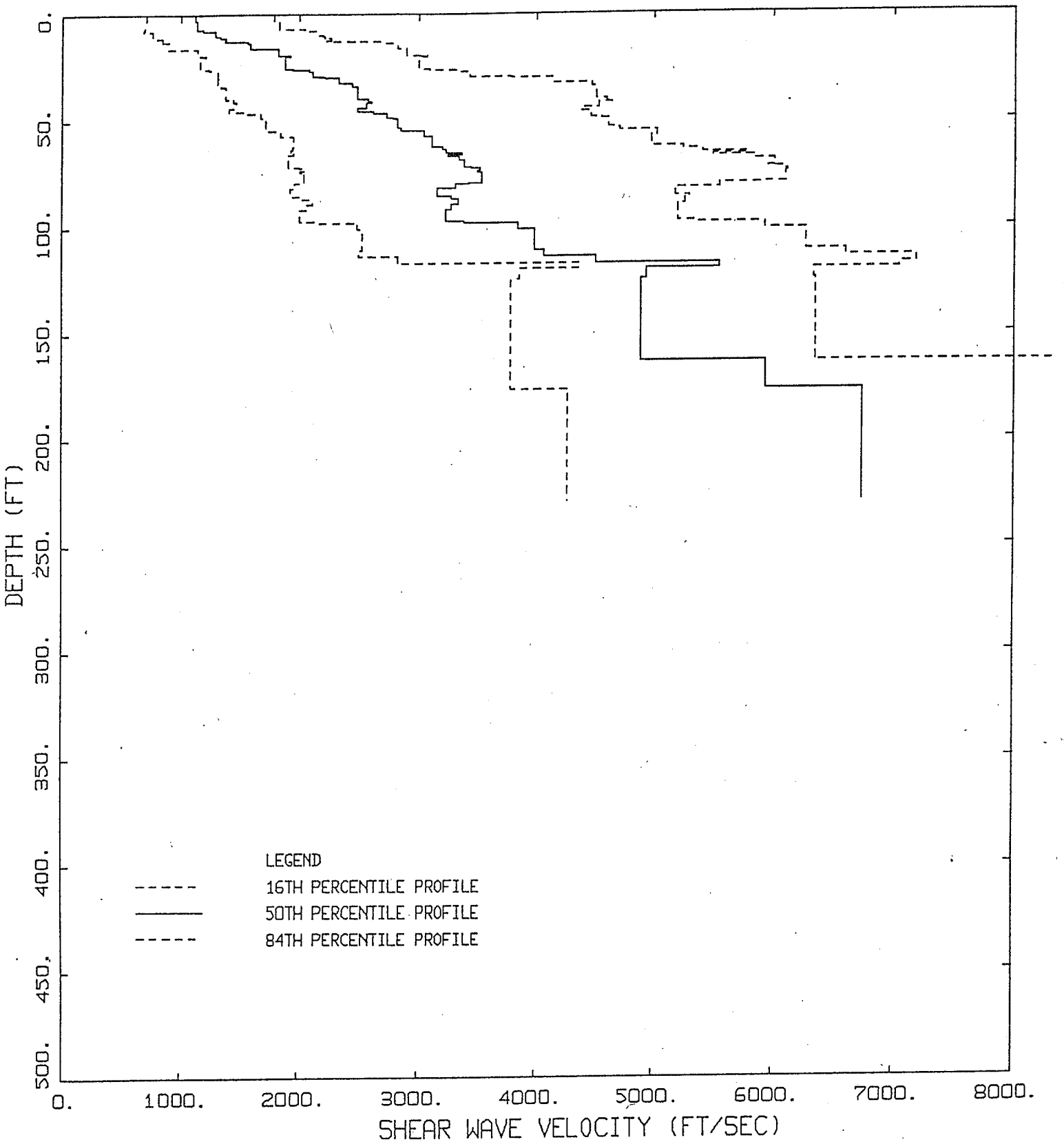

Figure 11. Median and $\pm$ 1σ shear-wave velocity profiles for accelerograph sites classified as rock.

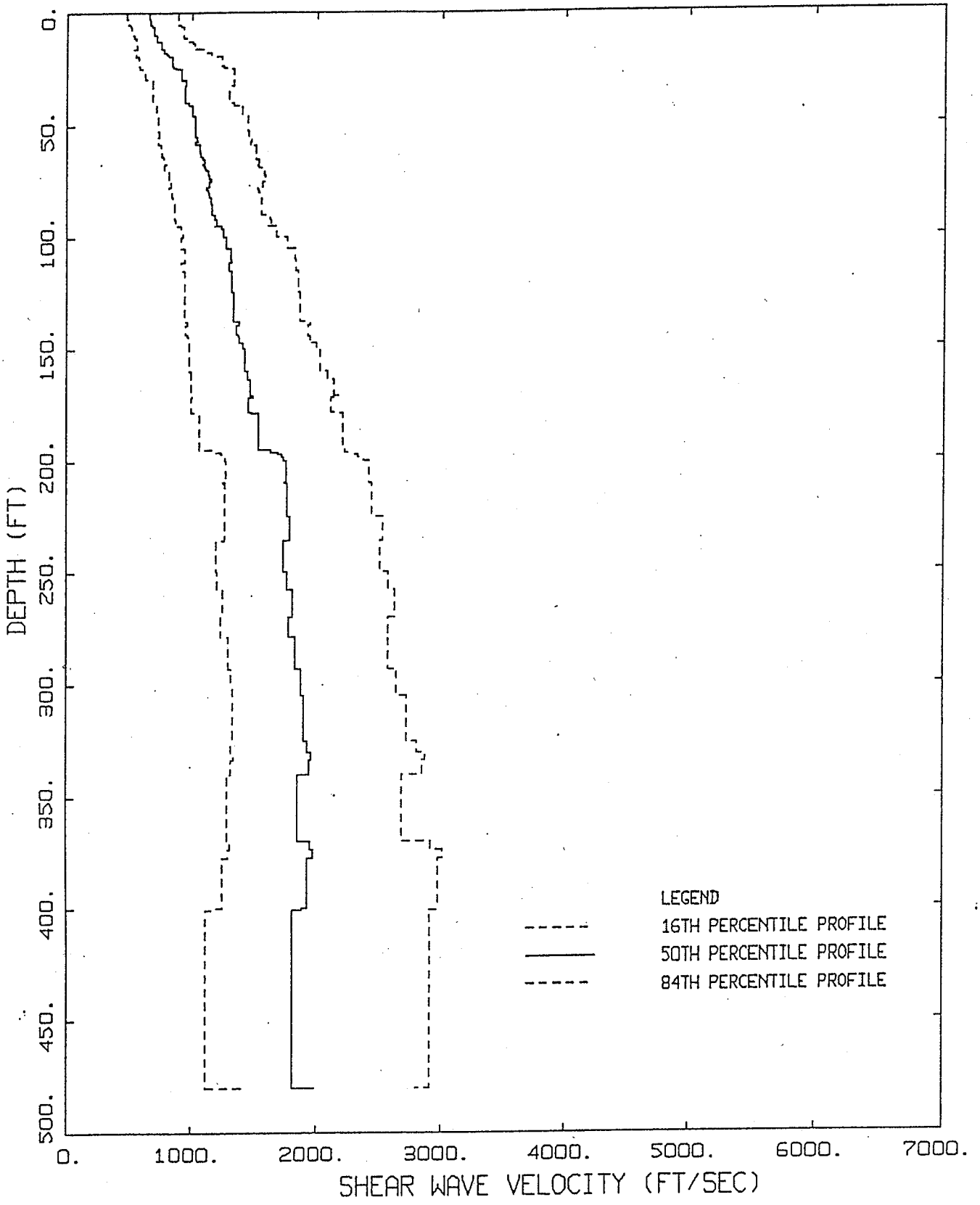

Figure 12. Median and $\pm$ 1σ shear-wave velocity profiles for accelerograph sites classified as soil.

APPENDIX A

EFFECTS OF MESA TOPOGRAPHY ON GROUND MOTIONS AT THE LOS ALAMOS NATIONAL LABORATORY*

The following example illustrates computed topographic effects due to mesas on strong ground motions. The Los Alamos National Laboratory is located in the mesa/valley region of Los Alamos and limited 2-dimensional analyses were performed to determine whether or not the mesa structures were likely to amplify strong ground motions. For the analyses, a "generic" mesa was developed (Figure 1) which has a base dimensions of about 400m and a height of 70m. The average shear-wave velocity to depths of about 200m is about 650 m/sec. Because topographic effects are most pronounced for wavelengths roughly corresponding to the base dimensions of the topographic structure, analyses were done for frequencies in the 1-5 Hz band.

Description of the Numerical Code

The computational algorithm used to model the effects of the 2-dimensional structure is an elastic explicit time-domain-finite-difference formulation (Vidale and Helmberger, 1988). The algorithm was developed by Dr. John Vidale who is currently at USGS (Menlo Park). The computer code, AMOD is fourth order in accuracy of spatial derivatives resulting in minimal grid dispersion. Absorbing boundary conditions are imposed on the sides and bottom of the finite difference grid. In the SH mode implemented here the top of the grid has free surface boundary conditions (reflection coefficient is equal to 1). In the analyses, the source is input as plane SH waves incident at specified angles from either the left or right side of the grid.

The effects of material damping have been implemented in the code in an approximate manner to attenuate high frequency scattered wavefields. Because of the approximate nature of the damping algorithm, the effective damping is frequency dependent and only modest levels are permissible (1.25% at 3 Hz in this case). In general, for very high levels of ground motions

*Source: Woodward-Clyde Federal Services

material damping is expected to increase substantially, especially in the shallow portions of the profiles ($\approx$ 100 ft), as a result, the amplifications predicted by the modeling should not be viewed as average values.

Topographic Model

To model the effects of the mesa structures on strong ground motions, three dimensional effect (along mesa axes) are assumed to be less important than the generally steeper cross-sectional relief. For the purpose of modeling, a generic mesa cross-section was developed from local topographic maps and is shown in Figure 1. This generic mesa is intended to represent an average mesa near the midpoint along axis. For more extensive modeling, necessary to quantify amplification effects, a large suite of structures and average velocities should be considered to define median values and their uncertainties. For the purpose of modeling, the generic mesa cross-section was simplified to straight line segments and is shown in Figure 2. The finite difference grid is about 5 km wide and 5 km deep with a grid spacing of 6.5m. Two mesas are considered to allow for any coupling (scattering) effects between structures which may affect both mesa and valley sites. Ten site locations are evaluated, representing valley (1, 2, 7, and 10), mesa (4, 5, 8, and 9), and mesa side (3 and 6) sites. Valley sites 1 and 10 are located a mesa dimension away from the closest mesa. This location was chosen to show minimum potential mesa effects while site 7 is located between the mesa at one-half a mesa dimension. This site should show the maximum effect of the mesas on valley sites.

The average shear-wave velocity for the mesas and underlying material is 0.65 km/sec and is based on measured velocity profiles.

Results of Analyses

To assess the effects of the mesa topography, Fourier amplitude spectra are computed at each site using both the 2-dimensional crustal structure and a 1-dimensional structure for the same angles of incidence. The 1-dimensional structure consists of simply the plane halfspace. Taking the ratios of the 2-dimension simulations to the 1-dimension simulations cancels source and propagation effects thereby isolating the effects of the topographic structures.

For completeness, a suite of incidence angles and shear-wave velocities are considered. In the analyses, incident inclined plane SH waves are considered. Angles of incidence are at 0°, 10°, 20°, and 40° (corresponding to varying source distances and depths) and analyses are performed for the base case velocity as well as a 50% variation (V_S x 1.5, V_S/1.5).

To present an example of time histories, Figure 3 shows both 1-D and 2-D displacement seismograms at the 10 site locations for a vertically propagating plane SH wave. For the mesa sites the 2D results (dashed lines) show a delay relative to the 1D arrivals due to the additional propagation distance (35-70m, Figure 2). There is also a slight decrease in amplitude of the initial dominant motion and an increase thereafter. In general, the effects of the topographic features are not strong for this case and suggest a that the mesas do not have a strong or dominant influence on ground motions.

In order to better quantify these results and to include the effects of different incidence angles and shear-wave velocities, Fourier amplitude spectral ratios (2D/1D) were computed for a suite of deterministic analyses. For each incidence angle of 0°, 10°, 20°, and 40°, with the inclined waves incident from the right in Figure 2, analyses were performed for each velocity: average; average x 1.5, and average /1.5. The results were then averaged (assuming a lognormal distribution) to compute a median and 1-sigma estimates of the Fourier amplitude ratios. Because a deterministic selection of incidence angles and velocities was used, the computed standard error should not be strictly interpreted as representing the range of 16th to 84th percentiles. It likely encompasses a broader range and should be viewed more as a qualitative estimate of the range of effects for the range of incidence angles and velocities. A true parametric analyses would also vary the geometry as well as include incident inclined P-SV waves for a complete and thorough study. As previously mentioned, the intent of the current study is to determine whether or not stable features of amplification do exist and which warrant further study, possibly resulting in accommodation into design motions.

The median and $\pm$ 1-sigma estimates based on the deterministic analyses are shown for sites 1-10 in Figures 4-13 for frequencies from about 1 to 5 Hz. For all the sites, a broad resonance is shown between 4-5 Hz. This is likely due to surface waves generated by the mesa

topography. The resonance is strongest at the sites located on the mesa sides (sites 3 and 6, Figures 6 and 9) and has a peak of about 1.2, which is associated with a large variability. The large variability suggests a high degree of sensitivity to velocity and/or incidence angle and indicates that the variability of ground motions should be high at sites located on slopes. Interestingly, these sites also show a slight deamplification at lower frequencies indicating the effects of wave cancellation.

At the mesa sites (4, 5, 8, and 9; Figures 7, 8, 11, and 12) the average amplification between 4-5 Hz is approximately 10% for sites 5 and 9 and near 1 for sites 4 and 8. The difference is likely due to inclusion of waves incident from only the right in the analyses. Additional analyses for waves incident from the left would probably average the median amplifications and increase the variability. As with the side sites, the variability is large near the resonance indicating a strong sensitivity to velocity and/or incidence angle. Unlike the side sites however, the mesa sites show a slight lower frequency amplification with a maximum of about 10% near 1 Hz. These results suggest that a more complete analysis may result in stable, perhaps broad-band amplification of ground motions at mesa sites.

At the valley sites (1, 2, 7 and 10; Figures 4, 5, 10, and 13) similar patterns exist. There is an asymmetry in response between sites 1 and 10, again possibly due to the inclusion of incident waves from the right only. The net amplification for these sites, located at a distance corresponding to 1 mesa base dimension away, is, on average, about 1. For site 2, located at the base of the mesa, the motions are generally deamplifyed with a maximum slightly greater than 1 near 4 Hz. The remaining valley site (7, Figure 10) is located symmetrically between the mesas at a distance of 1/2 of a base dimension and shows a slight broad-band amplification of 5-10%.

In general, the results of the 2-D topographic modeling suggest that stable features of topographic amplification are likely to occur at the Los Alamos National Laboratory. For mesa sites, amplifications of 10-20% over the frequency range studied (1-5 Hz) are suggested. At valley sites, the amplifications depend on distance from the mesas, being near 1 or less at distant ($\geq$ 1 base dimension) and adjacent sites and 5-10% for sites between. These results are for a

material damping of 1.25%. At high levels of motion, the damping will increase significantly which should result in a reduction of amplification.

REFERENCES

Geli, L., Bard, P.Y., and Jullien, B. (1988). "The effect of topography on earthquake ground motion: a review and new results." *Bull. Seism. Soc. Am.*, 78(1), 42-63.

Vidale, J.E. and Helmberger, D.V. (1988). "Elastic finite-difference modeling of the 1971 San Fernando, California earthquake." *Bull. Seism. Soc. Am.*, 78(1), 122-141.

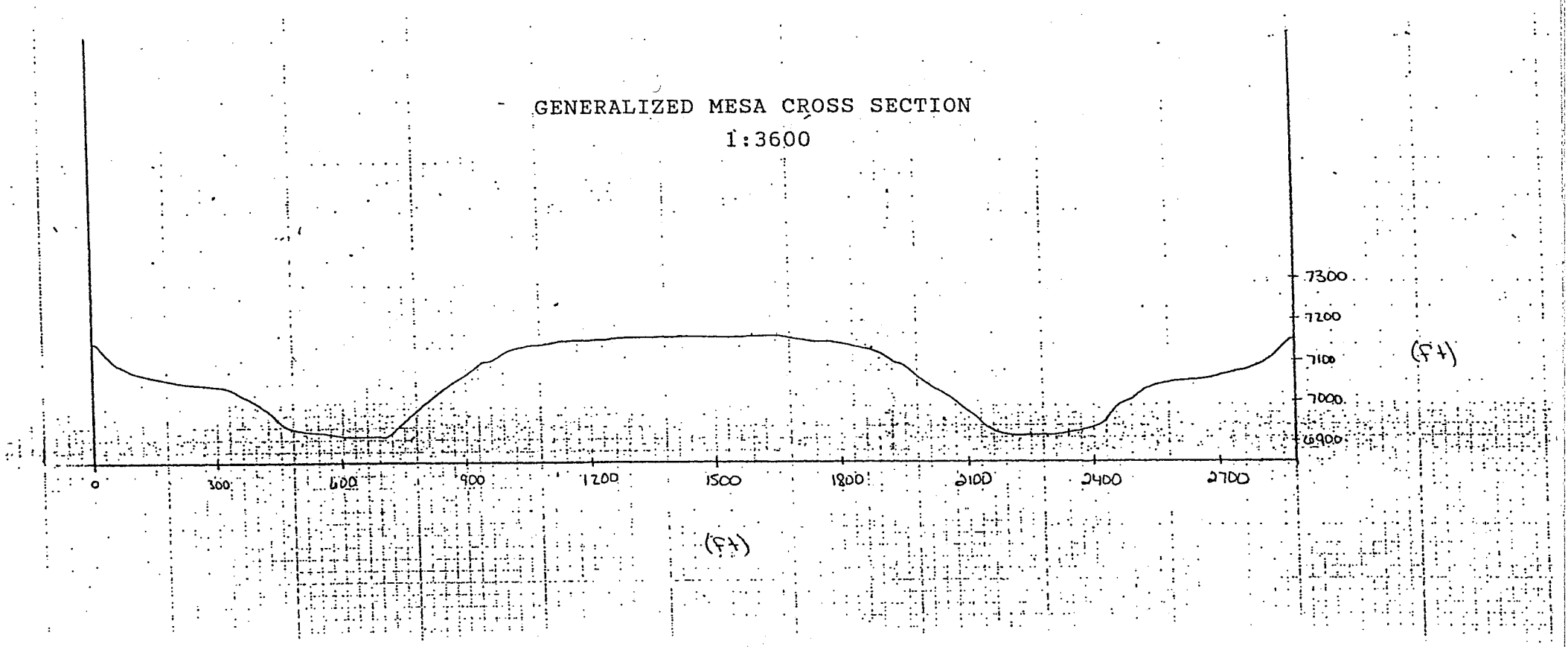
GENERALIZED MESA CROSS SECTION
1:3600
7300
7200
7100
7000
6900
(ft)
0
300
600
900
1200
1500
1800
2100
2400
2700
(ft)

Figure 1.

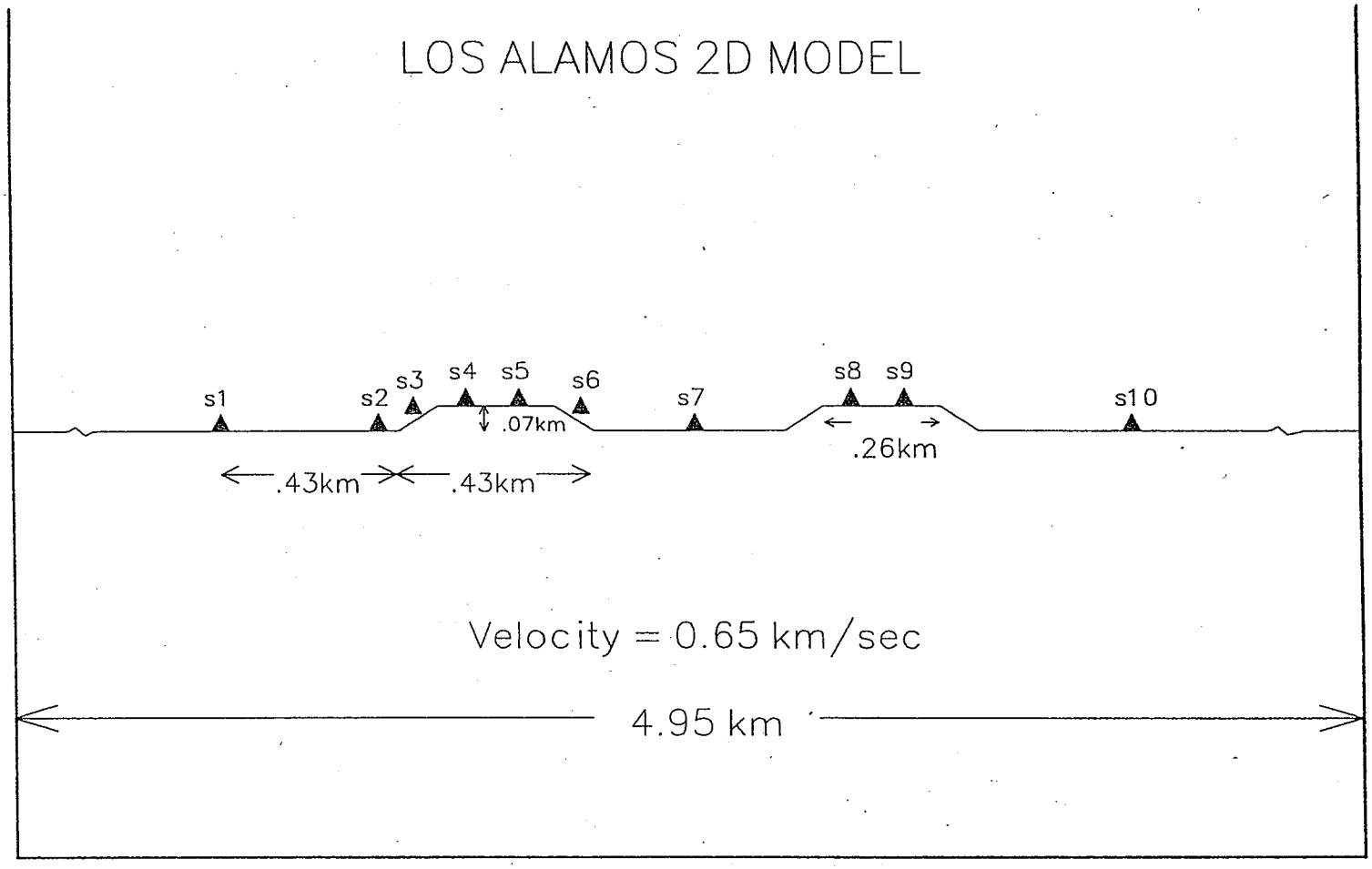

Figure 2. Two-dimensional model used in the finite difference simulations (based on Figure 1). The mesas are 70m wide at the top and 430m wide at the base. Sites are numbered 1-10. The grid is 4.95 km wide with an average shear wave velocity of 0.65 km/sec.

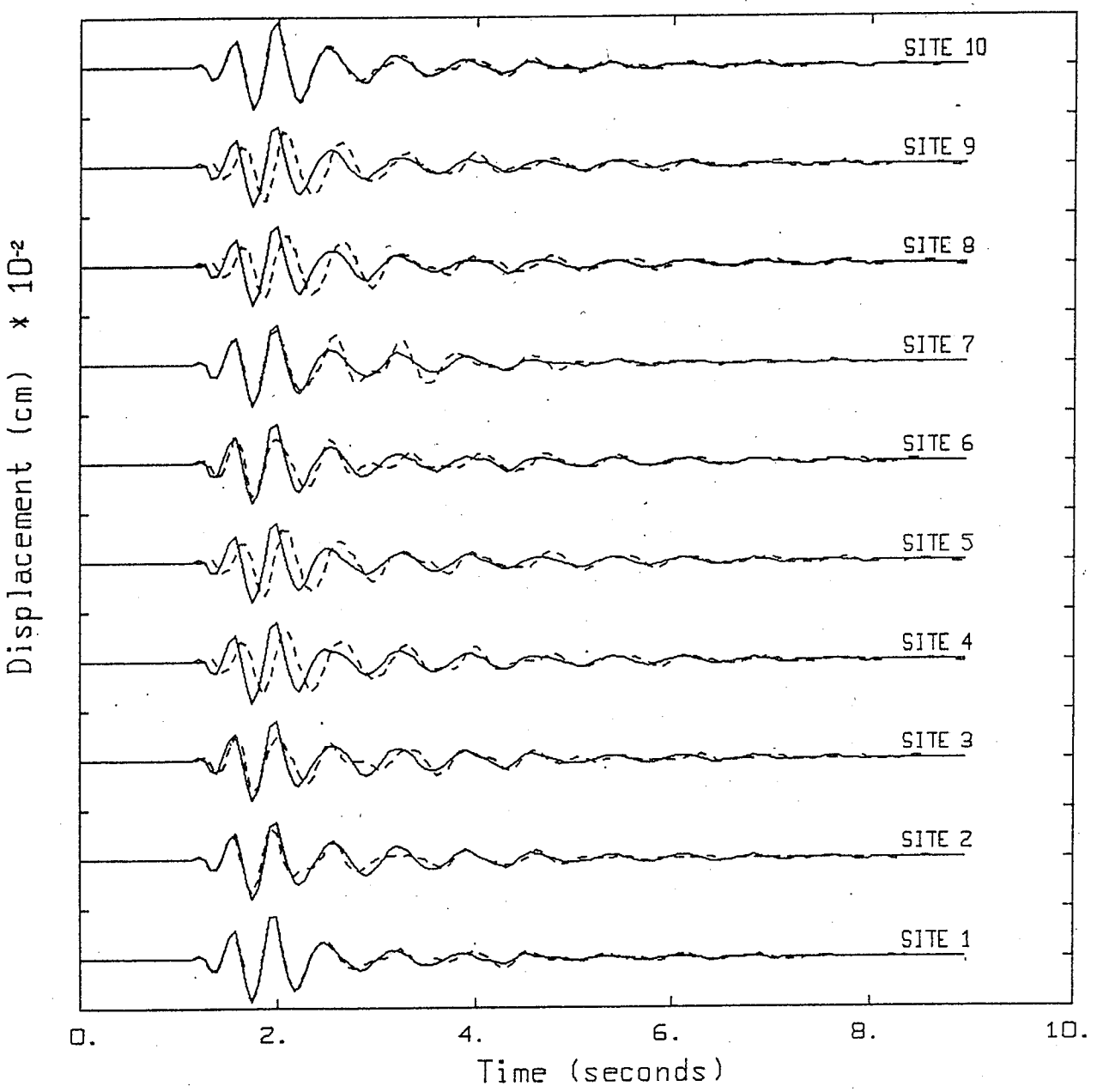

Figure 3. Simulated displacement time histories at sites 1-10 for a vertically propagating plane shear wave (SH): solid lines 1-D structure; dashed lines 2-D structure. Sites 3, 4, 5, 6, 8, and 9 are mesa sites (Figure 2) and reflect a slight delay in arrival.

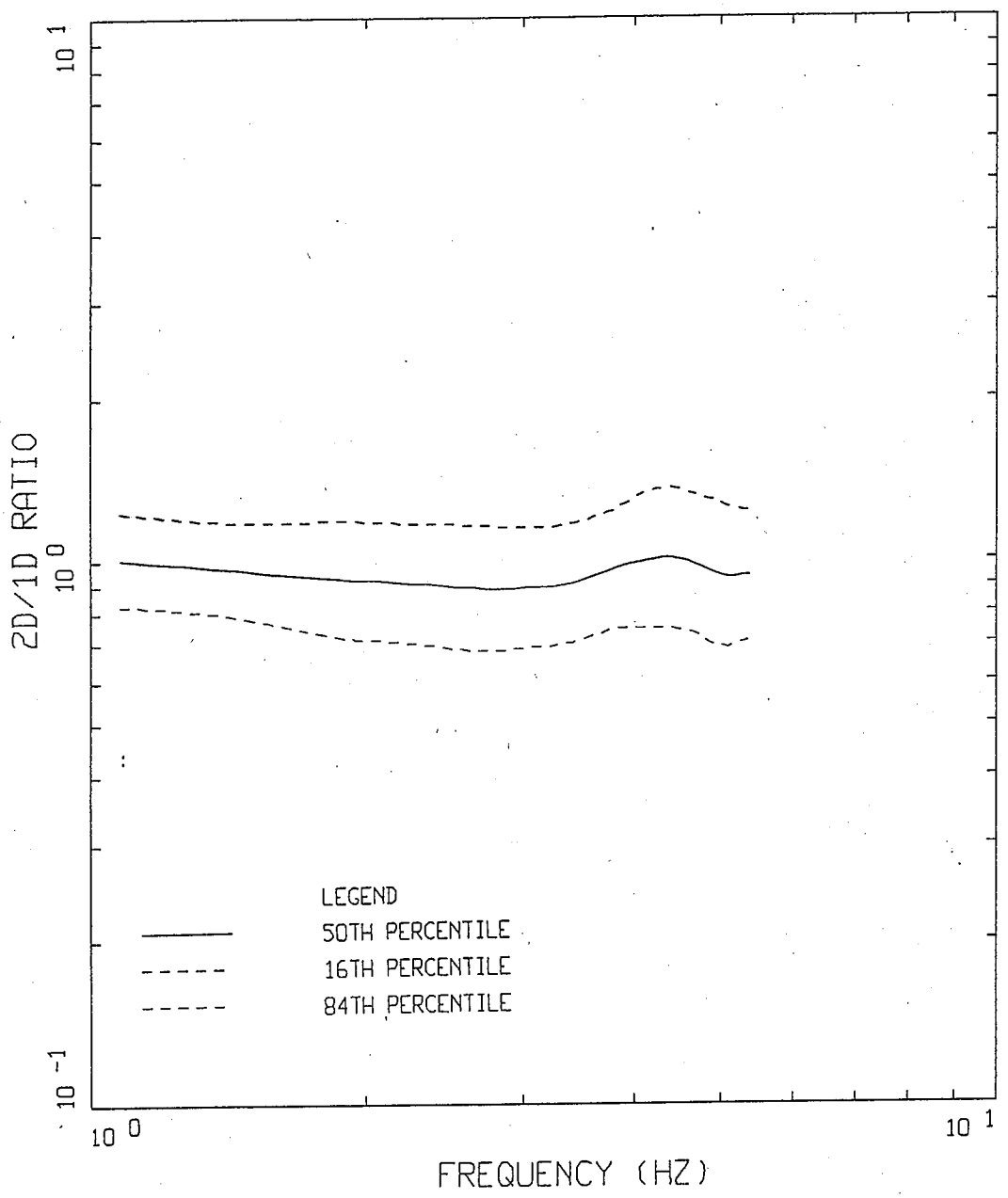

Figure 4. Site 1 Fourier amplitude spectral ratio (2D/1D) for incidence angles 0°, 10°, 20°, 40°, and shear wave velocities of 0.43 km/sec, 0.65 km/sec, and 0.98 km/sec. Fourier amplitudes have been smoothed over 2 Hz.

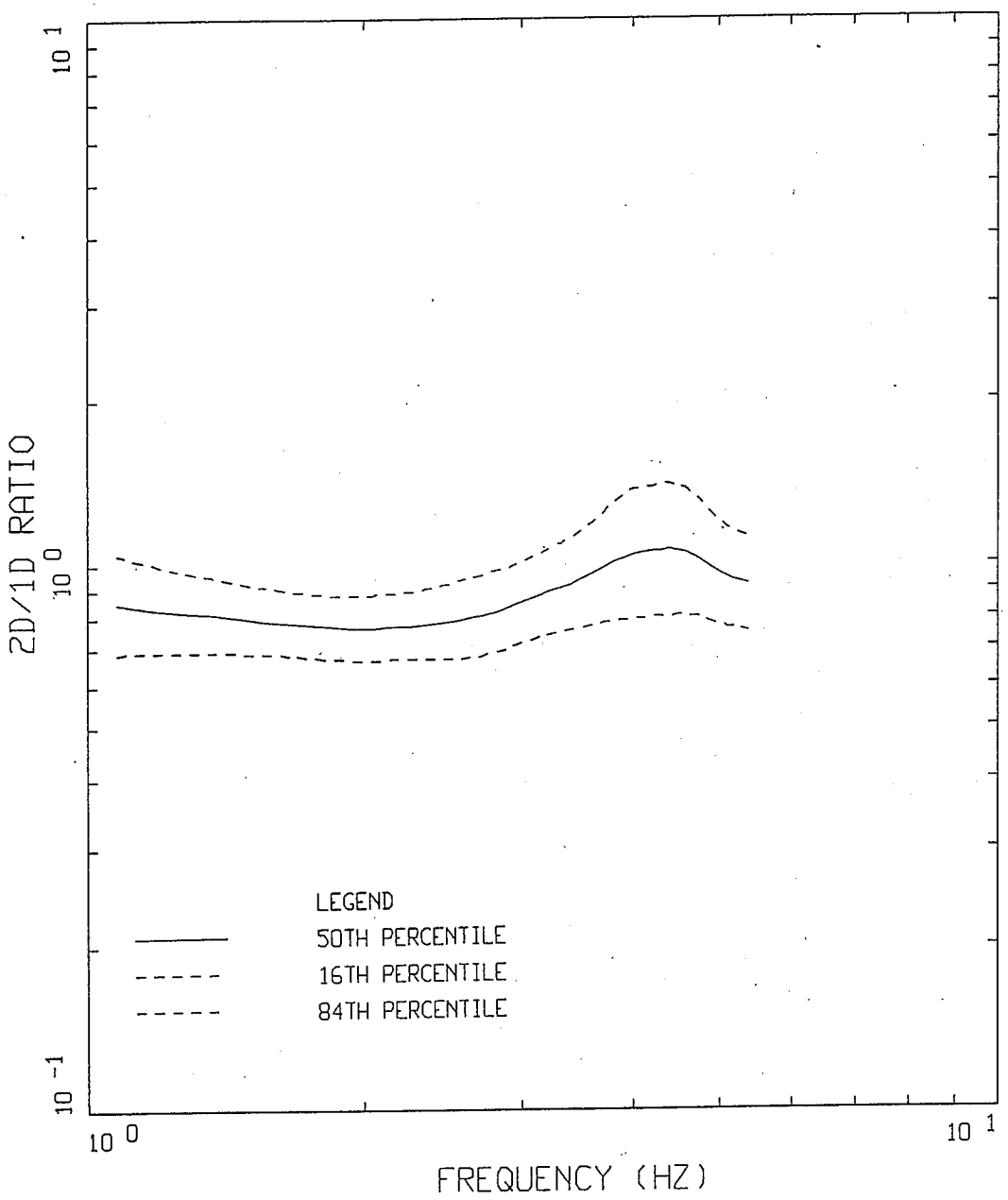

Figure 5. Site 2 Fourier amplitude spectral ratio (2D/1D) for incidence angles 0°, 10°, 20°, 40°, and shear wave velocities of 0.43 km/sec, 0.65 km/sec, and 0.98 km/sec. Fourier amplitudes have been smoothed over 2 Hz.

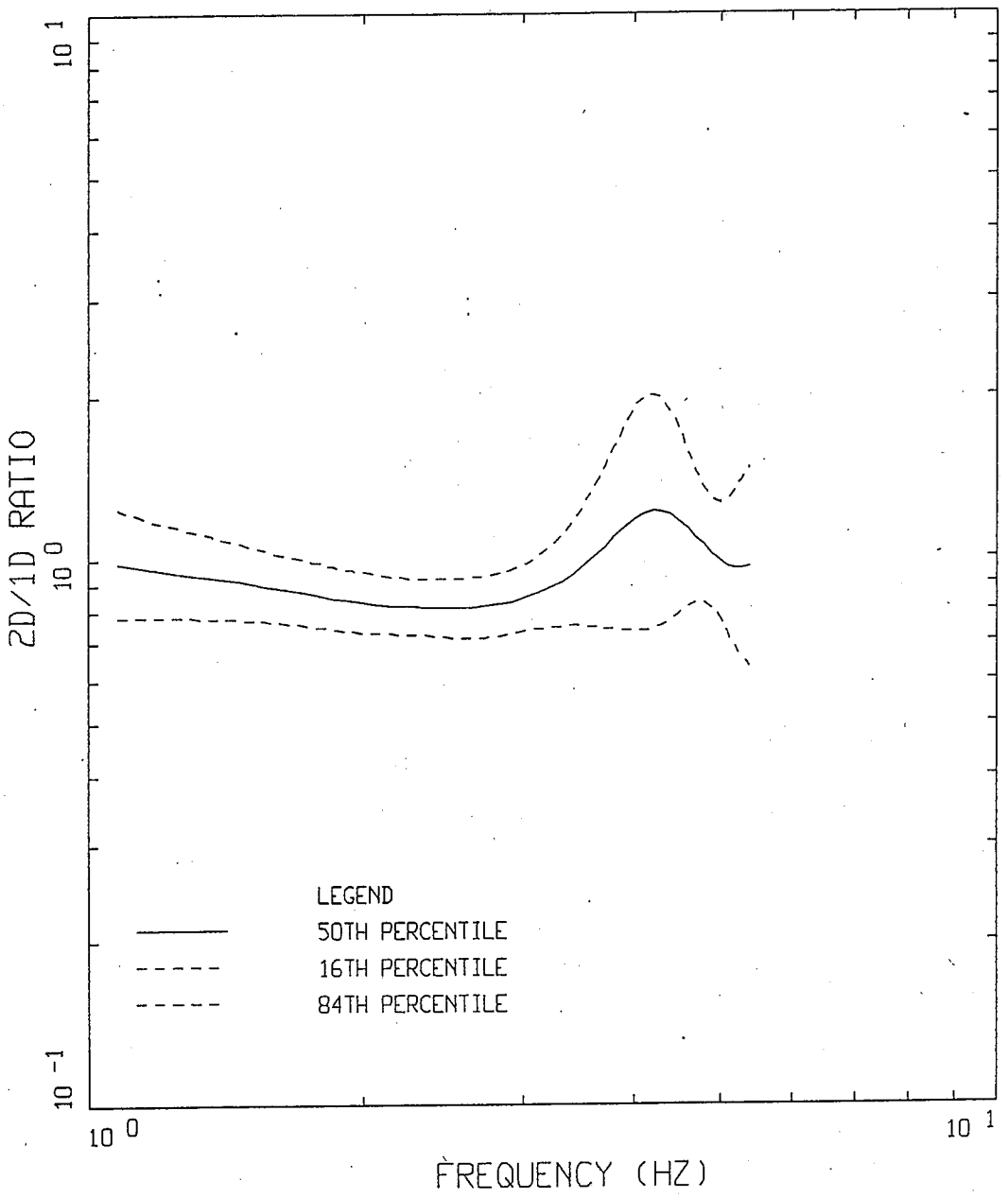

Figure 6. Site 3 Fourier amplitude spectral ratio (2D/1D) for incidence angles 0°, 10°, 20°, 40°, and shear wave velocities of 0.43 km/sec, 0.65 km/sec, and 0.98 km/sec. Fourier amplitudes have been smoothed over 2 Hz.

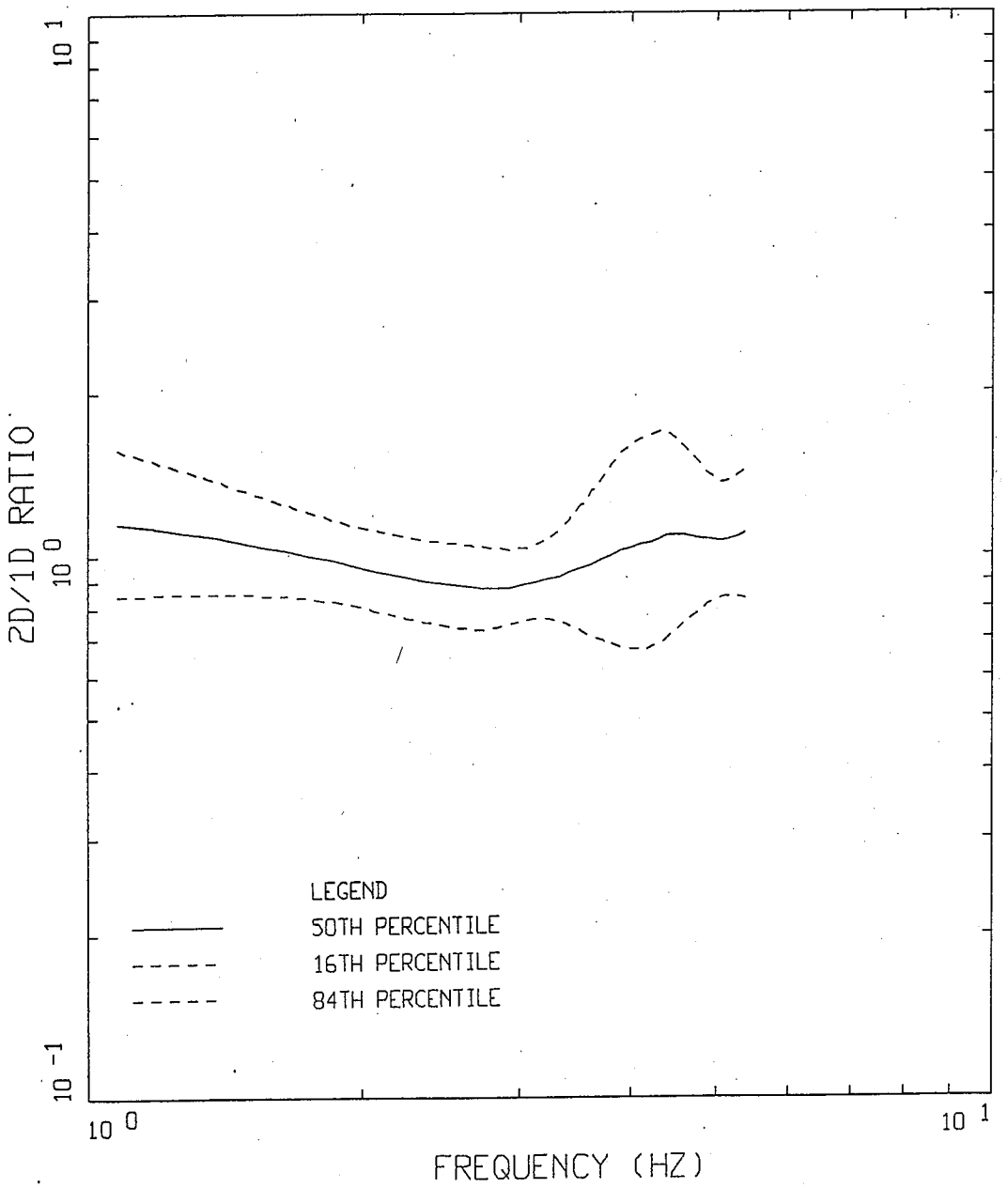

Figure 7. Site 4 Fourier amplitude spectral ratio (2D/1D) for incidence angles 0°, 10°, 20°, 40°, and shear wave velocities of 0.43 km/sec, 0.65 km/sec, and 0.98 km/sec. Fourier amplitudes have been smoothed over 2 Hz.

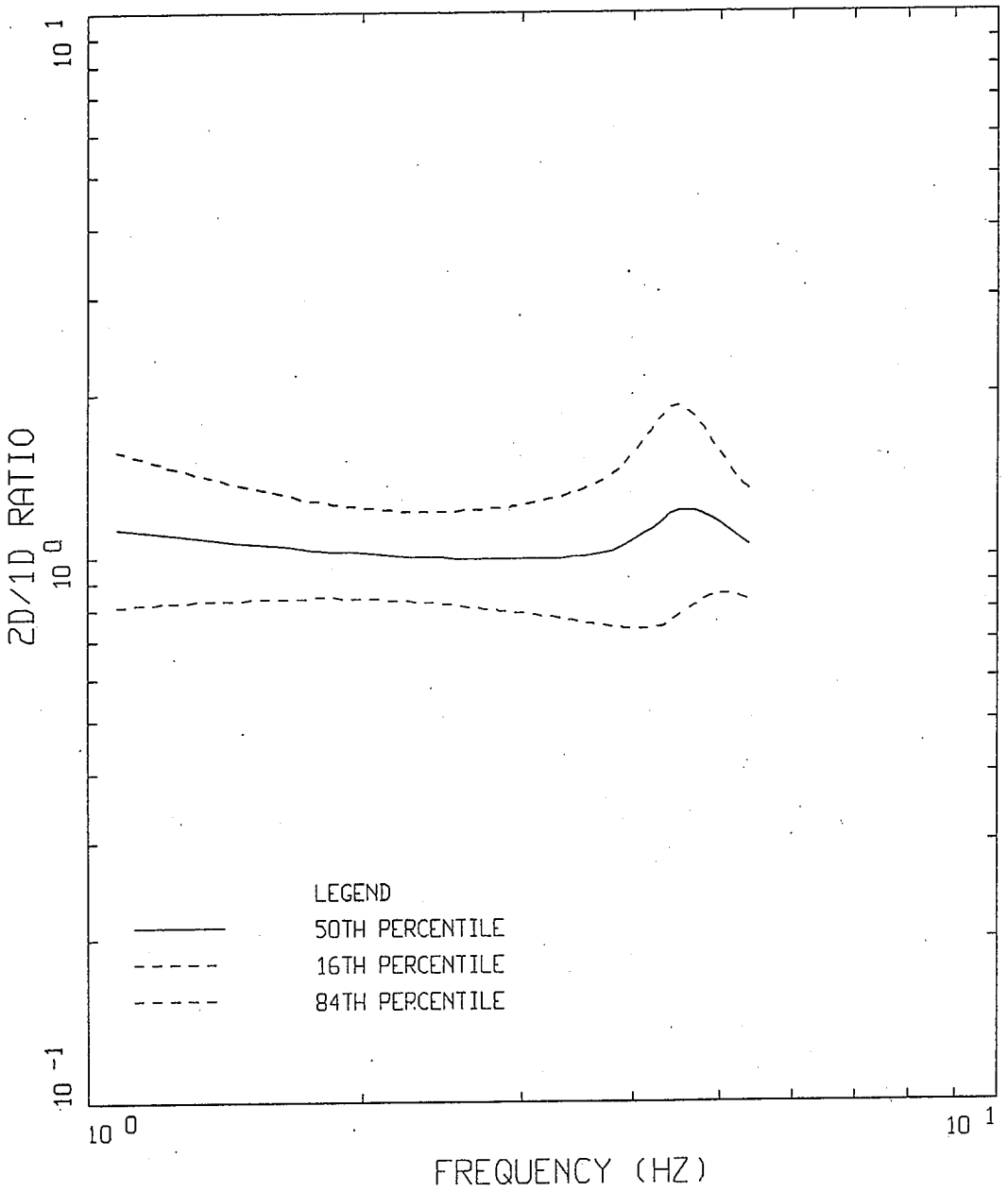

Figure 8. Site 5 Fourier amplitude spectral ratio (2D/1D) for incidence angles 0°, 10°, 20°, 40°, and shear wave velocities of 0.43 km/sec, 0.65 km/sec, and 0.98 km/sec. Fourier amplitudes have been smoothed over 2 Hz.

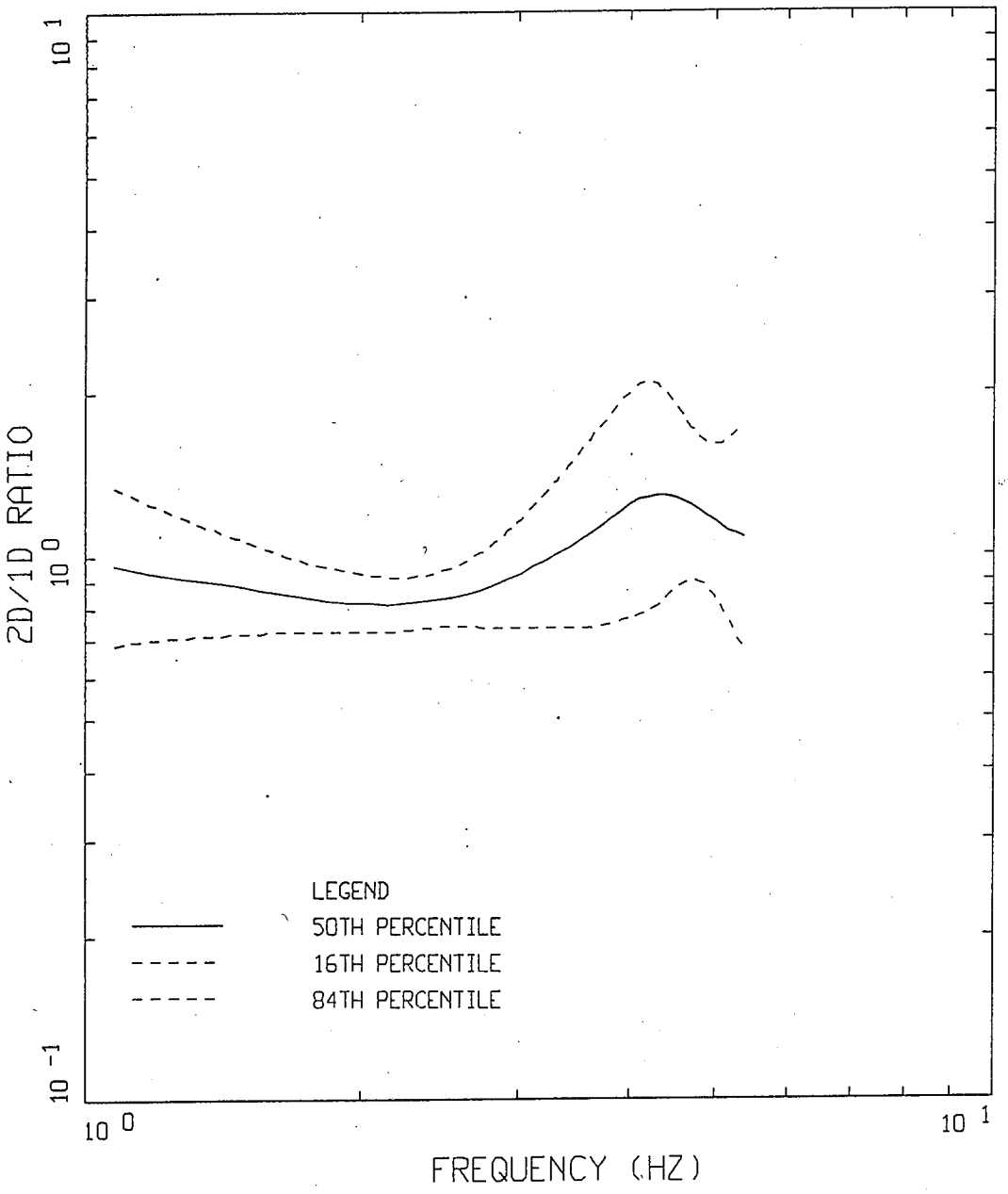

Figure 9. Site 6 Fourier amplitude spectral ratio (2D/1D) for incidence angles 0°, 10°, 20°, 40°, and shear wave velocities of 0.43 km/sec, 0.65 km/sec, and 0.98 km/sec. Fourier amplitudes have been smoothed over 2 Hz.

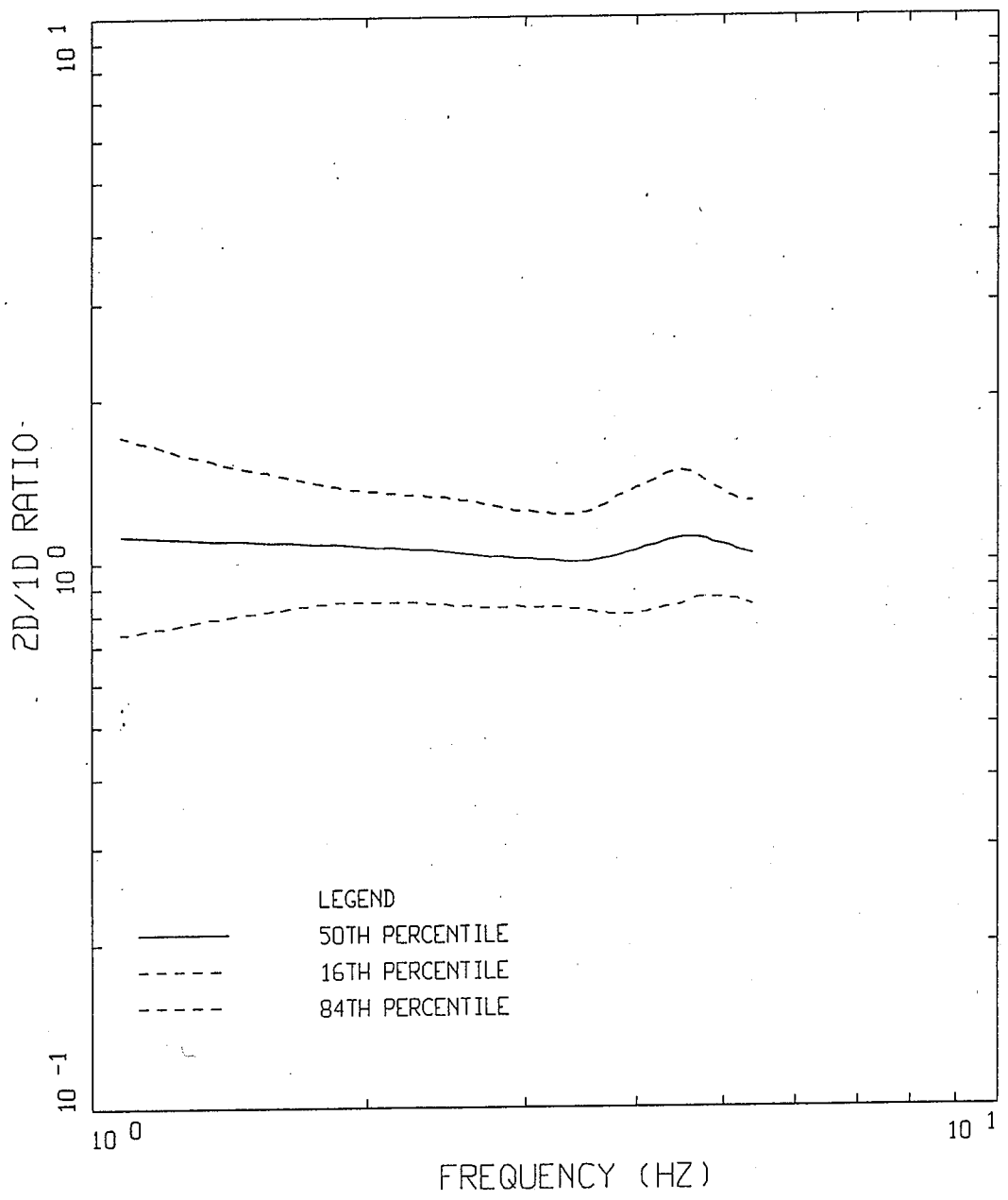

Figure 10. Site 7 Fourier amplitude spectral ratio (2D/1D) for incidence angles 0°, 10°, 20°, 40°, and shear wave velocities of 0.43 km/sec, 0.65 km/sec, and 0.98 km/sec. Fourier amplitudes have been smoothed over 2 Hz.

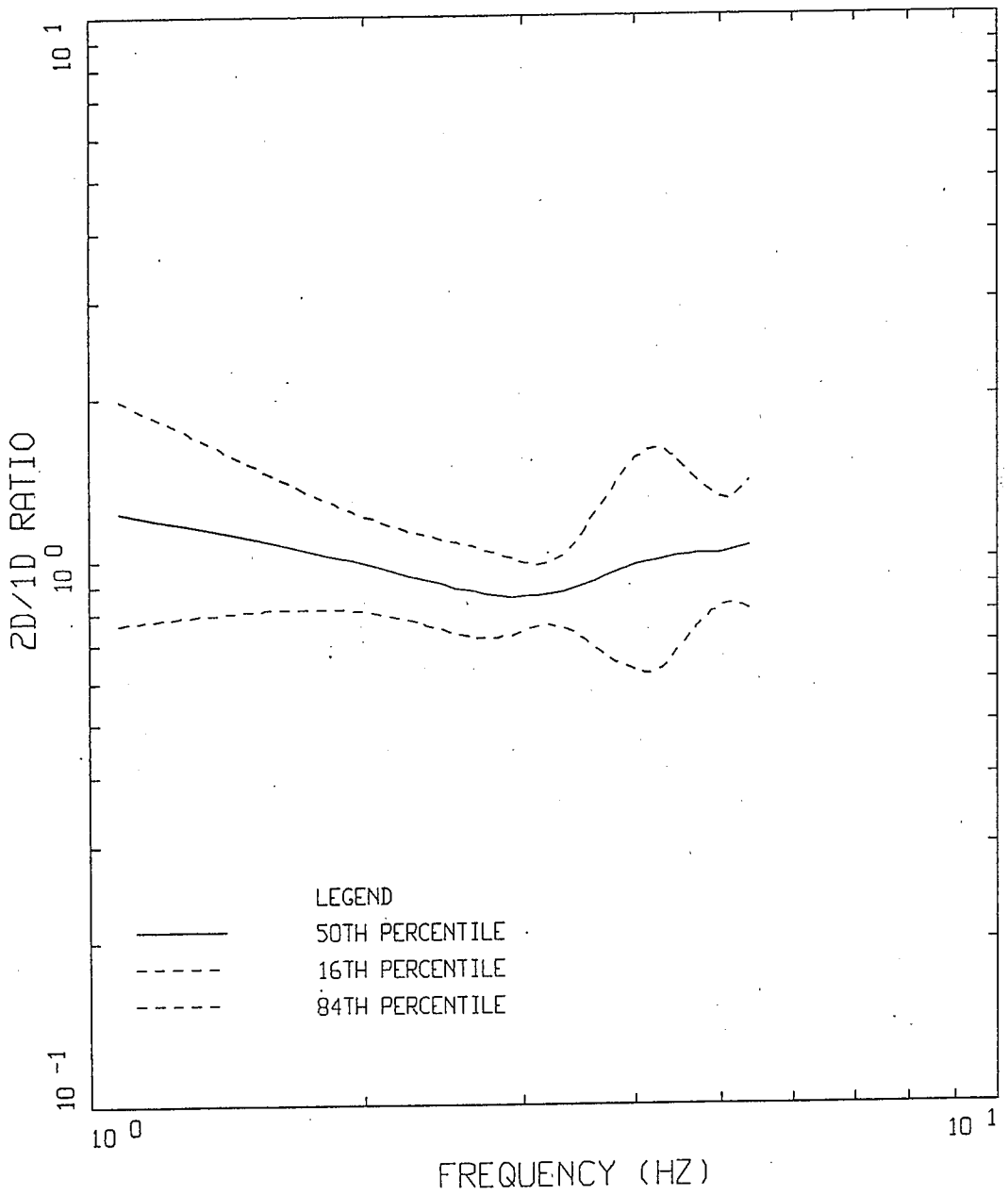

Figure 11. Site 8 Fourier amplitude spectral ratio (2D/1D) for incidence angles 0°, 10°, 20°, 40°, and shear wave velocities of 0.43 km/sec, 0.65 km/sec, and 0.98 km/sec. Fourier amplitudes have been smoothed over 2 Hz.

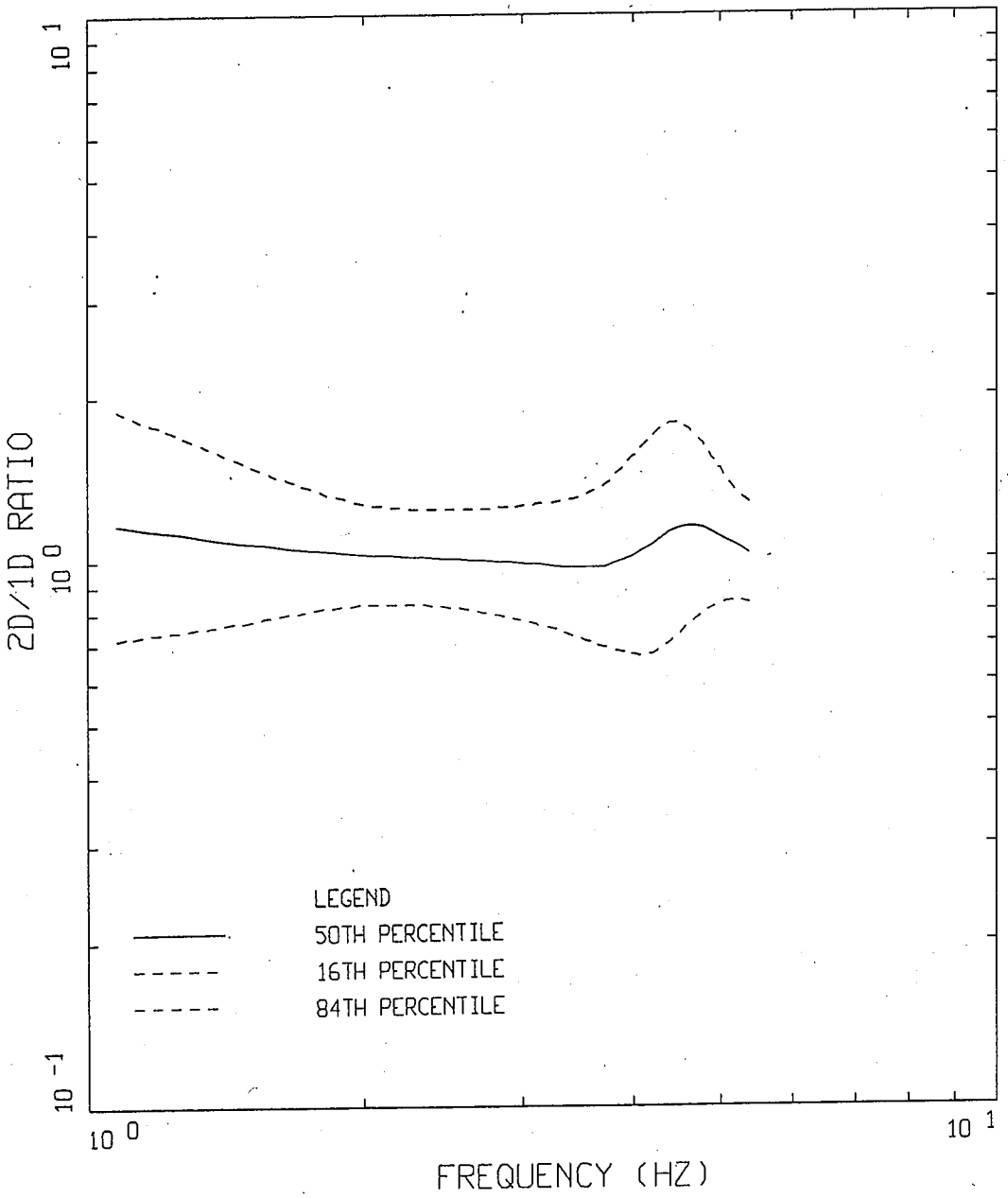

Figure 12. Site 9 Fourier amplitude spectral ratio (2D/1D) for incidence angles 0°, 10°, 20°, 40°, and shear wave velocities of 0.43 km/sec, 0.65 km/sec, and 0.98 km/sec. Fourier amplitudes have been smoothed over 2 Hz.

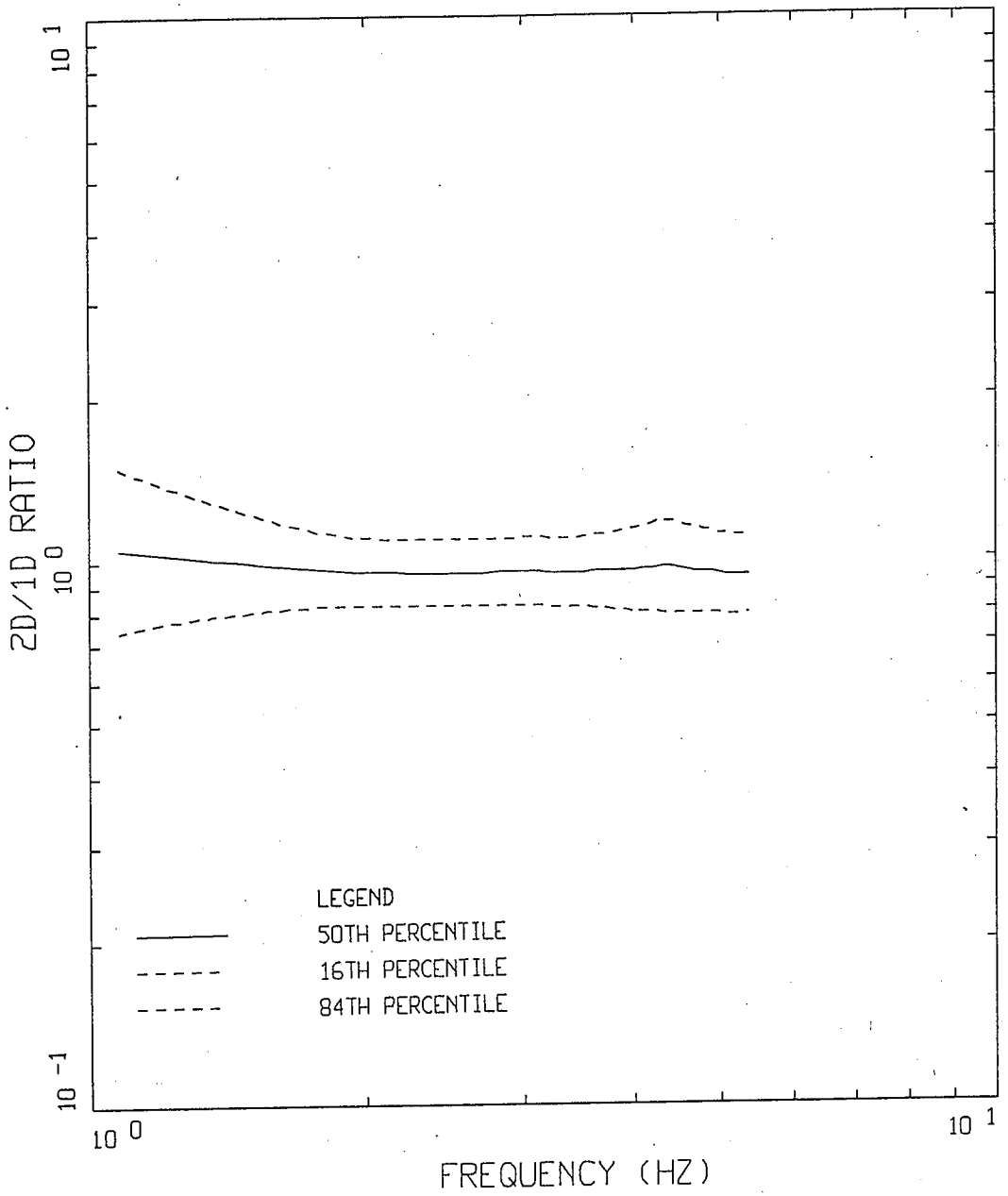

Figure 13. Site 10 Fourier amplitude spectral ratio (2D/1D) for incidence angles 0°, 10°, 20°, 40°, and shear wave velocities of 0.43 km/sec, 0.65 km/sec, and 0.98 km/sec. Fourier amplitudes have been smoothed over 2 Hz.

APPENDIX B

EFFECTS OF SUBSURFACE TOPOGRAPHY ON GROUND MOTIONS AT THE IDAHO NATIONAL ENGINEERING LABORATORY*

To illustrate the effects of subsurface topography on ground motions, an example is presented of a 2-D analysis done for an intrusive (magma) body beneath the Idaho National Engineering Laboratory. The intrusive body was outlined using refraction and gravity data and is schematically depicted in Figure 1 which shows a cross-section of the crust to a depth of 50 km. The purpose of the 2-dimensional modeling was to assess the effects of the intrusive body on ground motions recorded at the INEL from the 1983 M 7 Borah Peak earthquake and from a postulated Lemhi earthquake on the NPR (New Production Reactor) facility. The Lemhi earthquake is postulated to occur on the boundary of the SRP (Snake River Plane) with a maximum magnitude of about 7.0. Figure 2 shows the model used in the finite difference modeling along with the locations of the two earthquakes.

The SH-wave propagation through the 2-D model was carried out using an explicit time-domain finite-difference code (Vidale and Helmberger, 1988). The grid spacing of the finite-difference mesh was 40m, insuring that the computations are numerically stable up to 3 Hz. Synthetic seismograms at eight equally-spaced sites, 69 to 104 km from the northwest end of the crustal model, were generated (Figure 2). The NPR site is located at about 14 km from the boundary of the ESRP and 94 km from the northwest end of the crustal model.

To investigate the effects of lateral heterogeneities on ground motions, ratios of the finite difference synthetic seismograms using the 2-D model to those using 1 a-D model were computed. Synthetic ground displacements for both the Borah Peak earthquake and the Lemhi fault MCE were computed. Both sources were assumed to have fault strikes parallel to the 2-D profile with a dip of 45 degrees to the south and to exhibit pure normal faulting. The source

*Source: Woodward-Clyde Consultants

mechanism is not critical because it is approximately canceled in the process of computing the ratios.

Lemhi Earthquake

The hypocenter for the Lemhi fault was placed at three different focal depths, 5, 10, and 15 km to encompass the range of fault width for a finite source (Figure 2). The hypocenters were located at the boundary of the ESRP.

The ratios of the mean Fourier amplitude spectra between 1 and 3 Hz for the three hypocenters are shown in Figure 3. For the two deeper hypocenters, the ratios with respect to the NPR 1-D model are near unity. For the shallow source at a depth of 5 km, the 2-dimensional effects are large and increase into the SPR. The larger motions are likely due to surface waves generated along the dipping interface just above the source. Because the analysis was for an elastic system, the amplification due to these high frequency surface waves is extreme and their effects would be greatly reduced with damping levels associated with large ground motions. Additionally for a large (M 7) source most of the energy is expected to come from depths exceeding 5-7 km. The conclusion from the analyses is that the 2-dimensional structure is not going to be a significant factor for the postulated Lemhi earthquake at the NPR facility.

Borah Peak Earthquake

To assess the effects of the laterally-heterogeneous crust on the ground motions predicted for the Borah Peak earthquake, 2-D finite-difference modeling was performed as described in the previous section. The hypocenter was placed at a depth of 16 km (Doser and Smith, 1985) as shown in Figure 2.

The site NPR is located at a distance of 94 km from the northwest edge of the crustal model (Figure 2).

The ratios of mean Fourier amplitude spectra (2D/1D) between 1 and 3 Hz are plotted in Figure 4).

These ratios show the effects of the magma body and shallow 2D structure as a gradual increase in motions moving onto the SRP. The maximum effect is about 1.7 which is significant amplification for this distant source and contributes to the explanation of the unusually high motions recorded at the INEL from the Borah Peak earthquake.

REFERENCES

Doser, D. I. and Smith, R. B. (1985). "Source parameters of the 28 October 1983 Borah Peak, Idaho earthquake from body wave analysis." *Bull. Seism. Soc. Am.*, 75, 1041-1066.

Sparlin, M. A., Braile, L. W., and Smith, R. B. (1982). "Crustal structure of the eastern Snake River Plain determined from ray trace modeling of seismic refraction data." *J. Geophysical Resear.*, 87, 2619-2633.

Vidale, J.E., and Helmberger, D.V. (1988). "Elastic finite-difference modeling of the 1971 San Fernando, California earthquake." *Bull. Seism. Soc. Am.*, 78(1), 122-141.

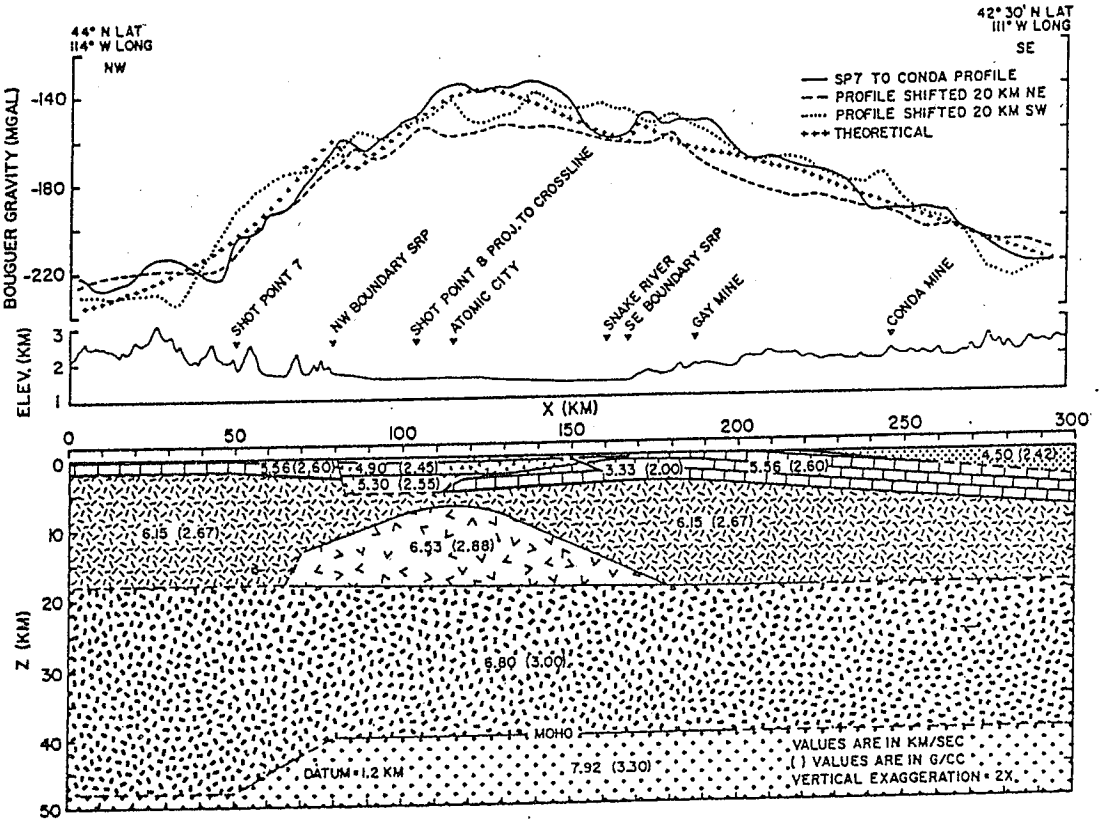

Note: The datum for the crustal model is 1.2-km elevation. Interfaces are dashed where no seismic control is available. Elevation and gravity profiles are also shown. Three observed simple Bouguer gravity profiles are shown. One is located along the Conda-SP7 profile, and the other two are oriented parallel to the Conda-SP7 profile but are shifted 20 km northeast and 20 km southwest. The gravity anomaly calculated from the two-dimensional density model (densities are values shown in parentheses) is also illustrated.

(from Sparlin et al., 1982)

Figure 1. Crustal model across the Eastern Snake River Plain (from Sparlin et al., 1982).

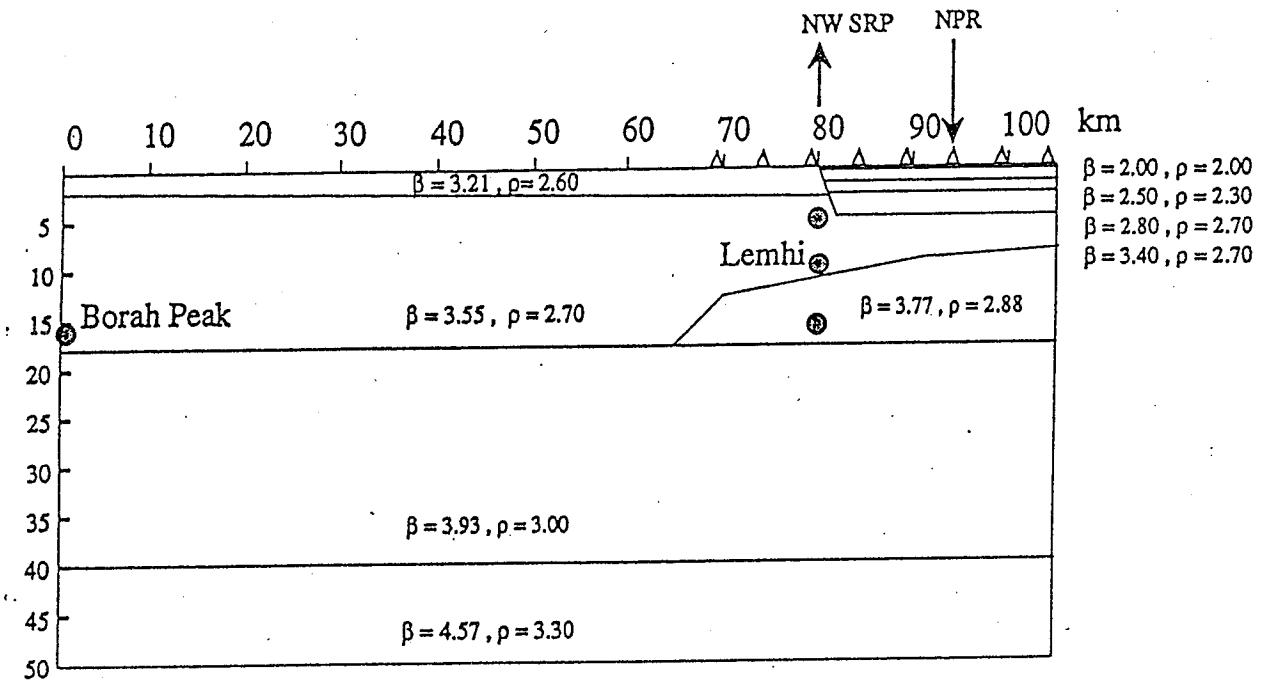

Figure 2. Crustal model used in 2-dimensional finite-difference modeling for the postulated Lemhi earthquake and the Borah Peak earthquake. Point sources are used.

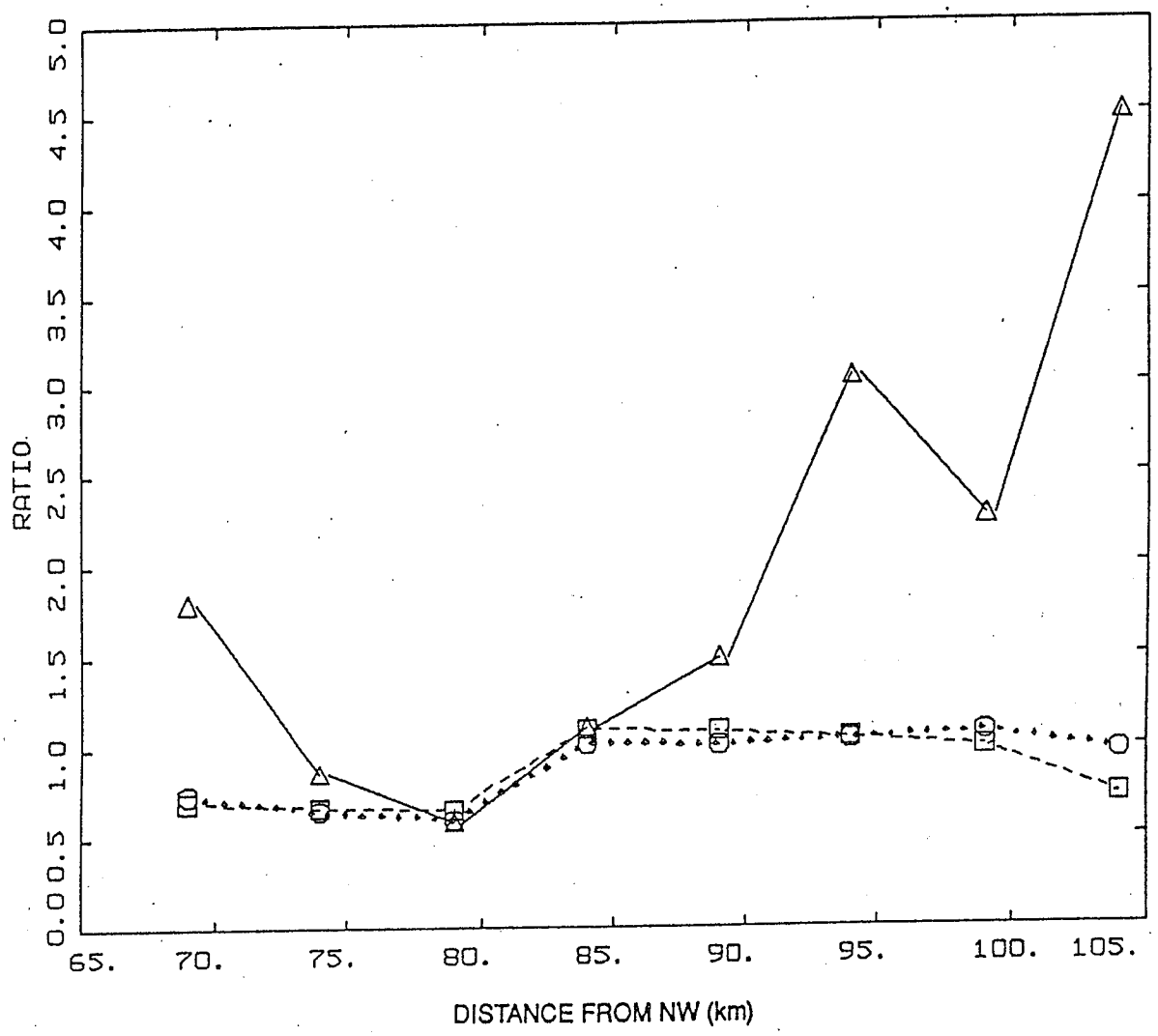

Figure 3. Ratios (2D/1D) of mean Fourier amplitude spectra between 1 to 3 Hz for the postulated Lemhi earthquake.

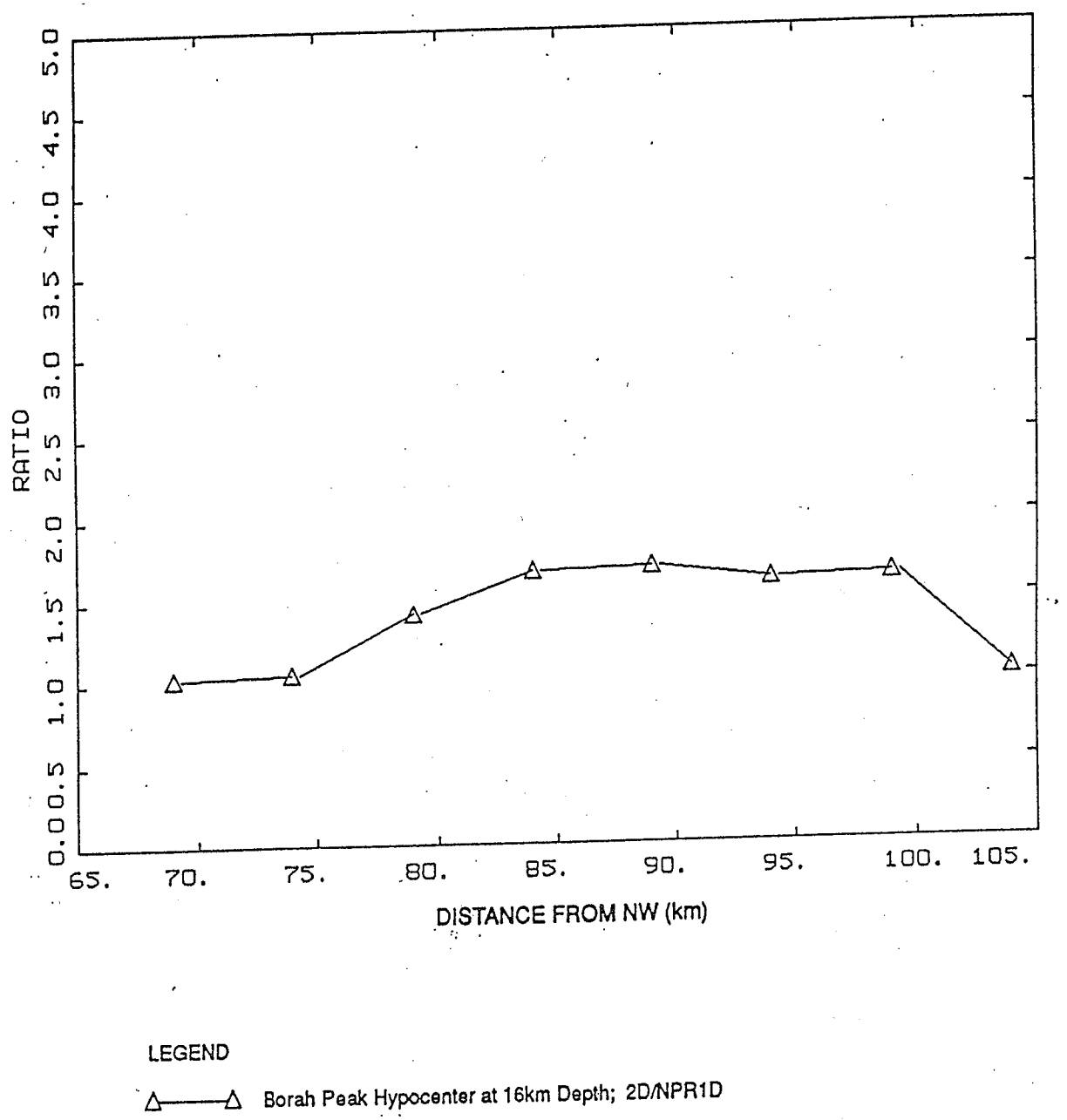

Figure 4. Ratios (2D/1D) of mean Fourier amplitude spectra between 1 to 3 Hz for the Borah Peak earthquake.

APPENDIX C

Paper submitted to Earthquake Spectra. It is included to illustrate the applicability of the three fundamental aspects of site response: 1) adequacy of the vertically propagating shear-wave model, 2) the appropriateness of combining shear-wave velocities determined in-situ with laboratory derived strain dependencies of dynamic material properties, and 3) the suitability of both equivalent-linear and fully nonlinear solution schemes using data from (2).

Evaluation and Implementation of an Improved Methodology for Earthquake Ground Response Analysis

Uniform Treatment of Source, Path and Site Effects

Application Example A

Variability in Site-Specific Seismic Ground Motion Design Predictions

Reference: ASCE Conference "Uncertainty in the Geologic Environment: From Theory to Practice", August 1-3, 1996.

Abstract:

Variability in computed site-specific seismic ground motion is examined over a wide range of periods using a stochastic model which incorporates both a finite source and an equivalent-linear formulation for non-linear site effects. A suite of examples involving a single scenario earthquake and a range of site conditions, source-to-site distances, and depths of characterization are used to illustrate how parametric variability can be systematically examined on a case-specific basis. Emphasis is placed on the relative contributions of geotechnical site parameters including the shear-wave velocity (Vs) profile and both modulus reduction (G/Gmax) and hysteretic damping (D) curves. It is shown that the parameters which control variability in ground-motion predictions are a case-specific function of site type, amplitude of motion, and period range of interest to the designer. The impact of site effects is shown to be the predominant source of parametric response-spectra variability for periods of up to several seconds for soil sites experiencing strong to moderate levels of ground motion. All results are described within the framework of parametric and modeling components of total variability in design predictions, and general trends are developed regarding conditions where extensive geotechnical site characterization efforts provide maximum benefit.

VARIABILITY IN SITE-SPECIFIC SEISMIC GROUND-MOTION DESIGN PREDICTIONS

C.J. Roblee[1] (M. ASCE), W.J. Silva[2],
G.R. Toro[3] (A.M. ASCE) and N. Abrahamson[4]

Abstract

Variability in computed site-specific seismic ground motion is examined over a wide range of periods using a stochastic model which incorporates both a finite source and an equivalent-linear formulation for non-linear site effects. A suite of examples involving a single scenario earthquake and a range of site conditions, source-to-site distances, and depths of characterization are used to illustrate how parametric variability can be systematically examined on a case-specific basis. Emphasis is placed on the relative contributions of geotechnical site parameters including the shear-wave velocity (Vs) profile and both modulus reduction (G/Gmax) and hysteretic damping (D) curves. It is shown that the parameters which control variability in ground-motion predictions are a case-specific function of site type, amplitude of motion, and period range of interest to the designer. The impact of site effects is shown to be the predominant source of parametric response-spectra variability for periods of up to several seconds for soil sites experiencing strong to moderate levels of ground motion. All results are described within the framework of parametric and modeling components of total variability in design predictions, and general trends are developed regarding conditions where extensive geotechnical site characterization efforts provide maximum benefit.

Introduction

Earthquakes pose one of nature's greatest engineering-design challenges due, in part, to the wide variability of possible motions which a particular site may experience. Empirical observations show that variations in spectral ordinates (e.g. peak ground acceleration) can span an order of magnitude for sites located at the same distance from a given earthquake. "Attenuation relationships", which provide a functional relationship of site response for a given combination of distance and magnitude, can be used to characterize median response as well as a range of possible motions. However, such relationships are quite generic in that they are developed from instrumental recordings obtained from sites overlying a wide range of subsurface conditions. Furthermore, these relationships are poorly constrained at

[1] Associate Engineer, Caltrans NT&R Program, 5900 Folsom Blvd., Sacramento, CA
[2] Seismologist, Pacific Engineering and Analysis, 311 Pamona Ave., El Cerrito, CA
[3] Vice President, Risk Engineering, Inc., 4155 Darley Ave., Suite A, Boulder, CO
[4] Consulting Seismologist, 5319 Camino Alta Mira, Castro Valley, CA

close distances to large magnitude events, an area of great concern to the design of many important facilities.

A variety of modeling approaches can be applied to develop ground-motion estimates for a particular site and earthquake scenario. For the design of important facilities, seismologists are often charged with developing scenario motions appropriate for "rock", and geotechnical engineers typically modify the "rock motion" on the basis of a local site profile to obtain a "site-specific" estimate of ground motion. Unfortunately, meaningful characterization of variability (often called "uncertainty"; see next section) is often lost in this chain-of-design approach. Recently, more comprehensive modeling approaches have become available which allow consistent treatment of parametric variabilities in source, path, and site parameters which contribute to overall ground motion estimates. Such approaches can be used either for site-specific estimation of ground motion, or as a means to extend existing empirically-based attenuation relationships into poorly constrained regions of magnitude-distance-site space. One such technique will be used herein to examine the role which geotechnical site characterization offers in terms of reducing variability in ground-motion estimation.

No discussion of ground-motion variability would be complete without noting that, in many cases, the greatest unknown in ground-motion estimation centers on the likelihood of occurrence of an event which has a potentially damaging combination of magnitude and distance within the "design life" of a facility. Such time-dependent considerations are the realm of probabilistic seismic hazard analysis [NRC, 1988], which is beyond the scope of this paper. However, even probabilistic hazard analyses are strongly influenced by variability in attenuation relations, and for highly active regions, the range of motion for a particular event may dominate the overall variability in hazard.

Nomenclature on Variability, Uncertainty, and Randomness

Modeling of physical phenomena, such as earthquake ground motions, generally yields a range of possible estimates which depend on model form, assumptions, and parameter values. In many disciplines, such a range in estimates is termed "uncertainty", however, this term is used quite generally and can have a variety of interpretations. An alternative nomenclature is used in the field of seismic hazard analysis which allows partitioning of the causes of a range of estimates into various components [Toro, et. al., 1994, Abrahamson, et. al., 1990]. This paper adopts this alternative nomenclature in which "variability" is the generic term used to denote the range of estimates (i.e. ground response), and variability is viewed as having components of both "uncertainty" and "randomness". Furthermore, for purposes of modeling ground motions, total variability is also partitioned into "modeling variability" and "parametric variability", each having components of uncertainty and randomness.

Table 1 outlines the four components of total variability identified by this nomenclature in the context of ground-response predictions. Generally, modeling variability is a measure of how well a model works when parameter values are known, while parametric variability is the sensitivity of a model to a viable range of values for model parameters. Viewing Table 1 from the other direction, uncertainty is that portion of both modeling and parametric variability which, in principle, can be reduced as additional information becomes available, whereas randomness represents the intrinsic or irreducible component of variability for a given model or parameter.

Table 1. Contributions to Total Variability in Ground-Response Estimates

	Modeling Variability	Parametric Variability
Uncertainty *(also Epistemic Uncertainty)*	Modeling Uncertainty: Variability in predicted response resulting from particular model assumptions, simplifications and/or fixed parameter values. *Can be reduced by adjusting or "calibrating" model to better fit observed earthquake response.*	Parametric Uncertainty: Variability in predicted response resulting from incomplete data needed to characterize parameters. *Can be reduced by collection of additional information which better constrains parameters*
Randomness *(also Aleatory Uncertainty)*	Modeling Randomness: Variability in predicted response resulting from discrepancies between model and actual complex physical processes. *Cannot be reduced for a given model form.*	Parametric Randomness: Variability in predicted response resulting from inherent randomness of parameter values. *Cannot be reduced a priori* by collection of additional information.*

* Some parameters (e.g. source characteristics) may be well defined after an earthquake.

In the context of earthquakes, modeling variability represents differences between the actual complex physical processes which generate and propagate a strong earthquake and a particular model used to predict ground motions. It is measured in terms of the residual, or misfit, between observations and predictions when model parameters are known. The topic of non-linear soil behavior can be used to illustrate both the distinction between modeling randomness and modeling uncertainty as well as the essential point that this distinction is model dependent. Say that a particular model 'A' considers soil behavior to be linear elastic (i.e. showed no change in stiffness or damping as a function of strain), and assume that soil behavior is indeed strain-dependent. Non-linear soil effects would then contribute to the scatter, or modeling variability, in the residuals between measured ground response and model 'A' predictions, and this scatter would be considered randomness (inherently unresolvable). However, if one examines the scatter as a function of ground-motion amplitude, one might find a systematic trend or "bias" to the scatter, say to overpredict high-amplitude motions and/or underpredict low-amplitude motions. This bias can be viewed as modeling uncertainty, and one could choose to "calibrate" or bias correct the linear-soil model (A*) in some fashion so as to eliminate this consistent trend for the strain levels represented in the data set, thus leaving only the randomness components to the scatter. As an alternative means to remove the amplitude-dependent bias, one might adopt a new model (B) which explicitly accounts for non-linear soil behavior. In this case, some modeling uncertainty would be eliminated, but only at the expense of introducing additional parametric variability associated with establishing the new non-linear parameters. Such a trade-off may, or may not, prove beneficial in terms of reducing total variability. However, the more "correct" model (B) should provide more accurate predictions (median values) for cases outside the empirical data base.

Using the same topic, an example of parametric variability is the range in predicted response associated with a range of possible functions (or "curves") describing non-linear material curves for the soil layers. The parametric uncertainty is that portion of response variability that could be reduced by better definition of the curves, say by using high-quality laboratory testing. However, such curves can never be perfectly defined due to both measurement errors and natural spatial variations within the soil deposit for a particular site. That portion of response variability associated with the undefinable range would be considered part of the parametric randomness. Another important example of parametric randomness stems from processes which cannot be foreseen in future events such as the distribution of slip along a fault plane or the location of the hypocenter.

It is important to emphasize that the distinction between modeling and parametric variability is model dependent. More complex models typically seek to reduce modeling randomness by more closely modeling physical phenomena. However, such models often require more comprehensive sets of observed data to constrain additional model parameters, and generally lead to increased parametric variability. If the increased parametric variability is primarily in the form of uncertainty, it is possible to reduce total variability, but only at the additional expense of constraining the additional parameters. Therefore, existing knowledge and/or available resources may limit the ability of more complex models to reduce total variability.

A central task in design is to select a model that strikes an appropriate balance between increased costs and reduction in total variability. This paper uses a limited set of examples to illustrate how a design engineer might investigate conditions where various levels of geotechnical site characterization may provide meaningful reduction in variability of ground-motion estimates.

Stochastic Finite-Fault Model

Figure 1 depicts central features of the simple, but comprehensive, stochastic finite-fault ground-motion model used herein to examine source, path, and site contributions to parametric variability. Detailed description of the model can be found in Silva [1992], Schneider et.al. [1993], and Silva et.al. [1990]. Generally, the method is based on an extension of a point-source model [Boore, 1983; Hanks and McGuire, 1981] which uses band-limited white noise (BLWN) and random vibration theory (RVT) to estimate site-specific response spectra. Major extensions include incorporation of a "finite fault" to approximate effects of a nearby extended source, and an RVT-based equivalent-linear site model to accommodate effects of strain-dependent soil behavior. A brief overview of the source, path, and site components of the stochastic model are outlined in separate paragraphs below.

The earthquake "source" is characterized as a plane rectangular fault, having specified strike and dip, located within the "seismogenic zone" or the depth range considered capable of significant seismic-energy release (typically >2 km). The fault plane is divided into a grid of subfaults, and each is assigned a different value of slip to simulate regions of high energy emission (i.e. "asperties"). For each subfault, a number of small-magnitude (M5) point sources are "fired" at random locations within the subfault at irregularly staggered time intervals to build up a heterogeneous energy release appropriate for the particular slip value assigned to the subfault. The rupture is initiated at a selected "nucleation point" (or "focus"), and the rupture propagates outward into adjacent subfaults at a rupture velocity, typically taken as about 80% of the shear-wave velocity for the host rock. The rupture velocity is

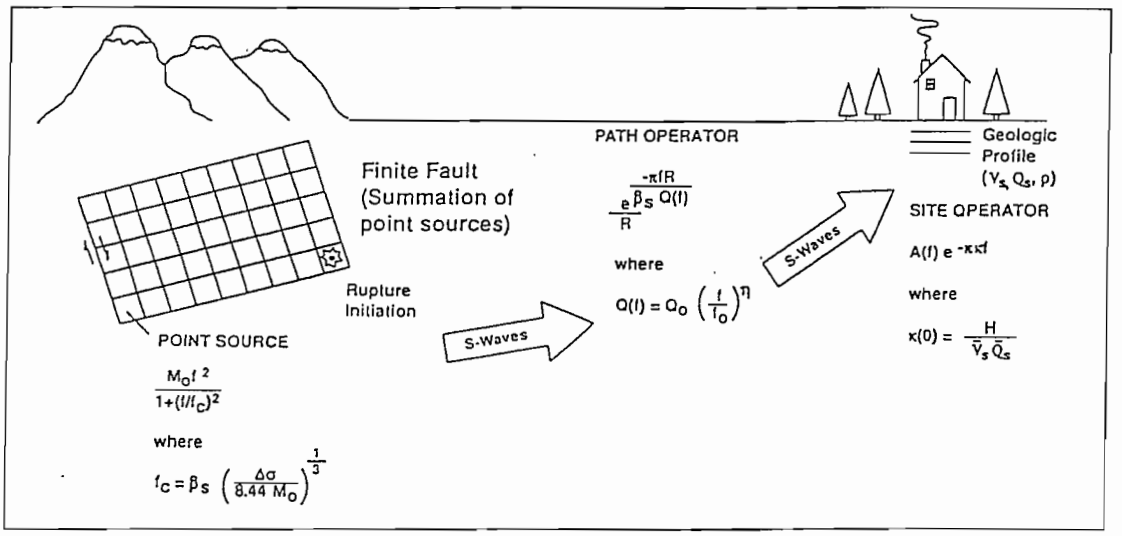

Figure 1. Schematic of Ground Motion Model

randomized within ±20% bounds to simulate an uneven rupture front propagating across the fault releasing spatially-dependent energy.

"Path" effects, which account for wave propagation from source to site, are modeled using simple relationships for geometrical spreading (typically 1/distance) and frequency-dependent crustal attenuation (Q{f}). Radiation-pattern effects are accommodated using an average over all the subfaults. Crustal amplification (A{f}) is modeled using one-dimensional inclined or vertically-propagating shear-waves through a specified regional crustal-velocity model, along with a near-surface (<2 km) exponential-decay parameter called "kappa" (κ) [Anderson and Hough, 1984]. Conventionally, seismologists consider both crustal amplification and the kappa term to be "site" effects, however for purposes of this paper (aimed primarily to an engineering audience), the term "site" is reserved for the very-near-surface region (say <300 m) which is accessible for purposes of geotechnical characterization.

"Site" effects, within the context of this paper, pertain only to the impact which both the velocity profile and non-linear (strain-dependent) soil behavior have on shear-wave propagation through the very-near-surface region. The stochastic model uses an RVT-based equivalent-linear approach to propagate outcrop power spectral density through a one-dimensional soil column, and can be viewed as a frequency-domain analog to time-domain analyses (e.g. SHAKE [Schnabel, et al., 1972]) familiar to most geotechnical engineers. Note that an advantage of the frequency-domain approach is that a single run provides a stable estimate of response without the need for a suite of control motions as would be required using a time-domain method.

The comprehensive nature of the stochastic finite-fault ground-motion model makes it well suited for evaluating the relative contributions of various components of parametric variability. Distributions for model parameters can be assigned and considered in various combinations using a Monte Carlo approach to yield both median relationships and statistics on parametric variability. Approximately 30 to 50 combinations of independently-varied parameters are typically required to provide stable estimates of median and one-sigma response over a wide frequency range.

This paper seeks to illuminate the impact of site-effects parametric variability in ground response by presenting median and one-sigma response spectra results for a single scenario earthquake using over 60 combinations of: 1) "known" model-parameter groups, 2) fault-to-site distances, 3) representative soil profiles, and 4) depth-of-characterization zones.

Scenario Earthquake

Figure 2 illustrates the geometry of the scenario earthquake modeled herein, in which a M7 event occurs on a simple vertical strike-slip fault. The top of the seismogenic region of the fault is located 2 km beneath the surface. The seismogenic region is given dimensions of 90 km along strike, and 12 km down dip (vertical). These values are based on both geologic constraints (for the western U.S.) and established correlations of fault area to moment magnitude [e.g. Wells and Coppersmith, 1994]. The sites considered are positioned at up to 4 separate perpendicular distances (3, 10, 30, and 100 km) from the one-third point along the fault trace. The purpose for selecting the third point of the fault rather than the middle is to allow some consideration of the variability associated with "rupture directivity" which can modify spectral shape and durations in a manner similar to a doppler effect depending upon whether a rupture front moves primarily toward or away from a site.

While all results presented herein must be interpreted in light of the particular nature of this selected scenario, the source/site geometry is not unusual, and is believed to provide sufficient generality to illuminate major trends regarding the impact of site effects on overall ground-motion variability.

Model Parameters and Distributions

The stochastic finite-fault model used herein allows randomization of several scalar and non-scalar parameters to capture major components of parametric variability associated with source, path, and site mechanisms contributing to ground response. Table 2 outlines the major parameters along with typical median values, standard deviations (σ), and distributions for those parameters which were not fixed. Figure 3 illustrates how the non-scalar parameter sets are distributed.

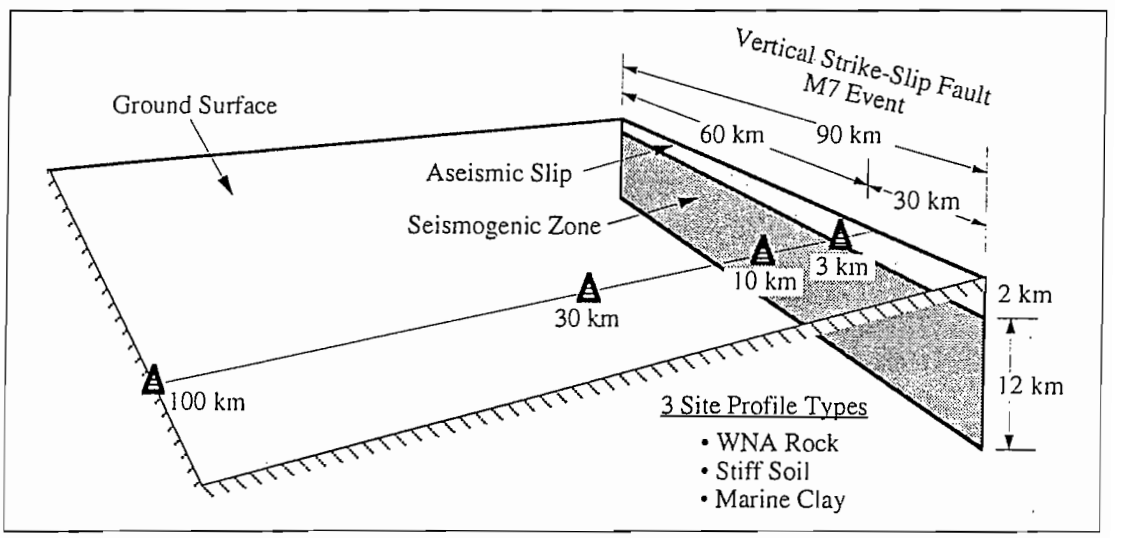

Figure 2. Scenario Earthquake Geometry and Recording Station Locations

Table 2. Model Parameters and Distributions

	Median	Std Dev (σ)	Distribution
Source Parameters			
Magnitude (M)	7.0	--	Fixed
Slip Distribution (See Fig. 3a)	--	--	[Silva, 1993]
Nucleation Point (See Fig. 3b)	Geometric Center	--	[Silva, 1993]
Source-Region Density (ρ)	2.7 g/cc	--	Fixed
Source-Region Velocity (β)	3.2 km/sec	--	Fixed
Path Parameters			
Fault-Site Distance (R)	3, 10, 30, 100 km	--	Fixed
Crustal Attenuation Coef. (Q_o)	150	0.18*	Log-Normal
Crustal Attenuation Coef. (η)	0.60	0.05	Normal
Near-Surface Attenuation** (κ)	0.04	0.30*	Log-Normal
Crustal Velocity Structure	[Boore, 1986]	--	Fixed
Site Parameters			
Near-Surface Velocity Profile (V_s)	3 Median Profiles	(See Fig. 4)	[Toro, 1993]
Material Model (G/G_{max} & D)	3 Curve Sets	(See Fig. 4)	[Silva, 1993]

* σ for log-normal distributions is based on the natural log (ln) of the parameter.
** Near-surface attenuation is often considered a "site" term.

The source modeling parameters include the geometric considerations described in the scenario earthquake section (fault dimensions, fault orientation, and site location) as well as both the distribution of slip on the fault and the nucleation point (focus) for initiation of rupture. For purposes of modeling future events, both slip and focus are varied randomly within empirically-derived constraints. Figure 3a shows three realizations of normalized slip generated using a procedure implemented by Silva [1993] which yields spatial variations of both the number, size, and "height" (amount of slip) of asperities having statistics which match those of observed events. Figure 3a also shows a typical set of 50 randomized nucleation points. Note that the nucleation point is constrained to both the lower half and to within 10% of the edges of the fault plane, also to be consistent with observed events (in California).

Path modeling parameters include the crustal velocity model, and both the frequency-dependent crustal damping function (Q{f}) and the frequency-independent attenuation factor kappa (κ). A single fixed regional crustal-velocity structure [Boore, 1986] is considered herein. The crustal damping function (Q{f}) is represented by a two-parameter function involving parameters Q_o and η. Therefore, the randomized path parameters include Q_o, η, and κ. Median values and distributions for these parameters are presented in Table 2, and were selected to be representative of California.

The fundamental parameters required for implementation of the equivalent-linear site model are the shear-wave velocity profile, and the strain-dependent values of both normalized secant modulus (G/Gmax) and hysteretic material damping (D) as illustrated in Fig. 3b. For purposes of estimating parametric variability, each of these functions are randomized within constraints of observed behavior. The left-hand chart of Fig. 3b shows a representative suite of randomized velocity profiles which includes a randomized depth to "bedrock". Profiles such as these are

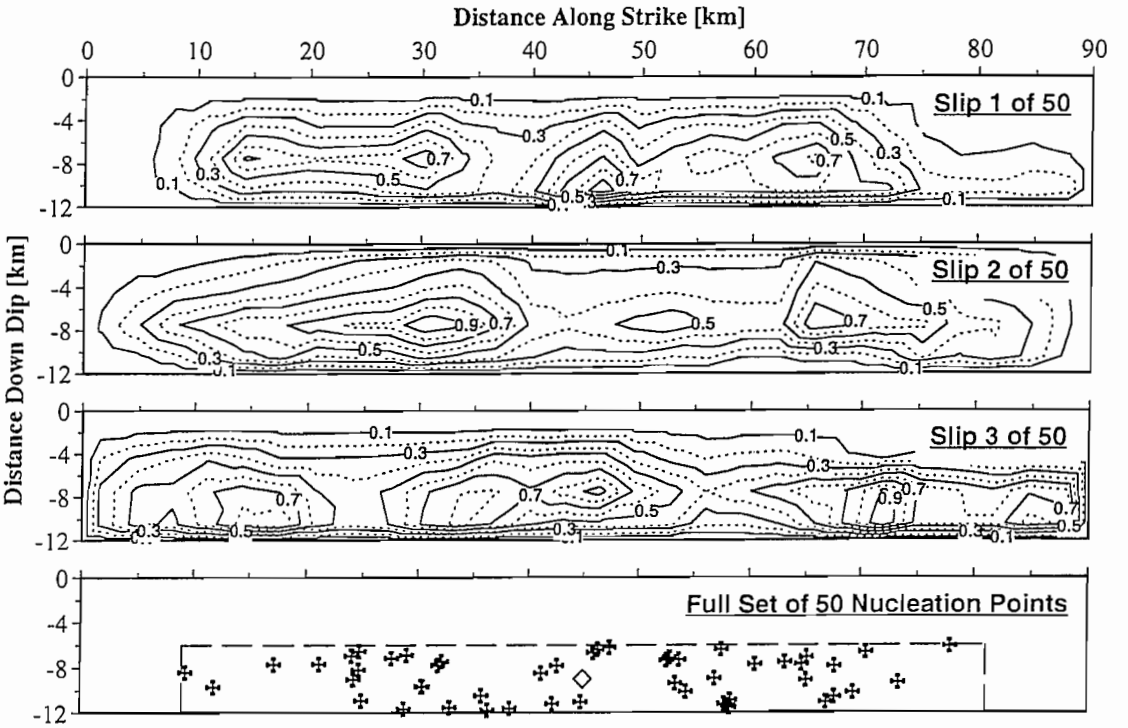

a) Source Parameters: Slip Distribution and Nucleation Point

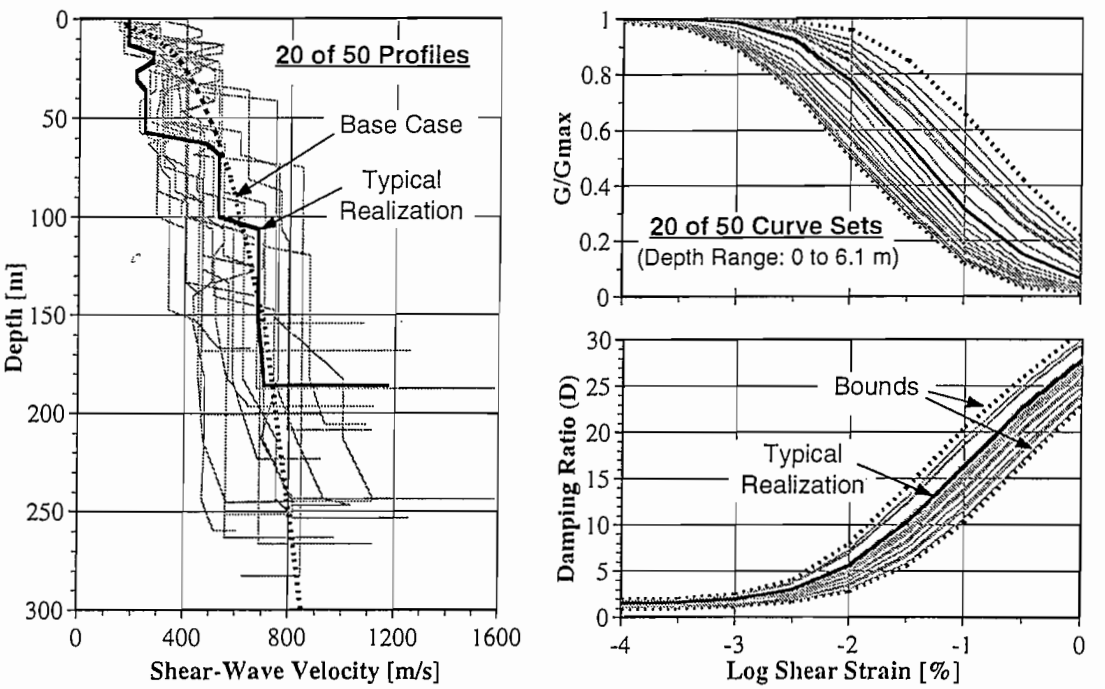

b) Site Parameters: Velocity Profile and Equivalent-Linear Material Curves

Figure 3. Examples of Randomized Non-Scalar Model Parameters

generated using a probabilistic model based on statistical analysis of approximately 650 measured profiles taken from locations throughout the U.S. [Toro, 1993]. In a similar fashion, randomized sets of material-properties curves, such as those shown in the right-hand charts of Fig. 3b, are generated using a routine implemented by Silva [1993]. Specific attributes of the site parameters considered herein are presented below.

Site Profiles and Non-Linear Material Models

Figure 4 shows both the median and plus-or-minus one standard deviation ($\pm\sigma$) of the set of randomized velocity profiles used for each of three different "base case" site types considered herein. The site types are identified as "rock", "stiff soil", and "marine clay", and sample a wide range in site conditions. The base-case velocity profiles for both the rock and stiff soil sites were developed from measured data where available, and on generic models beyond that depth. The rock site used measured data for the upper 25 m, and transitions to a generic regional rock model for Western North America (WNA) [Boore, 1986] for the remainder of the profile. In a similar fashion, the upper 150 m of the stiff-soil profile was constrained by measured data, while a generic soil model for WNA was adopted beyond that depth. Finally, the "marine clay" profile is a more specialized case involving a 15-m thick layer of marine clay underlying a 5-m thick fill. The base-case velocities for the marine-clay layer were based on a correlation for San Francisco Bay Mud [Dickenson, 1994]. A fixed 10-m-thick transitional layer of stiff clay was placed beneath the marine clay, and the WNA stiff-soil profile was used beyond that depth.

Note, for both the rock and stiff soil sites, the velocity profile was randomized to a depth of 300 m. For the stiff soil site, the depth to the crustal half-space was also randomized between 150 m and 300 m, resulting in an average value of 225 m. For the rock site, the "top of crust" was fixed at 225 m. Both the velocity profile and depth were randomized for the marine clay site. Velocities were varied to a depth of 75 m, and the half space was varied between 45 and 75 m with an average value of 60 m. All profiles shown in Fig. 4 reflect the median and $\pm\sigma$ velocity values for the entire depth of velocity randomization.

Figure 4 also presents typical median and bounding sets of non-linear material curves for key layers of each site profile. The randomization routine [Silva, 1993] for evaluating a single realization of both curves uses a normal distribution about base-case values at 0.03% strain, with the standard deviation value set at 0.10 and 0.04 for the modulus reduction and damping curves, respectively. A standard scaling relationship is used to establish values and preserve curve shape for the remainder of the strain range. The fixed bounds shown in Fig. 4 are used to eliminate non-physical statistical fluctuations. Note that the current routine does not incorporate coupling between modulus reduction and damping, and therefore has potential to misestimate parametric variability associated with accepted non-linear material behavior. The base-case curves identified as "rock" are one typical pair of the generic set of depth-dependent material properties developed for rock sites [Pyke, 1993], where this and other members of the set are used for all layers in the rock profile. The bounding rock curves were generally set to allow a factor of approximately ± 2 of the base-case value. A similar set of depth-dependent generic curves were used for the entire stiff-soil profile as well as for those portions of the marine clay profile where the WNA stiff soil was used. Finally, the base-case and bounding curves labeled "clay" are taken from an empirical relationship for clays having a plasticity index (PI) of 30, 0, and 100, respectively [Vucetic and Dobry,

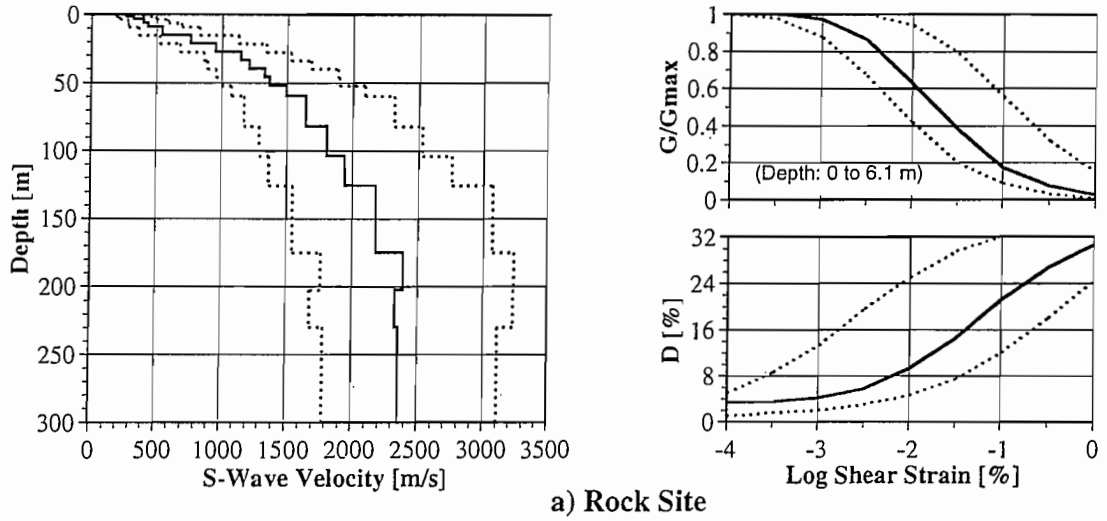

a) Rock Site

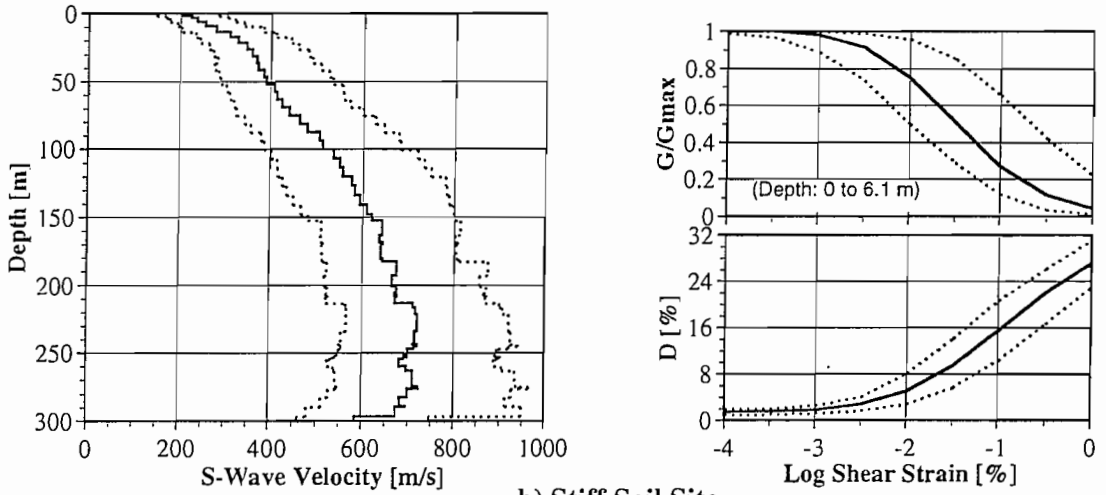

b) Stiff Soil Site

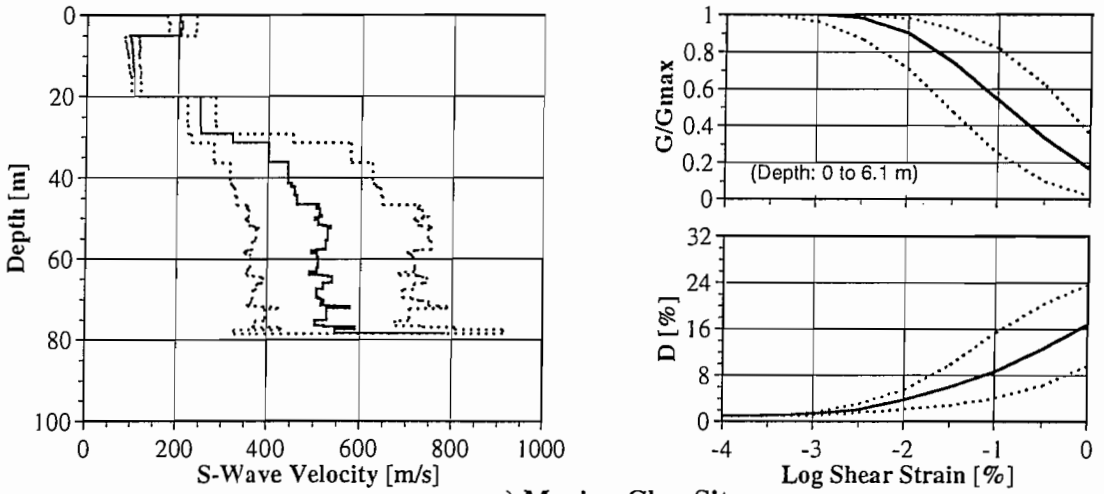

c) Marine Clay Site

Figure 4. Site Properties for Parametric Analysis: Median and ±σ Velocity Profiles and Typical Median and Bounding Nonlinear Material Curves

1991]. These curves are used for both the marine-clay and the stiff-clay layers of the marine clay profile.

Impact of Site Effects

The impact on ground-response parametric variability attributable to site effects can be assessed using the stochastic model by examining the effect on estimates of both σ and median spectral response caused by alternatively varying and fixing different parameter groups. This is done here in two ways, first by comparing individually varied groups of parameters while holding the remaining ones to fixed "base-case" (near median) values, and second by examining the change in response variability associated with holding only the site parameters fixed relative to that where all parameters are simultaneously varied.

Figures 5a and 5b present plots of standard deviation and median values, respectively, of 5%-damped spectral acceleration for distances of 3, 10, 30, and 100 km for each of the rock, stiff soil, and marine clay soil profiles described above. Each chart in both figures show 3 spectra, where each spectrum was generated holding one of the three parameter groups (source, path, and site) fixed to base case values while the remaining two parameter groups were randomly varied. For a linear system, this approach allows direct examination of the contribution to variability of each parameter group.

Figure 5a shows that the significance of each parameter group to parametric variability is a function of period, fault-to-site distance, and site type. Generally, site effects are shown to contribute greatly to parametric variability across most of the spectrum, with a peak in the short-to-intermediate period range (0.1 to 1.0 sec) and a distinct fall-off towards longer periods. The long-period fall-off occurs as wavelengths become significantly longer than the depth of the soil profile. Figure 5a also shows that site-effects variability is clearly a function of distance. For both the soft and stiff soil profiles, site-effects are important contributors to parametric variability to distances of at least 30 km for periods up to several seconds, and overwhelm other factors in this period range for soil sites within 10 km of the fault. For the stiffer rock profile, site effects are the primary contributor to variability from very-short periods to nearly 1 second for distances within 10 km. For 30 km and beyond, site-effects variability for the rock site are comparable or below those for source and path.

Figure 5a also shows that source effects contribute most to parametric variability at long periods, and are relatively insensitive to both site type and distance. As one would expect, path-effects are shown to have little impact on response variability near fault, but become much more pronounced as fault-to-site distance increases. Additionally, path effects have greater influence on both the stiffer profiles and the short-period end of the spectrum.

Figure 5b presents median spectral-response results for the same conditions presented in Fig. 5a. A very interesting trend pertaining to non-linear soil behavior is evident in these results. Note that the median spectra for the "vary site" case is below those of both the "vary source" and "vary path" cases (which nearly overlap), especially for the larger motions at close distances. This is because the "base case" velocity profile used when the site parameters are fixed is a smooth function of depth with values near the median of the randomized profiles. Under linear conditions, the median response of a randomly-varied velocity profile should nearly equal the response of the smooth base-case profile with only minor losses due to scattering at the layer contrasts. This behavior is observed in Fig. 5b for sites at large distance

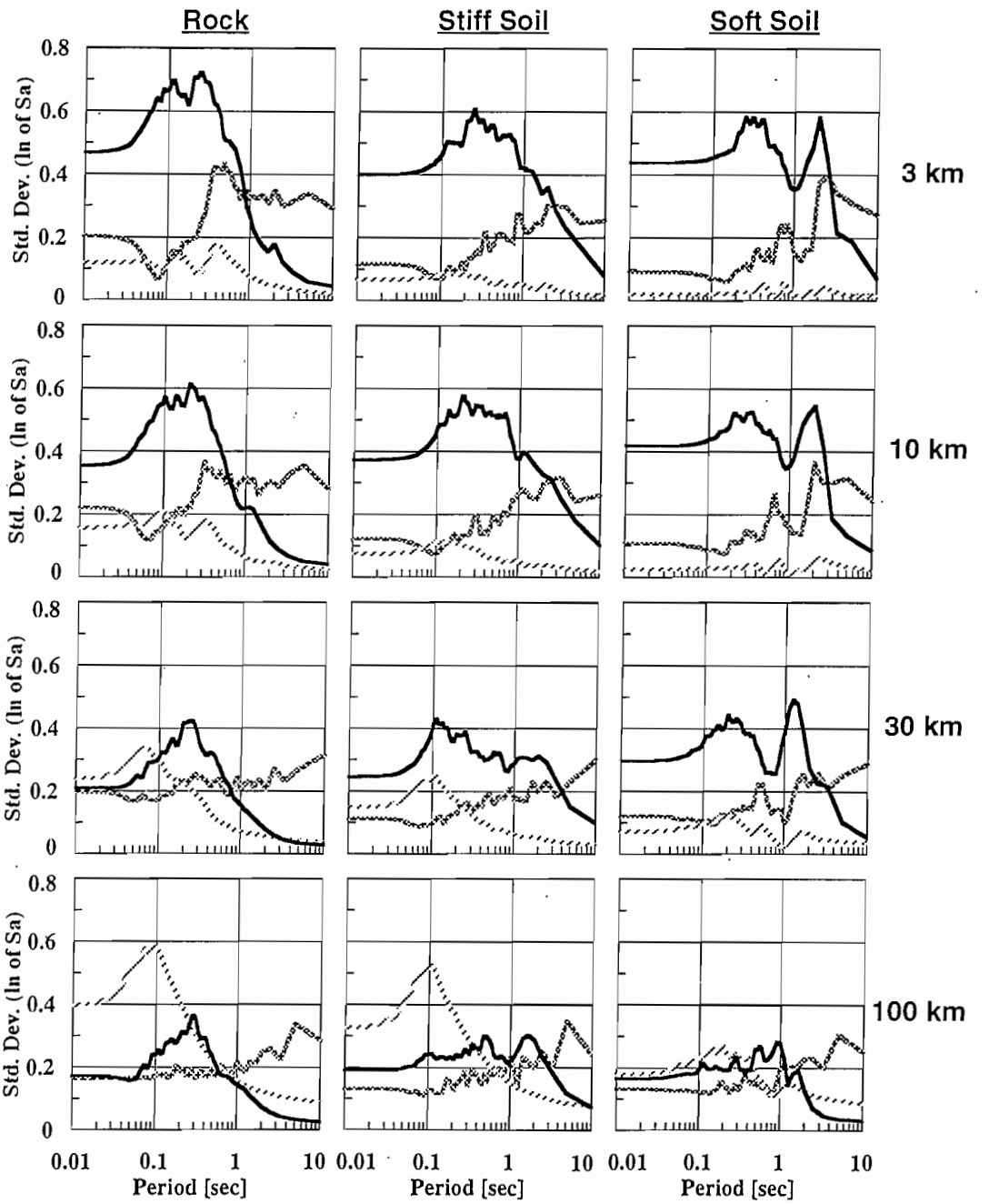

Key	Source (Slip, Focus)	Path (Q_o, η, κ)	Site (Profile, Material)
Vary Source	Randomized	Fixed	Fixed
Vary Path	Fixed	Randomized	Fixed
Vary Site	Fixed	Fixed	Randomized

Figure 5a. Spectral-Response Parametric Variability for Individually Randomized Source, Path, and Site Parameter Groups

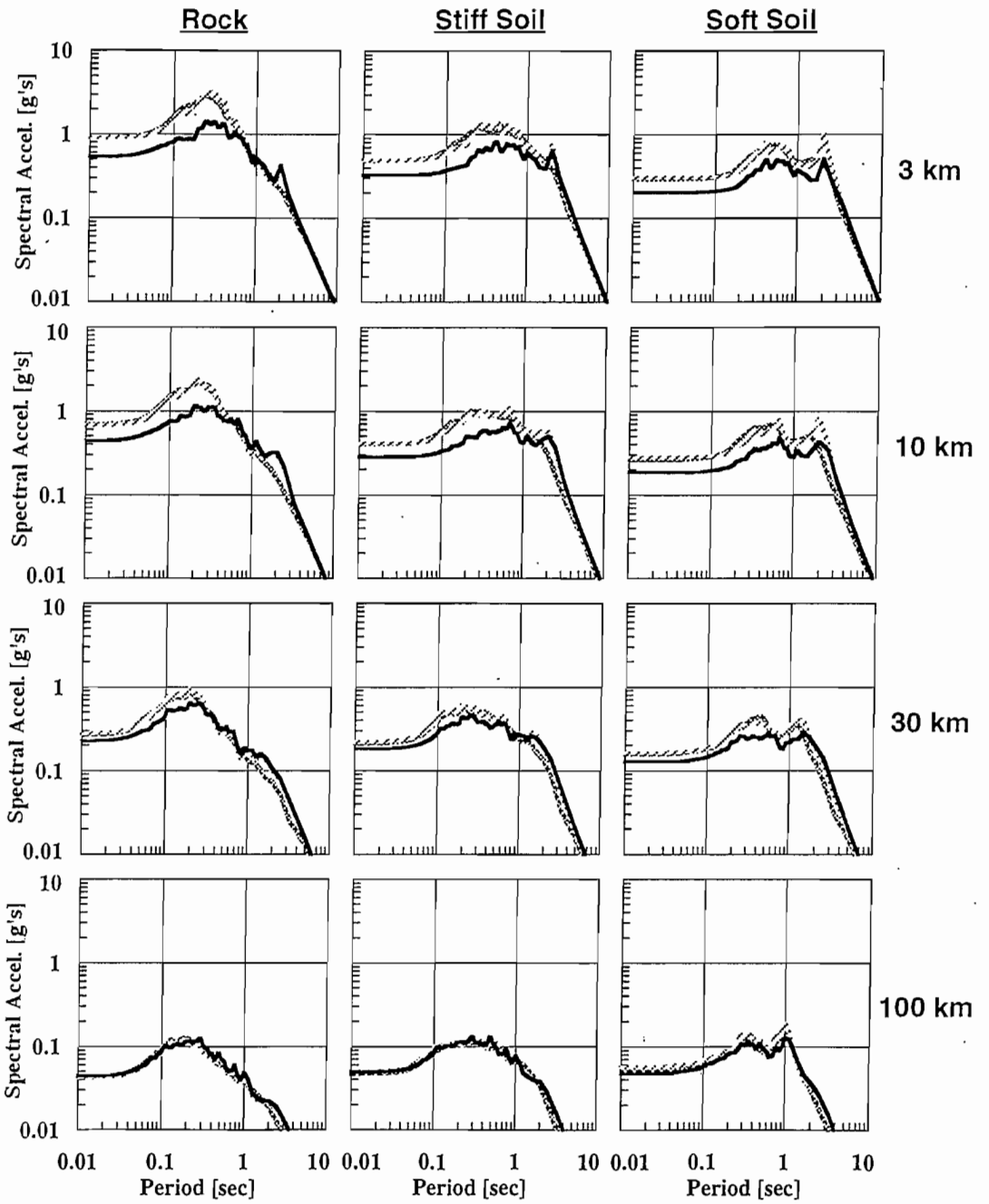

Key	Source (Slip, Focus)	Path (Q_o, η, κ)	Site (Profile, Material)
Vary Source	Randomized	Fixed	Fixed
Vary Path	Fixed	Randomized	Fixed
Vary Site	Fixed	Fixed	Randomized

Figure 5b. Median Spectral-Response for Individually Randomized Source, Path, and Site Parameter Groups

(100 km) where site response is nearly linear. However, as the level of motion increases (e.g. at closer distances), a randomized profile containing low-velocity layers, or "notches", will tend to accumulate high levels of strain at these notches. This, in turn, tends to both increase scattering due to higher velocity contrasts (lower modulus-reduction values) as well as increase the value of hysteretic damping (D) for the layers undergoing higher strain, thus reducing output motion. Therefore, since randomized profiles will include a certain number of realizations having low-velocity notches, the median output should be lower than the median response of the smooth base-case site profile. An interesting converse to this observation is that the output for a smooth median profile tends to approach the one-sigma motion of the randomized set for strong levels of motion.

Also notable in the median results of Fig. 5b is the somewhat peculiar dual-peak spectral shape for the marine-clay profile. This response is a result of the very particular nature of the specified velocity profile which leads to a site resonance near 1 to 2 seconds. Note that the resonsance peak shifts toward longer period as the level of motion increases and the materials soften.

An alternative approach for evaluation of the variability contribution of a particular parameter group is to examine the reduction in spectral-response variability associated with fixing that parameter group relative to the case where all parameters are varied simultaneously. Figure 6 presents such results for the case where the site parameters are fixed, which is analogous to having "perfect knowledge" (no uncertainty or randomness) of site conditions. The "vary all" baseline case can similarly be viewed as analogous to having "no knowledge" of site conditions. Note, due to both soil non-linearity and coupling between parameter variabilities, the "vary all" case may not be the sum of individual parametric contributions shown in Fig. 5a (as illustrated for the rock site at 100 km). The results shown in Fig. 6 are fully complimentary to those presented in Fig. 5a, and perhaps provide a clearer picture of the potential impact of site characterization. Very pronounced benefits for reducing parametric variability are shown to be possible for periods ranging upwards to several seconds for soil sites at distances to 30 km. Similar benefits could be achieved for rock sites through at least 10 km, however, the period range is somewhat more restricted.

Finally, one must note that while the results of Fig. 6 clearly illustrates the potential for reducing parametric variability through site characterization, it would be unrealistic to expect that the full extent of this reduction is attainable since site data will always be both imperfect and have a certain random component. Using the nomenclature of Table 1, the difference between the "vary all" and "site known" cases in Fig. 6 represents the total parametric variability which includes both a reducible uncertainty component and an irreducible randomness component.

Reduction in Variability with Increased Depth of Site Characterization

The focus of this paper now shifts from establishing the broad impact of site effects to the more narrow issue of examining the potential benefit of characterizing different parameters of a site profile to increasing depths. This exercise considers only the single case of the stiff-soil profile at a fault-site distance of 10 km. Individual and combined site parameters are considered "known" (fixed) within three separate "characterization zones" of progressively increasing depth. Zones 1, 2, and 3, are defined to extend from the ground surface to depths of 30, 100, and 300 m, respectively, and are intended to be representative of typical, extensive, and research-quality depths for geotechnical site characterization. For each zone, the

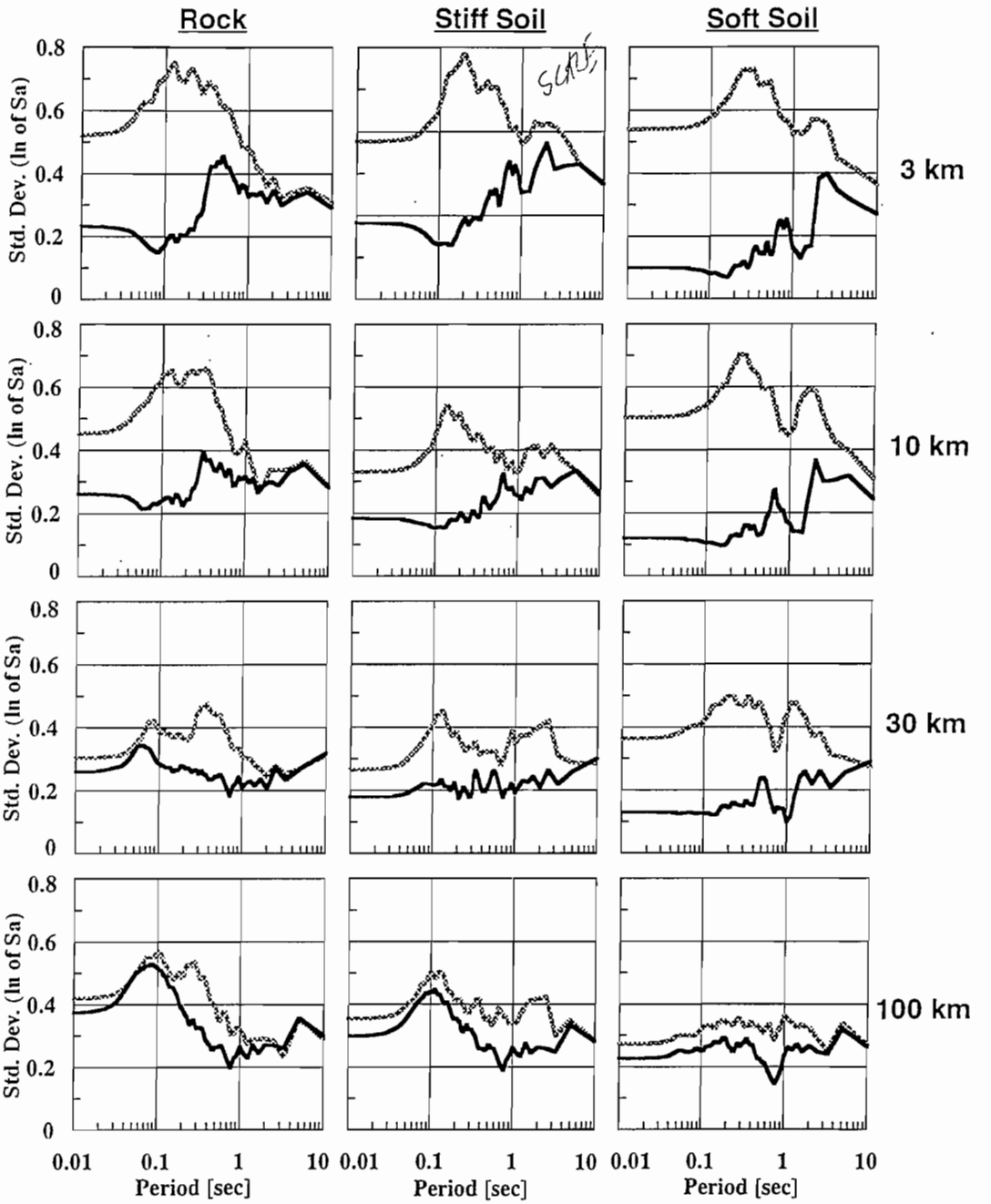

Key	Source (Slip, Focus)	Path (Q_o, η, κ)	Site (Profile, Material)
Vary All	Randomized	Randomized	Randomized
Site Known	Randomized	Randomized	Fixed

Figure 6. Change in Spectral-Response Parametric Variability Due To Fixing Only Site Parameters Group

parametric variability in spectral response is calculated for a fixed velocity profile, a fixed material model, and for the combination of both a fixed profile and fixed material model.

Figure 7 presents results of the characterization-zone analyses in each of two formats. A common baseline case where all parameters are varied is presented in all charts and is alternatively labeled "nothing fixed" and "zone 0". This baseline case serves as a reference from which to measure improvement or reduction in variability. Each chart in the upper row involves a single characterization zone, and shows variability results as site parameters are alternatively fixed both individually and in combination. For example, the cross-hatched line in the upper middle chart corresponds to having the velocity profile fixed and the material properties randomized for the upper 100 m of the profile, and both the velocity and the material model randomized below 100 m. The reduction in variability from the baseline case then corresponds to the benefit achieved by having perfect knowledge of only the velocity profile for the upper 100 m. The same results are rearranged and presented again in the lower row of charts. Here, each chart presents variability results as progressively deeper characterization zones are employed for a fixed single parameter or combination. For example, the cross-hatched line in the lower left chart shows results of fixing velocity only over the upper 100 m (same as above), while the heavy solid line represents velocity fixed over 300 m.

The results in Fig. 7 clearly show the well-anticipated trend toward reduced parametric variability as the depth of characterization progresses deeper. Furthermore, for this particular combination of ground-motion amplitude and site, fixing the velocity profile has a more substantial impact on reducing variability than fixing material properties alone, but fixing the combination of both profile and material properties provides a clear benefit for periods in the 0.1 to 1 second range. Note that one would expect the impact of the material curves to increase as strain amplitudes increase. The results in Fig. 7 also provide information regarding the incremental benefit of characterizing the profile to increased depths. These results suggest a very significant reduction in parametric uncertainty can be achieved for periods of up to approximately one second by extending the characterization zone to 100 m, while the marginal benefit of increasing the characterization depth to 300 m appears more limited.

The suite of examples presented in Figs. 5 through 7 are intended to provide some insight into general trends in site-response variability. Clearly, logical extensions of this work include examination of the impact of "realistic" rather than "perfect" site characterization, as well as performing characterization-zone analyses for a wider range of ground-motion amplitudes and site profiles. However, the more general purpose here has been to simply outline procedures whereby one can systematically examine the contribution of a particular parameter set to overall parametric variability in site response.

Modeling Variability

The primary focus thus far has been an examination of parametric variability in ground response, with particular emphasis placed on the role of geotechnical site effects. Modeling variability, as described in Table 1, represents the other component of variability in design ground-motion prediction. Detailed discussions of modeling variability for the stochastic finite-fault ground-motion model can be found in Silva [1992] and Schneider et. al. [1993]. A cursory review is presented here in the context of one of the case examples to provide a broader perspective of

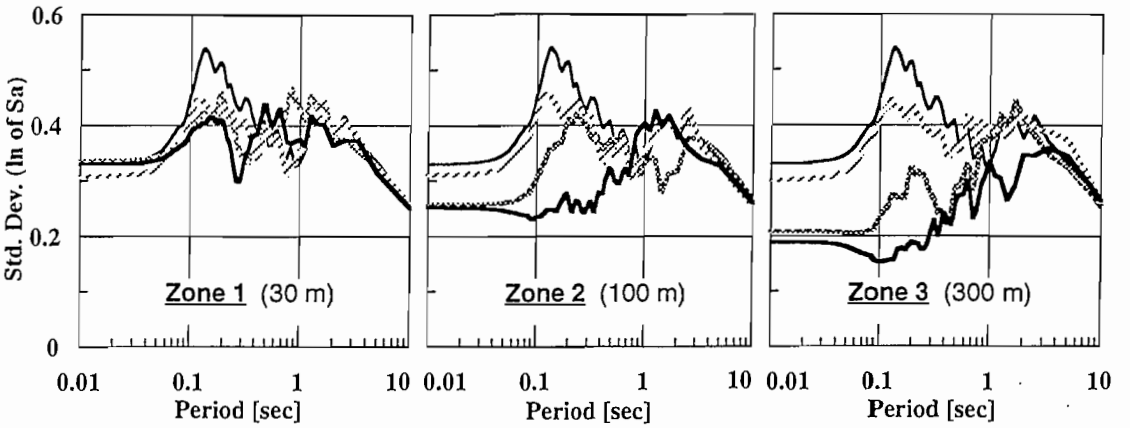

Key	Source (Slip, Focus)	Path (Q_o, η, κ)	Site (Profile)	Site (Material)
Nothing Fixed	Randomized	Randomized	Randomized	Randomized
Material Fixed	Randomized	Randomized	Randomized	Fixed in Zone
Velocity Fixed	Randomized	Randomized	Fixed in Zone	Randomized
Both Fixed	Randomized	Randomized	Fixed in Zone	Fixed in Zone

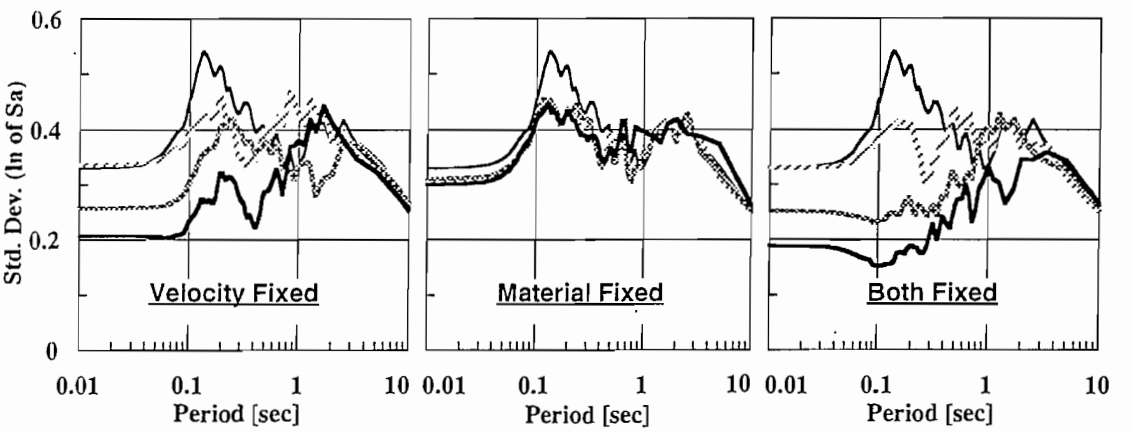

Key	Source (Slip, Focus)	Path (Q_o, η, κ)	Site (Profile or/and Material)
Zone 0 (0 m)	Randomized	Randomized	Randomized
Zone 1 (30 m)	Randomized	Randomized	Randomized Below 30 m
Zone 2 (100 m)	Randomized	Randomized	Randomized Below 100 m
Zone 3 (300 m)	Randomized	Randomized	Randomized Below 300 m

Figure 7. Change in Spectral-Response Parametric Variability Due To Fixing Individual and Combined Site Parameters Over 3 Depth Ranges for a Stiff Soil Profile Located 10 km from Fault.

the relative contributions of both modeling and parametric components to total variability.

Estimates of modeling variability are typically developed through a "calibration" exercise where model "predictions" are compared and optimized against a suite of strong-motion recordings. Quantitative assessment of modeling variability is typically calculated as the average squared residual for each period for a collection of sites and events, where the residual is defined as the difference between the logarithms of the observed and predicted 5%-damped spectral acceleration [Abrahamson et. al., 1990]. To assure the general applicability of the results of such a calibration exercise to future design predictions, it is important to sample as wide a suite of earthquakes, site conditions, and ground-motion-amplitude levels as possible using model parameters which are fixed by a consistent set of rules. A level of confidence can then be assigned to ground-motion predictions for future earthquake scenarios.

One estimate of modeling variability for the stochastic finite-fault model is shown in Fig. 8 (dotted line), and was developed from calibrations against the 1989 Loma Prieta and the 1987 Whittier Narrows earthquakes [Silva 1992]. Other validation exercises for the 1992 Landers and the 1994 Northridge events yielded similar results, and also showed that the site-specific estimates of ground motion produced by this stochastic model fit measured data as well as any comprehensive model currently available [Aki et.al., 1996]. Furthermore, Schneider et. al. [1993] show that modeling uncertainty for the stochastic model is comparable to the variance in attenuation relations developed from earthquake recordings, thus indicating a comparable level of predictive capability.

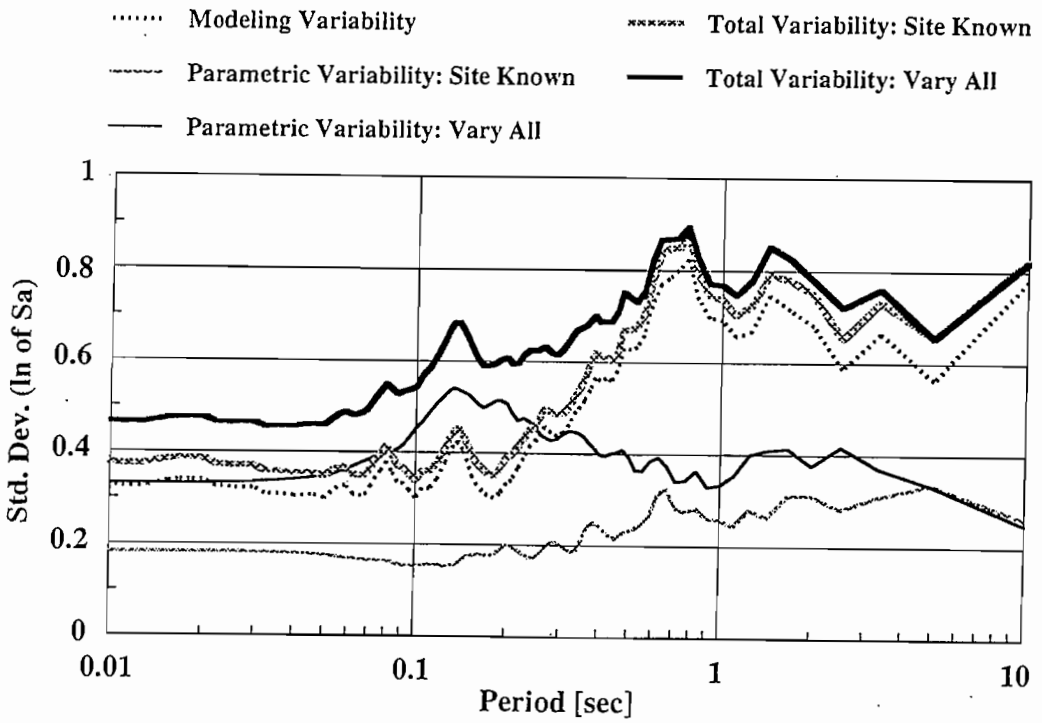

Figure 8. Comparison of Components of Variability for the Scenario Event and the Stiff-Soil Site at a Fault-Site Distance of 10 km.

In addition to modeling variability, Figure 8 also presents a comparison of two estimates each of both parametric variability and total variability for the stiff soil site at 10 km from the previous examples. The upper and lower estimates of parametric variability are based on the "vary all" and "site known" analyses, respectively, shown in Fig. 6. The total variability values are then computed as the vector sum of the modeling and parametric variabilities.

The comparison in Fig. 8 shows that for periods up to several tenths of a second, site-effects components of parametric variability comprise a significant proportion of total variability. For longer periods, modeling variability overshadows all sources of parametric variability including site-effects contributions. Therefore, for scenario conditions similar to those considered here, there is considerable value in extensive site characterization in terms of reducing variability in design predictions up to several tenths of a second. For longer oscillator periods, extensive site characterization is unlikely to provide meaningful reduction in the variability of predictions given the capabilities of current ground-motion models. Note that similar levels of variability exist for current empirical attenuation relationships, so target-spectra design approaches are constrained by the same lack of predictive capability for long-period motions. However, it is critical to keep in mind that even though total variability at long periods is little affected by knowledge of site properties, such information can have a very significant impact on predictions of median response.

Finally, it is important to note that the calibration exercises used to estimate modeling variability inherently include a considerable component of parametric uncertainty regarding site effects. This stems from using very simple generic rock and/or soil profiles during the calibration since little site-specific data are currently available for most strong-motion recording stations. Therefore the estimates of total variability shown in Fig. 8 are somewhat misleading in that they may "double count" site-effects variability to some extent. Therefore, significant improvements in modeling may become possible as more information from recording sites becomes available.

Summary and Conclusions

Variability in computed earthquake ground response has been examined using a stochastic finite-fault model which allows even treatment of source, path, and site components of ground-motion variability. A suite of examples were presented which illustrate how parametric variability can be systematically examined on a site-specific basis, and it was shown that the parameters which control ground-motion predictions are a function of the site-profile type, the amplitude of motion, and the period range of interest to the designer. The impact of site effects, as characterized by the near-surface velocity profile and non-linear material parameters, was shown to be the predominant source of parametric response-spectra variability up to several seconds for soil sites experiencing strong to moderate levels of motion. The example of varying drilling depth for a single scenario was used to illustrate how specific parameters controlling response variability can be isolated. A comparison of parametric and modeling variability for the same scenario showed clear benefits of performing detailed site characterization in terms of reducing variability of design predictions for response periods through several tenths of a second, but for longer periods, the benefit of extensive site characterization is primarily related to median response rather than reduction in variability due to the poorly-constrained nature of current ground-motion models at these periods. While the suite of examples presented herein are insufficient to comprehensively evaluate either the role of site

effects or the impact of geotechnical characterization on ground-response predictions, the results presented do illustrate major trends in behavior, and most importantly, provide a clear road map for treatment of such issues on a case-specific basis within the broader framework of total ground-motion variability.

Acknowledgments

This work was supported under Federal Project F94TL18 of the State Planning and Research Program of the California Department of Transportation (Caltrans). The authors wish to acknowledge Sylvia Li, Cathy Stark, and Ky Lang Silva of Pacific Engineering and Analysis for their assistance in developing the results presented herein. Also, the lead author would like to acknowledge both Joe Holland and Wes Lum of Caltrans' Office of Research for providing a supportive environment in which to explore these and other significant earthquake ground-motion issues.

References

Abrahamson, N.A., P.G. Somerville, and C.A. Cornell, 1990, "Uncertainty in Numerical Strong Motion Predictions", Proceedings of the Fourth U.S. National Conference on Earthquake Engineering, Palm Springs, CA, Vol. 1, pp 407-416.

Aki, K., G. Martin, J. Chin, N. Abrahamson, A. Cornell, and M. Mahdyiar, 1996, "The Characteristics of Earthquake Ground Motions for Seismic Design", Report on Task H7, Southern California Earthquake Center.

Anderson, J.G., and S.E. Hough, 1984, "A Model for the Shape of the Fourier Amplitude Spectrum of Acceleration at High Frequencies", Bulletin of the Seismological Society of America, Vol. 74, pp. 1969-1993.

Boore, D.M., 1983, "Stochastic Simulation of High-Frequency Ground-Motions Based on Seismological Models of the Radiated Spectra", Bulletin of the Seismological Society of America, Vol. 73, No. 6, pp. 1865-1894, December.

Boore, D.M., 1986, "Short Period P and S-Wave Radiation from Large Earthquakes: Implications for Spectral Scaling Relations, Bulletin of the Seismological Society of America, Vol. 76, No. 1, pp. 43-64.

Dickenson, S.E., 1994, "Dynamic Response of Soft and Deep Cohesive Soils During the Loma Prieta Earthquake of October 17, 1989", Ph.D. Dissertation, University of California at Berkeley, June, 331 p.

Hanks, T.C., and R.K. McGuire, 1981, "The Character of High-Frequency Strong Ground Motion", Bulletin of the Seismological Society of America, Vol. 71, No. 6, pp. 2071-2095, December.

National Research Council, 1988, "Probabilistic Seismic Hazard Analysis", Report of the Committee on Seismology, National Academy Press, Washington, D.C., 97 p.

Pyke, R., 1993, "Modeling of Dynamic Soil Properties", Early Site Permit Demonstration Program: Guidelines for Determining Design Basis Ground Motions, EPRI Project RP3302, Volume II, Appendix 7A.

Schnabel, P.B., J. Lysmer, and H.B. Seed, 1972, "SHAKE: A Computer Program for Earthquake Response Analysis of Horizontally Layered Sites", Report EERC 72-12, Earthquake Engineering Research Center, University of California at Berkeley.

Schneider, J.F., W.J. Silva,and C. Stark, 1993, "Ground Motion Model for the 1989 M6.9 Loma Prieta Earthquake Including Effects of Source, Path, and Site", Earthquake Spectra, Vol. 9, No. 2, pp. 251-287.

Silva, W.J., 1993, "Quantification of Site Effects", Early Site Permit Demonstration Program: Guidelines for Determining Design Basis Ground Motions, EPRI Project RP3302, Volume I, Section 6.

Silva, W.J., 1992, "Factors Controlling Strong Ground Motion and Their Associated Uncertainties", Proceedings of the ASCE Symposium on Dynamic Analysis and Design Considerations for High-Level Nuclear Waste Repositories, San Francisco, CA, August.

Silva, W.J., R.B. Darragh, C. Stark, I. Wong, J.C. Stepp, J. Schneider, and S.J. Chiou, 1990, "A Methodology to Estimate Design Response Spectra in the Near-Source Region of Large Earthquakes Using the Band-Limited-White-Noise Ground-Motion Model", Proceedings of the Fourth U.S. National Conference on Earthquake Engineering, Palm Springs, CA, EERI, Vol. 1, pp 487-494.

Toro, G.R., N.A. Abrahamson, and J.F. Schneider, 1995, "Engineering Model of Strong Ground Motions from Earthquakes in the Central and Eastern United States", (submitted for publication) Earthquake Spectra, EERI

Toro, G.R., 1993, "Probabilistic Model of Soil-Profile Variability", Early Site Permit Demonstration Program: Guidelines for Determining Design Basis Ground Motions, EPRI Project RP3302, Volume II, Appendix 6A.

Vucetic, M., and R. Dobry, 1991, "Effect of Soil Plasticity on Cyclic Response", ASCE, Journal of Geotechnical Engineering, Vol 117, No. 1, pp. 89-107.

Wells, D.L., and K.J. Coppersmith, 1994, "New Empirical Relationships Among Magnitude, Rupture Length, Rupture Width, Rupture Area, and Surface Displacement", Bulletin of the Seismological Society of America, Vol. 84, No. 4, pp. 974-1002, August.

Evaluation and Implementation of an Improved Methodology for Earthquake Ground Response Analysis

Uniform Treatment of Source, Path and Site Effects

Application Example B

Case Study: Site-Specific Motions at I-10 La Cienega Bridge in LA

Reference: ROSRINE Data Workshop, December 15-16, 1998

Abstract:

Extensive geotechnical site characterization work was completed as part of the installation of the Caltrans/CDMG deep strong-motion array located at the I-10 La Cienega site in Los Angeles and as part of the ROSRINE (Resolution of Site Response Issue from the Northridge Earthquake) research project to explore uncertainties in earthquake site response. Key geotechnical parameters affecting site response are the shear-wave velocity profile and the non-linear properties (normalized modulus and material damping) assigned to soil strata. To capture uncertainty in velocity profile, alternative geophysical methods including P-S suspension, crosshole, downhole and Spectral-Analysis-of-Surface-Waves (SASW) surveys were performed in close proximity by independent organizations. Similarly, three different types of laboratory testing equipment were employed by independent organizations on near-identical soil specimens to capture uncertainty in non-linear properties caused by testing differences. Extensive sampling and testing of specimens obtained at depths up to 240 m allowed development of a *preliminary* depth-dependent model for non-linear properties including representation of uncertainties related to differences in soil type and potential sampling disturbance effects.

The stochastic method described in Application Example A is used to conduct sensitivity analyses using the extensive data available from the La Cienega site. First, the sensitivity of calculated surface motion to level of detail in the interpretation of shear-wave profile is explored; Differences are shown to be minimal with less detail (smoother velocity gradient) providing a slightly higher surface motion. This is conducted using both randomized and non-randomized velocity profiles. An important finding is that calculated median surface motions for the non-randomized profiles (regardless of level of detail) are significantly (50% to 100%) higher than those from the randomized analysis. Next, another series of analyses are conducted to explore the sensitivity of surface motions to the non-linear soil model employed; Results show very high sensitivity to non-linear model with depth-dependent models producing much higher motions. Linearizing the soil model below 100 m achieves substantial convergence. Finally, the impact of potential soil disturbance is shown to be about a 20% effect for this site profile.

La Cienega: Case Study

Site Background

Validation of, & Uncertainty in Measurements

- Geophysical Methods for In Situ Velocity
- Laboratory Methods for Non-Linear Properties

Site Idealization & "Engineering Models"

- Velocity Profile
- Stratigraphy
- Non-Linear Models

Parametric Analyses

- Sensitivity to Profile Detail
- Impact of Disturbance-Adjustment Factor
- Alternate Non-Linear Models

La Cienega Site Location Relative to Northridge

1. Portero P-2 (Canyon Edge)
   Portero P-3 (Canyon Center)
2. Portero P-1 (USC SM Station)
3. Newhall Fire Station
4. Pacoima Downstream
5. Olive View Hospital (OVH)
6. Jensen Main Building
   Jensen Generator Building
7. Sylmar Converter West (SCW)
   Sylmar Converter East (SCE)
8. LA DAM (LAD)
9. Kagel Canyon
10. Rinaldi (RIN)
11. Sepulveda VA (Rosrine)
    Sepulveda VA (USGS)
12. Arleta (Nordhoff) Fire Station
13. Epiphany Luthern (ELC)
14. Tarzana
15. Sherman Oaks Park (SOP)
    Sherman Oaks Wood (SOW)
16. La Cienega
17. Baldwin Hills

Caltrans Geotechnical Research

OLD LA RIVER CHANNEL

Location and Conceptual Depiction of Caltrans I-10 La Cienega Vertical Seismic Array

(Not To Scale)
12/7/96, CJR

Plan View

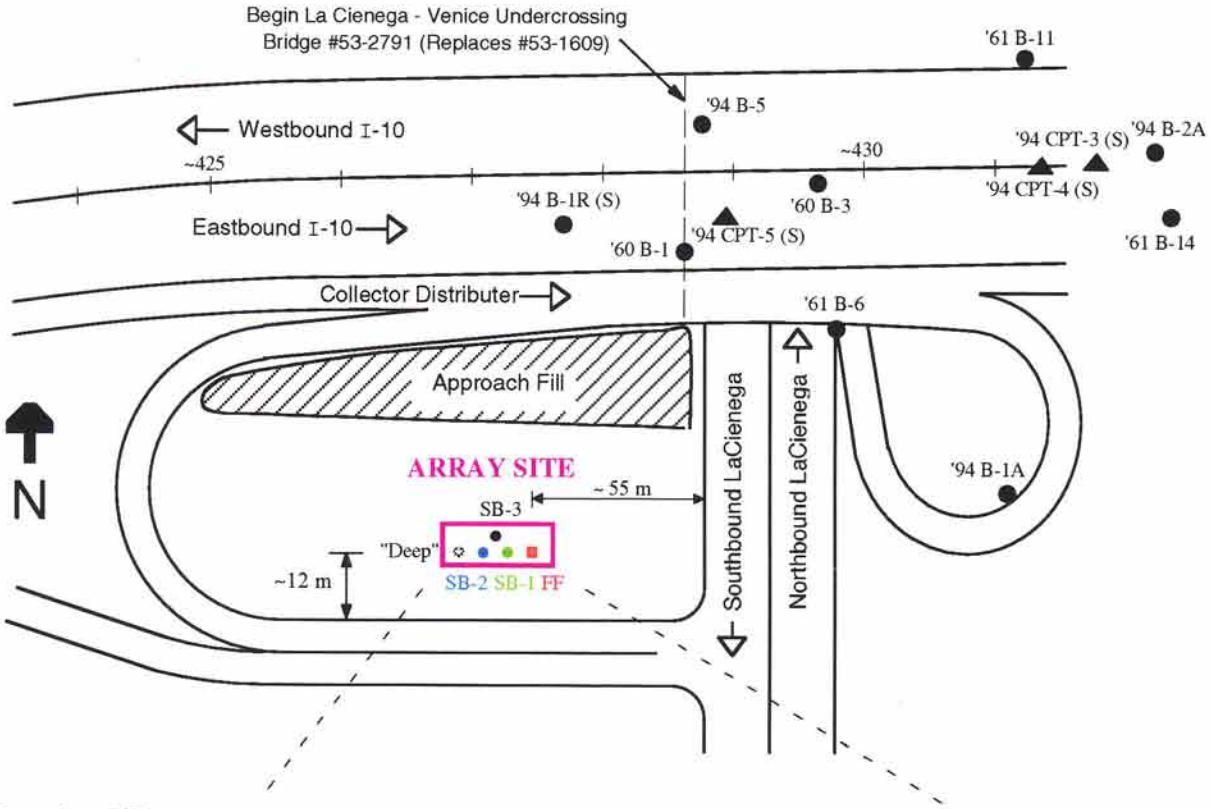

Elevation View

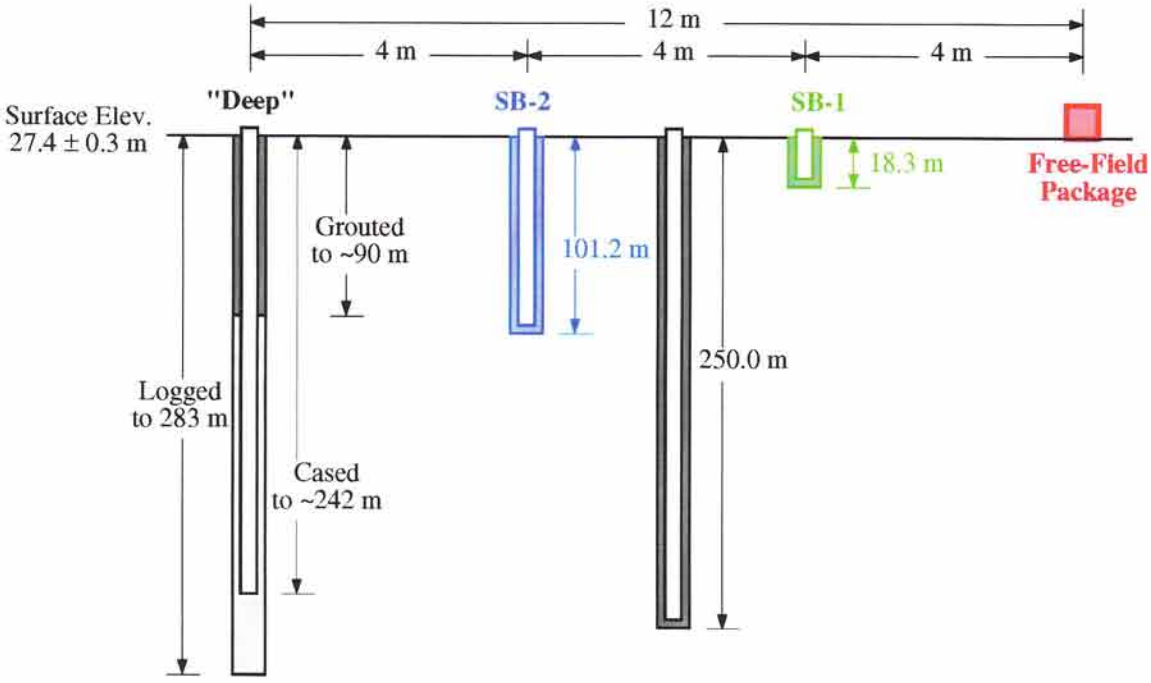

"Basic Array": SB-1 and SB-2 installed by CALTRANS. CDMG instrumentation operational in 1995.
"Enhanced Array": SB-3 and "Deep" site characterization by ROSRINE. CDMG to instrument in 1998.

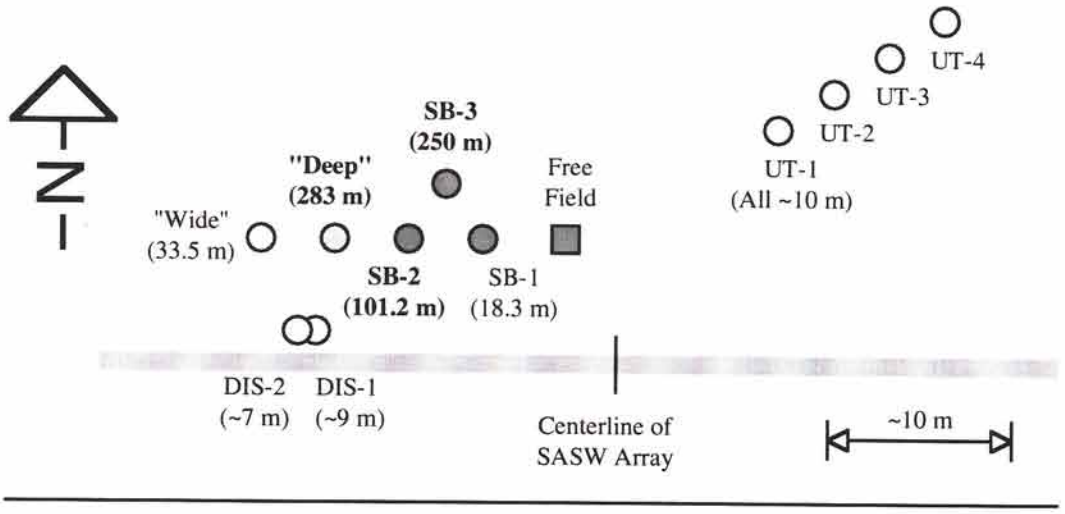

Fig. 4a) Relative Testing Locations at Caltrans I-10 La Cienega Geotechnical Array Site

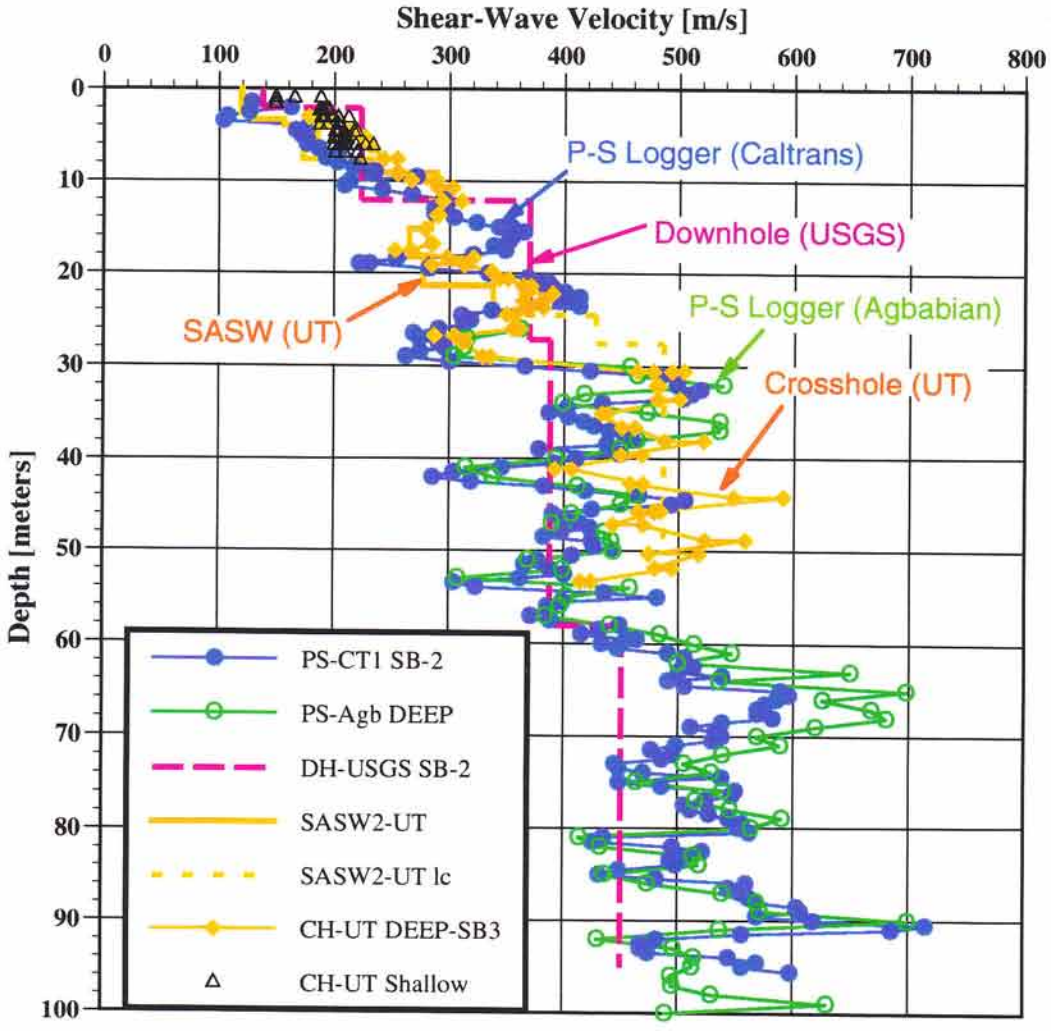

Fig. 4b) Comparison of In Situ Shear-Wave Velocity Measurements

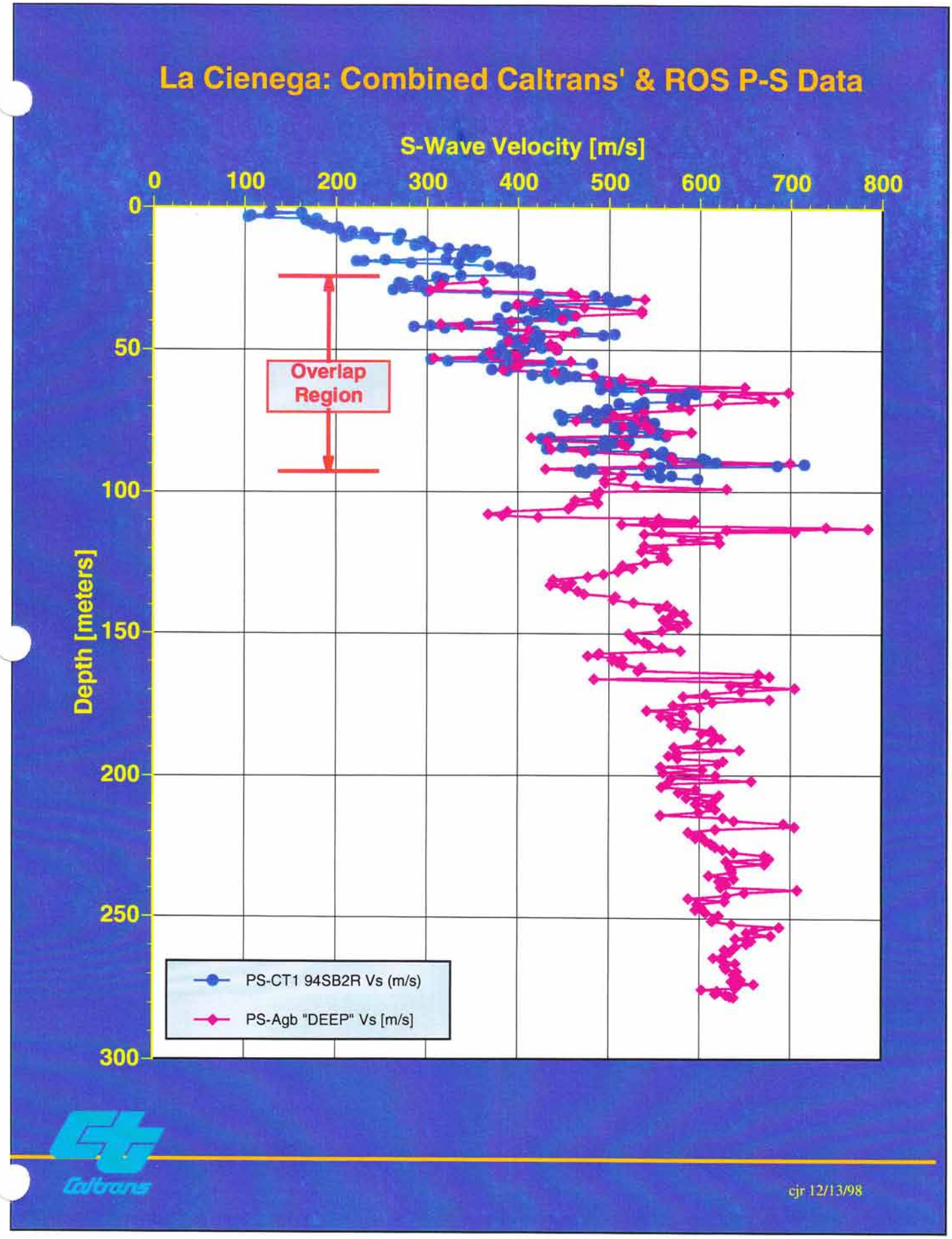
La Cienega: Combined Caltrans' & ROS P-S Data
S-Wave Velocity [m/s]
0
100
200
300
400
500
600
700
800
Depth [meters]
0
50
100
150
200
250
300
Overlap Region
PS-CT1 94SB2R Vs (m/s)
PS-Agb "DEEP" Vs [m/s]
Caltrans
cjr 12/13/98

La Cienega: Overlap of Caltrans' & ROS P-S Data

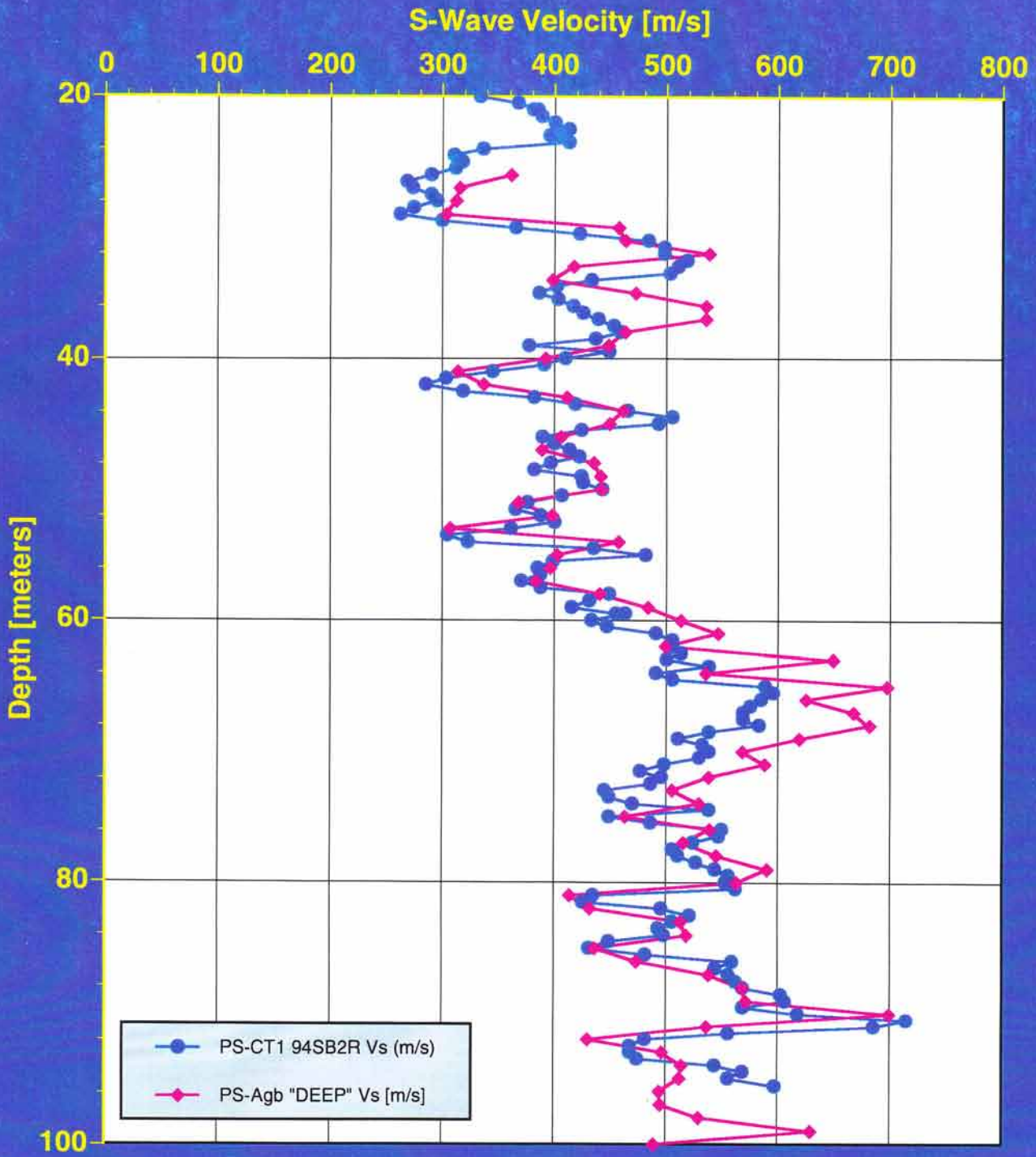

Caltrans

cjr 12/13/98

La Cienega: Comparison of Downhole & P-S Profiles

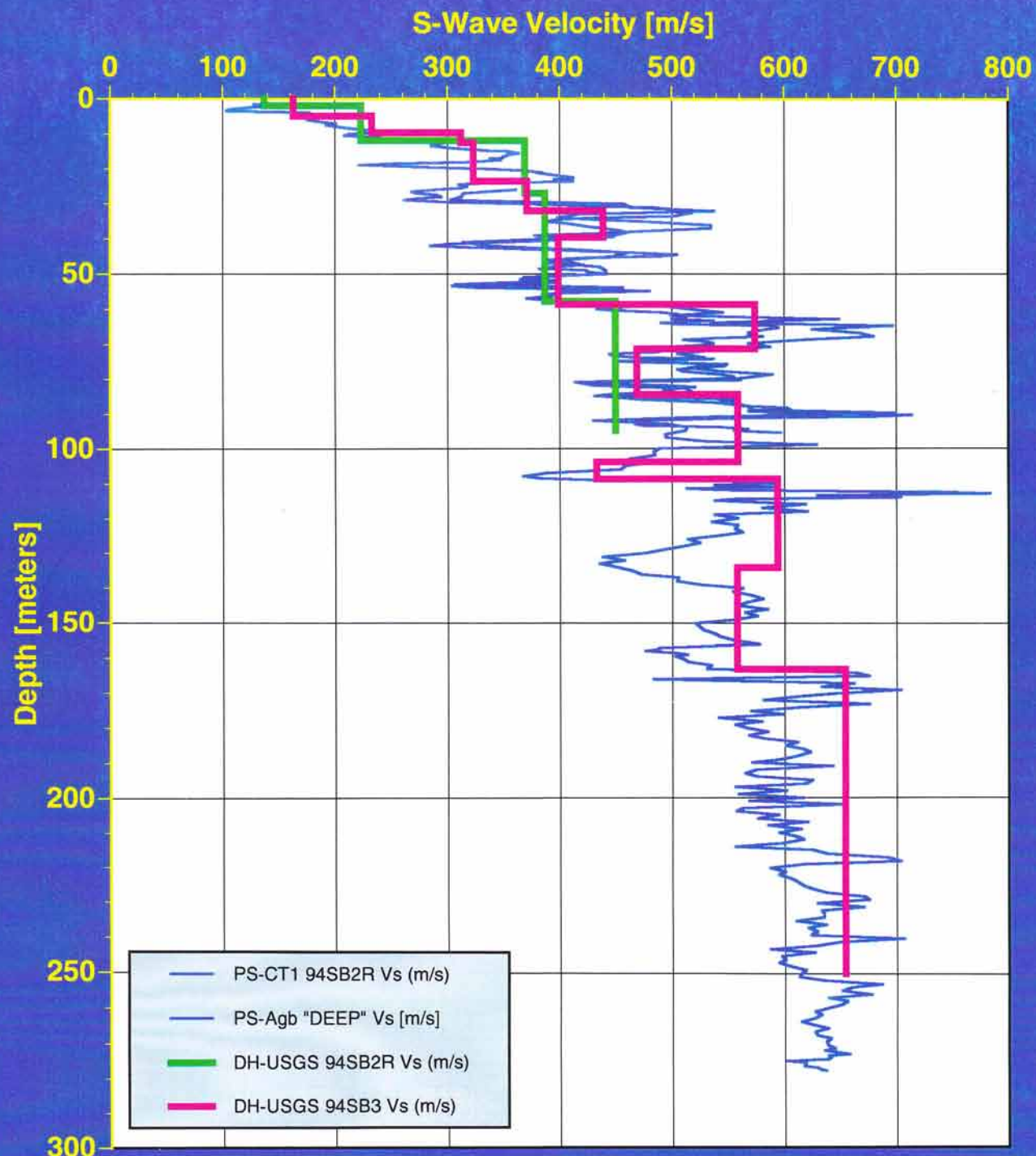

Caltrans

cjr 12/13/98

La Cienega: Comparison of DH & P-S Slowness Profiles

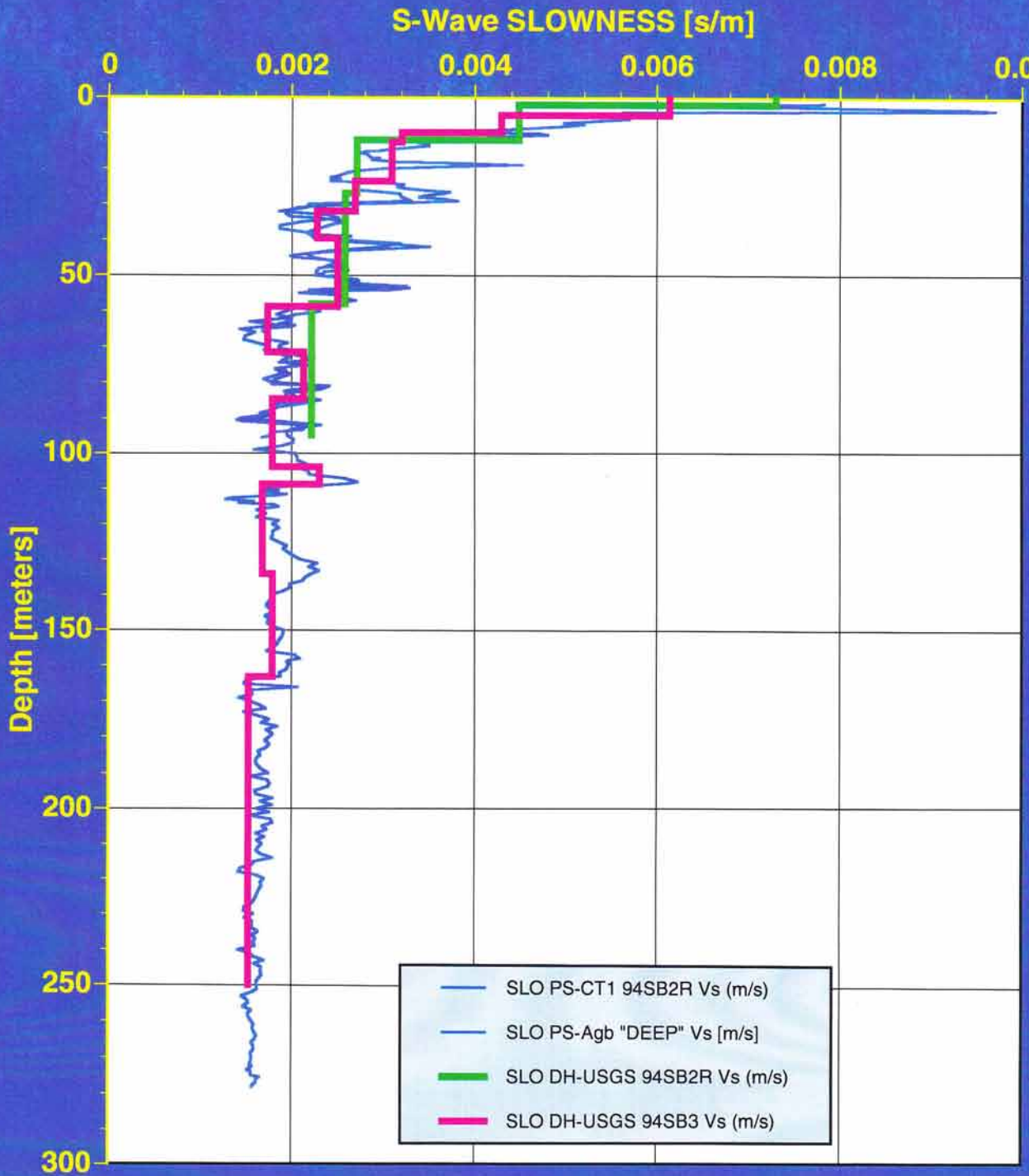

Caltrans

cjr 12/13/98

La Cienega: Borehole Deviation for Crosshole Test

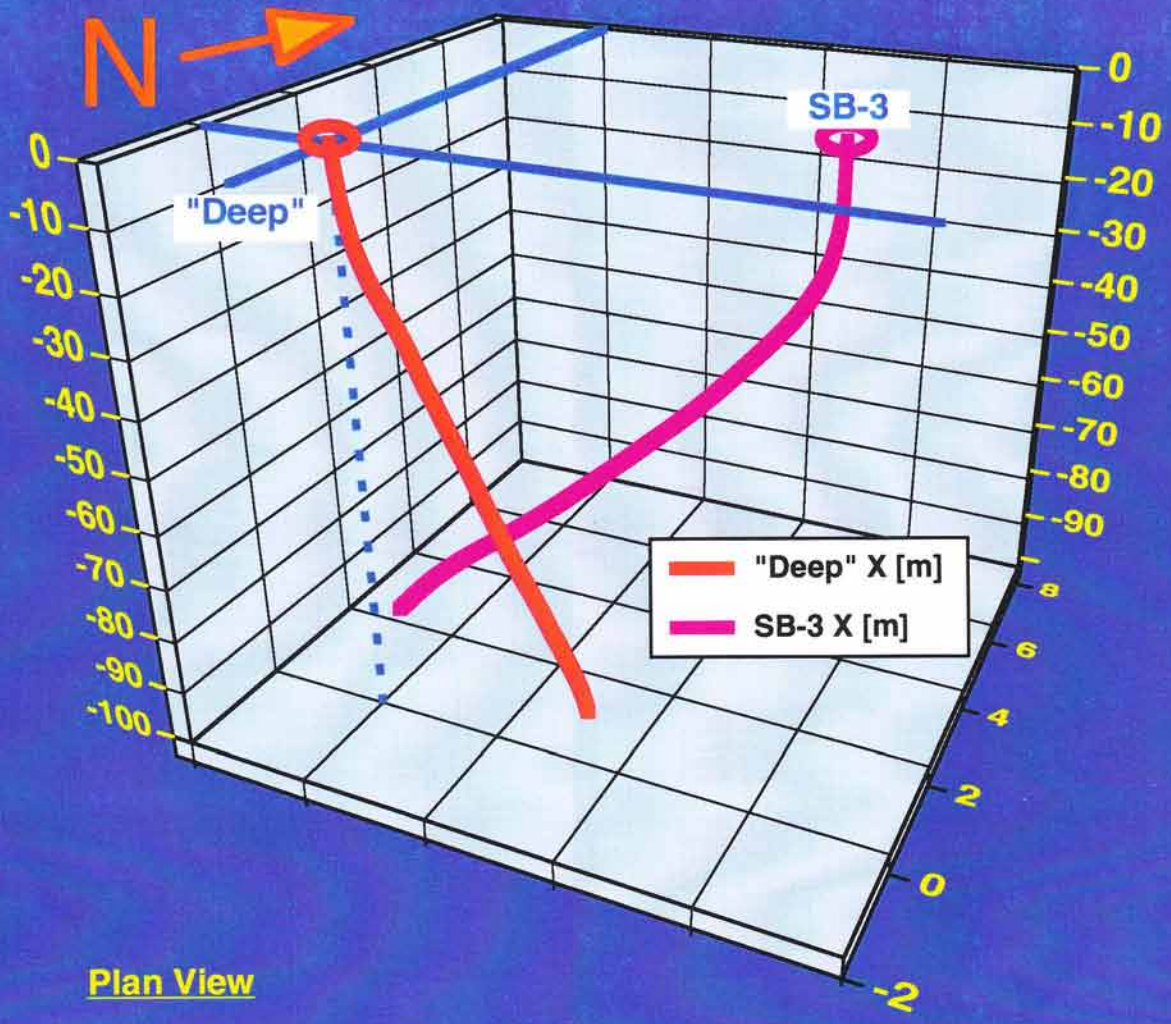

Plan View

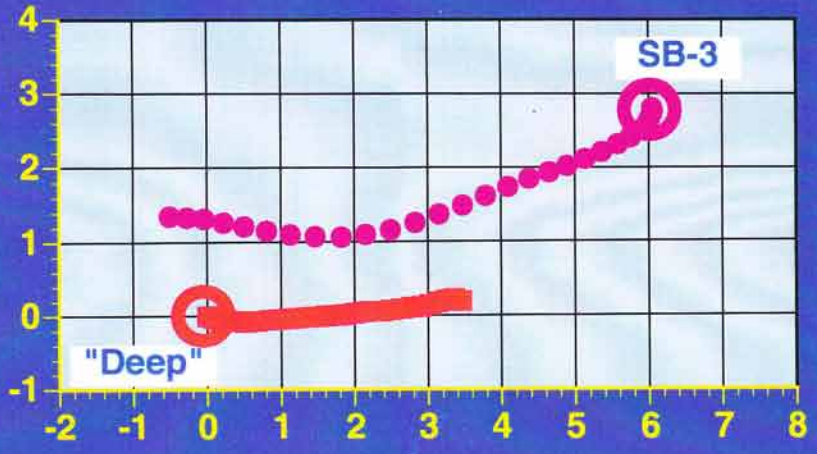

Caltrans

cjr 12/13/98

La Cienega: Comparison of Crosshole & P-S Profiles

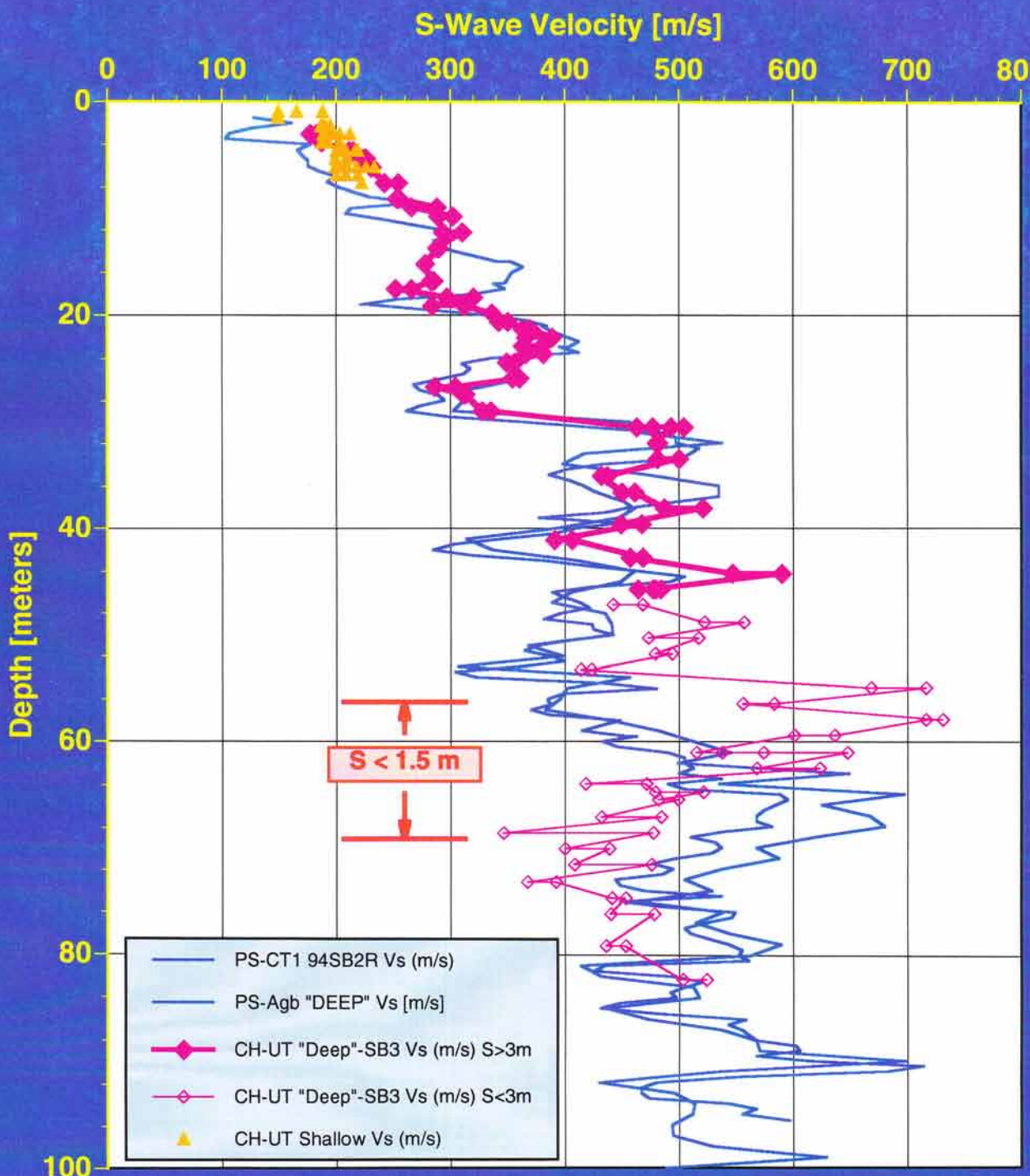

Caltrans

cjr 12/13/98

La Cienega: Comparison of SASW & P-S Profiles

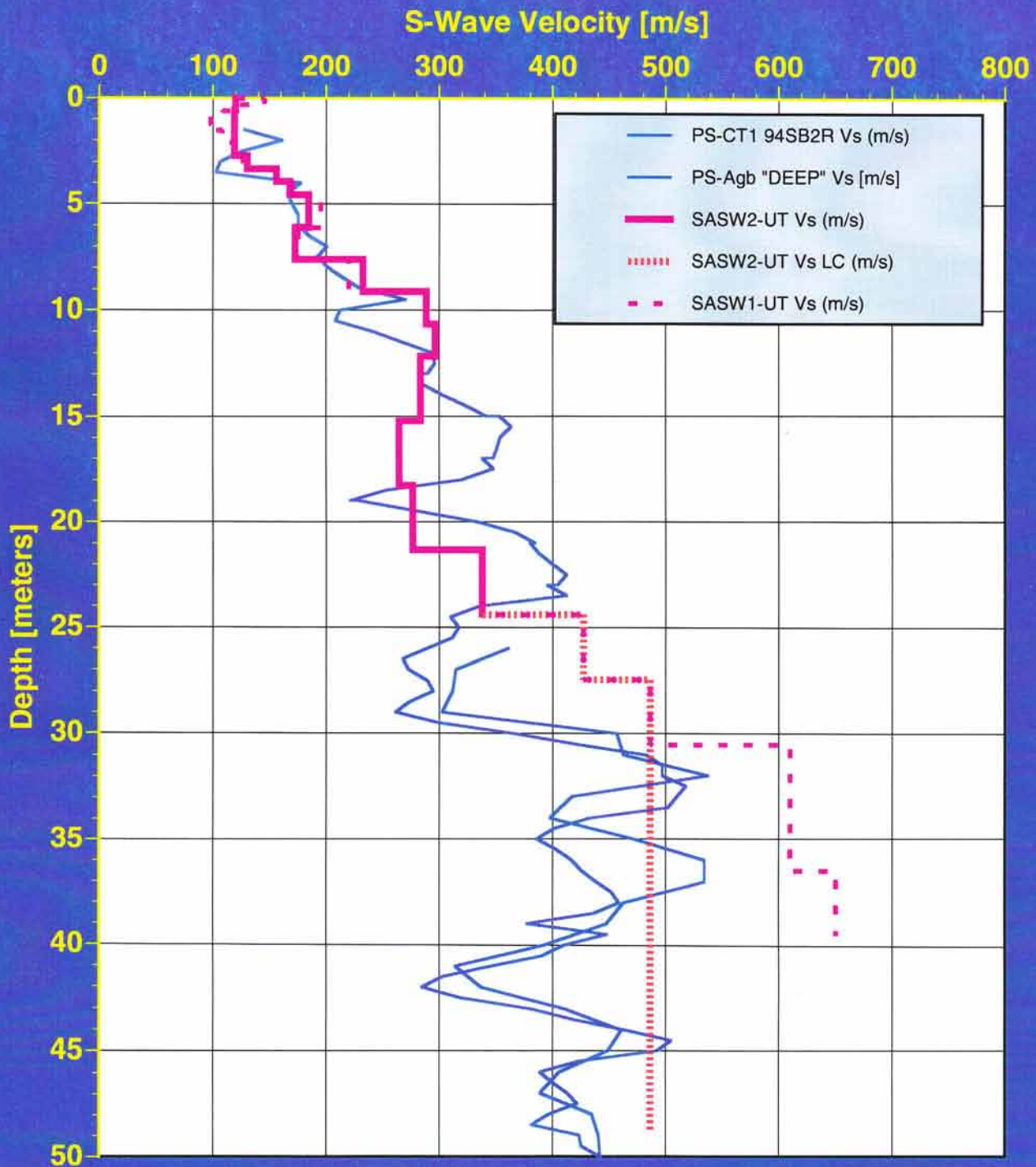

Caltrans

cjr 12/13/98

La Cienega: Comparison of All S-Wave Profiles

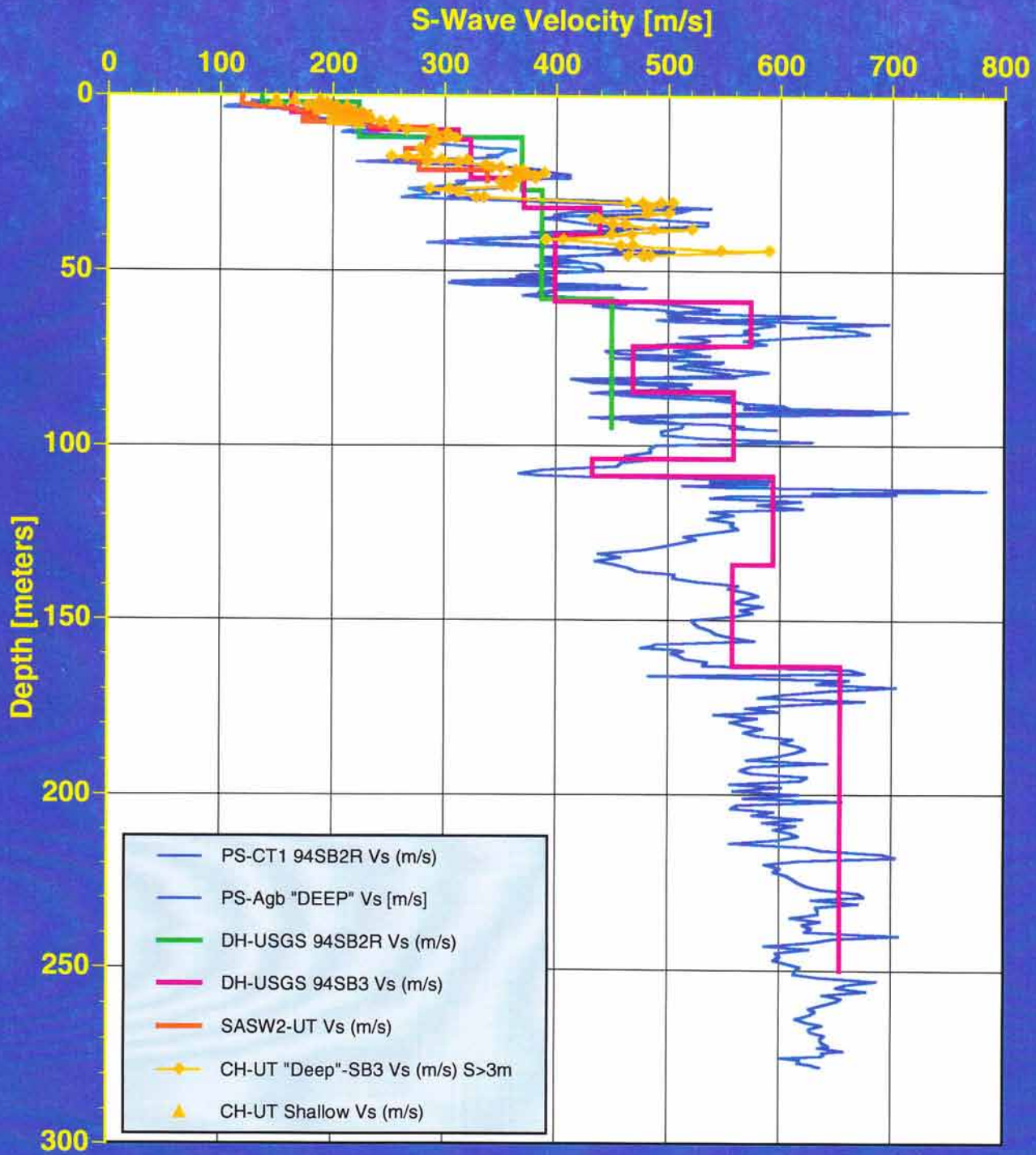

Caltrans

cjr 12/13/98

12

La Cienega: CT P-S Data for 2 Holes at ~60-m Separation

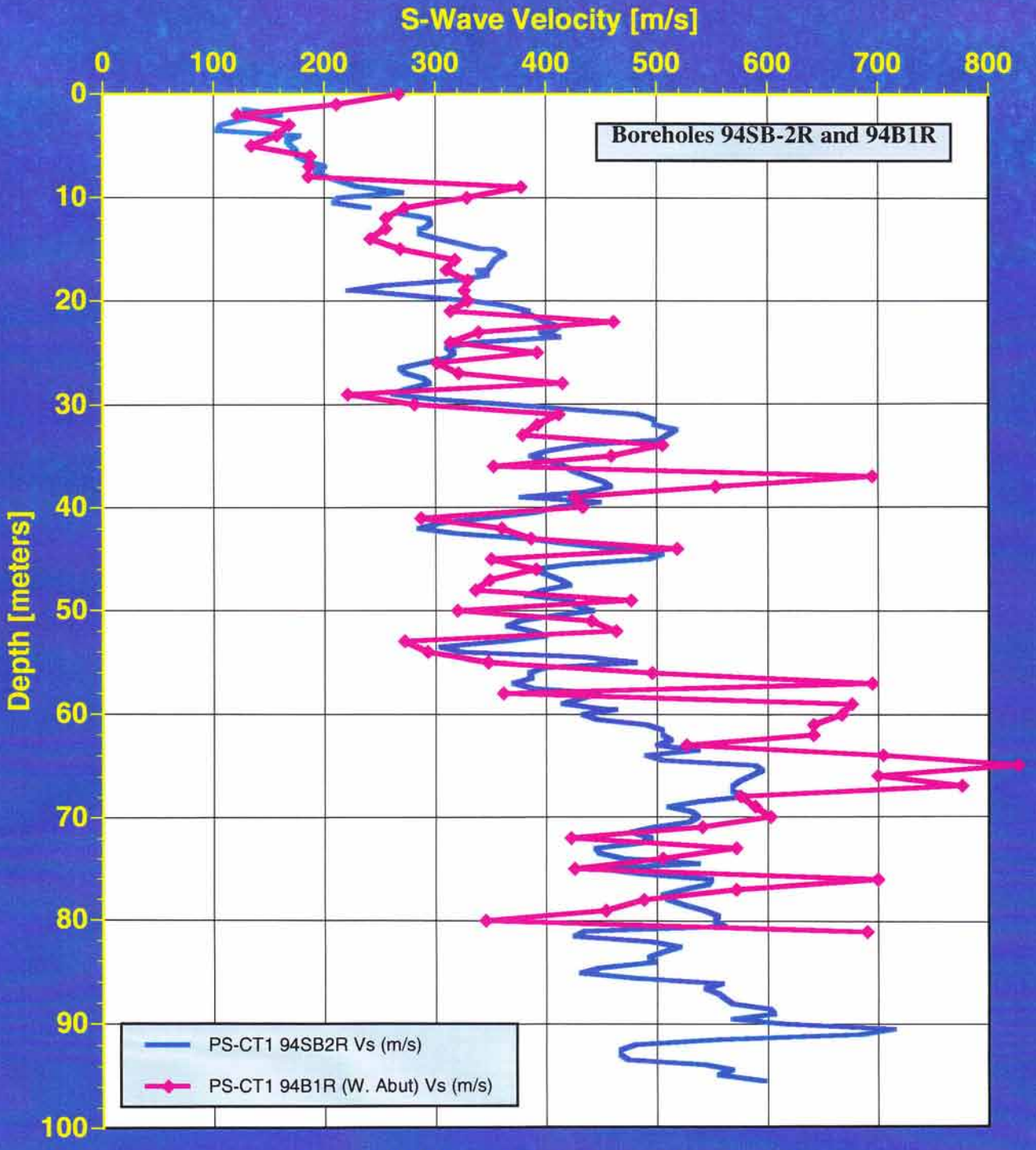

Depth for 94B1R Adjusted for Elevation Difference of Borings

Referenced to Ground Surface Elevation at Array Location: 27.6±0.1 m (90.7±0.3 ft)

Caltrans

cjr 12/13/98

La Cienega: 100-m Comparison of All P-Wave Profiles

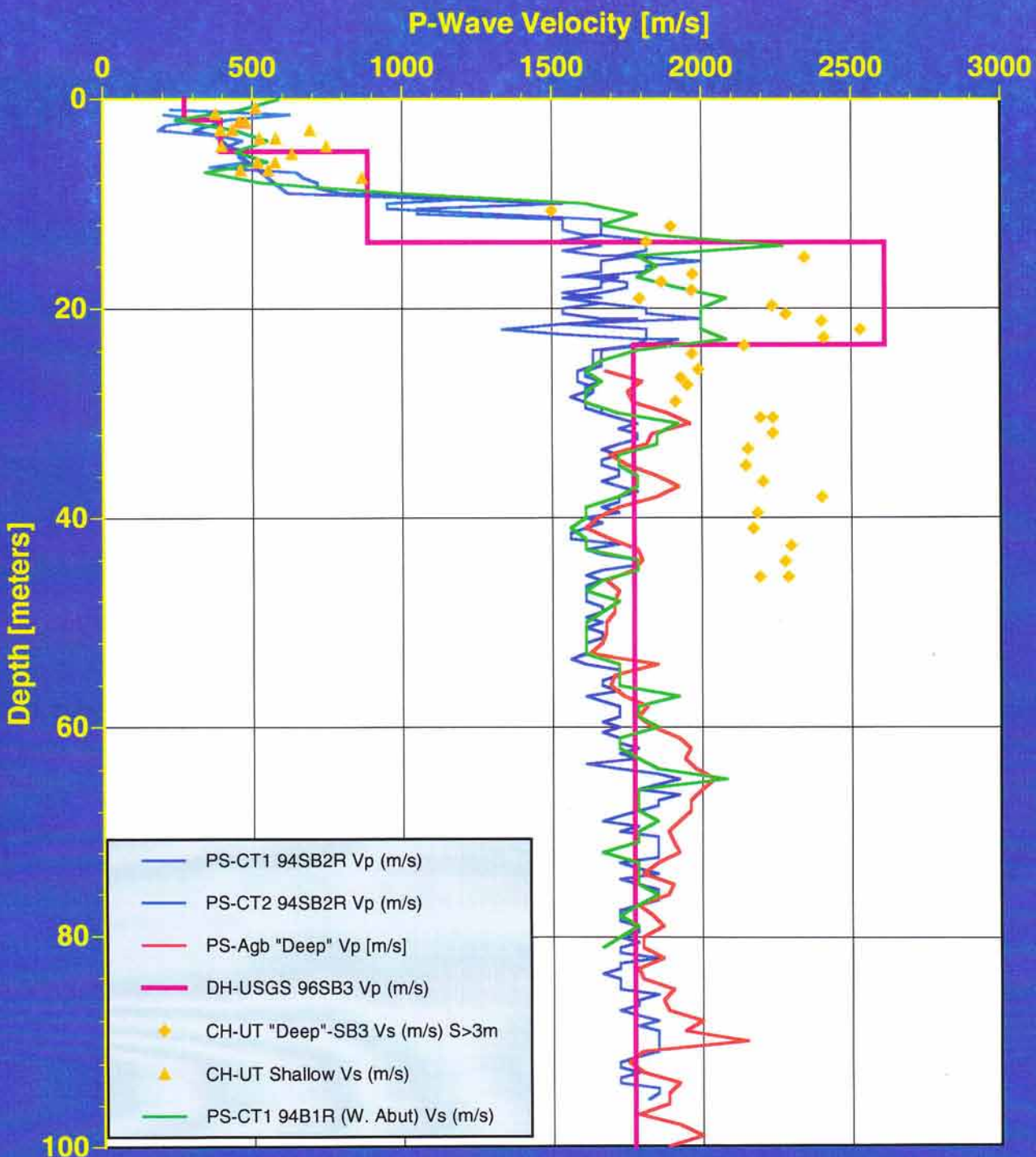

Caltrans

cjr 12/13/98

Controlled Comparison of Laboratory Tests for Non-Linear Material Properties

Extruding Laval Sample at La Cienega Site

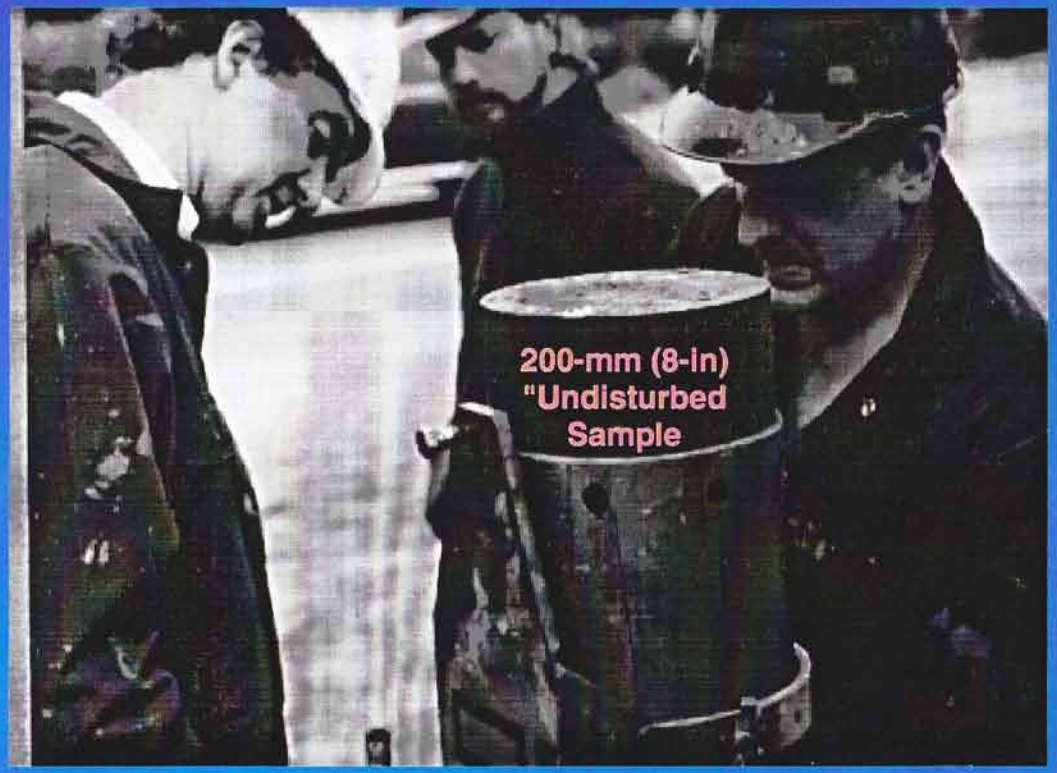

Subcutting Sample at UCLA

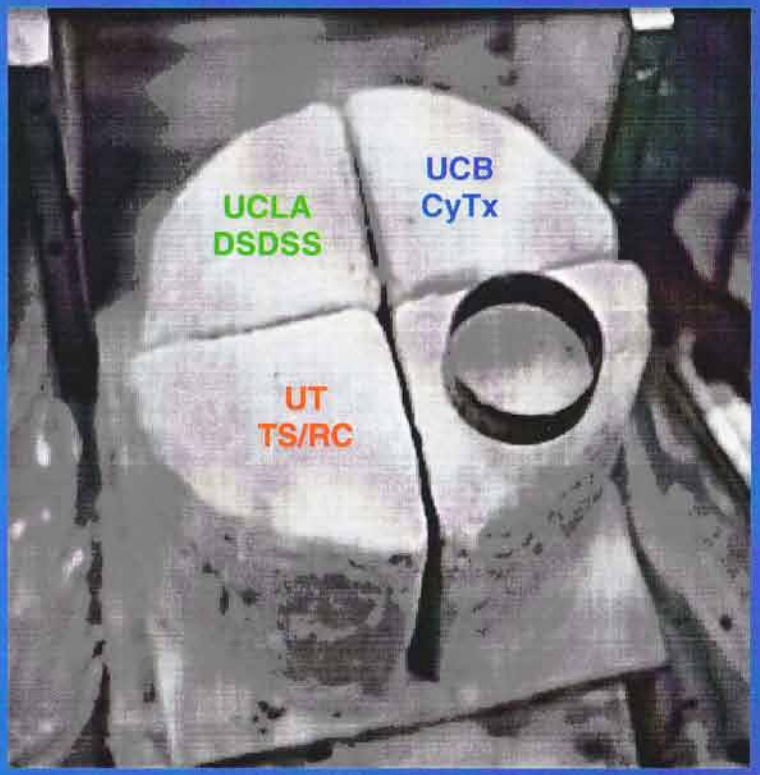

Caltrans Geotechnical Research

La Cienega: Comparison of Lab Results for Laval Samples

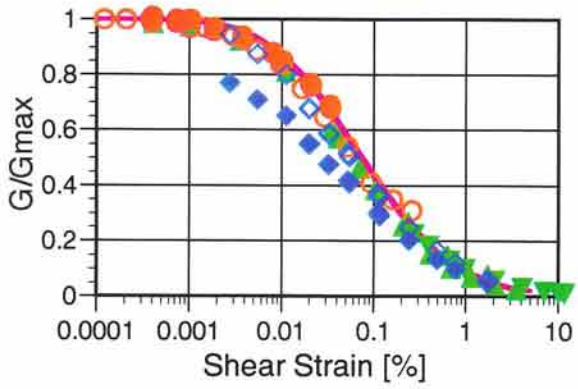

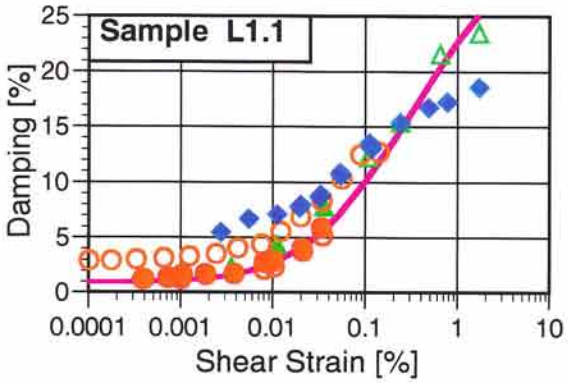

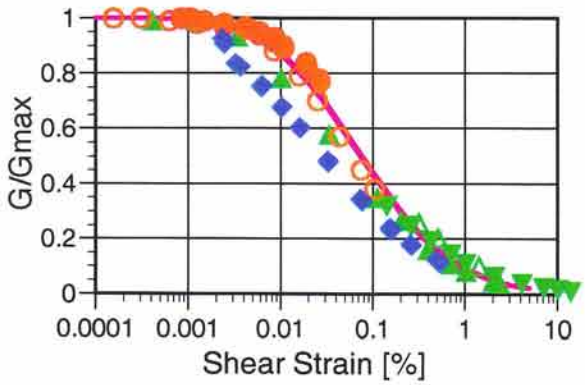

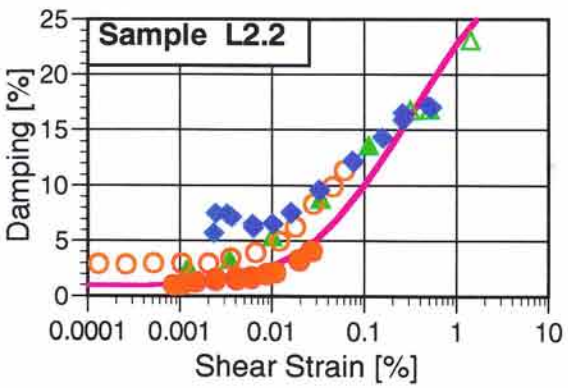

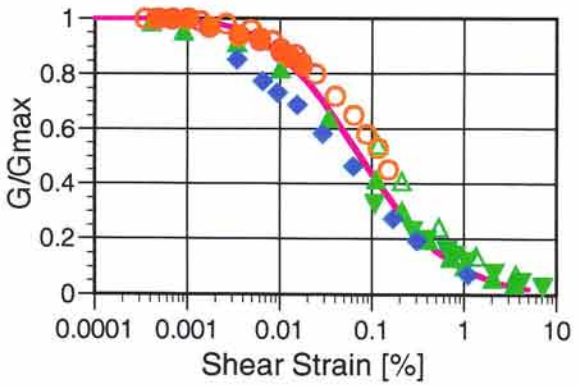

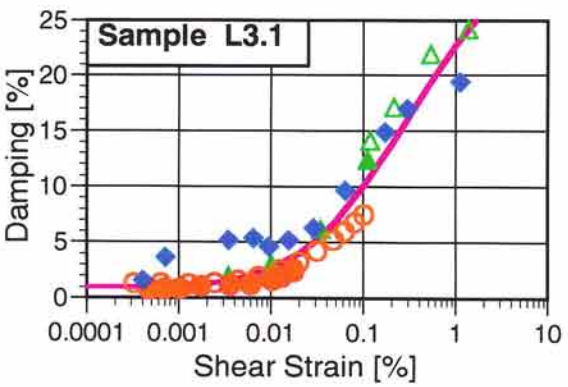

Texas	UCLA	UC-Berk
● TS-1	▲ DSDSS	◆ CyTx (bender Gmax)
⊙ TS-10	△ DSS-M	◇ CyTx (lab Gmax)
○ RC	▼ DSS-L	

La Cienega Site - Simplified CJR Model

Layer Depth [m]

From	To	Generalized Description	USC	Vs	Vp	Unit Wt.	Ref Strain	Dmin
0	4	Sandy Lean Clay w/ Silty Sand Lenses	CL	150	400	2.00	0.10	1.00
4	10	"	"	220	550	"	"	"
10	20	Mixed Coarse Alluvium	SM	300	1800	2.01	"	"
20	30	"	"	340	"	2.02	"	"
30	60	Mixed Fine Alluvium	CL	450	"	2.03	0.15	0.75
60	165	Mixed Coarse Alluvium	SM	540	"	2.04	0.20	"
165	204	"	SM	620	1900	2.05	0.30	0.50
204	280	Mixed Fine Alluvium	CL	640	1950	"	"	"

La Cienega Site - Detailed CJR Model

Layer Depth [m]

From	To	Generalized Description	USC	Vs	Vp	Unit Wt.	Ref Strain	Dmin
0	2	(Holocene) Sandy Lean Clay w/ Silty Sand Lenses	CL	140	400	2.00	0.10	1.00
2	4	"	"	180	"	"	"	"
4	7	"	"	210	500	"	"	"
7	10	"	"	240	600	"	"	"
10	13	Sands & Gravels w/ Silty Sand Lenses	SW-SM	280	1600	2.01	"	"
13	18	"	GM	310	1900	"	"	"
18	20	"	SW-SM	290	1850	"	"	"
20	22	"	GM	350	"	2.02	"	"
22	24	"	SW-SM	370	"	"	"	"
24	26	Lean to Fat Clay	CL	340	1800	"	"	"
26	30	"	"	320	"	"	"	"
30	34	Silty Sands and Sandy Lean Clays	SM	490	"	2.03	0.15	0.75
34	40	"	"	460	"	"	"	"
40	43	Lean Clay & Silt w/ Layers of Fat Clay	CL	390	1700	"	"	"
43	46	"	"	480	"	"	"	"
46	51	"	"	420	"	"	"	"
51	54	"	"	370	"	"	"	"
54	59	"	"	410	"	"	"	"
59	64	Silty Sands w/ Gravel	SM	520	1800	2.04	0.20	"
64	69	"	GM	600	"	"	"	"
69	72	"	SM	550	"	"	"	"
72	85	Silty Sands and Silts	SM	500	"	"	"	"
85	92	Sands & Gravels w/ Silty Sand Lenses	SP-SM	570	"	"	"	"
92	103	"	"	540	"	"	"	"
103	109	Fat Clay	CH	450	1700	"	"	"
109	120	Silty Sand	SM	590	1900	"	"	"
120	126	"	"	550	1800	"	"	"
126	136	"	"	500	"	"	"	"
136	154	Silt & Lean Clay	ML	560	"	"	"	"
154	166	Interbed Sand & Silt	SM	530	1900	"	"	"
166	175	Silty Sand & Sandy Silt	SM	640	"	2.05	0.30	0.50
175	182	"	"	570	"	"	"	"
182	204	"	"	600	"	"	"	"
204	218	Lean Clay	CL	600	"	"	"	"
218	242	Interbed Clayey Sand & Silty Sand	SC	640	1950	"	"	"
242	252	"	"	610	"	"	"	"
252	262	Silt to Fat Clay (near LL=50%)	ML-CH	650	"	"	"	"
262	280	"	"	630	"	"	"	"

La Cienega: "Detailed" & "Simplified" Interpretations

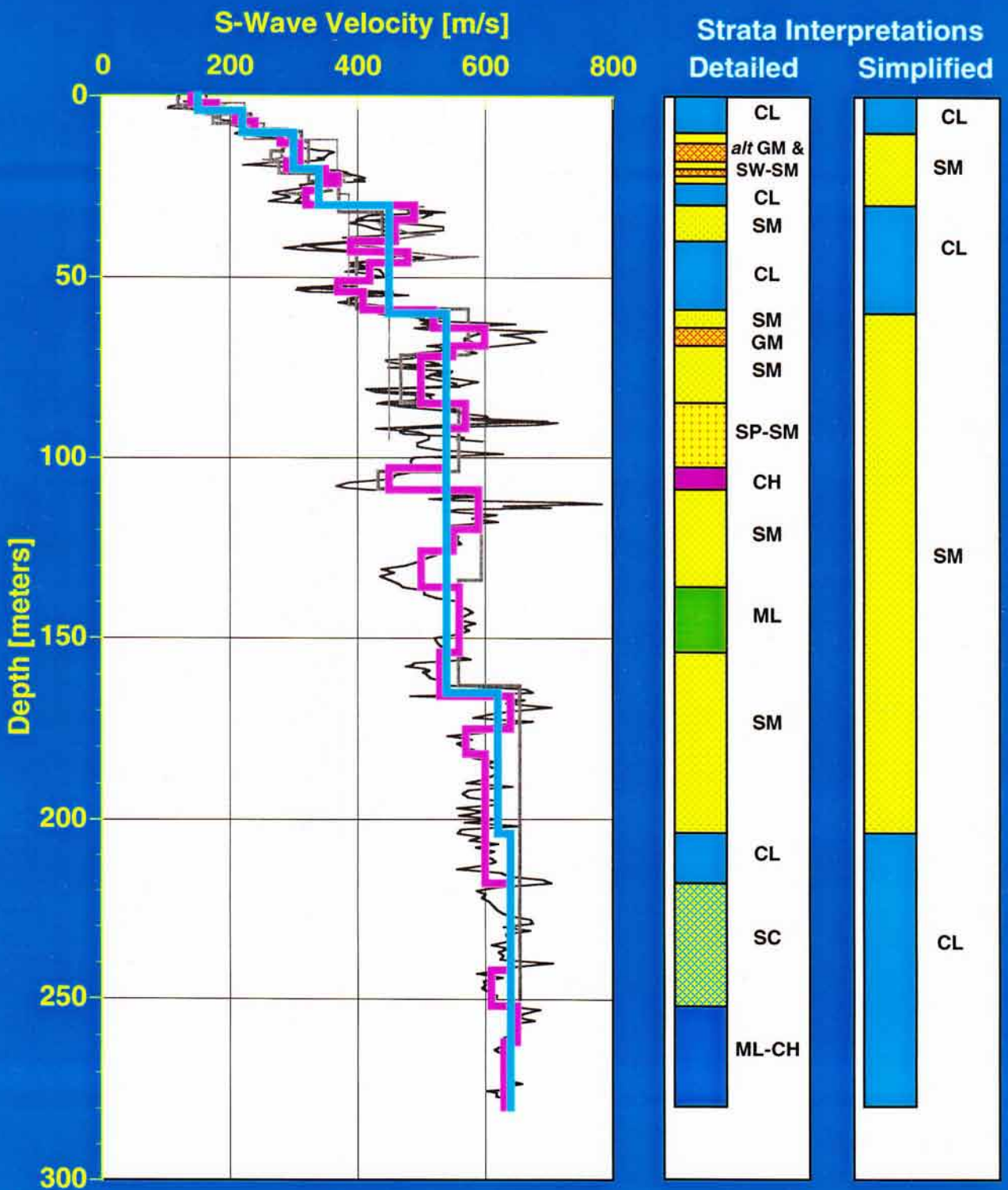

Caltrans

cjr 12/13/98

La Cienega: 100-m S-Wave Models vs. All Data

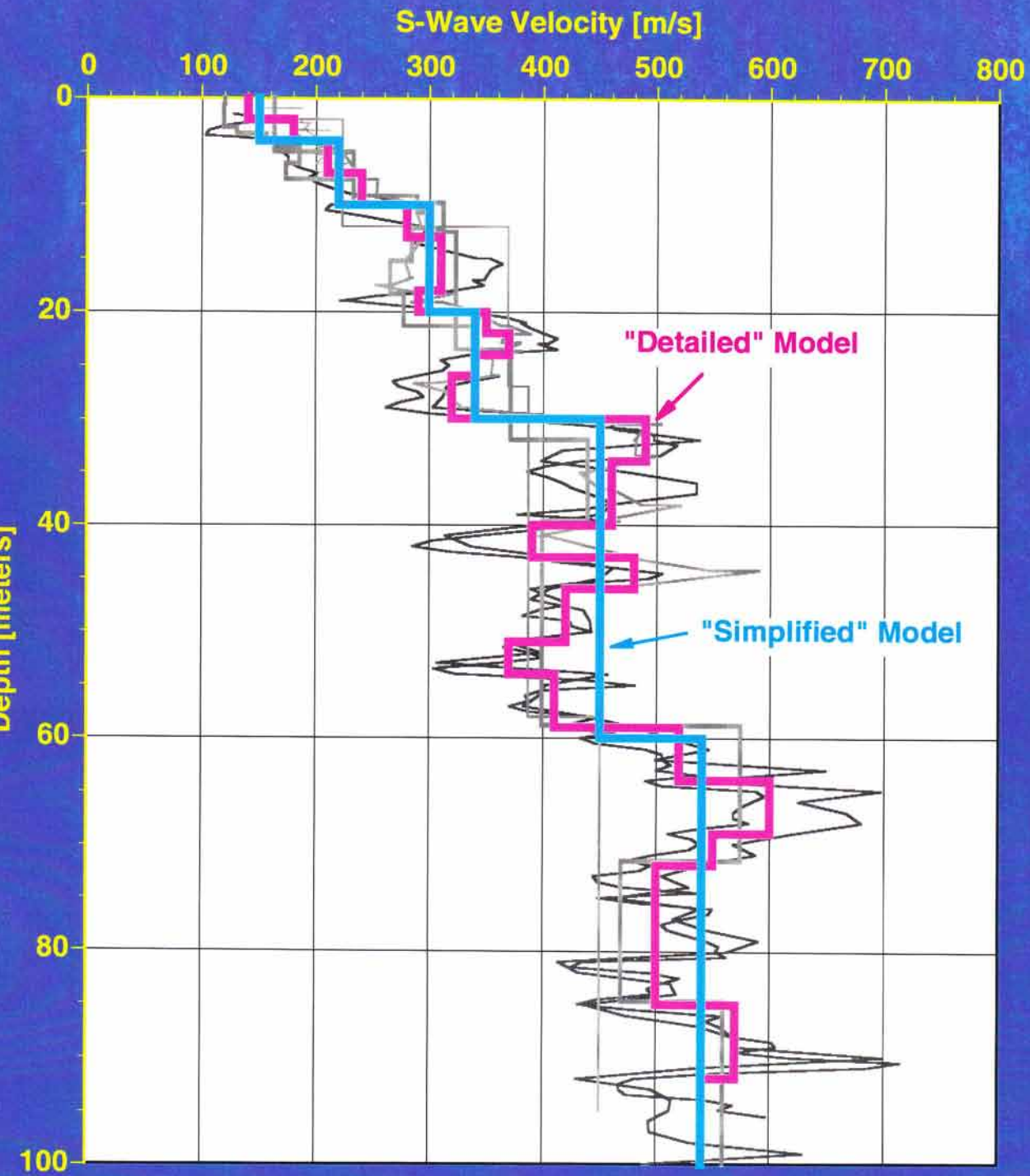

Caltrans

cjr 12/13/98

La Cienega: Geotechnical & Geophysical Data

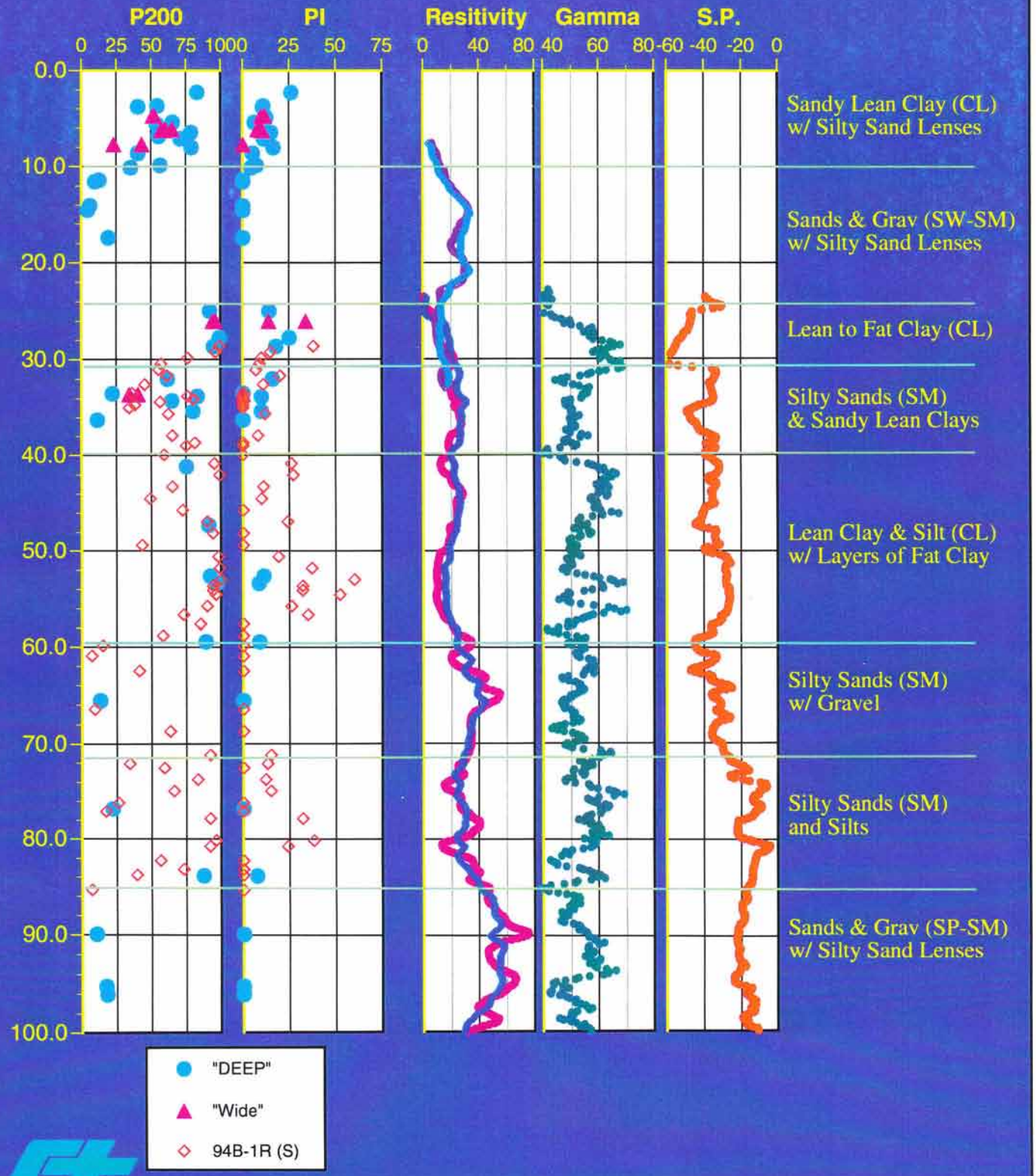

Caltrans

ejr 12/13/98

Typical Non-Linear Material Properties

Hyperbolic Model: Reference Strain = Shear Strength / Shear Modulus

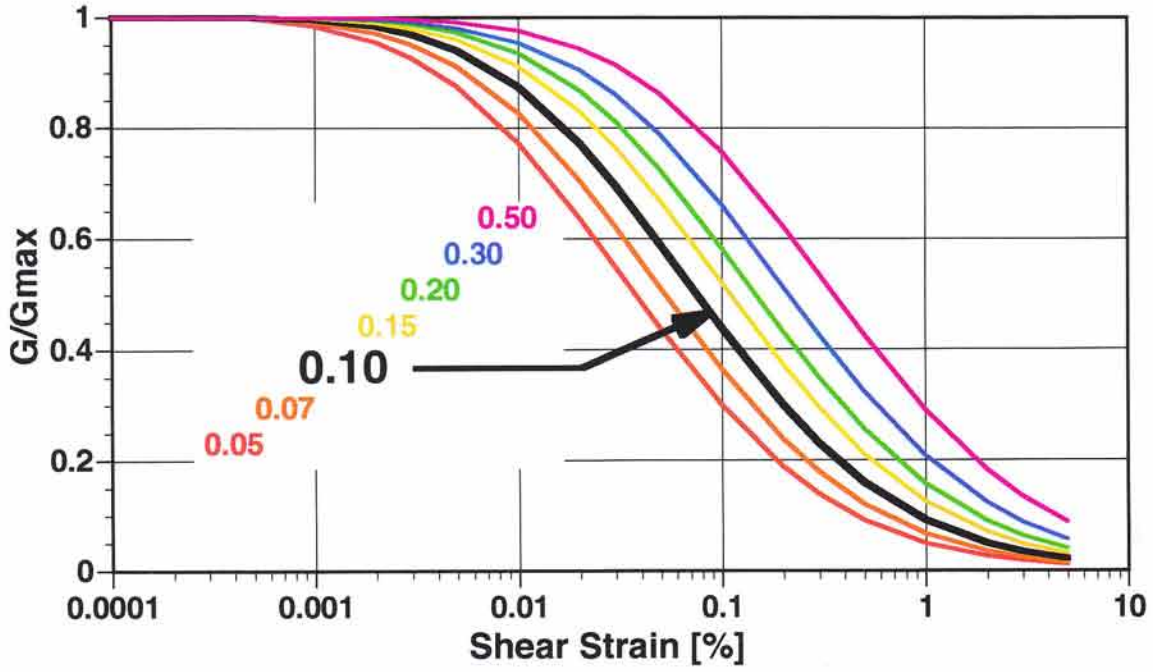

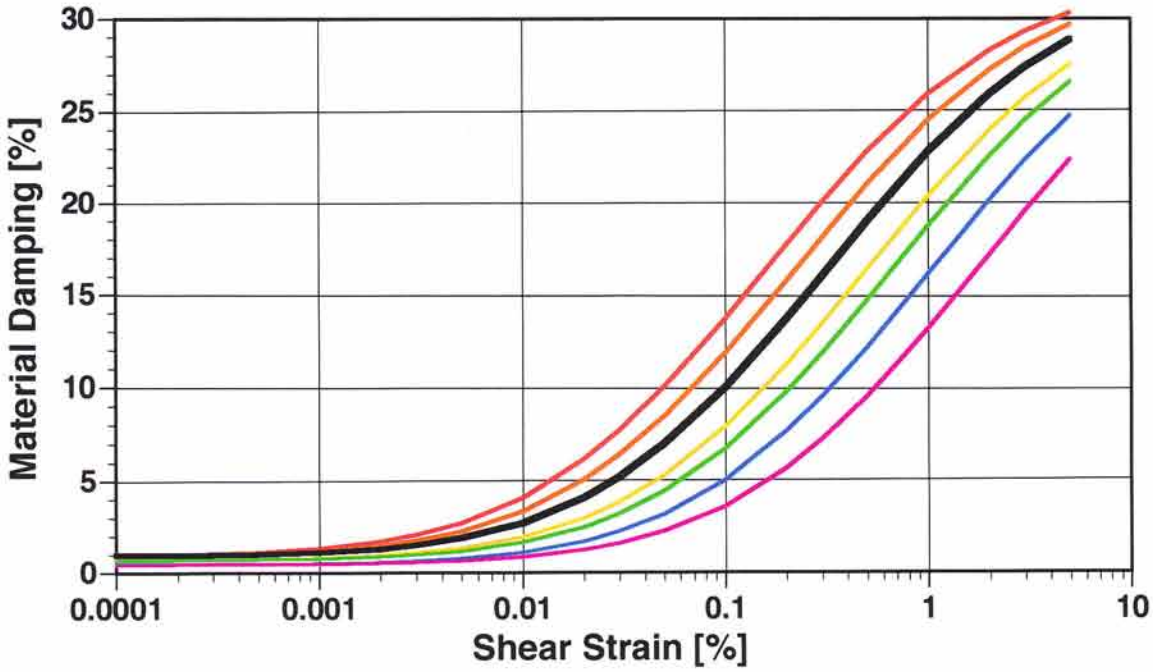

CL
PI = 18
P200 = 94

Example: Fitting Lab Data with Hyperbolic Curve

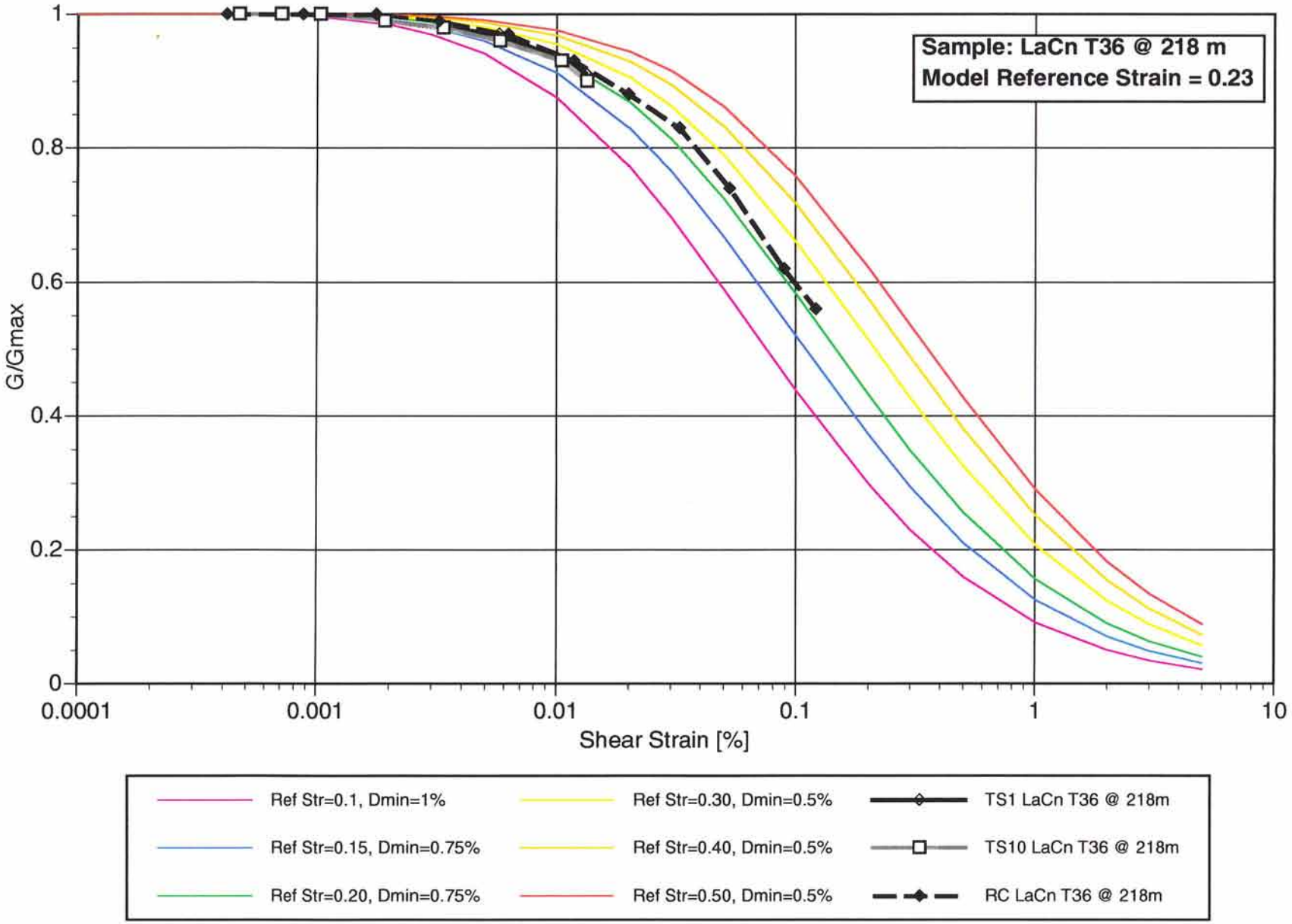

CH
PI = 36 %
P200 = 99%

Example: Poor Fit to Hyperbolic Model

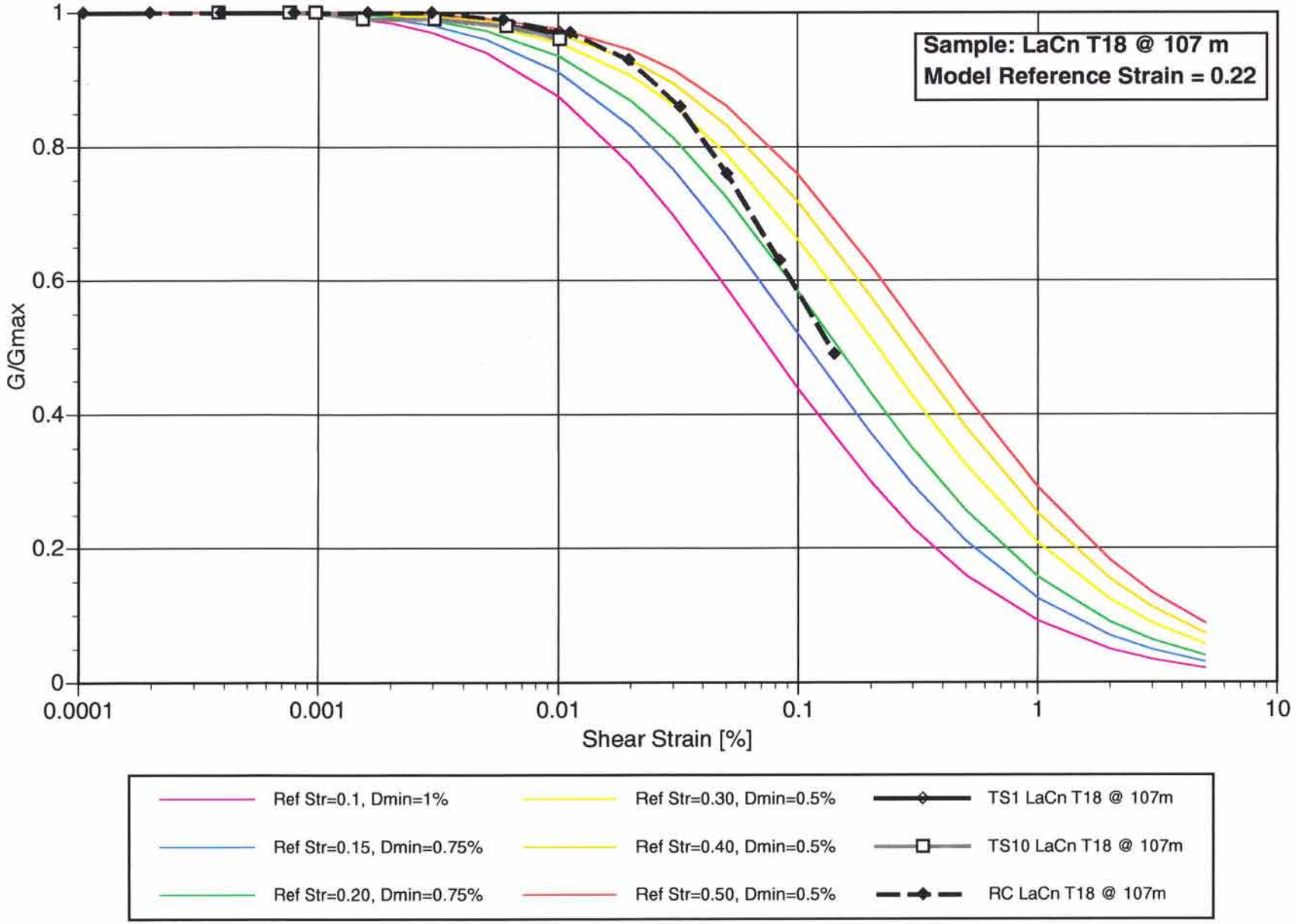

La Cienega: ROSRINE Non-Linear Models

UT Data Only

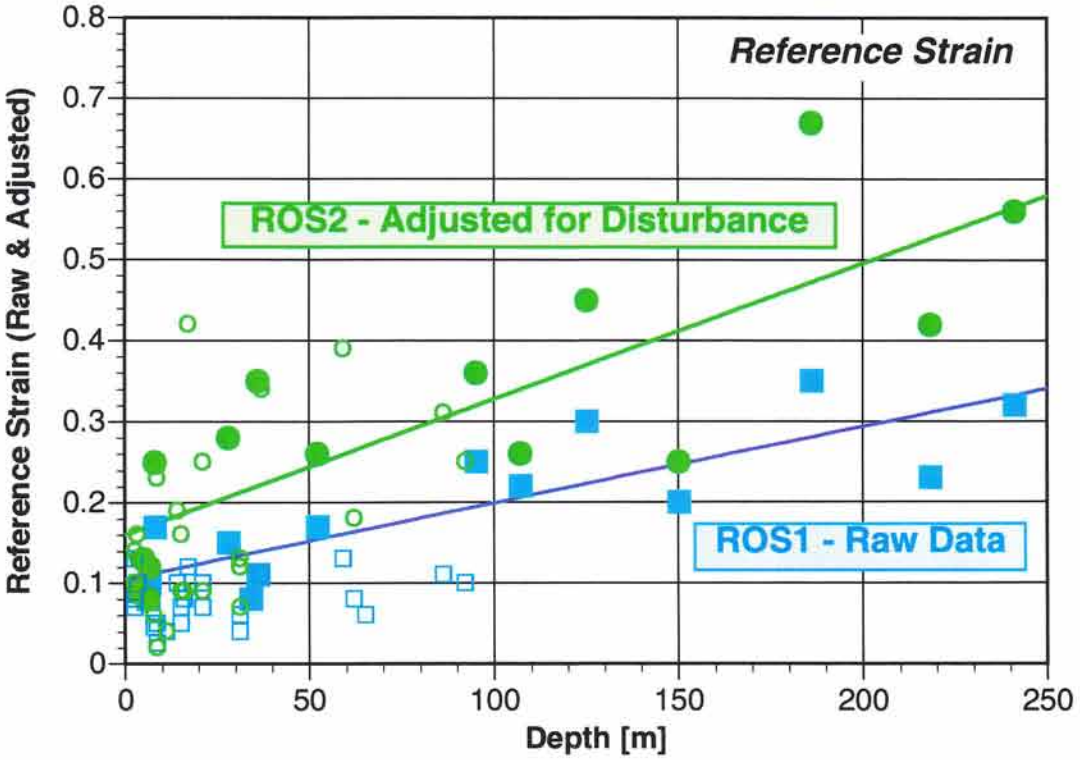

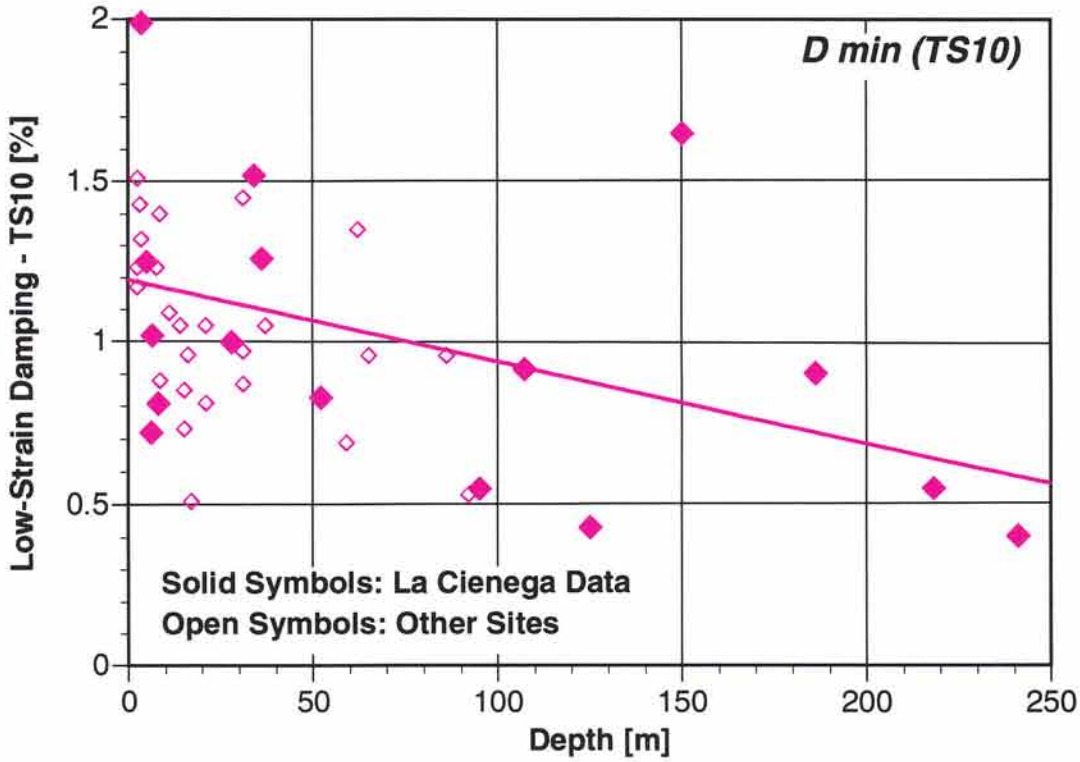

La Cienega Example: Analyses

Low-Strain Profile Interpretation

- **Level of Detail**
- Alt. Profiles from Alt. Geophysical

Alternative Non-Linear Soil Models

- **Common Design & More Recent Models**
- **Impact of Proposed Adjustment for Disturbance**
- **Impact on Motions of Alternative Models**
  - **Full 280-m Depth**
  - **Linear Below 100 m (Typical Design)**
- Uncertainty = f (Level of Motion)

La Cienega Example: Influence of Profile Detail
Fig. 1 Not Randomized

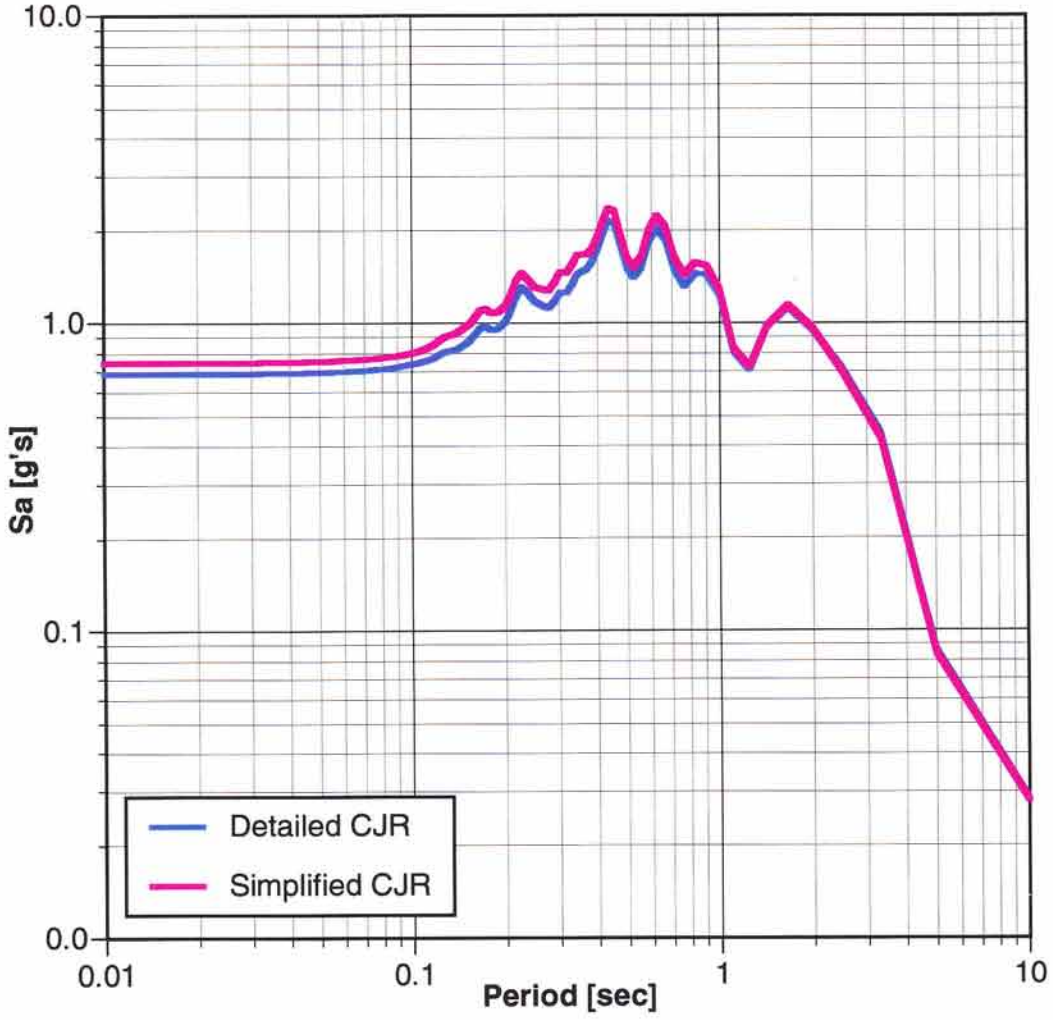

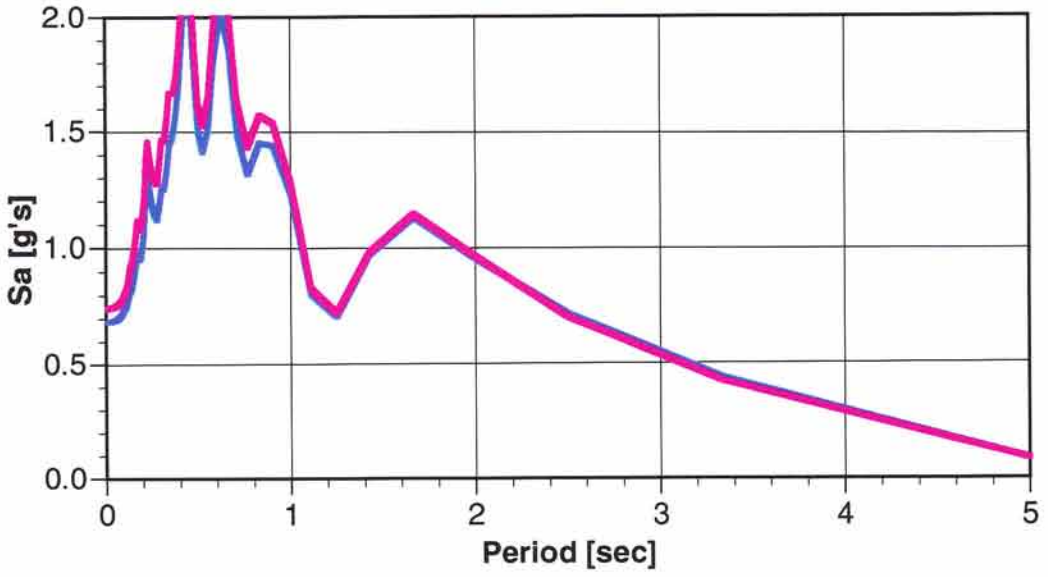

La Cienega Example: Influence of Vs Profile Detail
Fig. 2a Profiles Randomized, Lab Model

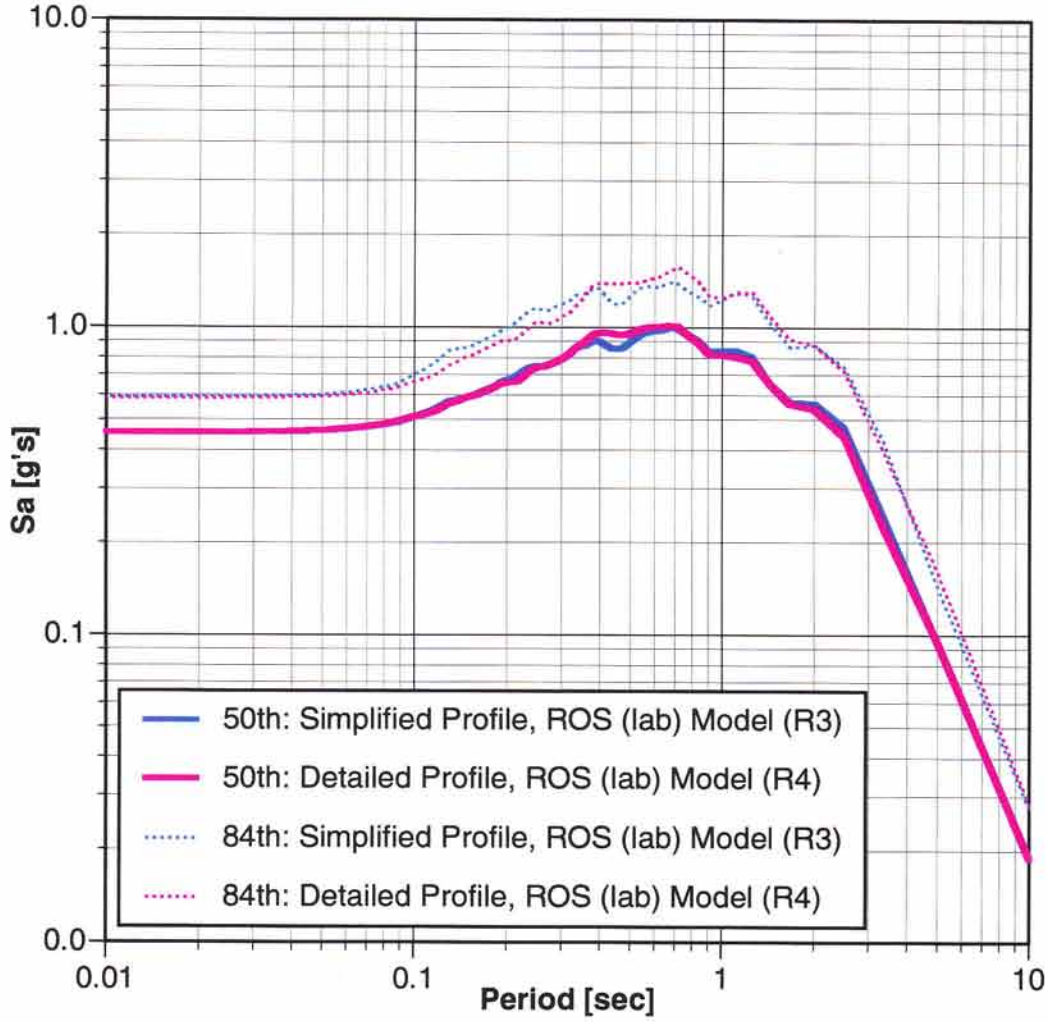

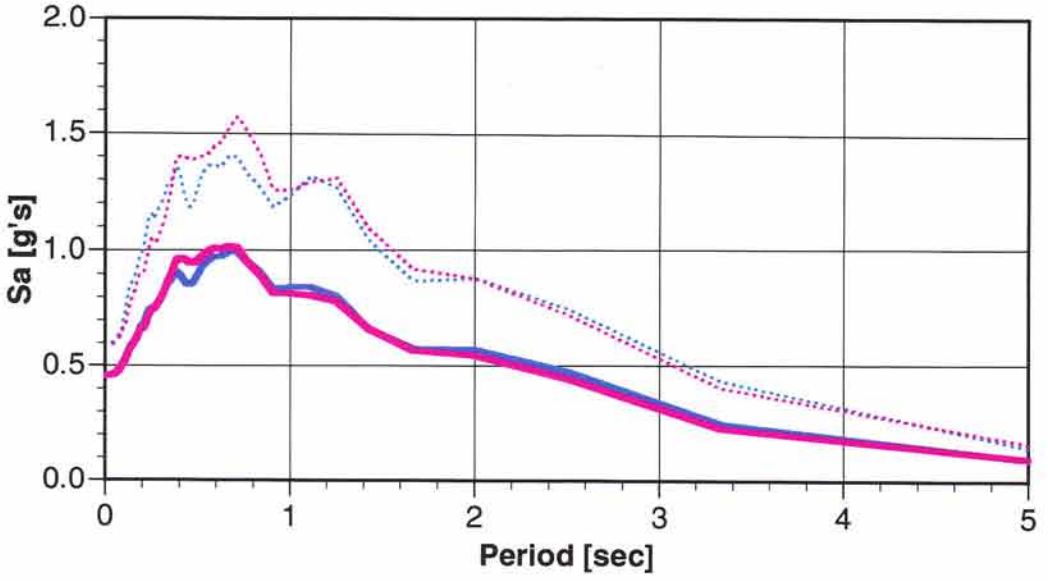

ROSRINE La Cienega Example: Alternative Non-Linear Models

La Cienega - Detailed CJR Profile Alternative Non-Linear Models					(1) ROSRINE SS INTERP RAW Lab Values		(2) ROSRINE SS INTERP ADJUSTED Lab Values		(3) '93 EPRI	(4) '96 BNL	(4) '91 V&D	(5) '91 SHAKE	(7) CT/UCB-88	(8) LINEAR
Layer Depth [m]		Velocity Profile [m/s]			Pyke Ref Strain Curves		Pyke Ref Strain Curves				PI-Based	Sand/Clay	Sands = f(conf.)	G/Gmax=1
From	To	Vs	Vp	Unit Wt.	Ref Strain	Dmin	Ref Strain	Dmin	Depth Range (ft)	Depth Range (ft)	Curves	Curves	Clays= '91 V&D	D=?
0	2	140	400	2.00	0.10	1.00	0.10	1.00	0-20' (E1)	0-50' (B1=E3)	15	Clay	V&D PI=15	
2	4	180	"	"	"	"	"	"	"	"	"	"	"	"
4	7	210	500	"	"	"	"	"	"	"	"	"	"	"
7	10	240	600	"	"	"	"	"	20-50' (E2)	"	"	"	"	"
10	13	280	1600	2.01	"	"	"	"	"	"	0	Sand	Sand S2	"
13	18	310	1900	"	"	"	"	"	"	"	"	"	"	"
18	20	290	1850	"	"	"	"	"	50-120' (E3)	50-500' (B2=E6)	"	"	"	"
20	22	350	"	2.02	"	"	0.15	"	"	"	"	"	"	"
22	24	370	"	"	"	"	"	"	"	"	"	"	"	"
24	26	340	1800	"	"	"	"	"	"	"	30	Clay	V&D PI=30	"
26	30	320	"	"	"	"	"	"	"	"	"	"	"	"
30	34	490	"	2.03	0.15	0.75	0.20	0.75	"	"	15	"	V&D, PI=15	"
34	40	460	"	"	"	"	"	"	120-250' (E4)	"	"	"	"	"
40	43	390	1700	"	"	"	"	"	"	"	"	"	"	"
43	46	480	"	"	"	"	"	"	"	"	"	"	"	"
46	51	420	"	"	"	"	"	"	"	"	"	"	"	"
51	54	370	"	"	"	"	"	"	"	"	"	"	"	"
54	59	410	"	"	"	"	"	"	"	"	"	"	"	"
59	64	520	1800	2.04	0.20	"	0.30	"	"	"	0	Sand	Sand S3	"
64	69	600	"	"	"	"	"	"	"	"	"	"	"	"
69	72	550	"	"	"	"	"	"	"	"	"	"	"	"
72	85	500	"	"	"	"	"	"	250-500' (E5)	"	"	"	"	"
85	92	570	"	"	"	"	"	"	"	"	"	"	"	"
92	103	540	"	"	"	"	"	"	"	"	"	"	"	"
103	109	450	1700	"	"	"	"	"	"	"	30	Clay	V&D PI=30	"
109	120	590	1900	"	"	"	0.40	"	"	"	0	Sand	Sand S3	"
120	126	550	1800	"	"	"	"	"	"	"	"	"	"	"
126	136	500	"	"	"	"	"	"	"	"	"	"	"	"
136	154	560	"	"	"	"	"	"	"	"	15	Clay	V&D, PI=15	"
154	166	530	1900	"	"	"	"	"	500-1000' (E6)	Linear, D=0.6%	0	Sand	Sand S3	"
166	175	640	"	2.05	0.30	0.50	0.50	0.50	"	"	"	"	"	"
175	182	570	"	"	"	"	"	"	"	"	"	"	"	"
182	204	600	"	"	"	"	"	"	"	"	"	"	"	"
204	218	600	"	"	"	"	"	"	"	"	15	Clay	V&D, PI=15	"
218	242	640	1950	"	"	"	"	"	"	"	"	"	"	"
242	252	610	"	"	"	"	"	"	"	"	"	"	"	"
252	262	650	"	"	"	"	"	"	"	"	30	"	V&D PI=30	"
262	280	630	"	"	"	"	"	"	"	"	"	"	"	"

La Cienega Example: Alternate Non-Linear Models
Fig. 3a 280-m Profile; Median

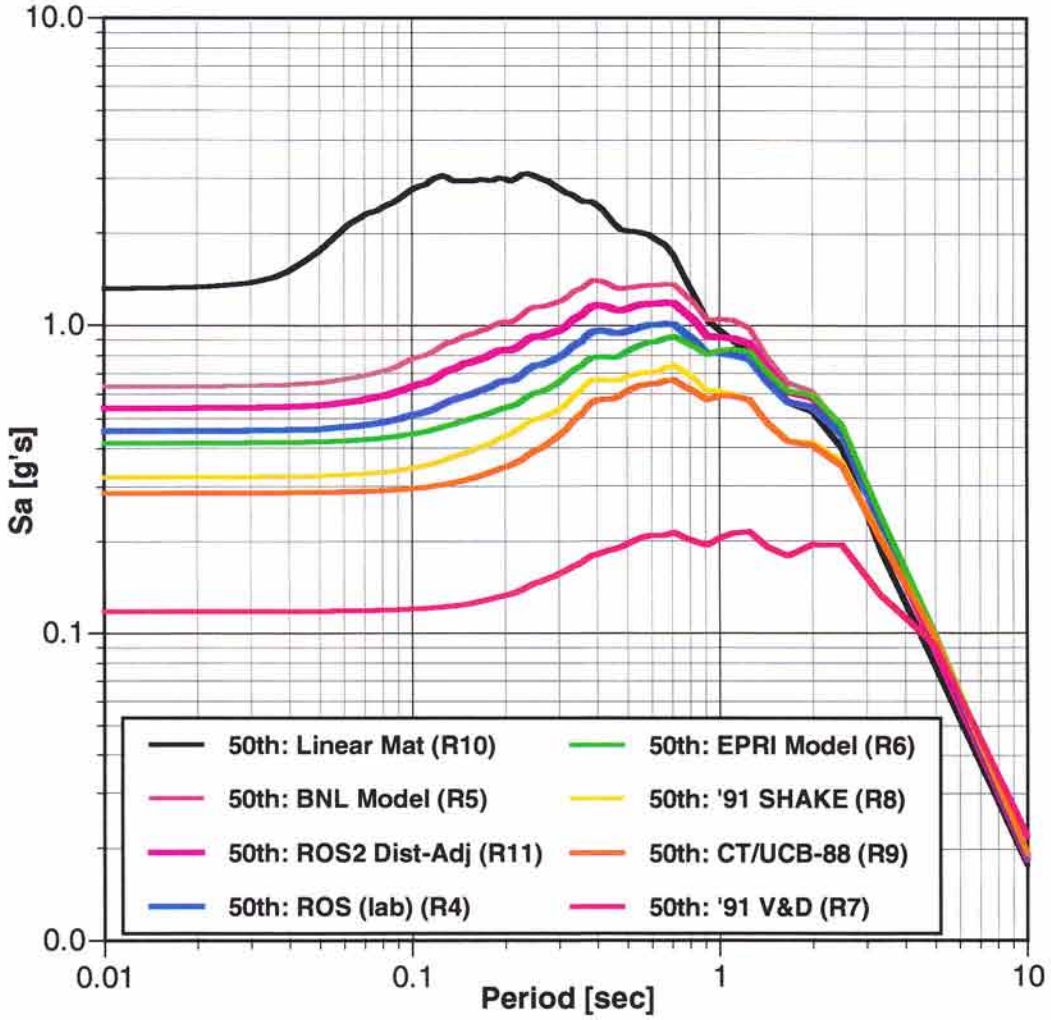

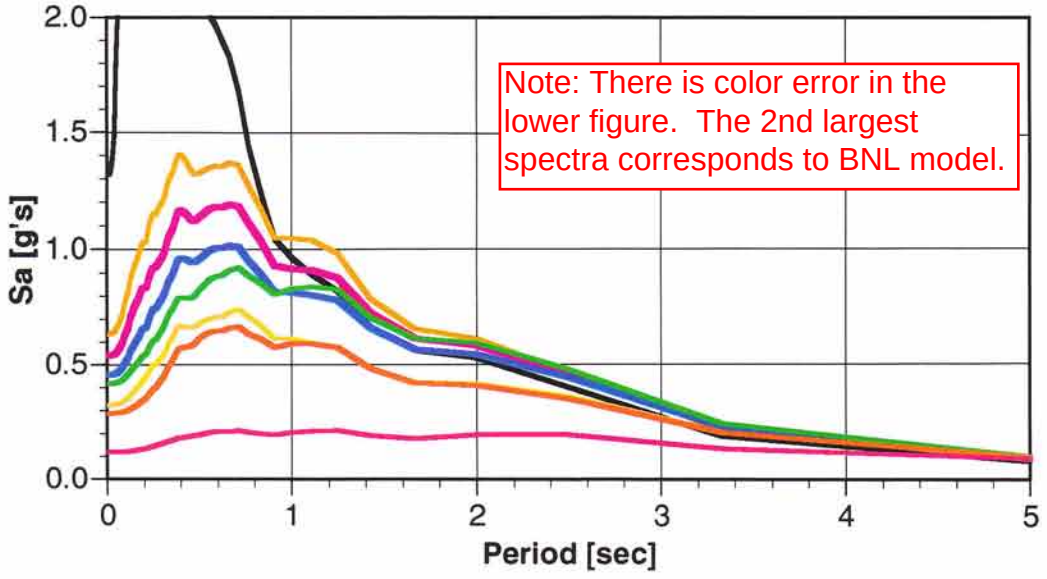

Note: There is color error in the lower figure. The 2nd largest spectra corresponds to BNL model.

La Cienega Example: Alternate Non-Linear Models
Fig. 4a

280-m Profile; Median

100* = Linear Below 100 m

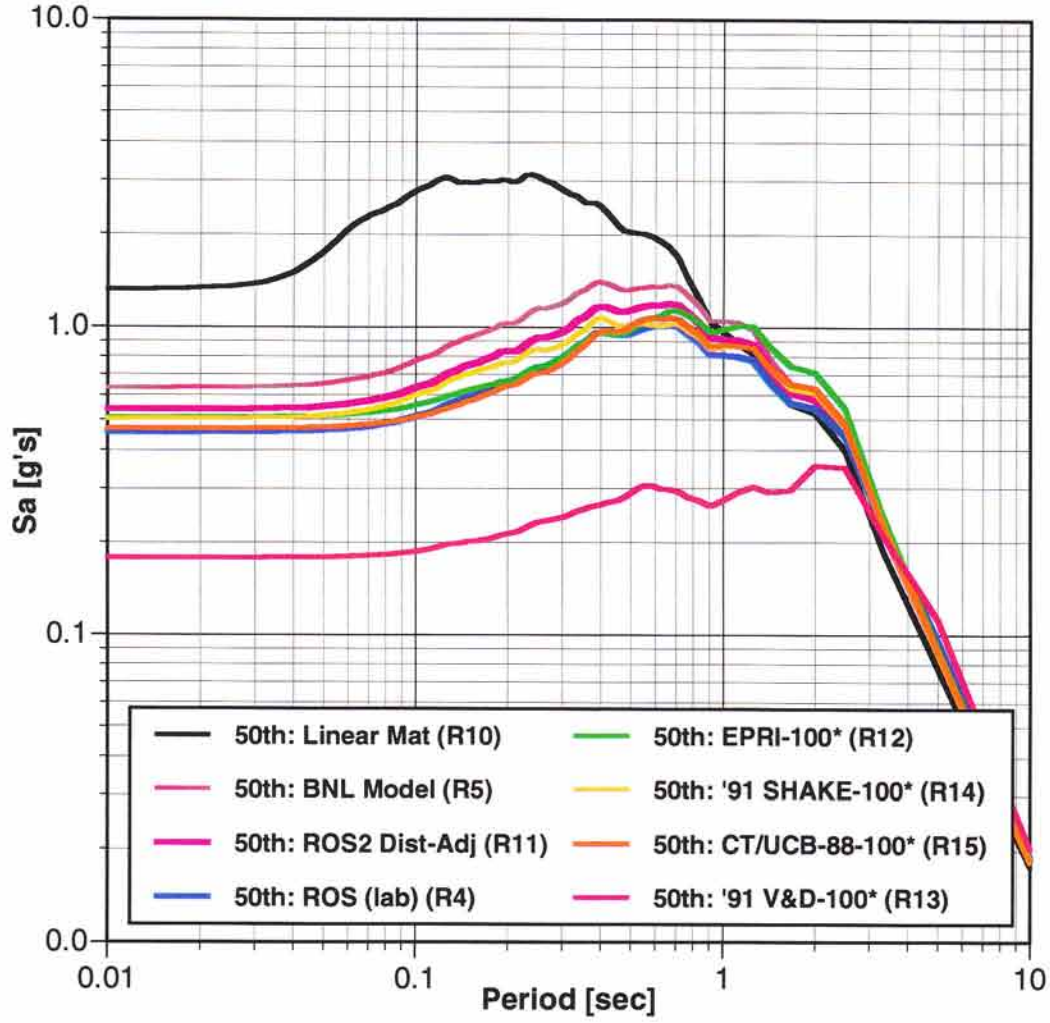

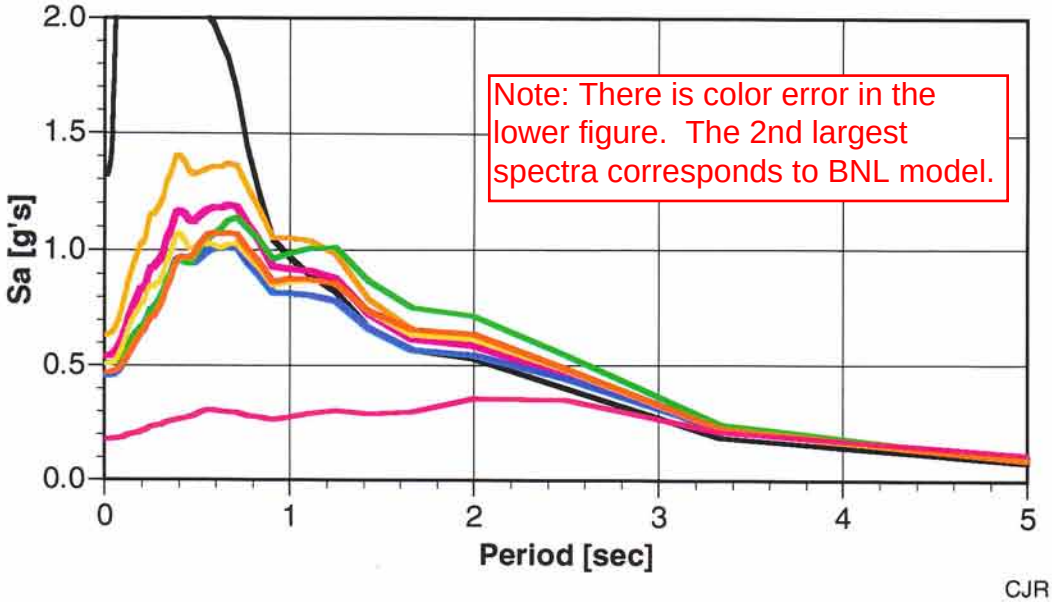

Note: There is color error in the lower figure. The 2nd largest spectra corresponds to BNL model.

CJR 12/12/98

La Cienega Example: Influence of Disturb-Adjust Factor
Fig. 7a Detailed Profile, Randomized